

ADVERTIMENT. La consulta d'aquesta tesi queda condicionada a l'acceptació de les següents condicions d'ús: La difusió d'aquesta tesi per mitjà del servei TDX (www.tesisenxarxa.net) ha estat autoritzada pels titulars dels drets de propietat intel·lectual únicament per a usos privats emmarcats en activitats d'investigació i docència. No s'autoritza la seva reproducció amb finalitats de lucre ni la seva difusió i posada a disposició des d'un lloc aliè al servei TDX. No s'autoritza la presentació del seu contingut en una finestra o marc aliè a TDX (framing). Aquesta reserva de drets afecta tant al resum de presentació de la tesi com als seus continguts. En la utilització o cita de parts de la tesi és obligat indicar el nom de la persona autora.

ADVERTENCIA. La consulta de esta tesis queda condicionada a la aceptación de las siguientes condiciones de uso: La difusión de esta tesis por medio del servicio TDR (www.tesisenred.net) ha sido autorizada por los titulares de los derechos de propiedad intelectual únicamente para usos privados enmarcados en actividades de investigación y docencia. No se autoriza su reproducción con finalidades de lucro ni su difusión y puesta a disposición desde un sitio ajeno al servicio TDR. No se autoriza la presentación de su contenido en una ventana o marco ajeno a TDR (framing). Esta reserva de derechos afecta tanto al resumen de presentación de la tesis como a sus contenidos. En la utilización o cita de partes de la tesis es obligado indicar el nombre de la persona autora.

WARNING. On having consulted this thesis you're accepting the following use conditions: Spreading this thesis by the TDX (www.tesisenxarxa.net) service has been authorized by the titular of the intellectual property rights only for private uses placed in investigation and teaching activities. Reproduction with lucrative aims is not authorized neither its spreading and availability from a site foreign to the TDX service. Introducing its content in a window or frame foreign to the TDX service is not authorized (framing). This rights affect to the presentation summary of the thesis as well as to its contents. In the using or citation of parts of the thesis it's obliged to indicate the name of the author



UNIVERSITAT POLITÈCNICA
DE CATALUNYA
BARCELONATECH

PhD Dissertation

Geosynchronous Synthetic Aperture Radar for Earth Continuous Observation Missions

Author

Josep Ruiz Rodon

Thesis Advisor:

Prof. Antoni Broquetas Ibars

**Department of Signal
Theory and Communications**



PhD. Program on Signal Theory and Communications Remote sensing
Lab. Group. Barcelona, July 2014

Abstract

This thesis belongs to remote sensing field, particularly Synthetic Aperture Radar (SAR) systems from the space. These systems acquire the signals along the orbital track of one or more satellites where the transmitter and receiver are mounted, and coherently process the echoes in order to form the synthetic aperture.

The study presented in this thesis is centred in a novel concept in SAR, which is known as Geosynchronous SAR or GEOSAR, where the transmitter and/or receiver are placed in a platform in a geostationary orbit. In this case, the small relative motions between the satellite and the Earth surface are taken to get the necessary motion to form the synthetic aperture and focus the image. The main advantage of these systems with respect to the current technology (where LEO satellites with lower height are considered) is the possibility of permanently acquire images from the same region thanks to the small motion of the platform.

The different possibilities in the orbital design that offer this novel technology as well as the geometric resolutions obtained in the final image have been studied. The system presented in this thesis is based on large integration time (from minutes to hours) to reach the desired resolutions and Signal to Noise Ratios.

On the other hand, the use of long integration time presents some drawbacks such as the scene targets decorrelation, atmospheric artefacts due to the refraction index variations in the tropospheric layer, transmitter and receiver clock jitter, clutter decorrelation or orbital positioning errors; which will affect the correct focusing of the image. For this reason, a detailed theoretical radiometric study is presented in the thesis in order to characterize and model these artefacts.

Finally, a ground receiver to reuse signals of opportunity from a broadcasting satellite have been designed and manufactured. This hardware is expected to be an important tool for experimental testing in future GEOSAR analysis.

Acknowledgements

First and foremost, I would like to specially thank my thesis advisor, Prof. Antoni Broquetas, for his advice, guidance and dedication in the difficult problems during the last five years.

I want to express my sincere gratitude to the other people that I work with in the challenging concept of GEOSAR, concretely Prof. Andrea Monti Guarnieri and Prof. Fabio Rocca from Politecnico di Milano; Farid Djelaili, Vu Khang, Delft Schulz and Ray Sperber from SES ASTRA; Davide Guidici, Andrea Recchia and other colleagues from European Space Agency, Reading University, Cranfield University and Tales Alenia Space.

I would also like to acknowledge the support of other colleagues from the department, specially to Eduardo Makhoul for his generous help and discussions on SAR topics.

Last but not least, I give thanks to my family and friends for their unconditional emotional support. Special thanks to Laura for giving me the support crucial for the consecution of this thesis.

Finally, this work has been supported in part by the Spanish Ministry of Science and Innovation (MICINN) under projects TEC2011-28201-C02-01 and CONSOLIDER CSD2008-00068, by the ESA Contract No. 4000108594/13/NL/CT “*Study of future Telecom Satellites for Earth Observation (GeoSTARe)*”, and by FI-AGAUR Research Fellowship Program, Generalitat de Catalunya, contracts 2011FI_B 00179, 2012FI00087.

Contents

List of Figures	v
List of Tables.....	xv
Abbreviations	xvii
Symbols	xxi
Chapter 1 Introduction.....	1
1.1 Synthetic Aperture Radar basic concepts	1
1.1.1 History and context of SAR remote sensing imaging	1
1.1.2 Real Aperture Radar vs. Synthetic Aperture Radar	2
1.1.3 SAR basic performance and parameters.....	5
1.2 GEOSynchronous Synthetic Aperture Radar	9
1.3 State of the art of GEOSAR.....	11
1.4 GEOSAR opportunities and limitations.....	14
1.5 Potential applications of GEOSAR.....	15
1.6 Thesis motivation and objectives	17
1.7 Thesis organization	20
Chapter 2 Geosynchronous SAR geometry.....	21
2.1 Geosynchronous orbits analysis.....	21
2.1.1 Orbital ephemerides and parameters.....	21
2.1.2 Geosynchronous orbital parameters definition for a nearly-zero inclination quasi-circular orbit.....	24
2.2 Geosynchronous SAR acquisition parameters	26
2.2.1 Review of basics on the geometry of the sphere	26

2.2.2	Geosynchronous satellite track.....	29
2.2.3	Satellite-targets slant range.....	34
2.2.4	Satellite location: elevation and azimuth angles.....	38
2.2.5	Target location: look and incidence angles.....	42
2.3	Geosynchronous SAR coverage.....	44
2.4	Orbital design impact on the resolution.....	48
2.4.1	Orbital ephemerides impact on GEOSAR synthetic aperture.....	48
2.4.2	GEOSAR achievable resolution: integration time requirements.....	62
2.4.3	Non-linear orbital track: daily variations of the achievable resolution.....	71
2.5	Analysis of current broadcasting telecommunications satellites orbits for GEOSAR purposes.....	75
Chapter 3	Geosynchronous SAR radiometric analysis.....	79
3.1	Antenna design: gain, coverage and dimensions.....	79
3.2	Doppler analysis of received data: Doppler centroid compensation.....	83
3.2.1	Doppler shift in SAR acquisition.....	83
3.2.2	Doppler history in GEOSAR.....	84
3.2.3	Doppler centroid estimation and compensation.....	87
3.3	Timing and PRF selection: diamond and dartboard diagrams.....	91
3.4	Ambiguity analysis for GEOSAR acquisition.....	100
3.4.1	Range Ambiguity to Signal Ratio (RASR).....	102
3.4.2	Azimuth Ambiguities to Signal Ratio (AASR).....	107
3.5	Power link budget.....	111
3.5.1	Power link budget of a dedicated GEOSAR mission.....	113
3.5.2	Radiometric feasibility of current broadcasting satellites as illuminators of opportunity.....	115
3.5.3	Clutter decorrelation impact on the power link budget.....	124
3.5.4	Stable target analysis: minimum RCS.....	130
3.5.5	Parabolic antennas as reflectors of opportunity.....	131
3.6	Image reconstruction via Time-Domain Back-Projection.....	135
3.6.1	GEOSAR system model.....	135
3.6.2	Digital reconstruction via Time Domain Back-Projection.....	138
3.6.3	GEOSAR simulator.....	140

3.6.4	Monostatic GEOSAR focusing	142
Chapter 4	Geosynchronous SAR applications and limitations	151
4.1	Sub-daily surface imaging	151
4.1.1	Full-resolution acquisition	152
4.1.2	Half-resolution acquisition	153
4.1.3	Dual-resolution acquisitions	153
4.1.4	Constant resolution acquisitions.....	155
4.1.5	Continuous acquisitions with varying resolution	156
4.2	Daily interferometric acquisitions.....	157
4.2.1	Geosynchronous orbit perturbations	158
4.2.2	Satellite longitudinal orbital drift and repositioning.....	160
4.2.3	GEOSAR repeat pass interferometry	164
4.3	Atmospheric Phase Screen (APS) retrieval.....	172
4.3.1	APS behaviour and effects to SAR acquisition	172
4.3.2	APS retrieval algorithm for point-like targets: auto-focusing technique.....	180
4.3.3	Interferometric APS retrieval.....	192
4.4	Fine orbit and clock drift determination for GEOSAR processing.....	194
Chapter 5	Dual-beam Dual-frequency GEOSAR for Terrain and Atmosphere with short Revisit. Bistatic baseline design	197
5.1	Mission overview	197
5.1.1	Motivation of bistatic GEOSAR	197
5.1.2	Mission definition and requirements: dual beam concept	199
5.1.3	Bistatic Synthetic Aperture Radar parameters definition	200
5.2	Bistatic observation geometry and possible flying formations.....	201
5.2.1	Satellites location impact on the mission coverage.....	202
5.2.2	Bistatic orbital design impact on the resolution.....	206
5.3	GEOSAR radiometric analysis for bistatic acquisition.....	214
5.3.1	Antenna design: coverage and pointing requirements.....	215
5.3.2	Backscattering profiles for bistatic acquisition	219
5.3.3	Timing and PRF selection for bistatic acquisition	222
5.3.4	Power requirements.....	227
5.4	Bistatic GEOSAR synchronisation.....	230

5.4.1	Oscillators analysis for bistatic GEOSAR	230
5.4.2	Bistatic synchronisation strategies	234
5.4.3	On-ground synchronisation errors	237
5.5	Bistatic GEOSAR baseline design.....	248
Chapter 6 Experimental bistatic system with passive on ground receiver and illuminator of opportunity		251
6.1	System description	252
6.1.1	Geometrical analysis.....	252
6.1.2	Achievable resolution	254
6.1.3	Bistatic GEOSAR with on-ground receiver focusing.....	255
6.1.4	Power link budget	257
6.2	Hardware design	260
6.2.1	DVB-S2 receiver: 2-channel simultaneous acquisition	260
6.2.2	LNB study: external oscillator	274
6.2.3	Acquisition with on-ground receiver scheme	282
Conclusions and future work.....		285
List of Publications.....		289
References.....		293

List of Figures

Figure 1.1. Basic geometry and parameter for RAR and SAR.....	4
Figure 1.2. SAR image coordinate system for side-looking radar	6
Figure 1.3. Elevation plane geometry for SAR systems	8
Figure 1.4. Azimuth plane geometry for SAR systems.....	8
Figure 1.6. Ground track of a geosynchronous satellite with 50° inclination [35].....	11
Figure 1.7. Concept of the 30 m L-Band antenna with hexagonal elements proposed by Madsen [37].....	12
Figure 1.8. Focused image using the backscattered TV signal.	13
Figure 1.10. GEOSAR revisit time/coverage vs. current configurations.....	18
Figure 2.1. Satellite orbital ephemerides definition [64]	22
Figure 2.2. Orbital shape and satellite location parameters	23
Figure 2.3. Quasi-circular geosynchronous orbit example with eccentricity of 10^{-4}	24
Figure 2.4. Geosynchronous satellite instantaneous velocity history considering an orbital eccentricity of 10^{-4}	25
Figure 2.5. Geometry of the sphere: great circle definition.	27
Figure 2.6. Spherical triangles over the sphere surface.....	28
Figure 2.7. Spherical trigonometry over spherical triangles.	28
Figure 2.8. Vertex angle defined at point B between the tangents of the intersecting great circles at that point.....	29
Figure 2.9. Satellite track fixed Earth reference system.	30
Figure 2.10. Satellite track in a rotating Earth reference system	32
Figure 2.11. Satellite relative longitude evolution approximation. a) Considering an orbit eccentricity of 0.0001 and b) 0.1	33
Figure 2.12. Earth-satellite geometry	35
Figure 2.13. Na-A-B triangle used in slant-range computation	36

Figure 2.14. Slant range variations due to orbit perturbations. a) Absolute satellite-target range. b) Hodograph relative to the minimum slant range	37
Figure 2.15. Satellite location in the sky. Elevation angle computation.....	38
Figure 2.16. Determination of the azimuth angle.....	41
Figure 2.17. Elevation and azimuth angles evolution. a) Changes seen from a target-centred reference system. b) Satellite (0°N , 30°W) and target (41.23°N , 2.11°E) example.....	42
Figure 2.18 Maximum look angle. In the geosynchronous case, only a small range of look angles are allowed.	43
Figure 2.19 Geosynchronous satellite field of view.....	45
Figure 2.20 Ground coverage of the satellite.....	46
Figure 2.21 Flat surface approximation in swath ground coverage computation.	47
Figure 2.22 Along-track (azimuth) direction in Geosynchronous vs. LEO satellites.	49
Figure 2.23 Geosynchronous satellite track considering small eccentricity in the orbit and zero-inclination.....	50
Figure 2.24 3D satellite orbit representation considering a non-inclined orbit with eccentricity of 0.0004 and nominal longitude of 0 degrees with respect to an Earth centred rotating coordinate system.....	51
Figure 2.25 a) 3D orbital representation. b) Top view representation (reference meridian- 90° West cut). c) Satellite nadir plane (North- 90° West cut). d) Side view (North-Reference meridian cut).	51
Figure 2.26 Geosynchronous satellite track considering zero eccentricity in the orbit and small inclination.....	52
Figure 2.27 3D satellite orbit representation considering a 0.046 degrees inclined orbit with zero eccentricity and nominal longitude of -30 degrees with respect to an Earth centred rotating coordinate system.....	53
Figure 2.28 a) 3D orbital representation. b) Top view representation (reference meridian- 90° West cut). c) Satellite nadir plane. d) Side view (North-Reference meridian cut).....	54
Figure 2.29 Elliptical satellite track inscribed in a rectangle of side $4e$ by $2i$ given by the satellite motion.	55
Figure 2.30 Satellite track simulation considering an orbit eccentricity of 0.0004 and inclination of 0.046 degrees.	58

Figure 2.31 Satellite angle from nominal satellite position simulation considering an orbit eccentricity of 0.0004 and inclination of 0.046 degrees.....	58
Figure 2.32 3D satellite orbit representation considering a 0.046 degrees inclined orbit with 0.0004 eccentricity and nominal longitude of -30 degrees with respect to an Earth's centred rotating coordinate system.....	59
Figure 2.33 a) 3D orbital representation. b) Top view representation (reference meridian-90° West cut). c) Satellite nadir plane. d) Side view (North-Reference meridian cut).....	59
Figure 2.34 The Earth zones (yellow slashed lines) in a perpendicular direction to the along-track satellite motion for different orbital configurations will present the maximum along-track resolution.....	60
Figure 2.35 Target angle from the Equator at the satellite nadir point.....	61
Figure 2.36 Maximum synthetic aperture length vs. actual aperture length for a randomly positioned target.	62
Figure 2.37 On-ground cross-track resolution variation with incidence angle.	64
Figure 2.38 Incidence angle over the Earth map considering a geosynchronous satellite at 30° East nominal longitude.....	64
Figure 2.40 Satellite longitude variation considering an orbital eccentricity of 0.0004. Red zone presents higher variation than green ones in the same integration time.	68
Figure 2.42 Achievable resolution with 30 min of integration for different orbital eccentricities working at L-band (1.625 GHz) for slant range of 36950 Km.....	70
FIGURE 2.44 Along-track cut of a GEOSAR focused image. As seen along-track resolution is degraded as the acquisition goes away from the perigee. Along-track resolutions of 17 m, 25 m and 65 m are obtained considering 2 hours of acquisition centred at tp, tp+3h and tp+5h, respectively; while the Peak-to-Side-Lobes Ratio (PSLR) is reduced.....	73
FIGURE 2.45 Along-track cut of a GEOSAR focused image considering along-track weighting of the zones with slower velocities.	74
FIGURE 2.46 GEOSAR focused images of a 1 by 1 Km scene over Barcelona. 10 point targets have been randomly placed. The raw data from 2 hours of integration have been simulated considering acquisitions centred, from left to right, at tp, tp+3h and tp+5h.....	74
Figure 3.1 Antenna beamwidth requirements to fulfil the desired coverage.....	81
Figure 3.3 Antenna gain requirements vs. desired ground coverage.....	82

Figure 3.4 Antenna beamwidth requirements vs. desired ground coverage at different frequency bands.	83
Figure 3.5 Doppler history of targets from a scene of 100 by 100 Km.	85
Figure 3.6 Synthetic aperture for a slightly eccentric orbit.	86
Figure 3.7 Doppler bandwidth considering 4 hours of integration time.	86
Figure 3.8 Covered scene for the L-Band wide beam (~3000 Km) and satellites orbit configuration (0.0004 eccentricity and zero inclination) for the Doppler bandwidth analysis.	88
Figure 3.9 Doppler history of a bistatic GEOSAR acquisition at L-Band over a region covering the South-Eastern Europe with a pair of satellites with an orbital eccentricity of 0.0004.	88
Figure 3.10 Doppler history of a bistatic GEOSAR acquisition at L-band after Doppler centroid compensation.	90
Figure 3.11 Covered scene for the Ku-Band spot beam (~650 Km) and satellites orbit configuration (0.0004 eccentricity and zero inclination) for the Doppler bandwidth analysis.	91
Figure 3.12 Doppler history of a bistatic GEOSAR acquisition at Ku-Band over a region covering the South-Eastern Europe with a pair of satellites with an orbital eccentricity of 0.0004.	92
Figure 3.13 Doppler history of a bistatic GEOSAR acquisition at Ku-band after Doppler centroid compensation.	92
Figure 3.14 Timing diagram for PRF constraints: a) transmit interference and b) nadir interference.	93
Figure 3.16 Diamond diagram for GEOSAR working with a duty cycle of 40%.	96
Figure 3.17 Diamond diagram for GEOSAR working with a duty cycle of 20%.	97
Figure 3.18 Dartboard diagram for GEOSAR with PRF of 5.7 Hz.	99
Figure 3.19 Dartboard diagram for GEOSAR with PRF of 9.6 Hz.	99
Figure 3.20 Diamond diagram for GEOSAR at 9.5 Hz considering a duty cycle of 20% (left) and 40% (right).	100
Figure 3.21 PRF tolerance in function of duty cycle to avoid transmission interferences.	100
Figure 3.22 Origin of range ambiguities in SAR systems.	103

Figure 3.23 Range ambiguous zones for GEOSAR at very-low PRF of 7Hz.....	105
Figure 3.24 RASR for GEOSAR at 7Hz for incidence angles between 49 and 54 degrees..	105
Figure 3.25 Range ambiguous zones for GEOSAR at high PRF of 100Hz.....	106
Figure 3.26 RASR for GEOSAR at 100Hz for incidence angles between 49 and 54 degrees.	106
Figure 3.27 Azimuth aliasing due to finite sampling at PRF.....	108
Figure 3.29 AASR for a GEOSAR acquisition at PRF=5 Hz. Levels under -50dB are obtained in this particular configuration.....	110
Figure 3.30 QPSK digital modulation example dBW.	117
Figure 3.31 22 Mbps QPSK signal autocorrelation.	118
Figure 3.33 KA-SAT spot-beams over Europe.....	122
FIGURE 3.34 KA-SAT spot-beam 10 illuminates Barcelona with an EIRP of 61 dBW.....	124
Figure 3.35 Clutter power spectrum response for L-band acquisition at 1.625 GHz for different wind speeds.....	125
Figure 3.36 Clutter power spectrum response for Ku-band acquisition at 17.25 GHz for different wind speeds.....	126
Figure 3.37 Long term coherent components vs. diffuse components in Billingsley's clutter model.	127
Figure 3.39 Clutter decorrelation impact in the Ku-Band acquisition SNR for different wind speeds.....	129
Figure 3.40 Clutter decorrelation impact on GEOSAR power link budget for Ku- and L- band acquisitions.	129
Figure 3.41 Number of user home parabolic antennas.	132
Figure 3.42 a) Parabolic antenna working as a scatterer. b) Feeder mismatch: power reflected and not delivered to the load.....	133
Figure 3.43 SAR system model for a linear satellite trajectory.....	136
Figure 3.44 SAR system model for a non-linear satellite trajectory.....	137
Figure 3.45 Back-projection algorithm geometric scheme.	138
Figure 3.46 Backprojection algorithm performance scheme.	139
Figure 3.48 3D view of satellite path (eccentricity of 0.0004 and no inclination) and scene location (41.23°N, 2.11°E).....	143

Figure 3.49 a) 3D orbital representation. b) Top view representation (reference meridian-90° West cut). c) Satellite nadir plane (North-90°West cut). d) Side view (North-Reference meridian cut).	144
Figure 3.50 Simulated raw data from a point target in the central point of the scene.....	144
Figure 3.51 Simulated raw data from a point target in the central point of the scene after Doppler centroid compensation.....	145
Figure 3.52 Range compression of the raw data matrix and cut for slow time of 14 hours.	146
Figure 3.54 a) Focused image with squared pixel, b) Target response azimuth cut and c) Target response range cut.....	148
Figure 3.55 Focused 50 by 50 meters resolution image for 10 point targets scene.	148
Figure 4.1 Acquisition scheme to get two full-resolution images per day.....	152
Figure 4.2 Acquisition scheme to get four half-resolution images per day.....	153
Figure 4.5 Daily variations of the along-track resolution considering constant integration time per sub-aperture.....	157
Figure 4.6 Earth's gravitational potential over the Equator. The satellite tends to stay at zones with lower potentials (stable regions).....	158
Figure 4.7 Longitude drift histories considering different nominal satellite longitudes.....	160
Figure 4.8 Orbital drift affecting a GEO platform. A maximum longitudinal drift ($\pm\lambda_{\text{max}}$) is allowed.....	160
Figure 4.10 Typical baseline directions in LEOSAR and GEOSAR cases.....	165
Figure 4.11 2D Fourier transform of reflectivity and spectral overlap for interferometry ..	166
Figure 4.12 Interferometer imaging geometry for acquisition points A1 and A2 with total baseline (B) and baseline perpendicular to the look direction (B_n). The phase offsets of points P will be given by $y \sin \theta_1$ and $y \sin \theta_2$	167
Figure 4.13 Critical baseline in GEOSAR acquisition considering the latitudinal satellite motion.....	169
Figure 4.14 Typical longitude/latitude satellite histories considering an eccentricity of 0.0005 and inclination equal to 0°. The longitude drift caused by the Earth's gravitational potential displaces the elliptical track towards the East.	171
Figure 4.15 Sensitivity ratio of the refraction index with respect to water vapour partial	

pressure vs. temperature.	175
Figure 4.16 TEC world map estimated by GPS measurements.	177
Figure 4.17 APS retrieval from sub-matrices of a long integration GEOSAR acquisition..	182
Figure 4.18 APS retrieval results from two different time instants of a long integration GEOSAR acquisition.	184
Figure 4.19 Focused images before and after APS compensation.....	184
Figure 4.20 Azimuth cut of the reconstructed image with no APS correction (blue) and after compensation (green). The red dots shows the location and peak power of the targets in the reconstruction image without APS correction. Peak power loss, spatial displacement and secondary lobes level increase effects are reduced after APS compensation.	185
Figure 4.21 a) Standard deviation of the residual error in the APS retrieval algorithm for different temporal correlations of the phase map. b) Phase estimation for one of the points in the scene considering an atmospheric temporal correlation of 15 min.	186
Figure 4.27 Orbital configuration for a GEOSAR constellation for interferometric APS retrieval.....	194
Figure 4.29 Intermediate Range Compressed data correction by using a pseudo orbital parameters correction able to compensate for orbital errors, clock phase changes, and model able APS perturbations.	196
Figure 5.1 Bistatic GEOSAR dual-beam concept.	200
Figure 5.2 Bistatic SAR geometry in the bistatic plane.....	201
Figure 5.3 Satellites placed on 11° East covering all the area of interest.....	202
Figure 5.4 Close bistatic field of view considering two satellites with nominal longitudes around 22° East.	203
Figure 5.5 Close bistatic field of view considering two satellites with nominal longitudes around 0°	204
Figure 5.6 Open bistatic GEOSAR field of view considering two satellites with nominal longitudes of 0° and 22° , respectively.	205
Figure 5.7 Relation between the satellites longitude shift and bistatic angle.....	205
Figure 5.8 Bistatic and equivalent monostatic SAR.....	207
Figure 5.9 Spatial (a) and Spectral (b) domains of the imaged scene. The scene spectrum accessed from a bistatic observation is equivalent, to a monostatic observation.....	208

Figure 5.10 Bistatic and equivalent monostatic satellite tracks for a generic GEOSAR case.	209
Figure 5.11 Bistatic and equivalent monostatic considering 4 hours of acquisition.	209
Figure 5.13 Focused image with an integration time of 4 hours at Ku-band (19.25 GHz) considering two satellites with orbital eccentricity of 0.0002. An along-track resolution around 19 meters is obtained.	212
Figure 5.14 Focused image with an integration time of 30 min at L-band (1.625 GHz) considering two satellites with orbital eccentricity of 0.0002. An along-track resolution around 1.56 km is obtained.	213
Figure 5.15 Achievable resolution of a bistatic GEOSAR acquisition with 4 hours of integration for different orbital eccentricities working at C-band (5.4 GHz).	213
Figure 5.16 Achievable resolution of a bistatic GEOSAR acquisition with 30 min of integration for different orbital eccentricities working at C-band (5.4 GHz).	214
Figure 5.17 Coverage reduction due to antenna pointing mismatches.	216
Figure 5.18 Coverage reduction in bistatic SAR due to pointing errors (slant range/pointing error direction plane).	217
Figure 5.20 Bistatic out of plane geometry.	220
Figure 5.21 Scattering behaviour of desert areas vs. out-of-plane angle at different incident angles [145].	220
Figure 5.23 Scattering behaviour of snow vs. out-of-plane angle at different incident angles [145].	221
Figure 5.24 Scattering behaviour vs. out-of-plane angle for different surfaces with incidence angle of 60 degrees [145].	222
Figure 5.25 In-plane backscattering coefficients in bistatic SAR for different surfaces.	224
Figure 5.26 Diamond diagram for GEOSAR with a 20% duty cycle.	225
Figure 5.28 Simplified block diagram of the transmitter and receiver of a bistatic Radar.	231
Figure 5.29 Simplified block diagram of a SAR processor based on Range & Azimuth compression which can be used to focus bistatic radar raw data.	232
Figure 5.30 a) Direct synchronisation link and b) synchronisation link using on-ground station.	235
Figure 5.32 a) Phase error evolution received from echoes of one of the calibrators. b)	

Phase estimation from sub-apertures and c) residual error.	242
Figure 5.33 RCS of the calibrators impact on the phase error in Ku-band.	243
Figure 5.34 Evolution of phase errors (Ku-band) related to SNR, SCR and clock with integration time. The total phase error presents a minimum considering an integration time of 0.95 seconds.	244
Figure 5.35 RCS of the calibrators impact on the phase error in L-band.	244
Figure 5.36 Evolution of phase errors (L-band) related to SNR, SCR and clock with integration time. The total phase error presents a minimum considering an integration time of 6.8 seconds.	245
Figure 5.37 Evolution of phase errors (X-band) related to SNR, SCR and clock with integration time. The total phase error presents a minimum considering an integration time of 1.63 seconds.	245
Figure 5.38 Resolution limits with orbital eccentricity of 0.0003 and feasibility with user's requirements for lower band applications.	250
Figure 5.39 Resolution limits with orbital eccentricity of 0.0003 and feasibility with user's requirements for higher band applications.	250
Figure 6.1 Illuminator-receiver-scene geometry.	252
Figure 6.4 Focused image from a bistatic GEOSAR with on-ground receiver simulated raw data during 4 hours of acquisition.	256
Figure 6.5 Along-track and cross-track resolution in the GEOSAR with on-ground receiver simulated case with 4 hours of integration.	257
Figure 6.6 ASTRA 2C footprint over Europe.	258
Figure 6.7 Horn antenna used as a receiver station on the bistatic on ground receiver configuration.	258
Figure 6.8 Front and back views of TBS 6981 PCIe Card used in the receiver for the bistatic GEOSAR acquisition.	261
Figure 6.9 TBS 6981 components: tuner (CX24132) and demodulator (CX24117).	261
Figure 6.10 Block diagram for the CX24132 tuner.	262
Figure 6.11 Block diagram for the CX24117 demodulator.	263
Figure 6.12 AD8039 dual amplifier pin-out.	264
Figure 6.13 Single amplifier design schematic.	264

Figure 6.14 Single amplifier design circuit.	265
Figure 6.15 Single amplifier design circuit.	265
Figure 6.16 Voltage supply circuit schematic.....	266
Figure 6.17 Voltage supply circuit with the 78L09 voltage regulator and the voltage divisor step.	267
Figure 6.18 Voltage supply + buffering circuits schematic and connections.	267
Figure 6.19 Final PCB top (left) and bottom (right) designs.	268
Figure 6.20 Final PCB testing.	268
Figure 6.21 Buffering circuit testing results.	269
Figure 6.22 Buffering circuit testing circuit.	270
Figure 6.24 Buffering circuit connections and output lines.	272
Figure 6.25 TBS6981 with buffering circuit final design.	273
Figure 6.26 Final design detail of the two inputs (direct and backscattered signals) and four outputs (I and Q components of each signal).	273
Figure 6.27 Detail of the buffering circuit into the TBS6981 card.	274
Figure 6.29 Inside view of the LNB.	275
Figure 6.32 LNB PCB necessary modifications (II).	277
Figure 6.33 LNB PCB necessary modifications (III).	278
Figure 6.34 LNB ready for working with external oscillator (back view).....	279
Figure 6.35 LNB ready for working with external oscillator (front view).	279
Figure 6.36 Measurement scheme for the LNB with local oscillator.	280
Figure 6.37 Measurement scheme for the LNB with external oscillator.	281
Figure 6.38 Measurement set up for the LNB with external oscillator.....	281
Figure 6.39 Down-converted signal from the LNB with local oscillator (left) and with external oscillator with signal amplitude of 0 dBm (right).	282
Figure 6.40 Bistatic GEOSAR acquisition with on ground receiver.....	282

List of Tables

Table 1.1. Highlights in space-borne SAR history [5].....	3
Table 2.1. Geosynchronous orbital typical parameters and formulas for the examples considered in this analysis.....	25
Table 2.2. Azimuth angle computation depending on the satellite-target position.	41
Table 2.3. Ground coverage considering several antenna beamwidth at 5 degrees of look angle.	46
Table 2.4. Antenna beamwidth required considering several ground coverage at 5 degrees of look angle.....	48
Table 2.5. Range of achievable azimuth resolutions at different frequency bands for an orbital eccentricity of 0.0004 and slant range of 36950 Km.	68
Table 2.6. Integration time required to obtain an azimuth resolution of 25 meters for an orbital eccentricity of 0.0004 and slant range of 36950 Km.	70
Table 2.7. TLE line 1 parameters description.	76
Table 2.8. TLE line 2 parameters description.	76
Table 3.1. SNR computation for a monostatic ad-hoc GEOSAR mission with scene coverage of 190Km with a resolution cell of 15 by 15 meters.	115
Table 3.2. SNR computation for a monostatic ad-hoc GEOSAR mission with scene coverage of 1000 Km with a resolution cell of 800 by 800 meters.....	116
Table 3.3. Satellite target link geometric parameters.....	120
Table 3.4. SNR computation for the monostatic case re-using the signal of HISPASAT-1D.	122
Table 3.5. SNR computation re-using the signal of KA-SAT.....	123
Table 3.6. Antenna parameters requirements for Ku-band spot beam with 350 Km coverage.	131
Table 4.1. Linear acceleration over equatorial plane depending on the satellite longitude.	159

Table 4.2. Station-keeping requirements considering different nominal longitudes and resolution cell sizes to keep the satellite in the desired orbital box for interferometric purposes.	172
Table 4.3. Ionospheric artefacts on long integration SAR images.	180
Table 4.4. Datasets (DS) considered in the long term raw data generation. The time interval between two consecutive data acquisition is used to determine the number of positions in raw data matrix taken for each sub-aperture.	190
Table 5.1. Antenna parameters requirements for L-band wide beam and Ku-band spot beam.	216
Table 5.3. Transmitted power requirements to reach a minimum SNR of 10 dB in L-band and Ku-band acquisitions.	228
Table 5.4. Antenna parameters requirements for Ku-band spot beam with 350 Km coverage.	229
Table 5.5. Transmitted power requirements to reach a minimum SNR of 10 dB in C-band for wide coverage and SPOT beams.	230
Table 5.6. Amplifier requirements for calibrators to reach the desired RCS of 75 dBsm at Ku-band.	247
Table 5.7. Amplifier requirements for calibrators to reach the desired RCS of 110 dBsm at L-band.	247
Table 5.9. Acquisition parameters for bistatic GEOSAR proposed beams (II)	249
Table 6.1. Geometric parameters for bistatic GEOSAR with on-ground receiver.	253
Table 6.2. Power link budget for the bistatic GEOSAR acquisition with on-ground receiver.	259

Abbreviations

AAP	Azimuth Antenna Pattern
AASR	Azimuth Ambiguity to Signal Ratio
AMC	Advanced Modulation and Coding
APS	Atmospheric Phase Screen
ARC	Active Radar Calibrator
ASR	Ambiguity to Signal Ratio
BRCS	Bistatic Radar Cross Section
CSAR	Circular Synthetic Aperture Radar
DC	Duty Cycle
DS	Data Set
DVB	Digital Video Broadcasting
EIRP	Equivalent Isotropic Radiated Power
ESA	European Space Agency
FFT	Fast Fourier Transform
GEO CSAR	GEOsynchronous Circular SAR
GEOSAR	GEOsynchronous Synthetic Aperture Radar
GNSS	Global Navigation Satellite System
GPS	Global Positioning System
IFFT	Inverse Fast Fourier Transform
InSAR	Interferometric Synthetic Aperture Radar
ISLR	Integrated Side-Lobe Ratio

IWV	Integrated Water Vapour
LEO	Low-Earth Orbit
LNB	Low Noise Block
LO	Local Oscillator
MPEG	Moving Picture Expert Group
MTI	Moving Target Indication
NESZ	Noise Equivalent Sigma Zero
NWP	Numerical Weather Prediction
PC	Personal Computer
PCB	Printed Circuit Board
PRF	Pulse Repetition Frequency
PRI	Pulse Repetition Interval
PSK	Phase-Shift Keying
PSLR	Peak-to-Side-Lobes Ratio
QPSK	Quadrature Phase-Shift Keying
RAAN	Right Ascension of the Ascending Node
RAR	Real Aperture Radar
RASR	Range Ambiguity to Signal Ratio
RCMC	Range Cell Migration Compensation
RCS	Radar Cross Section
RF	Radio Frequency
SA	Synthetic Aperture
SAR	Synthetic aperture Radar
SMA	SubMiniature version A
SMOS	Soil Moisture and Ocean Salinity
SNCR	Signal to Noise and Clutter Ratio

SNR	Signal-to-Noise Ratio
TDBP	Time Domain Back-Projection
TEC	Total Electron Content
TLE	Two-Line Element
TOPSAR	Terrain Observation by Progressive Scans
TS	Transport Stream
TWT	Travelling Wave Tube
UPC	Universitat Politècnica de Catalunya
USO	Ultra Stable Oscillator

Symbols

T_0	Ambient temperature
P_{amb}	Ambiguous received power
θ_{ant}^{-3db}	Antenna 3dB beamwidth
θ_{az}	Antenna beamwidth in azimuth
θ_{el}	Antenna beamwidth in range
D	Antenna Directivity
A_{eff}	Antenna effective area
X_{az}	Antenna footprint size (m) in azimuth
G	Antenna Gain
A_{geo}	Antenna Geometric Area
η_{il}	Antenna Illumination efficiency
L_a	Antenna length
η_{ohm}	Antenna ohmic efficiency
η_x	Antenna polarization efficiency
\wp	Antenna Power Density
η_s	Antenna spill over efficiency
η_t	Antenna Total efficiency
W_a	Antenna width
ω	Argument of the perigee
n	Atmospheric Refraction Index
N	Atmospheric refractivity

ρ_{az}	Azimuth resolution
k	Boltzmann constant
P_{CN}	Clutter non-desired power
S_C	Clutter spectrum
α	DC/AC ratio in Billingsley model
B_d	Doppler bandwidth
f_d	Doppler frequency
R_{Eq}	Earth equatorial radius
R_{Pol}	Earth polar radius
Ω_E	Earth rotation velocity
β	Exponential decay in Billingsley model
R_{far}	Far Range
φ_C	Geocentric latitude
ρ_{gr}	Ground Range Resolution
θ_{in}	Incidence angle
T_i	Integration time
Γ_L	Load power reflection coefficient
λ_{AN}	Longitude of the ascending node
θ_{look}	Look angle
R_{near}	Near Range
u	Nodal angular elongation
E	Orbital eccentric anomaly
e	Orbital eccentricity
i	Orbital inclination
M	Orbital mean anomaly
T_{orb}	Orbital period

Ω	Orbital Right Ascension of the Ascending Node (RAAN)
a	Orbital semi-major axis
b	Orbital semi-minor axis
v	Orbital true anomaly
$\Delta\phi_{APS}$	Phase error due to atmospheric changes
ϕ_{Clk}	Phase error due to clock unstabilities
$\Delta\phi_{Clutter}$	Phase error due to clutter interference
$\Delta\phi_{Noise}$	Phase error due to noise
h	Platform height
P_L	Power delivered to load
τ_{RP}	Pulse guard time
ρ_{rg}	Range resolution
τ_R	Received echo time delay
F_n	Receiver Noise Factor
θ_{az}^T	Satellite azimuth angle from the target
θ_{el}^T	Satellite elevation angle from the target
φ_{SL}	Satellite latitude
λ_{SL}	Satellite longitude
t_a	Satellite time pass through the apogee
t_p	Satellite time pass through the perigee
v_s	Satellite velocity
λ	Signal Wavelength
R_S	Slant range
c	Speed of light
S_w	Swath width (m) in range

L_{SA}	Synthetic Aperture Length
σ	Target radar cross section
Δt_{nad}	Time duration of the nadir return
L_T	Total losses
ϕ_T	Total phase error
τ_i	Transmitted pulse duration
β	Transmitter-receiver bistatic angle
P_{T-R}	Transmitter-receiver direct power
G_{2w}	Two way power antenna pattern
P_u, P_d	Useful/desired received power
χ	Vernal equinox
λ	Wavelength

Chapter 1

Introduction

1.1 Synthetic Aperture Radar basic concepts

In this section, the basic concepts of Synthetic Aperture Radar (SAR) are presented in a broad outline. This chapter is intended for introducing to the reader the necessary concepts that will be used all along this document. For further information about SAR concepts and performance, it is recommended to follow the references given in this section. Finally, the main objectives and motivation, as well as the organization, of the thesis are presented.

1.1.1 History and context of SAR remote sensing imaging

Remote sensing is a wide area which studies different techniques to get information of targets situated at far distances. These techniques can be classified in two different areas according to their basic operation. The first group, called passive remote sensing [1][2], uses passive sensors to acquire the energy radiated by the targets. This energy can come from an external source, such as Sun radiation, being reflected by the object or it can be emitted by the target itself. On the other hand, active remote sensing systems [2] emit their own signal to illuminate the scanned area. So, although it requires a more complex system, active sensing does not need an external source to operate which is an advantage when the conditions are not favourable.

Synthetic Aperture Radar (SAR) is an active remote sensing technique used in radar (RAdio Detection And Ranging) [3] systems to get high resolution images. The motion of a transmitting antenna is used to collect echoes from targets in different positions. The final image is obtained by coherently processing the received signals along the platform track.

SAR, Real Aperture Radars (RARs) or Ground-Based Radars (GB-SARs) are examples of active radar sensors, working at frequencies between 0.3 GHz and 300GHz. These systems send pulses towards the scanned area. Part of the energy interact with the surface and

return to the receiver. This echo is originated by the energy backscattered by the objects in the scene and it will be dependent of the backscattering profile of the targets (radar cross-section) [4]. The time delay, Doppler history and power received are processed to determine the target locations and features.

SAR techniques have been used for the last 40 years and present some advantages in comparison with other remote sensing techniques. The most significant are:

- Day/Night and all weather condition imaging since it does not depend on external power sources to detect the targets.
- Geometric resolution independent of transmitter height or transmitted wavelength.
- Use of microwave frequency signals which suffer less deterioration in atmosphere propagation.

The SAR systems started with aero-transported missions and later, first space missions were sent. The first theories in SAR date from 1951 when C. Wiley postulated the Doppler beam-sharpening concept. Highlights of SAR development are summarized in Table 1.1.

1.1.2 Real Aperture Radar vs. Synthetic Aperture Radar

Radar is a remote sensing technique based on transmitting one or more pulses and observing the echoes that return from the scene to determine the objects positions and features. The concept of Synthetic Aperture Radar (SAR) appeared as an alternative of Real Aperture Radar (RAR) [1] which was an extensively used technique in the beginnings of remote sensing. So, with SAR techniques better resolution images than in RAR can be obtained, independently of the central frequency of the transmitted signal and the distance between the transmitting antenna and the illuminated surface.

The idea of real/synthetic aperture is referred to the relative motion between the transmitter (usually an antenna mounted on a satellite or an airplane) and the imaged surface. The way to receive and process the echoes coming from the surface distinguishes the Real and Synthetic Aperture Radars.

The RAR technique provides a geometric resolution in the direction parallel to the relative transmitter motion which depends, basically, on the distance between the target and the illuminator and on the antenna beamwidth. So, two targets illuminated by the antenna footprint at the same time will not be separated during the image formation. Then, the RAR will be not useful for space-borne platforms neither airplane antennas if high resolution images are required. The basic scheme of a Real Aperture Radar acquisition is presented in Figure 1.1 (the geometrical concepts presented in Figure 1.1 are also valid for SAR geometry) where two main directions can be identified: azimuth (or along-track

direction) and range (or cross-track direction).

Date	Development
1951	Carl Wiley of Goodyear postulates the Doppler beam-sharpening concept.
1952	University of Illinois demonstrates the beam-sharpening concept.
1957	University of Michigan produces the first SAR imagery using an optical correlator.
1964	Analog electronic SAR correlation demonstrated in non-real time (U. Michigan).
1969	Digital electronic SAR correlation demonstrated in non-real time (Hughes, Goodyear, Westinghouse).
1972	Real-time digital SAR demonstrated with motion compensation (for aircraft systems)
1978	First space-borne SAR NASA/JPL SEASAT satellite [8]. Analog downlink; optical and non-real-time digital processing.
1981	Shuttle Imaging Radar series starts - SIR-A [6]. Non-real-time optical processing on ground.
1984	SIR-B digital downlink [7]; non-real-time digital processing on ground.
1986	Space-borne SAR Real-time processing demonstration using JPL Advanced Digital SAR processor (ADSP) [8]
1987	Soviet 1870 SAR is placed in Earth orbit.
1990	Magellan SAR images Venus [9]
1990	Evolution of SAR begins in space; Soviet ALMAZ (1991), European ERS-1 (1991) [10], Japanese JERS-1 (1992) [11], SIR-C (1994) [12], ERS-2 (1995) [13], Canadian RADARSAT-1 (1995) [14]
2000s	The last years the number of SAR missions increases significantly. Some examples are: SRTM (2000), ENVISAT (2002) [15], ALOS (2006), TerraSAR-X (2007) [16], RADARSAT-2 (2007) [17], SAR-LUPE (2007), SURVEYOR (2007)...

TABLE 1.1. Highlights in space-borne SAR history [5]

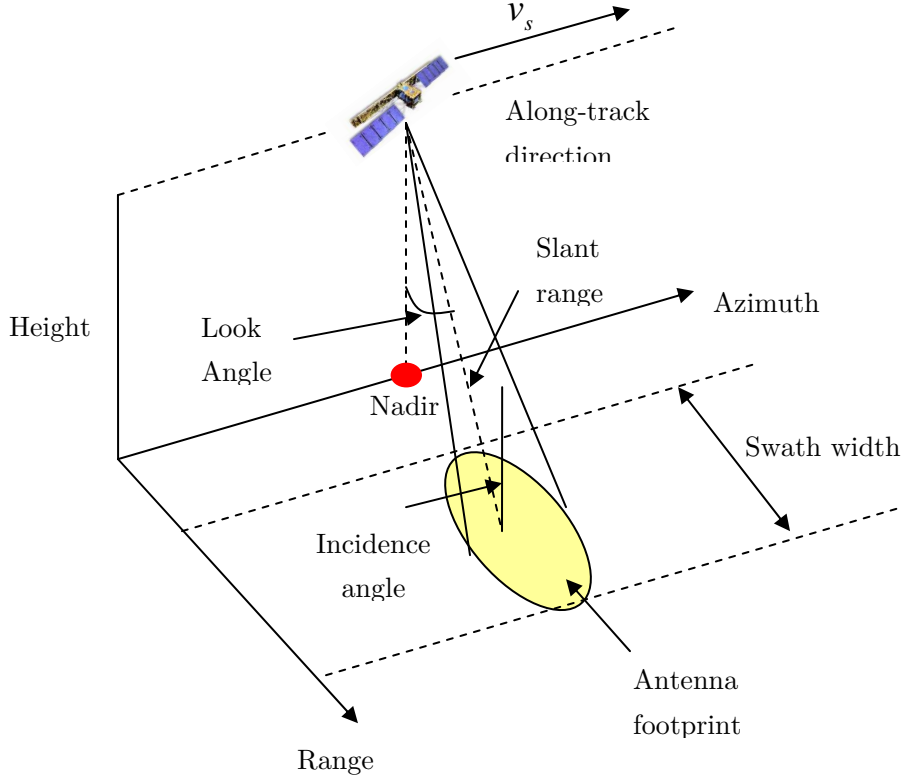


FIGURE 1.1. Basic geometry and parameter for RAR and SAR

In case of RAR, the system azimuth resolution will be given by the antenna footprint on ground. As a first approximation, the along-track resolution of a RAR acquisition can be obtained from the geometric parameters presented in Figure 1.1 as:

$$\rho_{az} = \frac{h\theta_{az}}{\cos\theta_{look}} = \frac{h}{\cos\theta_{look}} \frac{\lambda}{L_a} \quad (1.1)$$

where the antenna beamwidth (θ_{az}) has been approximated by λ/L_a being L_a the antenna length and λ the wavelength of the transmitted signal. θ_{look} corresponds to the look angle presented in Figure 1.1 while h is the transmitter height. So, $h / \cos\theta_{look}$ is the distance between the radar and the target (considering flat Earth approximation) known as slant range. Thus, as it has been previously commented, the resolution gets worse when the platform height and, consequently, the slant range to the target increase.

In Synthetic Aperture Radar (SAR), the different echoes from one object taken at different satellite positions are recorded and coherently processed. So, it is equivalent to have several antennas separated along the transmitter path simultaneously illuminating the scene (synthetic aperture antenna). A better azimuth resolution can be achieved with this technique. For a GEOSAR configuration, the azimuth resolution computation must be reformulated considering the novel acquisition geometry. For a generic SAR acquisition, the azimuth resolution can be computed as [19][20]:

$$\rho_{az} = \frac{\lambda}{2} \frac{R}{L_{SA}} \quad (1.2)$$

being L_{SA} the synthetic aperture length and R the distance between satellite and target.

Regarding the range or cross-track resolution, it will be determined by the transmitted signal bandwidth both in RAR and SAR.

1.1.3 SAR basic performance and parameters

In this section, the principal SAR parameters that will appear in this document are introduced and the notation is presented. This can be useful to have a clear vision of the geometry of our problem and get in touch with the parameters that will be used later on the Geosynchronous SAR discussion. Most of the parameters used in the Geosynchronous SAR analysis will be the same than in the conventional SAR.

1.1.3.1 SAR imaging coordinate system

Each positioning system has its own coordinate system to locate the targets in the scene univocally. So, while the real aperture radars have an angle-time delay format [1], in Synthetic Aperture Radar, a Doppler-time delay system is used. The Doppler shift is produced by the relative motion between the transmitting/receiving antenna and the illuminated targets while the time delay will be given by the slant range between the transmitter/receiver and the scene. The imaging coordinate system is presented in Figure 1.2.

Therefore, from the configuration shown in Figure 1.2, the echoes received from those points located on a sphere centred at the transmitter position will have the same delay. If these spheres are intersected with the surface plane of the Earth, the result is a family of concentric circles, centred at the nadir point which is the intersection of the direction pointing directly below the transmitter and the Earth surface. Thus, these circles define the lines of equidistance range to the sensor (iso-range lines).

On the other hand, points located on coaxial cones with the flight direction as the axis and the radar location as the apex will produce echoes with the same Doppler shift at the receiver. Once again, if these cones are intersected with the surface, a collection of hyperbolas with the same Doppler shift (iso-Doppler lines) is obtained over the Earth's surface.

As shown in Figure 1.2, for a given time delay and Doppler shift, there is an ambiguous region (point B) which has the same Doppler and time delay than the desired target (point A). It can be easily discriminated pointing the antenna to the side of the desired target (side-looking radar).

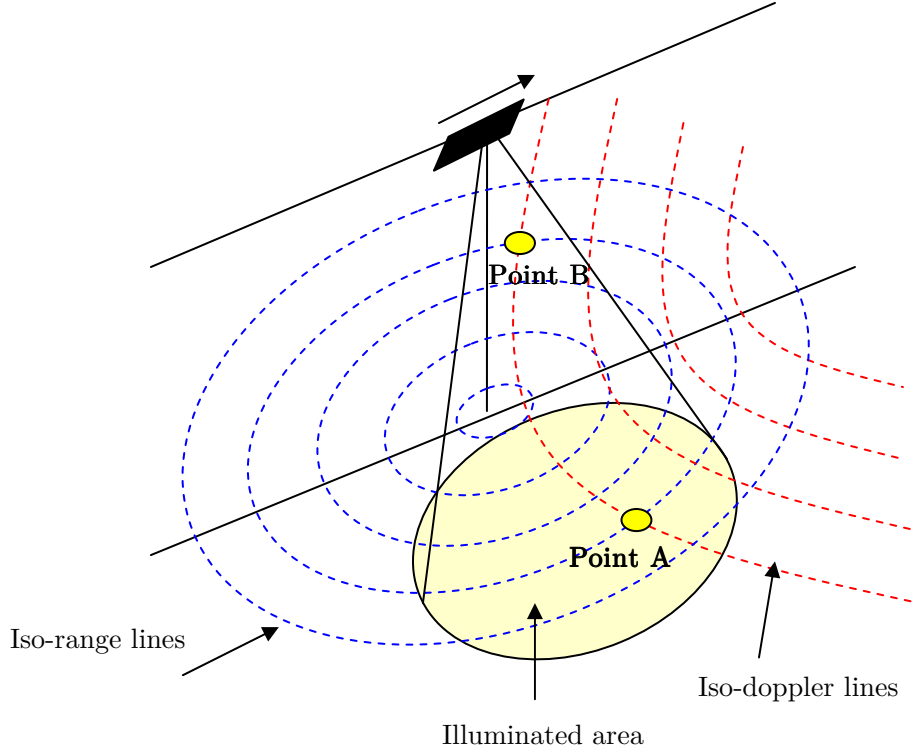


FIGURE 1.2. SAR image coordinate system for side-looking radar

The brightness that is assigned to a specific pixel of the final image will be proportional to the echo energy contained in the corresponding time delay Doppler shift bin which is unequivocally associated with a point on the scanned surface.

1.1.3.2 SAR parameters

Figure 1.1, Figure 1.3 and Figure 1.4 show the geometry corresponding to a side looking imaging and the range and the azimuth planes, respectively. The parameters shown in these figures, valid for a conventional SAR in a spacecraft or an airplane, will be also useful for the Geosynchronous SAR studied in this thesis.

In Figure 1.1, the basic SAR geometry can be observed. The orbital parameters such as platform height (h) and velocity (v_s) will define other geometric parameters of the system as it will be explained next. The radar antenna footprint illuminates a spot on the surface on one side of the nadir track. As the platform moves in the orbit, a continuous strip is illuminated over the surface along the flight direction known as swath.

As already mention in section 1.1.2, two perpendicular directions can be defined in SAR geometry. The along-track direction, parallel to the flight path of the satellite, is usually called azimuth. On the other hand, the direction perpendicular to this one is called cross-track direction or range.

An important parameter in SAR geometry that appears in Figure 1.3 is the look angle (θ_{look}). This corresponds to the angle between nadir direction and the direction where the antenna is pointing. Changing this angle, it is possible to switch between different swaths illuminating several zones of the Earth's surface. The combination of some swaths will provide higher range coverage for some scanning modes. Other important concepts in SAR geometry are the slant range (R_s), which is the distance between the platform and the illuminated surface. The ground range is the distance between the nadir point and the targets into the illuminated surface. The near and far ranges can be also defined as the distance between the radar and the nearest and furthest points in the swath respectively. The swath width (S_w) for a fixed look angle obtained from the parameters in Figure 1.3 as:

$$S_w \approx h \theta_{el} / \cos^2 \theta_{look} = \lambda h / W_a \cos^2 \theta_{look} \quad (1.3)$$

where θ_{el} is the elevation beamwidth of the antenna, which can be approximated as $\theta_{el} = \lambda / W_a$, being W_a the antenna width.

The antenna footprint width in the azimuth direction, defined as X_{az} in Figure 1.4, will determine the observation time of the targets which is equal to the time while a point target is illuminated by the main beam of the antenna. So, it will be related with azimuth beamwidth (θ_{az}) of the antenna. The observation (or integration) time per target is calculated from the satellite parameters as:

$$T_i = \frac{X_{az}}{v_s} = \frac{\theta_{az} \cdot R_s}{v_s} = \frac{\lambda}{L_a} \frac{h / \cos \theta_{look}}{v_s} \quad (1.4)$$

Regarding the azimuth resolution presented in equation (1.2), it can be related with the integration time as in (1.5). Integration time will be one of the key parameters to obtain the azimuth resolution in a GEOSAR acquisition. So, in a generic SAR acquisition, the azimuth resolution can be related with the integration time as:

$$\rho_{az} = \frac{\lambda}{2} \frac{R_m}{T_i \cdot V_s} \quad (1.5)$$

In the range plane (Figure 1.3), the look angle (θ_{look}) and elevation beamwidth (θ_{el}) are shown. The impact of the pulse duration (τ_i) on the range resolution (ρ_{gr}) can be also observed. The ground range resolution for a SAR acquisition is computed as [19] [20] [22]:

$$\rho_{gr} = c \tau_i / 2 \sin \theta_{look} \quad (1.6)$$

As it can be seen, neither the azimuth nor the range resolutions depend on the frequency or the platform height.

Another parameter that can be observed in Figure 1.3 and which will be used along this document is the incidence angle (θ_{in}) which corresponds to the angle between the direction

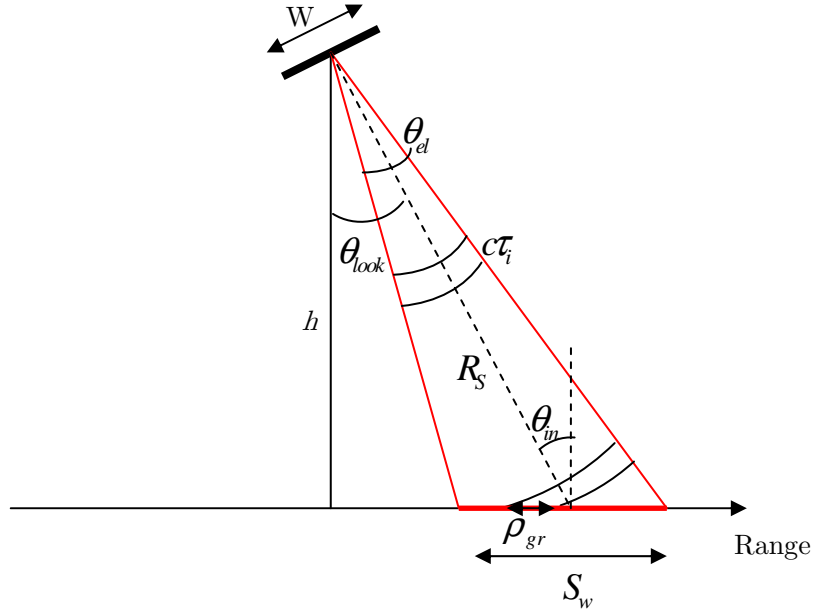


FIGURE 1.3. Elevation plane geometry for SAR systems

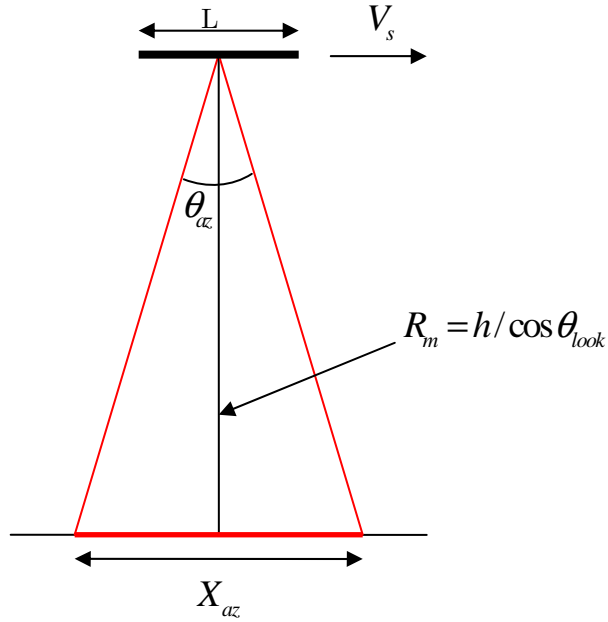


FIGURE 1.4. Azimuth plane geometry for SAR systems

of arrival of the transmitted signal into the surface and the normal vector perpendicular to the incidence plane. Most of the results of this document are given in function of this angle.

1.1.3.3 SAR achievable results and constraints

When a SAR imaging system is designed, a large number of parameters have to be chosen in order to fulfil the desired input requirements. The end-to-end design involves trade-offs between these parameters which are interrelated. The final design is the result of the

system designers, the hardware engineers, the platform engineers and scientific users' interactions. Consequently, it is necessary to do a large number of iterations to obtain the final configuration for the SAR system.

For a Geosynchronous SAR system, the same constraints must be fulfilled in order to assure the correct performance of the radar. However, the most critical parameter will be the signal to noise ratio since the satellite is placed at a Geosynchronous orbit 42.164Km far away from the Earth's centre. Furthermore, another critical parameter will be the achievable resolution due to the low satellite velocity with respect to the Earth surface. Both of them will be related to the integration time considered and orbital parameters of the transmitting/receiving satellite.

Other features to be studied in this report for the Geosynchronous SAR that will define the system performance are the desired swath coverage which mostly determine our antenna geometry, the desired range and azimuth resolutions, integration time, the ambiguity suppression, the noise equivalent sigma zero (NESZ), etc. In the following sections, all the geometric parameters for the Geosynchronous orbit will be accurately described and an analysis of the radiometric features of this kind of system for SAR observation purposes will be done.

1.2 GEOsynchronous Synthetic Aperture Radar

In this thesis, GEOsynchronous Synthetic Aperture Radar (GEOSAR) missions are analysed for Earth and atmosphere monitoring. A GEOSAR acquisition will use the relative motion of a geosynchronous satellite with respect to the Earth surface to obtain the SAR images. This motion can be achieved by combining slightly eccentric orbits with inclination of the orbital plane with respect to the Equatorial plane.

Current LEOSAR missions, such as RADARSAT [17] or TerraSAR-X [16] among others, present some limitations such as revisit time of several days or weeks, limited swath of a few hundreds of Kilometres or no permanent monitoring over the same region. The potential advantage of using a satellite on a geosynchronous orbit instead of a Low-Earth Orbit (LEO) is the possibility of having continuous illumination of a wide zone of the Earth. This can be really helpful in those kinds of applications that need to be continuously monitored due to its rapid evolution as the application presented in section 1.5. The revisit time of several days or weeks of LEO satellites limits the LEOSAR feasibility for these purposes.

The relative motion of a geosynchronous satellite with respect to the Earth surface presents some differences in front of conventional LEOSAR acquisition. The non-perfect geostationary orbit considered for GEOSAR will results in elliptical tracks that will determine the length of the synthetic aperture. These synthetic apertures must be carefully

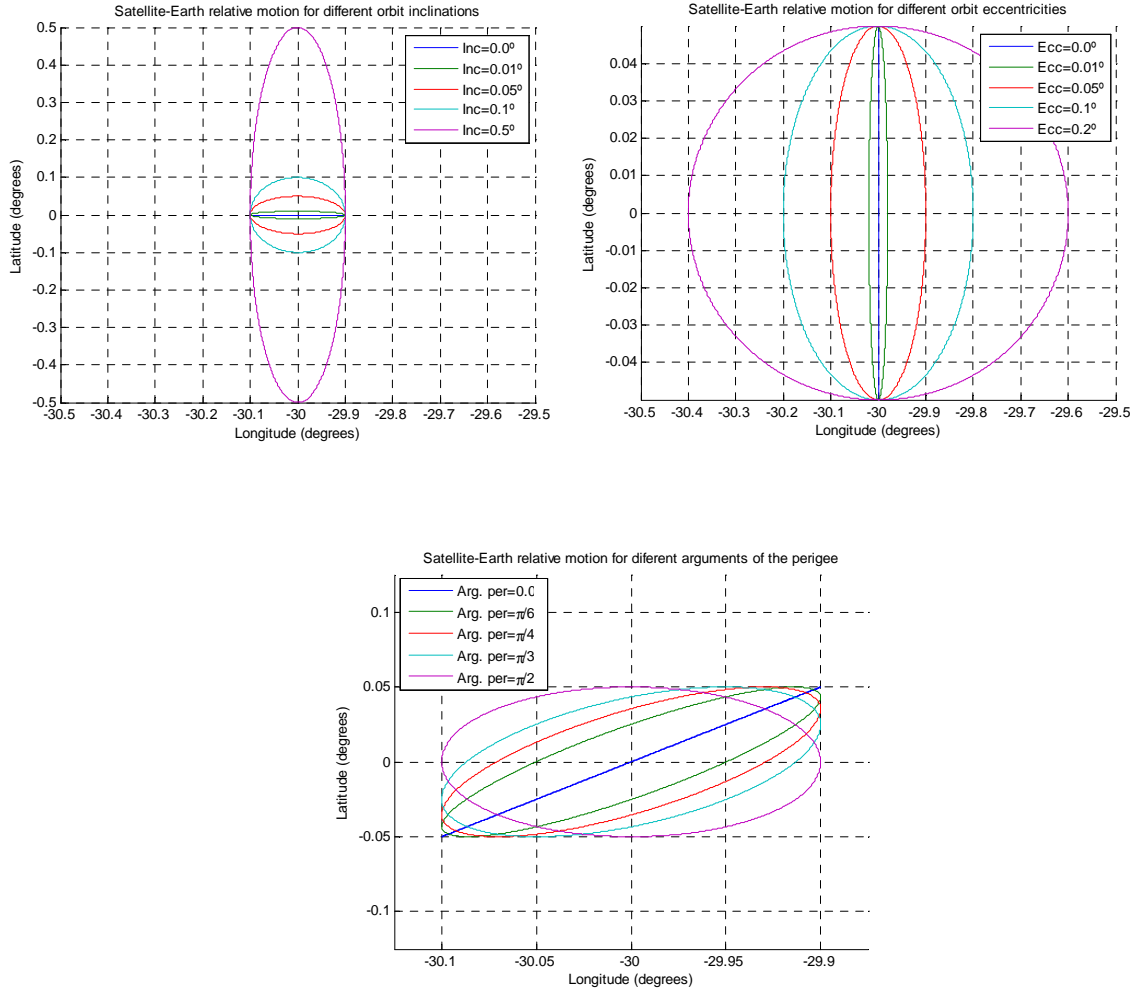


FIGURE 1.5. GEOSAR orbital track using different inclination of the orbital plane (top-left plot), eccentricities (top-right plot) and argument of the perigee (bottom plot).

characterized and the typical formulation for linear LEOSAR re-calculated to introduce the new features of GEOSAR acquisition. In Figure 1.5, the possibilities of the GEOSAR orbital design are presented for different values of the orbital parameters. A detailed geometric analysis of the geosynchronous orbital track is presented in Chapter 2.

Thus, GEOSAR provides daily coverage of wide Earth areas. Furthermore, it offers more flexibility since high resolution images of specific zones or low resolution images covering wider areas could be obtained depending on the acquisition parameters considered. Furthermore, the orbital design will also play an important role in the mission design and the most appropriate orbital configuration must be selected depending on the mission requirements.

1.3 State of the art of GEOSAR

The interest on GEOSynchronous Synthetic Aperture Radar (GEOSAR) has grown up in the last years. The idea of using the orbital motion of a geosynchronous platform to get SAR images was proposed by Kiyo Tomiyasu in 1978 [35][36]. Tomiyasu described a mission concept with high inclined geosynchronous orbit to obtain SAR images of the American continent with a resolution of 100 m by using the attitude of those satellites. In this way, the whole continent could be monitored in about three hours of segmented operation considering a circular orbit with an inclination of the orbital plane of 50° . The orbital track obtained by using this configuration is plotted in Figure 1.6. Regarding the power requirement, Tomiyasu proved that a sufficient SNR level could be reached working at 2450MHz with a transmitted average power of 1312W. However, the system studied by Tomiyasu used a 15 meter diameter antenna.

Since then several studies have been performed but they can be classified in three different blocks regarding their orbital, power and antenna parameters. On one hand, Tomiyasu and Madsen [37] proposals, as well as other recent studies [38]–[44], achieve continental coverage by considering high inclined orbits, obtaining an 8 figure satellite track (Figure 1.6). However, large antennas, as shown in Figure 1.7 with the 30 m L-Band antenna of Madsen proposal [37], and high transmitted powers are required to overcome the propagation losses due to the short illumination time per target.

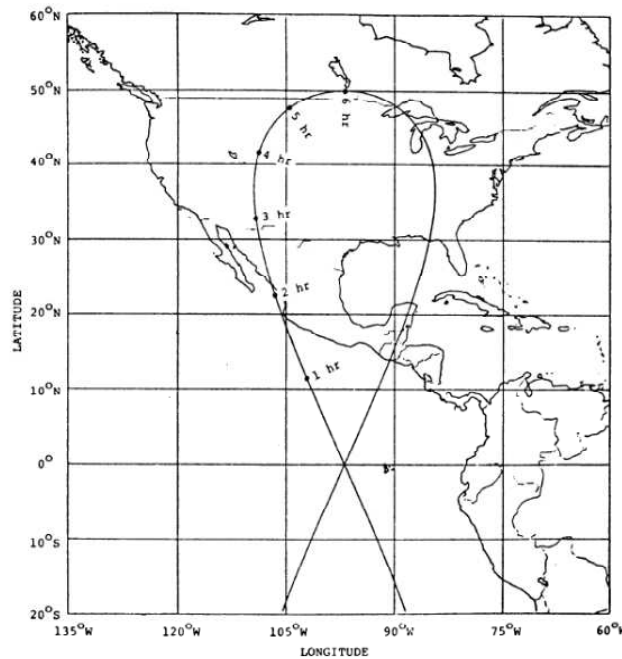


Figure 1.6. Ground track of a geosynchronous satellite with 50° inclination [35]

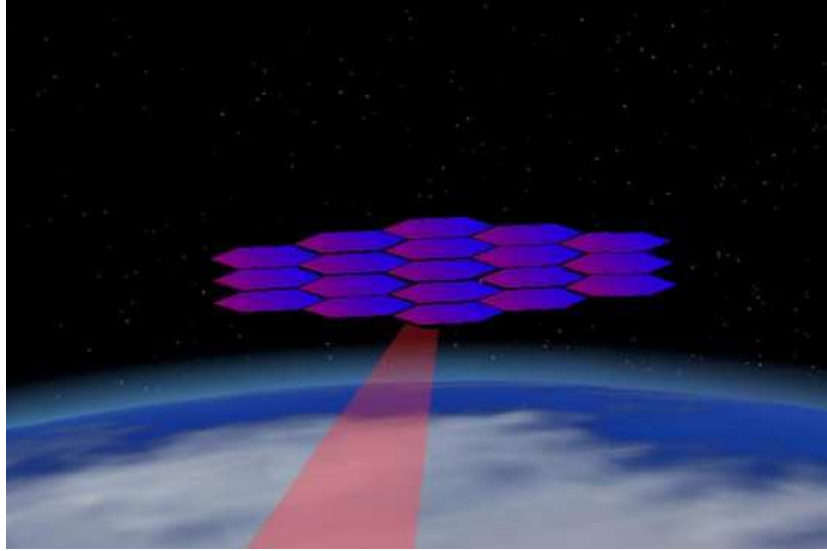


FIGURE 1.7. Concept of the 30 m L-Band antenna with hexagonal elements proposed by Madsen [37].

Secondly, a low-inclination ($\pm 1^\circ$) orbit with nearly circular satellite track, known as GEO CSAR, has been studied for 3D imaging and interferometric applications [45]–[47]. This technique combines the concepts of GEOSAR proposed by Tomiyasu with the acquisition features of Circular SAR (CSAR). In this case, lower inclinations of the orbital plane (a few degrees) than in high inclined orbit GEOSAR are considered. On the other hand, a non-perfect circular orbit (small orbital eccentricity) is taken in order to get the circular equivalent motion of the satellite. However, high transmitted powers are still required to overcome the large satellite-scene slant ranges. Daily repeat-pass interferometry over a specific area of the Earth may be obtained by GEO CSAR repeated acquisitions.

Finally, the radar payload may be placed on a geosynchronous orbit with nearly-zero inclination and small eccentricities resulting in a small synthetic aperture of a few hundreds of kilometres at most. Therefore, several hours of integration will be required to obtain a medium resolution image (10-20 meters). With this configuration, the high propagation losses working more than 36.000 Km away from the targets are overcome by long coherent integration of pulses. So, moderate powers and antenna sizes can be considered [48], which is not possible with the other geosynchronous SAR approaches presented above.

As mentioned before, the goal of the analysis presented in this thesis is to demonstrate the feasibility of a nearly-zero quasi-circular orbit GEOSAR working with transmitted powers and antenna size similar to LEOSAR acquisition. Therefore, orbital configurations with small inclination ($< 1^\circ$) and eccentricities (< 0.001) will be considered all along this thesis.

In the context of nearly-zero inclination GEOSAR, some studies on the feasibility of those systems have been done. A passive geosynchronous SAR system was proposed by Prati *et al* [49] in 1998. In this proposal, a SAR payload located in a geosynchronous satellite is

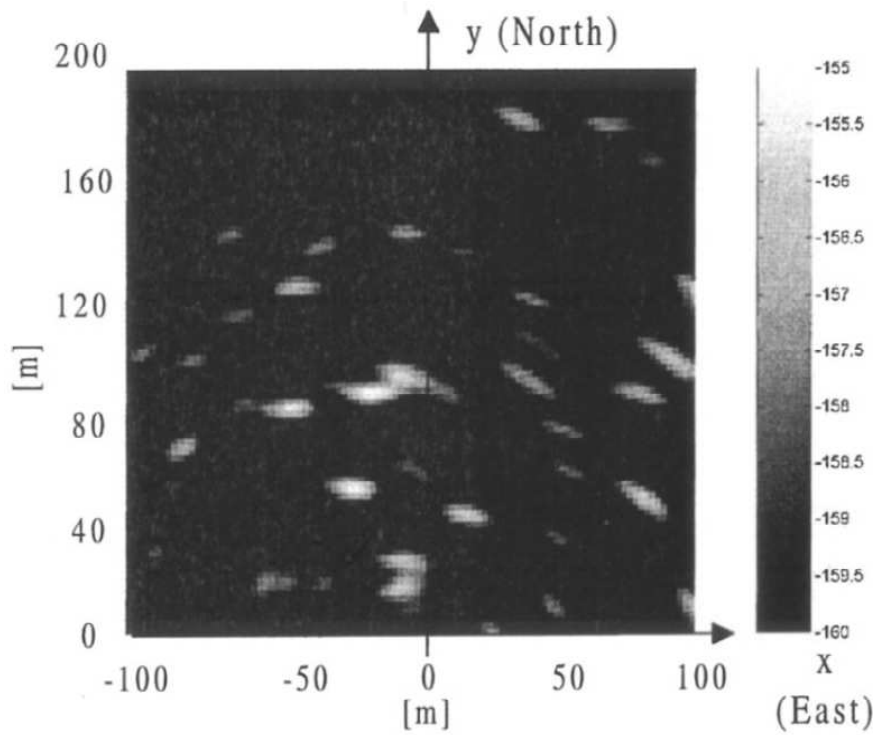


FIGURE 1.8. Focused image using the backscattered TV signal.

considered. The antenna collects the echoes from a scene which is illuminated by the transmitted signal of a TV broadcasting satellite (passive system). The concept of reusing the signal from another satellite (illuminators of opportunity) appears for the first time in the GEOSAR context. A preliminary performance evaluation in terms of spatial resolution, link budget and focusing techniques is given.

A ground based experiment of bistatic SAR was presented by Cazzani [50] in 2000. In this case, the experimental results of a bistatic configuration with a receiver on a ground station and using as illuminator a TV broadcasting satellite are presented. In this case, the SNR ratio limitations are reduced since the scene-receiver path is much shorter than in the case of working with a monostatic GEOSAR configuration or a bistatic one with two geosynchronous satellites. First images of an area of 200 by 200 meters were obtained (Figure 1.8). Problems related to atmospheric decorrelation are not considered in this study since the direct signal to the receiver (used as a reference) and the back-scattered from the scene are affected by the same atmospheric phase delay. This experiment was based on previous studies in *Politecnico di Milano* some years before [51][52].

Therefore, there are several open issues to be assessed in the GEOSAR analysis as introduced in [53]. Other studies in the field of GEOSAR focusing techniques and processing algorithms are being studied [54]–[63] at the same time of the development of this thesis. This is a consequence of the importance and potential applications of the GEOSAR acquisition as a complementary technology to the current LEOSAR missions.

1.4 GEOSAR opportunities and limitations

The feasibility of a GEOSAR system in terms of synthetic aperture formation has been briefly introduced in the previous section, showing that it is possible to obtain the necessary relative motion considering the non-perfect geostationary orbit of a geosynchronous satellite.

However, it is not the only requirement to assure the feasibility of a SAR system. The particular orbit of a GEOSAR acquisition, with an orbital period of one sidereal day, results in a slant range to targets of thousands of kilometres (from 36.000 to 40.000 Km). Therefore, the low power of the received echoes will be an important issue to take into account to achieve reasonable levels of Signal to Noise Ratio (SNR). A straight forward solution would be to increase the transmitted power and use larger antennas with higher gain in order to increase the received power. However, this solution would penalize the system coverage and will result in a very costly mission limiting the system life by the available power on board. Therefore, an alternative solution is considered in this study which consists in taking geosynchronous orbit with small eccentricities and inclinations of the orbital plane resulting in synthetic aperture of some hundreds of kilometres. So, the desired scene is continuously illuminated and the SNR can be improved by coherently processing echoes during hours with a final medium resolution image. In this way, typical LEOSAR transmitted power and antenna parameters will be considered obtaining the desired SNR by the proper selection of integration time and orbital parameters.

On the other hand, considering integration times of minutes or even hours, stable targets or regions with bright targets should be located to avoid defocusing and power blurring problems. A potential target of opportunity to be studied will be the user parabolic antennas. Many of the geostationary satellites are TV broadcasting satellites pointing to determined zones of the Earth with populated areas covered of parabolic antennas steered to these satellites. This kind of metallic reflectors will have high reflectivity and their orientation towards the satellite will increase their RCS mostly for monostatic configurations. Since these antennas need to have continuous direct link, it is expected that they will be in the line-of-sight of the satellite, well pointed and very stable mounted. The theoretical study and experimental validation of these reflectors as scatterers will be an important part in the development of the thesis.

Other problems related to long term integration time acquisition will be carefully studied for the GEOSAR case in this thesis. Atmospheric phase screen (APS) spatial and temporal decorrelation during the acquisition must be considered. The phase variations introduced by this phenomenon will result on final image defocusing. Therefore, a strong effort on APS theoretical characterization and simulations will be important to determine the feasibility of the long term GEOSAR acquisition. Besides, experimental test with Ground-Based SAR data have been used to validate the theoretical analysis.

Two main configurations would be studied in this report: monostatic or bistatic systems. Both of them present some advantages and drawbacks that have to be considered and studied carefully to determine the best option for each acquisition. In Chapter 2 and Chapter 3, a monostatic configuration is considered if not otherwise is specified.

In Chapter 5, a particular bistatic GEOSAR mission is analysed and the differences with respect to monostatic acquisition are pointed out. Finally, in Chapter 6, a bistatic system considering as a transmitter a TV broadcasting satellite and an on-ground receiver is studied.

As it has been previously introduced, the Geosynchronous SAR concept presents several conceptual and technical challenges to face up. However, it is an interesting system since it could allow a new range of applications that are not possible with the current LEO-SAR schemes such as the monitoring of the APS, daily interferometry or sub-daily acquisitions, as presented in Chapter 4.

1.5 Potential applications of GEOSAR

After the introduction to GEOSAR concept, in this section some potential applications of GEOSAR are presented. The possibility of using different timing and orbital configurations makes possible to consider a large variety of applications. The most interesting for surface and atmospheric imaging are listed next. Different configurations according to the scientific requirements from these applications are presented in Chapter 4.

Interferometric SAR (InSAR): Atmospheric Phase Screen (APS)

The InSAR acquisitions make possible to get millimetre-scale motions of the land surface. However, the signals travelling across the atmosphere suffer from spatial-temporal variations caused by the atmospheric turbulences associated to the water vapour content which changes the refractivity index of the different atmospheric layers (mostly in the troposphere). This phenomenon is known as Atmospheric Phase Screen (APS) which must be tracked and compensated to reduce its impact on the InSAR images.

Therefore, a GEOSAR wide coverage acquisition at low-frequency band could provide coarse resolution images (around 1 by 1 Km) in minutes (20-30 minutes). Since the APS usually present smooth spatial variations but rapid temporal changes, this GEOSAR configuration could be suitable for APS retrieval. The information retrieved could be used for reduce the atmospheric artefacts in images acquired at different frequencies for InSAR surface imaging. This application is exclusive of GEOSAR thanks to the permanent monitoring over large areas, impossible with current LEOSAR acquisition. APS is studied in depth in section 4.3.

Numerical Weather Prediction use external observations, mostly from satellites, in their

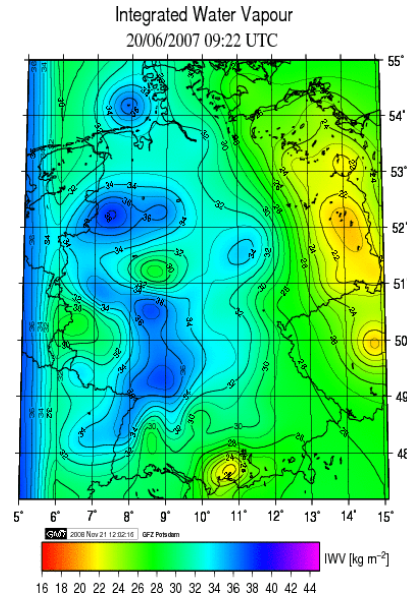


FIGURE 1.9. Integrated Water Vapour (IWV) from processed GPS data (from COPS-GRID project [24][25])

simulations to obtain the weather forecasts. Current predictions rely on Global Navigation Satellite System (GNSS)[23] to obtain the Integrated Water Vapour (IWV) maps over the land as shown in Figure 1.9. However, on-ground GPS stations are necessary to obtain the IWV maps. In some places, they might be sparse or non-existent which will degrade the spatial resolution of the obtained maps. As mentioned before, a GEOSAR image could be obtained every 20-30 minutes with spatial resolution of 1-2 Km. These images could be used in NWP to refine the meteorological forecast simulations.

Flooding: inundation monitoring and forecasting

The flooding across the surrounding lands of the rivers depends on the topography, the water flux, the nature of the surface and the flow paths taken. Therefore, knowing all the factors, hydrological flood models can be obtained. However, the major limitation of this approach is to know precisely the water flux of the rivers. So, additional information can be obtained from airborne or satellite imagery and integrated into flooding prediction models [26]. Information coming from LEOSAR acquisition present good results but it is constrained by the frequency of acquisition (from few to 10 days) which may be insufficient for a flooding hazard where the rising part of the flood last around 1 day. So, GEOSAR could be used to obtain frequent images (3-4 hours) with fine resolution (10-20 meters) to track and predict the evolution of flooding hazards.

Cryosphere: Glacier motion and snow cover and mass monitoring

To monitor the motion of glaciers, the advance or retreat of the glacier front and the vectors of motion of the surface must be determined. This information can be used to get the water resources of a specific zone, to understand the dynamics of ice and to get the mass budget of the cryosphere all of them related to climate change. The glacier motion can

be observed locally via GB-SAR acquisitions or by LEO imaging at larger scales [27]. However, the speed of glaciers in the order of centimetres or few meters per day is not suitable with revisit times of LEOSAR acquisitions. So, the more frequent observations from geosynchronous orbits will make possible to study the large scale fast moving glaciers not possible with current SAR acquisitions.

Regarding the snow cover monitoring, the changes on the backscatter signal from snow melting zones can be tracked for water resource management, flood warning, avalanche warning and land surface model parameterization and numerical weather prediction [28]. Additionally, with two acquisitions at different frequencies the snow mass can be also obtained. So, a dual beam GEOSAR acquisition could be considered to track both, the mass of dry snow and the location of the region with melting snow.

Earthquakes, volcanoes and landslides

Other natural hazards such as Earthquakes [29], volcanoes [30][31] and landslides [32][33], may produce changes on the land surface after the event. With a GEOSAR acquisition with a fixed beam pointing to particular zones with high risk of these phenomena would make possible to track the evolution of the surface deformations and detect potential zones with damaged buildings. Additionally, the monitoring of the surface changes before the event could be useful to predict these hazards in order to reduce some of their effect on human life. For this reason, it is necessary a fixed system, constantly monitoring those areas with large coverage which is only possible considering a GEOSAR mission.

Subsidence: monitoring anthropogenic and natural motion

The removal of liquids from pore spaces of rocks or the rocks themselves due to natural processes or due to human activities may result in surface subsidence which can be especially critical over urban areas. With current LEO radars the long-term secular deformation signal can be monitored from regional subsidence [34]. However, the localized subsidence (100 m scale) with more accelerated deformation caused by sinkhole formation or accelerating instability of building undergoing structural failure cannot be tracked. High resolution GEOSAR images could be useful to obtain this information with a day-by-day tracking of the local deformations.

1.6 Thesis motivation and objectives

In current SAR missions, the transmitting/receiving chain is usually carried either on an airplane or spacecraft or mounted in an on-ground station (GB-SAR). However, these techniques present several differences in acquisition geometry and performance. Regarding the acquisition geometry, the lower altitude of GB-SAR and airborne SAR makes necessary

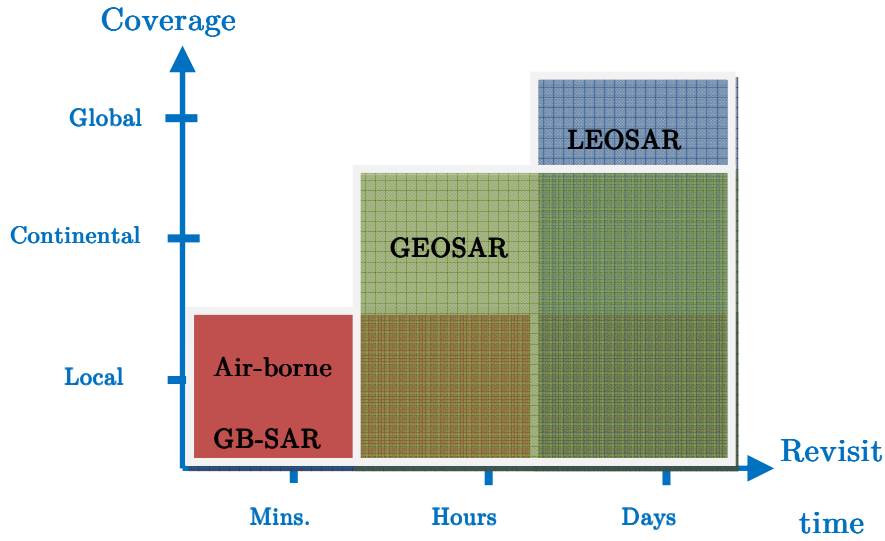


FIGURE 1.10. GEOSAR revisit time/coverage vs. current configurations

to image over a wide range of incidence angles to reach the desired coverage. On the other hand, the same coverage may be obtained with a space-borne configuration taking a narrower beam providing more uniform illumination over the scene. Therefore, GB-SAR and air-borne SAR acquisitions will be limited by the system coverage (few kilometres). However, the LEO orbit generally used in space-borne SAR (LEOSAR) to get global Earth coverage constrains the revisit time of a specific region which typically ranges from several days to weeks.

In this context, the novel GEOSAR technique is analysed in this thesis. The non-perfect geostationary orbits of geosynchronous satellites where the transmitter and receiver are placed are enough to get the necessary relative motion to form the synthetic aperture. Furthermore, the nearly fixed position of these satellites assures constant monitoring over large areas. Therefore, with GEOSAR, the revisit time may be reduced hours at the expenses of reducing the global coverage of a LEOSAR. Therefore, GEOSAR may fill the gap between the coverage/revisit time properties of current GB-SAR airborne SAR and LEOSAR technologies, as shown in Figure 1.10.

As previously mentioned, the solution proposed in this thesis consists on a SAR system, working with typical LEO parameters in terms of transmitted power and antenna size, and long coherent integration of pulses (during hours) to increase the low Signal-to-Noise Ratio (SNR) due to the large distances. Hence, the scope of this thesis is to analyse the main features of a GEOSAR system (geometric and radiometric analysis, parameters definition, focusing, etc.), as well as the potential problems and limitations, to determine its feasibility for SAR acquisition. The theoretical study will be completed by the design of a GEOSAR simulator tool in order to evaluate and validate the most relevant results.

Therefore, the main objectives of this thesis will be:

i) **LEOSAR performance and calibration revision:** during the last two years, the radiometric study of the operation modes (Stripmap, ScanSAR, Spotlight and TOPSAR) for SEOSAR PAZ system has been assessed. Therefore, the most relevant results obtained from these analyses will be used for the initial study of GEOSAR acquisition. Then, a strong effort to identify the similarities and differences between LEOSAR and GEOSAR acquisition is necessary to start with the GEOSAR analysis.

ii) **Study of the geometry in GEOSAR configuration.** The significant differences between LEO and geosynchronous orbits will be important to redefine the acquisition geometry. The main SAR geometrical parameters (i.e. satellite track, slant range to targets, incidence and look angles, azimuth and elevation angles, coverage, etc.) will be calculated considering the new geometry.

iii) **Radiometric performance analysis of GEOSAR.** The novel configuration makes necessary to study the main radiometric SAR parameters of GEOSAR acquisition such as synthetic aperture formation and achievable resolution, Doppler analysis of the received echoes, timing and PRF selection, Signal-to-Noise ratio limitations, ambiguity levels, GEOSAR image reconstruction, etc.

iv) **Development of a GEOSAR simulation tool.** The development of a GEOSAR simulator tool is essential to validate the theoretical analysis. The simulator must encompass from the generation of synthetic raw data to focusing. Other functionalities, such as atmospheric compensation techniques will be also incorporated in the simulator. Flexibility on the orbital parameters selection, scene definition and acquisition parameters will be important to provide the simulation with the versatility for GEOSAR simulations.

v) **Analysis of potential problems related to GEOSAR acquisition.** The design of a GEOSAR mission presents some problems that must be analysed to demonstrate its feasibility for SAR acquisition. SNR limitations and atmospheric decorrelation over the long integration time will be critical factors in the GEOSAR acquisition that must be carefully analysed.

vi) **Ground-Based SAR (GB-SAR) data to check the theoretical results.** In order to reinforce the theoretical results obtained in the GEOSAR analysis, experimental GB-SAR data will be used.

vii) **Bistatic Dual-beam dual-frequency GEOSAR mission analysis .** A mission performance analysis under an European Space Agency (ESA) contract carried by several partners such as SES ASTRA, Politecnico di Milano, Aresys, ThalesAlenia Space, Gamma Remote Sensing, Cranfield University, University of Reading and Universitat Politècnica de Catalunya (UPC) will be presented. The task presented in this thesis corresponds to

the analysis of the bistatic performance for the GEOSAR mission which was assigned to UPC.

1.7 Thesis organization

The work presented in this thesis is divided in six chapters corresponding to the different aspects studied during the GEOSAR mission analysis. In this first chapter, the basic concepts of SAR acquisition have been presented. Additionally, a quick look to GEOSAR concept and the possible applications have been also introduced. Finally, the motivation, objectives and organization of the thesis have been presented.

In Chapter 2, the GEOSAR geometry is studied in depth. First of all, an orbital analysis of the geosynchronous satellites is presented and the most relevant parameters of SAR acquisition are particularized for the GEOSAR case.

Chapter 3 includes the most relevant radiometric parameters of GEOSAR acquisition such as antenna design, Doppler analysis, timing and PRF selection, ambiguity analysis, power link budget and image reconstruction. The particularities of GEOSAR acquisition in the different analysis are studied in depth to identify the pros and cons of using a geosynchronous satellite for SAR purposes.

In Chapter 4, different possibilities on the acquisition configuration for surface and atmospheric monitoring are shown. Considering different integration time and orbital configuration the achievable resolutions can be adjusted depending on the user requirements for each application.

A bistatic analysis of a dual-beam dual-frequency GEOSAR mission is summarised in Chapter 5. The most critical aspects of the bistatic acquisition are assessed in this section.

Finally, in Chapter 6, the first steps on the design of a passive on-ground receiver for a bistatic GEOSAR acquisition are presented.

Chapter 2

Geosynchronous SAR Geometry

In this section the geosynchronous orbits are analysed. After the description of the orbital ephemerides that characterize a geosynchronous orbit, the most relevant parameters of SAR acquisition are recomputed for the GEOSAR geometry. Finally, the impact of the orbital design in the system resolution is studied for the proposed GEOSAR configurations.

2.1 Geosynchronous orbits analysis

2.1.1 *Orbital ephemerides and parameters*

The orbital ephemerides are the parameters that will identify univocally the satellite position at any time. They consist of three angular parameters which orientate the orbit (inclination, right ascension of the ascending node and argument of the perigee), two parameters defining the shape of the orbit (semi-major axis and eccentricity) and another parameter to locate the satellite within the orbital track (usually given by the time pass through the perigee or the true anomaly).

So, the *inclination* (i) and the *right ascension of the ascending node* (Ω) will establish the orbital plane in space. Besides, the orientation of the elliptical orbit in its plane will be given by the *argument of the perigee* (ω). These parameters are graphically presented in Figure 2.1.

The *inclination* is defined as the angle between the equatorial plane of the Earth and the orbital plane. This is counted positively between 0° and 180° at the ascending node. In the case of geosynchronous satellites considered in this analysis, this parameter will be some tens of a degree since quasi-equatorial orbits are desired.

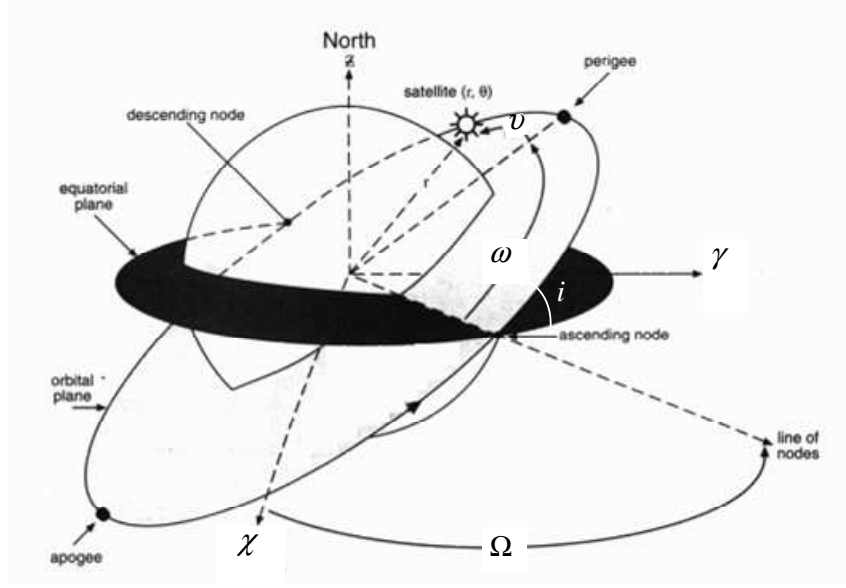


FIGURE 2.1. Satellite orbital ephemerides definition [64]

The other parameter that will define the position of the orbital plane was the *right ascension of the ascending node* (RAAN or Ω). This is the angle between the vernal equinox (χ) and the position of the ascending node. The orbital plane orientation is univocally determined by these two parameters.

Once the plane is located, a parameter fixing the orbit orientation in its plane is necessary. This parameter is known as the *argument of the perigee* (ω). This is the angle between the direction of the ascending node and the direction of the perigee (the closest satellite position with respect to the Earth) taken positively from 0° to 360° .

On the other hand, the orbit shape and satellite position at any time must be determined. The motion of a satellite in a geosynchronous orbit is governed, as well as all orbiting bodies, by the Kepler's laws. Kepler determined that the trajectories of planets around the Sun were elliptical. This concept can be applied to the satellite motion around the Earth as well. Then, a Keplerian system defines the relative motion between two point bodies (satellite-Earth system) under the sole influence of the gravitational attractions.

The Kepler laws were extended and mathematically characterized by the Newton's law. From that formulation, the orbit described by any satellite around the Earth can be characterized by the ellipse defined as [65]:

$$r = \frac{a(1 - e^2)}{1 + e \cos v} \quad (2.1)$$

where r is the distance between the satellite and the centre of the Earth, a is the semi-major axis of the ellipse described by the orbiting body, e is the orbit eccentricity and v is the true anomaly that defines the actual position of the satellite ranging from 0 to

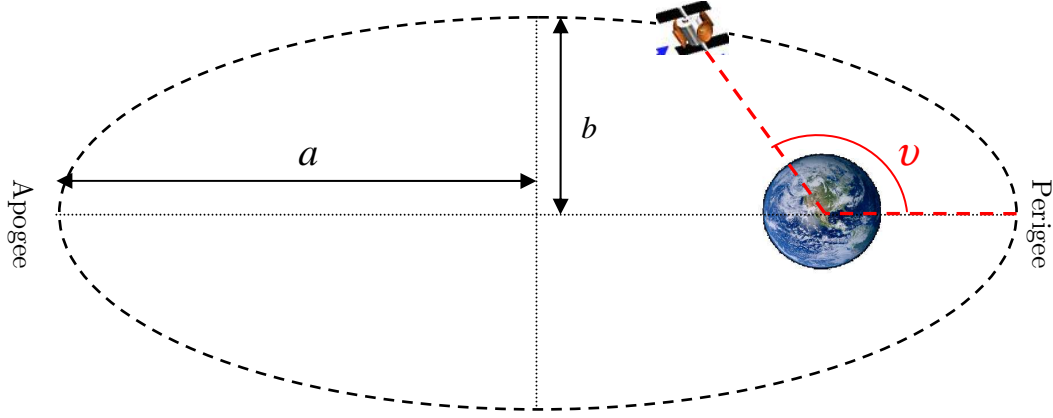


FIGURE 2.2. Orbital shape and satellite location parameters

360 degrees. The maximum radius of the orbit will be at 180° of true anomaly. The maximum distance to the Earth is called apogee. On the other hand, when the true anomaly is zero, the radius will be minimum and the satellite will be at the perigee. Then, the true anomaly is the angle between the direction of the perigee and the current position of the satellite. Instead of using the true anomaly, the position of the satellite can be described by the time elapsed from the pass through the perigee (t_p) which is considered as the reference initial time. The basic parameters that will define the satellite orbital position can be seen in Figure 2.2.

The orbit eccentricity (e) is obtained from the ratio between the semi-major axis (a) and semi-minor axis (b) of the ellipse shown in Figure 2.2 as in (2.2). Small eccentricities are also considered in this analysis since quasi-circular orbit will be taken to obtain synthetic apertures of a few hundreds of kilometres at most.

$$e = \sqrt{1 - \left(\frac{b}{a}\right)^2} \quad (2.2)$$

Other orbital important parameters may be obtained by using the third Kepler's law. So, it is possible to relate the semi-major axis of the orbit with the orbital period as [65]:

$$T_{orb} = 2\pi \frac{a^{3/2}}{\mu^{1/2}} \quad (2.3)$$

where μ is the Earth gravitational constant ($GM_E = 3.986 \cdot 10^{14} m^3 / s^2$). Furthermore, the satellite instantaneous velocity with respect to a fixed reference system centred at the Earth centre of mass may be obtained as [65]:

$$V_s = \sqrt{\mu \left(\frac{2}{r} - \frac{1}{a} \right)} \quad (2.4)$$

2.1.2 *Geosynchronous orbital parameters definition for a nearly-zero inclination quasi-circular orbit*

In this section, the orbital ephemerides and other parameters introduced in section 2.1.1 are particularized for a geosynchronous satellite in a nearly-zero inclined quasi-circular orbit which will be the focus of this thesis.

The main feature of a geosynchronous orbit is the orbital period which is equal to the Earth rotation period or one sidereal day (86164 seconds). Therefore, from equation (2.3), a semi-major axis of 42164 Km is obtained. As an example, considering a quasi-circular orbit with eccentricity of 10^{-4} , a radius variation ranging from 42160 Km at the perigee to 42168 Km at the apogee is found. This particular example is graphically presented in Figure 2.3.

So, as shown in equation (2.4), the orbital radius variations will result in a non-constant instantaneous satellite velocity. Particularizing expression (2.4) for the previous example with an eccentricity of 10^{-4} , the satellite instantaneous velocity history shown in Figure 2.4. As seen, the maximum velocity (3074.97 m/s) is obtained at the perigee when the satellite is closer to the Earth. On the other hand, the minimum velocity obtained at the apogee is 3074.35 m/s.

These results are consistent with the second Kepler's law. However, the relative motion with respect to the Earth surface considering a rotating reference system will be the interesting velocity to take into account in the GEOSAR performance analysis.

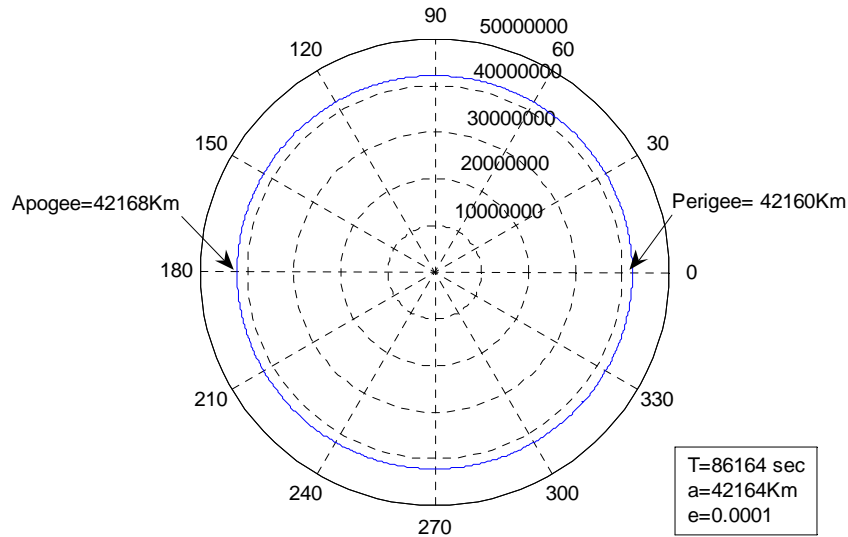


FIGURE 2.3. Quasi-circular geosynchronous orbit example with eccentricity of 10^{-4}

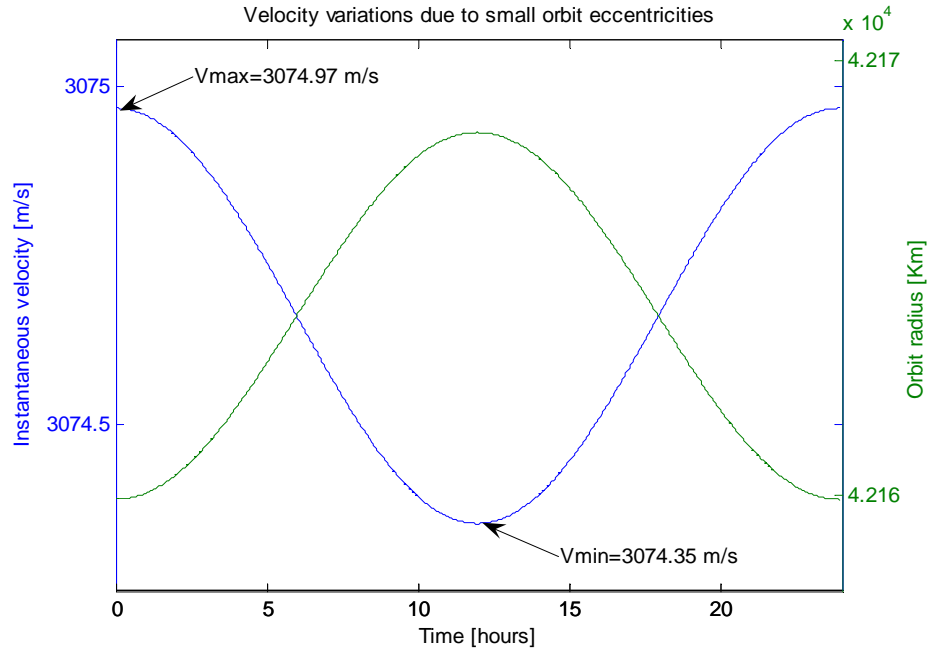


FIGURE 2.4. Geosynchronous satellite instantaneous velocity history considering an orbital eccentricity of 10^{-4}

Parameter	Symbol	Formula	Typical values considered
Orbit semi-major axis	a	$a = \left(\frac{T \mu^{1/2}}{2\pi} \right)^{2/3}$	42164Km
Orbital period	T	$T = T_{sidereal}$	86164sec
Radius vector of the orbit	r	$r = \frac{a(1 - e^2)}{1 + e \cos v}$	42100Km – 42200Km
Instantaneous velocity	V_s	$V_s = \sqrt{\mu \left(\frac{2}{r} - \frac{1}{a} \right)}$	3070m/s-3080m/s
Mean velocity	\bar{V}_s	$\bar{V}_s = \frac{2\pi a}{T}$	3074.66m/s
Orbit inclination	i	-	$< 1^\circ$
Orbit eccentricity	e	$e = \sqrt{1 - \left(\frac{b}{a} \right)^2}$	< 0.01

TABLE 2.1. Geosynchronous orbital typical parameters and formulas for the examples considered in this analysis.

Thus, the main parameters that will characterize a nearly-zero low-inclined orbits taken in the GEOSAR analysis of this thesis are summarized in Table 2.1. The parameters with a

fixed value determined by the geosynchronous orbital configuration are marked in bold type. On the other hand, for those parameters that will be constantly changing along the satellite orbit or that will depend on each acquisition, a range of reasonable values is provided in order to have an idea of which magnitudes will be considered. The orbital parameters such as the RAAN or the argument of the perigee have not been included in Table 2.1 since they can be chosen depending on the desired acquisition features.

2.2 Geosynchronous SAR acquisition parameters

The most important parameters of SAR acquisition will be particularized for a general GEOSAR acquisition considering low-inclined and low-eccentric orbits. This section starts with a brief review of the basics on the spherical geometry that will be used all along this section to derive the SAR parameters.

2.2.1 *Review of basics on the geometry of the sphere*

Firstly, before the analysis of the geosynchronous geometric parameters, in this section a brief introduction to the essential concepts on spherical trigonometry will be presented since they will be used to obtain the relations between the different geometric parameters that define a GEOSynchronous SAR system.

To understand the positions and motion of any celestial body, it is necessary to have a clear understanding of spherical geometry. This corresponds to the study of the geometry over the surface of a sphere. First of all, a great circle of a sphere is defined since all the formulas on spherical trigonometry are referred to this concept.

A great circle, as it can be seen in Figure 2.5 in red, is defined by the intersection of the sphere with a plane which contains the centre of the sphere. Any other intersection with a plane that does not contain the centre is known as small circle (green circle in Figure 2.5) and they will not be useful for this analysis. Any great circle divides the sphere in two identical parts. Once the great circles have been introduced, the spherical triangles are another concept necessary in the satellite motion analysis. A spherical triangle is a triangle drawn on the surface of a sphere whose sides are all arcs of great circles. Besides, any spherical triangle has to fulfil three additional properties:

- a) Any two sides are together longer than the third one.
- b) The addition of the three angles is greater than 180° .
- c) Each individual spherical angle is less than 180° .

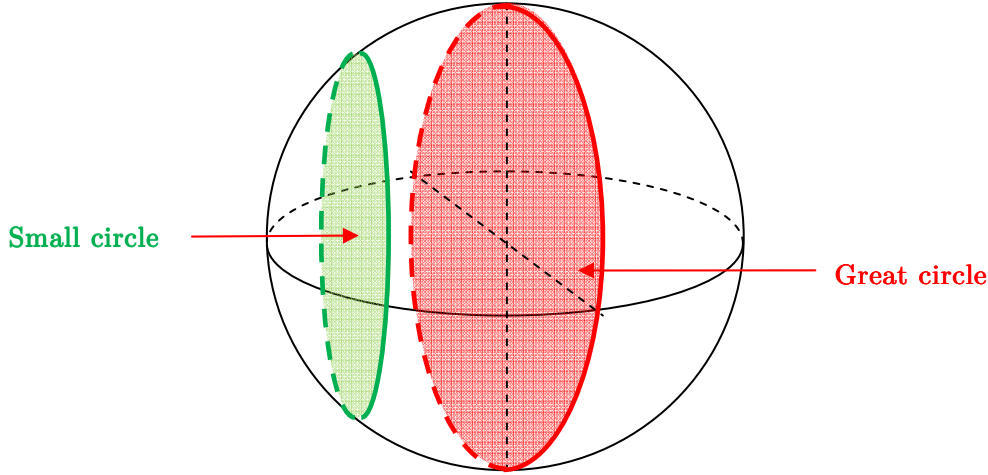


FIGURE 2.5. Geometry of the sphere: great circle definition.

Examples of what it is and what it is not a spherical triangle can be seen in Figure 2.6. The triangle P-A-B is not a spherical triangle since the side AB is an arc of a small circle.

On the other hand, the triangle P-C-D is a spherical triangle since all its sides are arcs of great circles.

It is important to see that the lengths of the sides of a spherical triangle are expressed in angular units. Considering that the length of an arc (s) which subtends an angle (θ) at the centre of a circle of radius (r) is given by $s = \theta r$; and knowing that all the arcs that compose the spherical triangle are segments of great circles with the same radius, a unitary radius can be taken. Then the arc s can be expressed directly as $s = \theta$ with radians units.

Similarly to working with triangles in planar trigonometry, it is necessary to use the formulation of spherical trigonometry to perform calculations with spherical triangles. The angle between two sides is defined as the angle between the tangents of the two crossing great circles at this point. In Figure 2.7, a spherical triangle formed by the arcs (a, b, c) and the vertex angles (A, B, C) is shown. In Figure 2.8, the angle at vertex B is shown in more detail. Considering the spherical triangle of Figure 2.8, some relations between them are given by the spherical trigonometric theorems.

Then, the arc lengths (a, b, c) and the vertex angles (A, B, C) of any spherical triangle are related by the *Spherical Law of Sines* and the *Spherical Law of Cosines* [66]. These are the spherical analogues laws of the planar *Law of sines* and *Law of Cosines*. The formulas, not demonstrated in this document, are given in (2.5) and (2.6), respectively.

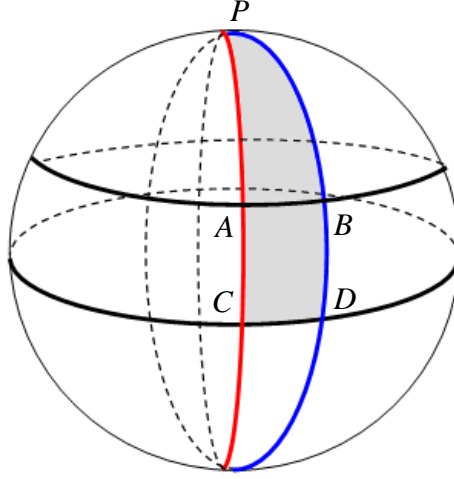


FIGURE 2.6. Spherical triangles over the sphere surface.

Spherical law of sines:

$$\frac{\sin a}{\sin A} = \frac{\sin b}{\sin B} = \frac{\sin c}{\sin C} \quad (2.5)$$

Spherical law of cosines:

$$\cos a = \cos b \cos c + \sin b \sin c \cos A \quad (2.6)$$

Other trigonometric properties of the spherical geometry that will be used in the following section are the polar cosine formula (2.7) and the cotangent formula (2.8) [66]:

$$\cos A = -\cos B \cos C + \sin B \sin C \cos a \quad (2.7)$$

$$\cos b \cos A = \sin b \cot c - \sin A \cot C \quad (2.8)$$

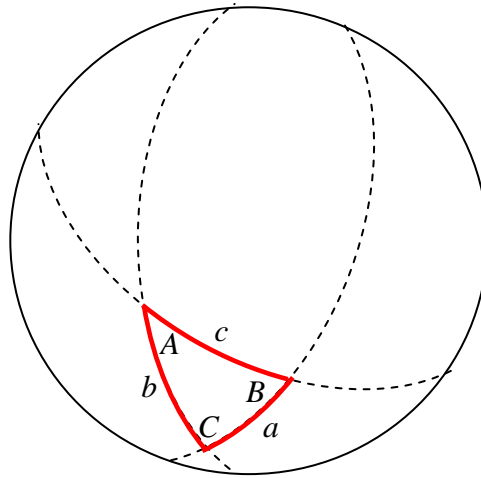


Figure 2.7. Spherical trigonometry over spherical triangles.

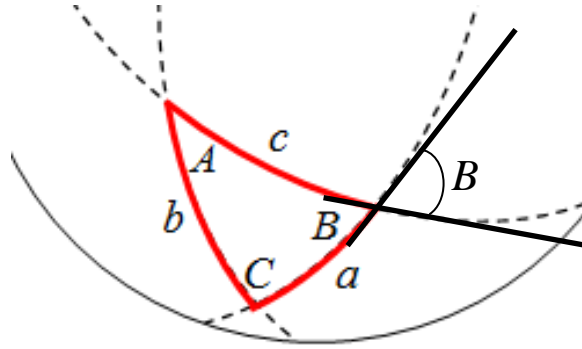


FIGURE 2.8. Vertex angle defined at point B between the tangents of the intersecting great circles at that point.

2.2.2 Geosynchronous satellite track

The satellite track is defined as the locus of the points of intersection of the Earth's centre-satellite vector with the surface of the Earth. In order to compute the satellite track, the satellite motion with respect to a rotating Earth centred system must be considered. Then, it will give information about the relative motion between the satellite and a fixed point over the Earth's surface. Firstly, the formulation for a fixed Earth will be presented and then the necessary modifications will be introduced to reproduce the actual situation with the rotating Earth.

The scheme considering a fixed Earth is shown in Figure 2.9. The coordinates of the satellite $(\lambda'_{SL}, \varphi_{SL})$ defines the longitude and latitude at a given time with respect to a reference meridian and to the equator, respectively. The longitude of the ascending node with respect to the reference meridian is called λ_{AN} and it will be used to relate the longitudinal and latitudinal coordinates of the satellite. This can be obtained using the cotangent formula (2.8) in the spherical triangle AN-SL-P from Figure 2.9 as follows:

$$\cos b \cos A = \sin b \cot c - \sin A \cot C$$

considering:

$$\begin{aligned} a &= u \\ b &= \lambda'_{SL} - \lambda_{AN} \\ c &= \varphi_{SL} \end{aligned} \quad \begin{aligned} A &= 90^\circ \\ C &= i \end{aligned}$$

where A, the angle at vertex P, is equal to 90° . Then:

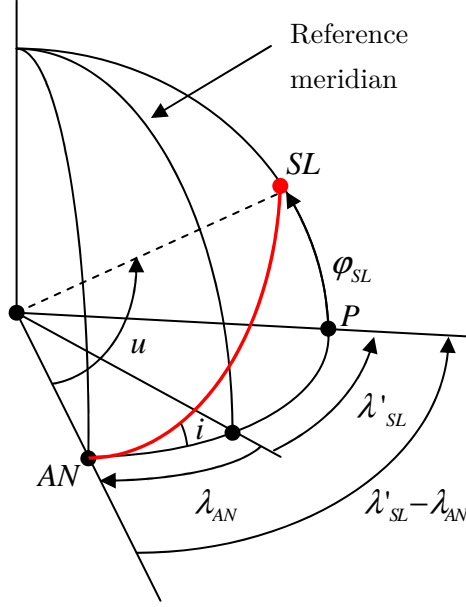


FIGURE 2.9. Satellite track fixed Earth reference system.

$$\cos(\lambda'_{SL} - \lambda_{AN}) \cos 90^\circ = \sin(\lambda'_{SL} - \lambda_{AN}) \cot \varphi_{SL} - \sin 90^\circ \cot i$$

$$0 = \sin(\lambda'_{SL} - \lambda_{AN}) \cot \varphi_{SL} - \cot i$$

$$\frac{1}{\tan i} = \sin(\lambda'_{SL} - \lambda_{AN}) \frac{1}{\tan \varphi_{SL}}$$

and finally:

$$\tan \varphi_{SL} = \sin(\lambda'_{SL} - \lambda_{AN}) \tan i \quad (2.9)$$

which relates the satellite latitude with the relative longitude, the orbit inclination and the longitude of the ascending node.

Furthermore, other relation between the parameters of the geometry shown in Figure 2.9 can be obtained. Considering the arc AN-SL that subtends an angle u (known as the *nodal angular elongation*), and taking the spherical law of sines (2.5) in the same spherical triangle, the *nodal angular elongation* can be related with the satellite orbital parameters as:

$$\frac{\sin \varphi_{SL}}{\sin i} = \frac{\sin(\lambda'_{SL} - \lambda_{AN})}{\sin SL} = \frac{\sin u}{\sin 90^\circ}$$

$$\sin \varphi_{SL} = \sin i \sin u \quad (2.10)$$

Considering the spherical law of cosines (2.6):

$$\cos u = \cos(\lambda'_{SL} - \lambda_{AN}) \cos \varphi_{SL} + \sin(\lambda'_{SL} - \lambda_{AN}) \sin \varphi_{SL} \cos 90^\circ$$

where $a = u$, $b = (\lambda_{SL} - \lambda_{AN})$, $c = \varphi_{SL}$ and $A = 90^\circ$ (angle at vertex P). This leads to:

$$\cos u = \cos(\lambda'_{SL} - \lambda_{AN}) \cos \varphi_{SL} \quad (2.11)$$

Combining both (2.10) and (2.11), the following relation can be obtained:

$$\begin{aligned} \tan u &= \frac{\sin u}{\cos u} = \frac{\sin \varphi_{SL} / \sin i}{\cos(\lambda'_{SL} - \lambda_{AN}) \cos \varphi_{SL}} = \frac{\tan \varphi_{SL}}{\sin i \cos(\lambda'_{SL} - \lambda_{AN})} \cdot \frac{\sin(\lambda'_{SL} - \lambda_A)}{\sin(\lambda'_{SL} - \lambda_A)} \\ &= \frac{\tan \varphi_{SL} \tan(\lambda'_{SL} - \lambda_{AN})}{\sin i \sin(\lambda'_{SL} - \lambda_{AN})} \end{aligned}$$

using (2.9) at the numerator:

$$\begin{aligned} \tan u &= \frac{\sin(\lambda'_{SL} - \lambda_{AN}) \tan i \tan(\lambda'_{SL} - \lambda_{AN})}{\sin i \sin(\lambda'_{SL} - \lambda_{AN})} = \frac{\tan(\lambda'_{SL} - \lambda_{AN})}{\cos i} \\ \tan(\lambda_{SL} - \lambda_{AN}) &= \tan u \cos i \end{aligned} \quad (2.12)$$

The point with highest latitude is called the vertex of the track. The longitude of this point is, by definition, $\pi / 2$ radians larger than the longitude of the ascending node: $\lambda_V = \lambda_{AN} + 90^\circ$.

Let's consider now a rotational Earth reference system. To do that, a rotation of the reference meridian along time has to be taken into account. Being Δt the time elapsed from the satellite pass through the reference meridian; the previous equations must be recomputed. The satellite cross through the perigee is usually taken as the reference time, so Δt can be written as $\Delta t = t_p - t_0$, where t_p is the time elapsed since the satellite reached the perigee and t_0 is the time of the initial position of the reference meridian computed from the passage through the perigee.

Then, the variation of the reference meridian position due to the Earth rotation (Ω_E) can be written as $\Delta\lambda = \Omega_E \Delta t = \Omega_E (t_p - t_0)$. This will change the relative longitude (λ_{SL}) of the satellite with respect this Earth rotating reference system. Now, the satellite longitude with respect to the new reference will be $\lambda_{SL} = \lambda'_{SL} - \Delta\lambda$. This new situation is shown in Figure 2.10. In next section, the relations between the longitude and latitude histories and the orbital ephemerides are derived.

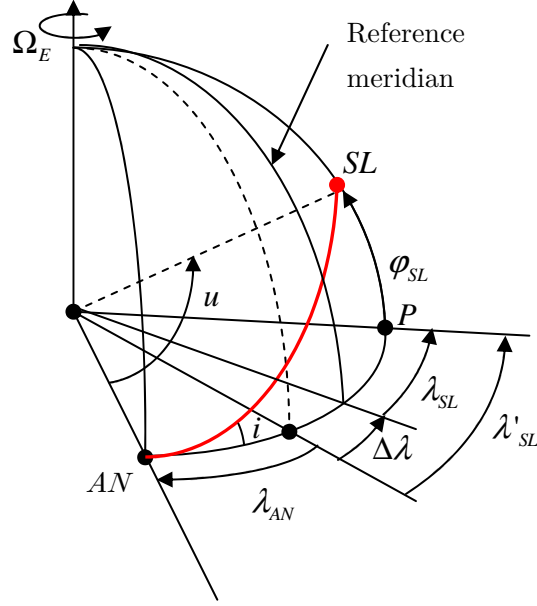


FIGURE 2.10. Satellite track in a rotating Earth reference system

2.2.2.1 Longitude history of the satellite track

For the sake of simplicity and without losing generality, let us consider as the reference meridian the meridian crossing at the longitude of the ascending node. This is equivalent to consider the longitude of the ascending node (λ_{AN}) equal to zero. Considering that, equations (2.9), (2.11) and (2.12) will be:

$$\sin \lambda'_{SL} = \frac{\tan \varphi_{SL}}{\tan i} \quad (2.13)$$

$$\cos \lambda'_{SL} = \frac{\cos u}{\cos \varphi_{SL}} \quad (2.14)$$

$$\tan \lambda'_{SL} = \tan u \cos i \quad (2.15)$$

So, the longitude of the satellite with respect to the meridian of the ascending node, considering a rotating reference system, can be obtained in different ways as follows:

$$\lambda_{SL} = \lambda'_{SL} - \Delta\lambda = \arcsin\left(\frac{\tan \varphi_{SL}}{\tan i}\right) - \Delta\lambda \quad (2.16)$$

$$\lambda_{SL} = \lambda'_{SL} - \Delta\lambda = \arccos\left(\frac{\cos u}{\cos \varphi_{SL}}\right) - \Delta\lambda \quad (2.17)$$

$$\lambda_{SL} = \lambda'_{SL} - \Delta\lambda = \arctan\left(\tan u \cos i\right) - \Delta\lambda \quad (2.18)$$

On the other hand, the term $\Delta\lambda$ can be re-written considering the mean anomalies of the satellite and the ascending node. The mean anomaly (M) is defined as the true anomaly of

an equivalent satellite in a circular orbit of the same period. This can be expressed as a function of the time with respect to the passage through the perigee as:

$$M = \frac{2\pi}{T}(t - t_p) = n(t - t_p) \quad (2.19)$$

being n the mean movement or mean angular velocity of a satellite with period T . Then:

$$\Delta\lambda = \Omega_E(t_s - t_0) = \Omega_E\left(\frac{M_s}{n} - \frac{M_0}{n}\right) = \frac{\Omega_E}{n}(M_s - M_0) \quad (2.20)$$

For a geosynchronous satellite with the same period than the Earth rotational period the mean movement (n) equals Ω_E . Furthermore, the angle u which is the angle between the ascending node and the position of the satellite can be computed as the addition of the argument of the perigee (ω) and the true anomaly of the satellite (v). Another parameter that usually appears on the orbital analysis is the *eccentric anomaly* (E). This corresponds to the true anomaly of the satellite at the present time mapped to an equivalent circular orbit [65]. The *mean anomaly* is related with the *eccentric anomaly* by:

$$M = E - e \sin E \quad (2.21)$$

With the previous consideration and equations (2.20) and (2.21), the longitude of the satellite can be finally written as:

$$\lambda_{SL} = \arctan\left(\tan(\omega + v)\cos i\right) - (E - e \sin E) + (E_0 - e \sin E_0) \quad (2.22)$$

For quasi-circular ($e \approx 0$) and non-inclined ($i < 1^\circ$) orbits, the satellite relative longitude with respect the nominal satellite longitude can be approximated as [50]:

$$\lambda_{SL} \cong \lambda_{SL_0} + 2e \sin(\Omega_E(t - t_p)) \quad (2.23)$$

being λ_{SL_0} the nominal satellite longitude if no eccentricities were considered.

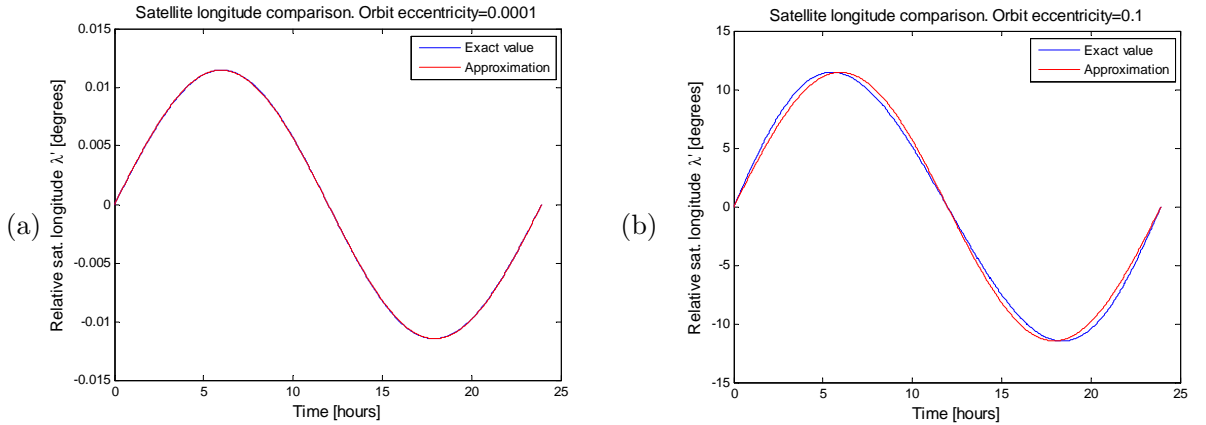


FIGURE 2.11. Satellite relative longitude evolution approximation. a) Considering an orbit eccentricity of 0.0001 and b) 0.1

The results given by the approximation (2.23) are compared in Figure 2.11 with the actual history given by equation (2.22). In Figure 2.11 a), the approximated and the exact longitude histories for an eccentricity of 10^{-4} are shown. In this case, the two functions have the same behaviour. Increasing the orbit eccentricity, as in Figure 2.11 b), up to $e = 10^{-1}$, slightly differences can be observed. However, higher eccentricities are out of interest in the geosynchronous satellites considered in this study. Then, (2.23) can be taken as a reasonable approximation for the nearly-zero inclination quasi-circular orbit GEOSAR case.

2.2.2.2 Latitude history of the satellite track

From the previous equations, the latitude of the satellite at any time can be also computed. In this case, the latitude is not affected by the Earth rotation and consequently, it does not depend on the choice of the origin position or reference meridian as in the longitude case. From (2.10), the satellite latitude can be written as:

$$\varphi_{SL} = \arcsin(\sin i \sin u) = \arcsin(\sin i \sin(\omega + v)) \quad (2.24)$$

Once again, considering the geosynchronous case with small inclinations of the orbit, the \arcsin function can be approximated by its argument while the $\sin i \approx i$. Therefore, the satellite latitude can be approximated as:

$$\varphi_{SL} = i \sin(\omega + \Omega_E(t - t_p)) \quad (2.25)$$

where the time across the perigee has been taken as a time reference like in longitude computation in (2.23). Therefore, combining the longitudinal and latitudinal motions given by (2.23) and (2.25) elliptical tracks will be typically obtained. So, the eccentricity will govern the longitudinal displacements of the satellite with respect to its nominal longitude. On the other hand, the inclination will determine the satellite latitudinal motion with respect to the equatorial plane. Finally, the argument of the perigee will establish the angular shift between both components, resulting in linear, elliptical or quasi-circular shapes of the relative satellite motion. Some example of the possible satellite tracks were shown in Figure 1.5.

2.2.3 *Satellite-targets slant range*

One of the key parameters of any remote sensing system is the distance to the illuminated targets. It will be important to identify the source of the received echoes as well as to compute the power link budget. The distance from the satellite to a target located at coordinates (λ_T, φ_T) over the Earth will depend on the satellite coordinates $(\lambda_{SL}, \varphi_{SL})$

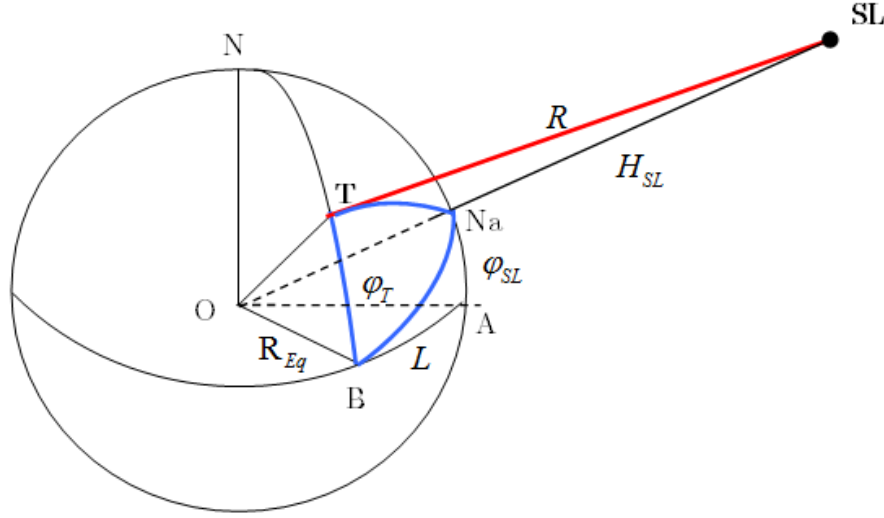


FIGURE 2.12. Earth-satellite geometry

and the geographical height (h_T) of the point over the Earth reference ellipsoid. The geometry for this analysis is shown in Figure 2.12.

The satellite latitude in Figure 2.12 is given by the centre angle $NaOA$, where Na is the sub-satellite point (or nadir) and the centre angle TOB corresponds to the target latitude. Another important parameter to take into account in the distance computation is the relative longitude between the satellite and the target. This angle, called $L = \lambda_T - \lambda_{SL}$, is defined by AOB .

To compute the distance between the satellite and the target (known in radar as *range*), the triangle with vertexes O-T-SL is used. The side OT which corresponds to the position of the target over the Earth's surface can be taken as the result of the local Earth's radius at that latitude plus the ellipsoidal height (h_T) of the considered target. The side OSL corresponds to the satellite distance from the Earth's centre. This can be obtained from the orbit analysis of the geosynchronous case with the two body problem (equation (2.1)) and corresponds to the addition of the local Earth's radius at the nadir point plus the satellite height over the nadir. Finally, the side TSL is the distance between the satellite and the desired target which is the goal of this section.

In order to obtain more precise results, on this analysis an ellipsoidal reference Earth model has been considered. The WGS84 [67] models the Earth as an ellipsoid with a semi-major axis (equatorial radius) of 6378,137 Km and a semi-minor axis (polar radius) of 6356,752 Km. Considering this model, the Earth's radius at arbitrary latitude φ can be easily obtained from the ellipse's formula as:

$$R_{ET}(\varphi_C) = \left(\frac{\cos^2 \varphi_C}{R_{Eq}} + \frac{\sin^2 \varphi_C}{R_{Pol}} \right)^{-1/2} \quad (2.26)$$

where φ_C is the geocentric latitude which is related with the geographical one (φ) by:

$$\tan \varphi_C = \frac{R_{Pol}^2}{R_{Eq}^2} \tan \varphi \quad (2.27)$$

Taking this consideration into account, the distance between the satellite (SL) and the target (T) can be obtained using the linear cosine law on the O-T-SL triangle. Then, the following equation is obtained:

$$R_{SL-T} = \sqrt{(R_{ET} + h_T)^2 + r^2 - 2(R_{ET} + h_T)r \cos \phi} \quad (2.28)$$

where R_{ET} is the local Earth's radius at the target latitude, h_T is the target height over the reference ellipsoid, r is the orbital radius of the satellite and ϕ is the angle $TONa$ shown in Figure 2.12. This angle can be obtained from the spherical triangle Na-T-B highlighted in blue in Figure 2.13 and Na-A-B by using the spherical sine (2.5) and cosine laws (2.6). From spherical cosine law, $\cos \phi$ can be written as:

$$\cos \phi = \cos \varphi_T \cos \xi + \sin \varphi_T \sin \xi \cos TBNa \quad (2.29)$$

The $\sin \xi$ and $\cos \xi$ can be obtained from the sine and cosine spherical laws applied on the triangle B-A-Na as in (2.30) and (2.31). On the other hand, $TBNa = \pi / 2 - i$ and, therefore, $\cos TBNa = \cos(\pi / 2 - i) = \sin i$. Then, combining the results obtained in (2.30) and (2.31) with equation (2.29), the expression obtained for $\cos \phi$ is shown in (2.32).

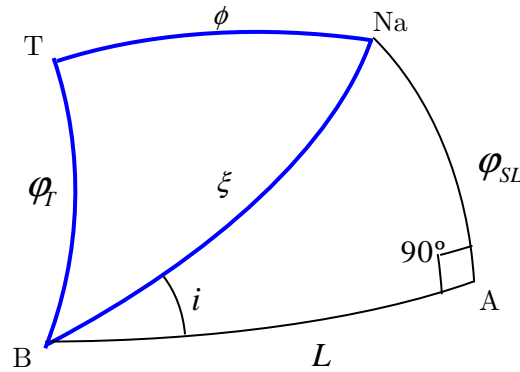


FIGURE 2.13. Na-A-B triangle used in slant-range computation

$$\frac{\sin \widehat{NaAB}}{\sin \xi} = \frac{\sin i}{\sin \varphi_{SL}} \rightarrow \sin \xi = \frac{\sin 90^\circ \sin \varphi_{SL}}{\sin i} = \frac{\sin \varphi_{SL}}{\sin i} \quad (2.30)$$

$$\begin{aligned} \cos \xi &= \cos \varphi_{SL} \cos L + \sin \varphi_{SL} \sin L \cos \widehat{NaAB} = \\ &= \cos \varphi_{SL} \cos L + \sin \varphi_{SL} \sin L \cos 90^\circ = \cos \varphi_{SL} \cos L \end{aligned} \quad (2.31)$$

$$\begin{aligned} \cos \phi &= \cos \varphi_T \cos \varphi_{SL} \cos L + \sin \varphi_T \frac{\sin \varphi_{SL}}{\sin i} \sin i = \\ &= \cos \varphi_T \cos \varphi_{SL} \cos L + \sin \varphi_T \sin \varphi_{SL} \end{aligned} \quad (2.32)$$

Using this result in (2.28), the target-satellite range can be computed as:

$$R_{SL-T} = \sqrt{(R_{ET} + h_T)^2 + r^2 - 2(R_{ET} + h_T)r(\cos \varphi_T \cos \varphi_{SL} \cos L + \sin \varphi_T \sin \varphi_{SL})} \quad (2.33)$$

In the particular GEOSAR case considered in this analysis with slight satellite longitude and latitude variations due to small inclinations and eccentricities, the slant range will change along the orbit accordingly to the satellite coordinates evolution obtained in (2.23) and (2.25). Besides, the small eccentricity of the orbit will cause variations on the orbit radius r , as given by equation (2.1), which will increase the fluctuations in the satellite-target distance. The parameters referred to the point target $(\varphi_T, \lambda_T, h_T)$ are fixed if a still point over the Earth's surface is considered.

Just as an example, a satellite placed on a geosynchronous orbit with coordinates 0° N and 30° W has been chosen (HISPASAT-1D). The orbit eccentricity has set up to $4 \cdot 10^{-4}$ and an orbit inclination to 0.05° . As a target, a point situated in Barcelona (41.23° N, 2.11° E) is considered. A target height of 450 meters (approximately the geographical height of Collserola communication tower) has been considered. The slant range variations obtained due to the satellite motion are shown in Figure 2.14.

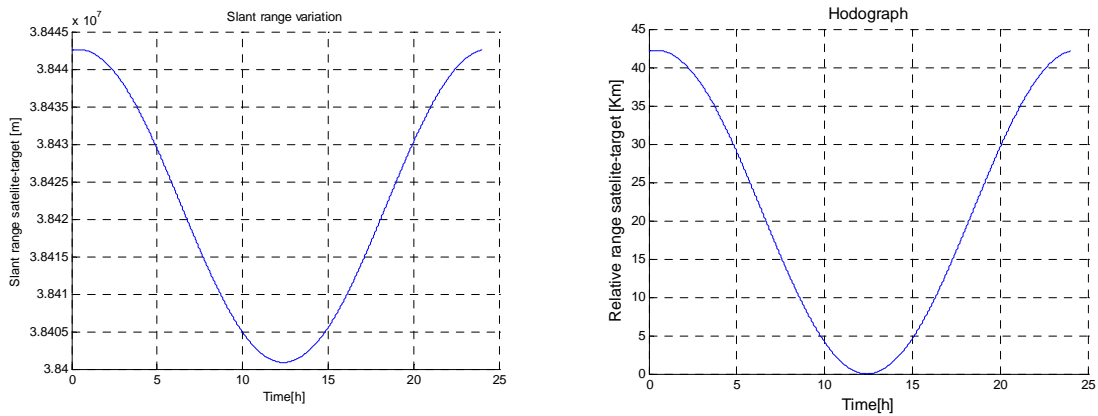


FIGURE 2.14. Slant range variations due to orbit perturbations. a) Absolute satellite-target range. b) Hodograph relative to the minimum slant range

The slant range obtained varies from 38442.6 Km to 38400.9 Km as it is plotted in Figure 2.14 a). Furthermore, in Figure 2.14 b), the hodograph is presented. It corresponds to the range variations relative to the closest distance. As it can be seen, a variation of 42 Km is obtained. Thus, a precise estimation of the satellite-target range considering all the features presented in this section has to be performed in order to get reliable results and process correctly the received echoes to focus the image.

2.2.4 Satellite location: elevation and azimuth angles

From a point of view of a target located at a point T, the satellite is seen on the sky in a fixed zone with slight variations due to the relative motion of the non-perfect geostationary orbit of the satellite. In order to define the location of the satellite, two angles are necessary and the most widely used are the elevation and azimuth angles. The satellite motion in the sky is usually called *analemma* of the satellite. These parameters will be important, for example, to point the on-ground stations towards the satellite for data downlink.

2.2.4.1 Elevation angle

The elevation angle is defined as the angle between the horizon at the point where the target is placed and the direction of the satellite measured in the plane that contains the satellite, the centre of the Earth and the considered target. In Figure 2.15, the triangle O-T-SL of Figure 2.12 is represented in the corresponding plane of interest. The elevation angle, called θ_{el}^T , can be computed using the right triangle O-T'-SL shown in Figure 2.15.

The angle $T'TSL$ in Figure 2.15 is equal to $\pi / 2 - \theta_{el}^T$. Since the angles of the triangle T-T'-SL must be equal to π radians, the angle $T'TSL = \pi - (\pi / 2 - \theta_{el}^T) - \pi / 2 = \theta_{el}^T$. Then, using planar trigonometry, the elevation angle can be obtained as:

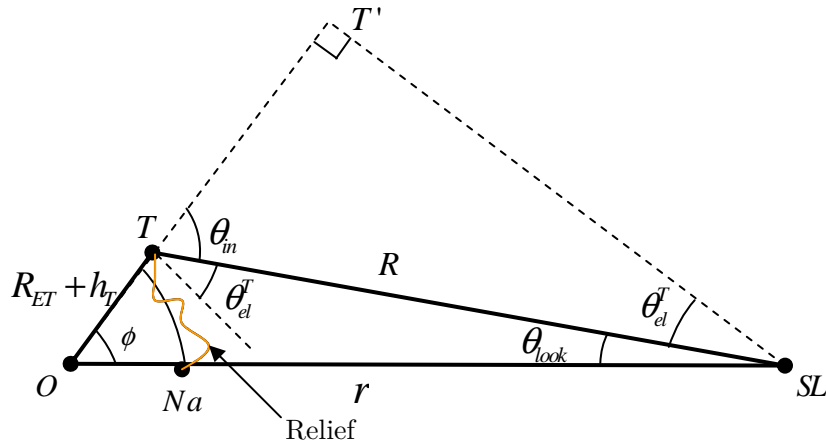


FIGURE 2.15. Satellite location in the sky. Elevation angle computation

$$\cos \theta_{el}^T = \frac{\overline{T'SL}}{R} \quad (2.34)$$

where the segment $\overline{T'SL}$ can be obtained from the triangle O-T'-SL as:

$$\sin \phi = \frac{\overline{T'SL}}{r} \quad (2.35)$$

Therefore, the elevation angle is computed with (2.36). The value of $\sin \phi$ can be easily found from (2.32) knowing that $\sin \phi = \sqrt{1 - \cos^2 \phi}$.

$$\theta_{el}^T = \arccos \left(\sin \phi \frac{r}{R} \right) \quad (2.36)$$

Similarly, the elevation angle can also be calculated considering the sine of the angle $TSLT'$. The analysis is presented next:

$$\sin \theta_{el}^T = \frac{\overline{T'T}}{R} \quad (2.37)$$

and

$$\cos \phi = \frac{(R_{ET} + h_T) + \overline{T'T}}{r} \rightarrow \overline{T'T} = r \cos \phi - (R_{ET} + h_T) \quad (2.38)$$

Using (2.38) in (2.37), another way to obtain the elevation angle is the following:

$$\theta_{el}^T = \arcsin \left(\frac{\cos \phi - (R_{ET} + h_T) / r}{R / r} \right) \quad (2.39)$$

Finally, taking the results of equations (2.36) and (2.39), the elevation angle is given in terms of the tangent as:

$$\begin{aligned} \tan \theta_{el}^T &= \frac{\sin \theta_{el}^T}{\cos \theta_{el}^T} = \frac{\frac{\cos \phi - (R_{ET} + h_T) / r}{R / r}}{\frac{\sin \phi}{R / r}} = \frac{\cos \phi - (R_{ET} + h_T) / r}{\sin \phi} \\ \theta_{el}^T &= \arctan \left(\frac{\cos \phi - (R_{ET} + h_T) / r}{\sin \phi} \right) \end{aligned} \quad (2.40)$$

2.2.4.2 Azimuth angle

The other angle necessary to univocally locate the satellite is the azimuth angle. This angle is measured in the incidence plane where the target is located between the direction of the

geographic north and the direction to the satellite nadir point over the Earth's surface. It corresponds to the spherical angle $NTNa$ in Figure 2.12. The azimuth angle takes values from 0 to 360 degrees depending on the orientation of the satellite with respect to the target considered. Using the spherical law of sinus in the spherical triangle N-Na-T, (2.41) is obtained.

$$\frac{\sin NTNa}{\sin(\pi / 2 - \varphi_{SL})} = \frac{\sin TNNa}{\sin \phi} \quad (2.41)$$

As it can be seen in Figure 2.12, the angle $TNNa$ is equal to BNA . This angle can be obtained from the spherical triangle N-B-A as:

$$\frac{\sin BNA}{\sin L} = \frac{\sin BAN}{\sin BON} = 1 \quad (2.42)$$

since $BAN = BON = 90^\circ$. Then, the angle $NTNa$ which will be called a from now on for simplicity, can be re-written as:

$$a = \arcsin\left(\frac{\sin TNNa}{\sin \phi} \sin(\pi / 2 - \varphi_{SL})\right) = \arcsin\left(\frac{\sin L}{\sin \phi} \cos(\varphi_{SL})\right) \quad (2.43)$$

The angle a computed with (2.43) always gives an angle between 0 and 90 degrees. Since the azimuth angle can be up to 360 degrees, a transformation will be necessary to obtain the final value of the azimuth angle. So, after computing the angle a , the azimuth angle (θ_{az}^T) will be obtained taking into account the relative position of the nadir point with respect to the target location.

The four possible situations are represented in Figure 2.16. The black dot represents the location of the target while the red one marks the position of the sub-satellite point or nadir. As it can be seen, depending on the position of the nadir point with respect to the target, the azimuth angle (θ_{az}^T) is computed in one way or another from a . The formulas required to obtain the azimuth angle are summarized in Table 2.2.

The behaviour of the relative motion of the satellite has been introduced in section 2.2.2, where the satellite longitude and latitude histories have been found in terms of the orbital ephemerides. Now that the satellite location has been characterized, the motion seen from the point of view of the targets in the Earth's surface can be better understood with the azimuth and elevation angles.

Just as an example, continuing with the scenario presented in the previous section where a satellite with nominal latitude and longitude of 0°N and 30°W and a point target near to Barcelona (41.23°N , 2.11°E) with a height of 450 meters were considered, the satellite *analemma* (or the figure described in the sky by the satellite) has been simulated.

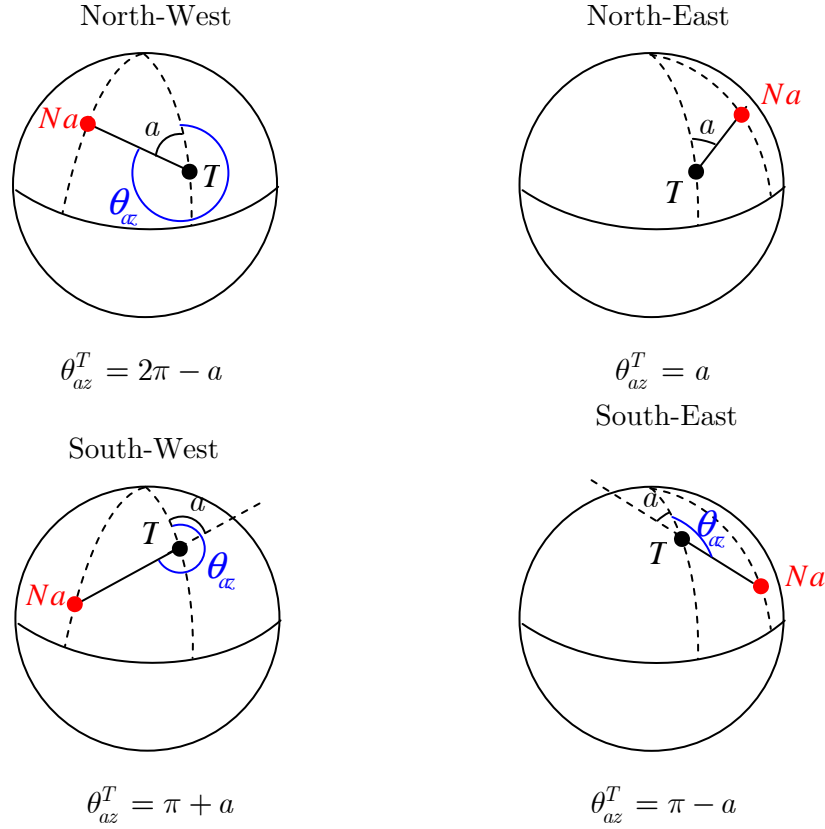


FIGURE 2.16. Determination of the azimuth angle

Sub-satellite point (Na) with respect to the target (T)	Relation between θ_{az} and a (degrees)
North-West	$\theta_{az}^T = 360^\circ - a$
North-East	$\theta_{az}^T = a$
South-West	$\theta_{az}^T = 180^\circ + a$
South-East	$\theta_{az}^T = 180^\circ - a$

TABLE 2.2. Azimuth angle computation depending on the satellite-target position.

In Figure 2.17, the situation is presented. As it is shown in Figure 2.17 a), the satellite describes an ellipse for low eccentricities and inclinations if a target-centred reference system is considered. If larger inclinations and/or eccentricities are considered, a figure 8 track [36] is obtained which is not the focus of this thesis. It means that the satellites movement on the sky is seen as an ellipse from the target point of view. The azimuth and elevation angles change all along the satellite orbital evolution. These variations are plotted in Figure 2.17 b) for the parameters presented in the previous paragraph. This figure on the sky is periodically repeated every day given the daily periodicity of the geosynchronous satellites.

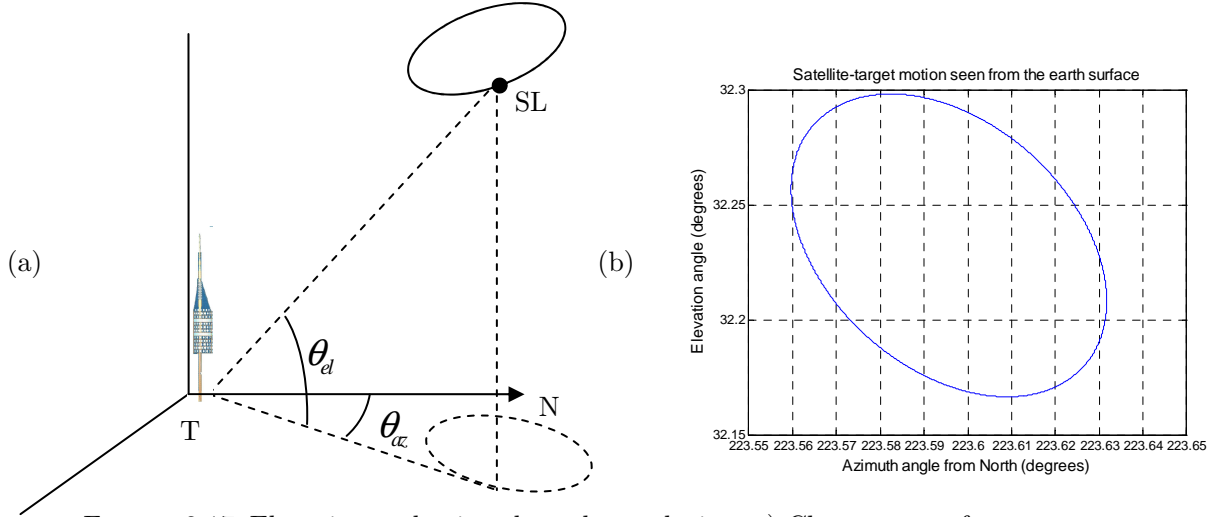


FIGURE 2.17. Elevation and azimuth angles evolution. a) Changes seen from a target-centred reference system. b) Satellite (0°N , 30°W) and target (41.23°N , 2.11°E) example.

2.2.5 Target location: look and incidence angles

Equivalently, the situation can be discussed from a point of view of the satellite. Then, a target over the surface is seen by the satellite in a determined position. The relative location of the target seen from the satellite can be defined by the look angle. Usually, the results are given in function of the incidence angle which will be defined in this section as well. These parameters will be important in the SAR acquisition analysis and they will be continuously appearing in the GEOSAR geometric and radiometric analysis.

2.2.5.1 Look angle

The look angle is defined as the angle between the nadir direction, perpendicular to the Earth's surface, and the direction of the illuminated target. This angle, called θ_{look} , corresponds to the angle \widehat{TSLO} in Figure 2.15. The look angle is also known as the nadir angle. From the cosine law in the triangle T-SL-O:

$$(R_{ET} + h_T)^2 = r^2 + R^2 - 2rR \cos \theta_{look} \quad (2.44)$$

where the look angle can be computed as:

$$\theta_{look} = \arccos \left(\frac{r^2 + R^2 - (R_{ET} + h_T)^2}{2rR} \right) \quad (2.45)$$

In the geosynchronous case, the range of possible look angles will be really small, given the large distance between the satellite and the Earth. The maximum look angle geometry is presented in Figure 2.18. As it can be seen, the maximum look angle is obtained when the incoming beam from the satellite is tangent to the Earth's surface. It means that the angle

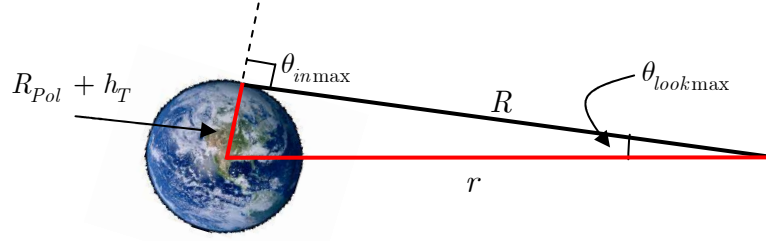


FIGURE 2.18 Maximum look angle. In the geosynchronous case, only a small range of look angles are allowed.

between the incoming beam and the Earth's radius at this point is a right angle. Then, from the law of sinus, the maximum look angle can be obtained easily as:

$$\frac{\sin \theta_{lookmax}}{R_{Pol} + h_T} = \frac{\sin 90^\circ}{r} \rightarrow \theta_{lookmax} = \arcsin\left(\frac{R_{Pol} + h_T}{r}\right) \quad (2.46)$$

Using the typical values of a geosynchronous satellite with an orbit radius of 42164 Km and considering an Earth's radius approximately at the poles with a target at 0 meters height, a maximum look angle of 8.7 degrees is obtained. So, the range of possible look angles will go from 0 to 8.7 degrees, a small range in the whole space seen by the satellite. The look angle will be a critical parameter on GEOSAR acquisition demanding high accuracy on the antenna pointing. Otherwise, small errors in pointing direction will result in large antenna footprint misalignment on the ground.

2.2.5.2 Incidence angle

Another way to express the position of the target with respect to the satellite is the incidence angle. This angle is related with the look angle so it does not provide any further information, but it is widely used in most of the SAR and radar backscattering analysis as shown in this thesis.

The incidence angle is the angle between the direction of the incoming satellite illumination and the direction perpendicular to the incidence plane which is the plane tangent to the Earth's sphere at the target location. It corresponds to the angle $\widehat{T'TSL}$ in Figure 2.15, where it is indicated by θ_{in} . The incidence angle can be obtained directly from the elevation angle as:

$$\theta_{in} = \frac{\pi}{2} - \theta_{el}^T \quad (2.47)$$

However, it will only be valid for a flat surface. The actual incidence angle should take into account the slopes or local topography of the imaged scene. On the other hand, it can also

be obtained from the look angle. Using the law of sinus in triangle O-T-SL in Figure 2.12:

$$\frac{\sin \theta_{look}}{R_{ET} + h_T} = \frac{\sin(\pi - \theta_{in})}{r} = \frac{\sin \theta_{in}}{r} \rightarrow \theta_{in} = \arcsin \left(\sin \theta_{look} \frac{r}{R_{ET} + h_T} \right) \quad (2.48)$$

In this case, the range of possible incidence angles for the geosynchronous case will vary from 0 degrees, corresponding to the nadir direction, to 90 degrees when the illumination is tangent to the Earth's surface. This maximum value can be seen in Figure 2.18 corresponding to the maximum look angle. This value can be also computed using the expression (2.48) with the maximum look angle (2.46). The result in (2.49) is obtained.

$$\theta_{in_max} = \arcsin \left(\frac{\cancel{R_{Pol}} + \cancel{h_T}}{r} \frac{r}{\cancel{R_{Pol}} + \cancel{h_T}} \right) = \arcsin 1 = 90^\circ \quad (2.49)$$

2.3 Geosynchronous SAR coverage

Another important parameter to take into account in the SAR design is the desired ground coverage or antenna footprint extension. This parameter is the ground patch that the radar is illuminating for a given look angle. Then, the swath will depend on the look angle at which the antenna is pointing and the antenna beamwidth considered.

One of the advantages of GEOSAR acquisition in front of current LEOSAR or GB-SAR is the large coverage of the system. So, the field-of-view of a single satellite will cover a large region of the Earth as shown in Figure 2.19. Therefore, with a single satellite, it will be possible to cover 1/3rd of the Earth, approximately. However, it would not be feasible to have simultaneous coverage of such large areas because the low gain of the antenna would result in too demanding transmitting power requirements. Thus, a narrower beam could be considered and the different zones accessible from the satellite can be illuminated periodically by changing the beam pointing. A mission analysis using this concept is presented in Chapter 5.

So, an acquisition scheme as the one presented in Figure 2.20 will be typically observed. In that case, the satellite points the antenna to a specific look angle and has an antenna beamwidth of $\Delta\theta_{look}$ that will determine the ground coverage of the system. Looking at the geometric parameters in Figure 2.20, the ground coverage (G_{cov}) can be obtained from the inner angles α_1 and α_2 as:

$$G_{cov} = \Delta\alpha \cdot R_{ET} = (\alpha_2 - \alpha_1)R_{ET} \quad (2.50)$$

being R_{ET} the local Earth's radius in the illuminated area. The inner angles α_1 and α_2 are obtained using the law of sinus:

$$\alpha_1 = \arcsin \left(\sin \theta_{look_near} \frac{R_{near}}{R_{ET}} \right) \quad (2.51)$$

$$\alpha_2 = \arcsin \left(\sin \theta_{look_far} \frac{R_{far}}{R_{ET}} \right) \quad (2.52)$$

where R_{near} stands for the range to the nearest point illuminated by the satellite while R_{far} corresponds to the furthest one. Similarly, the θ_{look_near} and θ_{look_far} are the look angle at which the nearest target is seen and the furthest one respectively. These angles can be easily obtained from the middle look angle and the beamwidth ($\Delta\theta_{look}$):

$$\theta_{look_near} = \theta_{look} - \frac{\Delta\theta_{look}}{2} \quad (2.53)$$

$$\theta_{look_far} = \theta_{look} + \frac{\Delta\theta_{look}}{2} \quad (2.54)$$

Finally, the near and far slant range can be computed from the look angles solving the second degree equations derived from the law of cosines (2.55) and (2.56). In those equations, r is the orbit radius while the look angles near and far corresponds to the ones computed in (2.53) and (2.54). Thus, the ground coverage can be computed from the look angle and the antenna beamwidth.

$$R_{near}^2 - 2r \cos \theta_{look_near} R_{near} = R_{ET}^2 - r^2 \quad (2.55)$$

$$R_{far}^2 - 2r \cos \theta_{look_far} R_{far} = R_{ET}^2 - r^2 \quad (2.56)$$

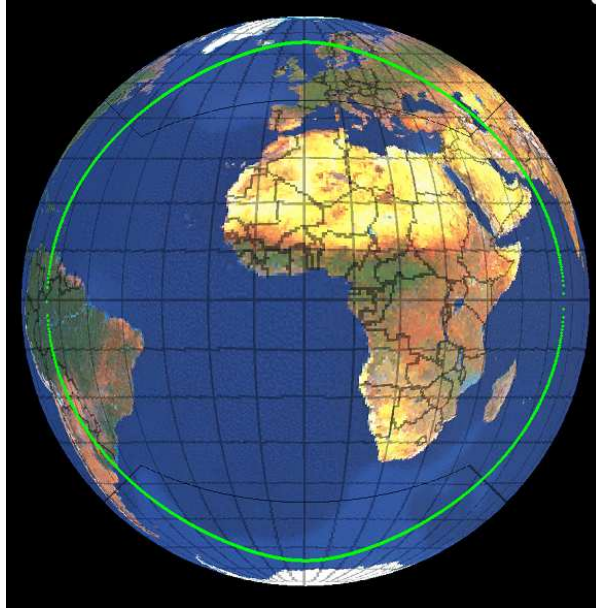


FIGURE 2.19 Geosynchronous satellite field of view.

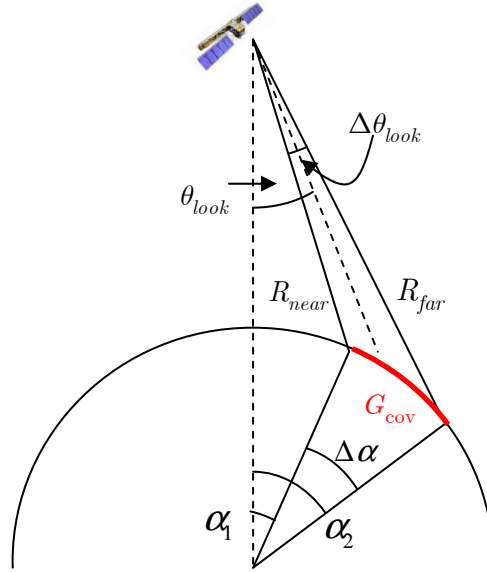


FIGURE 2.20 Ground coverage of the satellite.

$\Delta\theta_{look}$ [degrees]	$\theta_{look \ near}$ [degrees]	$\theta_{look \ far}$ [degrees]	R_{near} [Km]	R_{far} [Km]	$\Delta\alpha$ [degrees]	G_{cov} [Km]
0.15	4.925	5.075	36772	36840	0.0185	118.01
0.3	4.85	5.15	36739	36875	0.0371	236.05
0.5	4.75	5.25	36696	36923	0.0618	393.57
1.0	4	6	36595	37051	0.1239	788.53

TABLE 2.3. Ground coverage considering several antenna beamwidth at 5 degrees of look angle.

As an example to see which values will be obtained in the geosynchronous case, a look angle of 5 degrees has been considered and different antenna beamwidth have been tried. The results are shown in Table 2.3. As it can be seen, slight variation of the antenna beamwidth will provide a wide range of ground coverage or swath widths which can be really interesting depending on the acquisition purposes and applications of the system. So, in case of GEOSAR, very small beamwidth and high antenna gains will be considered to reach the desired coverage requirements.

On the other way around, sometimes it can be useful to obtain the necessary antenna beamwidth to reach a desired swath width or coverage for a given look angle. Looking at the previous equations, the isolation of the antenna beamwidth is really complicated and it cannot be solved by linear algebra. Thus, a reasonable approximation must be considered in order to obtain the required beamwidth. To do that, the Earth's surface in Figure 2.20 can

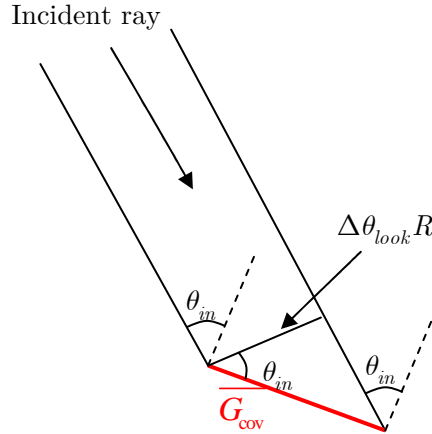


Figure 2.21 Flat surface approximation in swath ground coverage computation.

be considered locally flat. The new geometry is presented in Figure 2.21.

As it can be seen, the ground coverage can be approximated as:

$$\overline{G}_{cov} = \frac{\Delta\theta_{look} R}{\cos \theta_{in}} \quad (2.57)$$

where R is the slant range at the middle look angle and θ_{in} corresponds to the incidence angle, obtained from (2.48). So, the necessary antenna beamwidth can be obtained from the desired swath as:

$$\Delta\theta_{look} = \frac{\overline{G}_{cov} \cos \theta_{in}}{R} \quad (2.58)$$

To check the validity of the approximation presented in (2.58), different swath coverage has been evaluated as shown in Table 2.4. The values presented have been computed taking a middle look angle of 5 degrees. This corresponds to an incidence angle of 35.26 degrees and a middle slant range of 36805 Km.

As it can be seen, the values calculated with the approximation are close to the required coverage. The error increases with the width of the swath but, even in the worst case considered, it is not greater than a one per cent. In the analysis presented in this thesis, larger coverage will not be considered in order to avoid PRF selection and received power issues, as it will be seen in section 3.3 and section 3.5.

Desired G_{cov} [Km]	Approximated $\Delta\theta_{\text{look}}$ [degrees]	Actual G_{cov} [Km]	Swath width relative error (%)
100	0.1271	100.00	0.0038
200	0.2542	200.03	0.0151
300	0.3814	300.10	0.0339
500	0.6356	500.47	0.0943
1000	1.2712	1003.81	0.3810
1500	1.9067	1513.07	0.8716

TABLE 2.4. Antenna beamwidth required considering several ground coverage at 5 degrees of look angle.

2.4 Orbital design impact on the resolution

2.4.1 Orbital ephemerides impact on GEOSAR synthetic aperture

The length of the Synthetic Aperture achieved with a geosynchronous satellite will be determined by the relative motion between the platform and the scene considered. As it has been explained in section 2.2.2.1 and 2.2.2.2, the satellite longitude and latitude histories with respect to a rotating Earth coordinate system can be described by (2.23) and (2.25), respectively. The combination of both perpendicular directions will determine the length and shape of the Synthetic Aperture.

In the geosynchronous case, the definition of azimuth and range directions, introduced in section 1.1, is not as obvious as in a LEO system, where the along track and cross-track directions are well defined. Considering a geosynchronous orbit with an elliptical orbital track, the along and cross-track directions will depend on the time of the day considered. This phenomenon is shown in Figure 2.22. The red square represents the zone of interest illuminated by the radar (Europe in this example).

The slashed green lines represent the common LEO quasi-polar satellite tracks. Only some tracks have been plotted in Figure 2.22 for simplicity, but the behaviour is periodically repeated all over the Earth's surface. Furthermore, the ascending and descending tracks should be considered as well, but a similar behaviour should be obtained. However, the zone of interest will be only visible for the satellite for a short time during the entire satellite motion. As seen, for those satellites, the along-track (azimuth) and cross-track (range) directions are well defined in the scene. They do not depend on the time considered.

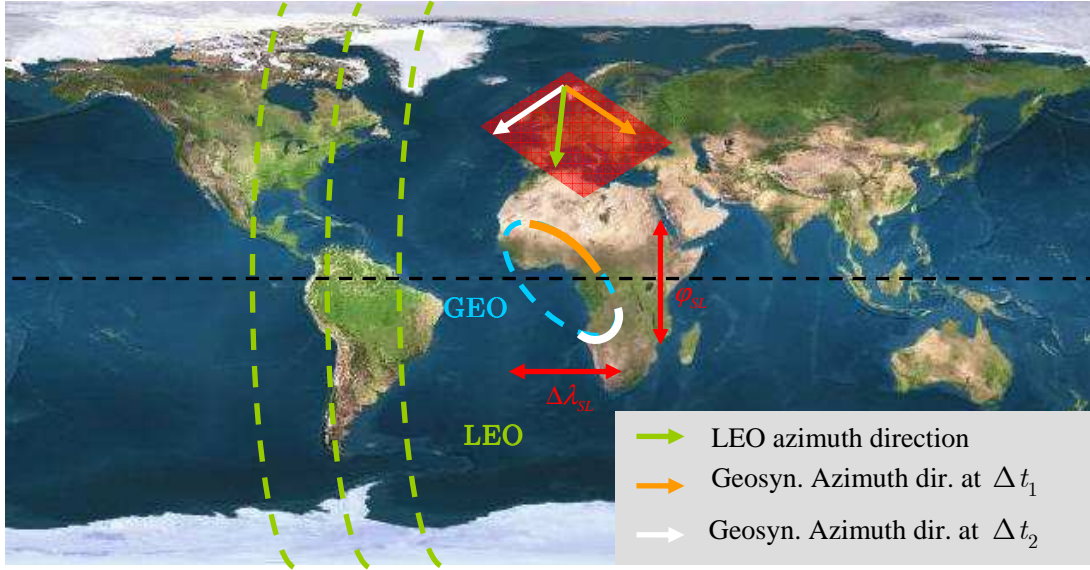


FIGURE 2.22 Along-track (azimuth) direction in Geosynchronous vs. LEO satellites.

On the other hand, the slashed blue line represents the typical behaviour of the satellite track of a Geosynchronous orbit. The satellite track is periodically repeated every day. Consequently, continuous monitoring of the zone of interest is achieved. In this case, depending on the time of the day considered to form the Synthetic Aperture, the along track direction will change. This phenomenon is shown in Figure 2.22 with the orange and white arrows which define the along-track direction at two different times. The cross-track directions have not been plotted in order not to hinder the understanding of the rest of the picture, but they will be perpendicular to the along-track direction in each case.

Then, several lengths and directions of the synthetic aperture can be achieved by playing with the duration of the acquisition and the instant when it is started. The maximum synthetic aperture length will be given by the semi-major axis of the ellipsoidal track described by the satellite and the relative position between the satellite and the zone of interest. In the following section, the impact of the different orbital ephemerides is studied.

2.4.1.1 Orbital eccentricity

As a first approximation, let's take a simple case with a geosynchronous satellite with only small eccentricity and zero-inclination, as shown in Figure 2.23. In this case, some variations from the satellite reference meridian are observed while the latitude is kept constant over the Equator. A swath over south Europe (yellow strip) at the same longitude than the satellite is considered. In Figure 2.23, the north-south illumination typical of those satellites can be appreciated. It is a new feature of the GEOSAR systems illuminating mid-latitudes, complementary to the LEO satellites which usually have East-West illumination.

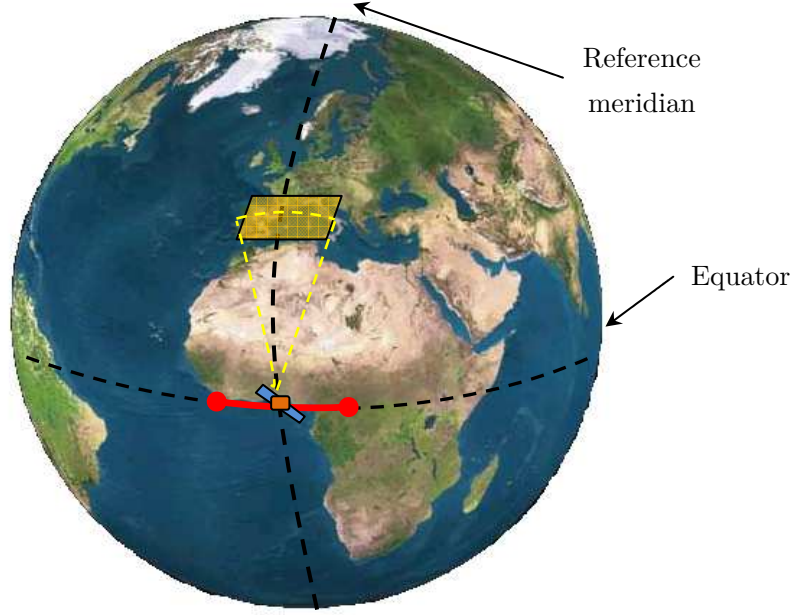


FIGURE 2.23 Geosynchronous satellite track considering small eccentricity in the orbit and zero-inclination.

So, taking the expression obtained in (2.23), the length of the synthetic aperture is computed as the angle variation (longitude in this case) multiplied by the distance of the satellite from the Earth's centre (mean orbit radius). Considering the maximum longitude variation (4e) given by equation (2.23), the maximum length of the synthetic aperture can be approximately obtained as:

$$L_{SA_{\max}} = r \cdot \Delta\lambda_{\max} = 4r \cdot e \quad (2.59)$$

Just as an example, let us consider a zero-inclined orbit with low eccentricity (0.0004) and an orbital mean radius of a 42.164,17 Km. With this parameters, a maximum synthetic aperture length of 67.5 Km is obtained. This example has been simulated and the results are plotted in Figure 2.24 and Figure 2.25. In Figure 2.24, a 3D representation of the satellite motion is plotted during a complete period (1 sidereal day: 86164 sec). As it can be seen, the maximum length of the synthetic aperture is achieved in 12 hours (half of the period) which is plotted as a green line in Figure 2.24. The rest of the orbit, plotted in blue, corresponds to West to East satellite motion until it reaches the initial position. So in a GEOSAR case, two quasi-identical maximum synthetic apertures lengths (just slight orbital radius variations) will be achieved with a geosynchronous satellite in one day of acquisition.

If the satellite motion during the 12 hours corresponding to the green line is computed, a total length of 81.7 Km is obtained. This result is larger than the theoretical synthetic aperture length previously calculated of 67.5 km. This difference arises from the non-constant radius of the orbit, which produces an approaching-moving away motion that does not contribute to the longitudinal satellite motion. The non-constant radius of the orbit can be appreciated in the orbital cuts presented in Figure 2.25 b) and d). This phenomenon will

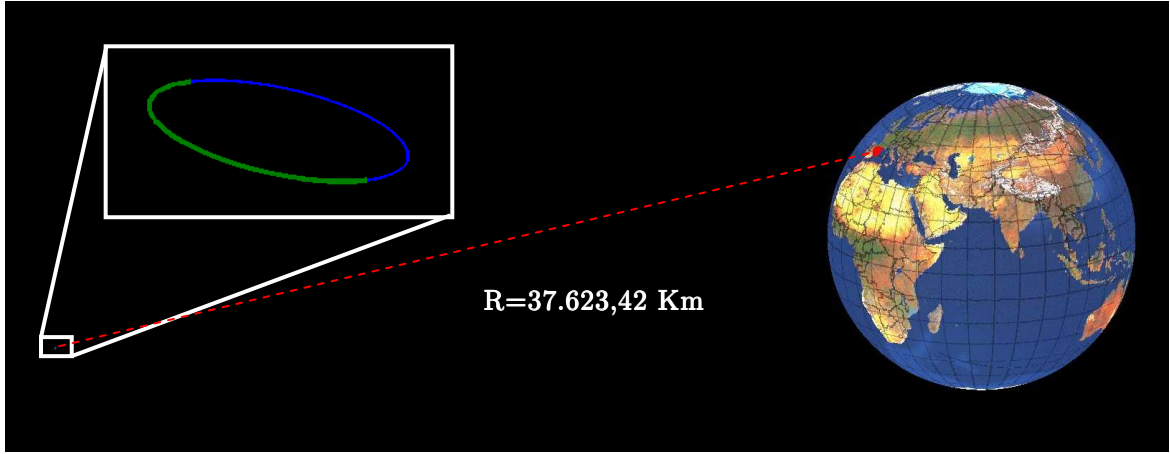


FIGURE 2.24 3D satellite orbit representation considering a non-inclined orbit with eccentricity of 0.0004 and nominal longitude of 0 degrees with respect to an Earth centred rotating coordinate system.

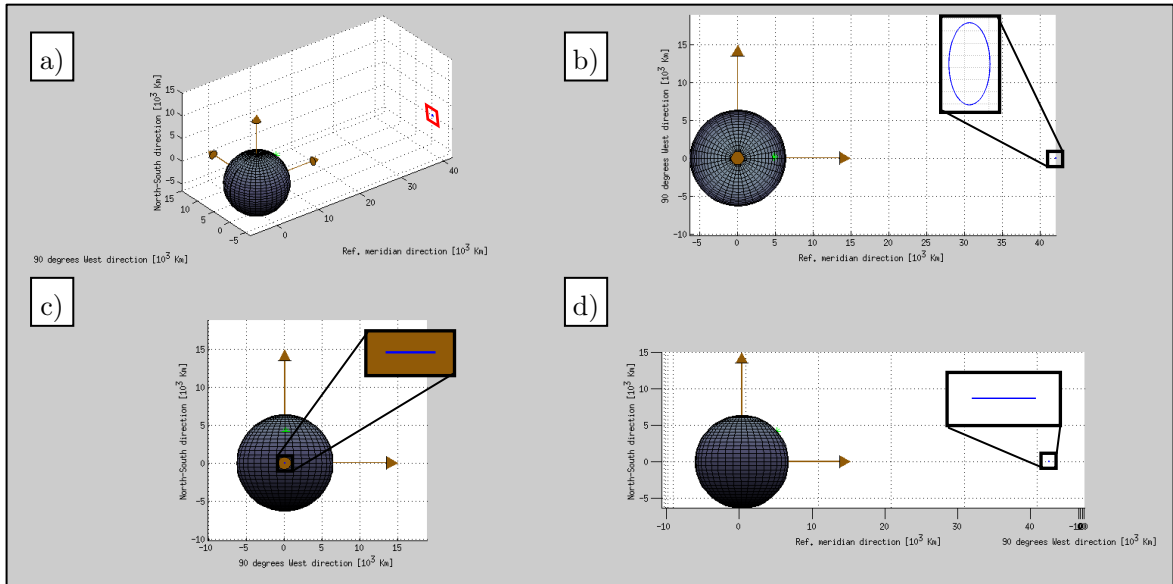


FIGURE 2.25 a) 3D orbital representation. b) Top view representation (reference meridian-90° West cut). c) Satellite nadir plane (North-90°West cut). d) Side view (North-Reference meridian cut).

introduce a common Doppler shift in the received raw data which is not useful to discriminate the targets in the scene and, therefore, it will not contribute to the effective synthetic aperture length. The Doppler history in GEOSAR is explained in section 3.2.

Therefore, the synthetic aperture length computation should only take into account the along-track variations (also cross-track variations if non-zero inclination is considered) between the satellite and the targets which correspond to the relative motion seen in Figure 2.25 c). Then, the radius variations must be subtracted from the satellite motion to obtain the along track movement of the satellite:

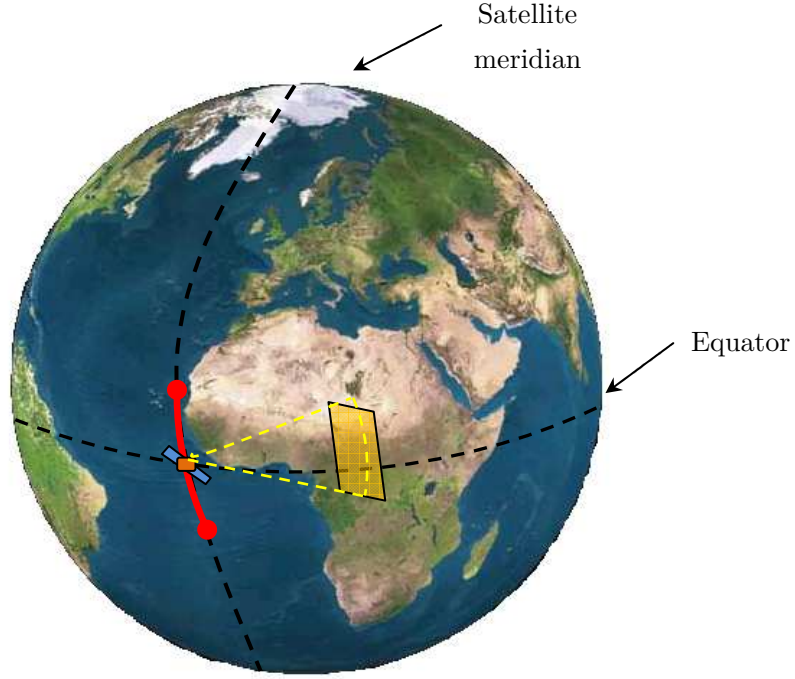


FIGURE 2.26 Geosynchronous satellite track considering zero eccentricity in the orbit and small inclination.

$$L_{SA} = \int_{t_{ac}} \sqrt{\left(\frac{dx_{sat}(t)}{dt}\right)^2 + \left(\frac{dy_{sat}(t)}{dt}\right)^2 + \left(\frac{dz_{sat}(t)}{dt}\right)^2 - \left(\frac{dr_{orbit}(t)}{dt}\right)^2} dt \quad (2.60)$$

With this consideration, the synthetic aperture length calculated for the previous example is 67.47 Km for both, the blue and green paths. These results are now consistent with the theoretical ones obtained with (2.59).

2.4.1.2 Inclination of the orbital plane

Alternatively, a GEOSAR system may be conceived with a perfect circular (zero eccentricity) but slightly inclined orbit. So, a North-South relative motion similar to the typical LEO SAR systems, but limited in the range on covered latitudes, could be achieved. This situation is complementary to the previous one so, once again, the versatility of a GEOSAR is demonstrated. Let us consider a similar situation than in the previous case but taking a scene over the equator and a nominal longitude of the satellite shifted with respect to the longitude of the scene. The new scenario is presented in Figure 2.26.

As it is shown, in this case only a latitudinal relative motion of the satellite is achieved since the longitude is fixed due to the zero eccentricity resulting in a the perfect circular orbit with the same period than the rotation period of the Earth. This latitude history is

computed with (2.25) whose maximum value depends basically on the orbit inclination (i). Similarly than in the previous case, the maximum length of the synthetic aperture in this case is computed as the angle variation of the satellite (latitude history) multiplied by the orbital radius as:

$$L_{SA_{\max}} = r \cdot \Delta\varphi_{\max} = 2i \cdot r \quad (2.61)$$

Thus, considering (2.61) and the synthetic aperture length obtained in the previous example (67.5 Km), an orbit inclination of 0.046 degrees should be taken to get the similar performance. Another simulation considering this new parameters (zero eccentricity and 0.046 deg of inclination), a nominal longitude of the satellite equal to -30 degrees and a scene placed over the equator at a longitude of 0 degrees has been performed. The orbital plots obtained are shown in Figure 2.27 and Figure 2.28. In this case, as it can be seen in Figure 2.27, the satellite describes a vertical line with only latitude variations as it was expected. Furthermore, the orbital radius is constant since a perfect circular orbit is considered. The constant orbit radius can be appreciated in Figure 2.28 b) where the top view shows only a point with no changes on the satellite Earth's centre distance.

So, equation (2.60) also applies in this situation but the last term, corresponding to the orbital radius variation, will be zero. Thus, computing the satellite motion over 12 hours of acquisition in this example, a synthetic aperture length of 67.49 Km is obtained. Once again, this result is in accordance with the expected value obtained from the theoretical approach.

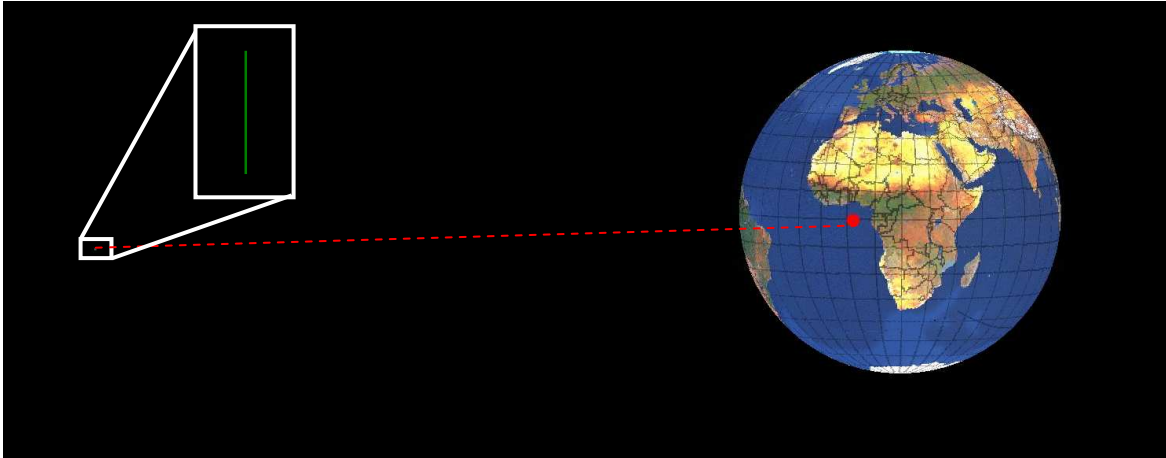


FIGURE 2.27 3D satellite orbit representation considering a 0.046 degrees inclined orbit with zero eccentricity and nominal longitude of -30 degrees with respect to an Earth centred rotating coordinate system.

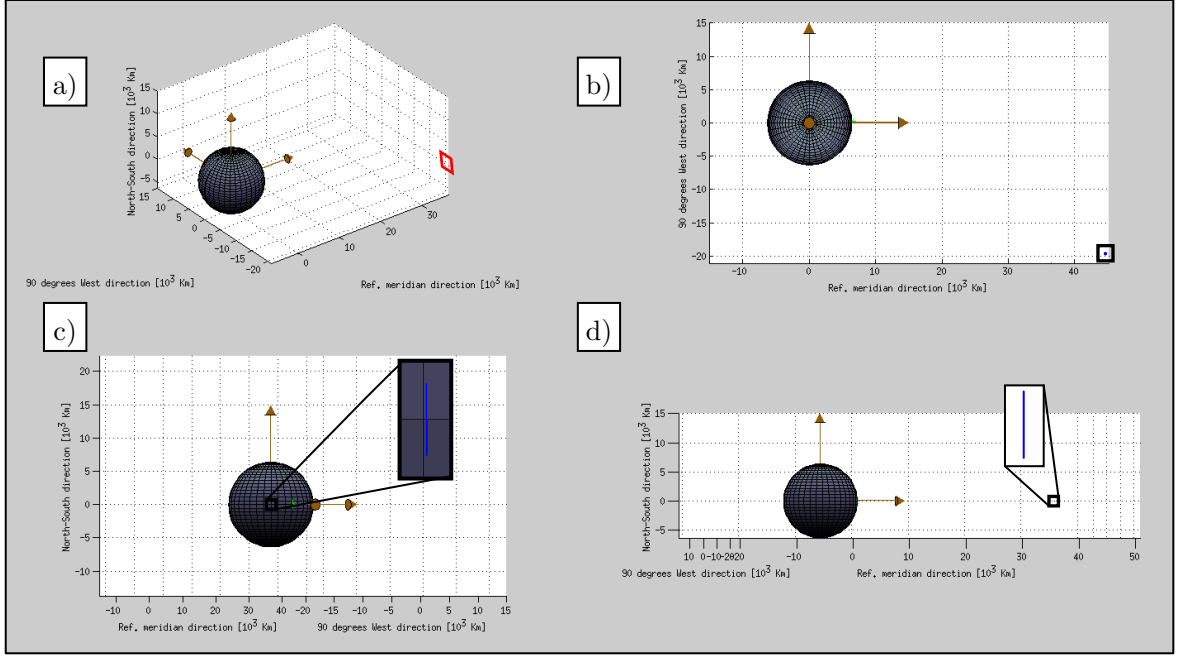


FIGURE 2.28 a) 3D orbital representation. b) Top view representation (reference meridian-90° West cut). c) Satellite nadir plane. d) Side view (North-Reference meridian cut).

2.4.1.3 Argument of the perigee: longitude and latitude combination

After these two basic examples, a more complex and general situation will be considered. In this case, a satellite in low eccentric orbit and small inclination of the orbital plane are considered. Therefore, the satellite track (section 2.2.2) will no longer be a vertical or horizontal line. The combination longitudinal and latitudinal motion, given by eccentricity and inclination respectively, will result in inclined lines or ellipses depending on the argument shift between the satellite longitude and latitude history governed by the argument of the perigee (ω), as given by equations (2.23) and (2.25).

In order to analytically compute the length of the synthetic aperture for an elliptical track, the basics on the ellipse geometry will be necessary. The purpose of this section is to give just the necessary concepts and justify their applicability to our problem to understand the calculations. So, equations (2.23) and (2.25) will describe an ellipse that will be inscribed in rectangle of sides $4e$ and $2i$, as shown in Figure 2.29.

To compute the maximum achievable synthetic aperture length, the semi-major axis (a) of the angular variation given by the ellipse shown in Figure 2.29 must be found and multiplied by the mean radius of the orbit, similarly than in the previous examples. The maximum length of the synthetic aperture will be related with the maximum longitude and latitude shift and with the tilt angle (τ) as well. In order to obtain the relation between the different angles that define the ellipse, the longitude and latitude histories will be

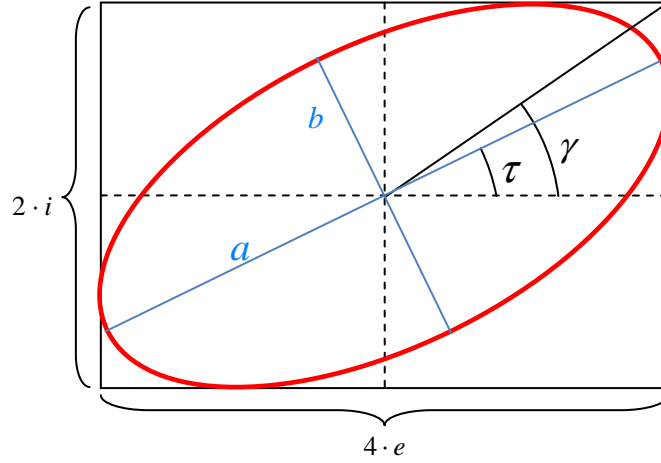


FIGURE 2.29 Elliptical satellite track inscribed in a rectangle of side $4e$ by $2i$ given by the satellite motion.

written as:

$$x = \Delta\lambda_{SL} = A_x \sin(\Omega_E(t - t_p)) \quad \text{where } A_x = 2e \quad (2.62)$$

$$y = \varphi_{SL} = A_y \sin(\omega + \Omega_E(t - t_p)) \quad \text{where } A_y = i \quad (2.63)$$

where ω is the argument of the perigee and it determines the phase shift (δ) between the two components while Ω_E stand for the Earth's rotation angular velocity. The other parameter in Figure 2.29 that can be easily computed is γ :

$$\gamma = \tan^{-1} \frac{A_y}{A_x} \quad (2.64)$$

From δ and γ , the tilt angle can be found by using (2.65). Another important parameter of an ellipse is the ratio between the major and minor axis. This is given by a parameter known as ellipticity (ε) computed as in (2.66).

$$\tan(2\tau) = \tan(2\gamma) \cdot \cos(\delta) \quad (2.65)$$

$$\sin(2\varepsilon) = \sin(2\gamma) \cdot \sin(\delta) \quad (2.66)$$

The axial ratio ($AR = a / b$) is obtained from the ellipticity as:

$$\varepsilon = \cot^{-1}(\mp AR) \quad (2.67)$$

All these parameters will give us information about the shape and orientation of the ellipse. Finally, the major axis of the ellipse must be determined from (2.62) and (2.63). It corresponds to the maximum angular variation of the satellite and can be found by computing the points of the ellipse at furthest distance from the centre ($x=0, y=0$). So, the

derivative of this distance must be computed and equalled to 0. The development is presented next. The angular shift of the points of the ellipse with respect to the nominal position of the satellite can be obtained as:

$$\phi = \sqrt{x^2 + y^2} \quad (2.68)$$

where x and y correspond are the orthogonal motion components given by (2.62) and (2.63), respectively. ϕ corresponds to the angle at the centre of the Earth between the nominal position and a point of the orbit. However, maximizing (2.68) is equivalent to maximize the distance squared whose derivative is easier to compute. So, the derivative of ϕ^2 is computed as:

$$\frac{\delta \phi^2}{\delta t} = \frac{\delta (x^2 + y^2)}{\delta t} = \frac{\delta \left([A_x \sin(\Omega_E(t - t_p))]^2 + [A_y \sin(\omega + \Omega_E(t - t_p))]^2 \right)}{\delta t} \quad (2.69)$$

To obtain the instants where the maximums and minimums of the angular shift occur (2.69) is equalled to 0:

$$\frac{\delta \left([A_x \sin(\Omega_E(t - t_p))]^2 + [A_y \sin(\omega + \Omega_E(t - t_p))]^2 \right)}{\delta t} = 0 \quad (2.70)$$

$$\begin{aligned} & A_x^2 \cdot 2 \sin(\Omega_E(t - t_p)) \cos(\Omega_E(t - t_p)) \cancel{\Omega_E} + \dots \\ & + A_y^2 \cdot 2 \sin(\omega + \Omega_E(t - t_p)) \cos(\omega + \Omega_E(t - t_p)) \cancel{\Omega_E} = 0 \end{aligned}$$

Using the trigonometric property (2.71) in the previous equation, (2.72) is obtained.

$$\sin \alpha \cdot \cos \alpha = \frac{1}{2} \sin 2\alpha \quad (2.71)$$

$$A_x^2 \cdot 2 \cancel{\frac{1}{2}} \sin(2\Omega_E(t - t_p)) + A_y^2 \cdot 2 \cancel{\frac{1}{2}} \sin(2(\omega + \Omega(t - t_p))) = 0 \quad (2.72)$$

And using $\cos(\alpha + \beta) = \cos \alpha \sin \beta + \sin \beta \cos \alpha$, (2.72) can be rearranged as:

$$A_x^2 \sin(2\Omega_E(t - t_p)) + A_y^2 [\sin(2\omega) \cos(2\Omega_E(t - t_p)) + \cos(2\omega) \sin(2\Omega_E(t - t_p))] = 0$$

$$\cancel{A_x^2 \sin(2\Omega_E(t - t_p))} + \cancel{A_y^2 \sin(2\Omega_E(t - t_p))} \left[\sin(2\omega) \frac{\cos(2\Omega_E(t - t_p))}{\sin(2\Omega_E(t - t_p))} + \cos(2\omega) \right] = 0$$

$$A_x^2 + A_y^2 \left[\frac{\sin(2\omega)}{\tan(2\Omega_E(t - t_p))} + \cos(2\omega) \right] = 0 \quad (2.73)$$

Finally, isolating the t and substituting A_x and A_y , the times with maxim (2.74) and minim (2.75) angular shift are obtained as:

$$t_{\max} = \frac{\arctan \left(\frac{\sin(2\omega)}{-\left(\frac{2e}{i}\right)^2 - \cos(2\omega)} \right) + (2n - 1)\pi}{2\Omega_E} + t_p \quad \text{with } n \in [-\infty \dots \infty] \quad (2.74)$$

$$t_{\min} = \frac{\arctan \left(\frac{\sin(2\omega)}{-\left(\frac{2e}{i}\right)^2 - \cos(2\omega)} \right) + 2n\pi}{2\Omega_E} + t_p \quad \text{with } n \in [-\infty \dots \infty] \quad (2.75)$$

As it can be seen, the periodicity of the arctangent function gives infinite results which correspond to the daily periodicity of the geosynchronous satellite but in one period only two minimums and maximums are obtained. Therefore, to determine the maximum length of the synthetic aperture, the angular aperture between the two consecutive maximum positions, which corresponds to the major axis of the ellipse in Figure 2.29, has to be computed and multiplied by the mean radius of the geosynchronous satellite:

$$L_{SA_{\max}} = r \cdot \Delta\phi_{\max} = r \cdot (\phi(t_{\max_1}) + \phi(t_{\max_2})) \quad (2.76)$$

In order to check the analysis presented above and compare the results obtained in this case with the previous ones, a new simulation considering both motion directions is performed. In this example, an inclination of 0.046 degrees and eccentricity of 0.0004 will be taken as input orbital parameters. The argument of the perigee will be set to 30 degrees. Later on, different values of ω will be tested in order to characterize its influence to the achievable synthetic aperture length. The time over the perigee (t_p) has been set to 0 since it is only a time reference. The resultant ellipse is plotted in Figure 2.30.

The longitude and latitude variations obtained correspond to the expected ones ($4e$ for longitude and $2i$ for latitude). The tilt angle, computed with (2.65), is equal to 45 degrees. The angle (ϕ) evolution from the nominal position of the satellite is shown in Figure 2.31. As it can be seen, the two maximum angles occur at $t_{\max_1} = 17925 \text{ sec}$ and $t_{\max_2} = 61038 \text{ sec}$ with a maximum angular shift of 0.0011 radians each one.

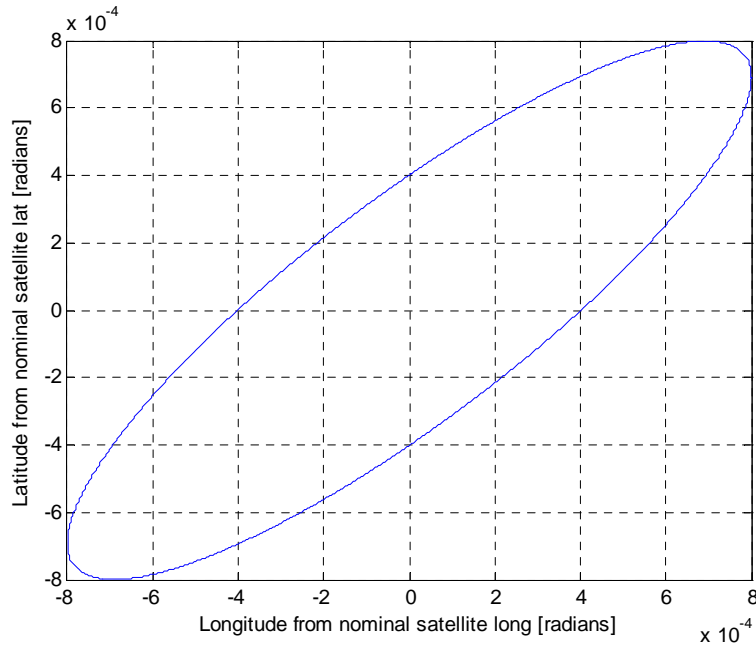


FIGURE 2.30 Satellite track simulation considering an orbit eccentricity of 0.0004 and inclination of 0.046 degrees.

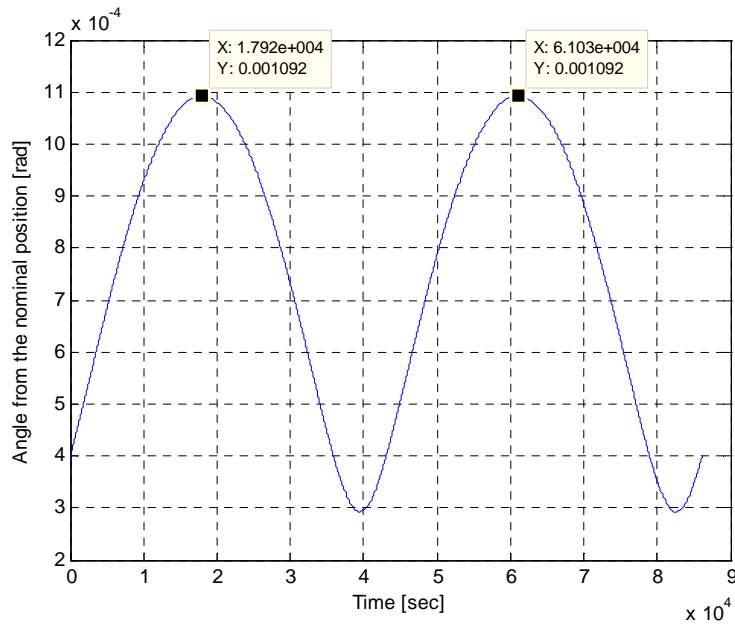


FIGURE 2.31 Satellite angle from nominal satellite position simulation considering an orbit eccentricity of 0.0004 and inclination of 0.046 degrees.

To corroborate the formulation previously derived, (2.74) is used to compute the t_{\max_1} and t_{\max_2} obtaining values of 17953 and 61036 seconds respectively, close to the simulated values. The small variations observed between the theoretical and simulated results arise from the approximations considered in the theoretical analysis of the longitude and latitude

histories. Computing $\phi(t_{\max_1})$ and $\phi(t_{\max_2})$ with (2.68) a value of 1.09 milliradians is obtained. So, the resultant synthetic aperture will have a theoretical length of:

$$L_{SA_{\max}} = r \cdot \Delta\phi_{\max} = 42164 \text{ Km} \cdot (2 \cdot 1.09 \cdot 10^{-3}) = 92.12 \text{ Km} \quad (2.77)$$

which is larger than the ones obtained in the previous example. It means that combining perturbations in eccentricity and inclination, larger synthetic aperture lengths and better image resolution can be achieved.



FIGURE 2.32 3D satellite orbit representation considering a 0.046 degrees inclined orbit with 0.0004 eccentricity and nominal longitude of -30 degrees with respect to an Earth's centred rotating coordinate system.

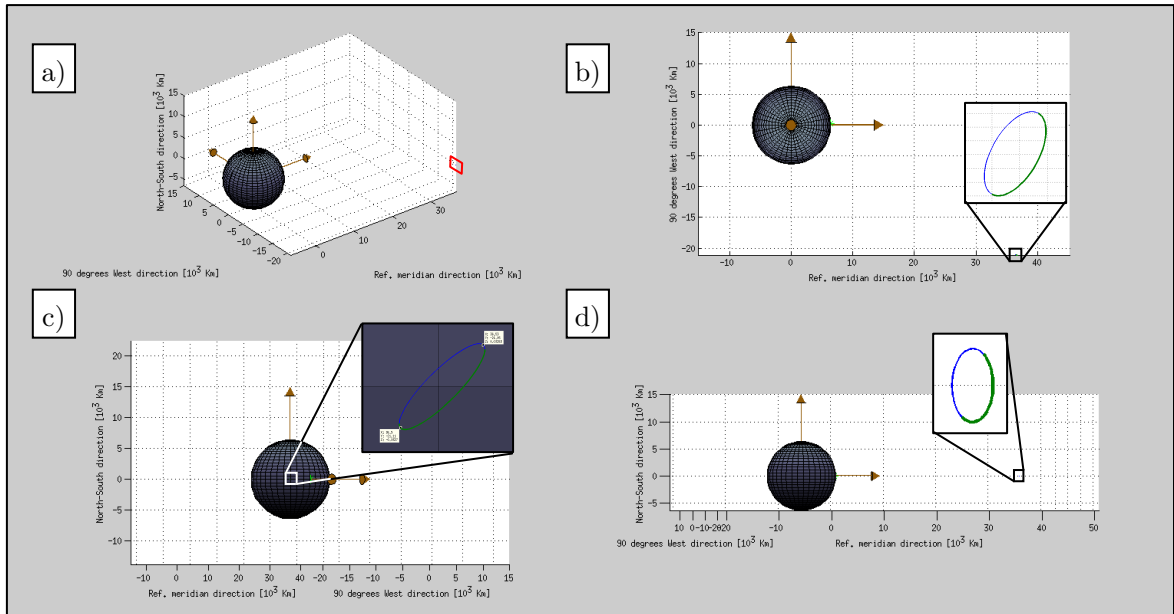


FIGURE 2.33 a) 3D orbital representation. b) Top view representation (reference meridian-90° West cut). c) Satellite nadir plane. d) Side view (North-Reference meridian cut).

As in the previous cases, let's compare the theoretical analysis with the ones obtained from actual orbital simulations. So, in Figure 2.32 and Figure 2.33, the resultant orbit with the above parameters is presented. It is interesting to take special attention to Figure 2.33 c) where the satellite track is shown. In this case the elliptical behaviour predicted with the analytical study shown in Figure 2.30 can be appreciated. The points used in the maximum synthetic aperture length computation are marked in Figure 2.33 c). In this case, the simulated maximum length is equal to 92.66 Km from equation (2.60), consistent with the result using equation (2.77). Therefore, the validity of the previous analysis to obtain the achievable synthetic aperture with a generic geosynchronous satellite has been checked.

2.4.1.4 Orbital orientation with respect to the illuminated scene

In the analysis presented in the previous sections, the synthetic aperture lengths computed were valid for a scene located perpendicularly to the direction of maximum satellite velocity. In Figure 2.34, the situation is graphically shown for the examples presented in sections 2.4.1.1, 2.4.1.2 and 2.4.1.3.

The best SAR cross-range resolution is obtained for scene points laying on the perpendicular direction with respect to the satellite track centre, as indicated by yellow slashed lines of Figure 2.34 left and centre plots. For a generic geosynchronous satellite, this strip will be situated perpendicularly to the direction of the major axis of the ellipse described by the satellite track as shown in the right plot in Figure 2.34.

Consequently, the effective synthetic aperture length for a scene placed at a random position has to be re-computed as the projection of the synthetic aperture length over the direction perpendicular to the illumination. To do that, the spherical angle β in Figure 2.35 (see section 2.2.1) must be obtained. It may be found from the spherical



FIGURE 2.34 The Earth zones (yellow slashed lines) in a perpendicular direction to the along-track satellite motion for different orbital configurations will present the maximum along-track resolution.

cotangent formula (2.8) as:

$$\begin{aligned} b &= \varphi_T - \varphi_{SL_0} & A &= 90^\circ \\ c &= \lambda_T - \lambda_{SL_0} & C &= \beta \end{aligned}$$

$$\cancel{\cos(\varphi_T - \varphi_{SL_0})} \cos 90^\circ = \sin(\varphi_T - \varphi_{SL_0}) \cot(\lambda_T - \lambda_{SL_0}) - \sin 90^\circ \cot \beta$$

$$\beta = \arctan \left(\frac{\tan(\lambda_T - \lambda_{SL_0})}{\sin(\varphi_T - \varphi_{SL_0})} \right) \quad (2.78)$$

Once the angle between the scene and nadir point is computed, it must be contrasted with the orientation of the ground track ellipse of the satellite. If we take the tilt angle (τ) of the ellipse from the equator, as shown in Figure 2.35, the relative angle between the major axis of the ellipse and the direction of the scene will be:

$$\alpha = |\pi + \beta - \tau| \quad (2.79)$$

The geometric interpretation of the problem is presented in Figure 2.36. As it can be seen, the actual length obtained for a determined orientation of the scene with respect to the satellite track ellipse is smaller than the maximum achievable length. This length is determined by the angle α , computed as in (2.79), which can be obtained approximately as:

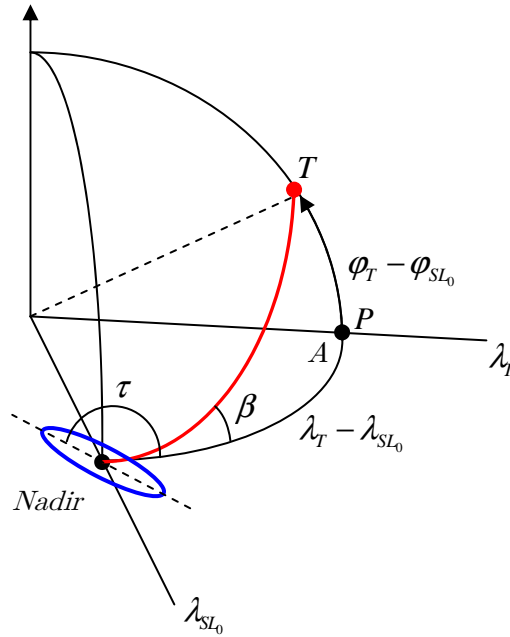


FIGURE 2.35 Target angle from the Equator at the satellite nadir point.

$$L_{SA} = L_{SA_{\max}} |\sin \alpha| = r \cdot \Delta \phi_{\max} |\sin \alpha| \quad (2.80)$$

As it has been shown in this section, the length of the synthetic aperture of a geosynchronous SAR will depend on a large number of factors, i.e. eccentricity of the orbit, inclination of the orbital plane, argument of the perigee and orientation of the ground track ellipse with respect to the scene location. Furthermore, as it is explained in section 2.4.2, the integration time will also play an important role to determine the length of each GEOSAR acquisition. So, if less than 12 hours of orbital motion are considered for SAR acquisition, the synthetic aperture length will be also reduced and, therefore, the achievable resolution will be worse.

2.4.2 GEOSAR achievable resolution: integration time requirements

In the previous section, the satellite-ground relative motion has been studied. The dependence of the effective synthetic aperture length with the orbital parameters and orientation of the scene with respect to the satellite motion has been analysed and the basic formulation proposed. However, in all the calculations, the integration time has not been taken into account, computing all the parameters with the whole satellite orbital motion. In this section, the cross-track and along-track resolution formulas for SAR are particularized and computed for GEOSAR case and their dependence with the acquisition parameters are analysed.

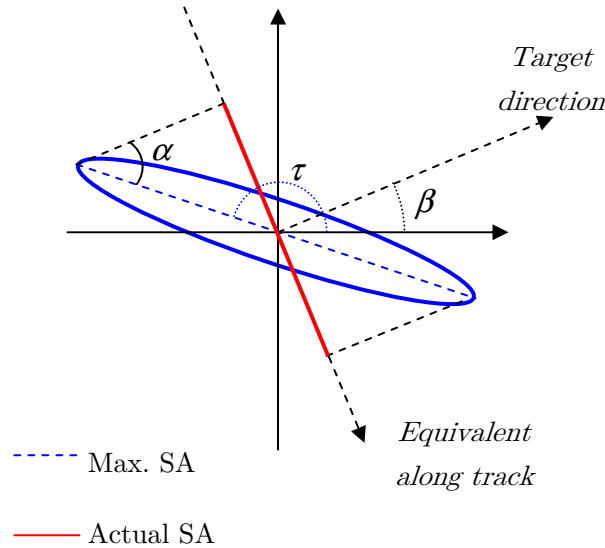


FIGURE 2.36 Maximum synthetic aperture length vs. actual aperture length for a randomly positioned target.

2.4.2.1 Cross-track resolution

The range resolution will depend on the pulse bandwidth and incidence angle as in the case of a typical LEO SAR. There is not any particularity in ground range resolution computation for GEOSAR configurations and, therefore, it will be given by [20]:

$$\rho_{gr} = \frac{c}{2B \sin \theta_{in}} \quad (2.81)$$

where c is the speed of light, B is the transmitted pulse bandwidth and θ_{in} is the incidence angle at the considered point.

However, the possibility of having large coverage in a GEOSAR acquisition could result in important variations of the ground range resolution within the scene. These variations, given by the on ground projection of the slant range resolution, indicated by the sine of the incidence angle in (2.81), will be more important for scenes near to the nadir point (small incidence angles). So, taking as an example a transmitted signal bandwidth of 10 MHz, which gives a slant range resolution of 15 meters, the ground cross-track resolution history vs. incidence angle shown in Figure 2.37 is obtained.

As seen, for small incidence angles, the ground range resolution starts to increase exponentially. Therefore, the images of regions close to the nadir point will have poor range resolution. Increasing the incidence angle, better resolutions are obtained. However, although going at larger incidence angles will improve the ground cross-track resolution, the backscattering response for most of the targets at high incident angles is usually very low, which will not be desirable for the power link budget requirements.

Therefore, the range of incidence angle that could be considered as valid would range from 40 to 70 degrees corresponding to mid-latitude Earth zones. In that case, taking the example presented in Figure 2.37 the ground cross-track resolution would change from 23 meters to 16 meters. So, if a GEOSAR configuration as the one presented in section 2.4.1.1 with longitudinal satellite motion, the cross-track direction would correspond to a meridian in the satellite nominal longitude. In that case, the range of observables latitude taking the incidence angle history from 40 to 70 degrees to avoid the resolution variation problems presented above will range from 30 to 60 degrees North and South.

This behaviour of the incidence angle over the European zone considering a satellite placed at 30° East is shown in Figure 2.38. As seen, the regions around the nadir point (central Africa) are seen under a low incidence angle while the most parts of the European continent are seen with incidence angles from 40 to 70 degrees which is in accordance with the limitations presented above.

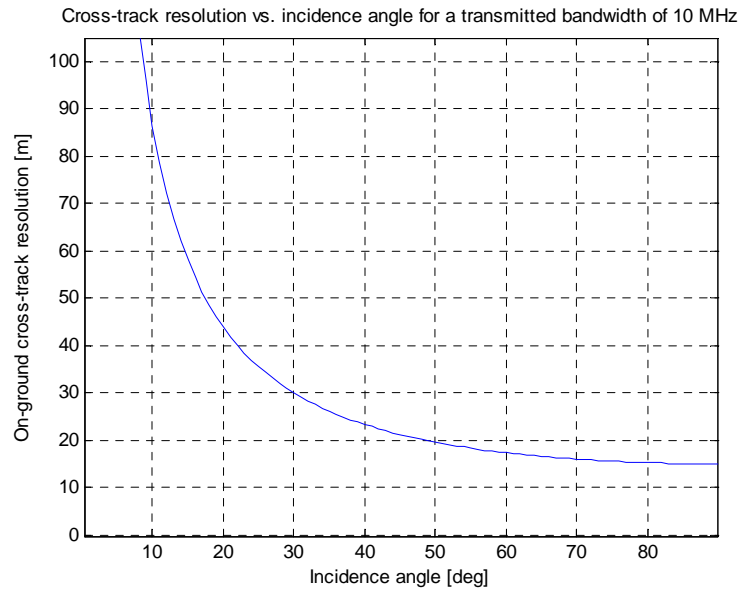


FIGURE 2.37 On-ground cross-track resolution variation with incidence angle.

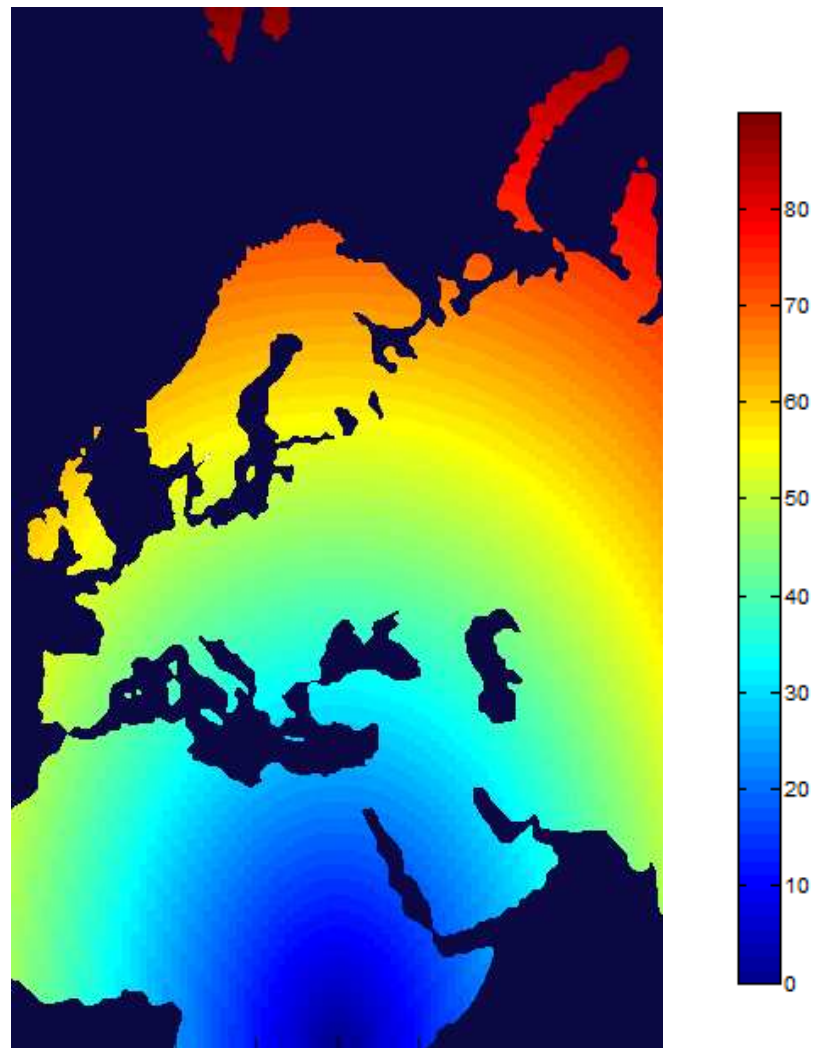


FIGURE 2.38 Incidence angle over the Earth map considering a geosynchronous satellite at 30° East nominal longitude.

On the other hand, the impact of the incidence angle over the Earth map for this particular case is shown in Figure 2.39. In this case, assuming the radar slant range resolution is 15 m, the ground range resolution at low latitudes under the satellite is above 50 meters. Regarding the European zone, resolutions from 25 to nearly 15 meters are obtained in this example.

Thus, considering a range of latitudes of interest from 30 to 60 degrees, a maximum ground range resolution variation under 10% within the image is obtained if a scene of 500Km is considered. For larger scenes or lower latitudes, a variable pulse bandwidth should be considered in order to reduce pixel geometric distortion, but it is not the case of this study.

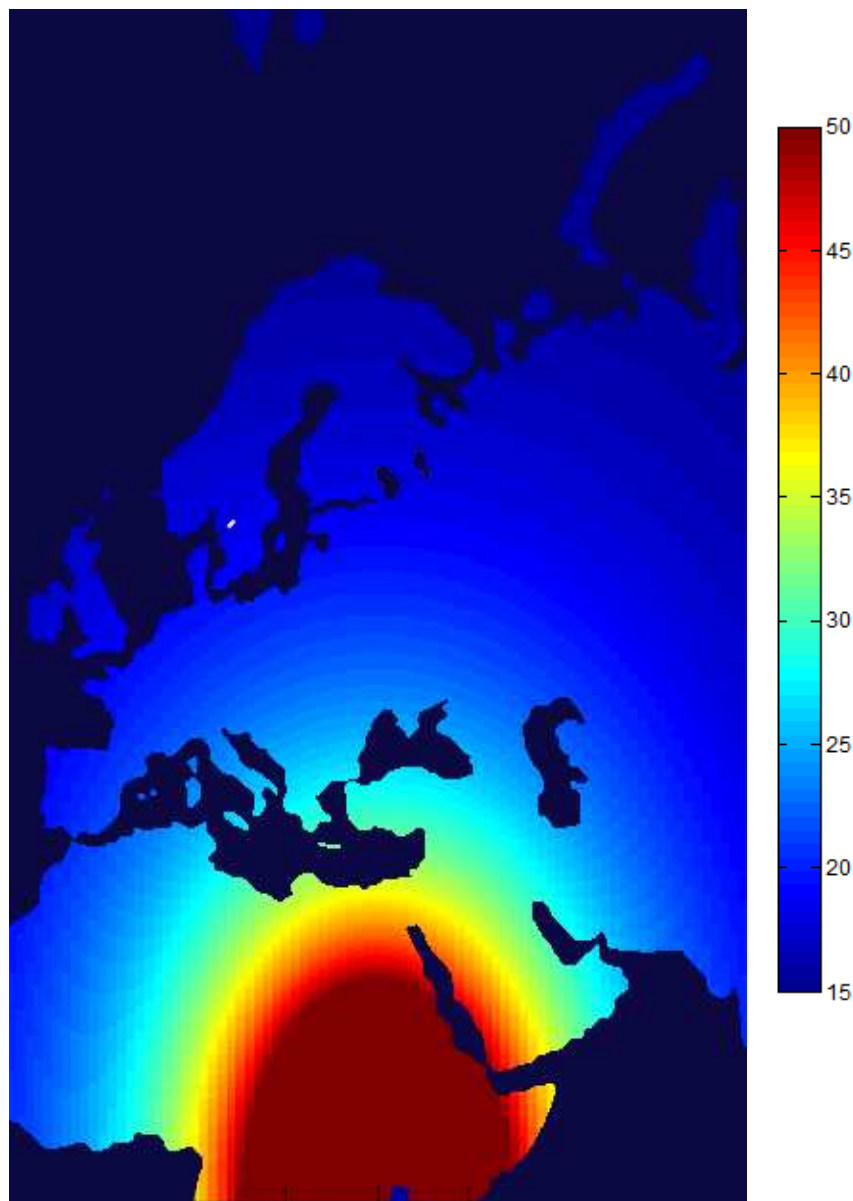


FIGURE 2.39 Ground range resolution over the Earth map considering a geosynchronous satellite at 30° East nominal longitude and a slant range resolution of 15 meters.

2.4.2.2 Along-track resolution

Until now, the duration of the acquisition has not been taken into account in the synthetic aperture length analysis. In a real acquisition, the integration time of the image acquisition will be finite and, most of the times, it will be shorter than half of the satellite period (12 hours). Therefore, only a part of the satellite daily motion will be considered in each acquisition, reducing the length of the synthetic aperture and, consequently, the achievable azimuth resolution. Furthermore, the time instant when the acquisition starts will be important in the determination of the synthetic aperture length as well due to the non-linear track and accelerations on the geosynchronous satellite motion.

In any SAR system, the azimuth or along-track resolution is related to the synthetic aperture length as follows [20]:

$$\rho_{az} = \frac{1}{2} \frac{\lambda}{L_{SA}} R \quad (2.82)$$

where λ is the wavelength of radar operation, L_{SA} the synthetic aperture length of the acquisition and R the slant range to the scene. The large number of possibilities in the synthetic aperture formation makes difficult to consider all the cases in this analysis. Therefore, in the following lines, some particular situations will be analysed and discussed to see the integration time requirements to reach the desired azimuth resolution or the other way around.

Let us start with a simple case, considering a geosynchronous satellite with small eccentricity in its orbit and no inclination of the orbital plane. As it has been studied in section 2.4.1.1, the maximum synthetic aperture length in this case is obtained from (2.59). Then, the maximum azimuth resolution achievable with this system considering the whole satellite motion can be computed as:

$$\rho_{az_{\max}} = \frac{1}{2} \frac{\lambda}{4 \cdot e \cdot r} R = \frac{\lambda}{8 \cdot e} \frac{R}{r} \quad (2.83)$$

On the other hand, the problem can be set out in the other way. Given a desired azimuth resolution, one can be interested in obtaining the orbital configuration necessary to satisfy the input requirements. For the previous example, if the signal and swath parameters are fixed, the only parameter available to be modified in the satellite orbital design is the orbit eccentricity. Then, this parameter must be tuned to fulfil the following equation:

$$e_{\min} = \frac{\lambda}{8 \cdot \rho_{az_{req}}} \frac{R}{r} \quad (2.84)$$

In Table 2.5, a summary of the range of expected azimuth resolutions for different frequency bands is presented. In this case, a mean range to the scene of 36950 Km and an orbital eccentricity of 0.0004 have been considered. As it can be seen, fine resolution can be achieved working at high frequencies. However, the frequency cannot be increased arbitrarily since other SAR aspects and technological limitations have to be taken into account. Furthermore, these values have been computed considering the whole synthetic aperture of the satellite which only can be achieved by integrating at least 12 hours. Such integration time will be too large compared with the temporal coherence of the scene for most of the GEOSAR applications.

To see how the acquisition duration affects to the synthetic aperture and, consequently, to the achievable resolution in the previous example, the equation (2.23) has been used considering a time of perigee equal to zero. Depending on the time interval considered, the longitude history of the satellite during the acquisition will be different as it shown in Figure 2.40 for an orbital eccentricity of 0.0004. As seen in Figure 2.40, the longitude variation during the 5 hours considered in the red line is higher than the variation considering the same acquisition time at green zones. The red line corresponds to the sine cross to zero in (2.23) and is where this function presents the highest slope which results in the highest longitudinal shift for a given integration time.

Therefore, in the red zone of Figure 2.40, the best trade-off between integration time and resolution will be obtained since. This corresponds to an acquisition centred to the time pass through the perigee or through the apogee. So, if the integration time (T_i) is defined between $t = [-T_i / 2, T_i / 2]$ considering $t_p = 0$, an acquisition centred at the pass through the perigee is simulated. Using this time interval directly on equation (2.23), the acquisition corresponds to the red longitude history in Figure 2.40, centred at the nominal longitude of the satellite ($\lambda(t = 0) = \lambda_{SL}$). The extreme values of the satellite longitude in function of the integration time will be:

$$\lambda_1 = \lambda_{SL} + 2e \sin\left(-\Omega_E \frac{T_i}{2}\right) \quad (2.85)$$

$$\lambda_2 = \lambda_{SL} + 2e \sin\left(\Omega_E \frac{T_i}{2}\right) \quad (2.86)$$

Knowing that $\sin(-\beta) = -\sin(\beta)$, the longitude variation during T_i can be written as:

$$\begin{aligned} \Delta\lambda = \lambda_2 - \lambda_1 &= \cancel{\lambda_{SL}} + 2e \sin\left(\Omega_E \frac{T_i}{2}\right) - \left[\cancel{\lambda_{SL}} - 2e \sin\left(\Omega_E \frac{T_i}{2}\right)\right] = \dots \\ &= 4e \sin\left(\Omega_E \frac{T_i}{2}\right) \end{aligned} \quad (2.87)$$

Frequency band	Frequency Range	λ	Achievable azimuth resolution
C band	4 to 8 GHz	7.5 to 3.75 cm	20.5 to 10.3 m
X band	8 to 12 GHz	3.75 to 2.5 cm	10.3 to 6.85 m
Ku band	12 to 18 GHz	2.5 to 1.67 cm	6.85 to 4.57 m
K band	18 to 26.5 GHz	1.67 to 1.13 cm	4.57 to 3.09 m
Ki-band	26.5 to 40 GHz	1.13 to 0.75 cm	3.09 to 2.05 m

TABLE 2.5. Range of achievable azimuth resolutions at different frequency bands for an orbital eccentricity of 0.0004 and slant range of 36950 Km.

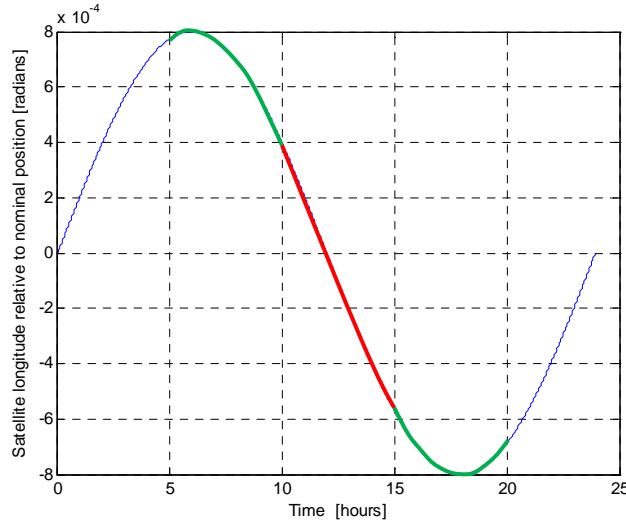


FIGURE 2.40 Satellite longitude variation considering an orbital eccentricity of 0.0004. Red zone presents higher variation than green ones in the same integration time.

And that corresponds to a length of the synthetic aperture of:

$$L_{SA} = r \cdot \Delta\lambda = r \cdot 4e \sin\left(\Omega_E \frac{T_i}{2}\right) \quad (2.88)$$

From (2.82), the azimuth resolution of the scene can be related to the integration time with the following equation for this particular example:

$$\rho_{az} = \frac{\lambda}{r \cdot 8e \sin\left(\Omega_E \frac{T_i}{2}\right)} R \quad (2.89)$$

Now, with (2.89), it is possible to obtain a relation between the minimum integration time required to get a desired resolution for a fixed parameters of the satellite orbit and the scene location. The integration time required will be:

$$T_{i_{req}} = \arcsin \left(\frac{\lambda}{r \cdot 8e \cdot \rho_{az}} R \right) \frac{2}{\Omega_E} \quad (2.90)$$

In Table 2.6, the required integration times at different bands to obtain an azimuth resolution image of 25 meters are presented. The satellite parameters are the same that the ones considered in the previous example: orbit eccentricity of 0.0004 and a distance to the scene of 36950 Km. A mean radius of the orbit of 42164 Km has been taken while the angular Earth's rotation velocity is $7.3 \cdot 10^{-5}$ rad/sec. The results show that, with a few hours of integration, it is possible to obtain a medium resolution SAR image at these frequency bands.

In order to see the dependence of the resolution with orbital ephemerides, in Figure 2.41 the achievable azimuth resolution for different orbital configurations is plotted. The theoretical results have been validated with simulation by using the MATLAB simulator presented in section 3.6.3. As seen, a medium resolution image of around 15 m can be obtained if a minimum orbital eccentricity of 0.0003 is considered.

Alternatively, for scene with low temporal correlation may be interesting to sacrifice spatial resolution reducing the integration time as in the case of the atmospheric sounding presented in section 4.3. In this case, the resolution obtained for an L-band acquisition at 1.625 GHz in front of the orbital eccentricity is represented in Figure 2.42. As seen, if a minimum orbital eccentricity of 0.0003 is taken as in the previous case, an along-track resolution around 1 km is obtained. Although coarser resolution is obtained in this case, it may be enough to track the spatial variations of atmospheric artefacts as explained in section 4.3.

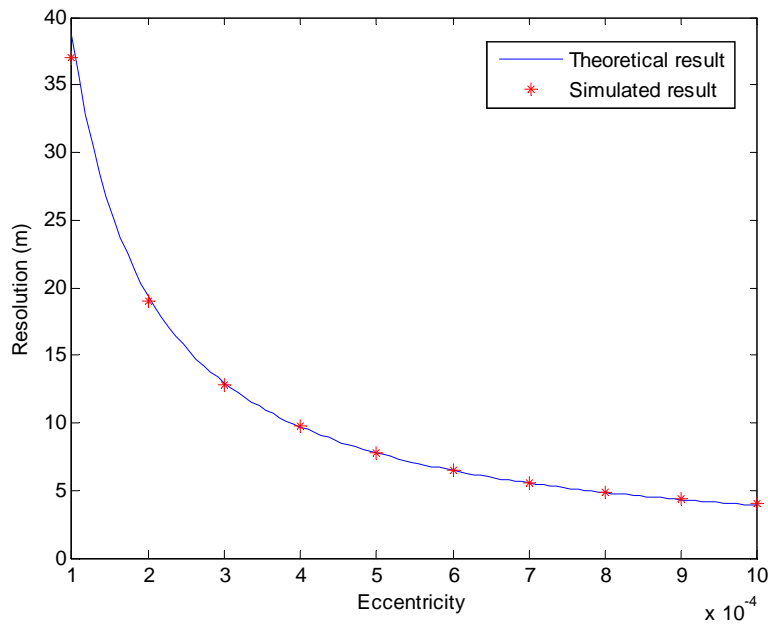


FIGURE 2.41 Achievable resolution with 4 hours of integration for different orbital eccentricities working at Ku-band (17.25 GHz) with slant range of 36950 Km.

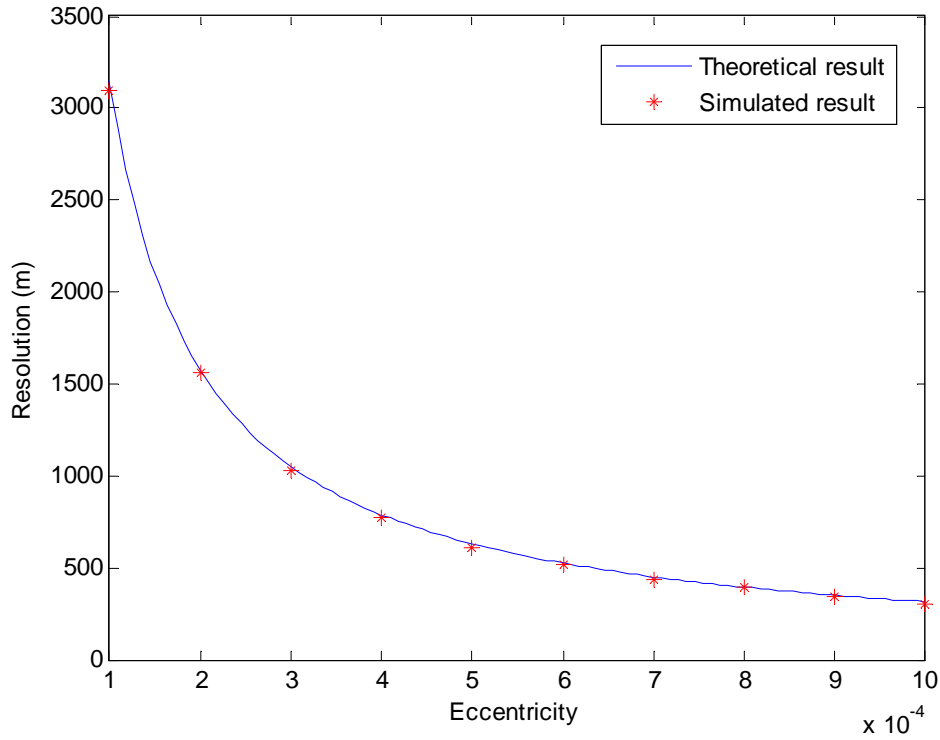


FIGURE 2.42 Achievable resolution with 30 min of integration for different orbital eccentricities working at L-band (1.625 GHz) for slant range of 36950 Km.

Frequency band	Frequency Range	λ	Integration time required
C band	4 to 8 GHz	7.5 to 3.75 cm	7.35 to 3.22 hours
X band	8 to 12 GHz	3.75 to 2.5 cm	3.22 to 2.11 hours
Ku band	12 to 18 GHz	2.5 to 1.67 cm	2.11 to 1.40 hours
K band	18 to 26.5 GHz	1.67 to 1.13 cm	1.40 to 0.95 hours
Ka-band	26.5 to 40 GHz	1.13 to 0.75 cm	0.95 to 0.63 hours

TABLE 2.6. Integration time required to obtain an azimuth resolution of 25 meters for an orbital eccentricity of 0.0004 and slant range of 36950 Km.

Equivalently to this example, the case with a non-eccentric orbit and only small perturbations on the inclination can be considered. The procedure is exactly the same only changing the longitude perturbations for the latitude history of the satellite. The final results obtained in this case are summarized in equations (2.91) to (2.94). As it can be seen, only the term $2e$ is changed by i .

$$\rho_{az_{\max}} = \frac{1}{2} \frac{\lambda}{2 \cdot i \cdot r} R = \frac{\lambda}{4 \cdot i} \frac{R}{r} \quad (2.91)$$

$$i_{\min} = \frac{\lambda}{4 \cdot \rho_{az_{req}}} \frac{R}{r} \quad (2.92)$$

$$L_{SA} = r \cdot \Delta\varphi = r \cdot 2i \sin\left(\Omega_E \frac{T_i}{2}\right) \quad (2.93)$$

$$T_{i_{req}} = \arcsin\left(\frac{\lambda}{r \cdot 4i \cdot \rho_{az}} R\right) \frac{2}{\Omega_E} \quad (2.94)$$

For more complex satellite motion is not feasible to obtain a closed formula for the relation between integration time and resolution and it must be obtained by simulations.

2.4.3 Non-linear orbital track: daily variations of the achievable resolution

Until now, an acquisition centred at time pass through the perigee has been considered. Considering an acquisition centred at this point or at the pass through the apogee, the best along-track resolution for a given integration time is obtained. However, sometimes may be interesting to consider an acquisition in other instant of the daily orbital motion. Therefore, in this section the daily history of the achievable resolution is analysed.

Taking the GEOSAR configuration with low-eccentric orbit and zero inclination, the satellite motion (given by equation (2.23)) is time dependent due to the sinusoidal function. So, the resulting along track motion may not be enough at the edges of the satellite elliptical track, where the satellite is moving slowly with respect to the Earth surface.

Thus, in order to study the daily history of the achievable resolution, the satellite motion all over the orbit must be analysed. So, for a given integration time, the longitude shift obtained for different acquisitions centred at different positions all along the satellite track will be considered. So, the position of the satellite (longitude) at the start and the end of the acquisition may be obtained as

$$\lambda_{SL}(t_{start}) = \lambda_{SL_0} + 2e \sin(\Omega_E(t_{start} - t_p)) \quad (2.95)$$

$$\lambda_{SL}(t_{end}) = \lambda_{SL_0} + 2e \sin(\Omega_E(t_{end} - t_p)) \quad (2.96)$$

where t_{start} and t_{end} will be $-T_i / 2$ and $T_i / 2$, respectively. The t_p will be used to consider the different positions of the centre of the acquisition being $t_p = 0$ an acquisition centred at time pass through the perigee and $t_p = 12 \text{ hours}$ an acquisition centred at time pass through the apogee. So, the length of the synthetic aperture for each particular acquisition will be:

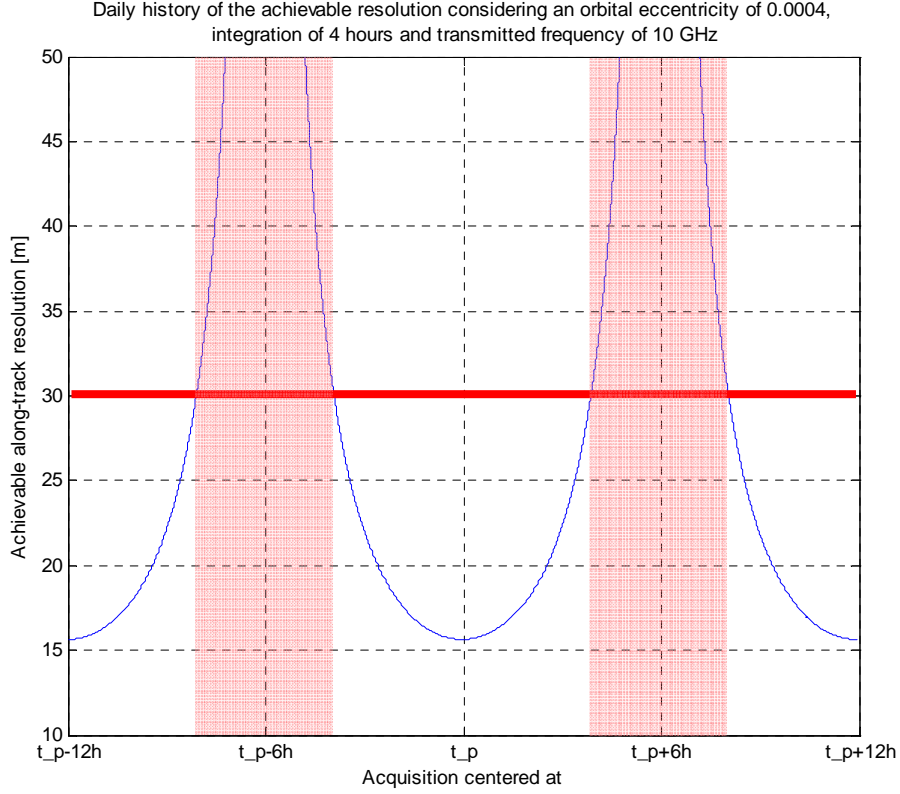


FIGURE 2.43 Daily along-track resolution variation considering acquisition centred at different time instants. An orbital eccentricity of 0.0004 has been taken and integration time of 4 hours and transmitted frequency of 10 GHz have been considered.

$$\Delta\lambda(t_p) = |\lambda_{SL}(t_{start}) - \lambda_{SL}(t_{end})| = \left| 2e \sin\left(\Omega_E \left(-\frac{T_i}{2} - t_p\right)\right) - 2e \sin\left(\Omega_E \left(\frac{T_i}{2} - t_p\right)\right) \right| \quad (2.97)$$

$$L_{SA}(t_p) = r \cdot \Delta\lambda(t_p) \quad (2.98)$$

From equations (2.97) and (2.98), and using equation (2.82), the daily variations of the azimuth resolution can be found. Just as an example, a geosynchronous satellite with 0.0004 eccentricity and zero inclination of the orbit has been considered. The integration time has been set up to 4 hours and a transmitted frequency of 10 GHz has been taken. The daily variation of the achievable resolution considering acquisitions centred at different time instants is presented in Figure 2.43.

As seen in Figure 2.43, poor resolution is obtained in acquisitions centred around $t_p \pm 6$ hours. In the previous example, if a maximum deterioration of the azimuth resolution up to 30 meters was allowed, there would be two regions (red zones in Figure 2.43) of 4.4 hours where the resolution requirements would not be fulfilled.

Therefore, this phenomenon must be taken into account in the orbital design of a GEOSAR

mission in order to reduce as much as possible these intervals with worse along-track resolution.

Furthermore, the daily relative motion variations may impact on the image quality if the regions around $t_p \pm 6 \text{ hours}$ are considered. In these regions, the relative speed of the satellite with respect to the Earth surface decreases significantly. This results in an accumulation of pulses from the satellite positions with slower velocity if constant PRF is considered which has a strong impact on the final image quality, increasing the lateral lobes.

So, if an acquisition centred at the time pass through the perigee, the longitudinal satellite velocity is nearly constant and therefore, considering a regular temporal sampling at inverse of the PRF, the satellite acquires signals at regularly spaced positions of the synthetic aperture. This results in the typical -13 dB side-lobe level as shown in Figure 2.44. However, as the centre of the acquisition goes further from at t_p , the resolution starts to get worse and the side-lobe level starts to increase. Two examples considering acquisitions centred at $t_p + 3 \text{ h}$ and $t_p + 5 \text{ h}$ are presented in Figure 2.44. In this case, the side lobe levels increase up to -12 dB and -9.8 dB, respectively. Additionally, the resolution loss due to the synthetic aperture length reduction may be also seen in Figure 2.44.

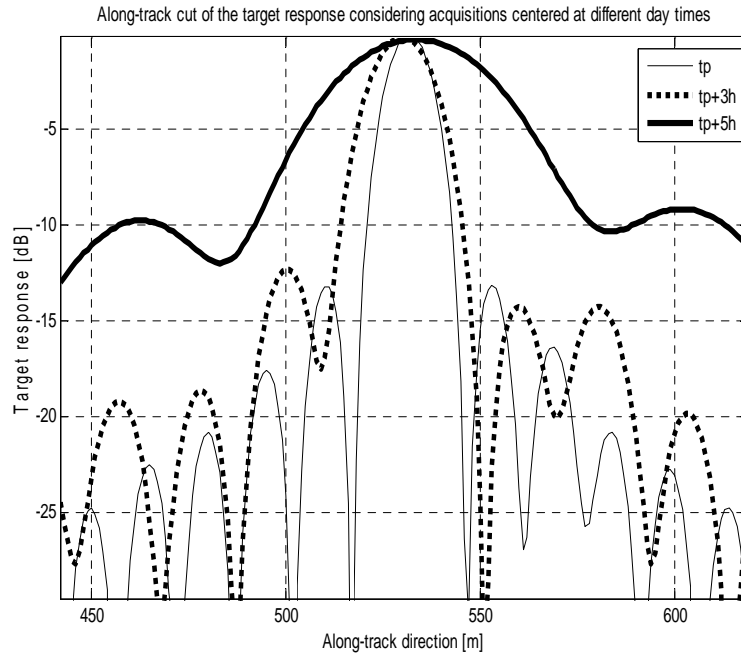


FIGURE 2.44 Along-track cut of a GEOSAR focused image. As seen along-track resolution is degraded as the acquisition goes away from the perigee. Along-track resolutions of 17 m, 25 m and 65 m are obtained considering 2 hours of acquisition centred at t_p , $t_p+3\text{h}$ and $t_p+5\text{h}$, respectively; while the Peak-to-Side-Lobes Ratio (PSLR) is reduced.

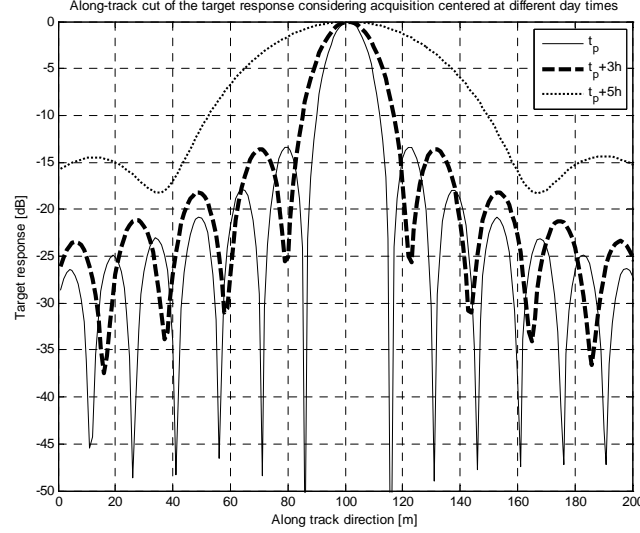


FIGURE 2.45 Along-track cut of a GEOSAR focused image considering along-track weighting of the zones with slower velocities.

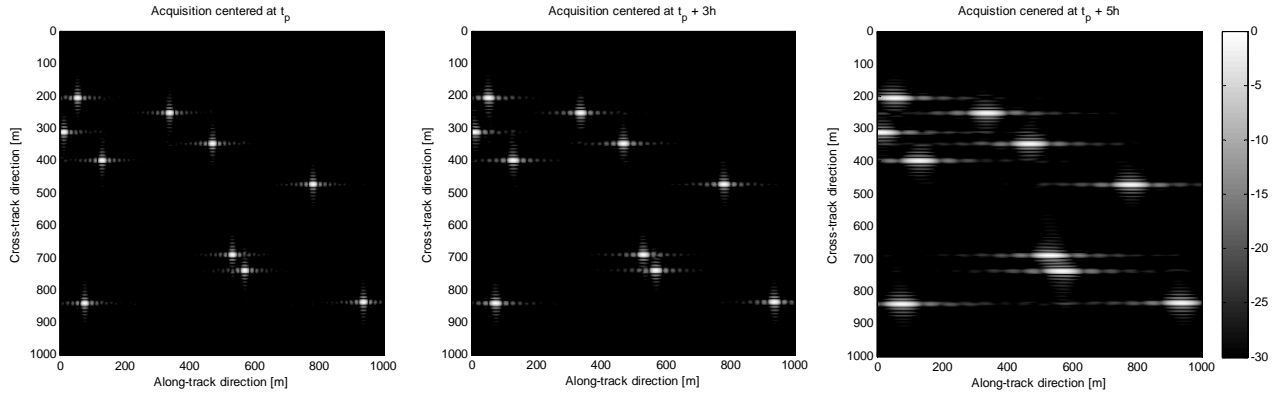


FIGURE 2.46 GEOSAR focused images of a 1 by 1 Km scene over Barcelona. 10 point targets have been randomly placed. The raw data from 2 hours of integration have been simulated considering acquisitions centred, from left to right, at t_p , $t_p + 3h$ and $t_p + 5h$.

Thus, this phenomenon must be taken into account when we consider those regions with higher orbital accelerations. In order to reduce this effect two possibilities may be considered. On one hand, an along-track filter could be considered in the processing raw data chain, reducing the weighting of those regions with slower relative velocities. However, it could reduce the received power level having an undesired effect to the SNR. On the other hand, a variable PRF could be taken in order to obtain a spatially constant sampling of the orbital track. So, the accumulation of pulses transmitted from the regions with slower velocity could be reduced significantly. In Figure 2.45, the azimuth cut of the same simulation presented in FIGURE 2.44 is presented after considering an azimuth weighting function. As seen, the resolution daily dependence is not corrected but the Peak-to-Side-Lobe (PSLR) degradation is corrected. The 2D image obtained after correction is shown in

Figure 2.46. In Figure 2.46, the daily changes of the azimuth resolution can be clearly seen, while the cross-track resolution is kept constant since it only depends on the signal bandwidth. Additionally, the reduction of side-lobe level in the whole image can be seen in Figure 2.46.

2.5 Analysis of current broadcasting telecommunications satellites orbits for GEOSAR purposes

After the theoretical analysis of the achievable resolution with a GEOSAR system, in this section the Two Line Elements (TLE) of current broadcasting satellites are studied. The TLEs of a satellite identify its orbital motion and orbital ephemerides evolution over time. This analysis will be suitable to check the feasibility of such satellites to carry a SAR payload transmitting and receiving SAR data in parallel with the broadcasting channels.

First of all, the structure and format of TLE must be described. So, in Figure 2.47 an example of a typical TLE file is presented. In Table 2.7 and Table 2.8, the TLE cells of line 1 and line 2 are described, respectively. As seen, in the first line parameters regarding the satellite name, year of launch and the time corresponding to each TLE are given. On the other hand, in the second line the orbital parameters are described: inclination, RAAN, eccentricity, argument of the perigee, etc.

In this thesis, geosynchronous satellites with nearly-zero inclination are being studied. The necessary relative motion is obtained from low-eccentricities of the orbit which results in longitudinal motion of the satellite. This motion, characterized by equations (2.23) and (2.25), will define the system along track resolution.

So, considering the analysis presented in section 2.4.2.2 a minimum orbital eccentricity would be required to reach the along-track resolution requirements. Let us take as a reference the orbital requirements computed in the example of the previous section. So, a minimum eccentricity of 0.0003 to obtain mid resolution images (15 meters) with 4 hours of integration and low resolution images (1 km) in 30 minutes was obtained.

In Figure 2.48, the orbital eccentricities of four broadcasting telecommunications satellites are presented. As seen, the orbital strategy of current broadcasting satellites presents a non-constant orbital eccentricity. In this example, the annual orbital eccentricities of these satellites may range from 0 to 0.0006 approximately. In Figure 2.48, the orbital eccentricity requirement of 0.0003 has been superimposed to the actual satellite behaviour. As seen, the orbital requirements of this example would not be fulfilled during one third of the year where coarser resolution would be obtained. Therefore, if future broadcasting satellites are intended for SAR purposes as well, the orbital design would have to assure a minimum eccentricity during the whole year in order to avoid this problem.

```

NOAA 14
1 23455U 94089A 97320.90946019 .00000140 00000-0 10191-3 0 2621
2 23455 99.0090 272.6745 0008546 223.1686 136.8816 14.11711747148495

```

FIGURE 2.47 TLE format.

Field	Columns	Content
1	01–01	Line number
2	03–07	Satellite number
3	08–08	Classification (U=Unclassified)
4	10–11	Last two digits of launch year
5	12–14	Launch number of the year
6	15–17	Piece of the launch
7	19–20	Epoch Year: Last two digits of year
8	21–32	Day of the year and fractional portion of the day
9	34–43	First Time Derivative of the Mean Motion divided by two
10	45–52	Second Time Derivative of Mean Motion divided by six (decimal point assumed)
11	54–61	BSTAR drag term (decimal point assumed)
12	63–63	Unused. Set to 0
13	65–68	TLE number counter.
14	69–69	Checksum (Modulo 10)

TABLE 2.7. TLE line 1 parameters description.

Field	Columns	Content
1	01–01	Line number
2	03–07	Satellite number
3	09–16	Inclination [Degrees]
4	18–25	Right Ascension of the Ascending Node [Degrees]
5	27–33	Eccentricity (decimal point assumed)
6	35–42	Argument of Perigee [Degrees]
7	44–51	Mean Anomaly [Degrees]
8	53–63	Mean Motion [Revs per day]
9	64–68	Revolution number at epoch [Revs]
10	69–69	Checksum (Modulo 10)

TABLE 2.8. TLE line 2 parameters description.

Alternatively, a multistatic design could be considered with a single receiver and switching between different satellites in order to maximize the achievable synthetic aperture during the whole year.

The other important parameter in the orbital design of a GEOSAR system is the orbital inclination. In this thesis, a nearly-zero inclination GEOSAR system has been proposed. Therefore, low inclinations are desired in order to avoid large longitudinal motions that could affect to the constant monitoring of the desired scene. In Figure 2.49, the orbital inclinations of the same satellites previously analysed are shown. In this case, the orbital inclination is kept under 0.1 degrees most of the time which will be suitable for the GEOSAR case studied in this thesis.

However, as explained in section 4.2.3, such inclination may degrade the quality of interferograms if daily repeat-pass GEOSAR interferometry is considered. Therefore, thinking on interferometric purposes, the inclination should be reduced as much as possible for future broadcasting geosynchronous satellites with SAR payloads. Alternatively, as it will be explained in section 5.2, the effects of the latitudinal undesired satellite motion may be reduced, or even suppressed, in a bistatic GEOSAR configuration.

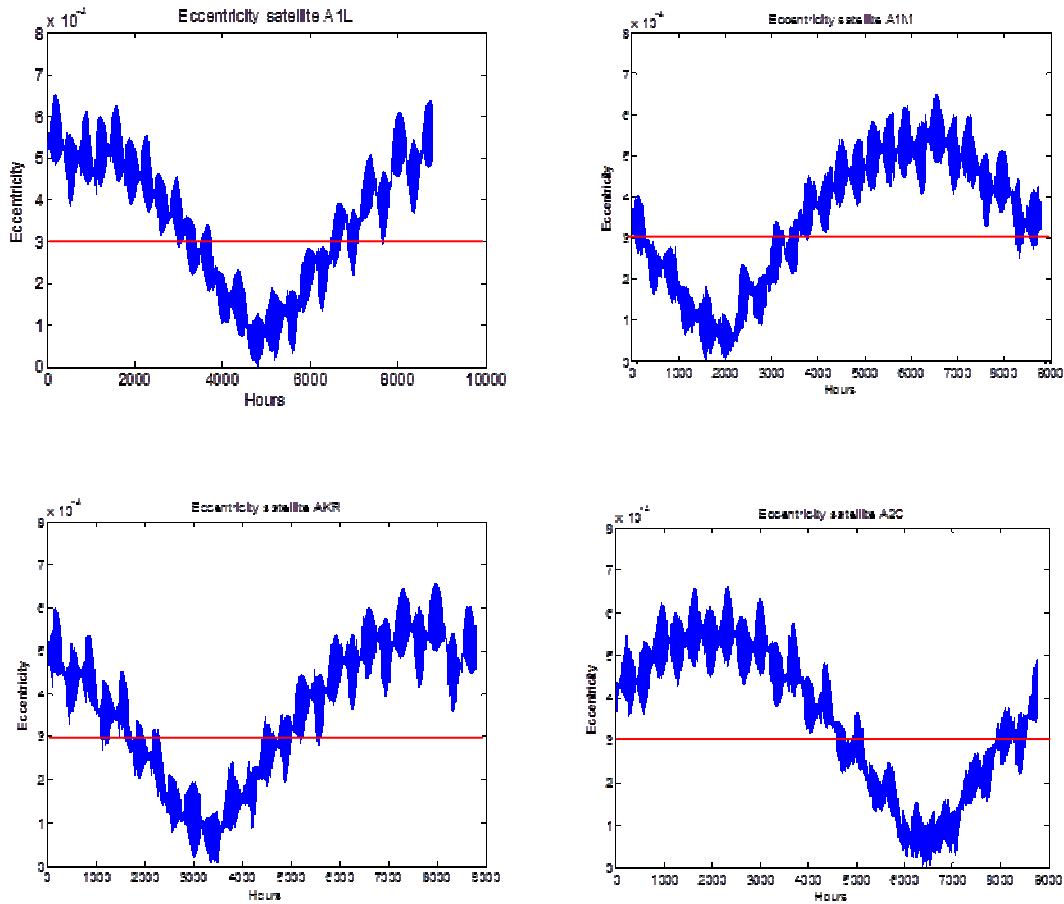


FIGURE 2.48 Orbital eccentricity of four broadcasting telecommunications satellites. Current orbital strategies for these satellites do not fulfil the eccentricity requirements for SAR purposes (eccentricity > 0.0003 has been chosen as inferior bound).

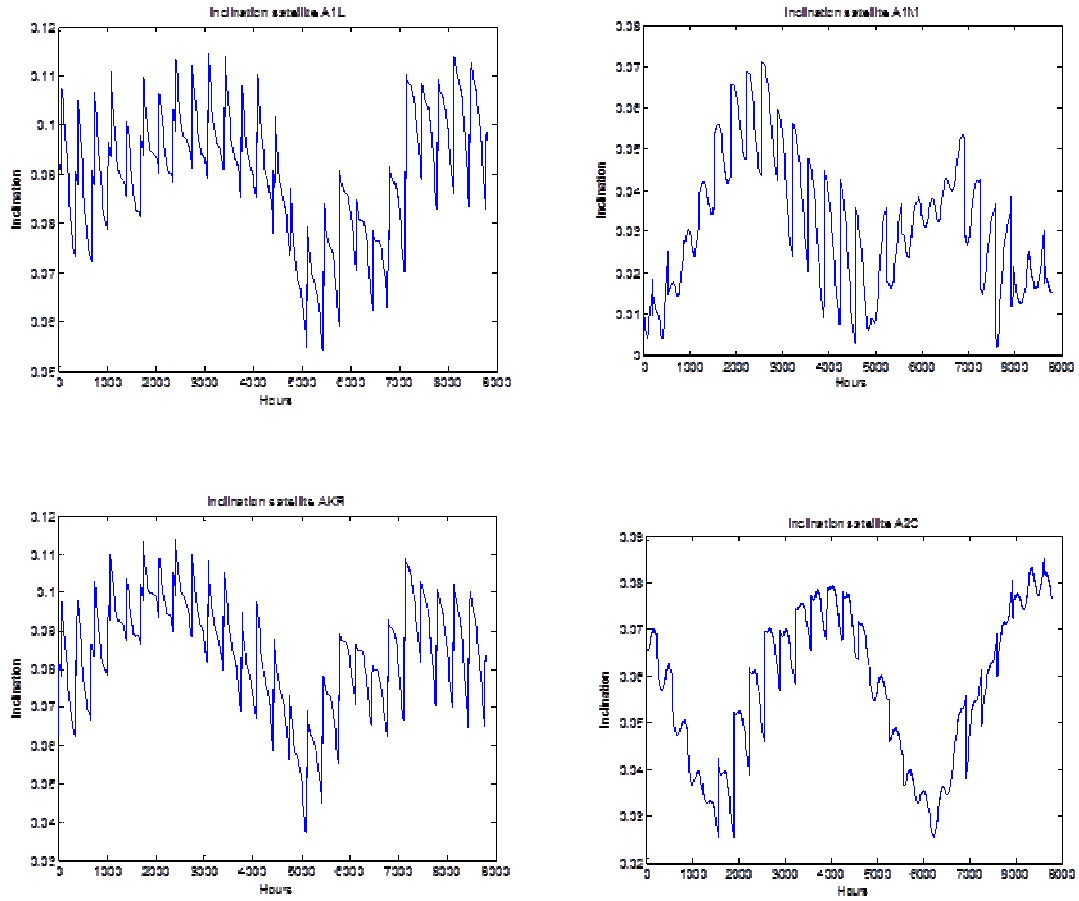


FIGURE 2.49 Orbital inclination of four broadcasting satellites. The inclinations of current satellites could be too large for SAR interferometric purposes causing cross-track decorrelation between acquisitions taken in several consecutive days (see section 4.2)

Chapter 3

Geosynchronous SAR Radiometric Analysis

3.1 Antenna design: gain, coverage and dimensions

In this section, the antenna parameters to reach the coverage requirements are defined. In the following analysis, parabolic reflectors have been considered to illuminate the scene. A brief theoretical introduction of the parabolic reflectors is presented. The antenna design (size, beamwidth, gain) will be studied and linked to the coverage requirements.

The goal of a parabolic reflector is to concentrate the radiated power of a feeder to a specific direction, with a certain gain and directivity. The far field directivity (D) of any antenna is defined as [68]:

$$D_{r \rightarrow \infty} = \frac{\wp_{\max}}{P_r / (4\pi r^2)} = \frac{4\pi r^2 |E_{\max}|^2}{\eta P_r} \Delta S \quad (3.1)$$

where \wp_{\max} and E_{\max} are maximum power density and electric field radiated by the reflector, respectively. The term P_r corresponds to the radiated power by the feeder, while η is the characteristic impedance of free space and r the distance between the antenna and the illuminated targets. In the case of the parabolic reflector, not all the power emitted by the feeder is collected by the parabolic dish. Therefore, just a fraction of the total power of the feeder (P_r) is intercepted by the reflector (P_a), while the rest ($P_r - P_a$) does not contribute to the antenna diagram. So, the equation (3.1) can be re-written as:

$$D = \frac{\wp_{\max} 4\pi r^2}{P_a} \frac{P_a}{P_r} = \frac{\wp_{\max} 4\pi r^2}{P_a} \eta_s \quad (3.2)$$

The quotient $\eta_s = P_a / P_r$ is called spill over efficiency. On the other hand, the parabolic reflector will generate a field distribution with a co-polar (P_{co}) and a cross-polar (P_{cx})

components. Since, we are only interested in the reference polarization, the polarization efficiency may be defined as $\eta_x = P_{co} / P_a$, and the previous equation can be written in terms of this new parameter as:

$$D = \frac{\wp_{\max} 4\pi r^2}{P_{co}} \frac{P_{co}}{P_a} \frac{P_a}{P_r} = \frac{\wp_{\max} 4\pi r^2}{P_{co}} \eta_x \eta_s \quad (3.3)$$

Finally, taking the reflector as an aperture, the illumination efficiency can be related to the power density and the co-polar power as [69]:

$$\frac{\wp_{\max} 4\pi r^2}{P_{co}} = D_{aperture} = \frac{4\pi}{\lambda^2} A_{geo} \eta_{il} \quad (3.4)$$

being λ the operation frequency and A_{geo} the geometric area of the reflector. So, using the relations (3.2)–(3.4) in (3.1), the directivity of the whole antenna (reflector+feeder) may be computed as:

$$D = \frac{\wp_{\max} 4\pi r^2}{P_{co}} \frac{P_{co}}{P_a} \frac{P_a}{P_r} = \frac{4\pi}{\lambda^2} A_{geo} \eta_{il} \eta_x \eta_s = \frac{4\pi}{\lambda^2} A_{geo} \eta_t \quad (3.5)$$

In this case, the total efficiency η_t is obtained as the product of the other efficiencies. Additionally, if the ohmic efficiency (η_{ohm}) of the antenna is considered, the antenna gain is obtained as:

$$G = \frac{4\pi}{\lambda^2} A_{geo} \eta_t \eta_{ohm} = \frac{4\pi}{\lambda^2} A_{eff} \quad (3.6)$$

The term A_{eff} corresponds to the effective area of the reflector, and it is computed as the product of the geometric area by the total and ohmic efficiency of the antenna. Finally, in case of a parabolic reflector, the antenna angular beamwidth in radians (θ_{ant}^{-3db}) can be related to the transmitted wavelength and the antenna diameter (ϕ_{ant}) as [70]:

$$\theta_{ant}^{-3db} = \frac{70^\circ \lambda}{\phi_{ant}} \frac{\pi}{180^\circ} \text{ rad} = 1.22 \frac{\lambda}{\phi_{ant}} \text{ rad} \quad (3.7)$$

From the acquisition geometry and the desired coverage, the antenna beamwidth requirements can be obtained. So, considering the scheme presented in Figure 3.1, the antenna beamwidth can be related with the slant range to the scene (R_s) and swath coverage (ΔS) with linear trigonometry as:

$$\theta_{ant}^{-3db} = 2 \arctan \left(\frac{\Delta S / 2}{R_s} \right) \quad (3.8)$$

In order to check the range of expected gains and antenna size in a GEOSAR configuration for different coverage, several frequency bands (L-, C-, X- and Ku-band) have been

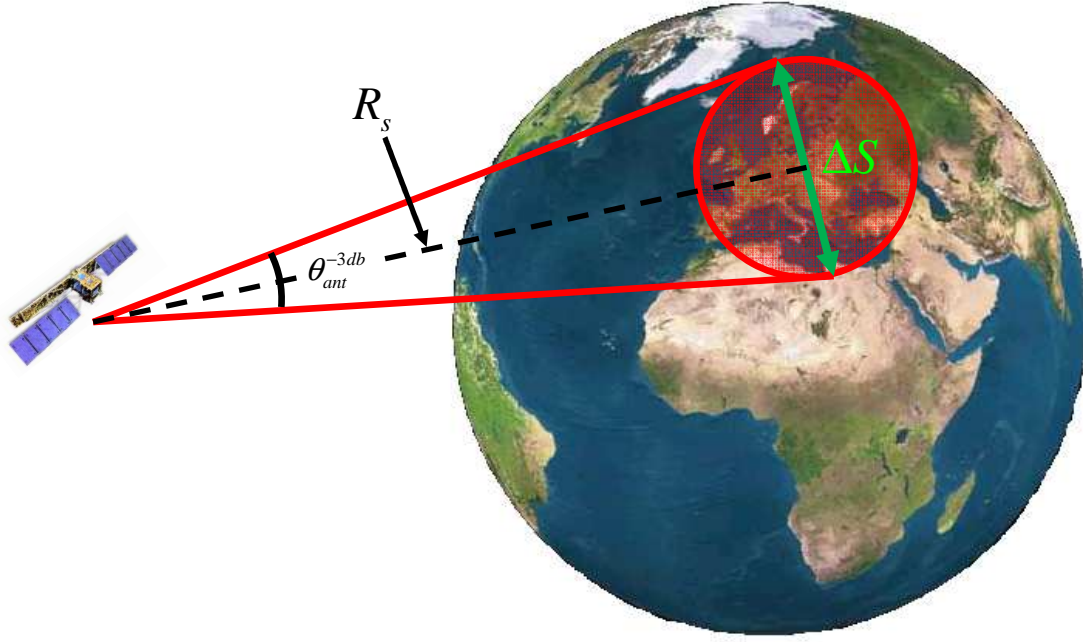


FIGURE 3.1 Antenna beamwidth requirements to fulfil the desired coverage.

analysed. A range of coverage from 100 Km to 5000 Km has been analysed. The antenna beamwidth requirements for a desired coverage are independent of the transmitted frequency, as given by equation (3.8). Similarly, antenna directivity does not depend on the frequency for a given coverage since the wavelength dependence shown in (3.5) is cancelled when the antenna diameter obtained by (3.7) is used in the antenna area computation.

Therefore, the antenna beamwidth requirements and the obtained antenna gain are shown in Figure 3.2 and Figure 3.3, respectively. Obviously, for larger coverage, larger antenna beamwidth is required and, consequently, lower antenna gain is obtained. Therefore, the system coverage will be limited, as it is studied in section 3.5, by the power link budget requirements in order to avoid using high transmitted powers.

However, the antenna gain cannot be increase arbitrary in order to improve the Signal to Noise Ratio of the acquisition since it will penalize the system coverage. Furthermore, reducing the system coverage, would result in large antennas which are not the focus of the GEOSAR mission analysed in this thesis. So, the antenna size requirements obtained for different frequency band and different ground coverage are summarized in Figure 3.4. Considering a maximum antenna size around 4.5 m, the minimum swath coverage to be considered at L-band will be around 1850 km, while at Ku-band it could be reduced up to 175 km.

Then, it will have a clear impact on the SNR analysis presented in section 3.5 since the antenna size limitations will impact on the maximum antenna gain that could be considered in the power link budget computation for the different frequency bands. So, considering the minimum coverage obtained from the antenna size requirements of Figure 3.4, a maximum

antenna gain of **35.83 dB**, **46.01 dB**, **51.20 dB** and **56.27 dB** are obtained for L-, C-, X- and Ku-bands, respectively.

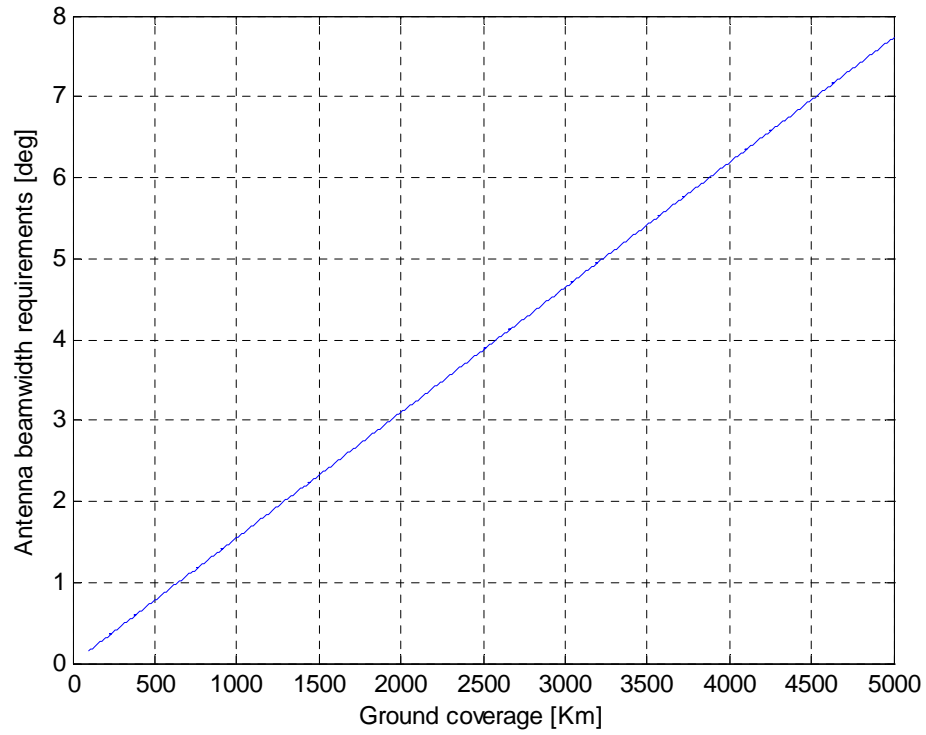


FIGURE 3.2 Antenna beamwidth requirements vs. desired ground coverage.

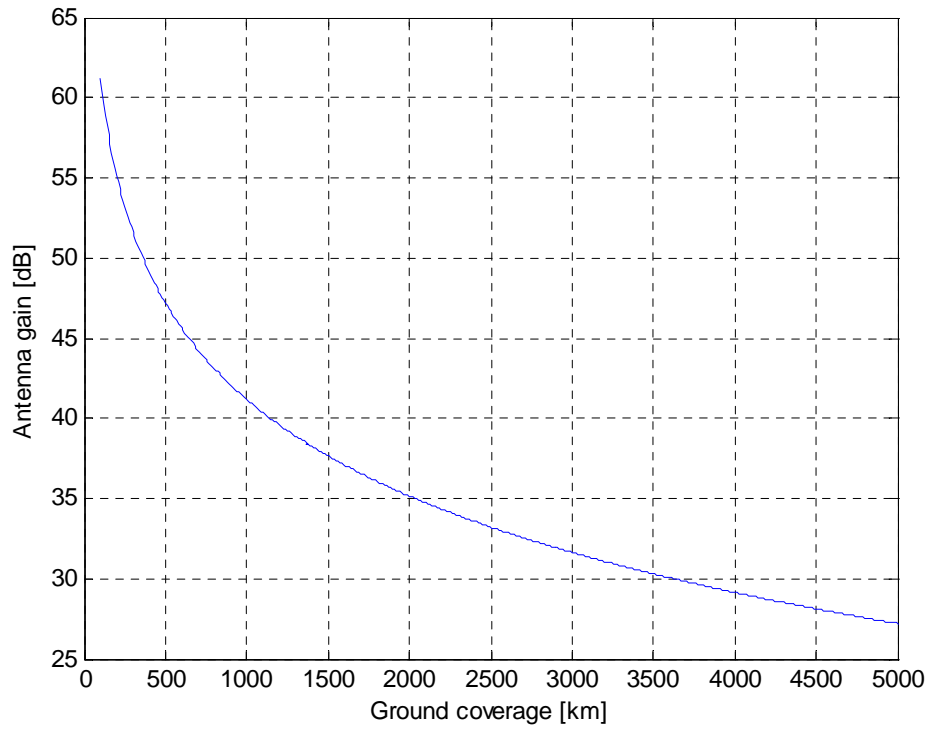


FIGURE 3.3 Antenna gain requirements vs. desired ground coverage.

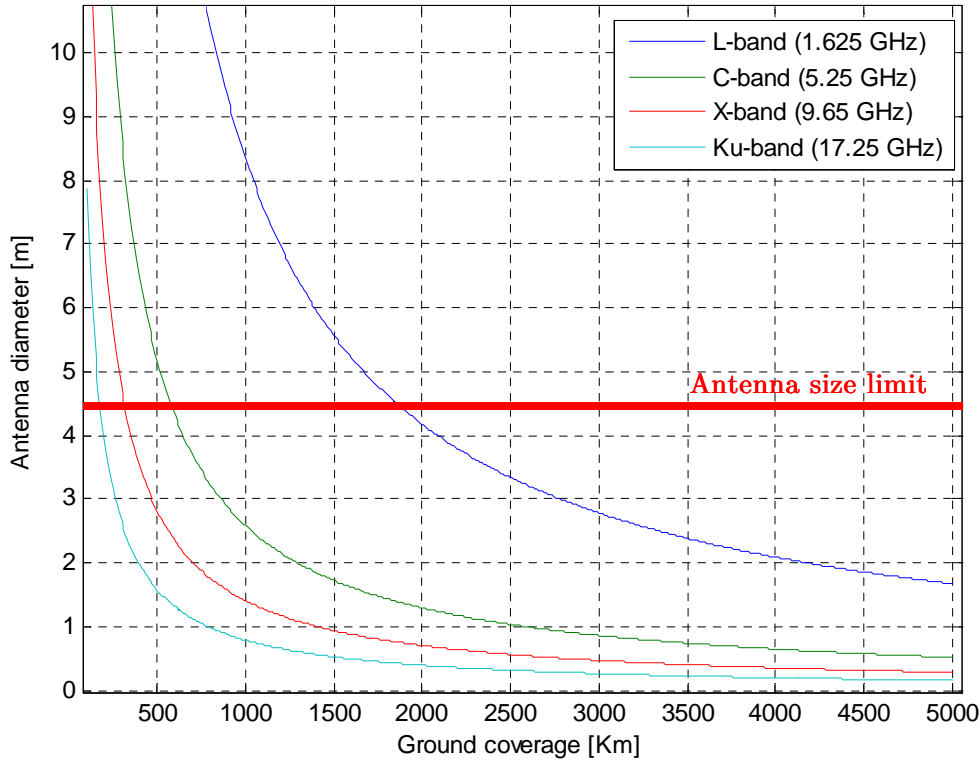


FIGURE 3.4 Antenna beamwidth requirements vs. desired ground coverage at different frequency bands.

3.2 Doppler analysis of received data: Doppler centroid compensation

In this section, the Doppler history of the received echoes along the acquisition will be analysed. As described in section 2.1, the orbital radius of a geosynchronous orbit with small eccentricity will not be constant (equation (2.1)). As explained later in this section, these variations will introduce a common Doppler shift in the whole imaged scene which will not be useful to discriminate the origin of the received echoes. Therefore, this component must be tracked and compensated. Then, the residual Doppler will determine the useful bandwidth for processing within the antenna footprint. The Doppler bandwidth of the imaged scene will be essential to determine the minimum PRF of the system in order to satisfy the Nyquist criteria. Furthermore, this instantaneous Doppler within the antenna footprint will be related to the achievable along-track resolutions shown in section 2.4.2.

3.2.1 Doppler shift in SAR acquisition

The Doppler Effect is a phenomenon that modifies the apparent received frequency when transmitter and/or receiver are moving with respect to the illuminated surface. It is not the purpose of this report to give a complete analysis and derivation of the precedence of the

Doppler, but the basic formulas which affect to the SAR acquisition will be given in this section.

The Doppler shift appreciated at any system with the transmitter and/or the receiver in motion can be computed as:

$$f_d \cong -\frac{1}{\lambda} \frac{\partial R}{\partial t} \quad \text{for} \quad \frac{\partial R}{\partial t} \ll c \quad (3.9)$$

where $\partial R/\partial t$ is the derivative of the slant range between the satellite and the targets in function of the time. This term is equivalent to the radial velocity towards the line of sight direction. Equation (3.9) accounts for the one way Doppler shift. In monostatic SAR, the two-way shift is obtained by multiplying by 2 the equation (3.9), since the transmitter and the receiver are placed at the same satellite and, consequently, they have the same Doppler history. In case of bistatic SAR, the motion of the transmitting and receiving satellites can be completely independent. Therefore, each Doppler component must be computed separately and then added to obtain the final Doppler shift.

In LEO SAR systems with linear satellite path, the Doppler history of the different targets follows a linear behaviour, starting from positive values, decreasing until zero Doppler shift when the target position is perpendicular to the satellite velocity and, then, increasing negatively until the target goes out of the antenna processing beam. However, the non-linear motion characteristic of the GEOSAR mission analysed in this report makes difficult to give a simple formulation for this phenomenon.

The Doppler history of targets, and more specifically the Doppler bandwidth within the antenna footprint, will determine the SAR performance in terms of along-track resolution. The along-track resolution can be related to the Doppler bandwidth of the acquired signal as [20]:

$$\rho_{az} = \frac{v_{sat}}{B_d} \quad (3.10)$$

In the following section, the Doppler history of a GEOSAR system is studied. As it will be explained, the Doppler bandwidth is related to the orbital ephemerides of the satellite since they will govern the relative motion between the scene and the satellite.

3.2.2 Doppler history in GEOSAR

In a GEOSAR system, the Doppler history of the targets will be quite different from the one obtained by a linear LEO SAR acquisition. The non-constant radius of the orbit will add a Doppler component to the common along track motion of the LEO satellites. This frequency shift produced by the radius changes will not be of our interest during the SAR

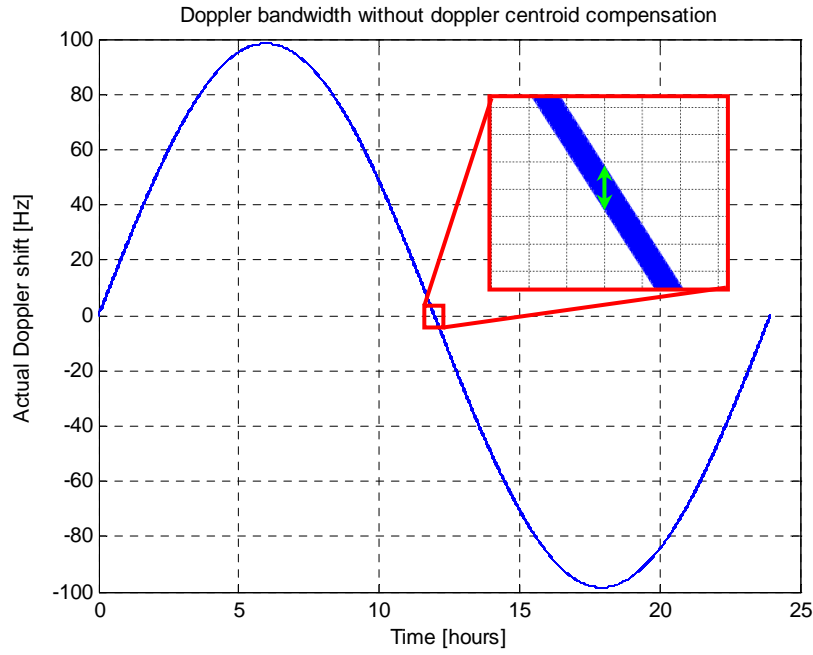


FIGURE 3.5 Doppler history of targets from a scene of 100 by 100 Km.

processing since it is a common shift for all the targets in the scene and, consequently, it cannot be used to discriminate the different targets on the azimuth direction. Therefore, it only adds a non-constant Doppler centroid to the raw data acquisition. So, the instantaneous Doppler bandwidth within the antenna footprint from the different targets of the desired scene will be the one used to process the received signal.

So, the whole Doppler bandwidth will depend on different factors such as the orbital configuration, the scene size or the transmitted frequency. Just as an example, the Doppler history of 100 by 100 Km scene placed over Barcelona and illuminated by a geosynchronous satellite at 10°W with an eccentricity of 0.0004 and inclination of 0.046 degrees is presented in Figure 3.5. A transmission signal frequency of 12 GHz has been considered. As seen, a total bandwidth around 200 Hz is obtained if the Doppler centroid is not compensated. However, the useful instantaneous Doppler bandwidth is the one shown with a green arrow in Figure 3.5.

The Doppler shift behaviour will strongly depend on the GEOSAR configuration (monostatic or bistatic) and the orbital parameters of the satellite/s. So, it is not easy to find a closed formula to easily compute the associated bandwidth for a generic GEOSAR acquisition as in LEO satellite. However, some approximations can be done in order to find an equation valid for particular GEOSAR configurations.

Let us consider a simpler case with a monostatic GEOSAR configuration with a single satellite in a low eccentric and no inclined orbit. The satellite is looking perpendicular to

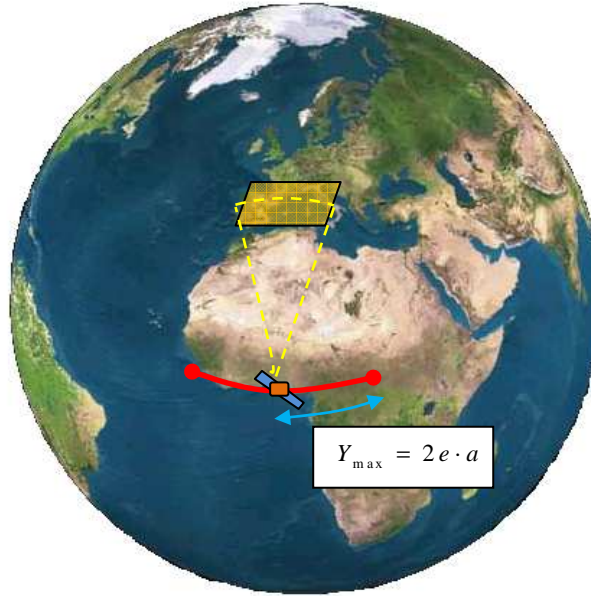


FIGURE 3.6 Synthetic aperture for a slightly eccentric orbit.

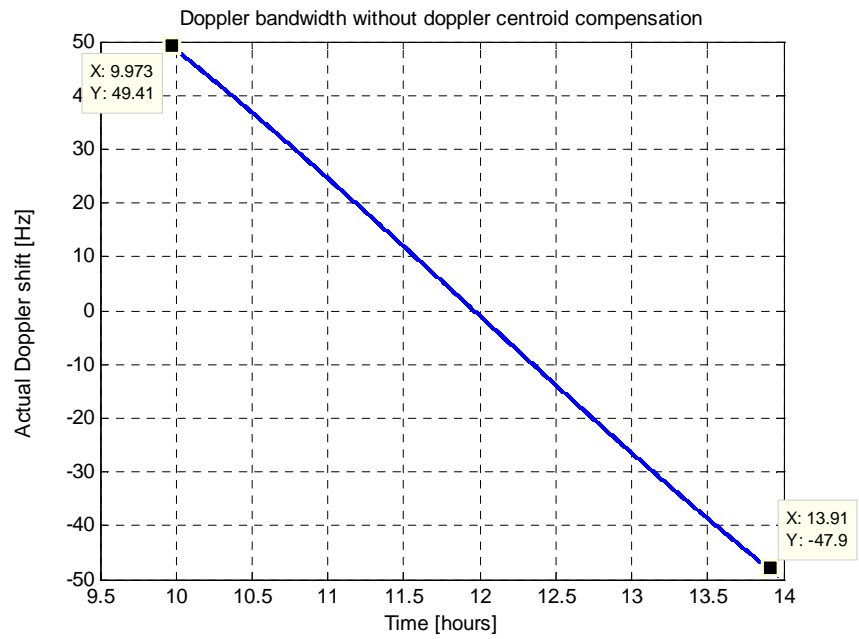


FIGURE 3.7 Doppler bandwidth considering 4 hours of integration time.

the equatorial line. The situation is schematically represented in Figure 3.6.

As it has been analytically computed in section 2.4, the synthetic aperture of the satellite with respect to the target can be obtained as in (2.59). So, the maximum longitudinal displacement of the satellite will be obtained as the half of the achieved synthetic aperture length:

$$Y_{\max} = 2e \cdot a \sin\left(\Omega_E \frac{T_i}{2}\right) \quad (3.11)$$

being e the orbit eccentricity, a the semi-major axis of the orbit ellipse, Ω_E the Earth's rotation angular velocity and T_i the integration time. From this maximum along track motion, the maximum Doppler bandwidth received from the scene can be computed as:

$$B_d = 2\Omega_E \frac{Y_{\max}}{\lambda} = 4\Omega_E \frac{e \cdot a}{\lambda} \sin\left(\Omega_E \frac{T_i}{2}\right) \quad (3.12)$$

If the previous formula is particularized for the orbital and signal parameters used in Figure 3.5, and an integration time of 4 hours is considered, a Doppler bandwidth of 98.63Hz is obtained. If this result is compared with the simulated results using this configuration, they are consistent since the obtained simulated Doppler bandwidth is around 97.31Hz as shown in Figure 3.7.

So, this approximation is valid for time intervals where the Doppler history presents a quasi-linear behaviour. Therefore, looking at Figure 3.5, (3.12) would be correct around the time interval from hour 9 to 15. On the other hand, it would not have any sense at intervals with maximum Doppler shift, around hours 6 or 18. However, it is only valid for this particular configuration.

In the next section, the Doppler bandwidth compensated with the Doppler centroid all along the GEOSAR acquisition is analysed. The compensated Doppler bandwidth will be the one used in reception to process the raw data from the scene.

3.2.3 *Doppler centroid estimation and compensation*

In any SAR system, the Doppler shift is essential to distinguish two targets at the same range whose echoes arrive to the receiver at the same time. However, the Doppler bandwidth computed in the previous section was not useful in SAR processing since it takes into account the common Doppler shifts that affect in the same way to all the targets in the scene due to the orbital radius variations.

Therefore, only the relative Doppler shifts between the points of the scene have to be considered. From these relative shifts, the useful Doppler bandwidth will be obtained. In order to get the useful Doppler bandwidth within the antenna footprint, the total Doppler of the received signal has to be compensated by the Doppler shift of one point within the scene (the central point for instance) in order to get the relative Doppler of all the targets with respect to this point. This Doppler centroid tracking and compensation will give as a result a lower Doppler bandwidth to be processed which will require a smaller PRF to accomplish Nyquist.

In order to see the typical behaviour of the Doppler shift in a GEOSAR acquisition let us

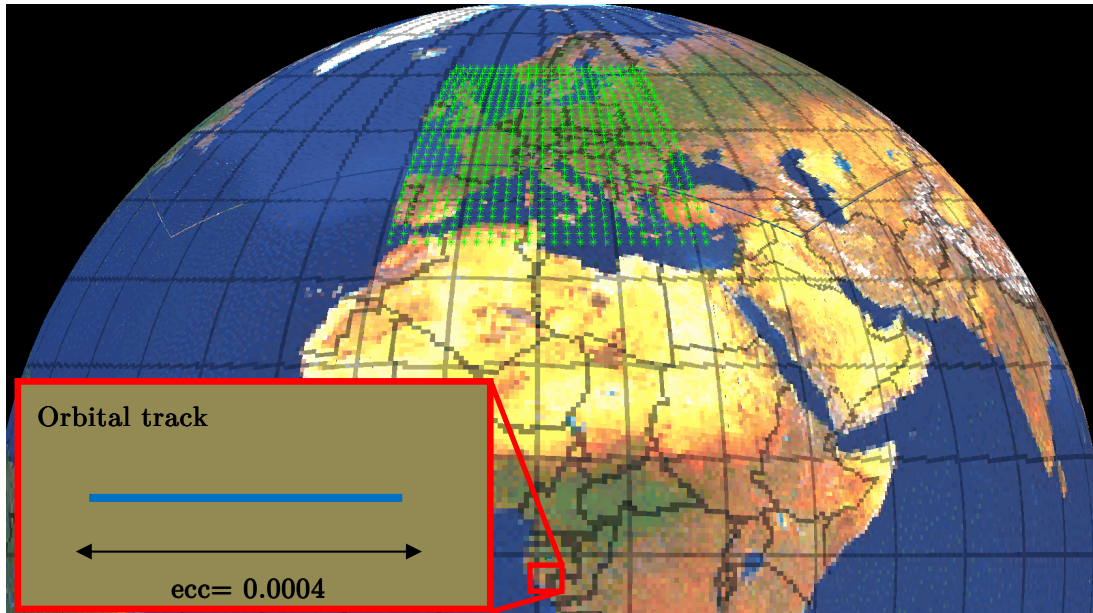


FIGURE 3.8 Covered scene for the L-Band wide beam (~ 3000 Km) and satellites orbit configuration (0.0004 eccentricity and zero inclination) for the Doppler bandwidth analysis.

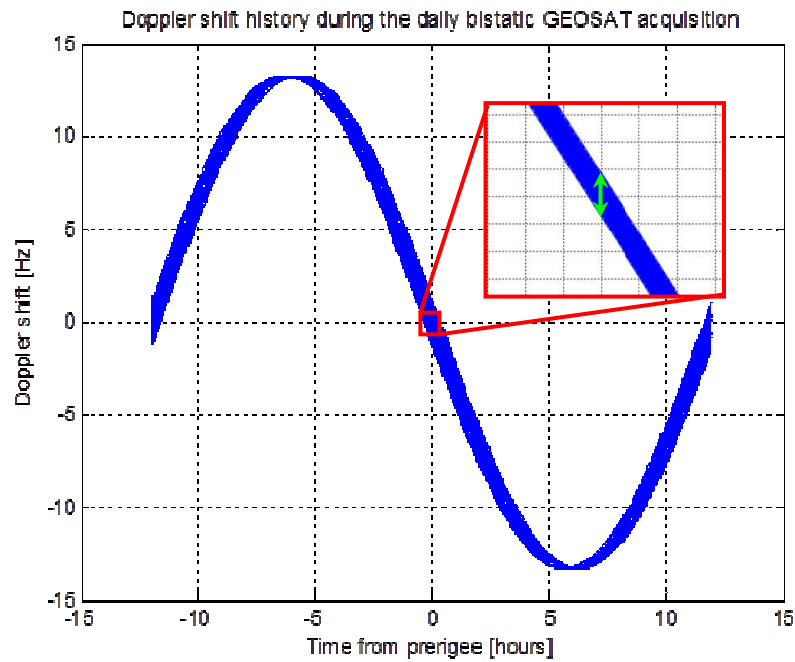


FIGURE 3.9 Doppler history of a bistatic GEOSAR acquisition at L-Band over a region covering the South-Eastern Europe with a pair of satellites with an orbital eccentricity of 0.0004.

consider two different situations. According to the results obtained in section 3.1, a wide beam covering a 3000 Km swath at L-band (1.625 GHz) and a narrower beam of 650 Km at Ku-band (17.25 GHz) will be considered. So, the Doppler behaviour in two opposite situations can be compared.

For the L-band acquisition, a wide coverage beam covering the south-western region of

Europe, centred at 11°E 48°N , has been taken. A satellite with nominal longitudes of 11°E and orbital eccentricity of 0.0004 has been used. Zero inclination of the orbital plane has been considered. The satellite-scene acquisition geometry is schematically presented in Figure 3.8 where the covered region is shaded with green points and the satellites motion is zoomed-in.

So, the Doppler history obtained taking the parameters presented above is presented in Figure 3.9. As seen, the total Doppler span goes from -13.2 to 13.2 Hz with maximum Doppler shifts corresponding to the maximum temporal derivative of orbital radius (at $t_p \pm 6 h$). As mention before, the Doppler centroid history during the daily motion is mainly caused by the orbital radius variations. Therefore, the system must be capable of tracking and compensate this Doppler centroid evolution previous the raw data focusing. However, even the total Doppler bandwidth is not worth for SAR focusing purposes; our receiver needs to acquire the whole bandwidth in order to follow the Doppler shift received. So, a total bandwidth of around 30 Hz would be required in this case.

However, other SAR parameters and constraints will be limited by the instantaneous Doppler shifts within the antenna footprint. This is the case of the minimum Pulse Repetition Frequency (PRF) required to fulfil the Nyquist criteria. Once again, going back to the previous example, the instantaneous Doppler bandwidth after Doppler centroid compensation is shown in the zoom-in of Figure 3.9 as a green double arrow. As it can be seen, the instantaneous Doppler bandwidth will be much smaller than the total Doppler span of the acquisition.

In order to show the behaviour of this instantaneous Doppler bandwidth, the Doppler shift of the central point of the scene has been used as a Doppler centroid reference of the acquisition. Therefore, subtracting this Doppler history to the Doppler shifts of the whole scene, the results presented in Figure 3.10 are obtained. In this case, the maximum instantaneous Doppler bandwidth is less than 3 Hz, going from -1.3 to 1.3 Hz. This bandwidth is the one that will determine the minimum pulse repetition frequency which is in fact the azimuth sampling rate taking into account the Nyquist limit and desired margin to prevent aliasing.

Furthermore, as seen in Figure 3.10, the instantaneous Doppler bandwidth is time dependent being maximum around the time pass through the perigee and apogee and nearly zero around $t_p \pm 6 h$. This happens due to the larger longitudinal motion when the satellites cross the perigee and the apogee which results in larger Doppler bandwidth and, consequently, better along-track resolution. On the other hand, at $t_p \pm 6 h$ the satellite motion is completely radial and, after Doppler centroid compensation, the resultant Doppler shifts are mostly cancelled. These results are consistent with the resolution analysis presented section 2.4.1.1.

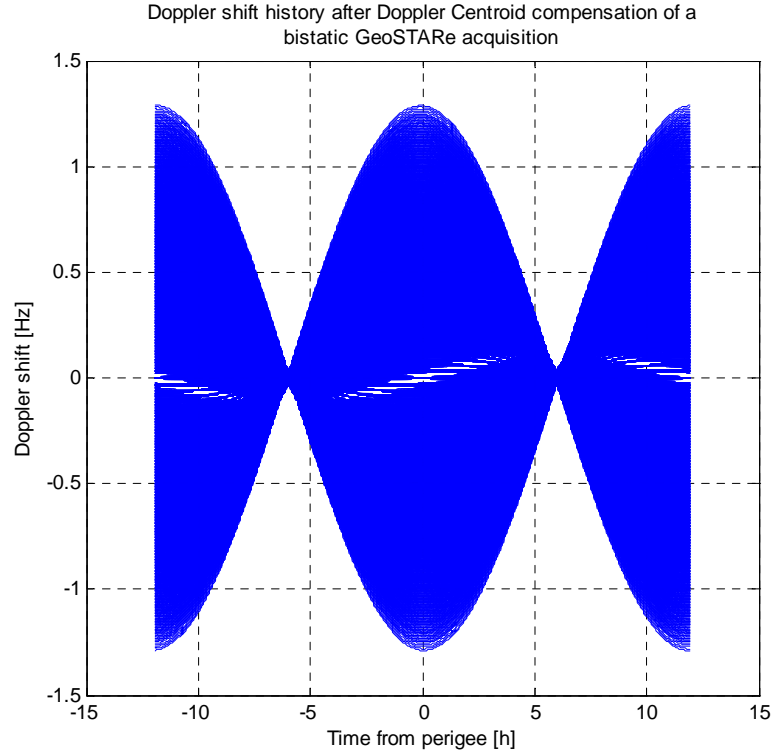


FIGURE 3.10 Doppler history of a bistatic GEOSAR acquisition at L-band after Doppler centroid compensation.

On the other hand, the same analysis is proposed for a Ku-band beam. In this case, considering a spot beam with smaller coverage, the Doppler shifts within the scene should be lower. However, working at Ku-band with smaller transmitted wavelength, the Doppler shifts will increase. So, let us consider the same orbital configuration than in the L-band beam Doppler analysis: 0.0004 orbital eccentricity and zero inclination. In this case, a smaller antenna footprint of 650 Km diameter has been considered. The acquisition geometry is schematically presented in Figure 3.11.

The Doppler history obtained in this case is shown in Figure 3.12. As it can be seen, the whole Doppler bandwidth is around 280 Hz, larger than in L-band due to the smaller wavelength. However, if the Doppler bandwidth within the antenna footprint is computed subtracting the Doppler centroid, the result obtained is shown in Figure 3.13. In this case, as in the L-band Doppler analysis, the Doppler bandwidth within the antenna footprint is about few Hertz, from -2.5 to 2.5 Hz.

So, on conclusion, the receiver needs to be capable of receive a whole band of around 30 Hz in L-band and 300 Hz at Ku-band. However, other SAR parameters and constraints (PRF selection, azimuth resolution, etc.) will be given by the instantaneous Doppler within the antenna footprint which is around 2.6 Hz at L-band and 5.0 Hz at Ku-band. These will be the effective bandwidths to be considered during the raw data processing.

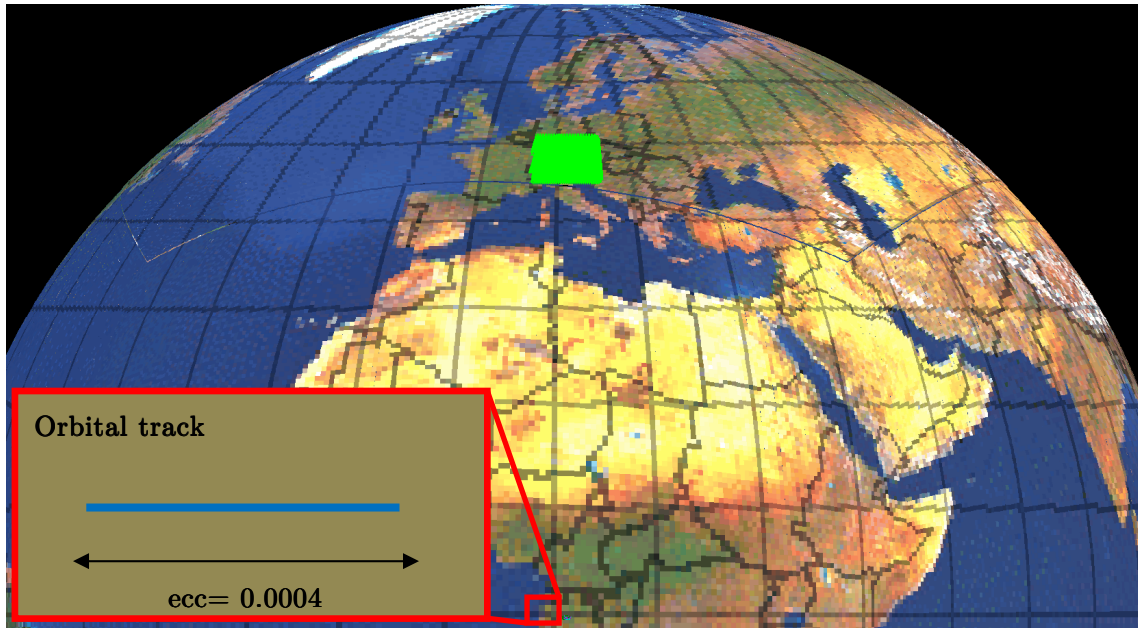


FIGURE 3.11 Covered scene for the Ku-Band spot beam (~650 Km) and satellites orbit configuration (0.0004 eccentricity and zero inclination) for the Doppler bandwidth analysis.

The Doppler bandwidth after Doppler centroid compensation will vary from one GEOSAR configuration to another. However, if smaller scenes are considered when the system operates at higher frequencies and the other way around, the final bandwidth will always be of a few Hz. This is a particular feature of the GEOSAR acquisition studied in this thesis with small orbital eccentricities and inclination. Typical Doppler processed bandwidth in LEOSAR or other GEOSAR configurations with larger orbital tracks are in the order of KHz. So, this result must be taken into account in the timing analysis presented in section 3.3 where the PRF requirements are analysed.

3.3 Timing and PRF selection: diamond and dartboard diagrams

The choice of the Pulse Repetition Frequency (PRF), which is the inverse of the period between two consecutive pulses sent by the radar, is constrained by a large number of factors. The ambiguity level, azimuth and range, is highly dependent on the PRF but, at the same time, it has other constraints that has to be taken into account in the PRF selection.

In this section, the PRF restrictions related to the SAR interferences will be analysed [20]. In a monostatic SAR systems the same antenna is used for both transmit and receive. Therefore, the time must be divided between transmission and reception intervals periodically. The received echoes must be interspersed between two transmitted pulses in order not to lose any part of the received information. In case of open bistatic

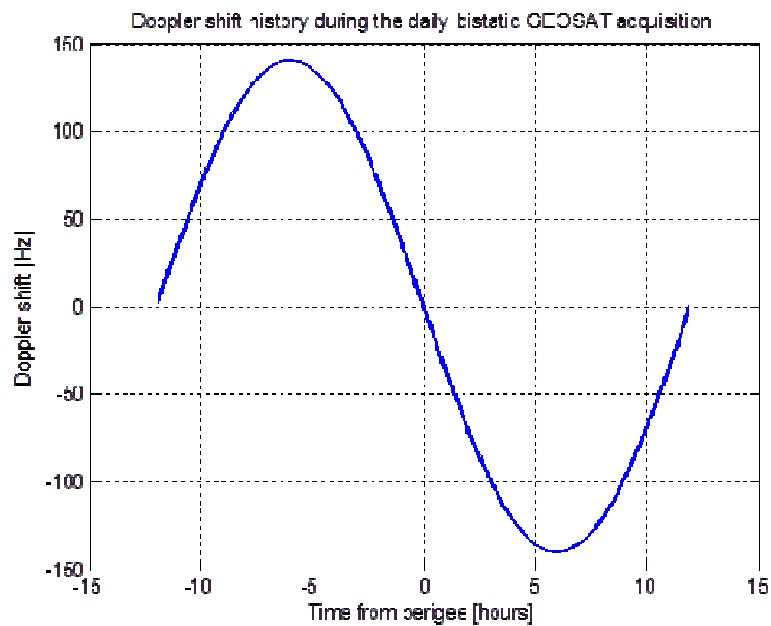


FIGURE 3.12 Doppler history of a bistatic GEOSAR acquisition at Ku-Band over a region covering the South-Eastern Europe with a pair of satellites with an orbital eccentricity of 0.0004.

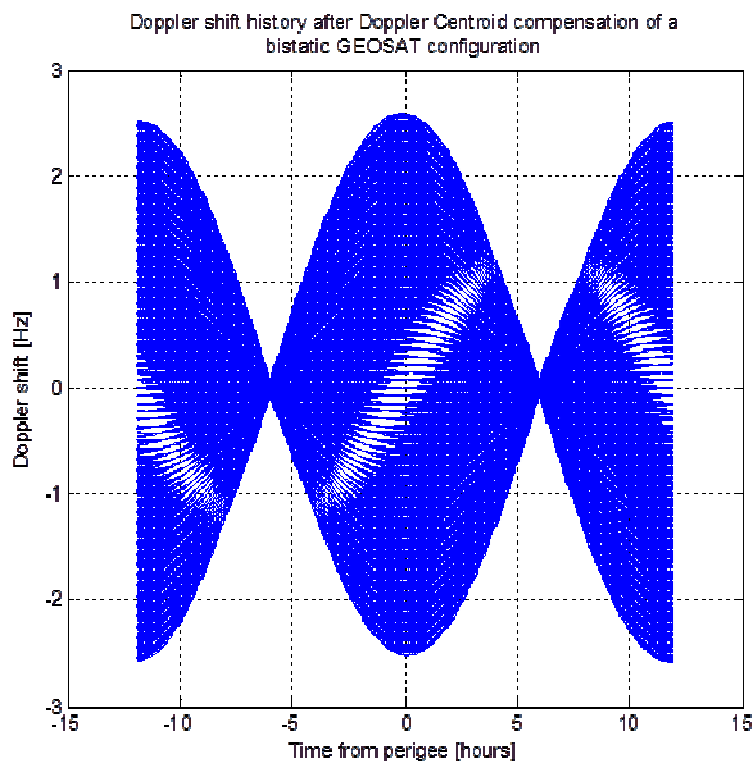


FIGURE 3.13 Doppler history of a bistatic GEOSAR acquisition at Ku-band after Doppler centroid compensation.

configuration, with separate transmitting and receiving satellites, this issue is avoided. However, for closer bistatic formations, the transmission interferences could be important if no isolation is assured between the transmitting and receiving antennas.

On the other hand, in the monostatic case the values of the PRF are selected such that the strong nadir echoes (echoes coming from the sub-satellite point) from succeeding pulses do not arrive at the same time that the data reception window since it could mask the useful returns. In case of bistatic configurations, the nadir point under the satellites will not be a problem but, on the other hand, there will be a point between both satellites where the specular reflection could result in a strong received echo. In this section, the PRF selection analysis is centred to the monostatic case. The bistatic configuration will be studied in detail in Chapter 5.

Therefore, the transmitting interferences in a monostatic configuration can be modelled with the next equations [20]:

$$\text{Frac}(2R_1 PRF / c) / PRF > \tau_i + \tau_{RP} \quad (3.13)$$

$$\text{Frac}(2R_N PRF / c) / PRF < \frac{1}{PRF} - \tau_{RP} \quad (3.14)$$

$$\text{Int}(2R_N PRF / c) = \text{Int}(2R_1 PRF / c) \quad (3.15)$$

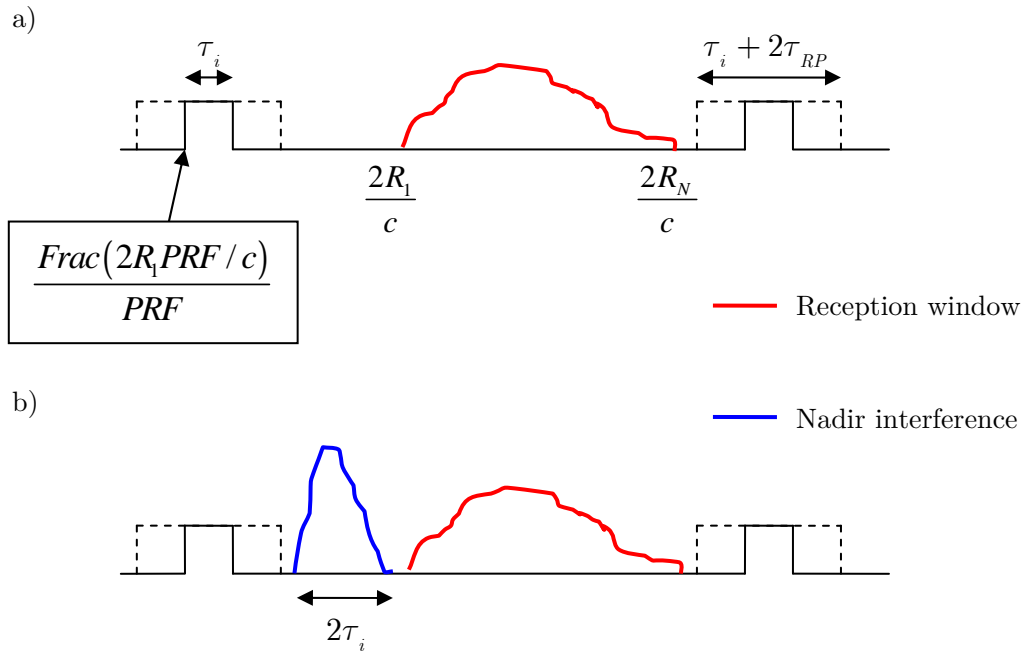


FIGURE 3.14 Timing diagram for PRF constraints: a) transmit interference and b) nadir interference.

In these equations, R_1 is the slant range to the nearest point of the scene, R_N is the slant range to the furthest scene point, τ_i is the duration of the transmitted pulse, and τ_{RP} is a guard time used in reception to avoid emitted-received pulse interferences. Finally, the function *Frac* extracts the fractional part of its argument, while the function *Int* takes the integer part of the value. In order to illustrate the meaning of these equations, Figure 3.14 a) shows the timing diagram of the radar transmission-reception events.

The reception burst, as shown in Figure 3.14 a), has to be interspersed between two consecutive pulse transmission events. This is imposed by equation (3.15) where the first and last data of the received burst are in the same inter-pulse period. Furthermore, equation (3.13) guarantees that the first data arrives after the guard time, while (3.14) adjusts the PRF such that the last data taken arrives before the guard interval of next emitted pulse.

On the other hand, the nadir return must not interfere with the reception windows. For this reason, as it can be observed in Figure 3.14 b), the selected PRF has to fulfil equations (3.16) and (3.17) for the monostatic LEOSAR case [20].

$$2h / c + j / PRF > 2R_N / c \quad j = 0, \pm 1, \pm 2, \dots \pm n_h \quad (3.16)$$

$$2h / c + \Delta t_{nad} + j / PRF < 2R_1 / c \quad j = 0, \pm 1, \pm 2, \dots \pm n_h \quad (3.17)$$

where h is the platform height over the nadir point and Δt_{nad} is the temporal extension of the nadir return. The duration of the nadir return depends on the illuminated terrain. Equation (3.16) adjusts the PRF such that all the nadir returns of succeeding and preceding pulses (j index) arrive after the last echo of the recording window. On the other hand, equation (3.17) assures that the nadir eclipses do not extend further than the beginning of the first echo of the next reception window.

In case of LEOSAR, the high power received from the nadir return may saturate the receiver during all the echo duration being impossible to compress neither the nadir nor the desired echoes. Therefore, if one of the previous constraints are not fulfilled the zone must be discarded since the received echo will be partially loss.

On the other hand, from a geosynchronous orbit, it is expected that the nadir return will mask the desired echo (it will be more powerful than the echoes from the scene) but it will not be powerful enough to saturate the receiving chain due to the far distances where the satellite is orbiting. For this reason, the nadir return could be range compressed. Therefore, only those received echoes that completely overlap with the nadir return will be eclipsed after range compression.

So, in case of GEOSAR acquisition the restrictions given by (3.16) and (3.17) must not be fulfilled at the same time to consider a zone as interfered by the nadir return which would

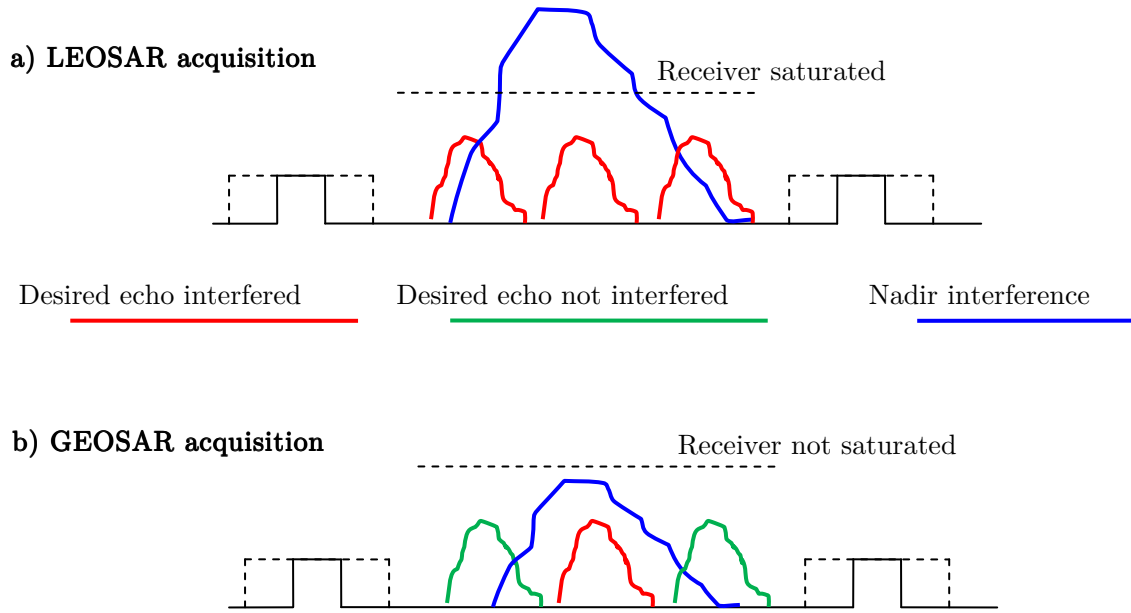


FIGURE 3.15 Nadir eclipses in LEOSAR vs. GEOSAR.

mean that the received echo is completely overlapped with one of the nadir returns.

In Figure 3.15, both cases are compared. As shown, in LEOSAR acquisition, all the desired returns partially overlapped with the nadir returns will be interfered since the receiver is saturated and, therefore, the desired information will be lost. On the other hand, in GEOSAR, the nadir return does not saturate the receiver and only those returns overlapped with the compressed nadir return will be interfered after range compression.

In SAR systems, it is common to use the diamond diagram [20] to identify the zones interfered by the transmission events or nadir returns for a range of possible PRFs. So, in the diamond diagram, the interfered zones are plotted in a PRF-incidence angle diagram. In GEOSAR, the range of selectable PRFs will be lower in order to have larger coverage which is not a problem taking into account the instantaneous Doppler bandwidth of few Hz obtained in section 3.2.

In order to see the diamond diagram in GEOSAR different Duty Cycles (DCs) have been considered in the following analysis. The duty cycle is the ratio of the pulse duration with respect to the inter-pulse period. Therefore, the transmission free interference slots will be smaller when the DC increases. As an example, the diamond diagrams for a typical GEOSAR configuration considering a duty cycle of 40% and 20% are presented in Figure 3.16 and Figure 3.17, respectively. As seen, the transmission interferences (in red) are more important in the case of 40% duty cycle due to the larger pulse length considered.

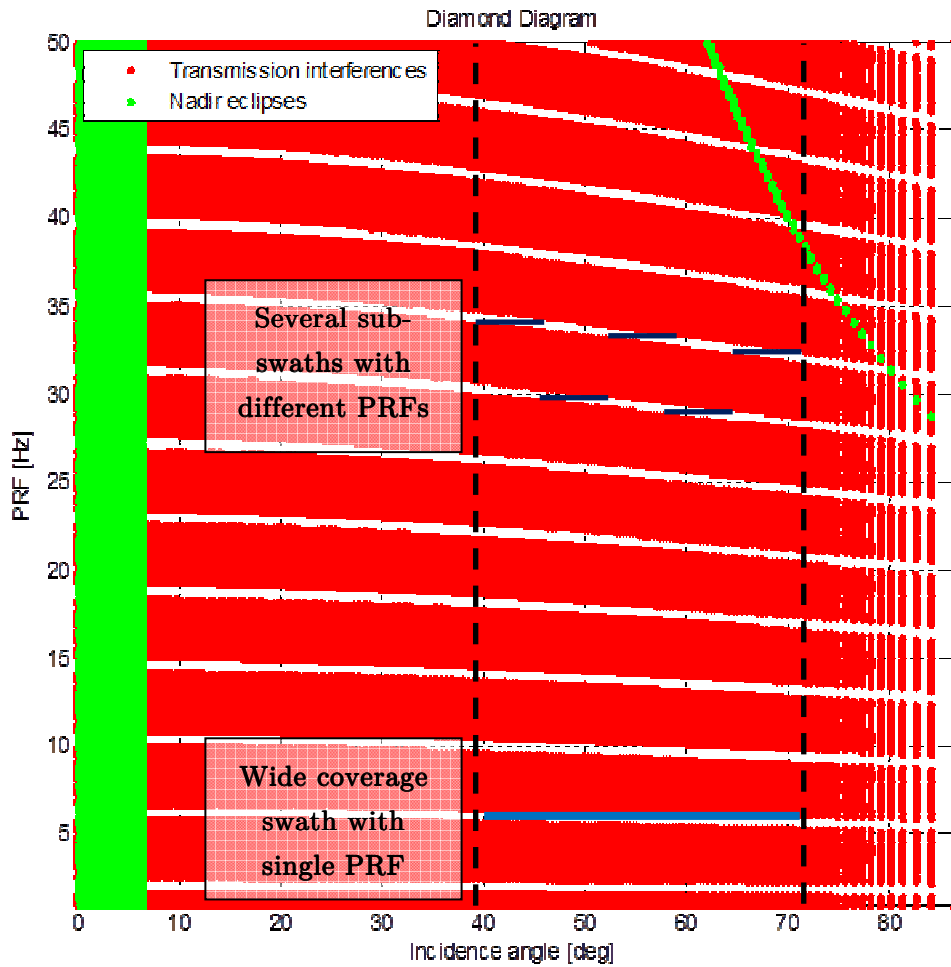


FIGURE 3.16 Diamond diagram for GEOSAR working with a duty cycle of 40%.

On the other hand, as shown in Figure 3.16 and Figure 3.17, the nadir eclipses are not affected by the DC variations since a fixed extension of 1 degree in look angle around the nadir point has been considered for the nadir return duration. This corresponds to the green strip of Figure 3.16 and Figure 3.17 going from 0 to 6.5 degrees of incidence angle. As seen, the nadir interference of first order does not appear until a PRF of 27 Hz. Furthermore, considering the nadir return range compression capabilities of GEOSAR presented in Figure 3.14, the nadir interference is a thin line that will only affect to small part of the illuminated scene at worst.

If the region of interest is within the 40° to 70° incidence angle interval, a free interference slot in the diamond diagram must be found in order to avoid transmission and nadir eclipses. As seen in Figure 3.16, for a duty cycle of 40%, there is a free slot around 2 Hz, another at 5.7 Hz and the last one at 9.8 Hz if the whole range of incidence angle from 40 to 70 degrees is considered. On the other hand, for the 20% duty cycle diagram presented

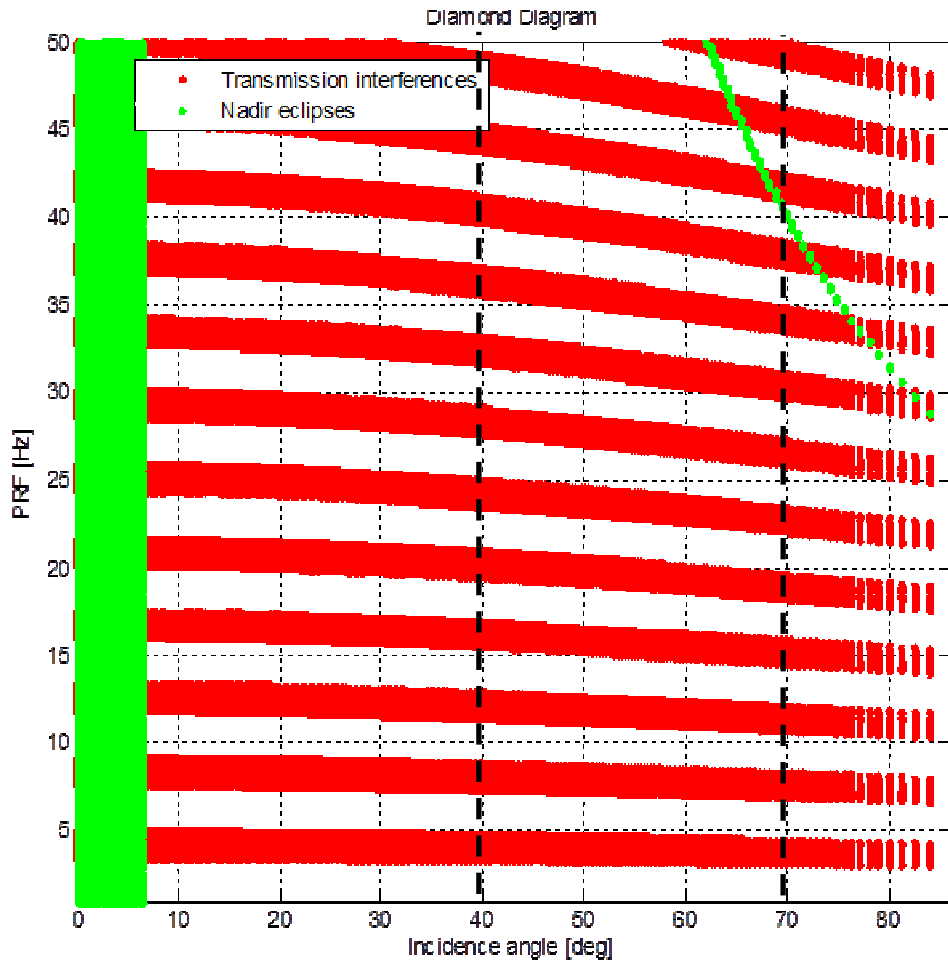


FIGURE 3.17 Diamond diagram for GEOSAR working with a duty cycle of 20%.

in Figure 3.17, free interferences slots up to 40 Hz PRFs can be found. Fortunately, as shown in the Doppler analysis presented in section 3.2, the minimum PRF to fulfil the Nyquist criteria will be of a few Hz which is in accordance with the range of selectable PRFs to avoid nadir and transmission interferences. However, if higher PRFs would be desired, the duty cycle could be decreased in order to reduce the span of transmission interferences. Alternatively, working with smaller swaths within the 40 to 70 degrees margin would make possible to use different PRFs depending on the zone of the Earth observed by each swath. This is schematically shown in Figure 3.16.

Another important aspect to take into account in the diamond diagram analysis is the tolerance on the PRF selection. This corresponds to the range of PRFs around the selected one that will be free of interference in order to avoid interference problems if PRF is slightly modified. So, in the diamond diagram presented in Figure 3.16, there is not much tolerance in the PRF selection, since the free interference zones are quite small. Therefore, a

small change in the PRF could be critical for the correct performance of the GEOSAR mission. To reduce that problem, the duty cycle can be decreased, at the expenses of the Signal to Noise Ratio as explained in section 3.5, in order to increase the range of valid PRFs. Therefore, if the diagram of Figure 3.17 with a duty cycle of 20% is considered, the range of selectable PRF presents more tolerance.

In order to see the effects of the PRF selection in the system coverage and interferences a new SAR tool useful for GEOSAR interference analysis is presented. In case of a low-inclined quasi-circular geosynchronous orbit, the orbital position of the satellite will be nearly fixed with respect to the Earth surface. This makes possible to represent the interfered zones in a novel way. This new diagram, never presented before in GEOSAR or other SAR analysis, has been called dartboard diagram. In a dartboard diagram the interfered zones due to transmission interferences and nadir eclipses are projected over the Earth map once the operating PRF has been chosen. So, it will be easier to interpret the diamond diagram and see which will be the free-interference zones of the acquisition.

So, taking as a reference the diamond diagrams obtained in Figure 3.16 and Figure 3.17, the dartboard diagrams considering a duty cycle of 40% and a PRF of 5.7 Hz and 9.6 Hz are shown in Figure 3.18 and Figure 3.19, respectively. As seen, in both cases, the region of interest from 40 to 70 degrees incidence angle (European continent) is free of interferences in both cases. Using a duty cycle of 20%, no transmission interferences are obtained in the diamond diagram, while only the regions around the sub-satellite point are affected by nadir eclipses.

However, small changes on the PRF may cause strong variations in the dartboard diagram. So, let us consider a PRF change of 0.1 Hz around 9.6 Hz (1% from the PRF previously considered). In Figure 3.20, the diamond diagram considering a PRF of 9.5 Hz is presented for a duty cycle of 20% and 40% in the left and right plots, respectively. As seen, if a duty cycle of 20% is considered, there are not problems with the transmission interference. On the other hand, considering the duty cycle of 40%, the desired scene is partially interfered by the transmission interferences.

Therefore, in order to see the tolerance in the PRF selection, the diamond diagrams for different duty cycles have been computed. From each one, the ranges of suitable PRF around 5.7 Hz and 9.6 Hz to assure interference free acquisitions have been computed. The results obtained are shown in Figure 3.21. As seen, in order to assure a tolerance of 1 Hz (± 0.5 Hz) around 5.7 Hz, a maximum duty cycle of 30% should be considered. On the other hand, with higher PRFs the tolerance becomes smaller. It is important to remember that different PRF could be considered for different sub-swaths with smaller coverage to increase the PRF tolerance at higher PRFs.

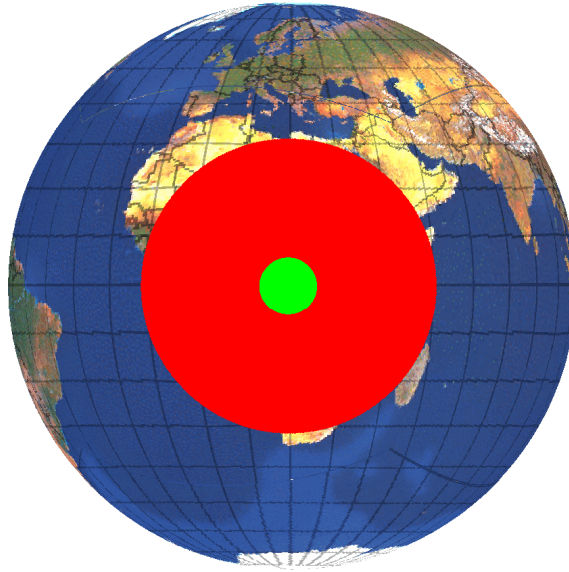


FIGURE 3.18 Dartboard diagram for GEOSAR with PRF of 5.7 Hz.

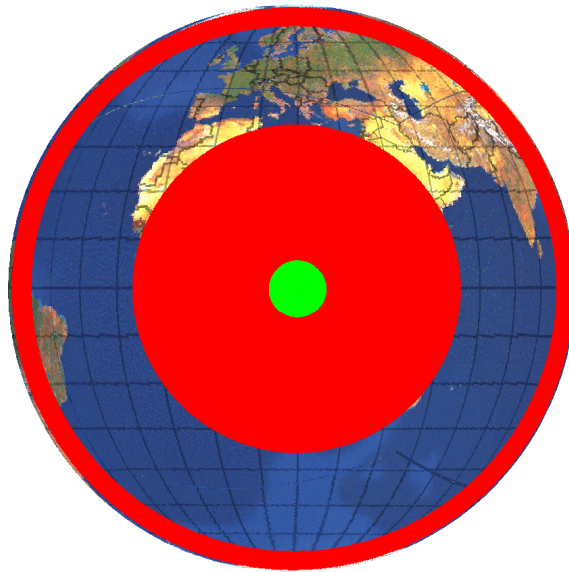


FIGURE 3.19 Dartboard diagram for GEOSAR with PRF of 9.6 Hz.

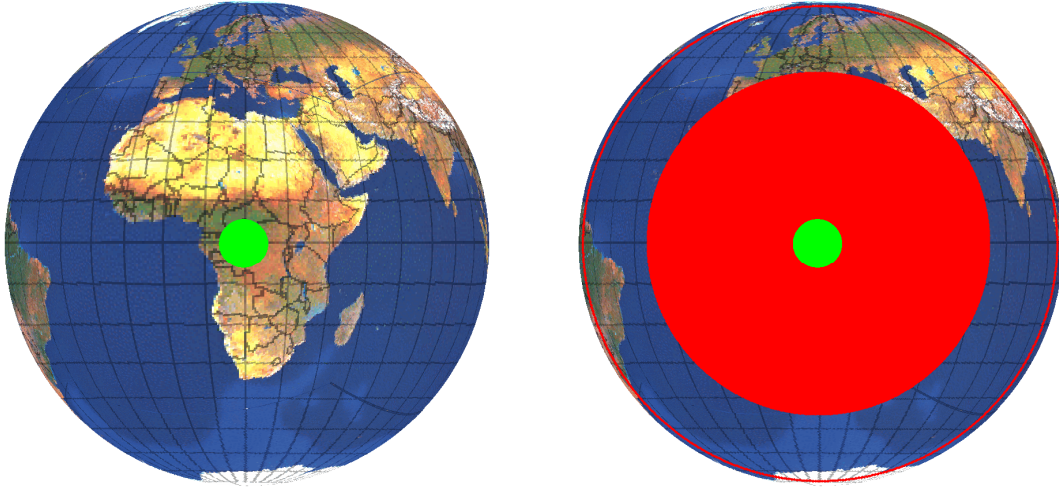


FIGURE 3.20 Diamond diagram for GEOSAR at 9.5 Hz considering a duty cycle of 20% (left) and 40% (right).

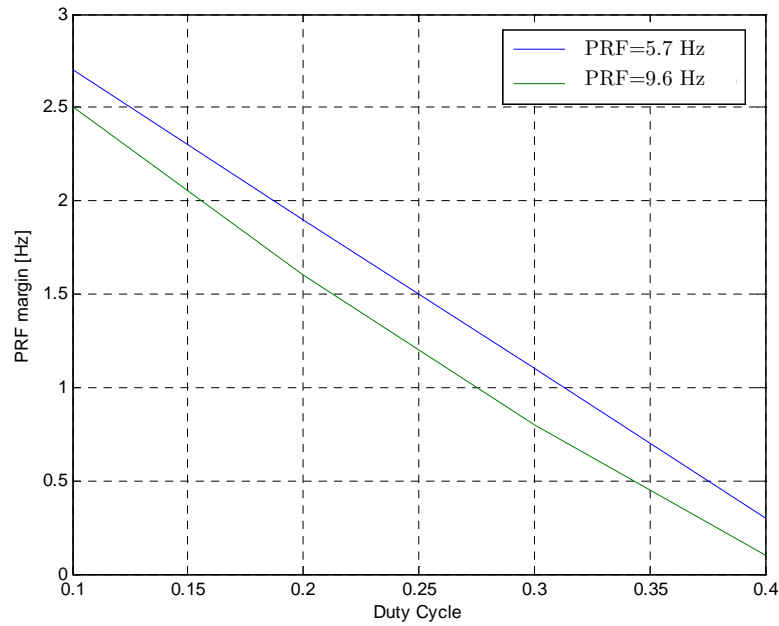


FIGURE 3.21 PRF tolerance in function of duty cycle to avoid transmission interferences.

3.4 Ambiguity analysis for GEOSAR acquisition

Ambiguity analysis will be another of the key elements to assure the correct performance of any radar system [20]. The ambiguities in range and azimuth axis are related to the antenna shape and dimensions, the processed Doppler bandwidth and other design parameters of the radar such as the PRF. The ambiguities are originated by echoes that do not correspond to the desired area illuminated by the antenna footprint. The ambiguous

echoes can cause image artefacts and misplaced replicas of bright targets. These ambiguities are classified in two categories depending on their origin. On one hand, azimuth ambiguities arise from aliasing caused by the finite sampling of the Doppler spectrum at intervals of the PRF. On the other hand, range ambiguities appear when the echoes from preceding and succeeding pulses arrive at the same time as the desired return. The total power of these ambiguous returns will determine the azimuth ambiguity to signal ratio (AASR) and the range ambiguity to signal ratio (RASR) of the SAR system.

Then, in order to improve the ambiguity to desired signal ratio, the antenna pattern and the PRF must be adjusted to fulfil the system requirements. So, for a given range and azimuth antenna pattern, it is necessary to select the right PRFs such that the power of the desired signal would be sufficiently higher than the total ambiguous power. On the other way around, for a given range of PRFs, the dimensions and weighting of the antenna must be accurately selected in order to get an antenna pattern that minimizes the ambiguity to signal ratio for the illuminated area.

In a first approximation the received ambiguous power can be computed as [20]:

$$P_{amb} = \sum_{\substack{m,n=-\infty \\ m,n \neq 0}}^{\infty} G_{2w} \left(f_{DC} + mPRF, \tau_R + \frac{n}{PRF} \right) \cdot \sigma_0 \left(f_{DC} + mPRF, \tau_R + \frac{n}{PRF} \right) \quad (3.18)$$

From (3.18), the dependency of the ambiguous returns with the PRF is clearly shown. The desired power received from one point, determined by its Doppler frequency shift (f_{DC}) and the time delay of the received echo (τ_R), is calculated multiplying the two way power antenna pattern (G_{2w}) by the surface reflectivity (σ_0) [71] of the desired target. On the other hand, the total ambiguous power received for a given Doppler frequency and a time delay bin will be calculated as the summation of the echoes from preceding and succeeding pulses, represented in (3.18) with the n -index (n / PRF); and the power of the replicas of the Doppler spectrum, which correspond to the m -index of the summation ($m \cdot PRF$). This power will mask the desired part of the spectrum. Obviously, the combination of indexes $m=n=0$ must be ignored in the ambiguous power computation because it corresponds to the desired return. So, using (3.18), the integrated ambiguity to signal ratio (ASR) for a given processed Doppler bandwidth (B_p) can be computed as [20]:

$$\begin{aligned} ASR(\tau) &= \frac{P_{amb}}{P_u} = \\ &= \frac{\sum_{\substack{m,n=-\infty \\ m,n \neq 0}}^{\infty} \int_{-B_p/2}^{B_p/2} G_{2w} \left(f_{DC} + mPRF, \tau_R + \frac{n}{PRF} \right) \cdot \sigma_0 \left(f_{DC} + mPRF, \tau_R + \frac{n}{PRF} \right) df}{\int_{-B_p/2}^{B_p/2} G_{2w}(f, \tau) \cdot \sigma_0(f, \tau) df} \quad (3.19) \end{aligned}$$

Unfortunately, (3.19) is not handy for space-borne SAR imaging since it requires the complete knowledge of the antenna pattern, while most specifications of the antenna are given by their azimuth or range cuts separately. For this reason, to facilitate the computation of the ASR, it is possible to separate the ambiguities in azimuth and range, calculating them independently [20]. In the following sections the effects of azimuth and range ambiguities will be analysed to see their impact in the GEOSAR operation.

3.4.1 Range Ambiguity to Signal Ratio (RASR)

As it was previously introduced, range ambiguities are the result of echoes from preceding and succeeding pulses that arrive at the same time that desired return at the antenna. The Range Ambiguity to Signal Ratio (RASR) will be computed as the quotient between the total power received from these ambiguous zones and the power from the desired target.

In Figure 3.22, a simple diagram illustrates the origin of range ambiguities. The zone of interest is identified as a yellow strip on the ground. The antenna illuminates this zone but the side lobes can receive echoes from further or nearer distances. A simplified antenna pattern in range is plotted in blue in Figure 3.22. As it can be seen, the main beam points to the centre of the scene while the side lobes are illuminating undesired zones.

In Figure 3.22, the desired pulse is sent at t_0 , so the echo will arrive to the antenna at $t_1 = t_0 + 2R_1 / c$, where R_1 is the distance to the middle of the swath. The pulses that will cause higher ambiguous returns are sent at times $t_0 - T_p$ and $t_0 + T_p$, where T_p is the inverse of the PRF (also known as Pulse Repetition Interval or PRI). The returns from the desired scene of these pulses, will arrive at $t_0 + 2R_1 / c - T_p$ and $t_0 + 2R_1 / c + T_p$, so these echoes would not affect the desired signal. However, the radar is illuminating further and nearer zones than the desired scene. So, for the previous emitted pulse, a return from a target placed at $R_2 = R_1 + cT_p / 2$ will be received at:

$$t_2 = t_0 - T_p + \frac{2R_2}{c} = t_0 - T_p + \frac{2\left(R_1 + \frac{cT_p}{2}\right)}{c} = t_0 + \frac{2R_1}{c} \quad (3.20)$$

Consequently, the echo of this point will arrive at the same time than the desired pulse since $t_2 = t_1$ and it will be considered as an ambiguous return. With a similar reasoning, the ambiguous distances for succeeding pulses can be determined. Considering a target situated at distance $R_3 = R_1 - cT_p / 2$ and knowing that the pulse will be sent at $t_0 + T_p$, in (3.21) is shown that it will be an ambiguous zone.

$$t_3 = t_0 + T_p + \frac{2R_3}{c} = t_0 + T_p + \frac{2\left(R_1 - \frac{cT_p}{2}\right)}{c} = t_0 + \frac{2R_1}{c} \quad (3.21)$$

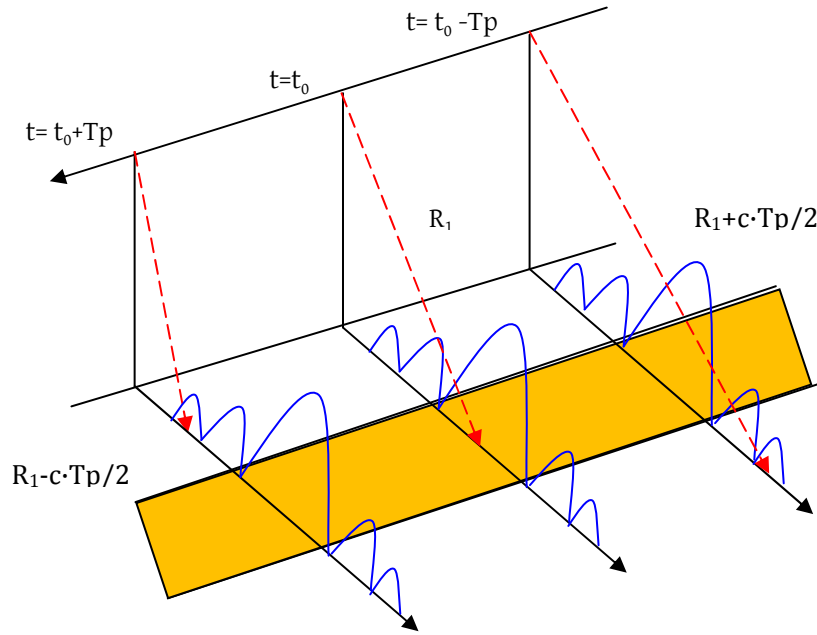


FIGURE 3.22 Origin of range ambiguities in SAR systems.

However, not only the adjacent pulses will cause ambiguous returns. It is necessary to consider previous and succeeding pulses to do a complete analysis of the range ambiguities. The location of the ambiguous zones of a point situated at R_1 equation (3.22) will be obtained as:

$$R_{amb} = R_1 \pm n \frac{cT_p}{2} \quad n = \pm 1, \pm 2 \dots n_h \quad (3.22)$$

where n is an integer that represents the pulse number (0 for desired pulse, negative for succeeding pulses and positive for preceding ones) and n_h is the number of pulses considered in RASR computation. Theoretically, the number of pulses is large, but in practice when n increases the distance increases as well and the antenna gain at such angles decreases considerably, so the received power will be insignificant for large values of n .

Once the ambiguous distances are determined, the RASR can be calculated from the radar equation (3.23), where the constant values will not have interest in the computation because they will be in the numerator and denominator of the ratio. So, finally, the required parameters to compute the range ambiguities will be the incidence angle and the backscattering coefficient of the illuminated surface, as well as the ambiguous distances of these pulses determined by (3.22). Also, the weighting of the antenna diagram in range will be necessary to compute the total RASR.

$$P_r = \frac{P_t G_t G_r \sigma_0 S \lambda^2}{(4\pi)^3 R^4 L} = \left(\frac{P_t G_t G_r \sigma_0 \lambda^2}{(4\pi)^3 R^4 L} \right) (R_0 \theta_{az}) \left(\frac{c \tau_0}{2 \sin \theta_{in}} \right) = K \frac{G_t G_r \sigma_0}{R^3 \sin \theta_{in}} \quad (3.23)$$

Then, the RASR for each point can be determined by taking the power of all ambiguous returns from the previous and succeeding echoes, and the desired power. Taking the ratio between these powers the RASR will be:

$$RASR = 10 \log_{10} \left(\frac{P_{amb}}{P_d} \right) \quad (3.24)$$

The desired power (P_d) received at the radar is obtained from (3.25) without considering the constant parameters which will be cancelled in (3.24). The total ambiguous power (P_{amb}) will be computed with (3.26).

$$P_d = \frac{\sigma_0(\theta_{in}) G_t G_r}{R^3 \sin(\theta_{in})} \quad (3.25)$$

$$P_{amb} = \sum_{\substack{n=-n_h \\ n \neq 0}}^{n_h} P_{amb}^+ + \sum_{n=-n_h}^{n_h} P_{amb}^- = \sum_{\substack{n=-n_h \\ n \neq 0}}^{n_h} \frac{\sigma_0(\theta_{ian}) G_{Tn}^+ G_{Rn}^+}{R_{amb_n}^3 \sin(\theta_{ian})} + \sum_{\substack{n=-n_h \\ n \neq 0}}^{n_h} \frac{\sigma_0(\theta_{ian}) G_{Tn}^- G_{Rn}^-}{R_{amb_n}^3 \sin(\theta_{iar})} \quad (3.26)$$

where θ_{in} is the incidence angle of the desired return while θ_{ian} is the incidence angle for the n_{th} ambiguous pulse, $\sigma_0(\theta_{ian})$ is the backscattering coefficient at each incidence angle and G_t, G_r are the antenna pattern in transmission and reception. Finally, the terms P_{amb}^+ and P_{amb}^- stand for the total ambiguous power in the pointing direction and the opposite side, considering a side-looking radar illumination.

As it has been commented, the PRF is one of the important elements on any SAR system implementation. In section 3.3, the PRF selection to avoid transmission and/or nadir interferences has been studied. However, the PRF has also to be selected thinking on the ambiguity level requirements. In the following examples it is shown how the PRF affects to the RASR. However, the level of range ambiguities is expected to be low due to the low PRF considered in the GEOSAR systems studied in this analysis.

A first GEOSAR example working at very-low PRF (7 Hz) and a desired scene swath covering a range of incidence angles from 49 to 54 degrees are considered. As shown in Figure 3.23, only the zone at same incidence angle but at the opposite illumination direction will be ambiguous to the radar at those small PRFs since the first ambiguity will be out of antenna range. Then, considering an approximated *sinc* shape antenna pattern,

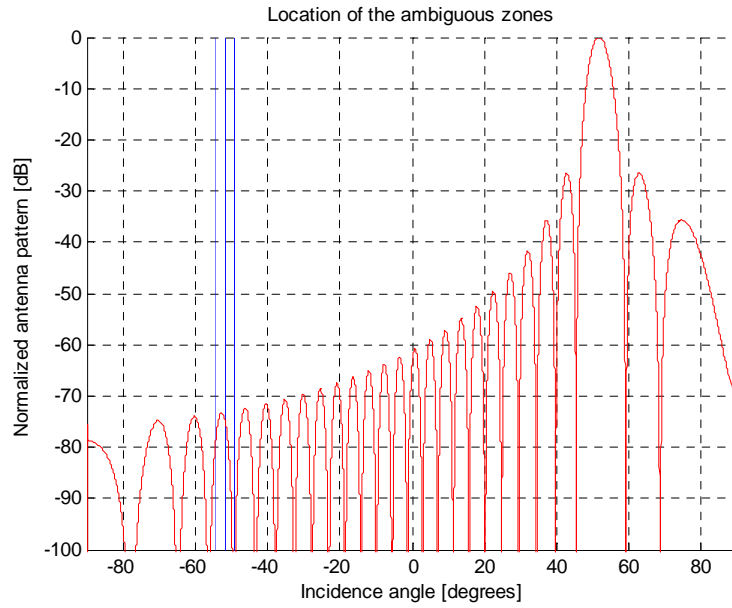


FIGURE 3.23 Range ambiguous zones for GEOSAR at very-low PRF of 7Hz.

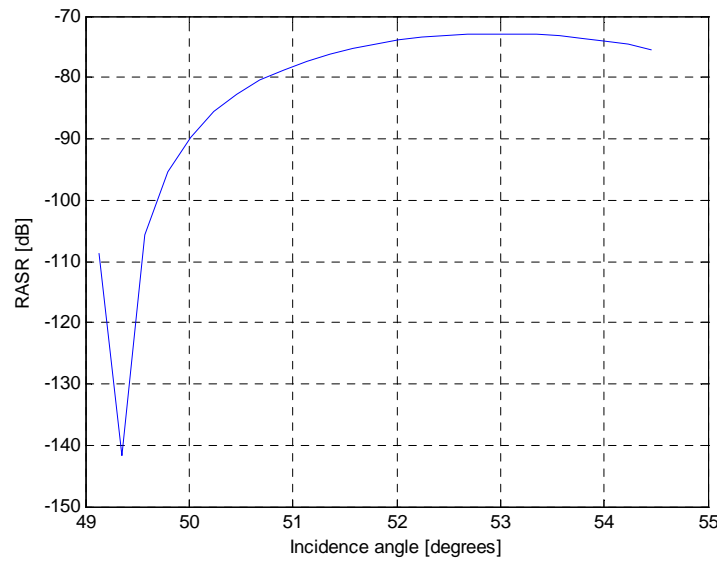


FIGURE 3.24 RASR for GEOSAR at 7Hz for incidence angles between 49 and 54 degrees.

this zone is more than 70 dB below the desired scene illumination. Consequently, the RASR level obtained for this configuration will be really low (acceptable values for RASR in a LEO SAR system are around the -20dB). In this example, as it is shown in Figure 3.24, RASR under -70dB is obtained.

It is difficult to obtain such results in a real system since the antenna pattern will not have the theoretical behaviour presented by the *sinc* function considered in this analysis but it is a good academic example to see the feasibility, regarding the range ambiguities, of the GEOSAR system presented in this thesis in terms of range ambiguities rejection.

To see the problems that higher PRF may cause to GEOSAR range ambiguities, a system working at a PRF of 100Hz will be considered as a second example. As it has been seen in section 3.3, such PRF will not be used for GEOSAR configurations with wide swaths since it will not be possible to avoid the transmission interferences. However, in this section, this PRF has been taken as an upper limit for GEOSAR operation in order to see the RASR level considering an extreme value of the PRF.

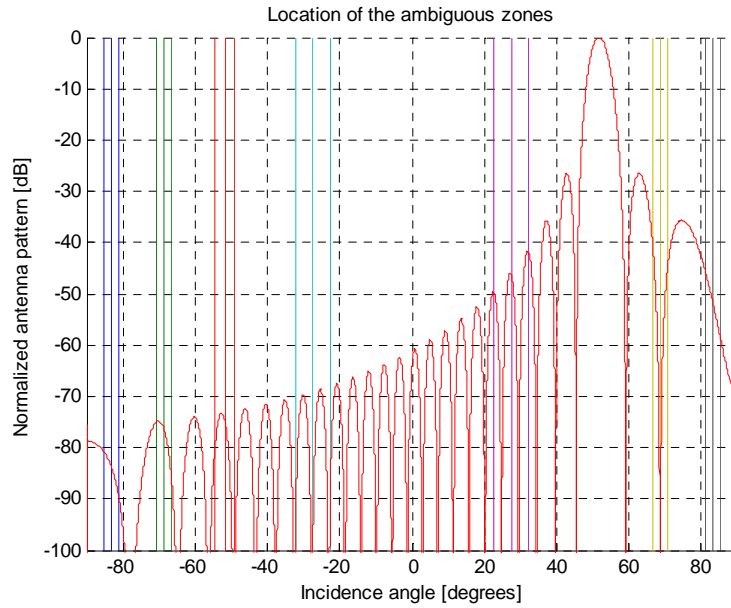


FIGURE 3.25 Range ambiguous zones for GEOSAR at high PRF of 100Hz.

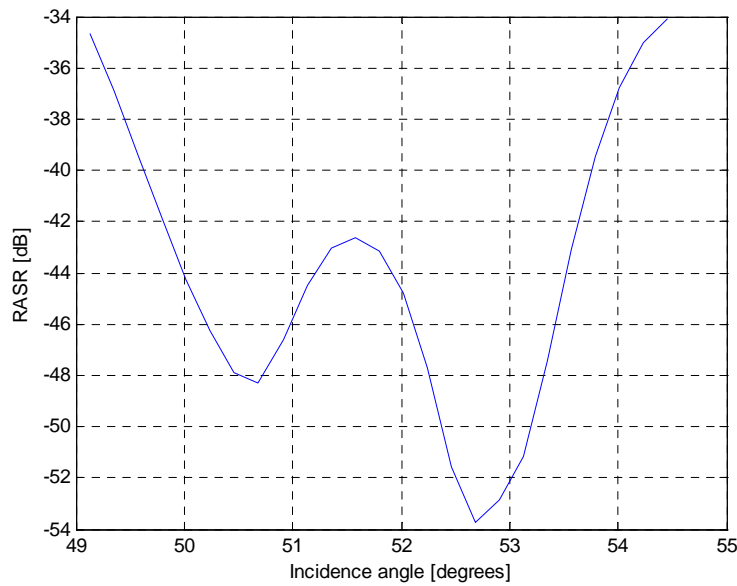


FIGURE 3.26 RASR for GEOSAR at 100Hz for incidence angles between 49 and 54 degrees.

The location of the ambiguous zones for this PRF is denser than in the previous case and, consequently, the level of RASR gets worse since more ambiguous zones will be considered. The location of the ambiguous zones and the RASR levels obtained with a PRF of 100 Hz are presented in Figure 3.25 and Figure 3.26. In this case, the RASR levels are under -30 dB which is enough for SAR application.

Therefore, it has been verified that the range ambiguities will not be a problem for SAR acquisition since such systems usually work at very low PRF (under 50 Hz).

3.4.2 Azimuth Ambiguities to Signal Ratio (AASR)

The relative motion of the radar with respect to the observed Earth surface results in different Doppler shifts due to diversity in observation direction within the antenna main beam. The radar samples the echoes along the azimuth direction according to the radar pulse repetition frequency (PRF) which depending on the echoes Doppler spectrum will result in azimuth ambiguities caused by aliasing. The Doppler spectrum in the GEOSAR geometry is band pass with a centre resulting from the radial satellite-scene centre velocity and a bandwidth which depends on the antenna beamwidth.

The azimuth signal bandwidth is limited by the accessible Doppler from the antenna lateral lobes. The resultant azimuth signal corresponds to a chirp. The azimuth aliasing, therefore, comes from the limited range of frequencies processed by the receiver which goes from $-PRF/2$ to $PRF/2$. The ambiguous aliasing in azimuth frequencies is schematically shown in Figure 3.27 where the antenna pattern should be superimposed to the received azimuth samples. Top plot in Figure 3.27 shows the chirp corresponding to the azimuth signal without aliasing since a sampling rate equal to the Nyquist criteria has been considered. In the middle plot in Figure 3.27, the sampling rate has been reduced by a factor of four and, therefore, aliasing has occurred.

Aliasing can be also seen in the frequency history of the previous signals (bottom plot in Figure 3.27). The blue line corresponds to the frequency history of the unaliased signal while the green one to the signal with aliasing. As seen, in the second case, frequency replicas each PRF time are obtained. These replicas can not be distinguished from the useful signal and, therefore, they will be considered as ambiguous signals. The PRF time can be obtained as [21]:

$$\Delta\tau = \frac{cR_0}{2f_0v_e^2} PRF \quad (3.27)$$

where f_0 is the radar frequency, v_e the platform velocity and R_0 the slant range.

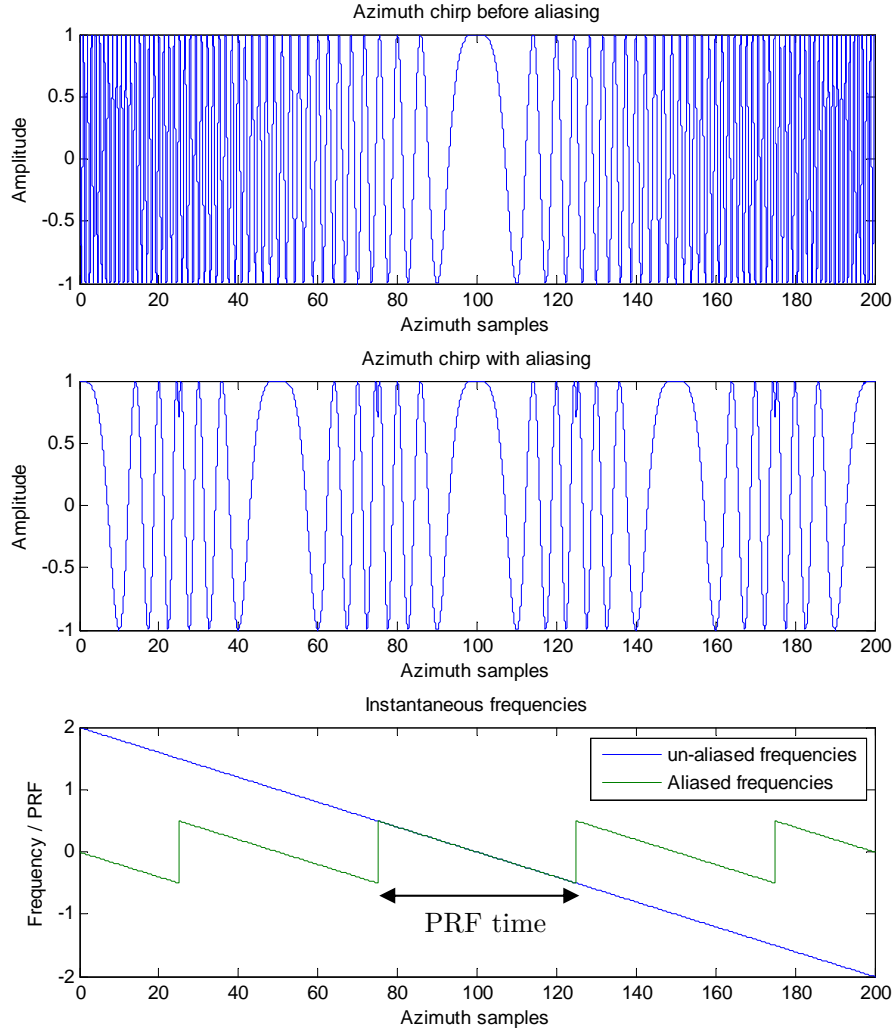


FIGURE 3.27 Azimuth aliasing due to finite sampling at PRF.

So, the desired integrated power in the receiver can be expressed as in (3.28), where T_i is the integration time, $W_{ai}(f)$ is the processing window in the receiver and G_{2az} is the azimuth two-way antenna pattern in the time domain.

$$P_d = \int_{-T_i/2}^{T_i/2} W_{ai}^2(\tau) \frac{G_{2az}(\tau)}{G_{2azMAX}} d\tau \quad (3.28)$$

On the other hand, the ambiguous signal that interferes in the desired Doppler bandwidth can be obtained as:

$$P_{amb} = \sum_{m \neq 0} \int_{-T_i/2}^{T_i/2} W_{ai}^2(\tau) \frac{G_{2az}(\tau + m\Delta\tau)}{G_{2azMAX}} d\tau \quad (3.29)$$

Finally, using (3.28) and (3.29) the AASR is calculated as the ratio between them:

$$AASR = 10 \log_{10} \left(\frac{P_{amb}}{P_d} \right) = 10 \log_{10} \left(\frac{\sum_{m \neq 0} \int_{-T_i/2}^{T_i/2} W_{ai}^2(\tau) \frac{G_{2az}(\tau + m\Delta\tau)}{G_{2azMAX}} d\tau}{\int_{-T_i/2}^{T_i/2} W_{ai}^2(\tau) \frac{G_{2az}(\tau)}{G_{2azMAX}} d\tau} \right) \quad (3.30)$$

This is the theoretical way to compute the AASR. Fortunately, the number of critical ambiguities, represented by index m , is not infinite because the AAP decays to negligible values when the Doppler frequency increases sufficiently. In practice, we will analyse the ambiguities for a finite number of ambiguities, which is a reasonable approximation to the exact result.

The AASR is extremely related to the Doppler bandwidth processed and the shape of the azimuth antenna pattern. In the GEOSAR case, this bandwidth will be a few Hz as obtained in 3.2. Therefore, if a higher PRF is used, the replicas in the spectrum will be separated enough to have a reasonable level of the AASR that will not mask or deteriorate the final image. A simple case will be analysed to see the expected level of azimuth ambiguities for a particular GEOSAR system.

In this example, a geosynchronous orbit with small perturbations in the eccentricity is considered. For an eccentricity of 0.0004, the maximum length of the synthetic aperture achieved was 67.4 Km in 12 hours. These values would give a mean relative velocity of the platform with respect the rotating Earth's surface of about 1.5 m/s. On the other side, a scene of 200 Km in azimuth placed at 37000 Km from the satellite will be considered. Then, considering the azimuth antenna pattern in time domain given by $G_{2az}(\tau)$, a pattern as the one shown in Figure 3.28 is obtained.

As it can be seen, the processing Doppler bandwidth for a GEOSAR system will be really small due to the low relative motion between the satellite and the scene and the long distances where the satellite is orbiting. Although low PRFs are considered in the GEOSAR systems (less than 50 Hz), the AASR will be really low due to the small Doppler bandwidth of the acquisition. So, considering a processing bandwidth of 1.5 Hz and working at a PRF of 5 Hz, the AASR obtained is shown in Figure 3.29. In this case, the AASR is under the -55dB which is a nice result for azimuth ambiguities.

As it has been seen, the small Doppler bandwidth considered in the acquisition due to the slow satellite relative motion makes that even the low PRFs chosen in this GEOSAR analysis, the level of AASR is low and will not cause any problem or artefacts in the SAR images. Once again, the results shown in the previous example have been obtained using a nice *sinc* shape antenna pattern. In a real situation, these results could be a bit worse, but anyway, it is not expected a significant increment of the AASR levels.

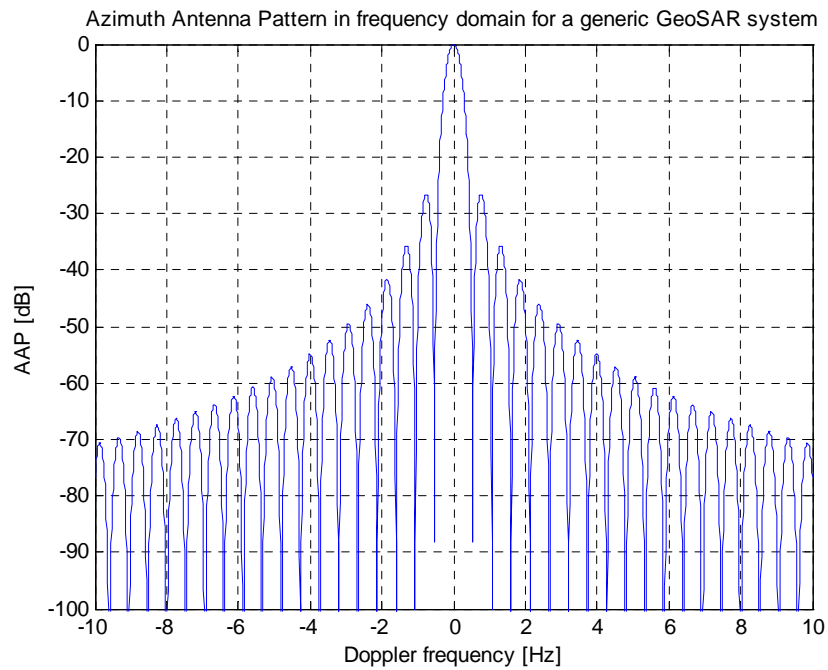


FIGURE 3.28 AAP in frequency domain considering the typical parameters of a GEOSAR system.

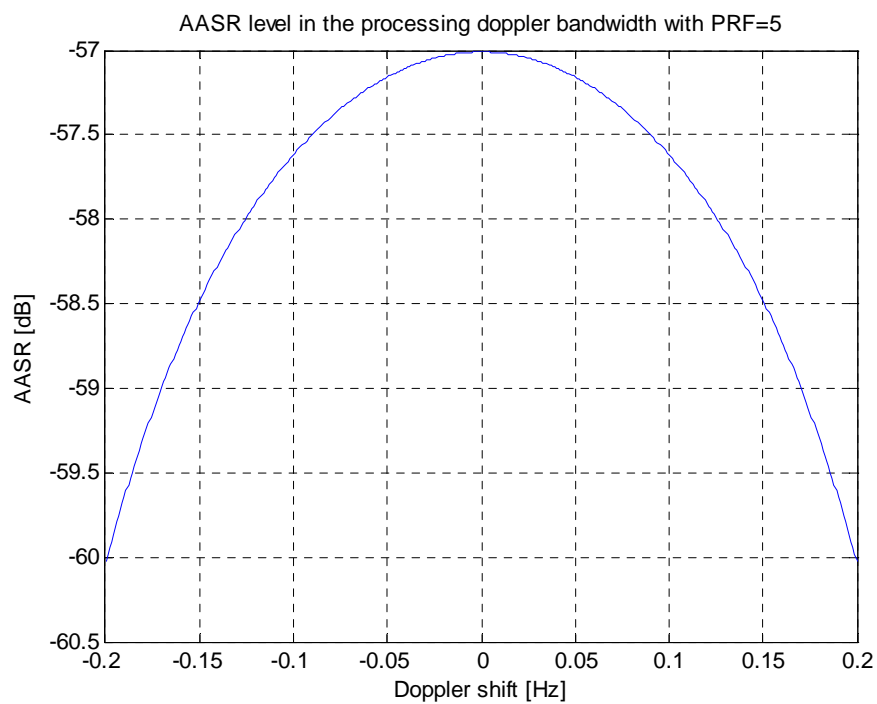


FIGURE 3.29 AASR for a GEOSAR acquisition at PRF=5 Hz. Levels under -50dB are obtained in this particular configuration.

3.5 Power link budget

To fulfil the coverage requirement the antenna dimension and gain have been computed in section 3.1. In this section, the GEOSAR signal to noise ratio will be obtained in order to find suitable values for the main radar system parameters to complete the power link budget. The idea is to obtain the SNR of a radar system which uses pulse compression and synthetic aperture techniques in the acquisition. So, as a first step, the signal to noise ratio for a single pulse transmitted by the radar is given by the well-known radar equation [20]:

$$SNR_1 = \frac{P_t G_t A_{eff,r} \sigma}{(4\pi)^2 R_{S_t}^2 R_{S_r}^2 k T_0 B_P F_n} \frac{1}{L_T} \quad (3.31)$$

where P_t is the radar transmitted power, G_t is the transmitter antenna gain, $A_{eff,r}$ is the effective area of the receiver antenna, σ is the target radar cross section (RCS), R_{S_t} and R_{S_r} are the transmitter and receiver slant ranges to the target, respectively. $k T_0 B_P F_n$ accounts for the noise power at the output of the receiver, being k the Boltzmann constant ($1.38 \cdot 10^{-23} J / K$), T_0 the ambient temperature (290 K), B_P the receiver chain bandwidth and F_n the noise figure of the receiver. L_T accounts for all the losses in the system considering the 2-way link (transmitter, receiver, atmospheric losses, etc.).

Equation (3.31) can be rearranged by taking the expression of the effective area of an antenna ($A_{eff,r} = G_r \lambda^2 / 4\pi$) and considering the RCS of a distributed target as $\sigma = \sigma_0 \cdot \rho_{az} \cdot \rho_{gr}$ where σ_0 is the surface backscattering coefficient of the terrain and $\rho_{az} \cdot \rho_{gr}$ the resolution cell area on ground determined by the azimuth and ground range resolutions, respectively. Then, the signal to noise ratio at the input of the receiver from a resolution cell is written as:

$$SNR_1 = \frac{P_t G_t G_r \sigma_0 \rho_{az} \rho_{gr} \lambda^2}{(4\pi)^3 R_{S_t}^2 R_{S_r}^2 L_T k T_0 B_P F_n} \quad (3.32)$$

The SNR obtained for a single pulse in the GEOSAR case would be really low and it could be compensated by using huge transmitted power. However, the purpose of this research work is to achieve GEOSAR operation with typical LEOSAR moderate antenna and power parameters. Thus, high range pulse compression and large pulse integration when forming the synthetic aperture will be needed to reach sufficient SNR considering low or medium transmitted powers. In case of considering an illuminator of opportunity, the transmitted power and transmitter antenna gain will be given and the design will focus on the receiver and processing parameters.

The pulse compression is given by the ratio between the transmitted pulse duration (τ_0) and the length of the compressed pulse ($\Delta\tau$). On the other hand, the number of pulses integrated during the synthetic aperture formation is obtained by multiplying the pulse

repetition frequency (PRF) by the integration time (T_i). In the GEOSAR case, the integration time is not limited by the synthetic aperture length as in the LEO SAR case. The constant line of sight between the satellite, at nearly fixed position, and the targets makes possible to increase the integration time and still have a medium resolution image. However, very long integration times are not desirable since the coherence loss of the terrain can degrade the final SNR. So, the improvement factor due to the pulse compression and pulse integration will be:

$$\Delta P = \frac{\tau_0}{\Delta\tau} \cdot PRF \cdot T_i \quad (3.33)$$

Therefore, the SNR after SAR processing with the improvement factor computed in (3.33) results in:

$$SNR_0 = SNR_1 \cdot \Delta P = \frac{P_t G_t G_r \sigma_0 \rho_{az} \rho_{gr} \lambda^2}{(4\pi)^3 R_{st}^2 R_{sr}^2 L_T k T_0 B_P F_n} \cdot \frac{\tau_0}{\Delta\tau} \cdot PRF \cdot T_i \quad (3.34)$$

To maximize the Signal to Noise Ratio on the receiver output a matched filter [20] is used. In this case, the receiver bandwidth is the pulse bandwidth which is the inverse of $\Delta\tau$. Furthermore, the product of the pulse duration by the PRF is known as the duty cycle (DC). Then, the SNR can be re-written as:

$$SNR_0 = SNR_1 \cdot \Delta P = \frac{P_t G_t G_r \sigma_0 \rho_{az} \rho_{gr} \lambda^2}{(4\pi)^3 R_{st}^2 R_{sr}^2 L_T k T_0 F_n} \cdot DC \cdot T_i \quad (3.35)$$

As it can be seen in equation (3.35), once the radar, antenna and geometry parameters are chosen, a trade-off between the desired resolution and the achieved SNR must be considered. Note the dependence of SNR (3.35) with the spatial resolution and integration time which are both affected by the orbital design. Thus, the relation between SNR after SAR processing and the resolution cell area will be fixed by the system parameters:

$$\frac{SNR_0}{\rho_{az} \rho_{gr}} = \frac{P_t G_t G_r \sigma_0 \lambda^2}{(4\pi)^3 R_{st}^2 R_{sr}^2 L_T k T_0 F_n} \cdot DC \cdot T_i \quad (3.36)$$

In the following sections, different bistatic GEOSAR configurations are analysed and the SNR levels expected are computed. A dedicated bistatic GEOSAR mission is firstly studied in order to determine the power requirements to achieve a minimum Signal-to-Noise Ratio (SNR). Current and future broadcasting satellites footprints, antenna and power parameters are analysed to determine which of them may be used as illuminators of opportunity.

3.5.1 Power link budget of a dedicated GEOSAR mission

In this section, the power link budget for a SAR dedicated geosynchronous satellite will be presented. Obviously, the number of possibilities in this case is infinite depending on the user's requirements. For this reason, in this section a particular example taking standard power and timing values of a possible GEOSAR mission will be considered to see its feasibility in terms of SNR requirements.

A monostatic GEOSAR acquisition from a zero inclination and low-eccentric orbit will be considered. Accordingly, a 15% DC has been adopted as a reference value in this study. A transmitted peak power similar to the one used in current LEOSAR mission, according the output power offered by the current technology of TWT, is selected. In this example, a transmitted power of 1500 W will be considered (31.8 dBW).

The other main difference is the transmission and reception antenna gains. If the purpose of the acquisition is to image a small region, spot beam antennas with high directivities can be used. The telecommunications satellite antennas are usually broadcasting antennas for high number of users in extensive areas with low directivities which also penalize the final SNR obtained. In this example, an antenna gain of 55dB will be considered. Such antenna working at 12GHz will have effective area (A_{eff}) given by (3.37), which corresponds to a circular reflector of effective diameter (ϕ_{eff}) and ground spot given by (3.38) and (3.39).

$$G_t = A_{eff} \frac{4\pi}{\lambda^2} \rightarrow A_{eff} = 10^{55dB/10} \frac{0.025^2}{4\pi} = 15.72m^2 \quad (3.37)$$

$$A_{eff} = \pi \cdot \left(\frac{\phi_{eff}}{2} \right)^2 \rightarrow \phi_{eff} = 2\sqrt{\frac{A_{eff}}{\pi}} = 4.47m \quad (3.38)$$

$$\Delta R = 0.88 \frac{\lambda}{\phi_{eff}} R = 0.88 \frac{0.025m}{4.47m} \cdot 38422Km = 189Km \quad (3.39)$$

A mid-resolution image of 15 by 15 meters is considered for this example with an integration time of 4 hours. Considering the analysis presented in section 2.4.2.2, and more specifically the relation between integration time, eccentricity and resolution given by equation (2.89), an orbital eccentricity of 0.0004 is required. A signal bandwidth of 17.7 MHz has been considered to reach a ground range resolution of 15 meters for mid-latitudes. Other noise and receiver parameters considered in the SNR computation are summarized in Table 3.1. In this case, a SNR of 19.22 dB is obtained which is quite good taking into account the adverse conditions of the GEOSAR acquisition.

Therefore, this configuration could provide continuous images of 15 by 15 meters resolution each 4 hours. It is important to take into account the non-linear satellite velocity studied in section 2.4.3 which results in non-constant along-track resolution. The strategies to increase

the daily acquisition preserving as much as possible the along-track resolution are presented in section 4.1.

In the power link budget presented in Table 3.1, an integration time of 4 hours has been considered. Such long integration may not be a problem for stable target or regions, but other scenarios, such as the Atmospheric Phase Screen (APS) retrieval [73]–[76] studied in section 4.3, present low temporal correlation and needs to be much more continuously monitored. Fortunately, the spatial correlation of atmospheric phase screen map is high, being possible to degrade the spatial resolution without losing information of the atmospheric artefacts. Therefore, if the integration time is reduced, the along track resolution will increase proportionally and the SNR ratio would be kept. Furthermore, the ground range resolution may be degraded reducing the signal bandwidth in order to square the pixel and the extra dBs gained can be used to reduce the antenna gain and increase the system coverage to have an APS map of a larger region. The considered parameters are presented in Table 3.2.

In this case, an L-band acquisition at 1.625 GHz has been considered. An antenna gain of 40 dB has been taken. The new values give a coverage of:

$$G_t = A_{eff} \frac{4\pi}{\lambda^2} \rightarrow A_{eff} = 10^{40dB/10} \frac{0.1846^2}{4\pi} = 27.11m^2 \quad (3.40)$$

$$A_{eff} = \pi \cdot \left(\frac{\phi_{eff}}{2} \right)^2 \rightarrow \phi_{eff} = 2\sqrt{\frac{A_{eff}}{\pi}} = 5.87m \quad (3.41)$$

$$\Delta R = 0.88 \frac{\lambda}{\phi_{eff}} R = 0.88 \frac{0.1846m}{5.87m} \cdot 38422Km = 1063Km \quad (3.42)$$

A shorter integration time of 30 minutes has been considered in order to be able to retrieve the rapid temporal changes of the atmosphere. Considering the same orbital design than in the previous example (eccentricity of 0.0004 and no inclination), it results in an along-track resolution of 800 meters. The signal transmitted bandwidth has been also reduced in order to have a ground range resolution around 800 m as well. In this case, a final SNR of 32.2 dB is obtained. In order to reduce the power consumption of the system, lower transmitted peak power could be considered in this case. So, for a transmitted peak power of 19.6 dBW, the SNR of 20.0 dB could be still obtained.

Therefore, the power link budget for a low coverage (200 Km) mid-resolution (15 by 15 m) acquisition at X-band (12 GHz) and for a wide coverage (1000 Km) low-resolution (800 by 800 meters) acquisition at L-band (1.625 GHz) have been computed obtaining values above 20 dB in both cases. As seen, the power requirements in the first case will be more stringent than in the APS retrieval acquisition.

SNR COMPUTATION PARAMETERS FOR HIGH RCS POINT TARGET					
Parameter	Symbol	Value	SNR impact	SNR budget	Units
Transmitted power	P_t	31.8 dBW	EIRP	+86.8	dBW
Gain trans.	G_t	55.0 dB			
Gain rec.	G_r	55.0 dB	-	+55.00	dB
Slant range	R_t^2, R_r^2	38422 km	$\frac{\lambda^2}{(4\pi)^3 R^4}$	-368.4	dBsm ⁻¹
Wavelength	λ	0.0249827 m			
Pixel area	$\rho_{az}\rho_{gr}$	15m x 15m	RCS	+13.5	dBsm
Backscattering coefficient	σ_0	-10 dB			
System losses	L_T	3 dB	-	-3	dB
kT_0	-	$4 \cdot 10^{-21}$ J	Noise power	+129.5	dB
Noise factor	F_n	2 dB			
Signal Bandwidth	B	17.7 MHz			
SNR single pulse (per res. cell)			SNR_1	-86.6	dB
Pulse duration	τ_i	0,015 sec	Pulse compression (τ_i / τ_0)	54.24	dB
Compressed pulse duration	$\tau_0 = 1 / B$	56.5 nsec			
PRF	-	10 Hz	Integrated pulses ($PRF \cdot T_i$)	51.58	dB
Integration time	T_i	$4 \cdot 3600$ sec			
SNR after SAR processing			SNR_0	19.22	dB
Noise Equivalent Sigma Zero			NESZ	-29.22	dB

TABLE 3.1. SNR computation for a monostatic ad-hoc GEOSAR mission with scene coverage of 190Km with a resolution cell of 15 by 15 meters.

3.5.2 Radiometric feasibility of current broadcasting satellites as illuminators of opportunity

3.5.2.1 Transmitted signal of current broadcasting TV satellites

For this study, current TV broadcasting satellites will be considered. Such systems use the DVB-S2 standard [77] to transmit the TV and radio signals. DVB-S2 is the successor of the previous satellite TV standard known as DVB-S. The radiometric features that will affect to the GEOSAR acquisition if these signals are considered for SAR applications will be the type of modulation used and the signal bandwidth.

SNR COMPUTATION PARAMETERS FOR APS MONITORING					
Parameter	Symbol	Value	SNR impact	SNR budget	Units
Transmitted power	P_t	31.8 dBW	EIRP	+71.8	dBW
Gain trans.	G_t	40.0 dB			
Gain rec.	G_r	40.0 dB	-	+40.00	dB
Slant range	R_t^2, R_r^2	38422 km	$\frac{\lambda^2}{(4\pi)^3 R^4}$	-351.0	dBsm ⁻¹
Wavelength	λ	0.1846 m			
Pixel area	$\rho_{az}\rho_{gr}$	800 m x 800 m	RCS	+48.06	dBsm
Backscattering coefficient	σ_0	-10 dB			
System losses	L_T	3 dB	-	-3	dB
kT_0	-	$4 \cdot 10^{-21}$ J	Noise power	+146.54	dB
Noise factor	F_n	2 dB			
Signal Bandwidth	B	0.35 MHz			
SNR single pulse (per res. cell)			SNR_1	-47.6	dB
Pulse duration	τ_i	0,015 sec	Pulse compression (τ_i / τ_0)	37.20	dB
Compressed pulse duration	$\tau_0 = 1 / B$	56.5 nsec			
PRF	-	10 Hz	Integrated pulses ($PRF \cdot T_i$)	42.55	dB
Integration time	T_i	30 · 60 sec			
SNR after SAR processing			SNR_0	32.2	dB
Noise Equivalent Sigma Zero			NESZ	-42.2	dB

TABLE 3.2. SNR computation for a monostatic ad-hoc GEOSAR mission with scene coverage of 1000 Km with a resolution cell of 800 by 800 meters.

So, the used modulations for TV transmission in DVB-S2 are typically phase modulations: QPSK and 8-PSK. The Phase-Shift Keying (PSK) is a digital modulation that sends information by changing the phase of the reference signal. An example of a transmitted QPSK sequence is presented in Figure 3.30. So, the transmitted QPSK modulated signal can be obtained as:

$$s_i(t) = K \cos(2\pi f_0 t + \Theta_i) \quad (3.43)$$

where Θ_i is the phase value corresponding to each transmitted symbol. The typical values for the modulated phase are 45°, 135°, 225° and 315°.

During the SAR focusing the received signal backscattered from the scene is convolved with a conjugated replica of the transmitted signal which performs the range compression. After range compression, the echo origin can be determined. Therefore, in order to check the feasibility of this kind of signal for SAR purposes the autocorrelation of a random QPSK sequence has been computed. The result is presented in Figure 3.31. As seen, the autocorrelation of the QPSK signal shows a thin peak, which is necessary to assure the correct range focusing.

The other important parameter to take into account is the transmitted signal bandwidth which will determine the width of the autocorrelation function and, therefore, the range resolution. The channel capacity in case of ASTRA 2C, for example, is 26 MHz. Therefore, as explained in section 2.4.2.1, a range resolution of 7.5 m could be achieved with this channel bandwidth. Projecting this range resolution to ground, a varying ground range resolution from 11.67 m to 8 m for the range of incidence angles going from 40 to 70 degrees is obtained.

Therefore, the obtained ground range resolution with this kind of signal and this transmitted bandwidth is in the order of the one desired in GEOSAR. Thus, the transmitted signal by TV broadcasting satellites may be considered as signals of opportunity for SAR purposes.

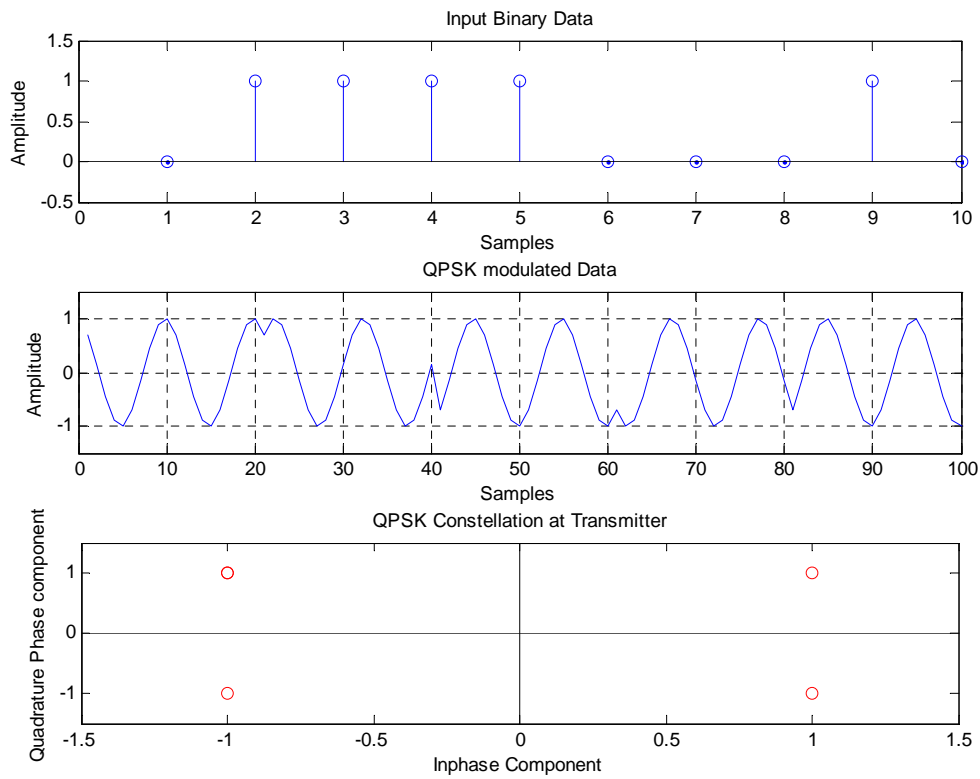


FIGURE 3.30 QPSK digital modulation example dBW.

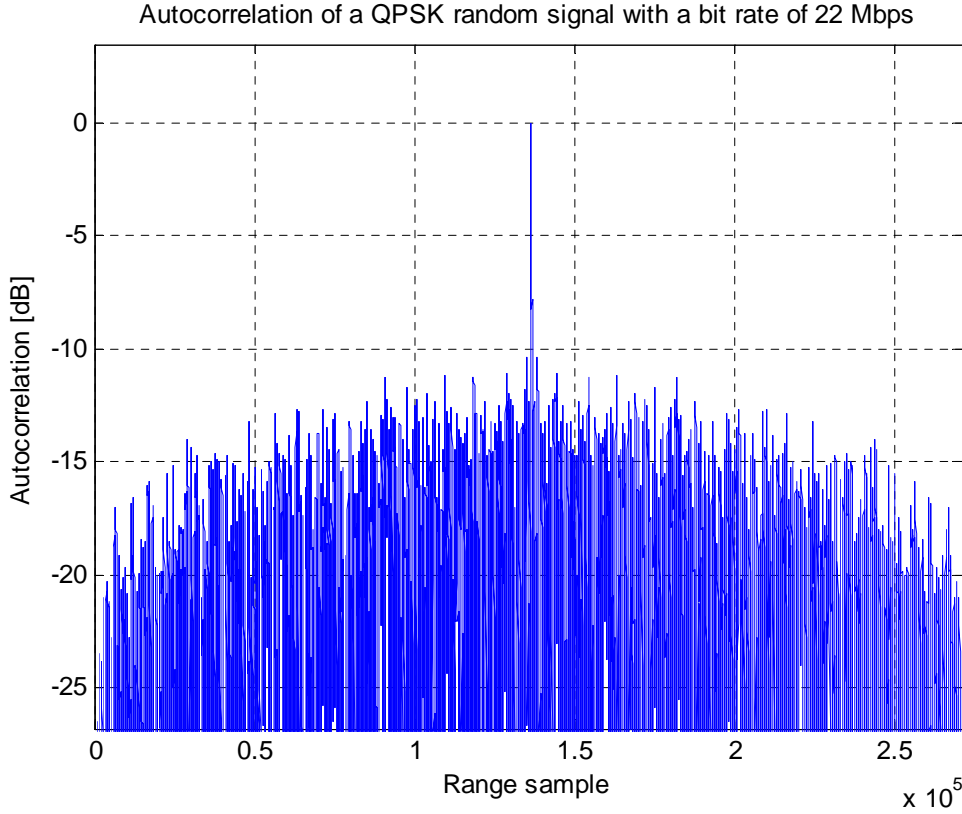


FIGURE 3.31 22 Mbps QPSK signal autocorrelation.

3.5.2.2 Large coverage low EIRP beam for APS retrieval

As it has been analysed in section 2.5, it is possible to have a receiver on board of a telecommunications satellite tuned at the same frequency of one of the transmitters of another satellite collecting the echoes in an open bistatic configuration. The two satellites must be separated enough to avoid transmitting interferences. In this case, the signal transmitted by the broadcasting satellite is used as signal of opportunity for SAR purposes. In such configuration, the orbital, antenna and transmitted signal parameters are fixed by the telecommunication operator and cannot be modified to improve the SNR or any other SAR feature. Therefore, to reach an acceptable level of SNR, only the parameters related to SAR acquisition (duty cycle, integration time and pixel area) can be adjusted.

Let us consider, as an example, the HISPASAT-1D satellite that covers the Western Europe region. The satellite where the receiver has to be mounted must be selected accordingly with the Earth's zone of interest since constant line of sight must be assured to perform the integration during several hours. For targets placed in Europe (longitudes from 10° West to 40° East), HISPASAT-1D is a good candidate since it is placed at a longitude of 30° West. Furthermore, HISPASAT-1D has one of the beams pointing and covering part of Europe as shown in Figure 3.32. The Equivalent Isotropic Radiated Power ($\text{EIRP} = P_t G_t$) over Barcelona is 54dBW as shows Figure 3.32.

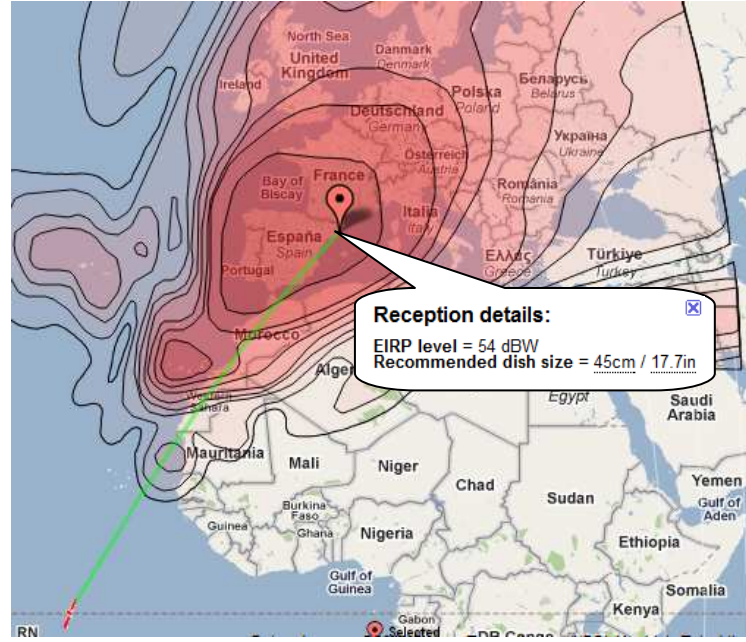


FIGURE 3.32 HISPASAT-1D footprint over Europe. EIRP level at Barcelona of 54dBW.

From the footprint coverage presented in Figure 3.32, an estimation of the antenna parameters of the satellite can be computed. Considering a main beam extension at -3dB of 1000 x 1000 Km approximately, a slant range to Barcelona of 38422Km, a frequency of 12GHz, the approximated size of the transmitter dish antenna can be obtained as:

$$\Delta R = 0.88 \frac{\lambda}{\phi} R \rightarrow \phi = 0.88 \frac{\lambda}{\Delta R} R \quad (3.44)$$

where ΔR is the ground coverage, λ the working wavelength, ϕ the transmitter dish diameter and R the slant range to the target. (3.44) would be only valid for a uniform illumination of the antenna which is not the case presented, where beamforming or reflector shaping is used in order to get the desired footprint. However, (3.44) has been considered as a good approximation to obtain the antenna gain necessary to compute the SNR. Using the parameters above, a diameter of 0.85 meters is obtained. From the diameter, the effective area of the antenna is easy to obtain as follows:

$$A_{eff} = A_{geo} \cdot \eta_{eff} = \pi \cdot \left(\frac{\phi}{2} \right)^2 \cdot \eta_{eff} \quad (3.45)$$

Where an efficiency of the antenna (η_{eff}) of 0.85 has been considered. With these values, the effective area of the antenna is equal to 0.476 m². Finally, the antenna gain can be calculated from the effective area as:

$$G_t = A_{eff} \frac{4\pi}{\lambda^2} = 0.476 \cdot \frac{4\pi}{(3 \cdot 10^8 / 12 \cdot 10^9)^2} = 39.8dB \quad (3.46)$$

The obtained gain is consistent with the values used in Table 3.2 for the ad-hoc power link budget for APS retrieval. The geometrical and orbital parameters of the satellite-target link are summarized in Table 3.3 for a zone around Barcelona. It is important to note that HISPASAT 1D has several channels at Ku-band, but there are no channels at L-band, as it was considered in the previous section for APS retrieval. However, in the power link budget presented in Table 3.4 a hypothetical channel at L-band (1.625 GHz) with the same properties than the Ku-band channels has been considered since Ku-band would result in too small pixel cell size for APS retrieval deteriorating the final SNR.

As seen in Table 3.3, the orbital eccentricity is in accordance with the values considered in section 3.5.1 (0.0004 eccentricity) and, therefore, an along-track resolution similar to the values in Table 3.2 for the same integration time will be obtained. As shown in Table 3.4, a final SNR of 14.35 dB is obtained re-using the signal from a satellite such as HISPASAT-1D. However, a channel at L-Band with similar transmitted power and bandwidth than the current Ku-band ones should be considered for futures broadcasting satellites if it is desired to put a L-Band SAR payload on them.

SYSTEM & GEOMETRY PARAMETERS			
Satellite			
Orbit Period	T	24	hours
Satellite latitude	φ_{sat}	0	deg
Satellite longitude	λ_{sat}	-30	deg
Orbital eccentricity	e	0.0004	-
SAT height over Earth	h_{sat}	35786	Km
Orbit radius	r_{sat}	42164.2	Km
Target			
Local Earth's radius	R_{earth}	6368.8	Km
Target Latitude	φ_T	41.23	deg
Target Longitude	λ_T	2.11	deg
Satellite-Target Link			
Sat-Target: Range	R	38422	Km
Azimuth angle	θ_{az}	223.6	deg
Elevation angle	θ_{el}	32.2	deg
Look angle	θ_{look}	7.3	deg
Incidence angle	θ_m	57.8	deg

TABLE 3.3. Satellite target link geometric parameters.

Additionally, the transmitting interferences could be avoided by considering a dedicated SAR channel in future telecommunication satellites. This configuration will give more flexibility in the SAR payload design offering better performance in terms of SNR.

3.5.2.3 Spot beam high EIRP beam for mid-resolution surface imaging

Recently, Eutelsat has launched KA-SAT which is the first multi-beam satellite to operate in Ka-band for broadcasting purposes [78][79][80]. This satellite will provide broadband in Europe, the Mediterranean Basin and parts of the Middle East. The satellite is configured to work with 80 spot-beams. A scheme of the KA-SAT coverage is shown in Figure 3.33. Each cell covers an area of 250 Km approximately which is in the order of the coverage requirements for terrain observation considered in Section 3.5.1 for the ad-hoc mission.

If the spot-beam 10 is considered, it illuminates the region around Barcelona with an EIRP of 61 dB as shown in FIGURE 3.34. As done in section 3.5.2.2, the antenna gain and transmitted power can be approximately found from the EIRP and the footprint coverage. Therefore, considering a cell diameter of 250Km, a diameter of the effective aperture of 3.2 meters can be obtained at Ka-band. Then, the effective area of the reflector will be:

$$A_{eff_{KA-SAT}} = \pi \cdot \left(\frac{\phi_{eff}}{2} \right)^2 = 8.04 m^2 \quad (3.47)$$

which results in an antenna gain of:

$$G_t = A_{eff} \frac{4\pi}{\lambda^2} = 8.04 \cdot \frac{4\pi}{(3 \cdot 10^8 / 12 \cdot 10^9)^2} = 52.01 dB \quad (3.48)$$

Therefore, the transmitted peak power will be around 9 dBW for each beam. So, considering a transmitted signal from one of the Ka-band (26.5 GHz) transponders and an orbital motion similar to HISPASAT 1D, the SNR budget is shown in Table 3.5. As seen, a mid-resolution image of 15 by 15 meters in 4 hours of integration with SNR of -16.5 dB is obtained. Thus, this satellite will not be useful as illuminator of opportunity for SAR purposes. However, the orbital design could be slightly modified to reduce the system resolution (lower eccentricity) and some extra transmitted power should be sent for the channels considered for SAR. So, taking a transmitted power of 31.8 dBW as in Table 3.1 and degrading the resolution cell to 30 by 30 meters, a final SNR of 12.3 dB would be obtained. However, although the spot beam configuration of KA-SAT is a good starting point for thinking in illuminators of opportunity in GEOSAR mid-resolution imaging, a more powerful transponder would be required to reach a minimum SNR to assure the right performance of the SAR system.

SNR COMPUTATION PARAMETERS					
Parameter	Symbol	Value	SNR impact	SNR budget	Units
Transmitted power	P_t	14 dBW	EIRP	+54	dBW
Gain trans.	G_t	40 dB			
Gain rec.	G_r	40 dB	-	+40	dB
Slant range	R_t^2, R_r^2	38422 km	$\frac{\lambda^2}{(4\pi)^3 R^4}$	-351.0	dBsm ⁻¹
Wavelength	λ	0.1846 m			
Pixel area	$\rho_{az}\rho_{gr}$	800 m x 800 m	RCS	+48.06	dBsm
Backscattering	σ_0	-10 dB			
System losses	L_T	3 dB	-	-3	dB
kT_0	-	$4 \cdot 10^{-21}$ J	Noise power	+146.54	dB
Noise factor	F_n	2 dB			
Signal Bandwidth	B	0.35 MHz			
SNR single pulse (per res. cell)			SNR_1	-65.4	dB
Pulse duration	τ_i	0,015 sec	Pulse compression (τ_i / τ_0)	37.20	dB
Compress pulse duration	$\tau_0 = 1 / B$	56.5 nsec			
PRF	-	10 Hz	Integrated pulses ($PRF \cdot T_i$)	42.55	dB
Integration time	T_i	30 · 60 sec			
SNR after SAR processing			SNR_0	14.35	dB
Noise Equivalent Sigma Zero			NESZ	-24.35	dB

TABLE 3.4. SNR computation for the monostatic case re-using the signal of HISPASAT-1D.

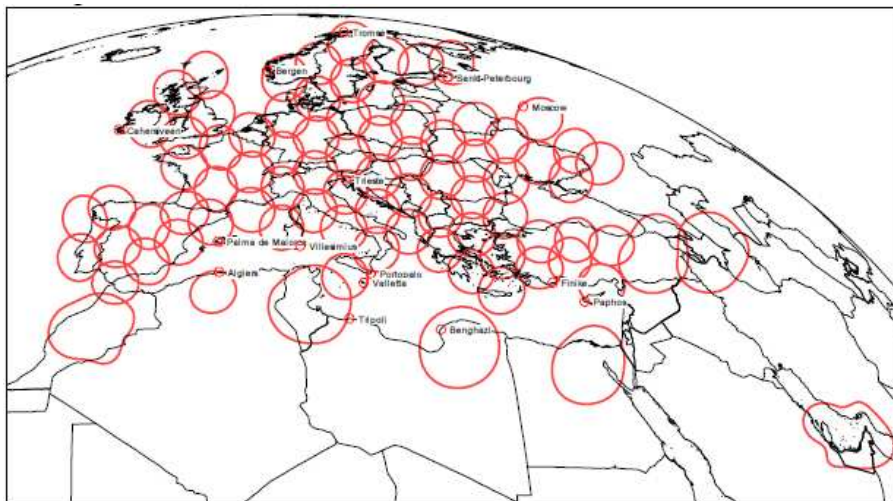


FIGURE 3.33 KA-SAT spot-beams over Europe.

SNR COMPUTATION PARAMETERS					
Parameter	Symbol	Value	SNR impact	SNR budget	Units
Transmitted power	P_t	9.0 dBW	EIRP	+61.0	dBW
Gain trans.	G_t	52.01 dB			
Gain rec.	G_r	52.01 dB	-	+52.01	dB
Slant range	R_t^2, R_r^2	38422 km	$\frac{\lambda^2}{(4\pi)^3 R^4}$	-375.3	dBsm ⁻¹
Wavelength	λ	0.0113 m			
Pixel area	$\rho_{az}\rho_{gr}$	15 m x 15 m	RCS	+13.5	dBsm
Backscattering coefficient	σ_0	-10 dB			
System losses	L_T	3 dB	-	-3	dB
kT_0	-	$4 \cdot 10^{-21}$ J	Noise power	+129.5	dB
Noise factor	F_n	2 dB			
Signal Bandwidth	B	17.7 MHz			
SNR single pulse (per res. cell)			SNR_1	-122.3	dB
Pulse duration	τ_i	0,015 sec	Pulse compression (τ_i / τ_0)	54.24	dB
Compressed pulse duration	$\tau_0 = 1 / B$	56.5 nsec			
PRF	-	10 Hz	Integrated pulses ($PRF \cdot T_i$)	51.58	dB
Integration time	T_i	$4 \cdot 3600$ sec			
SNR after SAR processing			SNR_0	-16.48	dB
Noise Equivalent Sigma Zero			NESZ	6.48	dB

TABLE 3.5. SNR computation re-using the signal of KA-SAT.

So, after analysing two types of current broadcasting satellites to be used as illuminators of opportunity, we may conclude that current technology is still not prepared for SAR acquisition. The main reason is because these systems are intended for sending signal to the parabolic antennas placed on ground and, therefore, only a single path transmission is taken into account in the power link budget. Thus, if a radar payload is equipped in future telecommunications broadcasting satellites for GEOSAR purposes, higher power should be considered in the channel dedicated to SAR acquisition.



FIGURE 3.34 KA-SAT spot-beam 10 illuminates Barcelona with an EIRP of 61 dBW.

3.5.3 Clutter decorrelation impact on the power link budget

An important aspect to take into account on the GEOSAR acquisition will be the clutter decorrelation during the long integration considered. Clutter is typically modelled as stationary, but the internal motion results in a non-zero Doppler bandwidth response. This is known as the internal or intrinsic clutter motion. Billingsley found a mathematical model [81] for the power spectrum of the internal clutter motion from experimental results that depends on the radar frequency and wind speed. This model presents two components, a stationary term (DC) and a noise term (AC) with exponential frequency spectrum. The clutter spectrum can be modelled as [81][82][83]:

$$S_C(f_D) = \frac{\alpha}{\alpha + 1} \delta(f_D) + \frac{1}{\alpha + 1} \frac{\beta \lambda}{4} e^{-\frac{\beta \lambda}{2} |f_D|} \quad (3.49)$$

where f_D is the clutter Doppler shift (in Hz), λ corresponds to the radar wavelength and $\delta(f_D)$ is the Dirac delta function. α and β are parameters that depend on the transmitted frequency and wind speed. The spectrum function presented in (3.49) is normalized to 1.

A relation of the transmitted power and wind speed with the ratio α between the power of the DC and AC components of the ground clutter has been experimentally found [81]:

$$\alpha = 489.9 \cdot w^{-1.55} F_0^{-1.21} \quad (3.50)$$

being w the wind speed in miles per hour and F_0 the radar carrier frequency in GHz.

On the other hand, the exponential decay of the power spectrum is given by β . This

parameter is function of the wind parameters but it has been experimentally shown that it is not dependent on the carrier frequency. The expression of β is:

$$\beta^{-1} = 0.1048 [\log w + 0.4147] \quad (3.51)$$

Therefore, considering two different frequency bands, L-band (1.625 GHz) and Ku-band (17.25 GHz), the clutter spectrum responses for different wind speeds obtained are presented in Figure 3.35 and Figure 3.36, respectively. As seen, the clutter power spectrum is more disperse in case of Ku-band due to the lower DC/AC ratio working at higher frequency. Furthermore, the DC term also decrease with respect to the AC component when the wind speed increases. Regarding the AC component decay, the negative exponential term decreases for high wind speeds, resulting in higher level for non-zero Doppler components.

Due to the long integration time considered in this mission to overcome the low backscattered power from the scene, only those targets with long term coherent components will provide the useful signal. On the other hand, targets with slow diffuse components will spread clutter noise everywhere in the antenna footprint. Therefore, only the part of the spectrum corresponding to Doppler frequencies under the inverse of the integration time has to be taken into account as useful clutter power. The rest of the spectrum will be added to the noise term in the signal to noise ratio computation.

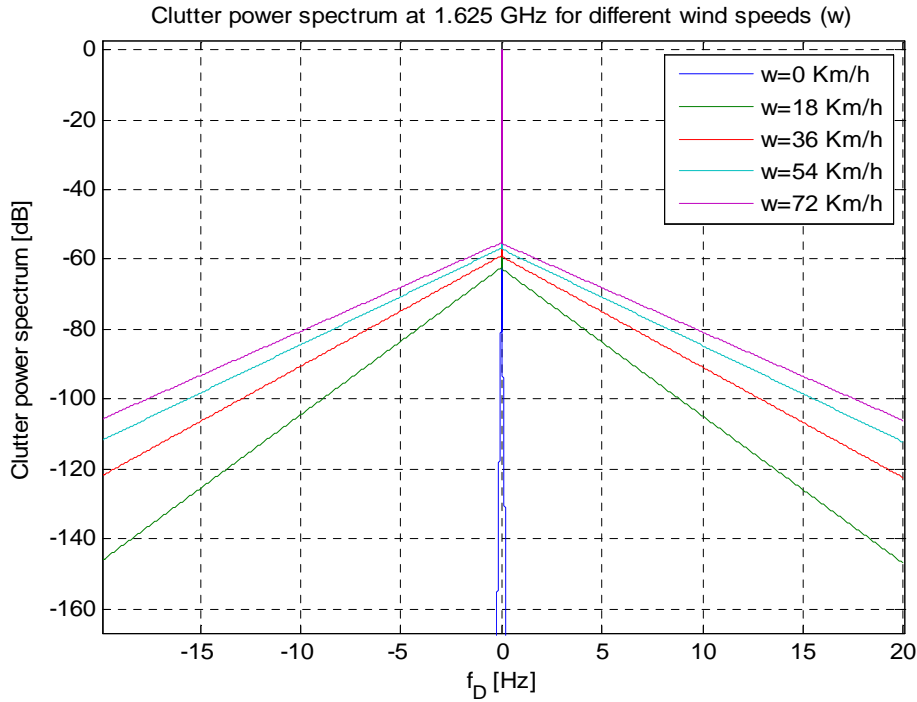


FIGURE 3.35 Clutter power spectrum response for L-band acquisition at 1.625 GHz for different wind speeds.

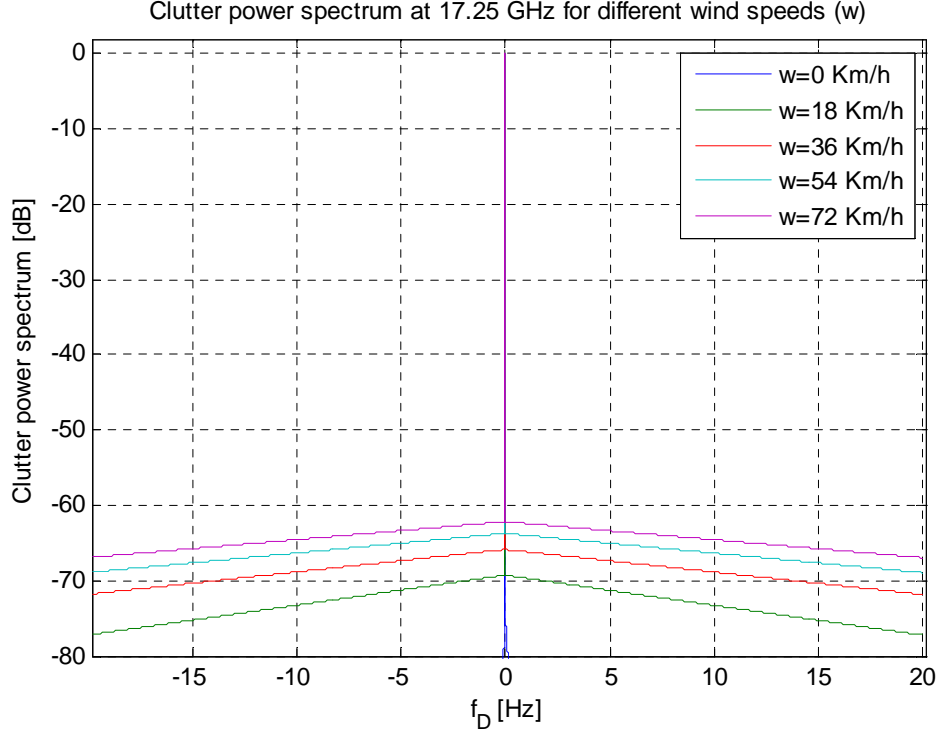


FIGURE 3.36 Clutter power spectrum response for Ku-band acquisition at 17.25 GHz for different wind speeds.

So, considering the schematic Billingsley's clutter response presented in Figure 3.37, only the blue shaded part of the spectrum will contribute in the received power. Therefore, a decorrelation coefficient in the received power level will be considered. This term can be obtained as:

$$C_U = \int_{-1/T_i}^{1/T_i} S_C(f_D) df_D \quad (3.52)$$

So, following the analysis presented in section 3.5.1, the backscattered power received after SAR processing will be now computed as:

$$P_r' = \frac{P_t G_t G_r \sigma_0 \rho_{az} \rho_{gr} \lambda^2}{(4\pi)^3 R_{St}^2 R_{Sr}^2 L_T k T_0 F_n} \cdot DC \cdot T_i \cdot B \cdot C_U = P_{r_0} C_U \quad (3.53)$$

where P_{r_0} is the received power without considering the clutter decorrelation.

On the other hand, the clutter power that will contribute to the noise can be obtained integrating the diffuse components of the power spectrum. Therefore, taking into account that the power spectrum function presented in (3.49) is normalized, the clutter factor of the power spectrum will be obtained as:

$$C_N = 2 \int_{1/T_i}^{f_{D_{\max}}} S_C(f_D) df_D \quad (3.54)$$

where $f_{D_{\max}}$ is the maximum Doppler of ground clutter affecting the desired signal. In our analysis, maximum Doppler shifts around 20 Hz has been considered. The clutter noise power will be given by:

$$P_{CN} = \frac{P_t G_t G_r \sigma_0 \rho_{az} \rho_{gr} \lambda^2}{(4\pi)^3 R_{St}^2 R_{Sr}^2 L_T k T_0 F_n} \cdot DC \cdot T_i \cdot B \cdot C_N \quad (3.55)$$

Therefore, the Signal to Noise and Clutter Ratio (SNCR) considering the clutter decorrelation terms will be given by:

$$SNCR = \frac{P_r'}{k T_0 FB + P_{CN}} \quad (3.56)$$

So, the clutter decorrelation will penalize the SNCR decreasing the useful received power from the scene and increasing the noisy term. The impact on the power link budget in two different bands is studied next.

Let us consider an L-band acquisition with a SNR of 10 dB without considering the clutter decorrelation. The impact on the SNCR of the clutter decorrelation for different wind speeds is summarized in Figure 3.38. In blue, the SNCR for a transmitted power of 36.5 W is shown. Other link budget parameters have been adjusted to obtain a SNCR of 10 dB if

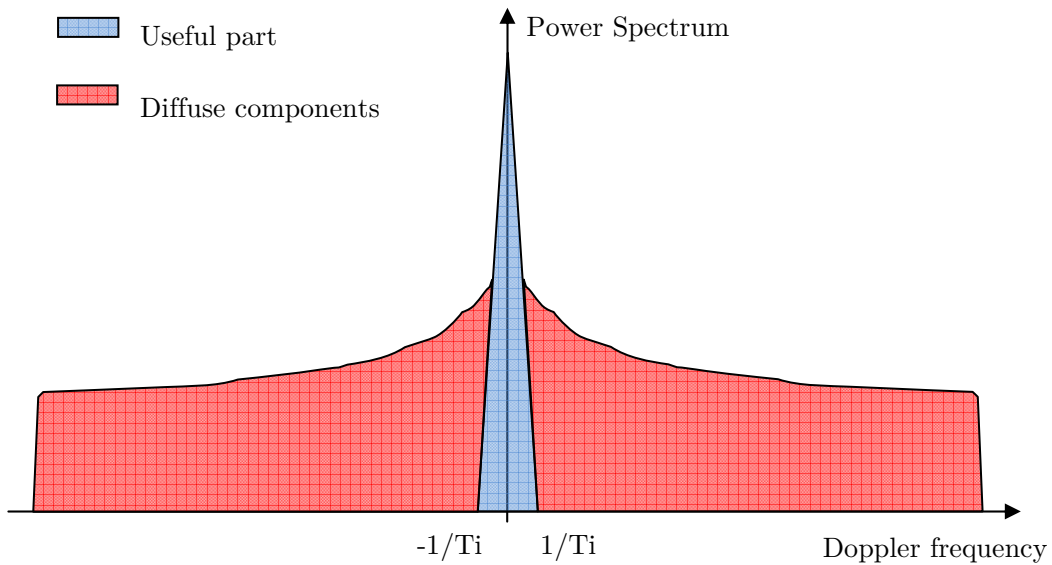


FIGURE 3.37 Long term coherent components vs. diffuse components in Billingsley's clutter model.

no wind is considered (quasi-static clutter). However, as the wind speed increases, lower values of SNCR are obtained. A possible solution for increasing the SNR under windy conditions would be to increase the transmitted power. Considering an extra 6 dB of transmitted power, the green curve of Figure 3.38 is obtained. As it can be seen, SNCRs above 10 dB are obtained for wind speeds up to 50 Km/h.

However, sometimes increasing the power will not be possible or it would not improve significantly the SNCR since the clutter power also depends on the transmitted power. This is the case when higher frequencies were used, where the transmitted power requirements were more stringent. Let us study the impact on the SNR of the clutter decorrelation in a Ku-band acquisition. In this case, a transmitted power of 457 W has been considered, and the rest of the parameters have been adjusted to obtain a SNR of 10 dB without wind. As shown in Figure 3.39, the SNCR decreases faster than in L-band when the wind speed increases. Furthermore, the required transmitted power to reach 10 dB SNR in absence of wind was larger than in L-band and, therefore, it cannot be increase as much as in the L-band example. So, increasing the transmitted mean power from 457 W to 1000 W, the SNR is above 10 dB only for wind speeds under 14 Km/h as shown by the green line in Figure 3.39.

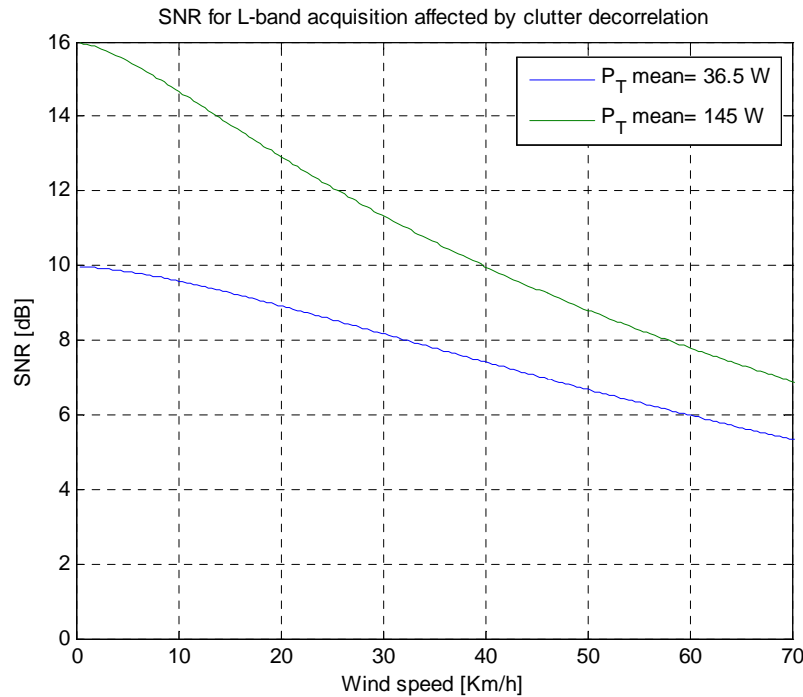


FIGURE 3.38 Clutter decorrelation impact in the L-Band acquisition SNR for different wind speeds.

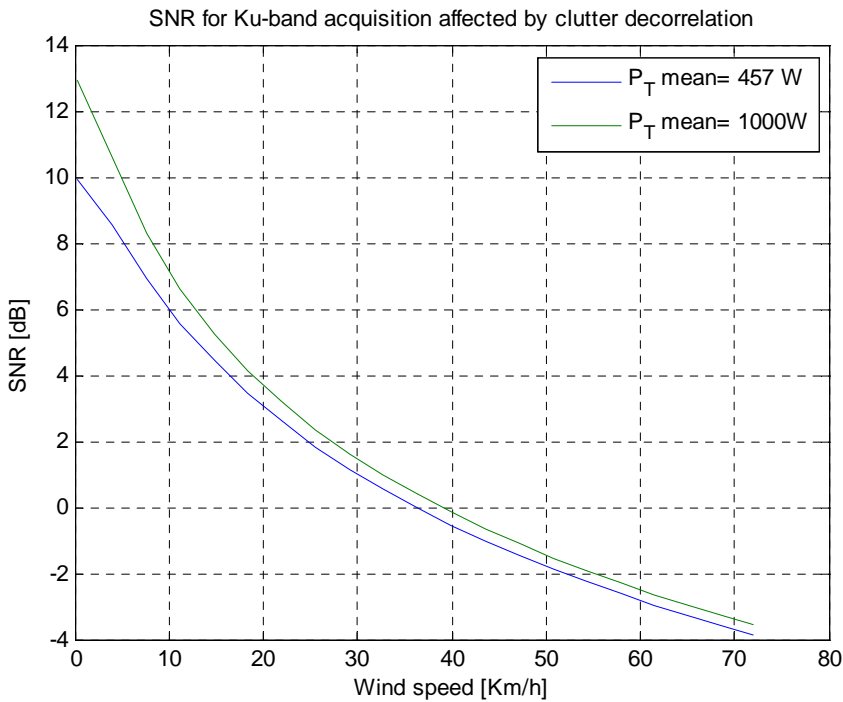


FIGURE 3.39 Clutter decorrelation impact in the Ku-Band acquisition SNR for different wind speeds.

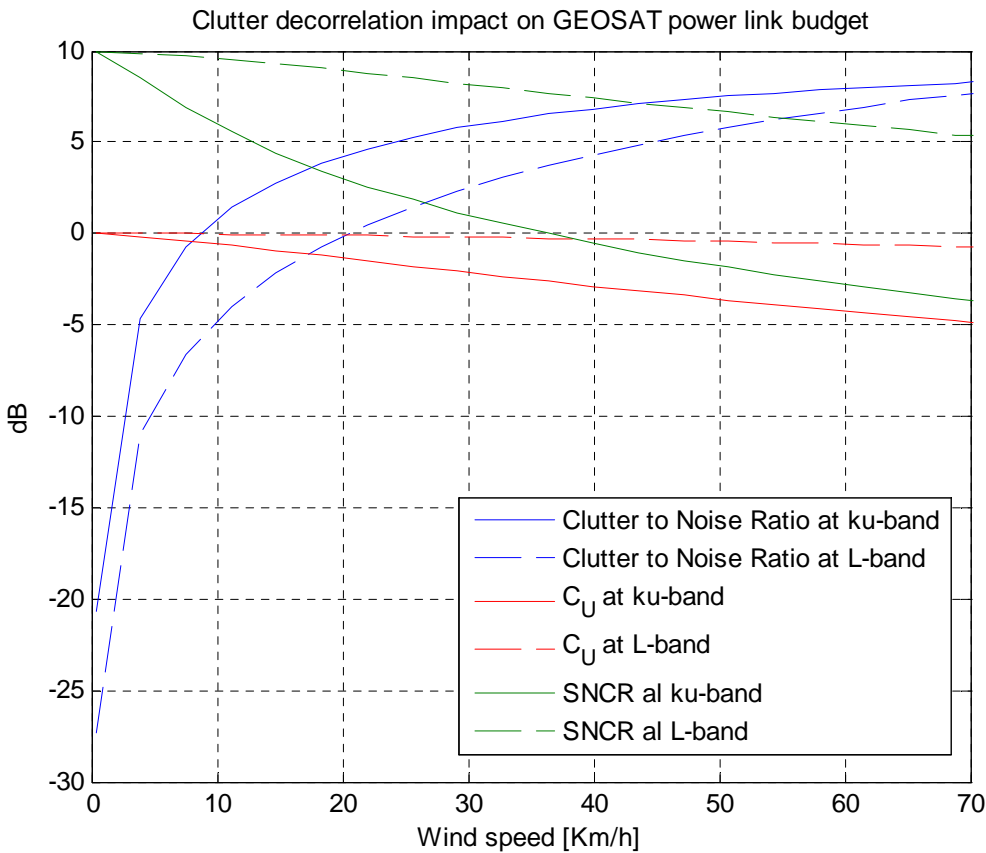


FIGURE 3.40 Clutter decorrelation impact on GEOSAR power link budget for Ku- and L-band acquisitions.

Thus, the clutter decorrelation will have deeper impact on higher frequencies link budget while the SNR in lower frequency band acquisitions can be preserved above 10 dB for wind speed up to 50 Km/h (in L-band example). As shown in Figure 3.40, the clutter to noise ratio for Ku-band is higher than in L-band as a consequence of the higher clutter decorrelation at higher frequencies. As a consequence, as seen in Figure 3.40, the C_U decorrelation coefficient is higher in Ku-band, with deeper impact on the SNCR.

Therefore, for Ku-band acquisition, stable targets should be found to assure the correct performance of the system for windy conditions. This is the case of urban areas with trihedral structures and parabolic user's antennas which can be interesting targets of opportunity. The analysis of such reflectors and their impact on the power link budget for Ku-band acquisition is presented in section 3.5.5.

3.5.4 *Stable target analysis: minimum RCS*

As seen in section 3.5.3, the clutter decorrelation will have strong impact in higher frequency band acquisitions considering large integration times. Therefore, the presence of permanent scatterers in the scene will be necessary to overcome the clutter defocusing problems. This kind of scatterers is expected to be stable during the acquisition presenting high RCS. The minimum RCS to reach the desired SNR will be determined in this section reformulating the SNCR calculation for the case of a point target. In section 3.5.5, a theoretical approach to the expected values for user's parabolic antennas RCS is presented.

So, considering a point target, the formulation regarding the useful power will change with respect to the distributed target (or clutter) analysis. Therefore, the $\sigma_0 \rho_{az} \rho_{gr} C_U$ term corresponding to the clutter power per resolution cell will be substituted by the point target RCS. Other terms of equation (3.56) regarding the thermal and clutter decorrelation noise will still be present in the power link budget computation in the case of point targets. Therefore, the SNCR will be computed as:

$$SNCR = \frac{P_{r_{PT}}}{kT_0 FB + P_{CN_{PT}}} \quad (3.57)$$

where $P_{r_{PT}}$ is the received power from the point target obtained as:

$$P_{r_{PT}} = \frac{P_t G_t G_r \lambda^2 \sigma_{RCS}}{(4\pi)^3 R_{St}^2 R_{Sr}^2 L_T} \cdot DC \cdot T_i \cdot B \quad (3.58)$$

while the clutter power, considered as noise in this case will be obtained as:

$$P_{CN_{PT}} = \frac{P_t G_t G_r \lambda^2 \sigma_0 \rho_{az} \rho_{gr}}{(4\pi)^3 R_{St}^2 R_{Sr}^2 L_T} \cdot DC \cdot T_i \cdot B \quad (3.59)$$

Frequency	17.25 GHz
Wavelength	0.0174 m
Antenna gain	50.1 dB
Required transmitted peak power	31.83 dBW
System Losses	3 dB
Duty cycle	0.3
Integration time	4 hours
Resolution cell	15 x 15 meters
Receiver noise factor	2 dB

TABLE 3.6. Antenna parameters requirements for Ku-band spot beam with 350 Km coverage.

So, if the target RCS is isolated from (3.57) using the expressions (3.58) and (3.59), the RCS requirements to reach the minimum SNCR can be obtained as:

$$\sigma_{RCS_{req}} = SNCR_{\min} \left(\sigma_0 \rho_{az} \rho_{rg} + \frac{(4\pi)^3 R_{st}^2 R_{sr}^2 L_T}{P_t G_t G_r \lambda^2 DC \cdot T_i} k T_0 F \right) \quad (3.60)$$

Considering a minimum SNCR of 10 dB to assure the correct reception of echoes from the scene, and the parameters presented in Table 3.6 as a particular example of a Ku-band acquisition, a RCS of 23.93 dBsm would be necessary taking a clutter backscattering coefficient of -10 dB. A theoretical approach to the expected RCS of user's parabolic antennas in urban areas is presented next. Other stable target and trihedral structures on urban areas could be targets of interest for the Ku-band GEOSAR acquisition.

3.5.5 Parabolic antennas as reflectors of opportunity

Most of the geostationary satellites are TV broadcasting satellites pointing to users zones of the Earth where a lot of parabolic antennas are steered to them. This kind of metallic reflectors are expected to have high RCS in the direction of the main beam. Since these antennas need to have continuous direct link, it is expected that they always be visible for the satellite, well pointed and very stable mounted.

Furthermore, the development of the satellite TV during the last years has increased the number of these parabolic antennas making them really interesting for Geosynchronous SAR purposes. The density of parabolic antennas is particularly high in urban areas which are regions of high interest for GEOSAR monitoring. Figure 3.41 shows the distribution of the parabolic antennas in the world. As it can be observed, the major concentration of these reflectors is in Europe. Furthermore, an increase of a 22% in the world during the period from 1999 to 2002 is observed. Then, they will be an interesting opportunity to

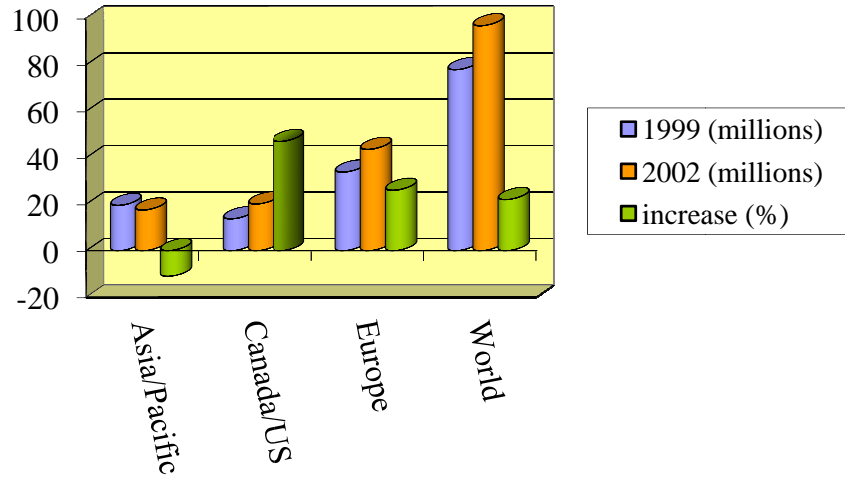


Figure 3.41 Number of user home parabolic antennas.

monitor urban areas and assure at least in those zones (especially in Europe) a very dense coverage of stable and bright targets.

However, the response of a parabolic antenna as a remote sensing scatterer has to be studied. It will depend on the reflector characteristics and the mismatch produced due to the feeder which will reflect a fraction of the satellite signal back to the dish again. In the following lines, a detailed theoretical approach is presented taking the basic backscattering formulas of radar. The radar backscattering coefficient or RCS (σ) can be defined as the coefficient between the electric field scattered by the target (E_s) squared and the electric field incident to the target (E_i) squared for far distances. Equivalently, it can be related to the scattered and incident power densities, \wp_s and \wp_i respectively, as in (3.61).

$$\sigma = \lim_{R \rightarrow \infty} 4\pi R^2 \frac{|E_s|^2}{|E_i|^2} = \lim_{R \rightarrow \infty} 4\pi R^2 \frac{\wp_s}{\wp_i} ; \quad \text{since} \quad \wp = \frac{|E|^2}{\eta_{wave}} \quad (3.61)$$

Then, the field or power density scattered by the parabolic antenna must be computed to determine the RCS. Two different contributions will influence to the total reflected signal. The former one corresponds to the non-guided reflected power due to the reflexions on the structure, supports, etc. The non-guided reflections will be a second order term and, consequently, they are neglected in this RCS analysis. The dominant term, and the one studied in this section, corresponds to the guided reflection in the output port of the feeder.

The analysed scheme is presented in Figure 3.42 a). The incoming signal (red slashed lines) hits the parabolic dish which reflects the signal to the feeder (red lines). Considering an incidence power density \wp_i and taking the parabolic antenna geometrical area (A_{geo}), the power intercepted by the parabolic disc can be computed as:

$$P_i = \wp_i A_p = \wp_i A_{geo} \quad (3.62)$$

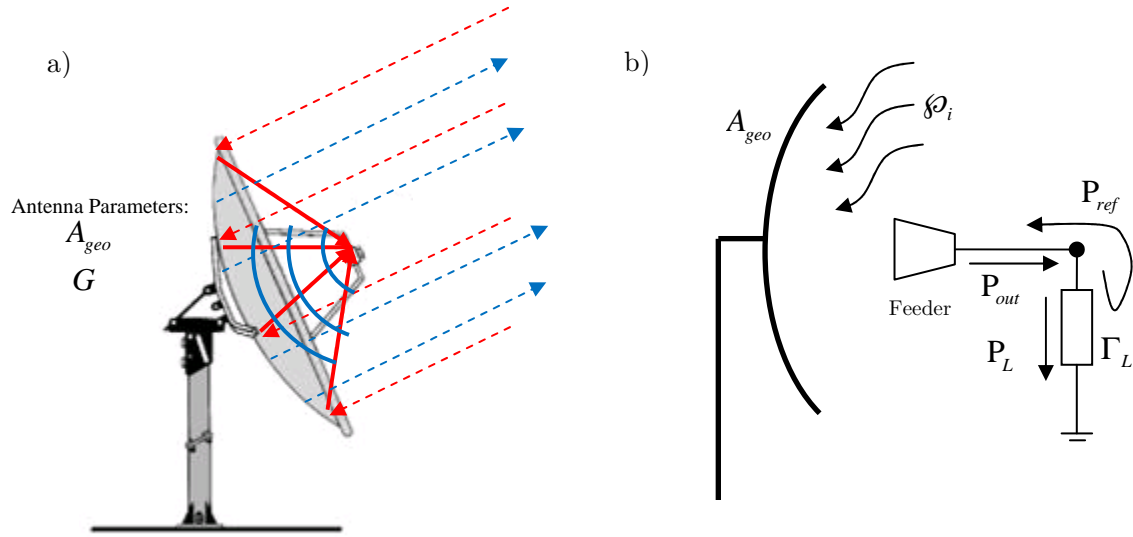


FIGURE 3.42 a) Parabolic antenna working as a scatterer. b) Feeder mismatch: power reflected and not delivered to the load.

where A_p corresponds to the projected area in the direction of illumination. In the case studied, the parabolic reflectors will be faced to the transmitting satellite to assure the correct reception of the signal. Then, the projected area can be approximated directly with the geometric area (A_{geo}). On the other hand, not all the intercepted power by the dish is reflected and transmitted to the feeder. Another important parameter of the parabolic antenna (dish + feeder) is the efficiency. So, the power delivered to the output port will be:

$$P_{out} = P_i \eta_{eff} = \mathcal{P}_i A_{geo} \eta_{eff} = \mathcal{P}_i A_{eff} \quad (3.63)$$

The efficiency of the antenna (η_{eff}) accounts for the ohmic losses and illumination efficiency of the whole antenna. It can be computed from the antenna gain as:

$$G = \frac{4\pi}{\lambda^2} A_{eff} = \frac{4\pi}{\lambda^2} A_{geo} \eta_{eff} \rightarrow \eta_{eff} \triangleq \frac{G}{A_{geo}} \frac{\lambda^2}{4\pi} \quad (3.64)$$

Once the signal is collected by the feeder, it is transmitted to a load which is not usually perfectly matched to the transmission line. The first stage of a low noise block (LNB) downconverter is an amplifier with an input matching network optimized for minimum Noise Factor which is usually slightly mismatched at the nominal LNB frequency band. This mismatch will increase in case the radar operates at a different frequency. Then, a fraction of the output power (P_{out}) is delivered to the load (P_L) while the rest is reflected and sent back to the reflector. The delivered and reflected powers can be obtained as:

$$P_L = P_{out} \left(1 - |\Gamma_L|^2 \right) \quad (3.65)$$

$$P_{ref} = P_{out} |\Gamma_L|^2 \quad (3.66)$$

The reflected power will be re-radiated by the antenna. So, the power density backscattered by the antenna is related with the incidence power density as follows:

$$\begin{aligned} \wp_s &= \frac{P_{ref} G}{4\pi R^2} = \frac{P_{out} |\Gamma_L|^2 G}{4\pi R^2} = \frac{P_{out} |\Gamma_L|^2 A_{eff} \frac{4\pi}{\lambda^2}}{4\pi R^2} = \frac{\wp_i A_{eff} |\Gamma_L|^2 A_{eff} \frac{4\pi}{\lambda^2}}{4\pi R^2} = \\ &= \wp_i |\Gamma_L|^2 \frac{A_{eff}^2}{\lambda^2 R^2} \end{aligned} \quad (3.67)$$

Finally, using (3.67) in the RCS equation (3.61), the backscattering coefficient for the parabolic antenna can be expressed as:

$$\sigma = \lim_{R \rightarrow \infty} 4\pi R^2 \frac{\wp_s}{\wp_i} = \lim_{R \rightarrow \infty} 4\pi R^2 \wp_i |\Gamma_L|^2 \frac{A_{eff}^2}{\lambda^2 R^2} \frac{1}{\wp_i} = \frac{4\pi}{\lambda^2} A_{geo}^2 \eta_{eff}^2 |\Gamma_L|^2 \quad (3.68)$$

In Table 3.7, the RCS has been computed taking the parameters of some commercial parabolic antennas for TV satellite at Ku band. The RCS is computed for different antenna diameters and gains. A typical low-noise reflection coefficient of -10dB ($20 \log |\Gamma_L|$) has been considered for the feeder-load mismatch. As seen, the SNR requirements of 10 dB are fulfilled for the 135 cm and 80 cm diameter parabolic dish. However, even in the case of 60 cm dish, a SNR of 9.22 dB is obtained which is close to the desired value.

Therefore, the user's parabolic antennas will be an interesting target of opportunity to take into account in GEOSAR acquisition. Experimental measurements should be considered in order to validate the analysis presented above.

Brand	Model	Freq.	Band	Diameter	Area	Gain	η_{eff}	RCS (dBsm)	SNCR (dB)
TECATEL	135+LNB	17.25 GHz	Ku	135 cm	1.43 m ²	45.74 dB	0.63	35.29	21.35
TECATEL	80+LNB	17.25 GHz	Ku	80 cm	0.50 m ²	41.05 dB	0.61	25.89	11.95
XINSHI	XS-KU-60-I	17.25 GHz	Ku	60 cm	0.28 m ²	39.56dB	0.77	22.95	9.22

TABLE 3.7. RCS of parabolic antennas depending on the geometric and frequency parameters.

3.6 Image reconstruction via Time-Domain Back-Projection

A very important part of any SAR system is the image reconstruction. The raw data collected from a scene must be correctly processed in order to give the final product to the user. There are several algorithms to process the SAR raw data but not all of them will be appropriate for GEOSAR systems due to the linear trajectory approximations that some of them consider. In this section, the basic SAR concepts on reconstruction will be shortly explained and the selected algorithm for GEOSAR processing, the Time Domain Back-Projection (TDBP), will be presented. After that, the results obtained with this algorithm for different situations in a simulated GEOSAR system will be presented and the image characteristics analysed and compared with the expected resolutions from the theoretical approach presented in section 2.4.

3.6.1 GEOSAR system model

First of all, the geometrical model used in a SAR system is presented to clarify the basic concepts on acquisition and processing. Consider a scene with several point targets with different reflectivities σ_n . Each point target is placed at an arbitrary position (x_n, y_n) in the scene. The coordinate system is defined such as the x axis corresponds to the range or cross-track domain, while the y axis to the azimuth or along track domain. A satellite with the antenna radar placed at $(0, u)$ which illuminates the scene with a signal $p(t_r)$ is assumed. In this case, the measured echo from each transmitted pulse will be:

$$s_r(t_r, u) = \sum_n \sigma_n p \left[t_r - \frac{2\sqrt{x_n^2 + (y_n - u)^2}}{c} \right] \quad (3.69)$$

The summation on (3.69) accounts for the different targets on the scene while

$$\frac{2\sqrt{x_n^2 + (y_n - u)^2}}{c}$$

is the 2-way delay associated to each target on the scene considering the satellite position $(0, u)$ at each transmission event. This example, presented in Figure 3.43, is valid for a rectilinear satellite path but it will not model the general situation for a GEOSAR acquisition where several curvilinear trajectories can be obtained depending on the geosynchronous satellite orbital ephemerides.

Therefore, considering an arbitrary trajectory as in Figure 3.44, the satellite motion must be defined in a 3D coordinate system. The reference system considered in the GEOSAR simulations is an Earth centred rotating coordinate system. In this way, the $(x_{sat}, y_{sat}, z_{sat})$ coordinates of the satellite can be obtained from the satellite longitude and latitude

histories computed in (2.23) and (2.25) as a change from spherical to Cartesian coordinates as:

$$x_{sat}(t_a) = r(t_a) \sin(90^\circ - \varphi_{sat}(t_a)) \cos(\lambda_{sat}(t_a)) \quad (3.70)$$

$$y_{sat}(t_a) = r(t_a) \sin(90^\circ - \varphi_{sat}(t_a)) \sin(\lambda_{sat}(t_a)) \quad (3.71)$$

$$z_{sat}(t_a) = r(t_a) \cos(90^\circ - \varphi_{sat}(t_a)) \quad (3.72)$$

where $r(t_a)$ is the temporal evolution of the orbital radius computed in (2.1) while $\varphi_{sat}(t_a)$ and $\lambda_{sat}(t_a)$ stands for the satellite latitude and longitude histories of the satellite. A similar procedure has been used to determine the target locations in the Cartesian coordinate system. The position of the targets considering the Earth's centred rotating coordinated system is fixed if the target is not moving. So, from the target latitude, longitude and height over the Earth reference ellipsoid, the target coordinates will be obtained as:

$$x_{tar_n} = (R_{earth}(\varphi_{tar_n}) + h_{tar_n}) \sin(90^\circ - \varphi_{tar_n}) \cos(\lambda_{tar_n}) \quad (3.73)$$

$$y_{tar_n} = (R_{earth}(\varphi_{tar_n}) + h_{tar_n}) \sin(90^\circ - \varphi_{tar_n}) \sin(\lambda_{tar_n}) \quad (3.74)$$

$$z_{tar_n} = (R_{earth}(\varphi_{tar_n}) + h_{tar_n}) \cos(90^\circ - \varphi_{tar_n}) \quad (3.75)$$

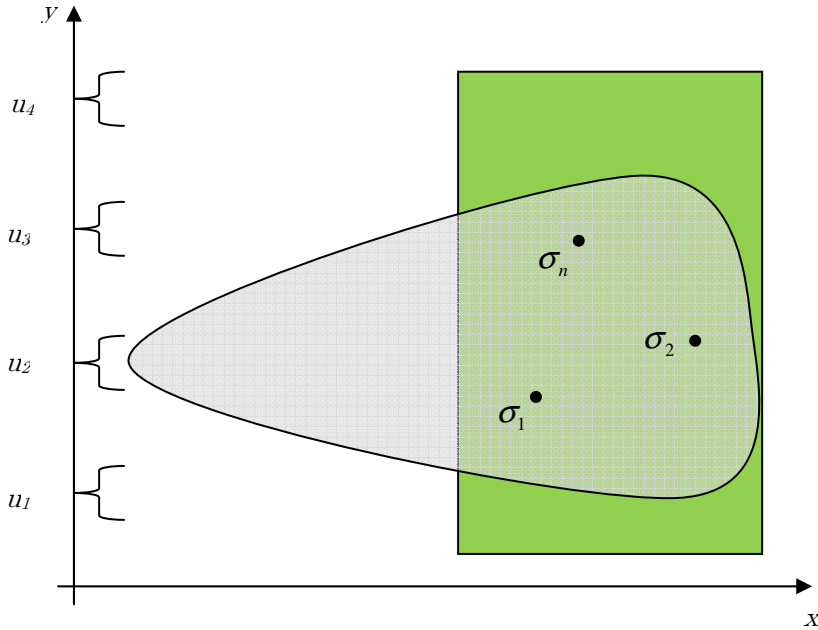


FIGURE 3.43 SAR system model for a linear satellite trajectory.

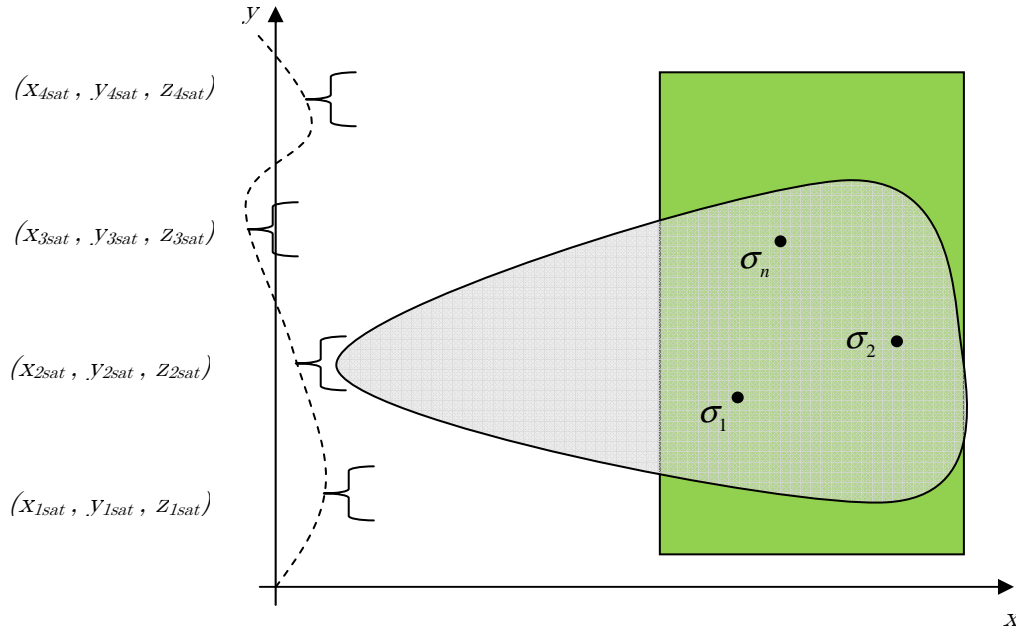


Figure 3.44 SAR system model for a non-linear satellite trajectory.

In this case, $R_{earth}(\varphi_{tar_n})$ is the Earth's radius at the target's latitude. In this study, the WGS84 model [67] has been used to model the Earth ellipsoid. h_{tar_n} corresponds to the target height over the reference ellipsoid and the coordinates of the target are defined by φ_{tar_n} and λ_{tar_n} for the latitude and longitude, respectively.

Then, considering the new geometry of the problem, the received signal in the radar can be modelled as follows:

$$s_r(t_r, t_a) = \sum_n \sigma_n p \left[t_r - \frac{2\sqrt{(x_{tar_n} - x_{sat}(t_a))^2 + (y_{tar_n} - y_{sat}(t_a))^2 + (z_{tar_n} - z_{sat}(t_a))^2}}{c} \right] \quad (3.76)$$

Typically in SAR, the t_r domain is known as *fast time or range domain* since it models the signal propagation which travels at the speed of light. On the other hand, the variable t_a accounts for the satellite position at the different transmission events which has a slower evolution. Hence, it is known as the *slow time or azimuth domain*. Every PRI (Pulse Repetition Interval), the satellite transmits a pulse to the scene. For this reason, the slow time domain must be sampled each PRI to model the transmitted pulses.

3.6.2 Digital reconstruction via Time Domain Back-Projection

The raw data obtained from a SAR system must be processed in order to obtain a focused image from the two dimensions matrix (t_r, t_a) presented in the previous section. The geosynchronous satellites describe non-linear tracks preventing the direct application of SAR algorithms based on linear track/constant speed assumptions. The Time Domain Back-Projection (TDBP) algorithm is one of the most versatile SAR processing tools since does not consider any approximation and can be used for any system geometry and acquisition parameters. It makes this algorithm suitable for the GEOSAR case considered in this report.

The first step to reconstruct the image by TDBP is to perform a matched filtering in the fast time domain of the raw data. The fast time matched filter used in this case is a conjugated and reversed replica of the transmitted signal [84]. So, the fast-time matched-filtered SAR matrix will be obtained as:

$$s_M(t_r, t_a) = s_r(t_r, t_a) * p^*(-t_r) \quad (3.77)$$

In (3.77), a convolution in the fast time domain is performed for each received echo. So, considering the integration of several pulses all along the synthetic aperture formation, the pixel brightness for each target of the scene is computed as:

$$f(x_i, y_i) = \int_{x_{sat}, y_{sat}, z_{sat}} s_M \left(\frac{2\sqrt{(x_{tar_n} - x_{sat}(t_a))^2 + (y_{tar_n} - y_{sat}(t_a))^2 + (z_{tar_n} - z_{sat}(t_a))^2}}{c}, t_a \right) dt_a \times A_{ij} e^{-j\phi_{ij}t} \quad (3.78)$$

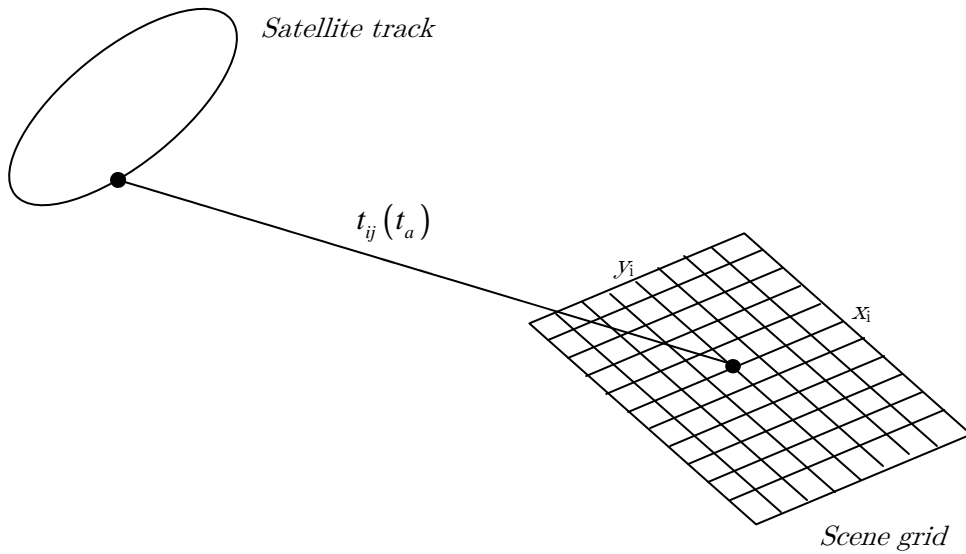


FIGURE 3.45 Back-projection algorithm geometric scheme.

where the fast time matched filtered response position corresponding to the 2 way delay from the satellite position at each slow time and the target position (x_i, y_i) is integrated for the whole synthetic aperture formation. The term $A_{ij}e^{j\phi_{ij}t}$ accounts for the amplitude and parabolic phase compensation due to the radar motion. The previous equation can be re-written as:

$$f(x_i, y_i) = \int_{x_{sat}, y_{sat}, z_{sat}} s_M(t_{ij}(t_a), t_a) dt_a \times A_{ij}e^{-j\phi_{ij}t} \quad (3.79)$$

In TDBP SAR reconstruction algorithm, the data of the fast-time bins that corresponds to the location of each scene point at each received pulse for all the synthetic aperture locations determined by the slow time are added coherently. So, a reconstruction grid over the scene must be defined and the corresponding echoes from each point located in the fast time matched raw data matrix and added to retrieve the total power that comes from each scene position.

The situation is presented schematically in Figure 3.45. For each position of the scene grid, the two way delay must be computed for each satellite position at each slow time transmission event. Once the delay is computed for each slow time, the corresponding samples of the raw data matrix range compressed must be added coherently. If a bright target is placed in the position (x_i, y_i) , the echoes from different slow times will give a strong power since all they will have high amplitude and the phases will be added constructively. On the other hand, if no target is placed in the computed grid position, the different samples of the raw data matrix will be added destructively giving a residual low power for that position of the scene grid.

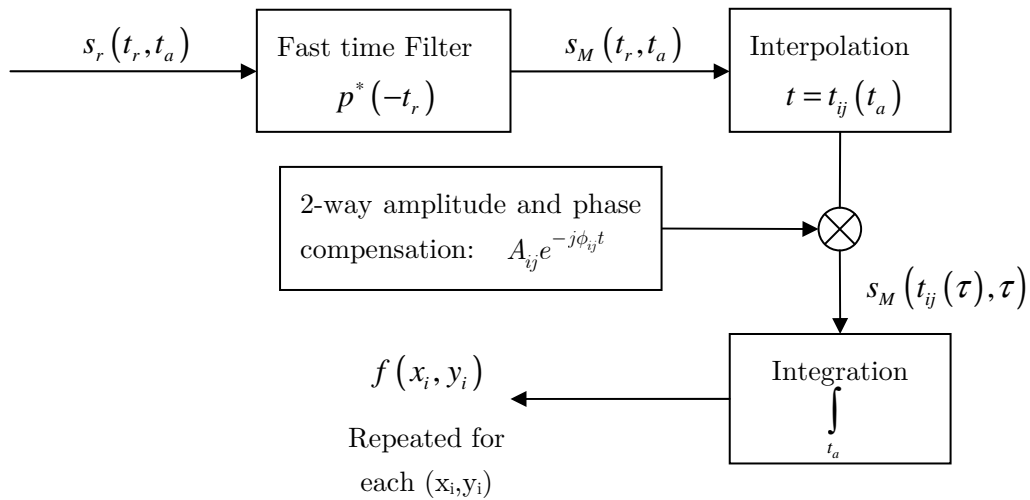


FIGURE 3.46 Backprojection algorithm performance scheme.

This procedure must be repeated for each scene point to obtain the final reconstructed image. The scene grid must be sampled enough to properly focus the image (much more sampled than the ground range and azimuth resolution) to avoid wrong target positioning. It may be also necessary to interpolate the range compressed raw data matrix in the fast time domain in order to get the sufficient samples and more accurate results.

The complete algorithm is schematically summarized in Figure 3.46. As it has been explained, the received data is range compressed and the sample corresponding to the delay from each transmitted pulse is integrated for all the position of the synthetic aperture. This algorithm, interesting for its versatility, has as a major drawback: the computational cost. For large areas, the procedure must be repeated for all the points of the scene which can take long times. Several articles propose some strategies to decrease this time [85][86]. However, for the GEOSAR images with long integration time and medium resolution presented in this thesis, it will not be a problem by now. These algorithms could be analysed and applied to see their impact in the processing time in future GEOSAR studies.

3.6.3 *GEOSAR simulator*

In order to simulate the GEOSAR acquisition and generate raw data, a MATLAB simulator has been developed. This has been an important tool for checking the theoretical analyses presented all along this document since no real SAR data from a geosynchronous satellite is available nowadays. In Figure 3.47, the block diagram for the GEOSAR simulator is presented. The most important parts of the simulator are summarized next:

- **Input parameters:** in this block the user defines the parameters that affect to the GEOSAR analysis and focusing.
 - Constant definitions: speed of light, Earth's model, sidereal day, etc. In principle, they are fixed parameters and should not be modified.
 - Satellite parameters: acquisition configuration (monostatic or bistatic) and satellites ephemerides (inclination, eccentricity, nominal position, argument of the perigee, etc.). It models the orbital behaviour presented in section 2.4.
 - Signal parameters and timing: signal type, signal duration, carrier frequency, bandwidth, Pulse Repetition Frequency, Duty Cycle, integration time, etc. These parameters should be taken in accordance with the different studies presented in sections 3.1, 3.2 and 3.3
 - SAR processing options: block processing in raw data generation and/or focusing for large raw data matrices. This is an important block to avoid

large matrices during the raw data processing due to the long integration time considered in GEOSAR.

- Scene parameters: target locations and RCS, scene temporal decorrelation.
- Atmospheric phase inputs: spatial-temporal correlation of atmospheric phase map. Input parameters to simulate the atmospheric temporal and spatial decorrelation in order to see its impact to the raw data focusing of long integration time SAR acquisitions. The Atmospheric Phase Screen (APS) properties are studied in section 4.3.
- **Orbit computation:** the satellite track is computed from the input satellite parameters. The satellite orbit behaviour presented in section 2.2.2 is used to obtain the satellite motion with respect to a rotating Earth centred reference system.
- **Scene definition:** the scene is defined from the input scene parameters. Different scene sizes and configuration can be analysed in order to check the feasibility of GEOSAR focusing in different situations.
- **Raw data generation:** the simulated raw data is obtained from the slant range computation given by the satellite orbit and scene considered (section 2.2.3). Additionally, the atmospheric phase disturbances will be considered to check the APS effects on GEOSAR raw data focusing as will be studied in section 4.3.
- **SAR features results:** the simulator gives to the user the most important results obtained with for the analysed GEOSAR configuration: Doppler history of received echoes (section 3.2), PRF selection and diamond/dartboard diagrams (section 3.3), ambiguity results (section 3.4) and SNR budget (section 3.5).
- **Atmospheric phase map generation:** a simulated behaviour of the atmospheric phase map is computed from the atmospheric phase inputs. This block considers the atmospheric properties described in the literature as presented in section 4.3.
- **Back-projection focusing:** raw data focusing via time-domain back projection as presented in section 3.6.2.
- **Sub-acquisition focusing:** sub-focusing technique to obtain several low-resolution images from sub-matrices of the long-term raw data matrix and retrieve the atmospheric phase behaviour. This APS retrieval algorithm is explained in section 4.3.2.
- **Atmospheric phase map retrieval:** results obtained from the APS retrieval algorithm.
- **Raw data compensation:** the phase information obtained from the APS retrieval algorithm is used to compensate the atmospheric phase in the long term raw data.

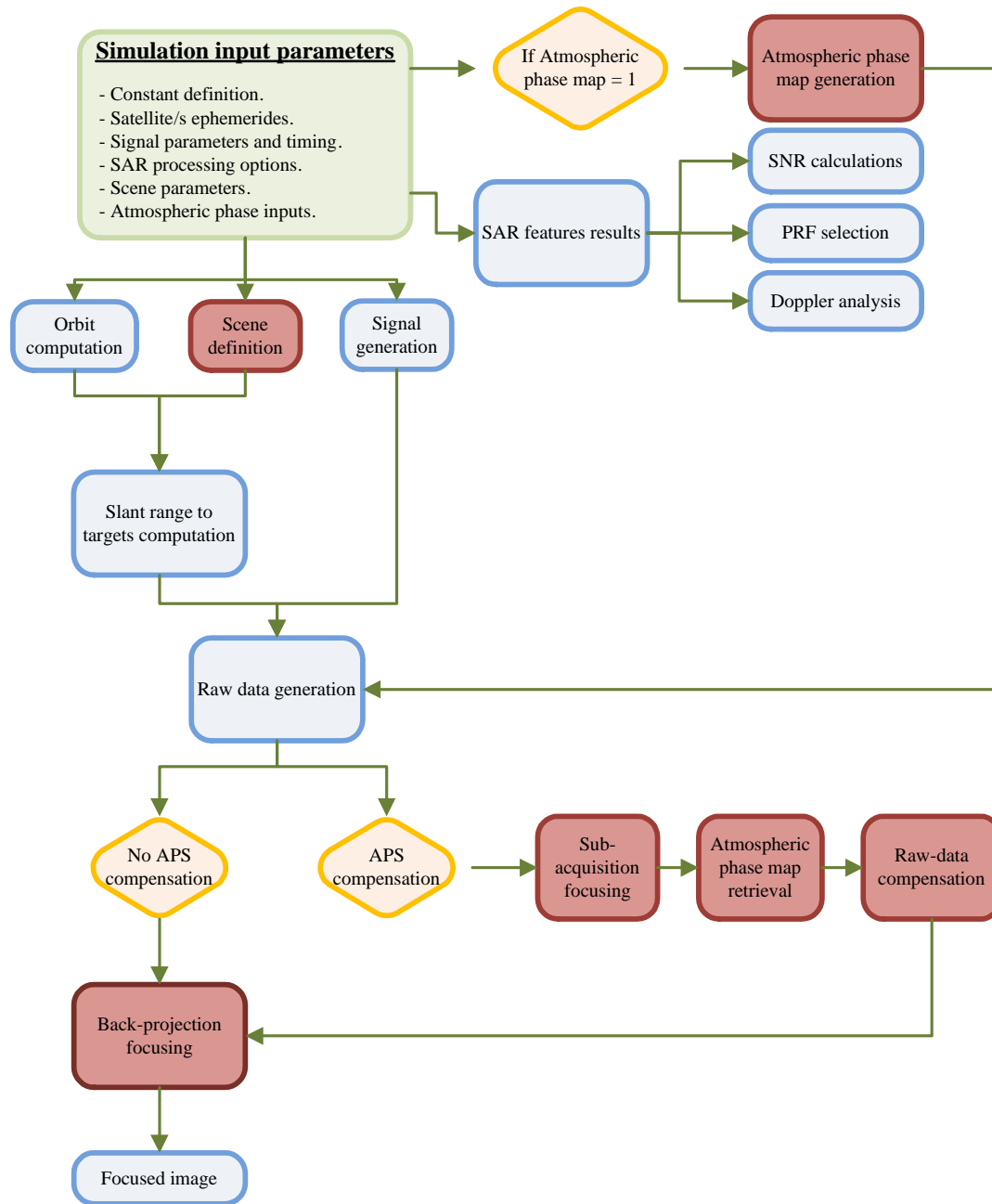


FIGURE 3.47 GEOSAR simulator block diagram.

3.6.4 Monostatic GEOSAR focusing

In this section, a particular monostatic GEOSAR acquisition is analysed to determine the correct performance of the Time Domain Back-projection algorithm to focus the raw data. A scene of 1 by 1 Km scene placed over Barcelona (41.23°N, 2.11°E) with a single target in

the central position is firstly considered. The scene is illuminated by a satellite placed at the same longitude with an orbit eccentricity of 0.0004 and no inclination of the orbital plane. In this case, the effects of the atmospheric phase map variation have been neglected.

Then, the first step performed by the GEOSAR simulation tool is to compute the satellite orbital motion and the satellite track. As a result, it shows a 3D plot and the cuts from different views as presented in Figure 3.48 and Figure 3.49 for this particular case. So, the user can identify the satellite motion and the scene and target locations and determine if the chosen orbital parameters are suitable for the acquisition requirements. The red square in Figure 3.48 is a zoom in for the satellite motion while in green one is the zoom in for the scene targets distribution. As it can be seen, in the middle of the scene, a red dot shows the location of the target for the particular example considered in this section. The green line shown in the satellite motion of Figure 3.48 and Figure 3.49 corresponds to the part of the orbital motion considered for the acquisition. Therefore, it is the actual synthetic aperture length of the acquisition. In this example, the integration time is 12 hours.

Considering the different cuts of the orbital motion shown in Figure 3.49, some of the GEOSAR motion particularities presented in Chapter 2 can be observed. In Figure 3.49 b), the non-constant radius of the orbit due to the eccentricity can be appreciated. On the other hand, in Figure 3.49 c), the left-right motion or along track relative movement of the satellite with respect to the scene, as a consequence of the orbital eccentricity, can be seen. This is the satellite motion that will determine the azimuth resolution of the system and it is the one that must be considered in the synthetic aperture formation analysis.

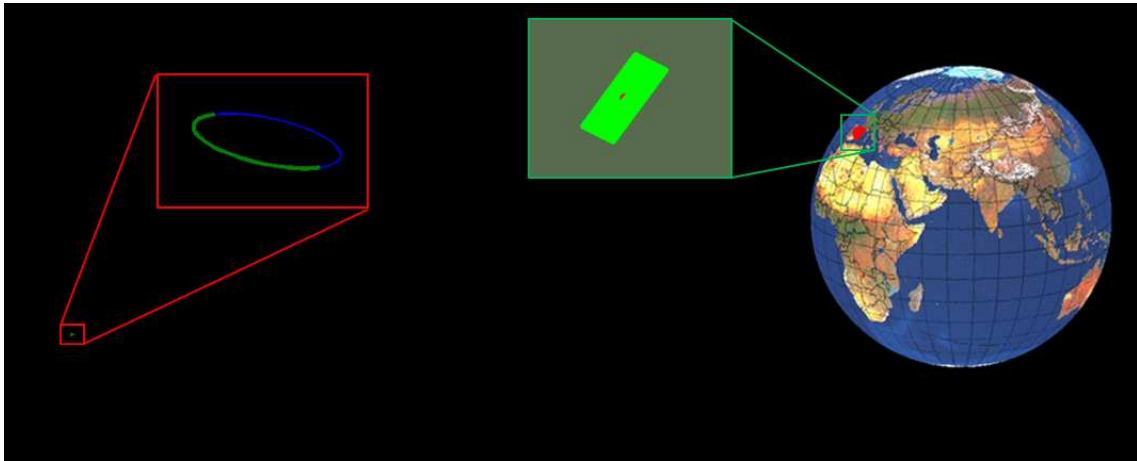


FIGURE 3.48 3D view of satellite path (eccentricity of 0.0004 and no inclination) and scene location (41.23°N , 2.11°E).

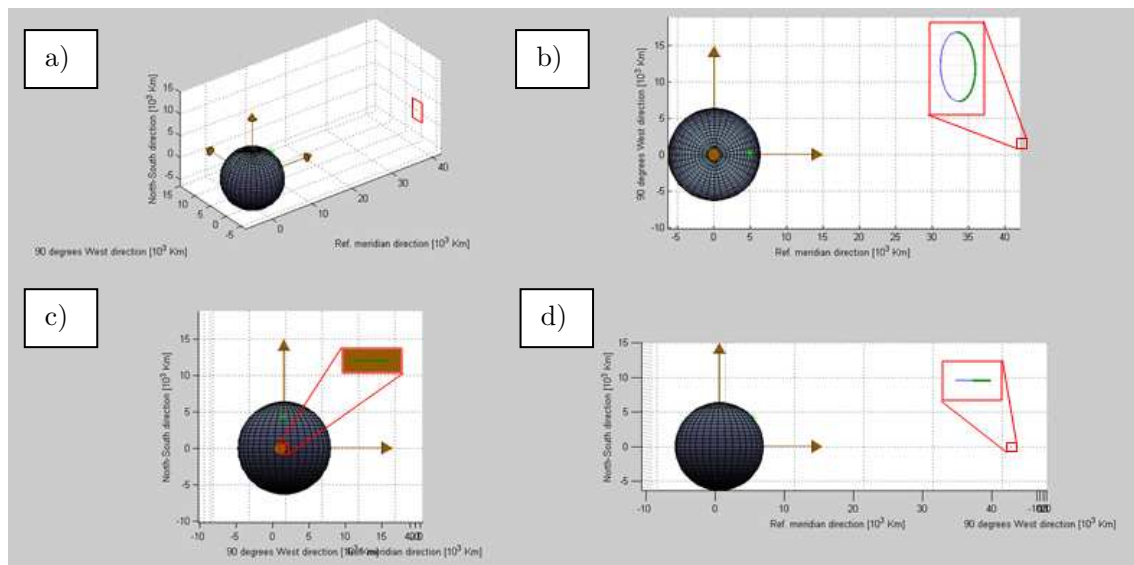


FIGURE 3.49 a) 3D orbital representation. b) Top view representation (reference meridian- 90° West cut). c) Satellite nadir plane (North- 90° West cut). d) Side view (North-Reference meridian cut).

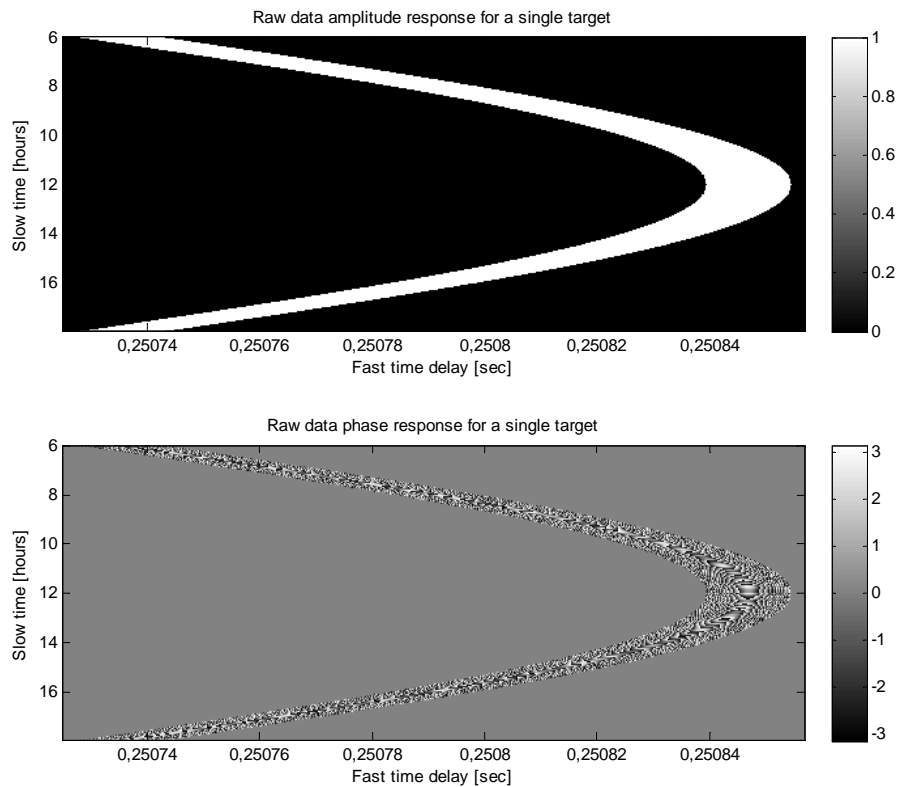


FIGURE 3.50 Simulated raw data from a point target in the central point of the scene.

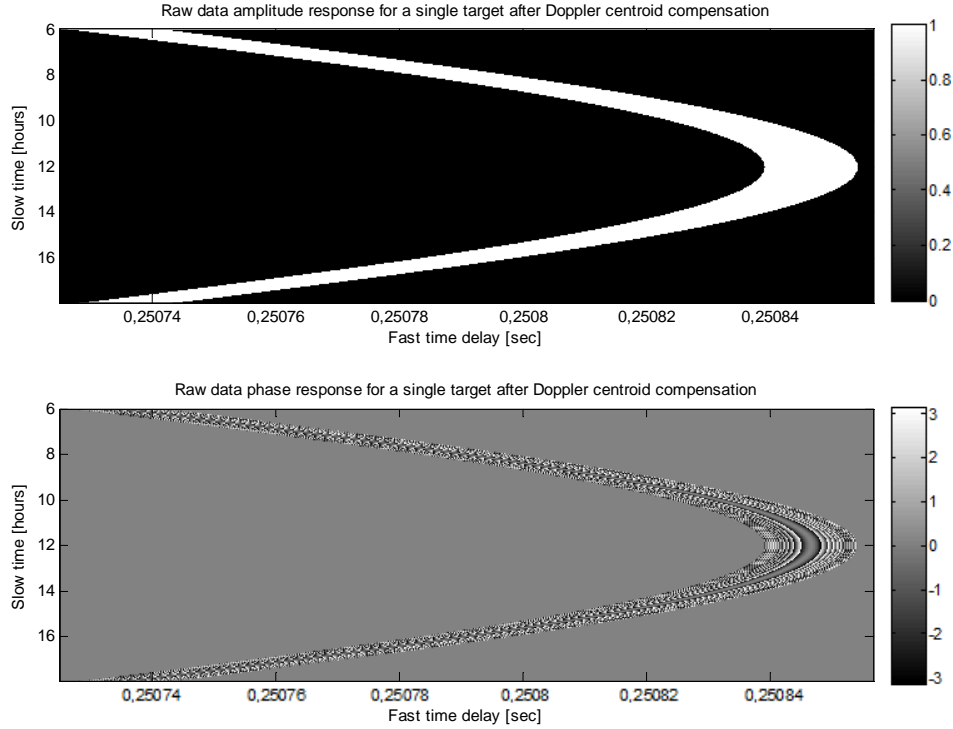


FIGURE 3.51 Simulated raw data from a point target in the central point of the scene after Doppler centroid compensation.

Once the satellite and target location are well defined, the raw data matrix is computed by using equation (3.76). In order to obtain the raw data matrix of the acquisition, the satellite-target slant range for the different position of the satellite are computed using the equation (2.33) obtained in section 2.2.3. The raw data matrix amplitude and phase obtained for this case are shown in Figure 3.50. As explained in the Doppler history analysis of GEOSAR acquisition, Doppler centroid compensation has to be considered previous the raw data focusing in order to cancel the Doppler shift produced by the orbital radius variations which are not useful for focusing. This compensation corresponds to an additional phase term and, therefore, the amplitude is not affected as shown in Figure 3.51 where the raw data matrix amplitude and phase after Doppler centroid compensation are presented.

After the raw data matrix generation, the range compression, as introduced in section 3.6.2, must be performed. In this example, a chirp pulse has been considered as a transmitted signal. The raw data compressed matrix is shown in Figure 3.52. As it can be seen, the orbital radius variations introduce a common delay in the received raw data from the scene obtaining a maximum delay at twelve hours from the perigee which corresponds to the apogee. This is consistent with the orbital analysis of section 2.1 and the Doppler history presented in section 3.2. A range cut at 14 hours from the perigee is shown in Figure 3.52 bottom plot. As seen, the range compression is correctly performed and the origin of the echo can be identified univocally with a specific delay.

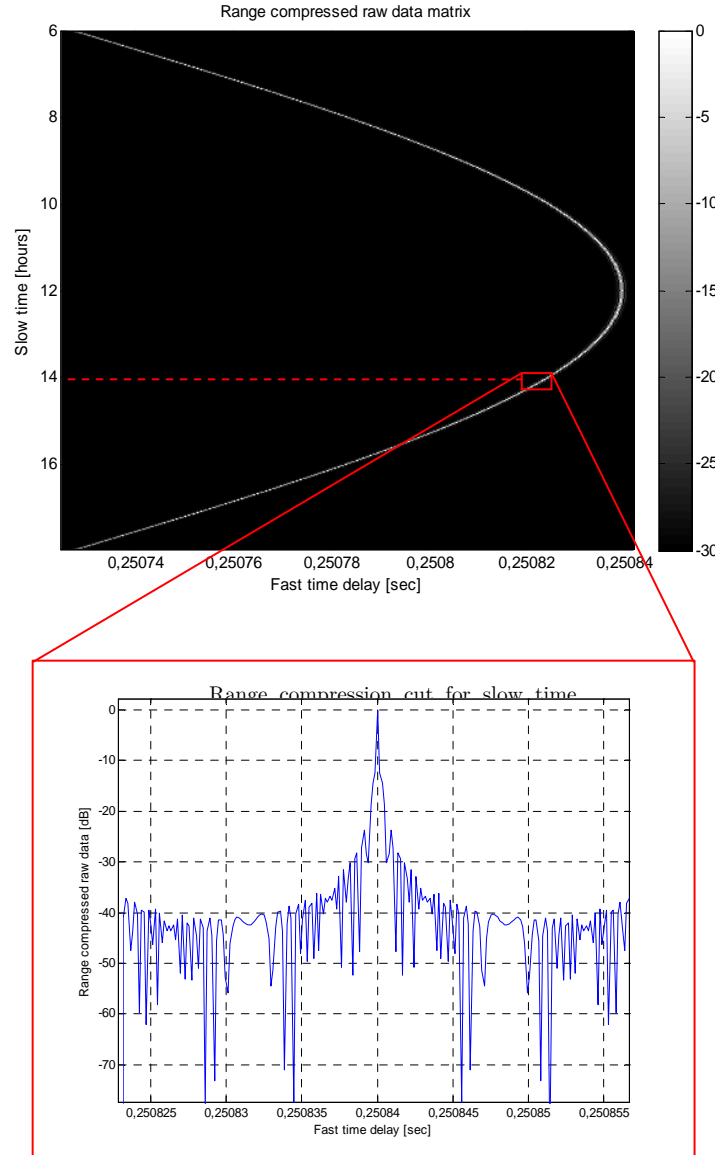


FIGURE 3.52 Range compression of the raw data matrix and cut for slow time of 14 hours.

Once the range compressed raw data matrix is computed, the back-projection focusing is done. First, a grid over the scene must be defined. In this case, 1000 by 1000 points has been considered to sample the 1 by 1 Km scene. Then, for each point in the grid, the 2 way slant ranges from the satellite are computed. The corresponding bins of the compressed data matrix are added coherently after the phase shift compensation associated to the signal path delay. An interpolation 1:10 in the fast time domain has been implemented to get more precise results. Once, the algorithm has been computed for all the points in the scene grid the focused image presented in Figure 3.53 is obtained. As it can be seen, a bright point in the middle of the scene is focused as it was defined in the input parameters.

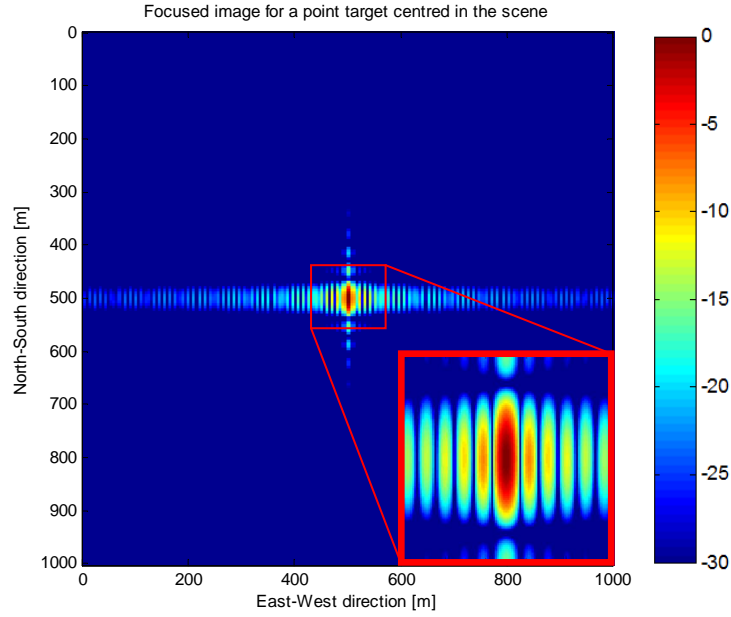


FIGURE 3.53 Focused image for the raw data from a single point target in the centre of the scene.

If the equations (2.81) and (2.83) obtained from the theoretical approach for the azimuth and ground range resolutions are particularized for this example, considering the 12 hours of integration and a signal transmitted frequency of 12 GHz with a bandwidth of 4 MHz, an azimuth and ground range resolution of 6.85 meters and 60 meters are obtained, respectively. If these values are compared with the simulated focused image, an azimuth resolution of 7.5 meters and a ground range resolution around 55 meters are obtained. These results from the simulation are close to the expected ones from the theoretical analysis.

As explained in section 2.4.2, the integration time will play an important role to determine the achievable resolution of the acquisition. So, in the previous example, considering 12 hours of integration, the maximum achievable resolution for this particular case is obtained. However, such integration time will be too large in most of the cases where the scene decorrelation may affect to the SAR focusing.

Thus, if in the previous example the integration time is reduced to 1 hour, the synthetic aperture length is shortened and, consequently, the azimuth resolution is worsened. In this case, the theoretical azimuth resolution given by equation (2.89) would be 52 meters. The simulated results are presented in Figure 3.54. As it can be seen, with the shorter integration time, worse azimuth resolution is obtained and the target impulse response is squared. Taking a look to the azimuth and range cuts presented in Figure 3.54 b) and Figure 3.54 c) respectively, a resolution of around 50 by 55 meters is obtained. As seen, the range resolution is not affected by the integration time considered.

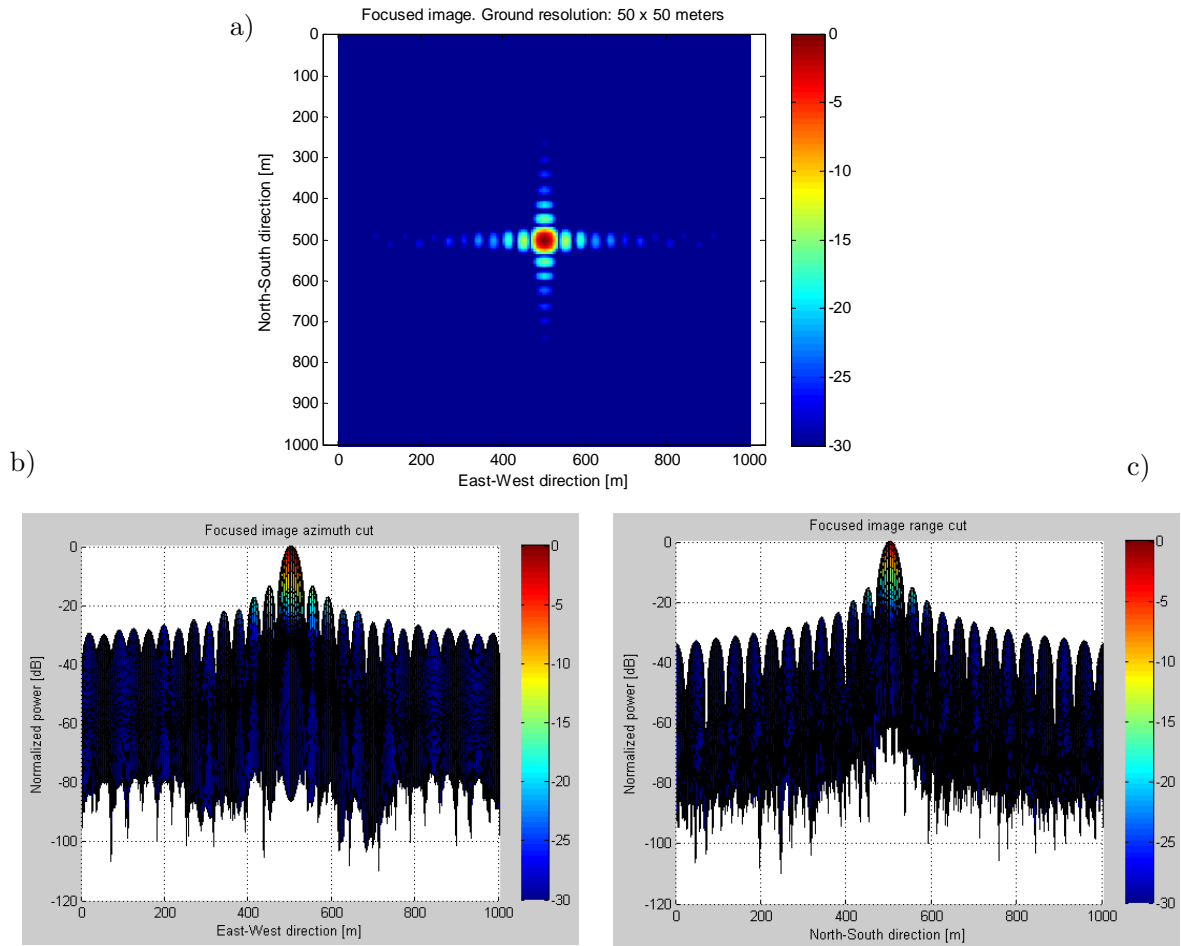


FIGURE 3.54 a) Focused image with squared pixel, b) Target response azimuth cut and c) Target response range cut.

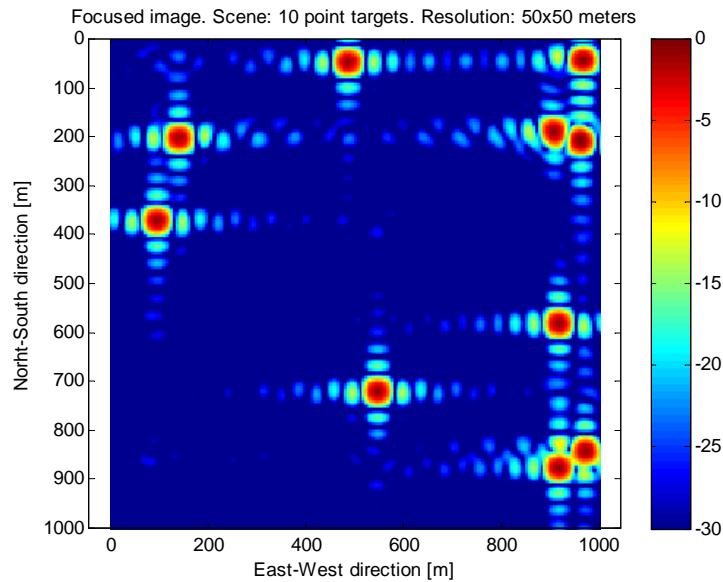


FIGURE 3.55 Focused 50 by 50 meters resolution image for 10 point targets scene.

Once the feasibility of the back-projection reconstruction for a monostatic GEOSAR acquisition with a single point target within the illuminated scene has been checked, more complex scenes and/or systems can be simulated. In Figure 3.55, an image considering the

same orbital and scene parameters than in the previous example but taking 10 point targets randomly placed at the scene is presented. The 10 point targets can be distinguished since their separation is larger than the SAR resolution of the considered configuration.

Other GEOSAR geometries (two geosynchronous satellites in a bistatic configuration, bistatic acquisition with on-ground receiver) and more complex scenarios (multiple targets, atmospheric decorrelation effects, target decorrelation effects, etc.) are presented in Chapter 4.

Chapter 4

Geosynchronous SAR Applications and Limitations

The nearly fixed position of the geosynchronous satellite considered in this thesis, with low-eccentric orbits and zero-inclination, makes it possible to monitor permanently a specific region of the Earth. This feature, impossible to fulfil with current LEOSAR, limited by the revisit time, neither with air-borne or GB-SAR with reduced coverage, makes possible to consider a new range of applications for GEOSAR.

GEOSAR acquisition will be interesting for those scenarios affected by changes with time scales in the order of hours or longer, or with constant evolution. This could be the case on risk zones monitoring and disaster management (Earthquakes, floods, volcanoes, etc.) which needs to be permanently monitored in order to react as fast as possible. With current LEOSAR, it would be only possible to get information about these phenomena if, luckily, a LEO satellite would have been crossing above the scene at this moment and, even so, it would not be possible to follow the temporal evolution of the phenomenon. Otherwise, it can be difficult to access to the damage zone in order to get information via GB-SAR or air-borne SAR acquisition, due to their limited coverage commented above.

Thus, applications and limitations have been put together in this chapter since some of the potential applications, such as APS monitoring, are at the same time a limiting factor that needs to be compensated in other GEOSAR applications such as interferometry.

4.1 Sub-daily surface imaging

The nearly fixed position with respect to the Earth of the geosynchronous satellites studied in this section will make it possible to have several SAR acquisition per day. However, as already studied in section 2.4.2, the resolution of the obtained image will strongly depend, apart from the orbital ephemerides, on the integration time considered in each acquisition.

Therefore, several acquisition strategies could be considered depending on the mission requirements and features of the imaged scene. In the following section, some of them are briefly introduced and analysed.

4.1.1 *Full-resolution acquisition*

Given a GEOSAR orbital design, two full-resolution images may be obtained by considering two acquisitions of twelve hours of integration centred at the satellite pass through the perigee and through the apogee, respectively. The acquisition scheme is presented in Figure 4.1.

As seen in Figure 4.1, two maximum synthetic aperture lengths are obtained by considering this acquisition scheme. Increasing the integration time above 12 hours will not represent better resolution since the satellite motion is enclosed in the orbital box defined by the orbital eccentricity and inclination. However, these full-resolution acquisitions will only be possible over very stable scene due to the long integration time considered (12 hours) to get each image.

In order to compare the performance of the different acquisition schemes presented in these sections, a satellite with orbital eccentricity of 0.0003 and no inclination will be considered. A C-band acquisition (5.4 GHz) from a slant range of 38.000 km will be assumed for these examples. Therefore, considering the resolution analysis presented in section 2.4 and particularly the equation (2.83), two images with an along-track resolution of 20.8 meters can be obtained. As it will be seen in the other examples, this will be the maximum achievable resolution for this configuration and, for this reason, this acquisition mode has been called full-resolution acquisition.

The effects of the satellite relative velocity daily variations in the PSLR presented in section 2.4.3 should be considered in the different examples presented in this section.

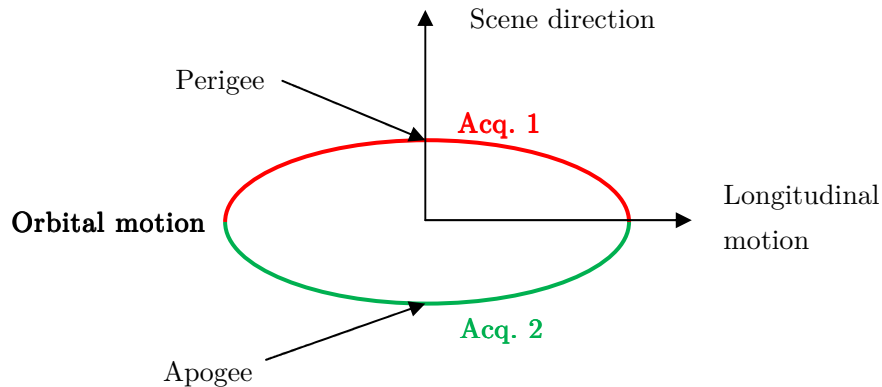


FIGURE 4.1 Acquisition scheme to get two full-resolution images per day.

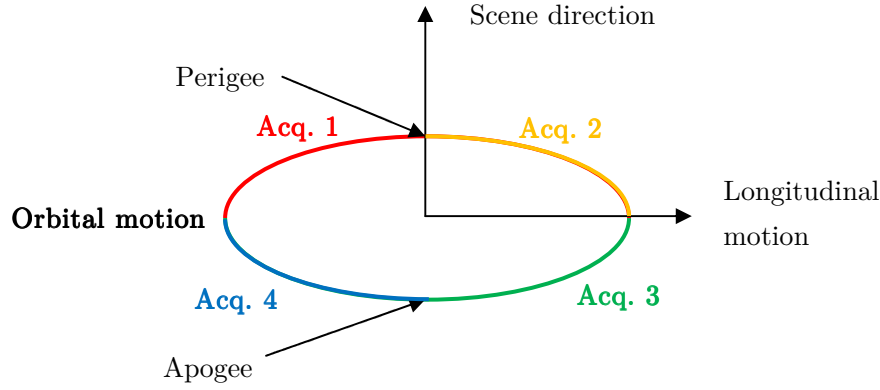


FIGURE 4.2 Acquisition scheme to get four half-resolution images per day.

4.1.2 Half-resolution acquisition

Alternatively, for scenarios with lower temporal correlation a shorter integration time should be considered. Obviously, reducing the integration time below 12 hours, coarser along-track resolution will be obtained. This will be the case of most of the scenarios, where 12 hours of integration will be too long considering the temporal decorrelation of the scene.

Therefore, four half-resolution images can be obtained by considering 6 hours of integration for each one. In this case, the acquisitions should start at the time pass through the perigee (t_p), at t_p+6h , at time pass through the apogee (t_a) and at t_a+6h , respectively. This new acquisition mode is schematically shown in Figure 4.2. As seen, four acquisitions with a synthetic aperture length of half the maximum orbital longitudinal displacement are obtained.

So, considering the same orbital design than in the previous section (orbital eccentricity of 0.0003) and the transmitting signal parameters (C-band 5.4 GHz), an along-track resolution of 41.7 meters would be obtained by considering the analysis of Section 2.4. As seen, half resolution with respect to the acquisition mode presented in the previous section is obtained.

4.1.3 Dual-resolution acquisitions

Until now, the daily orbital motion of the satellite has been split in sub-aperture of the same length obtaining several images per day with the same along-track resolution. In the example presented in section 4.1.2, an along track resolution of 41.7 meters was obtained from 6 hours of integration. However, considering an acquisition centred at the time pass through the perigee or through the apogee, the achievable resolution would be maximized for a given integration time since the relative velocity of the satellite with respect to the Earth is higher around this point (see section 2.4.3).

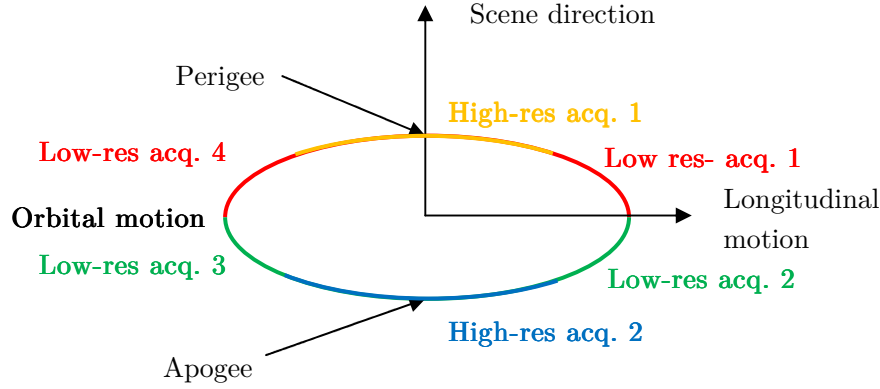


FIGURE 4.3 Dual-resolution acquisition mode scheme.

Therefore, other acquisition schemes can be considered in order to maximize the along-track resolution for a given integration time for two images per day. Additionally, other coarser resolution images could be obtained considering the orbital motion between these two maximum resolution acquisitions. This acquisition mode is schematically presented in Figure 4.3. As seen, two high-resolution and four low-resolution images would be obtained by considering this scheme. The along-track resolution of each image will depend on the integration time defined for each sub-acquisition.

Let us consider an integration time of 6 hours for the high resolution acquisition centred at the perigee and apogee in order to compare the results obtained for this configuration with the one considered in the previous section. This integration time for the high-resolution acquisition will result in an integration time of 3 hours for the four low resolution images. An orbital eccentricity of 0.0003 and a transmitted frequency of 5.4 GHz (C-band) have been used as in the previous cases.

So, for the 6 hours integration acquisition centred at the time pass through the perigee and through the apogee, an along-track resolution of 29.4 meters is obtained with equation (2.89). As seen, for the same integration time than in the scheme analysed in section 4.1.2, better along-track resolution can be obtained with this configuration. However, it may be achieved at expenses of reducing the number of high-resolution images to two per day.

On the other hand, for the low-resolution images with an integration time of 3 hours at the edges of the orbital motion, coarser resolution will be obtained. So, taking the analysis presented in section 2.4.3, with $t_p = -7.5$ h, -4.5 h, 4.5 h and 7.5 h, respectively, an along-track resolution for these low resolution acquisition of 140 meters has been obtained.

Therefore, for this particular example, two high resolution (29.4 meters) and four low-

resolution (140 meters) images per day could be obtained. This configuration may be interesting for monitoring different phenomena during the day one requiring high spatial resolution with less temporal sampling and others requiring more frequent images but with lower spatial resolution.

4.1.4 Constant resolution acquisitions

The acquisition modes presented in sections 4.1.1 and 4.1.2 with two and four acquisition with the same resolution per day may be extended to an arbitrary number of acquisitions per day with coarser along-track resolutions. So, there will always be a trade-off between the number of acquisitions per day and the achievable resolution of each obtained image.

So, in order to obtain constant resolution along the daily different acquisition of the satellite, the same synthetic aperture per sub-acquisition must be assured. Taking into account the non-constant satellite velocity with respect to the Earth surface, the integration time requirement to reach the desired synthetic aperture length will vary depending on the instant of the day considered.

So, taking into account the analysis of section 2.4.3, the required orbital longitude span can be related to the synthetic aperture length requirements as:

$$L_{SA} = r \cdot \left| 2e \cdot \sin \left(\Omega_E \left(\frac{-T_i}{2} - t_p \right) \right) - 2e \cdot \sin \left(\Omega_E \left(\frac{T_i}{2} - t_p \right) \right) \right| \quad (4.1)$$

Using the trigonometric identity

$$\sin x - \sin y = 2 \sin \left((x - y) / 2 \right) \cos \left((x + y) / 2 \right)$$

the equation (4.1) can be re-written as:

$$\begin{aligned} L_{SA} &= 2e \cdot r \cdot \left| \sin \left(\frac{\Omega_E}{2} \left(\frac{-T_i}{2} - t_p' - \frac{-T_i}{2} + t_p' \right) \right) \cos \left(\frac{\Omega_E}{2} \left(-\frac{T_i}{2} - t_p + \frac{T_i}{2} - t_p \right) \right) \right| = \\ &= 2e \cdot r \cdot \left| \sin \left(-T_i \frac{\Omega_E}{2} \right) \cos \left(-\Omega_E t_p \right) \right| \end{aligned} \quad (4.2)$$

where the integration time and time pass through the perigee impacts have been separated. Then, the integration time required for different values of t_p for a desired along-track resolution (ρ_{az}) can be obtained as:

$$T_i = \frac{2}{\Omega_E} \arcsin \left(\frac{L_{SA}}{4e \cdot r \cdot \cos \left(-\Omega_E t_p \right)} \right) = \frac{2}{\Omega_E} \arcsin \left(\frac{\lambda R}{8e \cdot r \cdot \rho_{az} \cos \left(-\Omega_E t_p \right)} \right) \quad (4.3)$$

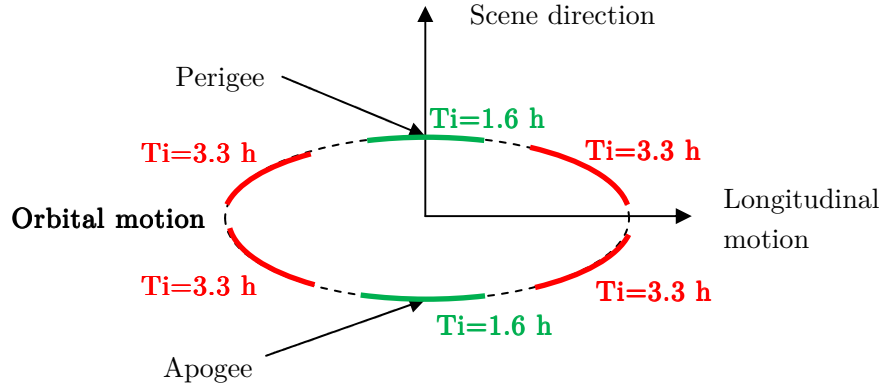


FIGURE 4.4 Constant resolution acquisitions.

So, let us consider an acquisition at C-band (5.4 GHz) with the same orbital design used all along this section (eccentricity of 0.0003). Additionally, consider a mission that requires 6 daily images, one each 4 hours, with an along track resolution of 100 meters. In this case, acquisitions centred at t_p , t_p+4h , t_p+8h , t_a , t_a+4 , t_a+8 have been taken into account. Using the equation (4.3), integration times of 1.6 h, 3.3 h, 3.3 h, 1.6 h, 3.3 h and 3.3 h are obtained for each acquisition to get the desired resolution.

The scheme of this acquisition mode is presented in Figure 4.4. As seen, in the 6 daily acquisitions, the satellite covers a similar range of longitudes obtaining a similar length of the synthetic aperture in all the cases although the integration times required in each case are not the same.

4.1.5 Continuous acquisitions with varying resolution

Finally, an opposite configuration to the one presented in the previous section can be defined. In this case, continuous images with the same integration time per image and varying resolution may be desired. This would be the case of atmospheric phase map retrieval presented in section 4.3 with rapid temporal changes that need to be continuously monitored having less importance the spatial resolution of the resultant image due to the high spatial correlation of atmospheric turbulences.

In this case, the whole daily satellite motion can be divided in several sub-acquisitions with the same integration time per sub-aperture. The resultant synthetic aperture lengths will change during the day providing images with different along-track resolutions.

As an example, the daily motion of a satellite with the same orbital parameters than in the previous cases have been divided into 48 sub-acquisitions of 30 minutes each one. A transmitted frequency of 5.4 GHz as in the previous examples has been adopted. The obtained along-track resolutions for the different sub-acquisitions are presented in Figure 4.5.

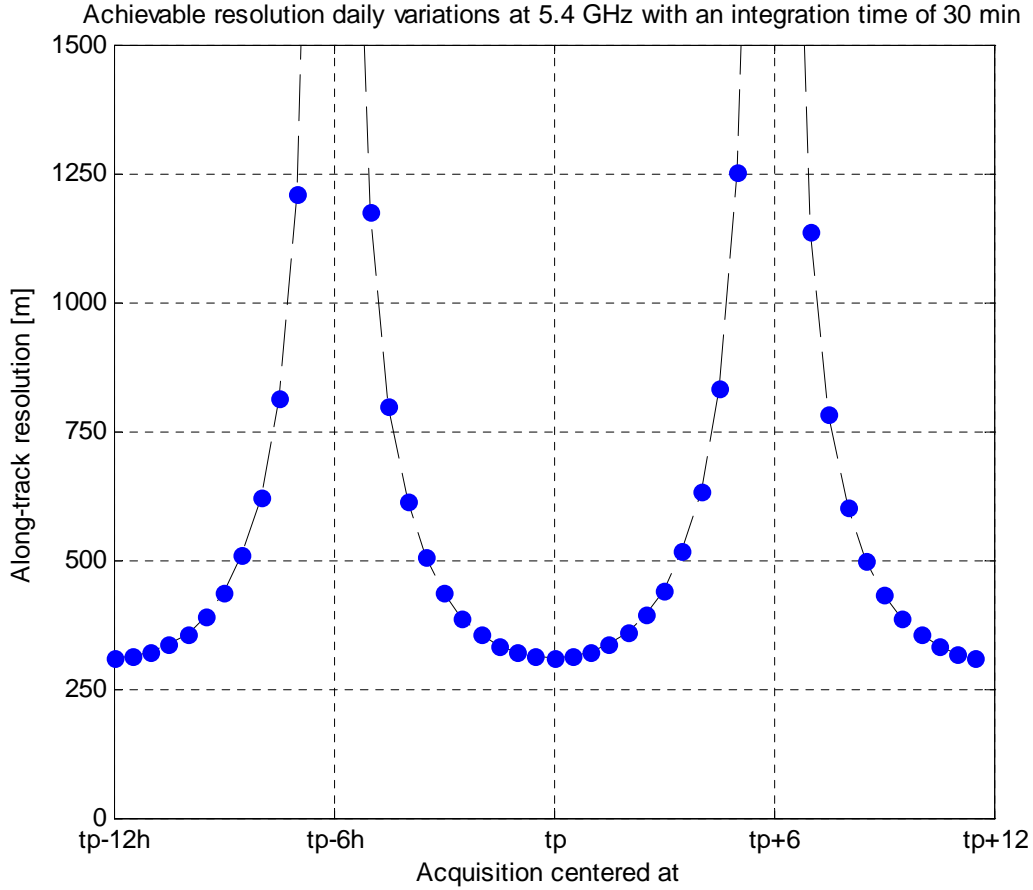


FIGURE 4.5 Daily variations of the along-track resolution considering constant integration time per sub-aperture.

As seen in this example, a maximum along-track resolution will be obtained for the sub-aperture centred at the pass through the perigee and apogee. Furthermore, if it is desired to obtain an along-track resolution better than 1500 meters (which can be enough to track the atmospheric spatial changes), there will be 6 sub-acquisitions that will not fulfil the resolution requirements in the desired integration time. These points correspond to the sub-acquisitions around $tp-6h$ and $tp+6h$ and they would be above the along track resolution limits plotted in Figure 4.5. Therefore, it will be important to define the orbital and acquisition parameters to fulfil the acquisition requirements as much as possible during most of the time.

4.2 Daily interferometric acquisitions

Ideally, daily interferograms could be obtained by a GEOSAR system if the exact orbit was repeated day after day. However, a satellite placed at geostationary orbit suffers some disturbances which affects the nominal satellite position. These displacements will result in non-desired changes on the satellite-surface slant range that can modify the signal

(amplitude and phase) received from each pixel of the image producing strong errors in the final interferograms.

4.2.1 *Geosynchronous orbit perturbations*

The primary disturbances affecting any satellite orbiting around the Earth are the luni-solar perturbations, Earth triaxiality and solar radiation pressure [87][88]. In case of geosynchronous orbits, the dominant term is the Earth triaxiality perturbation produced by the non-uniform gravitational Earth's potential in the Equatorial plane. This gravity field produces a longitudinal drift of the geosynchronous platform as shown in the left plot in Figure 4.6. The force can be obtained as the derivative of the potential function. As known from basic physics, the force satellite motion tends to go to the positions with lower potential. The potential energy curve affecting a geosynchronous satellite is given in the right plot of Figure 4.6.

From the qualitative observation of the potential energy shown in Figure 4.6, the satellite longitudinal drift can be easily predicted. Given an initial longitude where the satellite is placed without relative velocity with respect to the Earth surface, the initial kinetic energy is equal to zero and, therefore, the satellite energy is directly the potential energy of the initial point. Since all the forces in the satellite are conservative, the total energy remains constant. Then, from the initial point, the satellite starts to move towards the minimum potential location, increasing its kinetic energy. When it reaches the minimum, the kinetic energy has a maximum. From that point the kinetic energy starts to decrease, until the

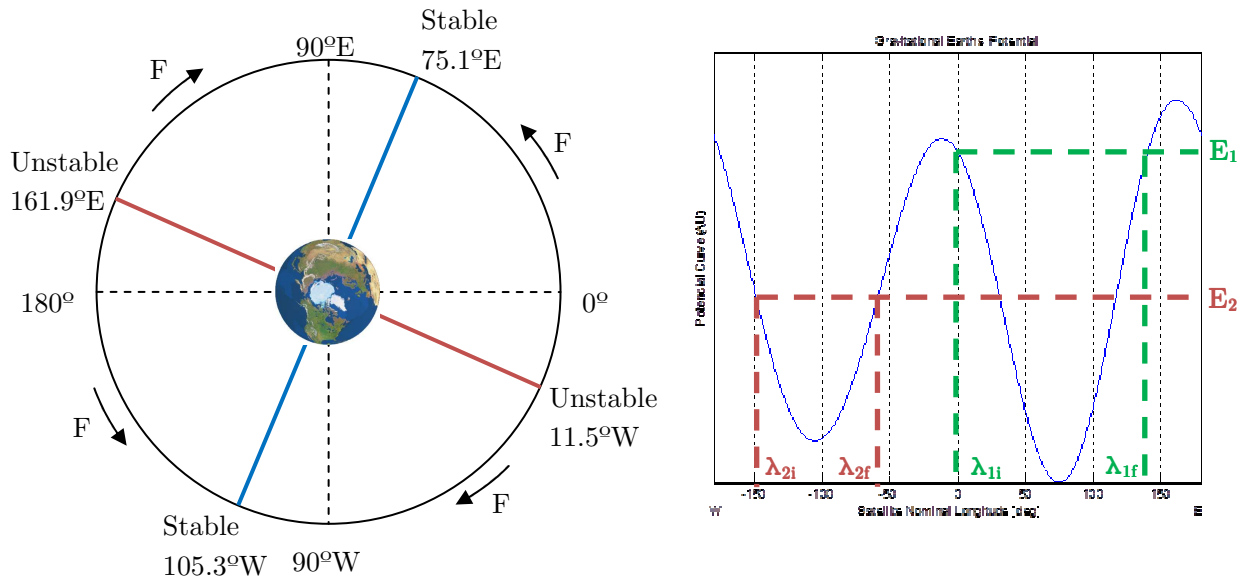


FIGURE 4.6 Earth's gravitational potential over the Equator. The satellite tends to stay at zones with lower potentials (stable regions).

platform reaches a location with the same potential than in the initial instant at the other side of the minimum potential position. This motion is periodically repeated around the minimum potential location.

Let us consider as an example two satellites with initial locations (λ_{1i} and λ_{2i} as shown in Figure 4.6) and energies E_1 and E_2 , respectively. As mention before, if the initial velocity is zero (there is no displacement of the platform with respect to the Earth surface), the energy of the satellite is equal to the initial potential. With the qualitative study shown in Figure 4.6, the angle sweep in these examples would be around 140° and 90° , respectively.

The qualitative potential curve shown in Figure 4.6 results in non-constant satellite acceleration depending on the nominal location of the satellite, as given in Table 4. So, considering the acceleration and potential curve that affects to the geosynchronous platforms, different longitude oscillation amplitudes and periods will be obtained depending on the starting position of the satellite. In Figure 4.7, the longitude shifts for three examples considering initial satellite positions at 150° West, 0° and 100° West are plotted. As seen, a satellite with nominal longitude 0° presents a periodic longitudinal drift from 0° to 141.2° while the one placed at nominal longitude -150° has a longitude variation going from -150° to -56.9° . These results are close to the qualitative description shown in Figure 4.6.

On the other hand, if a platform near the minimum potential location is considered small perturbation around the nominal position will be obtained. It is shown in the third example presented Figure 4.7 which corresponds to a satellite with nominal longitude of 100° West. Another aspect that can be appreciated in Figure 4.7 is the different longitude drift period depending on the case considered. So, large satellite longitudinal drift periods are obtained going from 4 to 6.5 years in the previous examples.

Longitude (degrees East)	Acceleration (m/s ²)	Longitude (degrees East)	Acceleration (m/s ²)
-160	$-5.30 \cdot 10^{-8}$	20	$-5.09 \cdot 10^{-8}$
-140	$-4.75 \cdot 10^{-8}$	40	$-5.73 \cdot 10^{-8}$
-120	$-2.30 \cdot 10^{-8}$	60	$-3.30 \cdot 10^{-8}$
-100	$8.10 \cdot 10^{-9}$	80	$1.17 \cdot 10^{-8}$
-80	$3.39 \cdot 10^{-8}$	100	$5.21 \cdot 10^{-8}$
-60	$4.61 \cdot 10^{-8}$	120	$6.49 \cdot 10^{-8}$
-40	$3.99 \cdot 10^{-8}$	140	$4.44 \cdot 10^{-8}$
-20	$1.48 \cdot 10^{-8}$	160	$4.08 \cdot 10^{-9}$
0	$-2.10 \cdot 10^{-8}$	180	$-3.40 \cdot 10^{-8}$

TABLE 4.1. Linear acceleration over equatorial plane depending on the satellite longitude

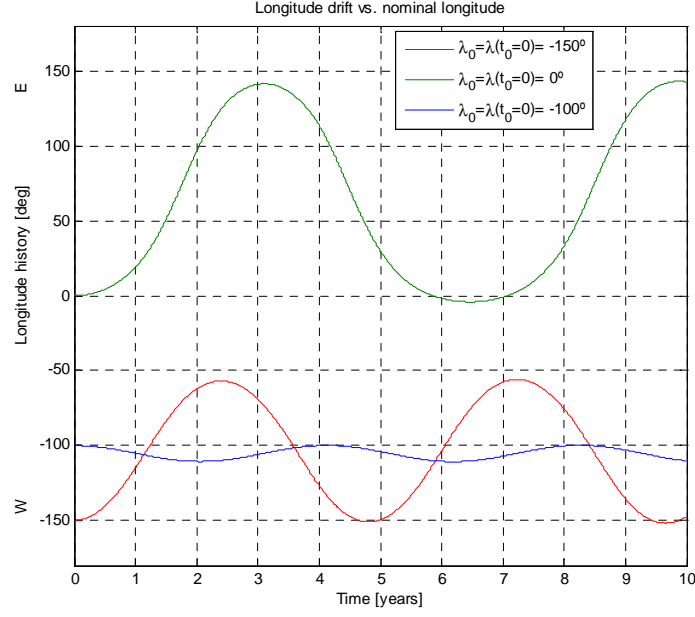


FIGURE 4.7 Longitude drift histories considering different nominal satellite longitudes.

4.2.2 Satellite longitudinal orbital drift and repositioning

As shown in Figure 4.7, longitude drifts of several degrees can be seen depending on the satellite position, which will result in a non-constant linear acceleration as presented in Table 4. However, in order to avoid large signal variations, the satellite longitude will be kept in a small satellite orbital box (longitude drifts under 1°) and, therefore, constant acceleration must be assumed. Then, the initial complex circular motion with non-constant accelerations can be simplified to a uniformly accelerated circular motion problem.

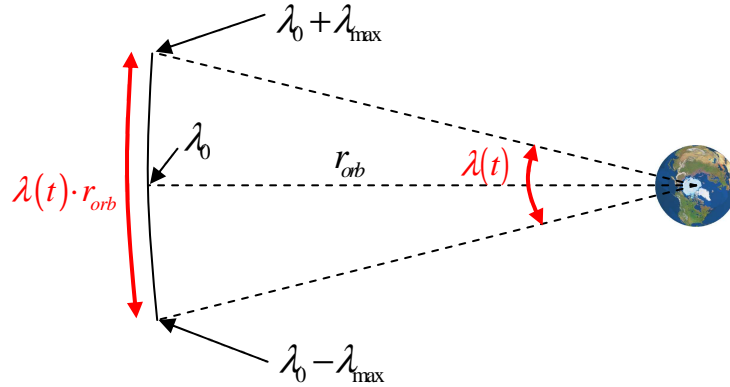


FIGURE 4.8 Orbital drift affecting a GEO platform. A maximum longitudinal drift ($\pm\lambda_{\max}$) is allowed.

Considering the orbital scheme presented in Figure 4.8, the nominal longitude history of the geosynchronous platform ($\lambda(t)$) will be constrained within an orbital box with maximum longitude deviation given by λ_{\max} . As mentioned before, since the maximum deviation will be kept under 1° to avoid high received signal variations, the acceleration that affects the orbital drift can be considered constant within the orbital box. Therefore, the longitude history can be written as:

$$\lambda(t) = \lambda_i + \omega_i(t - t_i) + \frac{\alpha(t - t_i)^2}{2} \quad (4.4)$$

where λ_i is the initial satellite location, ω_i is the initial angular velocity of the platform and α the constant angular acceleration. Besides, the angular velocity can be obtained as:

$$\omega(t) = \omega_i + \alpha(t - t_i) \quad (4.5)$$

The correspondence between the angular and linear parameters can be easily computed taking the orbital radius (r_{orb}) as:

$$\begin{aligned} x(t) &= \lambda(t) \cdot r_{orb} \\ v(t) &= \omega(t) \cdot r_{orb} \\ a(t) &= \alpha \cdot r_{orb} = ctn. = a(\lambda_0) \end{aligned} \quad (4.6)$$

As seen, the acceleration is considered constant in the whole satellite longitude drift. However, it will be strongly dependent on the nominal satellite longitude (λ_0). So, taking initially ($t_i = 0$) the satellite at one of the edges of the orbital box ($\lambda_0 - \lambda_{\max}$), without initial relative motion ($\omega_i = 0$) and considering a positive angular acceleration ($a(\lambda_0)$), the longitude drift is given by:

$$\lambda(t) = \lambda_0 - \lambda_{\max} + \cancel{\omega_i(t - t_i)} + \frac{a(t - t_i)^2}{2 \cdot r_{orb}} \quad (4.7)$$

At t_1 , the satellite reaches the other edge of the orbital box ($\lambda(t_1) = \lambda_0 + \lambda_{\max}$). Therefore, t_1 may be obtained from (4.7) as:

$$\cancel{\lambda_0} + \lambda_{\max} = \cancel{\lambda_0} - \lambda_{\max} + \frac{a(t_1)^2}{2 \cdot r_{orb}} \rightarrow t_1 = 2 \cdot \sqrt{\frac{\lambda_{\max} r_{orb}}{a(\lambda_0)}} \quad (4.8)$$

At this point, the angular velocity of the platform will be:

$$\omega_1 = \omega(t_1) = 0 + \frac{a}{r_{orb}} t_1 = 2 \cdot \sqrt{\frac{\lambda_{\max} a(\lambda_0)}{r_{orb}}} \quad (4.9)$$

In order to keep the satellite in the desired orbital box, an instant impulse (Δv) that changes the velocity must be applied at t_1 . The angular velocity after the linear impulse

will be:

$$\omega_1' = \omega_1 - \frac{\Delta v}{r_{orb}} \quad (4.10)$$

From this instant, the platform longitudinal position starts a new uniformly accelerated circular motion with initials conditions: $t_i = t_1$, $\omega_i = \omega_1'$ and $\lambda_i = \lambda_0 + \lambda_{\max}$. Then, the longitude drift is written as:

$$\lambda(t) = \lambda_0 + \lambda_{\max} + \omega_1'(t - t_1) + \frac{a(t - t_1)^2}{2 \cdot r_{orb}} \quad (4.11)$$

Equation (4.11) describes a parabolic function for the angle variation. It is necessary to find the value of ω_1' that equals the minimum of $\lambda(t)$ to $\lambda_0 - \lambda_{\max}$. If a higher impulse is set up, the platform will escape from the desired box. On the other hand, if the impulse is too low, the satellite would not reach the edge of the orbital box and, therefore, it will return to the other edge in a shorter time reducing the period between consecutive impulses. In order to find the exact value of ω_1' , the time instant (t_2) where the minimum occurs must be found:

$$\left. \frac{d\lambda}{dt} \right|_{t=t_2} = 0 \rightarrow \omega_1' + \frac{2a(t_2 - t_1)}{2 \cdot r_{orb}} = 0 \rightarrow (t_2 - t_1) = -\frac{\omega_1' r_{orb}}{a(\lambda_0)} \quad (4.12)$$

Considering the sign criteria used until now, ω_1' is negative in order to go from $\lambda_0 + \lambda_{\max}$ to $\lambda_0 - \lambda_{\max}$. Therefore, the value $(t_2 - t_1)$ is positive, as expected. As already mentioned, the minimum longitude at point t_2 must be equal to $\lambda_0 - \lambda_{\max}$. So,

$$\lambda(t_2) = \lambda_0 - \lambda_{\max} = \lambda_0 + \lambda_{\max} + \omega_1'(t_2 - t_1) + \frac{a(t_2 - t_1)^2}{2 \cdot r_{orb}} \quad (4.13)$$

Replacing $(t_2 - t_1)$ by the equation obtained in (4.12):

$$\lambda_0 - \lambda_{\max} = \lambda_0 + \lambda_{\max} + \omega_1' \left(-\frac{\omega_1' r_{orb}}{a(\lambda_0)} \right) + \frac{a \left(-\frac{\omega_1' r_{orb}}{a(\lambda_0)} \right)^2}{2 \cdot r_{orb}} \quad (4.14)$$

which leads to:

$$\omega_1' = -2 \sqrt{\frac{\lambda_{\max} a(\lambda_0)}{r_{orb}}} \quad (4.15)$$

As mentioned, the negative solution of the square root has been taken in order to counteract the positive sign of the acceleration in this example. The example for a negative

acceleration will be the same just considering the appropriate signs for each magnitude computed. From (4.15), the linear impulse obtained in (4.10) can be computed as:

$$\Delta v = r_{orb}(\omega_1 - \omega_1') = 4\sqrt{\lambda_{\max} a(\lambda_0) r_{orb}} \quad (4.16)$$

Finally, the time (t_2) when the satellite reaches the position where the first impulse was done must be computed in order to get the impulse periodicity. It can be easily found from (4.11) as:

$$\lambda(t_3) = \cancel{\lambda_0} + \cancel{\lambda_{\max}} = \cancel{\lambda_0} + \cancel{\lambda_{\max}} + \omega_1'(t_3 - t_1) + \frac{a(t_3 - t_1)^2}{2 \cdot r_{orb}} \quad (4.17)$$

The impulse period will be equal to $T = (t_3 - t_1)$. Therefore:

$$0 = \omega_1' T + \frac{aT^2}{2 \cdot r_{orb}} \rightarrow T = -\frac{\omega_1' 2r_{orb}}{a(\lambda_0)} = 4\sqrt{\frac{\lambda_{\max} r_{orb}}{a(\lambda_0)}} \quad (4.18)$$

In Figure 4.9, an example of the longitude history of a geosynchronous satellite placed at nominal longitude of 0° with a repositioning period of 102 days is presented. As seen, the maximum longitude deviation considering the repositioning is $\pm 0.16^\circ$. The repositioning period and the repositioning strength will be crucial to keep the satellite in a desired orbital box in order not to interfere with other satellite in similar positions.

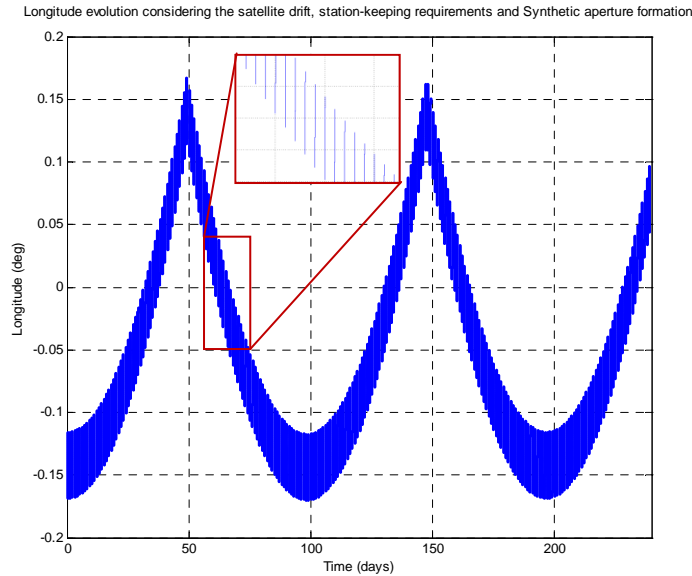


FIGURE 4.9 Longitude history of the GEOSAR satellite with nominal longitude of 0° and maxim orbital drift of $\pm 0.16^\circ$ with reposition period of 102 days.

4.2.3 *GEOSAR repeat pass interferometry*

Daily differential interferometry is one of the potential applications of a GEOSAR acquisition thanks to the shorter repeat period impossible to fulfil with current LEOSAR technology. In SAR interferometry, the phase changes between two SAR images of the same regions are compared. So, if a scatterer on ground suffers slightly changes in its relative position with respect to the satellite, the phase of the echo will shift according to the modified 2-way path. SAR interferometry is a well-studied topic in SAR [89]—[92] and it is not the purpose of this thesis to present a deep analysis of the interferometric techniques. Therefore, in the following sections, the critical baseline in GEOSAR case will be analysed and the required repositioning periods to perform daily interferometric acquisitions will be obtained.

In this analysis, we will be focused on repeat-pass interferometry [93][94]. In repeat-pass interferometry, two images acquired from two close passes of the satellite over the scene are used to generate the interferogram. In this case, the temporal and spatial correlation between both acquisitions will be crucial to get reliable information from the interferogram. So, if the time interval between the two acquisitions is too large, the temporal decorrelation will degrade the quality of the interferogram. It is the case of repeat-pass SAR interferometry from LEO satellite with a revisit time of several days. In case of GEOSAR, with a revisit time of 1 day, the temporal decorrelation between acquisitions will be lower, providing better interferometric results working with a single satellite.

On the other hand, partial frequency spectrum overlapping must be assured in order to avoid complete geometric decorrelation of two separated passes. So, the critical baseline [95] to assure cross-track partial correlation must be particularized for the GEOSAR acquisition in order to see how the orbital parameters affect to the interferometric acquisition. Additionally, the effects of longitudinal drift in along-track spectrum decorrelation need to be analysed to determine the repositioning requirements for GEOSAR repeat-pass interferometry.

So, the information on the path length between the transmitting/receiving satellite and the scene will be contained in the phase measured. However, the phase observed from each pixel of the scene ($\phi_P^{t_i}$) will be the result of the superposition of several contributions as:

$$\phi_P^{t_i} = \phi_{P,geom}^{t_i} + \phi_{P,prop}^{t_i} + \phi_{P,scat}^{t_i} \quad (4.19)$$

In equation (4.19), $\phi_{P,geom}^{t_i}$ is the phase term that arises from the geometric distance, $\phi_{P,prop}^{t_i}$ is related to the signal propagation velocity variations (related to atmospheric changes as studied in section 4.3) and $\phi_{P,scat}^{t_i}$ is the phase term related to scattering properties of the illuminated cell composed by an arbitrary number of scatterers randomly placed. The scattering phase term will be characterized by a uniform probability density function from $-\pi$ to π and, therefore, the sum of all components of (4.19) will be also

uniformly distributed. Thus, no useful information could be obtained from the direct analysis of the phase received from a single SAR image.

Thus, in repeat-pass interferometry, the phase information of two SAR images acquired at different times is subtracted which results in an interferometric phase:

$$\Delta\phi_P = \phi_P^{t_1} - \phi_P^{t_2} \quad (4.20)$$

which encompass the differential phase of the geometric component $\Delta\phi_{P,geom}$, the propagation component $\Delta\phi_{P,prop}$ and the scattering component $\Delta\phi_{P,scat}$. As mentioned before, if spectral frequency overlapping is assured by considering two orbits sufficiently close, the scattering behaviour of the two acquisitions will be similar ($\Delta\phi_{P,scat} \approx 0$). This is given by the critical baseline (section 4.2.3.1) and along-track spectrum overlapping (section 4.2.3.2). Therefore, the scattering component will be eliminated in the final phase of the interferogram. The assumption of stationary scattering component is essential for SAR interferometry. Otherwise, it will not be possible to obtain coherent phase observations if surfaces with rapid changes are considered.

Thus, a satellite placed at geostationary orbit will suffer some disturbances, which affects its nominal position as seen in section 4.2.1. For GEOSAR interferometric applications, these orbital drifts will result in non-desired changes on the received spectral band from the surface [96], which may degrade the quality of the final interferogram.

4.2.3.1 Critical baseline

In nearly-zero inclination GEOSAR acquisition, as shown in Chapter 2 orbital tracks around the equatorial plane of the Earth will be obtained. Typically, the regions of interest will be at mid-latitudes (such as European regions) and, therefore, the along-track motion required to perform the synthetic aperture will be given by the orbital eccentricity and longitudinal motion of the satellite.

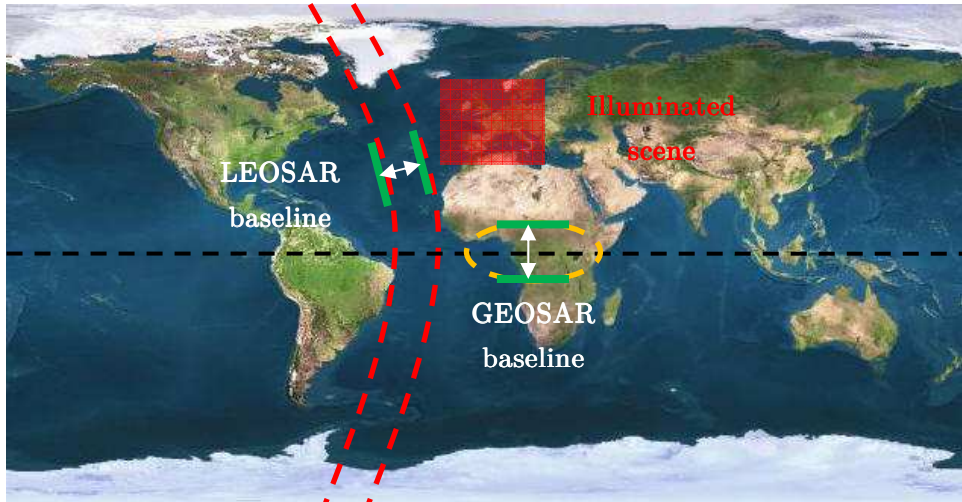


FIGURE 4.10 Typical baseline directions in LEOSAR and GEOSAR cases.

Therefore, in this GEOSAR case, the radius variations and inclination of the orbit may be seen as separate passes of the satellite above the scene which will result in a cross-track spectral shift. It would be equivalent to two passes in high-inclined LEOSAR shifted in the East-West direction. The typical baseline direction in case of LEOSAR and GEOSAR are schematically compared in Figure 4.10.

The interferometric acquisition is based on the overlapping of the part of the spectral response of the target seen from different acquisition positions. The spatial separation between both acquisitions is known as baseline of the interferometric pair. So, assuming that a radar scene is composed by a distribution of a large number of isotropic uncoupled scattering centres, the complex radar backscattered field provides information of the spatial Fourier Transform of the surface radar reflectivity. The part of the scene spectrum accessed is limited by the wavenumber vectors of illumination and backscattering. The synthetic aperture and the carrier and bandwidth of the transmitted pulses will define the angular and radial extension of the accessed spectrum which, finally, will provide the final spatial resolutions in the cross-range and range directions respectively.

Thus, in order to assure total or partial spectral overlap, the two acquisitions considered in for the interferometric image must access to the same region of the 2D spectrum. Otherwise, complete decorrelation between both images would be obtained resulting in a low-quality interferogram. The 2D Fourier transform of a scene reflectivity and the spectral overlapping of two acquisitions with signal bandwidth B_P and angular spread $\Delta\omega$ is schematically presented in Figure 4.11. In the left plot of Figure 4.11, the two acquisitions present complete decorrelation since the vectors of illumination and backscattering of the first acquisition (k_1^T and k_1^R) access to a different portion of the spectrum than the vectors of the second acquisition (k_2^T and k_2^R). On the other hand, in the right plot in Figure 4.11, the partial overlapping of the spectral access of both acquisition would make possible to perform an interferometric acquisition.

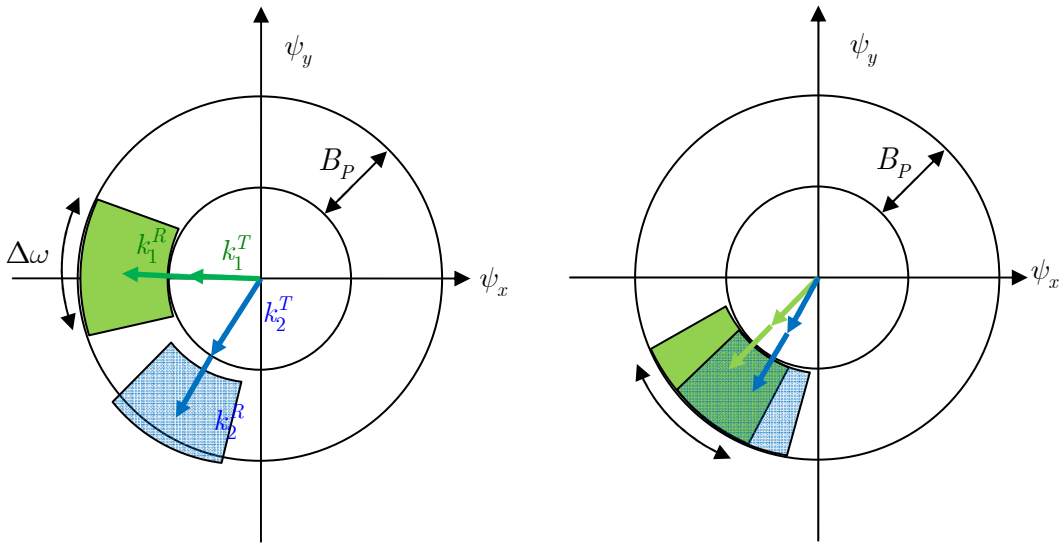


FIGURE 4.11 2D Fourier transform of reflectivity and spectral overlap for interferometry

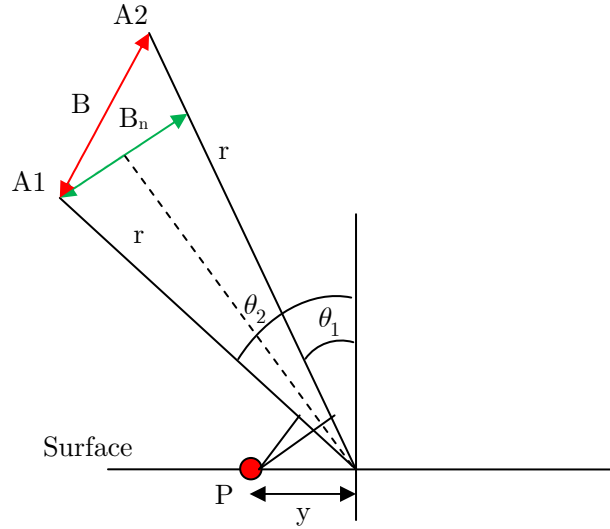


FIGURE 4.12 Interferometer imaging geometry for acquisition points A1 and A2 with total baseline (B) and baseline perpendicular to the look direction (B_n). The phase offsets of points P will be given by $y \sin \theta_1$ and $y \sin \theta_2$

Once the spectral correlation has been introduced schematically, the maximum spatial separation between acquisitions can be computed mathematically. So, the fraction of echo correlated between acquisitions may be obtained from the imaging geometry. The typical geometry for a generic SAR acquisition from two different location A1 and A2 is presented in Figure 4.12. The signals from A1 measured in the final image at position (x_0, y_0) in azimuth and ground range, respectively, from antennas A1 and A2 are:

$$s_1 = \iint f(x - x_0, y - y_0) \exp \left\{ -j \frac{4\pi}{\lambda} (r + y \sin \theta_1) \right\} W(x, y) dx dy + n_1 \quad (4.21)$$

$$s_2 = \iint f(x - x_0, y - y_0) \exp \left\{ -j \frac{4\pi}{\lambda} (r + y \sin \theta_2) \right\} W(x, y) dx dy + n_2 \quad (4.22)$$

Where $f(x, y)$ is the complex backscatter at each point, $W(x, y)$ the system impulse response and n the receiver noise. So, the cross-correlation between signals from which the interferometer phase is determined is:

$$s_1^* s_2 = \iint f(x - x_0, y - y_0) f^*(x' - x_0, y' - y_0) \exp \left\{ -j \frac{4\pi}{\lambda} y (\sin \theta_1 + \sin \theta_2) \right\} \cdot W(x, y) W^*(x', y') dx dy dx' dy' \quad (4.23)$$

In this case, the slant ranges (r) of both antennas towards the scene have been considered as equal. If they were unequal, only the mean phase of the correlation changes but not the correlation magnitude. For the surface backscattering, considering a scene with uniformly distributed and uncorrelated scattering points we can use

$$\left\langle f(x - x_0, y - y_0) f^*(x' - x_0, y' - y_0) \right\rangle = \sigma_0 \delta(x - x', y - y') \quad (4.24)$$

and (4.23) can be re-written as:

$$\left\langle s_1 s_2^* \right\rangle = \sigma_0 \int \int \exp \left\{ -j \frac{4\pi}{\lambda} y \cos \theta \delta \theta \right\} |W(x, y)|^2 dx dy \quad (4.25)$$

being θ the average look angle and $\delta \theta = \theta_1 - \theta_2$. Equation (4.25) can be interpreted as a Fourier transform relation between the correlation function and the radar system impulse response with the exponential term as the Fourier kernel. So, the correlation function is the transform of the intensity impulse response.

If a typical radar model is considered with impulse response as

$$W(x, y) = \text{sinc}(x / \rho_{az}) \text{sinc}(y / \rho_{gr}) \quad (4.26)$$

being ρ_{az} and ρ_{gr} the azimuth and ground range respectively, the solution of equation (4.25) results in a spatial correlation ($\rho_{spatial}$) as:

$$\rho_{spatial} = 1 - \frac{2 \cos \theta |\delta \theta| \rho_{gr}}{\lambda} \quad (4.27)$$

Additionally, considering the slant range (r) to the satellites and the angular separation between them ($\delta \theta$), the baseline in meters perpendicular to the look direction in the satellite can be obtained as $B_n = r \delta \theta$. So, the spatial correlation will be:

$$\rho_{spatial} = 1 - \frac{2 \cos \theta B_n \rho_{gr}}{\lambda r} \quad (4.28)$$

So, the critical baseline in the normal direction ($B_{n,c}$) will correspond to the satellites separation that results in null spatial correlation:

$$\rho_{spatial} = 1 - \frac{2 \cos \theta B_{n,c} \rho_{gr}}{\lambda r} = 0 \rightarrow B_{n,c} = \frac{\lambda r}{2 \cos \theta \rho_{gr}} \quad (4.29)$$

Finally, the critical baseline can be put in terms of slant range resolution (ρ_c) and considering a local terrain slope (α) as [97]:

$$B_{nc} = \left| \frac{\lambda R \tan(\theta - \alpha)}{2 \rho_c} \right| \quad (4.30)$$

So, B_{nc} corresponds to the critical baseline projected normal to the look direction. In case of GEOSAR, as shown in Figure 4.13, the latitudinal motion of the satellite is nearly perpendicular to the look direction due to the long satellite-Earth's distance which results in small look angles ($\theta_{\max} < 9^\circ$) and, therefore, the radius variations ($2 \cdot ea$) may be

neglected in the critical baseline computations. So, the maximum baseline normal to the look direction in a GEOSAR acquisition can be approximated by:

$$B_{n,\max} \approx 2i \bar{r} \quad (4.31)$$

where \bar{r} is the mean radius of the orbit. Combining (4.30) and (4.31), the maximum inclination of the orbital plane that assures a baseline shorter than the critical one can be computed as:

$$i_{\max} = \frac{\lambda R}{4\rho_c \bar{r}} \tan \theta_0 \quad (4.32)$$

Just as an example, taking $\lambda = 0.017m$, $R = 37000Km$, $\rho_c = 20m$ and $\theta_0 = 50^\circ$, a maximum inclination of $1.27 \cdot 10^3$ degrees should be taken in order to have a baseline under 10% of the critical one along the daily motion. If this requirement is fulfilled, two interferometric acquisitions per day could be performed by taking the satellite passes at the same range of longitudes but with different latitude guarantying partial cross-track spectral overlapping.

These values may be difficult to set up in a real situation, where typical values of inclinations in geosynchronous platforms are, at least, 0.001 degrees. A possible solution to that problem is to consider a bistatic system with two satellites in a proper formation in order to assure an equivalent monostatic acquisition with zero inclination. It will be studied in detail in Chapter 5. In the following section, the longitudinal drifts effects on the along-track spectrum overlapping for acquisition taken in consecutive days are analysed. In that case, an inclination equal to zero has been considered in order to assure cross-track spectral overlapping from any orbital position of the daily motion.

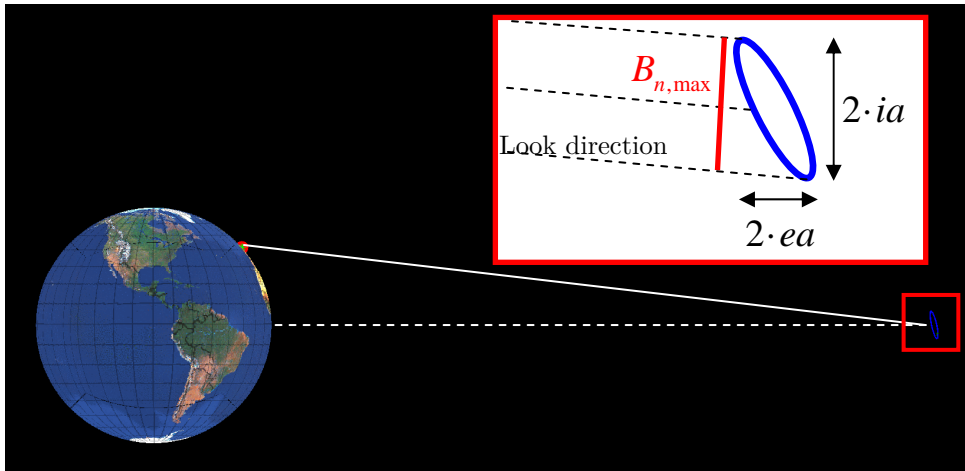


FIGURE 4.13 Critical baseline in GEOSAR acquisition considering the latitudinal satellite motion.

4.2.3.2 Longitudinal drifts effects on GEOSAR interferometry

On the other hand, the satellite orbital drifts that modify the nominal longitude must be taken into account in the along-track spectral shift besides the typical longitudinal motion. In the analysis of the along-track spectral shift, a non-inclined orbit has been considered. In order to assure that two images taken at different days are not completely decorrelated, the satellite longitude of both acquisitions must be partially coincident.

As explained in section 4.2.2, a uniform acceleration affecting the satellite can be considered since the longitude station-keeping will preserve the platform in a small orbital box of a few tenths of a degree in longitude while the acceleration changes with longitude are smoother [98]. As explained in section 4.2.2, the longitudinal drift may be obtained from the analysis of a uniformly accelerated circular motion. It is given by:

$$\Delta\lambda(t) = \frac{acc(\lambda_0)}{2\bar{r}}(t - t_0)^2 \quad (4.33)$$

Combining the daily motion of a geosynchronous satellite with no inclination (given by equation (2.23)) and the longitudinal drift given by (4.33), the longitude of the satellite will be:

$$\lambda_{SL}(t) = \lambda_0 + 2e \sin(\Omega_E(t - t_p)) + \frac{acc(\lambda_0)}{2\bar{r}}(t - t_0)^2 \quad (4.34)$$

Additionally, from the resolution requirement studied in section 2.4.2.2, the longitude shift of the satellite necessary to reach the desired along track resolution can be obtained as:

$$\lambda_{SA} = \frac{1}{2} \frac{\lambda}{\bar{r} \rho_a} R \quad (4.35)$$

In Figure 4.14, the daily longitude history of a geosynchronous satellite with initial nominal longitude of 0° , affected by a constant acceleration of $-2.1 \cdot 10^8 \text{ m/s}^2$, is plotted. An orbital eccentricity of $5 \cdot 10^{-4}$ has been considered in this example. Additionally, the necessary longitude shift (λ_{SA}) to obtain a resolution of 20 meters has been superimposed in red. As seen, the along-track spectral overlapping can be assured by taking one edge of the whole longitude history at day one and considering different parts of the daily motion in the following days until the other edge is reached. In Figure 4.14, the same range of longitudes could be preserved during 29 days of acquisition.

Therefore, the longitude station-keeping will be essential in order to keep the satellite in the desired orbital box to preserve the along-track spectrum overlapping for interferometric purposes. From Figure 4.14, the maximum satellite longitude drift $\Delta\lambda_{0,\max}$ (in radians) to avoid along-track spectral decorrelation is obtained as:

$$\Delta\lambda_{0,\max} = 4e - \lambda_{SA} = 4e - \frac{1}{2} \frac{\lambda}{\bar{r}\rho_a} R \quad (4.36)$$

From (4.33) and (4.36), the impulse strength and the periodicity obtained in equations (4.16) and (4.18) can be found again. If the parameters used in the example of Figure 4.14 are considered, a maximum longitudinal drift of 0.09 degrees is obtained by using (4.36). These results lead to a re-positioning period of 29 days taking equation (4.18) which is consistent with the simulated results shown in Figure 4.14.

As already mentioned, the longitude keeping requirements will change depending on the satellite nominal longitude (acceleration variations with satellite location), the resolution cell size considered (angular spread λ_{SA} required to reach the desired along track resolution) and orbital configuration. In Table 4.2, the re-positioning period and the maximum orbital drift obtained for different satellite nominal longitudes and eccentricities to get a 20 meters along-track resolution are summarized.

Satellite repositioning based on SAR coherence preservation allows an optimum usage of the available fuel. On the other hand, a two satellites constellation [99] could be considered. In this case, higher spectral superposition would be obtained offering more design flexibility.

On the other hand, the effects of the Atmospheric Phase Screen in differential interferometry should be considered. In section 4.3, the APS is studied and an algorithm to retrieve and compensate it from the raw data is presented. The residual phase error should be considered in the interferogram as an additional source of noise.

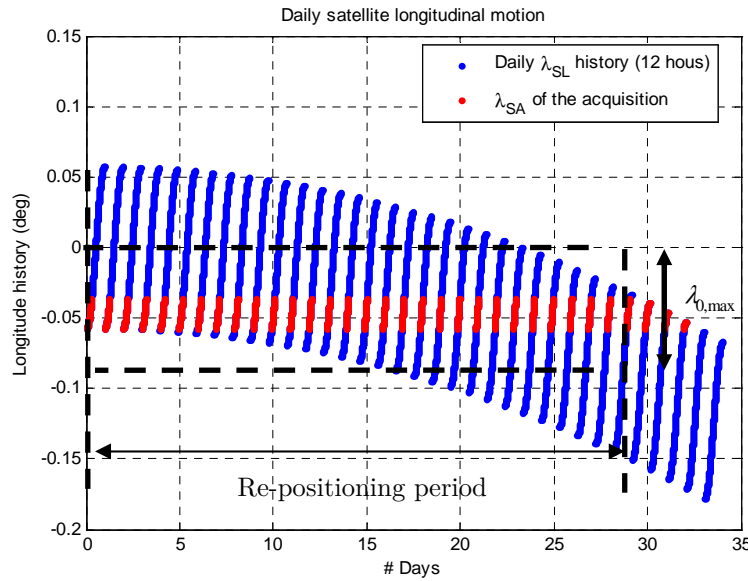


FIGURE 4.14 Typical longitude/latitude satellite histories considering an eccentricity of 0.0005 and inclination equal to 0° . The longitude drift caused by the Earth's gravitational potential displaces the elliptical track towards the East.

Satellite nominal longitude (deg)	Re-positioning period (days) to get 20 m resolution interferogram		
	Orbit eccentricity		
	0.0001	0.0005	0.001
180 °W	2	23	34
140 °W	2	19	29
100 °W	5	47	71
60 °W	2	19	29
20 °W	3	35	52
0	3	29	44
20 °E	2	19	28
60 °E	2	23	35
100 °E	2	18	28
140 °E	2	20	30
$\lambda_{\text{orb}}(\text{degrees})$	0.001	0.093	0.207

TABLE 4.2. Station-keeping requirements considering different nominal longitudes and resolution cell sizes to keep the satellite in the desired orbital box for interferometric purposes.

4.3 Atmospheric Phase Screen (APS) retrieval

4.3.1 APS behaviour and effects to SAR acquisition

The spatial distribution of water vapour in the atmosphere is an important parameter in meteorology and forecasting. The local concentrations of water vapour may vary significantly from 0 to 4% depending on the atmospheric conditions. Nowadays, ground-based and upper air sounding networks are being used to track the water vapour distribution but with an important limitation on the spatial coverage and resolution. The spatial variations in atmospheric moisture and temperature are commonly on a 1 km scale, impossible to track with ground acquisitions.

On the other hand, interferometric SAR acquisition from LEO satellites may provide wide coverage atmospheric maps with resolution of 10-20 meters (more than enough to track the spatial behaviour of atmospheric map) but with another limiting factor which is the temporal revisit time. So, revisit times of at least 1 day using a dense LEO constellation are achieved which are too large for retrieving the rapid changes of the atmospheric phase map in the order of minutes.

Therefore, GEOSAR is an interesting alternative to overcome the spatial and temporal problems of current technology for atmospheric sounding. So, from a geosynchronous satellite, continuous phase maps (20-30 minutes) with a spatial resolution of 500-1000 meters could be obtained.

In SAR acquisition, particularly in interferometry, the Atmospheric Phase Screen (APS) will be an undesired artefact that will affect to target phase estimation. Additionally, in GEOSAR acquisition, the atmospheric phase decorrelation during long integration times (several hours) has to be characterized and compensated from the acquired raw data to avoid undesired artefacts on the final image.

As mentioned in section 4.2, the phase received from a resolution cell in the scene will be composed of three components. So, apart from the scattering phase particular of each resolution cell and the phase corresponding to the geometric distance, an extra term related to signal propagation velocity variations must be considered. These velocity variations arise from the changes in the refraction index on the different atmospheric layers which results in signal path bending. The changes of velocity and the effects on the received phase from the cell may be seen as an extra path on the signal geometric distance.

The atmospheric contribution on the propagation phase delay will arise from two different layers of the atmosphere: the tropospheric and ionospheric delays. The troposphere corresponds to the lower part of the atmosphere and it is destabilized due to the irradiative heating and by vertical wind shear near the Earth surface. So, the irradiative heating will result in vertical convective motion while the vertical wind shear will results in horizontal instabilities. The water vapour distribution will be the dominant term affecting the signal propagation in the tropospheric layer. Unlike the troposphere, other atmospheric layers are water vapour free and, therefore, the major contribution of the signal delay will come from the troposphere. The effect in signal propagation of the free electron charges present in the ionosphere will be also introduced in this section.

4.3.1.1 Tropospheric phase delay

The troposphere is defined as the lower layer of the atmosphere where the temperature decrease with height since it is heated by surface heat radiation. This includes the range of heights from the surface to the tropopause, being around 17 km high at equator and 9 km high at poles.

The changes in temperature, pressure and water vapour content will modify the refractive index which will characterise the propagation of electromagnetic waves through this layer. So, the actual geometrical distance between the transmitter and the illuminated surface will not be equal than the optical path that will follow the electromagnetic wave. The difference between the geometrical distance and the optical path may be computed from the refractive index as:

$$\delta R_{Trop} = \int_{atm} n(s) ds - \int_{vacuum} 1 \cdot ds \quad (4.37)$$

where $n(s)$ corresponds to the refraction index of the different atmospheric layers along the signal path s . The second term of the equation (4.37) stands for the signal propagation across the vacuum which will correspond to the virtual path of the transmitted signal in absence of atmospheric deviations. It is usual to work with the non-dimensional parameter N obtained from the refractive index as:

$$N = (n - 1) \cdot 10^{-6} \quad (4.38)$$

The refractivity N can be written in terms of other atmospheric parameters as [114]:

$$N_{Trop} = k_1 \frac{P_d}{T} + \left(k_2 \frac{e}{T} + k_3 \frac{e}{T^2} \right) \quad (4.39)$$

where P_d is the partial pressure of dry air in hPa, e is the partial pressure of water vapour in hPa and T is the absolute temperature in Kelvin. k_1 , k_2 and k_3 are constants determined from experimental analysis [115] with values $k_1 = 77.6 \text{ K hPa}^{-1}$, $k_2 = 71.6 \text{ K hPa}^{-1}$ and $k_3 = 3.75 \cdot 10^5 \text{ K}^2 \text{ hPa}^{-1}$. The first term on the right side of (4.39) is usually known as *dry term* while the following two terms in brackets are known as *wet terms*.

Alternatively, the refractivity may be written in terms of the total atmospheric pressure ($P = P_d + e$) as [116]:

$$N_{Trop} = k_1 \frac{P}{T} + \left(k_2' \frac{e}{T} + k_3 \frac{e}{T^2} \right) \quad (4.40)$$

with

$$k_2' = k_2 - \frac{R_d}{R_v} k_1 \quad (4.41)$$

being $R_d = 287.053 \text{ J K}^{-1} \text{ Kg}^{-1}$ and $R_v = 461.524 \text{ J K}^{-1} \text{ Kg}^{-1}$. The first term in the right side of equation (4.40) is known as *hydrostatic term*. The hydrostatic delay related to this term can be obtained from the surface pressure (P_s):

$$\delta R_{hydrostatic} = k_1 \cdot 10^{-6} \frac{R_d}{g_m} P_s \quad (4.42)$$

with g_m the local gravity. The spatial scale of pressure variations will be of hundreds of km and, therefore, the hydrostatic term will be a common phase delay equal in all the points of the image. For larger scenes (thousands of kilometres) the hydrostatic term may be predicted and compensated by spatially distributed surface pressure measurements. Therefore, the image phase changes due to atmospheric variations will be given, majorly, by the changes on the wet part of the refractivity.

Assuming that the hydrostatic term can be compensated, let us study the wet component of the

tropospheric refractivity index. So, taking the part in brackets of equation (4.40), the wet tropospheric part sensitivity to changes in temperature and water vapour content can be obtained from their partial derivatives as:

$$\left. \frac{\partial N_{wet}}{\partial T} \right|_{e=ctn} = -\frac{k_2' e}{T^2} - \frac{2k_3 e}{T^3} \quad (4.43)$$

$$\left. \frac{\partial N_{wet}}{\partial e} \right|_{T=ctn} = \frac{k_2'}{T} + \frac{k_3}{T} \quad (4.44)$$

As it can be seen, an increase of temperature results in a decrease of the refractivity index which yields a relative increase in the propagation velocity. On the other hand, an increase on the water vapour pressure will mean a relative decrease in the propagation velocity. If the sensitivity of N_{wet} for 1 hPa change in partial pressure of water vapour is compared with the sensitivity to 1°C change in temperature, the obtained ratio

$$R = \frac{\partial N_{wet}}{\partial e} \bigg/ \frac{\partial N_{wet}}{\partial T}$$

is plotted in Figure 4.15. In the range of selected temperatures and water vapour partial pressure $|R| > 1$ which means that the refractivity is R times more sensitive to 1hPa change in water pressure than to a 1°C change in temperature. Furthermore, typically $4 < |R| < 20$ except for very dry air with partial pressure of water vapour under 5 hPa.

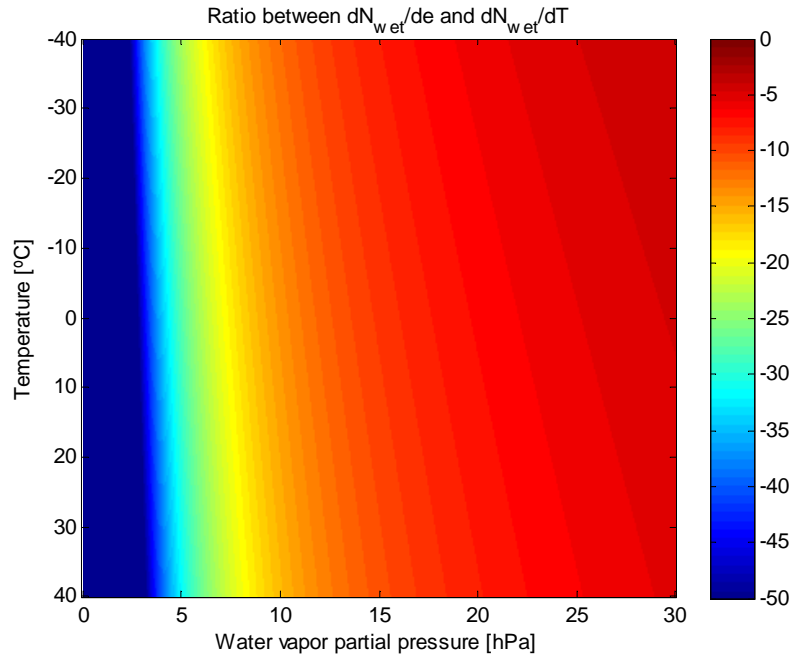


FIGURE 4.15 Sensitivity ratio of the refraction index with respect to water vapour partial pressure vs. temperature.

Therefore, the wet part of the tropospheric refractivity will be at least 4 to 20 times more sensitive to change of 1 hPa in water vapour pressure than of 1°C in temperature. Furthermore, moisture variations of 1 g/kg (equivalent to 1.2 hPa) are common in a 1 km spatial scale. So, relative phase delay differences between cells in a wide coverage image may be appreciated and, for this reason, the wet part of the tropospheric refractivity and, particularly, the variations on the water vapour partial pressure will be one of the critical parts of the atmospheric dynamics to study and retrieve to assure the correct performance of a GEOSAR long integration acquisition.

Additionally, the impact of liquid water on troposphere should be also considered. The effects of liquid water (droplets) in saturated air and clouds are often neglected since they only contribute in a small part of the total wet delay. However, for interferometric observation where relative differences between cells of the scene are computed, the impact of liquid water may be important.

The interaction of the electromagnetic signal with a droplet may be seen as a forward scattering problem where the principal wave front will interfere with the secondary front coming from the interaction of the incoming signal with the droplet. The liquid water content (W) of clouds is defined as particle number density times the volume per particle times the density of liquid water. This is related with the refractivity index by the Clausius-Mossotti equation [117]:

$$N_{liquid} = \frac{3}{2} \frac{W}{\rho_W} \frac{\varepsilon_0 - 1}{\varepsilon_0 + 2} \approx 1.45W \quad (4.45)$$

with ρ_W the density of liquid water and ε_0 the permittivity of water. It is important to note that droplets will only be present in saturated air mass, and therefore the water vapour concentration will be high. For this reason, the delays observed in the phase induced by the troposphere will come basically from water vapour [118].

To sum up, the theoretical analysis of tropospheric layer shows that the sensitivity of the refractivity is highest for spatial variations in water vapour content with spatial scale around 1 km. Nevertheless, the temperature effects and liquid water in troposphere cannot be ignored since they may result in deviations in the quantitative analysis of the delays.

4.3.1.2 Ionospheric phase delay

As mentioned before, the ionospheric delay will be related with the electron content. So, the refractivity of the ionospheric layer can be obtained as [119]:

$$N_{iono} = -4.028 \cdot 10^7 \frac{n_e}{f^2} \quad (4.46)$$

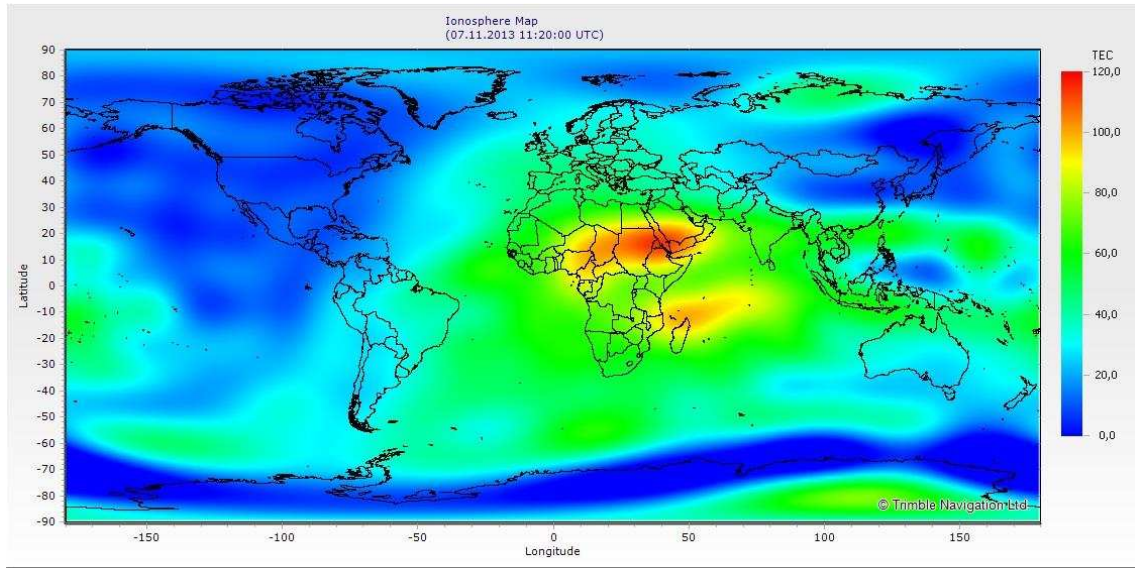


FIGURE 4.16 TEC world map estimated by GPS measurements.

being n_e the electron density per cubic meter and f the radar frequency. The ionospheric impact on the zenith range error can be formulated as:

$$\delta R_{iono} = \frac{K}{f^2} TEC \quad (4.47)$$

where TEC is the Total Electron Content. The factor $K = -40.28 \text{ m}^3 \text{ s}^2$. The TEC values may vary between 0 m^{-2} at night to $20 \cdot 10^{16} \text{ m}^{-2}$ at the minimum of the solar cycle to $100 \cdot 10^{16} \text{ m}^{-2}$ at the solar maximum. So, the ionospheric delays will present strong spatial correlation since the electron content on the atmosphere will vary very slowly in space as shown in Figure 4.16. On the other hand, the daily and seasonal variations on the TEC in the ionosphere may be important. However, permanent information of TEC constant is available from GPS measurements and, therefore, the large scale changes on the ionospheric layer may be estimated for long integration GEOSAR acquisitions. The major problem will come from the small scale turbulent scintillations. Both components are analysed next.

The effects of ionospheric layer may be classified into two different basic types [100]. First of all, there is a stable background that produces phase advance, group delay and Faraday rotation in most of the SAR acquisitions. These effects can be mostly reduced by suitable modelling of background ionosphere used in SAR processing [101] or via polarimetric acquisition measuring the Faraday rotation [102][103].

On the other hand, we may consider the effects introduced by small scale ionospheric structure, which results in scintillation in the signal and spatially varying phase delay patterns [100]. Therefore, if large scenes are considered, these small scale ionospheric changes can cause distortions in the SAR image. This kind of small scale ionospheric irregularities is more relevant around equatorial and polar zones which will not be the

major interest in GEOSAR design considered in this thesis at mid-latitudes. However, the possible impact that could have in the image will be studied in any case.

Thus, depending on the spatial-temporal correlation of the ionospheric effects on signal phase we can consider four possibilities: large scale spatial and temporal correlation, large scale spatial short temporal correlation, small scale spatial long temporal correlation and small scale spatial short temporal correlation. The effects and possibilities to track their behaviour and reduce their impact are presented next.

a) Large scale spatial and temporal correlation of ionospheric artefacts

Let us consider first the large spatial scale and long temporal correlation effects produced by the ionospheric layer. For long temporal correlation we mean that it can be considered stable during the acquisition. This large scale spatial evolution is currently continuously monitored and modelled from GNSS observations (TEC monitoring [104]) and therefore can be compensated from the received signals. The ionospheric behaviour can be also obtained via polarimetric acquisitions, measuring the Faraday rotation, so it could be considered as a future alternative for a polarimetric GEOSAR acquisition. It has been found recently that TEC maps can be also derived from L-Band radiometric-polarimetric observations provided by the SMOS mission [105].

b) Large scale spatial short temporal correlation of ionospheric artefacts

In case of having faster temporal changes in the ionospheric phase map, we can not assure the correct focusing of the images for large integration times. However, if the ionospheric map is still spatially correlated along the image, we may retrieve the temporal evolution of the ionosphere phase map from periodic calibration steps (each few seconds) recovering the phase information from the ground control points with high SNR thanks to the large RCS of the active calibrators considered. Particular attention must be taken in the distribution of the calibrators since, due to the short integration time considered for calibration (around 1 second) the image will have coarse azimuth resolution (the range focusing is not affected by integration time). Therefore, in order to avoid phase interferences coming from two calibrators at the same range and different azimuth cells, all calibrators should be placed in different range cells.

c) Small scale spatial and long temporal correlation of ionospheric artefacts

On the other hand, if the temporal correlation is on the order of the integration time or larger, no substantial defocusing is expected. In this way, we may extract the spatial pattern of the ionospheric layer observing the phase changes between the different stable

targets (ground control points, cities, etc.) distributed along the image. So, the spatial correlation in this case should be on the order of the separation between ground control points or other stable targets (10-20 Km) in order to make possible to extract the ionospheric spatial information.

d) Small scale spatial and short temporal correlation of ionospheric artefacts

Finally, the small spatial scale changes with a temporal correlation shorter than the integration time will cause image defocusing and it will not be possible to track them with a GEOSAR acquisition, except at active calibrator locations, since the phase information will vary all along the image and the spatial resolution obtained with short integration times will not be enough to track the ionospheric artefacts behaviour. Therefore, this will cause a residual phase error that must be studied in order to determine its impact on the final image quality.

Current literature in ionospheric behaviour [100][106][107] concludes that the most important effects on mid-latitudes will come from the ionospheric background with large spatial and temporal correlation and, therefore, its impact can be compensated via model predictions. The observations during years have shown a seasonal variation of TEC besides the diurnal variation of TEC [108]. So, the daily variations of TEC shows a steady increase from sunrise to afternoon where a maximum in TEC is obtained. Then, a gradual decrease after sunset is observed. Regarding the seasonal variations of TEC, higher values are observed in equinoctial months while the TEC daily variations are similar in summer and winter. Additionally, the solar activity and particular space weather events may change the TEC of the ionosphere [108].

On the other hand, the smaller component due to ionospheric scintillation will have a small impact in GEOSAR acquisition, with temporal phase errors with $\sigma < 0.15$ rad [106]. Typical autocorrelation values of ionospheric variations span from 10 to 100 Km (spatial) and from 1 to 10 minutes (temporal) for low latitudes. In case of mid-latitudes, which are the target of the system studied, higher correlations are expected but it needs to be studied in depth in order to determine the ionospheric impact on the final GEOSAR images. The occurrence of ionospheric scintillations has been studied in [109] for low-latitudes. In this case, a seasonal behaviour of the mean occurrence may be observed. So, the maximum occurrence is around 30% for months of February, March and April. On the other hand, the mean occurrence during the rest of the year is mostly under 15%. Thus, the occurrence of scintillation in mid-latitudes will be below these values. The different ionospheric effects and their possible corrections are summarized in Table 4.3.

After analysing the impact of tropospheric and ionospheric delays on the received signals, we may conclude that the important part to be assessed in a long term GEOSAR acquisition will be related to the wet delay on tropospheric layer and, concretely, to the water vapour partial pressure variations. This phenomenon will have a spatial scale

variation on the order of 1 km while rapid temporal variations (20-30 minutes) are expected. The temperature variations must add a daily slow variation in phase delay but it will be a second order term as demonstrated by the sensitivity analysis of section 4.3.1.1. Regarding the ionospheric delay, it may be ignored since it present larger spatial scales and it can be compensated by using the information from GPS measurements.

In the following sections, two techniques to retrieve the Atmospheric Phase Screen (APS) behaviour from continuous monitoring of a GEOSAR acquisition are presented. The first one is based in auto-focusing techniques and the atmospheric behaviour is obtained from the study of phase variations received from expected stable targets. On the other hand, the second technique is based on repeat-pass interferometry with a constellation of geosynchronous satellites.

4.3.2 APS retrieval algorithm for point-like targets: auto-focusing technique

A GEOSAR acquisition with integration time of several hours will be affected by the Atmospheric Phase Screen (APS) decorrelation. Here, an algorithm to retrieve the phase map directly from the long term raw data matrix is presented.

Ionospheric correlation		Effect	Phase perturbations	Frequency of occurrence	Corrected via
Spatial	Temporal				
>100 Km	~ hours	Ionospheric background	Smooth phase term applicable to the whole image	Continuous	Models based on GPS or polarimetric acquisitions
>100 Km	~ minutes	Azimuth defocusing of long integration SAR images	Temporal phase std. dev.: $\sigma < 0.15$ rad [106]	Daily variations (seasonal trends)	Periodic calibration data from ground control points
10-20 Km	~ hours	Spatial phase variations within the image	Spatial Variations	$<< 30\%$	Spatial phase maps obtained from focused images
10-20 Km	~ minute	Defocusing + spatial differences on the received signals	Spatial variations + temporal phase std: $\sigma < 0.15$ rad [106]	$<< 30\%$	Not possible. Except at ARC locations Residual phase error

TABLE 4.3. Ionospheric artefacts on long integration SAR images.

In this analysis, a statistical behaviour of the phase errors induced by the APS has been considered assuming a temporal stability of 10-20 minutes and spatial stability of 1-2 km. Additionally, the variograms from the statistical analysis of the atmosphere show a standard deviation of the difference in the atmospheric phase delay ranging from 2 to 11 mm [111]. Therefore, continuous low-resolution images are necessary to track the atmospheric phase variations.

4.3.2.1 Algorithm description

In this section, the algorithm proposed to retrieve the APS behaviour from a long integration GEOSAR acquisition is presented. The GEOSAR system studied all along this thesis is conceived to get medium resolution images (10-20 meters) with integration times of several hours. As seen before, these long integration times do not fit with the low temporal correlation of APS which needs to be constantly monitored. To compensate the rapid atmospheric phase changes we introduce a new focusing scheme that integrates atmospheric phase screen estimation in the kernel.

In Figure 4.17, the algorithm proposed is schematically summarized. The methodology proposed in this paper consists of dividing the long integration GEOSAR synthetic aperture in sub-apertures (sub-matrices of the raw data matrix) with integration time in the order of the temporal decorrelation of the APS (minutes). Therefore, a set of low along-track resolution images with temporal lapse of a few minutes is obtained.

From each image, the phase history of a set of known point-scatterers with large Signal-to-Clutter ratio may be retrieved. These scatterers should ideally present constant phase over time. Therefore, the phase variations observed from image to image can be directly related to undesired effects, mostly from the atmospheric phase delay. Therefore, the APS retrieval will be valid over scenes where many stable point targets are found in the APS space resolution cell like urban, periurban or rocky areas.

At this point, the phase information of a set of randomly located targets with low temporal resolution (one sample per sub-aperture) is obtained. Consequently, temporal and 2-D cubic interpolations are performed to have spatial-temporal continuous APS information. The quality of the retrieved APS can be evaluated in terms of the target density and the target quality, intended as the ratio between signal and total thermal plus clutter noise, as shown in [110].

Once the APS behaviour is obtained, it may be used for GEOSAR long integration raw data compensation to reduce the defocusing artefacts obtaining a medium resolution image. Furthermore, it may be a final product giving a set of low-resolution images for atmospheric sounding and meteorological applications.

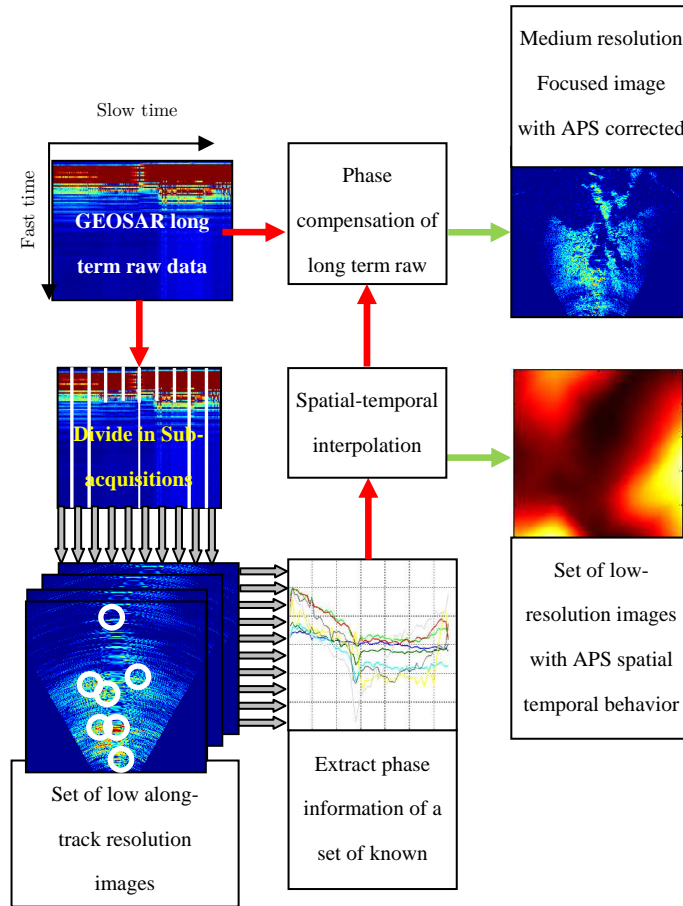


FIGURE 4.17 APS retrieval from sub-matrices of a long integration GEOSAR acquisition.

The phase information obtained from the low-resolution images is used to compensate the long term GEOSAR data and may be valuable information for meteorological applications or other phase sensitive systems

In order to check the performance of the APS retrieval algorithm presented in Figure 4.17 for a particular set of atmospheric conditions, the raw data from a long integration GEOSAR acquisition (4 hours) has been simulated. In this example, a satellite with orbital eccentricity of 0.0005 illuminating a scene of 10 by 10 km has been considered. An additional random phase term modelling the spatial-temporal APS changes has been added to the reflectivity of the terrain. In this case, an exponential temporal and spatial correlation with correlation factors of 30 minutes and 1 km have been considered.

Two different simulations with different stable target densities in the scene have been considered. In the first one, 25 targets in a regular grid spaced 2 by 2 km have been taken. On the other hand, 100 targets spaced 1 by 1 km have been considered in the second scenario. The whole long integration acquisition has been divided in 24 sub-apertures with

an integration time per sub-aperture of 10 minutes, shorter than the temporal coherence of the APS simulated. The phase histories of the targets have been retrieved from each low-resolution image and the atmospheric phase map of the whole acquisition over the scene has been obtained by spatial-temporal interpolation from these points.

Figure 4.18 shows the results obtained in these two scenarios. For each case, two different time instants of the acquisition after focusing and interpolation with different APS spatial distribution have been selected. For the most spatially correlated APS case (first and third rows of Figure 4.18), both simulations offer a good APS estimation, with a residual error with standard deviation under 26.87 degrees and 7.92 degrees, respectively. On the other hand, for the APS with higher spatial variations (second and fourth rows in Figure 4.18), the first case with the stable targets each 2 by 2 Km shows a poor estimation while in the case of a denser grid of stable points, the estimation is still quite good with a standard deviation of the residual error of 15.9 degrees. Therefore, the importance of having a dense grid of stable targets (1 per km approximately in the previous example) has been shown.

As mentioned before, the phase information may be used for raw data compensation in long integration GEOSAR acquisition. In Figure 4.19, the focused images considering the whole GEOSAR simulated raw data (4 hours) before and after compensation with the retrieved APS are presented in the 1 by 1 Km spaced target grid case. As seen, the along track defocusing caused by the APS variations is reduced even in the circled point, where the phase has been obtained interpolating the phase information from the neighbour targets. In the constant range cut of Figure 4.20 shows the effects of APS decorrelation.

4.3.2.2 Algorithm performance with varying atmospheric conditions and multi-scatterer cells

After presenting the algorithm and checking its performance with a particular example, the APS retrieval algorithm has been tested by simulating different atmospheric conditions. So, a known spatial-temporal varying atmospheric phase map has been added in the GEOSAR raw data generation and its evolution has been recovered using the presented algorithm.

The temporal correlation of the atmospheric phase map impact on the APS retrieval has been firstly studied. Different atmospheric temporal exponential correlation factors ranging from 1 to 60 minutes have been simulated and the phase evolution of 10 stable points over the scene has been retrieved. The spatial correlation in this case has been set up to 1 Km. A total integration time of 2 hours divided in twelve sub-apertures of 10 minutes each one have been considered. The phase information from each sub-aperture has been interpolated to obtain continuous atmospheric phase information for each received pulse.

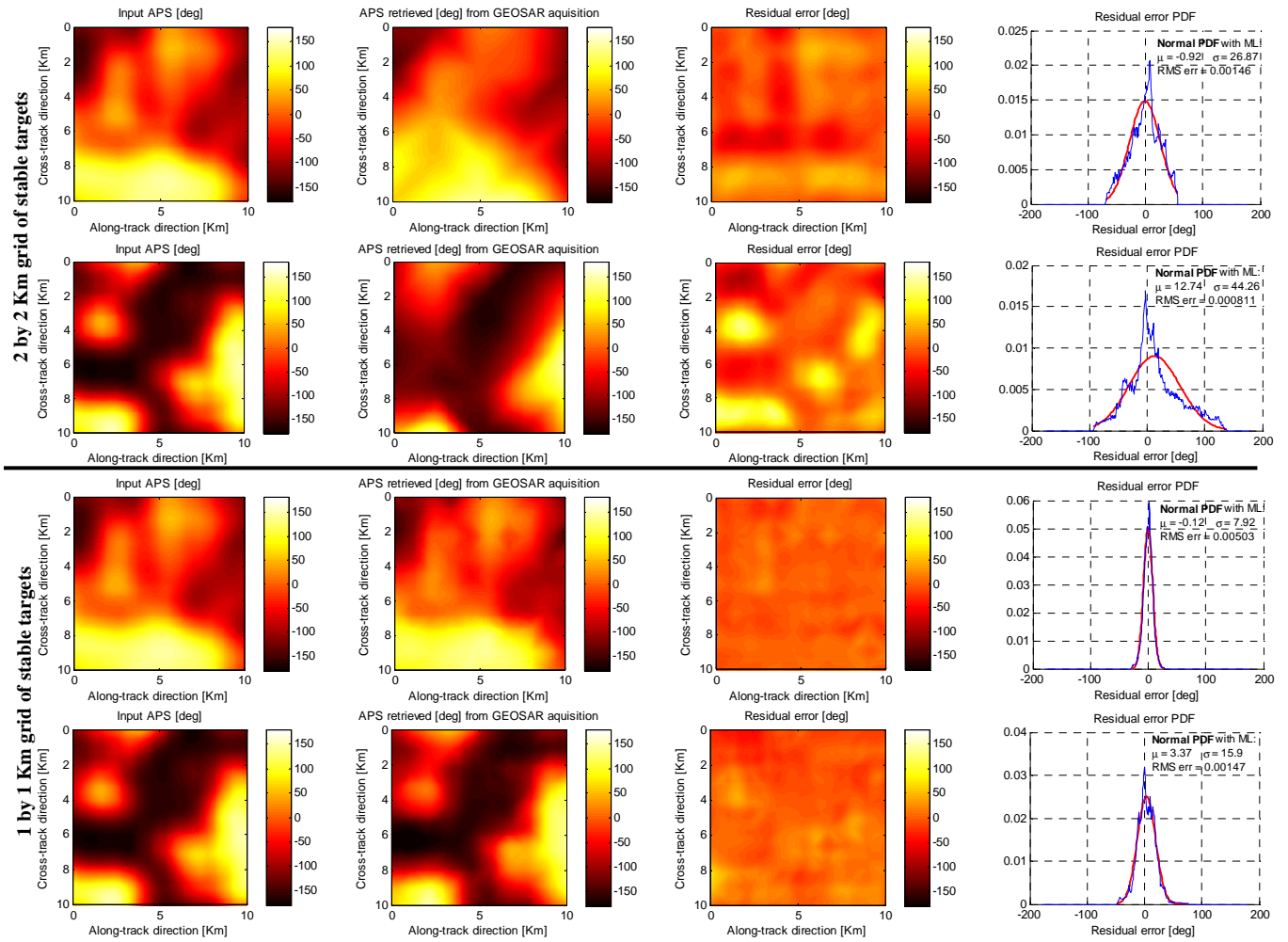


FIGURE 4.18 APS retrieval results from two different time instants of a long integration GEOSAR acquisition.

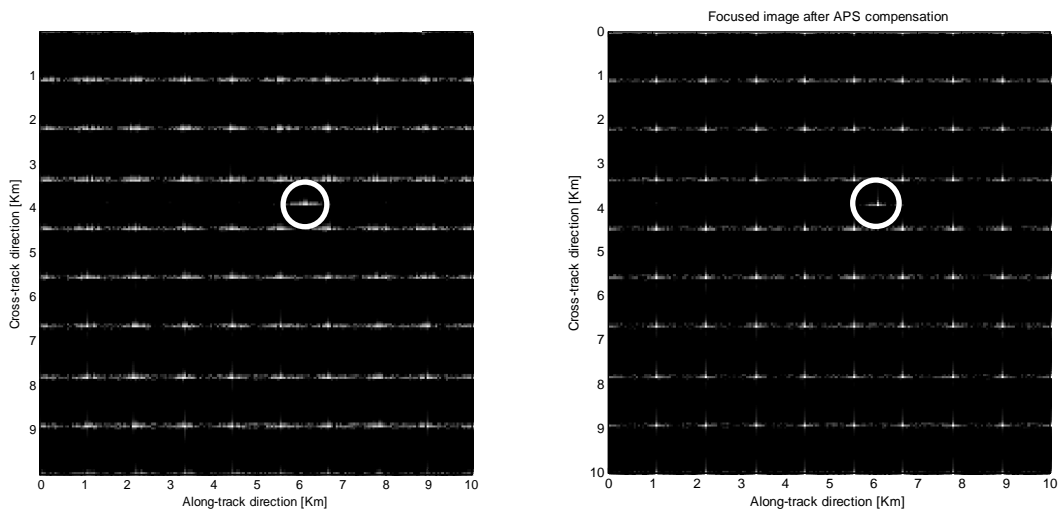


FIGURE 4.19 Focused images before and after APS compensation.

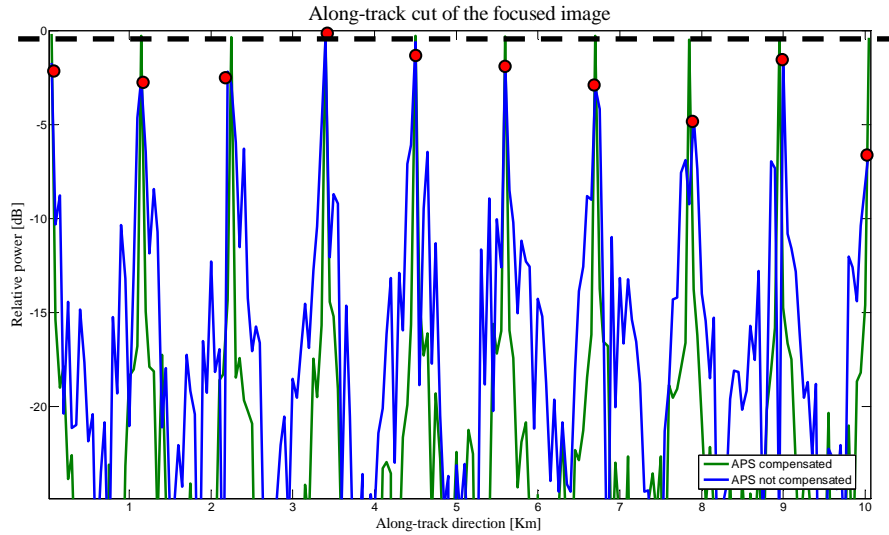


FIGURE 4.20 Azimuth cut of the reconstructed image with no APS correction (blue) and after compensation (green). The red dots shows the location and peak power of the targets in the reconstruction image without APS correction. Peak power loss, spatial displacement and secondary lobes level increase effects are reduced after APS compensation.

In Figure 4.21, the results obtained are presented. As seen in Figure 4.21 a), for atmospheric temporal correlation on the order of the sub-aperture time, the standard deviation of the residual error is 15 degrees. For more stable atmospheric conditions, i.e. 15 min. or above, the standard deviation of the error is reduced to less than 7 degrees. Figure 4.21 b) shows the temporal accuracy of the APS estimation from one of the simulated points in case of considering an atmospheric correlation of 15 minutes. As seen, the atmospheric behaviour is correctly track but there is a residual error corresponding to rapid temporal changes on the APS. Atmospheric temporal correlations around 10-20 min are expected in most cases, particularly at night with more stable atmospheric conditions.

On the other hand, the atmospheric spatial stability will be also important on the APS retrieval algorithm performance. To test the algorithm a 10x10 Km scene with uniformly spaced targets each kilometre has been used. Atmospheric maps with temporal correlation of 15 minutes and different spatial correlations have been added to the simulated raw data.

In Figure 4.22 a), the standard deviation of the phase estimation error over the 10x10 Km scene in a 2 hours acquisition is computed for different atmospheric spatial correlations. For correlations over 2 Km, standard deviation of the residual errors under 10 deg are obtained. Figure 4.22 b) shows one of the input phase maps and the retrieved one with the algorithm for a spatial correlation of 2 Km. For higher unstable meteorological conditions other methods should be considered. A posteriori knowledge of the APS behaviour could be obtained combining the information from other sensors to determine the optimum sub-aperture integration time [112].

Until now, isolated stable point targets have been considered in APS retrieval algorithm

tests. The impact of multi-scatterer cells and partially developed speckle in cells is analysed next. When more than one single point target is considered in each resolution cell, the effects of the speckle noise will deteriorate the estimation of the APS.

So, a single cell of 175x20 m with 20 randomly distributed targets with the same RCS has been considered. Additionally, a higher RCS target has been considered in different simulations varying the Signal-to-Clutter Ratio (SCR). 1000 iterations with different target cell distributions around the reference target have been considered. An atmospheric phase map with temporal correlation of 15 min has been added to the reflectivity of the terrain.

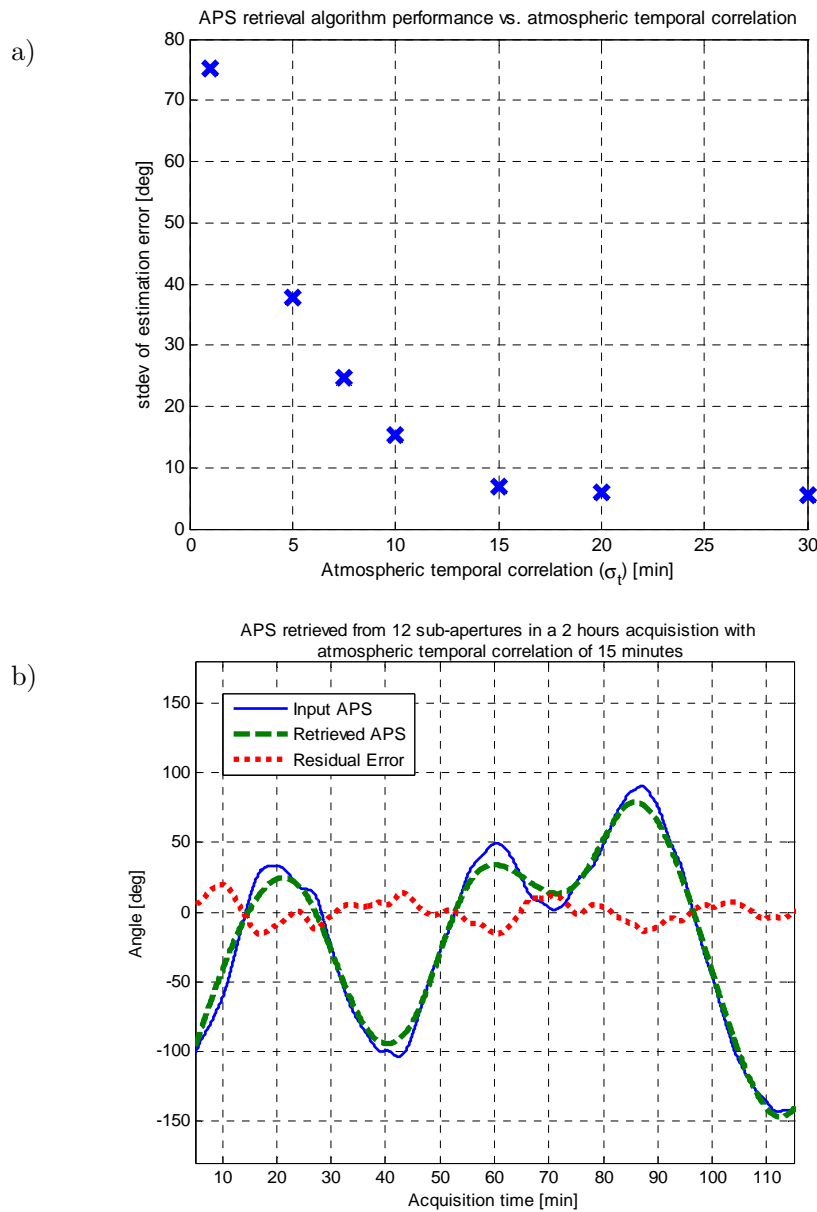


FIGURE 4.21 a) Standard deviation of the residual error in the APS retrieval algorithm for different temporal correlations of the phase map. b) Phase estimation for one of the points in the scene considering an atmospheric temporal correlation of 15 min.

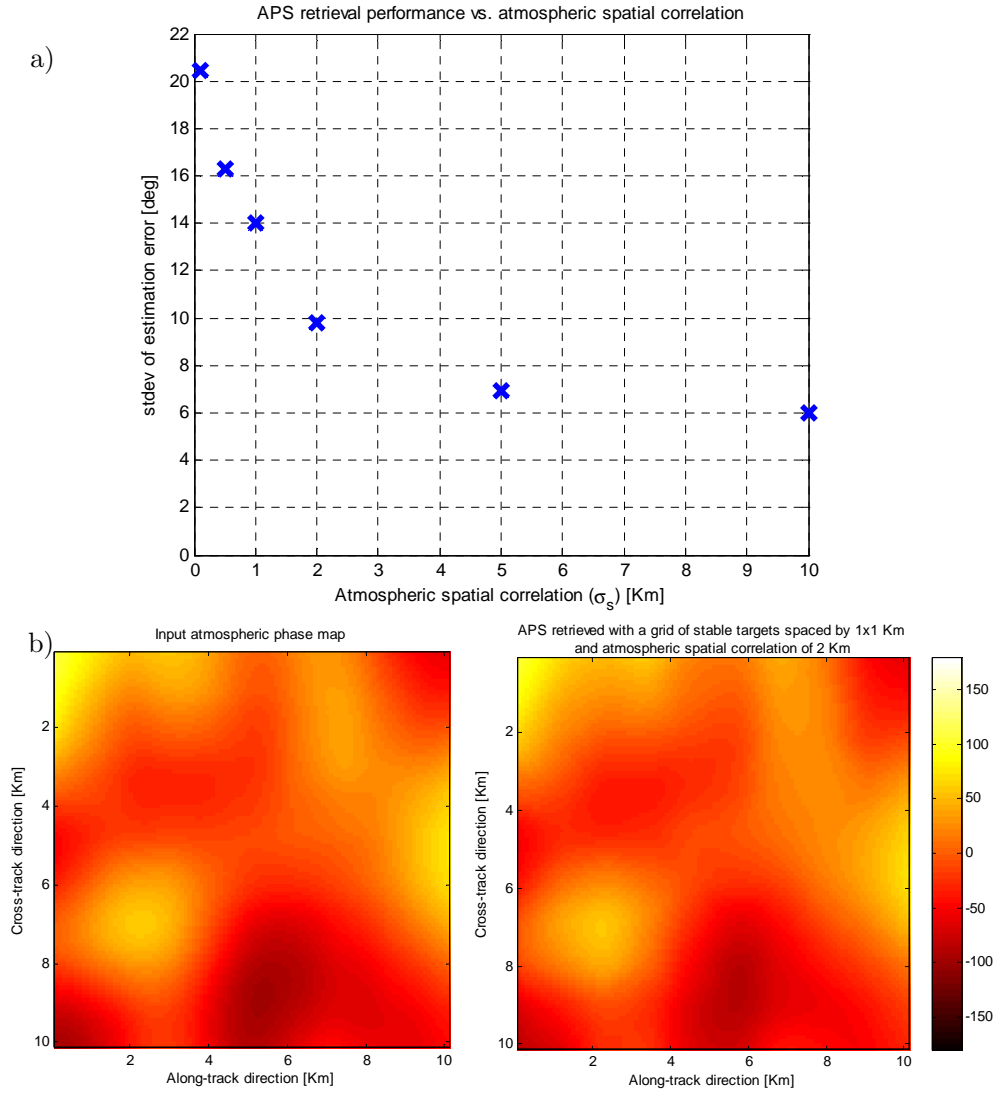


FIGURE 4.22 a) Standard deviation of the residual error in the APS retrieval algorithm for different spatial correlations of the phase map. b) Phase map estimation during the acquisition considering a grid of stable targets spaced 1x1 Km with APS spatial correlation of 2 Km.

The same APS algorithm inputs than in the previous examples has been considered: 2 hours of acquisition divided in 12 sub-apertures of 10 min each one.

The results obtained are presented in Figure 4.23. As seen, a minimum SCR of 14dB is required to get a standard deviation of final error below 10 degrees. On the other hand, for SCR above 17 dB the predominant term in the phase map estimation error will be the temporal sampling presented in the previous section.

In this case, the spatial fluctuations in the APS estimation due to partially developed speckle and noise could be reduced by differential phase spatial multi-look, averaging the phase differences from consecutive sub-apertures of contiguous pixels. This is possible since several pixels (175 x 20 meters resolution) will be affected by a common atmospheric delay due to the higher spatial correlation of the atmospheric phase map on the order of

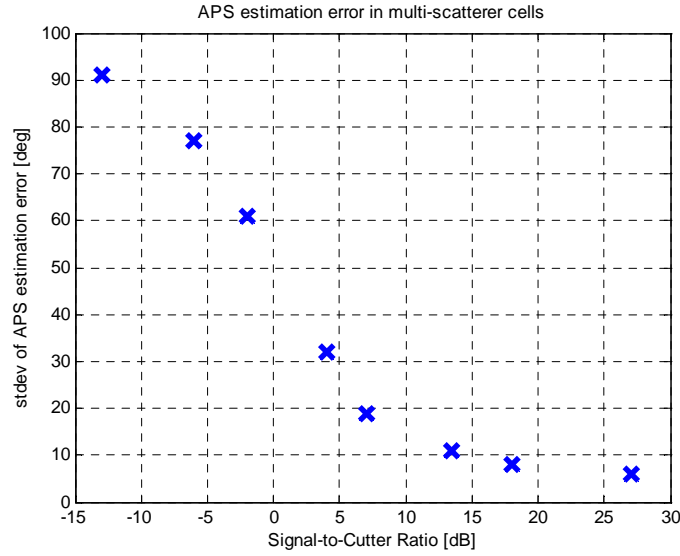


FIGURE 4.23 APS estimation error in multi-scatterer cells for different relative power between the reference target and the other targets in the cell.

Kilometres. For fully developed speckle scenes this approach does not properly work and thus, an interferometric based approach with a multistatic constellation could be considered [99] as explained in section 4.3.3.

4.3.2.3 Experimental test using data from GB-SAR system

In this section, the long term atmospheric phase history is analysed from data acquired with a Ground-Based SAR (GBSAR) system and the APS retrieval algorithm is tested with real data from a long integration GB-SAR acquisition. Although this system presents significant differences with respect to the GEOSAR technology, it will be useful to characterize the distortion produced in the raw data focusing due to the APS artefacts in long integration time acquisitions.

A GB-SAR system working at X-band [113] illuminating a valley in Canillo (Andorra) is presently being used for land-slide monitoring. The system takes periodical images from 220 different positions along a baseline of 2.2 m. From each position within the baseline, a total of 128 pulses are sent. So, a total time of 3 min 15 sec is necessary to cover the whole baseline. The acquisition is repeated every few minutes within a total time span of 6 hours.

Therefore, several short integration time acquisition (minutes) are distributed all along the acquisition campaign (hours). So, different portions of each raw data set, corresponding to a sub-aperture of the complete baseline, have been taken in order to obtain an equivalent long integration time acquisition combining different parts of the baseline of different acquisition datasets. The scheme to get the equivalent long integration acquisition is shown in Figure 4.24. As seen, different parts of each dataset are considered in order to form the complete baseline with an equivalent integration time of several hours.

In Table 4.4, the timing for the particular example considered is shown. In this case, 63 different datasets (DS) during 6 h 1min are taken. Each sub-aperture length is proportional to the interval between two consecutive acquisitions which is given by the difference between the acquisition times shown in Table 4.4. The number of positions of the raw data matrix taken for each dataset over the whole 220 is shown in the *Data* column of Table 4.4.

So, combining the different raw data matrix of the 63 datasets as summarized in Table 4.4, an equivalent 6 hours integration image may be obtained. In Figure 4.25, the images reconstructed with a single dataset (left plots) and the long term acquisition (right plots) are computed. As seen in top images of Figure 4.25, the power on the long acquisition reconstructed scene is blurred. Furthermore, in the zoom-in of the images in Figure 4.25, the point marked with a black square shows a power loss of 6 dB while the point highlighted with a white circle shows the along-track resolution defocusing as a consequence of the unpredictable atmospheric phase variations. Furthermore, a cross-track ripple is visible in the long term image. It comes from the constructive/destructive pulse integration when the atmospheric phase shift is added to the actual phase received from the targets.

Thus, the equivalent long integration data obtained from GB-SAR acquisition presented above is used to check the validity of the APS retrieval algorithm presented in section 4.3.2.1. In Figure 4.26, the APS correction results are presented for the previous example. In Figure 4.26 a), one of the short term images obtained with a single GB-SAR acquisition with an integration time of 3 min. 15 sec. is shown. On the other hand, in Figure 4.26 b), the effects of the long term integration during 6 hours can be seen. So, a power loss of 1.8 dB is obtained. Furthermore, the atmospheric uncompensated phase shift the along-track position of the target producing an azimuth positioning error of 4.8 meters. Finally, an important along-track defocusing is appreciable. The cross-track focusing is not affected by the APS decorrelation as expected.

So, the marked point of Figure 4.26 a) has been used as a reference to determine the APS history in the acquisition. The coherence analysis over this region shows that it was a good candidate to be used as a reference point since it present high amplitude and phase coherence between the different acquisitions and, therefore, constant phase should be expected from it. The phase variations obtained from this point are presented in Figure 4.26 c). These variations can be related to undesirable artefacts mostly from the atmosphere.

In Figure 4.26 c), the APS evolution computed directly from the long term acquisition using the APS retrieval algorithm is compared with the actual phase of the point obtained from the periodic short term acquisitions. As seen, a reliable approximation of the APS can be obtained from the low resolution images focused from several sub-apertures of the long term synthetic aperture. Finally, in Figure 4.26 d), the focused image from the long term data after APS compensation is presented. Target power loss is reduced to 0.4 dB while the along-track defocusing is clearly reduced from Figure 4.26 b).

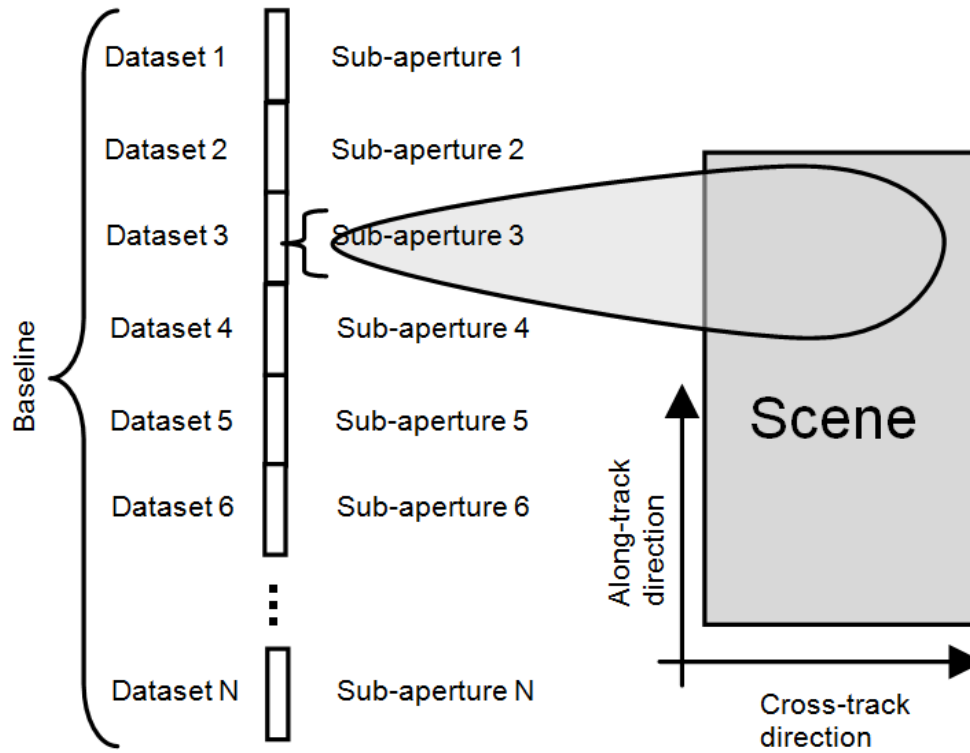


FIGURE 4.24 Sub-aperture acquisition scheme. Each sub-aperture takes the raw data acquired in different time intervals.

ACQUISIRION IN CANILLO (ANDORA) on April 6th 2011											
DS	Time	Data	DS	Time	Data	DS	Time	Data	DS	Time	Data
1	17:13	4.88	17	18:58	6.09	33	20:25	2.44	49	21:49	4.27
2	17:21	9.75	18	19:08	3.05	34	20:29	2.44	50	21:56	4.27
3	17:37	3.66	19	19:13	2.44	35	20:33	2.44	51	22:03	4.27
4	17:43	2.44	20	19:17	2.44	36	20:37	2.44	52	22:10	3.05
5	17:47	3.05	21	19:21	2.44	37	20:41	3.66	53	22:15	3.66
6	17:52	6.09	22	19:25	2.44	38	20:47	4.27	54	22:21	3.05
7	18:02	1.83	23	19:29	2.44	39	20:54	3.05	55	22:26	3.05
8	18:05	7.31	24	19:33	2.44	40	20:59	5.48	56	22:31	3.05
9	18:17	2.44	25	19:37	3.66	41	21:08	4.27	57	22:36	4.27
10	18:21	2.44	26	19:43	5.48	42	21:15	2.44	58	22:43	3.66
11	18:25	2.44	27	19:52	4.27	43	21:19	3.05	59	22:49	3.05
12	18:29	3.66	28	19:59	4.88	44	21:24	2.44	60	22:54	3.66
13	18:35	2.44	29	20:07	3.05	45	21:28	3.05	61	23:00	4.27
14	18:39	3.66	30	20:12	3.05	46	21:33	2.44	62	23:07	2.44
15	18:45	3.66	31	20:17	1.83	47	21:37	3.66	63	23:11	1.83
16	18:51	4.27	32	20:20	3.05	48	21:43	3.66	Total	6h1m	220

TABLE 4.4. Datasets (DS) considered in the long term raw data generation. The time interval between two consecutive data acquisition is used to determine the number of positions in raw data matrix taken for each sub-aperture.

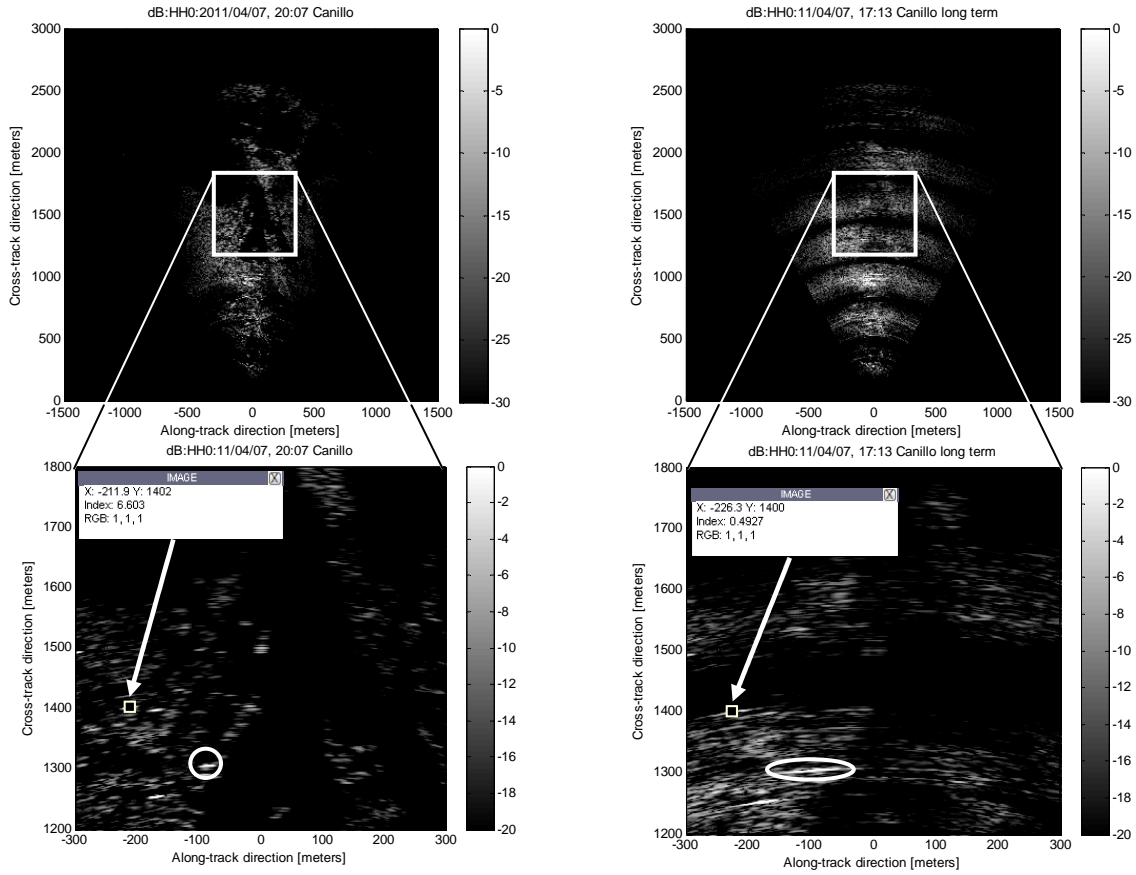


FIGURE 4.25 Reconstructed image from a single dataset at 20:07 (left plot) vs. long term reconstructed image considering the timing of the previous example (right plot). Although target power is degraded (6 dB) and the image is defocused in along-track direction, targets are still visible in the long term image. However, atmospheric compensation will be necessary to assure better image reconstruction.

In this example, the information from a single point has been considered to compensate the phase error of the whole image. Since a small part of the image (200 x 200 m) is considered, spatial fluctuation of the phase map will not be appreciated. However, since the atmospheric delay is range dependent, an additional term should be considered to have perfect reconstruction over the whole image in case of GB-SAR, where the range differences between the targets of the scene will be important.

So, larger scenes should be considered in future acquisitions in order to appreciate the spatial behaviour of atmospheric phase map. In this case, several reference targets should be taken to map the spatial variations of the APS as explained in section 4.3.2.1.

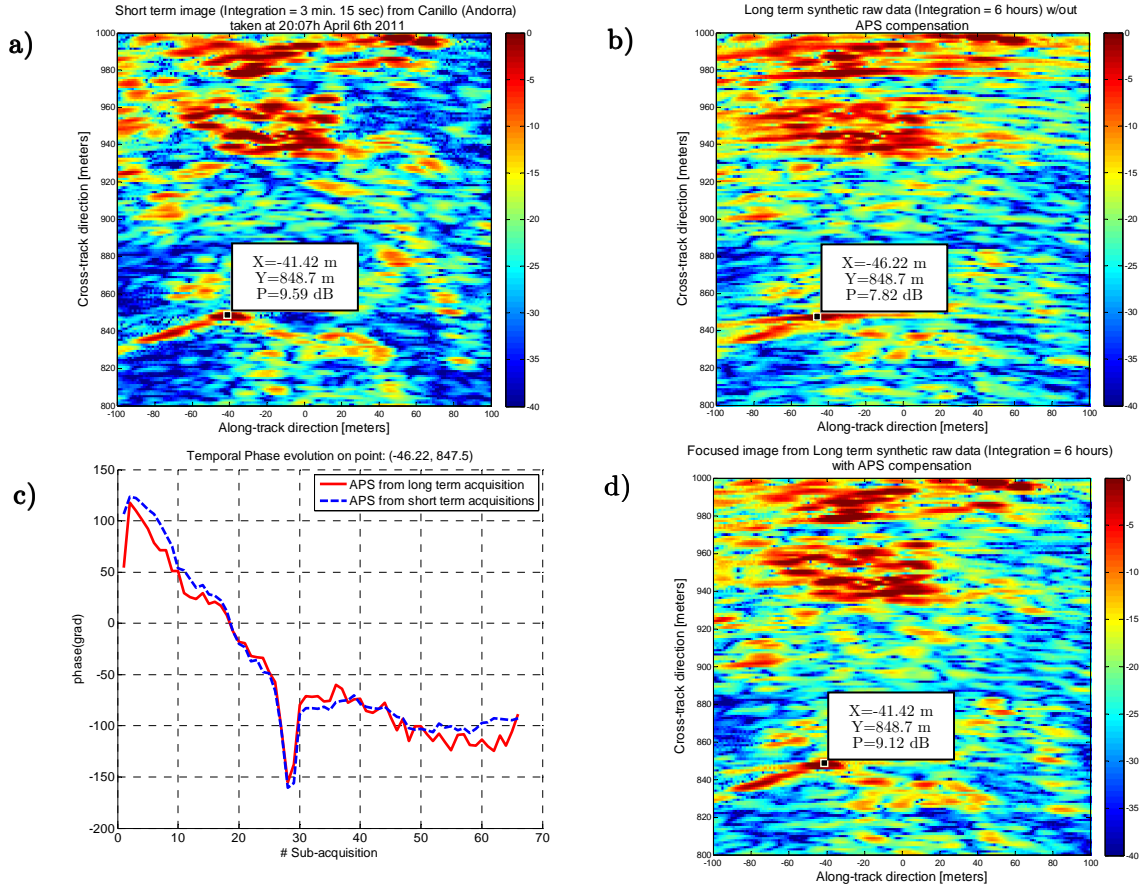


FIGURE 4.26 Long term image reconstruction and APS correction: a) short term acquisition, b) long term acquisition without APS correction, c) APS history from long term acquisition (section 3.3) and taking the short terms periodic acquisitions from GB-SAR and d) long term image with APS corrected.

4.3.3 Interferometric APS retrieval

In the previous section, an auto-focusing technique to retrieve the APS map from a monostatic acquisition with a single satellite has been presented and analysed. Alternatively, a more complex system working with a satellite constellation (two or more) can be considered for APS retrieval purposes with repeat-pass interferometry as introduced in section 4.2.3.

So, the phase received from a point in the scene was composed by several terms (equation (4.19)). As mentioned in section 4.2.3, the phase term coming from the geometry of the problem can be properly compensated by the focusing algorithm knowing the satellite and target location during the acquisition. On the other hand, the phase term corresponding to the scattering properties of the scene point will not vary from two acquisitions taken from closed orbital position and, therefore, they will disappear in the interferometric phase. Therefore, if two images from closed orbital positions can be obtained, the phase difference between the stable points in the scene will only come from propagation extra delays mostly from the tropospheric layer. Thus, the phase drift shown in the final interferograms will be

related to changes on the atmospheric phase map from one acquisition to the other.

Therefore, a pair of closely spaced geosynchronous satellites with the same orbital ephemerides can be considered for this purpose. From each satellite, low resolution images will be obtained considering a proper integration time in which the atmospheric variations can be neglected. Using a common geosynchronous orbit for both satellites, two equal passes over the scene can be obtained with a time separation of a few minutes.

Thus, the APS could be retrieved by subtracting the phase obtained from the two images acquired at different times (difference of minutes). The resultant phase drift may be directly related to propagation effects as mentioned above. The acquisition scheme is presented in Figure 4.27.

As seen, the satellites are in the same orbit with a time shift of ΔT . Therefore, the first satellite takes an acquisition from the orbital position φ_a obtaining a low-resolution image of the covered scene. The phase received from a point in the scene (x) will present the geometrical, the scattering and propagation terms. In order to isolate the propagation term related to atmospheric delay, a second acquisition is taken from the second satellite after ΔT when this satellite goes across the same positions than the first one in the first acquisition. So, differentiation of both terms, the geometrical and scattering phase of the total delay can be suppressed, obtaining the temporal derivative of the APS component over the scene.

As shown in Figure 4.27, a second interferogram could be obtained considering the acquisition from the first satellite at ΔT in an orbital position φ_b and the acquisition from the second satellite at $2\Delta T$ from the same orbital position. These acquisitions could be periodically performed (integration time of 10-30 minutes) all along the orbit in order to obtain the continuous behaviour of the atmospheric phase term. The separation between the satellites and the integration time per image should be properly selected to be consistent with atmospheric temporal decorrelation properties. The optimal integration time to optimize the APS estimation has been discussed in [112].

A mission designed for interferometric APS retrieval and imaging was presented in [147]. In this work, a dual beam concept is used to obtain wide and spot beam coverage for APS monitoring and surface imaging, respectively. A second alternative is presented in [99]. In order to avoid the time varying along-track resolution of a geosynchronous satellite, as presented in section 4.1.5, which would result in poor resolution images at the edges of the satellite orbital motion; a second pair of satellites at the same orbit but shifted 6 hours with respect to the former ones is considered. The link geometric and link budget presented in [99] shows the feasibility of such system to get continuous information of APS all over the day. In this case, the transmitter is placed in a broadcasting satellite while the pairs of satellites are conceived as received only microsatellites in order to reduce the mission cost of such configuration working with geosynchronous constellations.

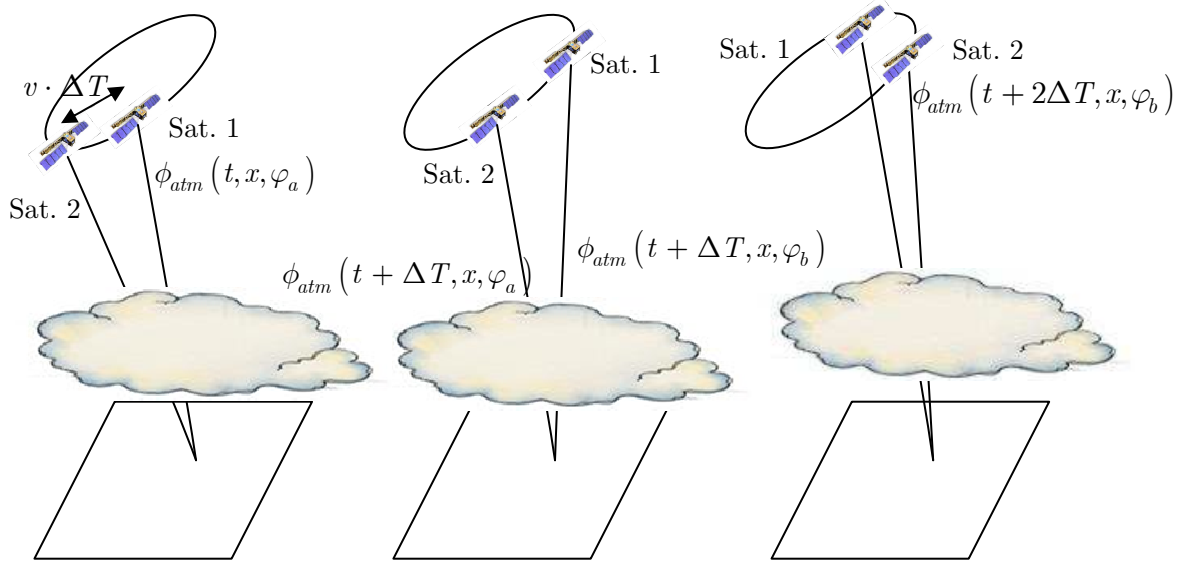


FIGURE 4.27 Orbital configuration for a GEOSAR constellation for interferometric APS retrieval.

4.4 Fine orbit and clock drift determination for GEOSAR processing

Orbital errors and clock phase errors can degrade severely the azimuth reference function to be used in the azimuth focusing step of the GEOSAR SAR processor. The determination of these errors and their compensation is a fundamental problem affecting bistatic, multistatic and monostatic configurations. The number of involved platforms determines the number of unknowns of orbital and clock parameters. However, the essence of the azimuth reference compensation is the same, allowing a common problem statement and the proposal of a common solution approach.

To obtain an accurate synthetic aperture focusing, the phase of azimuth reference function must reproduce the true phase history of every possible scattering point on the radar scene during the signal acquisition. The phase history is also affected by the APS changes during the radar data take, however in this section we will focus on the orbit and clock compensation since the APS compensation is addressed specifically in Section 4.3. Small random errors of few degrees in the azimuth reference function for SAR processing are considered tolerable. However the detailed impact of phase errors on the SAR azimuth impulsion response depends both on the error magnitude, shape and power spectrum of the phase changes. For example a constant bias error in range and the corresponding phase bias along the synthetic aperture results in perfect focusing and no other impact on the image than a constant phase which can be removed with a ground control point if necessary. This detail is relevant since in orbit control or GNSS applications a large bias range error would be intolerable but in the SAR case will have a small impact. A linear and parabolic phase components along the synthetic aperture produce image azimuth

misregistration errors and loss of resolution respectively. On the other hand the side-lobe level is degraded primarily by the high frequency components of the phase errors along the aperture [123]. A brute-force solution to minimise the clock and orbit errors impact on the SAR focusing would be to set stringent requirements in the orbit determination and clock stability, in such a way the combined impact on the azimuth reference phase errors becomes negligible. However the length of the synthetic aperture and the integration time in the order of several hours for fine resolution modes of bistatic/multistatic GEOSAR result in requirements not met by the available orbit determination methods nor ultra-stable clock present technologies as studied in Section 5.4.1. In this context it must be pointed out that in the monostatic case the clock phase drift does not impact at the time scale of the synthetic aperture integration time but only at the pulse delay scale (around 0.26 s in GEOSAR), since the received echo phase is measured with respect to the same oscillator used in transmission and therefore the long term echo phase drifts are inherently compensated.

The usage of scene scatterers of opportunity or radar calibrators may be used to provide bistatic synchronism of transmitter and receiver clocks. The phase information obtained from the calibration reflectors can also be exploited to refine the orbital track; however the number and geographical spread of the calibrators, the solution methodology and the expected phase compensation accuracy have not yet been studied.

Chapter 5

Dual-beam Dual-frequency GEOSAR for Terrain and Atmosphere with short Revisit. Bistatic baseline design

In this chapter, a bistatic/multistatic GEOSAR analysis is presented. This analysis is part of an ESA contract carried out jointly with other partners such as SES ASTRA, Politecnico di Milano, Aresys, Thales Alenia Space, Gamma Remote Sensing, Cranfield University and the University of Reading; to evaluate the feasibility of future Telecommunications broadcasting geosynchronous satellites for Synthetic Aperture Radar purposes.

5.1 Mission overview

5.1.1 Motivation of bistatic GEOSAR

In this chapter, the bistatic/multistatic concept for GEOSAR mission is analysed. In Bistatic Synthetic Aperture Radar, the transmitter and receiver are placed in a two separated spacecrafts.

Apart from the benefits of monostatic GEOSAR acquisition, such as permanent monitoring over a large area, reduction of revisit time, North-South illumination complementary to current East-West illumination of polar LEOSAR; bistatic SAR presents other advantages. First of all, using two separate antennas, the transmitter/receiver interferences are reduced. Furthermore, enough isolation between antennas is achieved, the switching between transmission and reception is not necessary, making possible to consider a 100% duty cycle.

The use of two spacecrafts offers an extra degree of freedom in orbital and antenna design which provides more possibilities in the study of possible flying formations and power link budget computation.

On the other hand, there are other issues to be assessed during the bistatic GEOSAR mission analysis. Since the transmitting and receiving chains are independent, there is a need of time, frequency and phase synchronization. Several synchronization techniques will be evaluated in this chapter for bistatic/multistatic GEOSAR. In order to assure the correct image reconstruction, an accurate antenna separation measurement and the trajectory control will be also important. On the other hand, the bistatic Radar Cross Section (BRCS) of user's parabolic antennas, a reflector of opportunity for monostatic GEOSAR acquisition as explained in section 3.5.5, will be deteriorated in bistatic acquisition. The BRCS of such reflectors needs to be studied and characterized.

Close bistatic formations (quasi-monostatic) and open bistatic formations (large separation between transmitter and receiver) will be analysed. The possibility of using an illuminator of opportunity as a transmitter can be an interesting solution to reduce the mission costs and complexity.

Going a step further, a multistatic SAR system could be also an interesting alternative for GEOSAR. So, combining the signals received in different receive-only satellites, the image quality can be improved offering a large range of new applications. In this case, an illuminator of opportunity can be used as a transmitter as well, and design only the constellation of low-cost receive-only satellite, reducing the overall multistatic mission costs. Alternatively, a mission with a single receiver with several illuminators of opportunity could be also considered, but it would increase the amount of data since each transmitting satellite would transmit its own signal. However, a single receiver would be enough to receive all the echoes from the scene.

A multistatic configuration would have several benefits with respect to the monostatic or bistatic ones. First of all, using an array of receivers (or transmitters) in different orbital positions would make possible to reduce the integration time to reach the desired resolution or, equivalently, it would increase the system resolution taking the same integration time. On the other hand, the current broadcasting telecommunications satellites are not intended for remote sensing purposes. Therefore, their orbital ephemerides are not optimized to maximize the synthetic aperture necessary for SAR acquisitions. Then, with a multistatic configuration the receiver could switch between different illuminators trying to maximize the achievable resolution.

The bistatic/multistatic SAR acquisition presents a large range of new applications:

- Evaluation of BRCS with Multi-angle Bistatic SAR Observations.
- Bistatic atmospheric mapping for meteorological applications [120][133].
- Along-track interferometry for oceanography [134] and velocity measurements and

Moving Target Indication (MTI) [135].

- Single-pass cross-track interferometry for high quality global DEMs [136].
- Polarimetric interferometry for retrieval of vegetation and volume parameters [137].
- Multi-baseline data acquisition in multistatic configurations.
- Tomography with an array of receive-only satellites [138].

So, in this chapter, a bistatic/multistatic GEOSAR mission analysis is presented. Starting from the mission requirements, the geometric and radiometric features of a bistatic/multistatic GEOSAR mission will be studied. Furthermore, the synchronism requirements as well as the possible synchronization techniques will be evaluated. Finally, with all the results obtained during the study, a preliminary bistatic/multistatic GEOSAR system design will be proposed.

5.1.2 *Mission definition and requirements: dual beam concept*

The bistatic/multistatic GEOSAR mission analysed is presented in this section. As already mentioned, bistatic GEOSAR may offer some advantages in front of monostatic configurations. So, the use of two satellites will reduce the transmitting/receiving interferences, making possible to use a 100% duty cycle which will result in some extra dB's in the power link budget computation. The multistatic design, using several transmitters or receivers, may be interesting to reduce the integration time requirements to achieve the resolution requirements, reduce the daily resolution variations due to the satellite accelerations or avoid long term resolution variations due to the satellite orbital ephemerides history.

The main concept of the bistatic/multistatic GEOSAR configuration is similar than in the monostatic GEOSAR proposed for the project which is schematically shown in Figure 5.1. So, a dual-beam dual-frequency acquisition would be studied in this analysis. A wide coverage L-Band beam, with around 3000Km spot, will be considered for atmospheric Water-Vapour Maps covering the Western part of Europe. With this beam, low-resolution images and interferograms, but enough to retrieve the atmospheric spatial changes, may be obtained every 20-30 minutes. On the other hand, several spot beams (around 650 Km coverage each one) at Ku-band that could cover the whole wide beam by antenna switching will be considered to obtain medium resolution images (in the order of 15 by 15 meters) with a revisit time of 12/24 hours, or even less in multistatic configurations.

Additionally, a single C-band beam will be also considered for both purposes: wide coverage low resolution continuous images and spot beam medium resolution images with long integration. A transmitted frequency of 5.4 GHz will be taken for this analysis. The best option for the mission requirements will be selected.

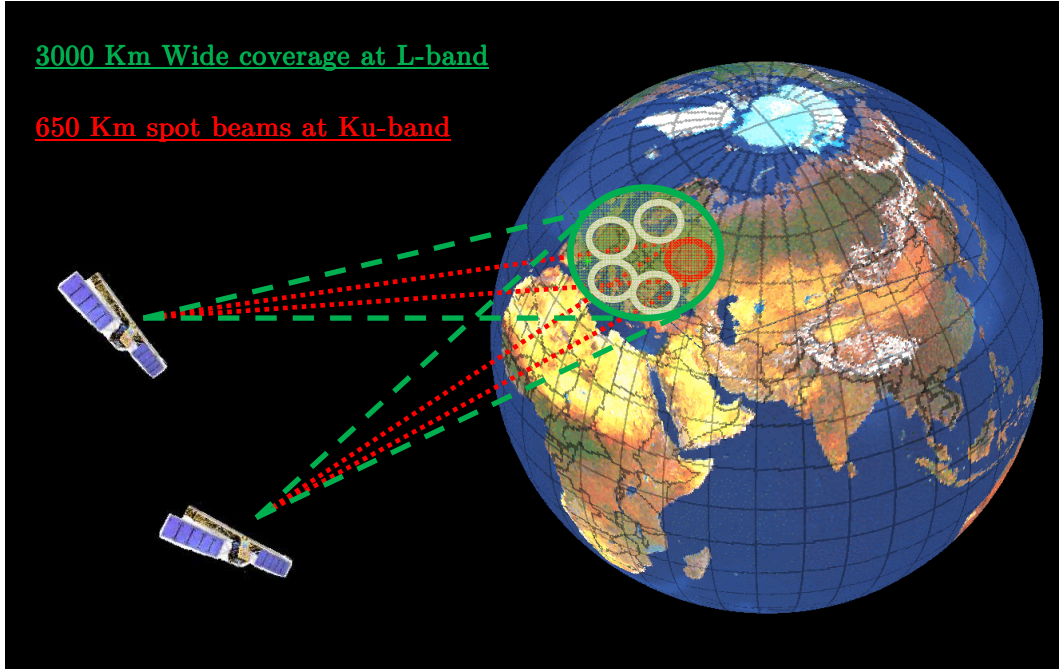


FIGURE 5.1 Bistatic GEOSAR dual-beam concept.

Therefore, several orbital designs will be analysed and the most suitable orbital ephemerides requirements (orbital eccentricity, inclination, argument of the perigee, etc.) for bistatic GEOSAR will be described. The separation between the possible transmitters and receivers, the bistatic angle, will also affect to the system performance (resolution and target bistatic Radar Cross Section) and it will be another parameter to be studied.

5.1.3 Bistatic Synthetic Aperture Radar parameters definition

In Figure 1.1, the basic monostatic SAR geometry was presented and the main parameters of a monostatic acquisition were defined. In case of bistatic SAR, some other parameters must be added to completely characterize the bistatic acquisition. In Figure 5.2, the bistatic range cut is shown. As seen, the acquisition is performed with two separated satellites, one used as a transmitter and the other as the receiver. In the bistatic acquisition, the same parameters described in Figure 1.1 for the monostatic case are still valid. In this case, the subscripts T and R are used to identify the parameters corresponding to the transmitting and receiving paths, respectively.

Additionally, the geometric parameters that will define the bistatic acquisition will be the distance between satellites which is described by the baseline vector (\vec{B}) from transmitting to receiving antenna and the transmitter-target-receiver angle, known as the bistatic angle (β). These parameters are presented in Figure 5.2. The bistatic angle can be derived from the baseline and the other geometric parameters as:

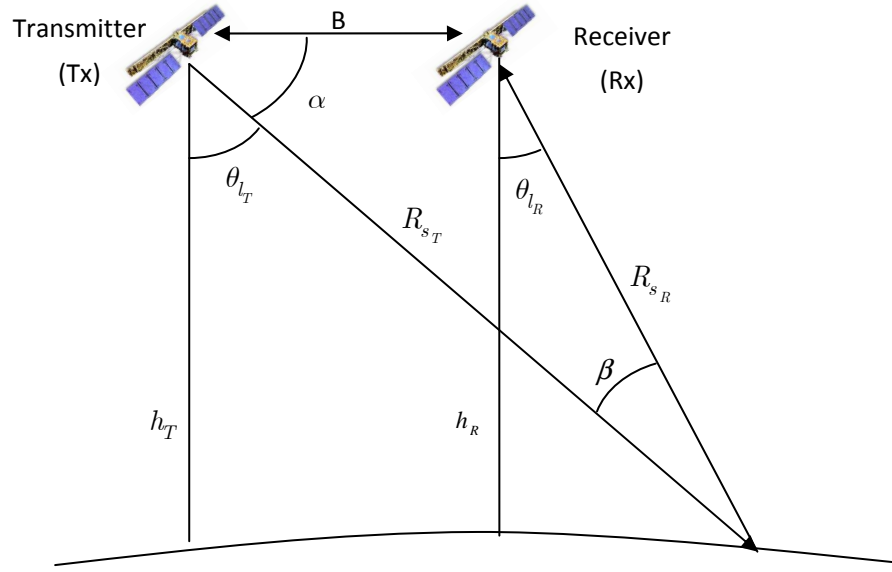


FIGURE 5.2 Bistatic SAR geometry in the bistatic plane.

$$\beta = \sin^{-1} \left(\frac{B}{R_{s_R}} \sin \alpha \right) \quad (5.1)$$

where

$$\alpha = \cos^{-1} \left(\frac{B}{2(R_e + h_T)} \right) - \theta_{l_T} \quad (5.2)$$

$$R_{s_R} = \sqrt{R_{s_T}^2 + B^2 + 2R_{s_T}B \cos \alpha} \quad (5.3)$$

$$R_{s_T} = (R_e + h_T) \cos \theta_{l_T} - \sqrt{R_e^2 - (R_e + H)^2 \sin^2 \theta_{l_T}} \quad (5.4)$$

5.2 Bistatic observation geometry and possible flying formations

In this section, the possible bistatic GEOSAR formations are analysed in order to determine the proper orbital configuration for SAR purposes. First of all, the range of possible nominal longitudes of the satellites to cover the desired scene must be defined. The separation between satellites may also affect to the system coverage and, therefore, a maximum bistatic angle to assure the desired coverage must be found. On the other hand, the orbital ephemerides will be studied to obtain the necessary relative motion to fulfil the resolution requirements of the system.

5.2.1 *Satellites location impact on the mission coverage*

As introduced in the mission requirements presented in section 5.1.2, the region of interest is Western Europe. Therefore, one important aspect is to determine the longitudes where the satellites can be placed to cover this region. As shown in section 2.3, a single geosynchronous satellite may cover $1/3^{\text{rd}}$ of the Earth approximately, but in a bistatic configuration, the superposition of both satellite fields of view must be assured over the region of interest.

First of all, let us consider a close bistatic formation with two satellites in the same orbital box. The achievable coverage in this case is equivalent to a monostatic acquisition since the both fields of view will be completely overlapped. In this case, taking as a reference longitude the centre of the desired scene around 11° East, the best nominal position of the satellites to avoid coverage reduction will be around this point. In Figure 5.3, the covered areas of two satellites placed at 10.95° East and 11.05° East are plotted as green and red circles over the Earth map, respectively. As seen in this case, both fields of view are completely overlapped and cover the region of interest shaded in blue over the Earth plot shown in Figure 5.3.

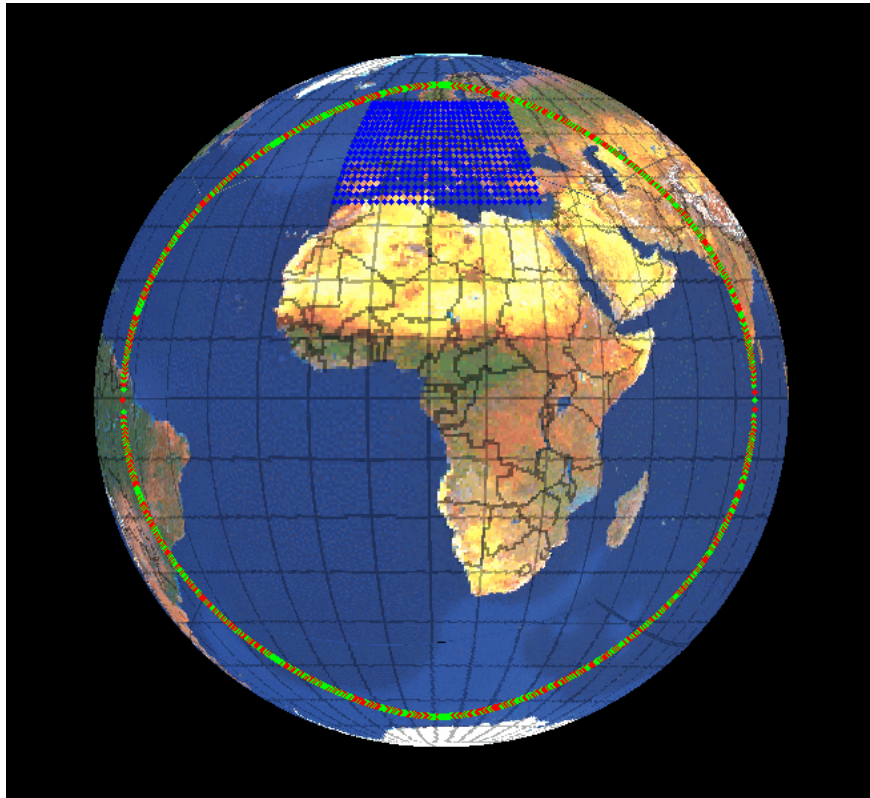


FIGURE 5.3 Satellites placed on 11° East covering all the area of interest.

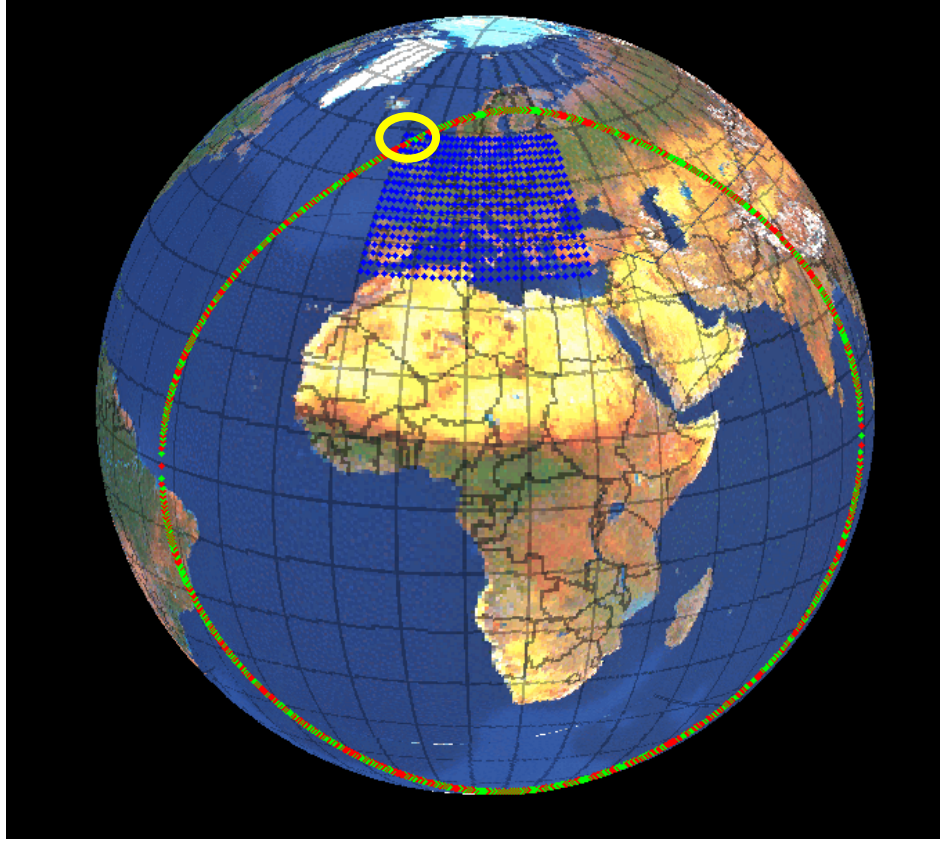


FIGURE 5.4 Close bistatic field of view considering two satellites with nominal longitudes around 22° East.

In order to evaluate the range of possible nominal longitudes in case of close bistatic formations, the previous analysis is repeated for several nominal satellites locations shifted to East and West with respect to the reference position at 11°E . So, in Figure 5.4, the satellite coverage considering a nominal longitude of 22° East is presented. As seen in this case, the North-Western part of the desired scene is already partially uncovered. Therefore, it has been considered as one of the limits in the satellite nominal longitude definition.

On the other hand, repeating the analysis but shifting the position to the West a similar result is found. So, in Figure 5.5, the same plot considering a nominal longitude of the satellites around 0° is presented. In this case, the North-Eastern part of the desired region is not seen by the satellites.

Therefore, for this particular mission covering the Western part of the European continent (centred at 11° East longitude), the range of nominal longitudes for a close bistatic GEOSAR acquisition will go from 0° to 22° East approximately. Considering further nominal longitudes, the scene will start to be partially uncovered.

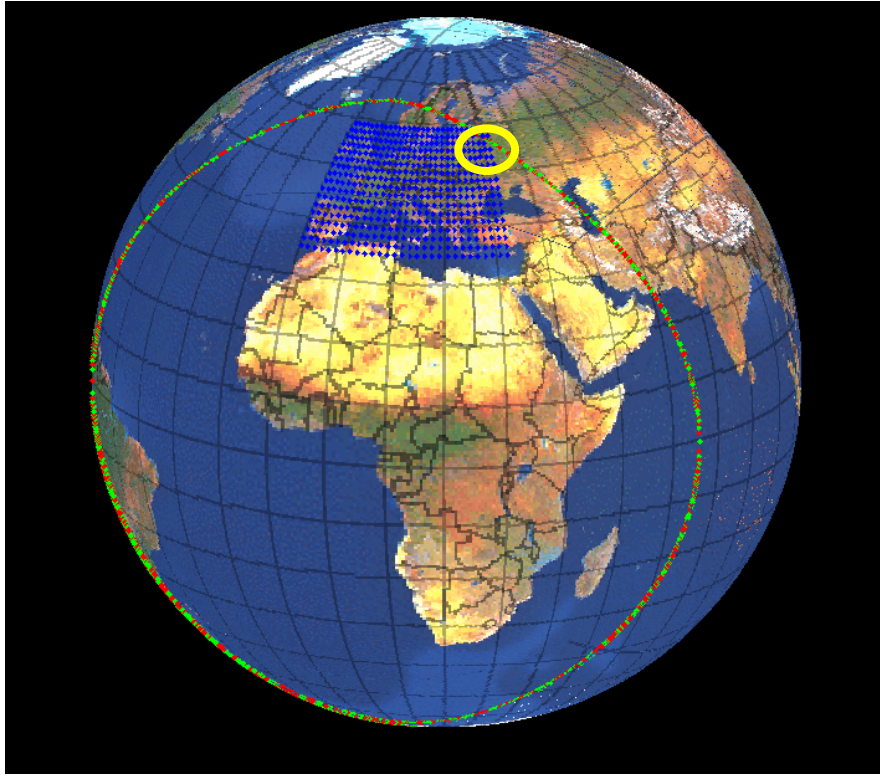


FIGURE 5.5 Close bistatic field of view considering two satellites with nominal longitudes around 0° .

On the other hand, the effect of the separation between the satellites in the coverage must be studied in order to identify the maximum bistatic angle of a bistatic GEOSAR acquisition. Therefore, as the bistatic angle between the transmitter and the receiver is increased, the overlapping between the satellites fields of view will start to decrease.

So, starting with a close bistatic formation centred at 11° East as the example shown in Figure 5.3, the bistatic angle has been progressively increased. In Figure 5.6, the bistatic GEOSAR configuration with two satellites placed at nominal longitudes of 0° and 22° East is presented. As seen in this case, the coverage of the desired scene is reduced for both Northern corners which are the result of the transmitter-receiver field of view overlapping reduction.

In order to define the maximum bistatic angle from the maximum longitudinal separation between the satellites, the scheme presented in Figure 5.7. So, the bistatic angle can be related with the longitude shift as:

$$\beta = \frac{\Delta\lambda \cdot a}{R} \quad (5.5)$$

Therefore, considering the maximum separation defined in Figure 5.6 of 22 degrees, the orbital radius of geosynchronous satellites (42164 km) and a slant range to the centre of the

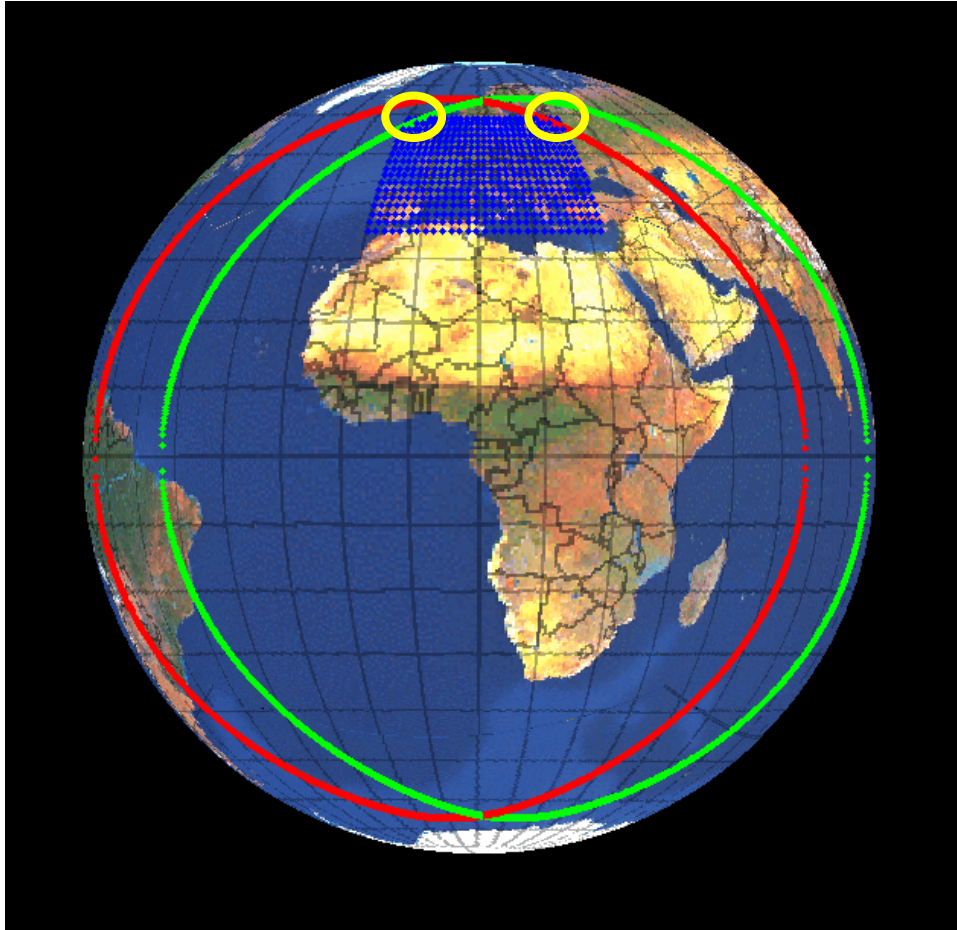


FIGURE 5.6 Open bistatic GEOSAR field of view considering two satellites with nominal longitudes of 0° and 22° , respectively.

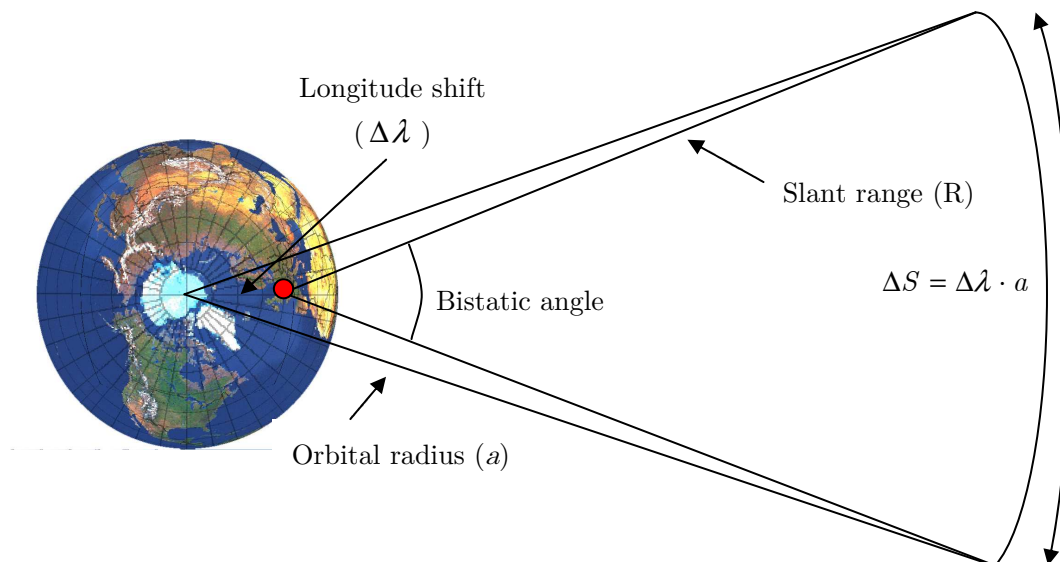


FIGURE 5.7 Relation between the satellites longitude shift and bistatic angle.

scene of 38500 km, a maximum bistatic angle between the satellites of for the presented mission of 24.1 degrees may be taken for the particular mission considered in this analysis.

5.2.2 *Bistatic orbital design impact on the resolution*

As in the monostatic GEOSAR case, along-track and cross-track directions can be defined in bistatic acquisition. For each one, the system resolution can be found.

On one hand, regarding the cross-track or range resolution, there is not any particularity with respect to the monostatic case. So, as presented in section 2.4.2.1, the ground range resolution will be related with the transmitted signal bandwidth (B) and the incidence angle (θ_{inc}) as:

$$\rho_{gr} = \frac{c}{2B \sin \theta_{inc}} \quad (5.6)$$

The incidence angle from the transmitter and the receiver could be significantly different in a bistatic acquisition. However, for close bistatic formations considering geosynchronous satellites with small eccentricities and inclinations, both angles can be considered equal for resolution calculation purposes. So, as introduced in section 5.1.2, a dual beam dual frequency acquisition is studied in this mission. On one hand, for the wide coverage coarse resolution L-band acquisition, a transmitted signal bandwidth of 0.25 MHz will be enough to reach a ground range resolution of 1 km considering the lowest incidence angles within the scene around 40 degrees. On the other hand, in case of spot beam fine resolution Ku-band acquisition, the signal bandwidth should be increase up to 15.5 MHz to reach a ground range resolution of 15 meters under the same assumptions than in the previous case. As seen, the ground range resolution will be independent of the orbital design.

On the other hand, special attention must be taken in the along-track or azimuth resolution analysis. In this case, considering separate transmitting and receiving satellites, each one with its own orbital ephemerides, the synthetic aperture definition can be a bit more complex than in the monostatic GEOSAR case.

In order to determine the effective synthetic aperture of a bistatic acquisition, an equivalent monostatic model [145] is used. The equivalent monostatic acquisition can be computed as an equivalent track considering the mid-points of the two satellites tracks of the bistatic pair as shown in Figure 5.8.

The bistatic and equivalent monostatic acquisitions will be equivalent if the same surface radar scattering spectrum is obtained from each one. In fact monostatic and bistatic synthetic aperture radar can be considered particular cases of microwave diffraction tomographic imaging [146]. Under the usual implicit assumption of a radar scene composed

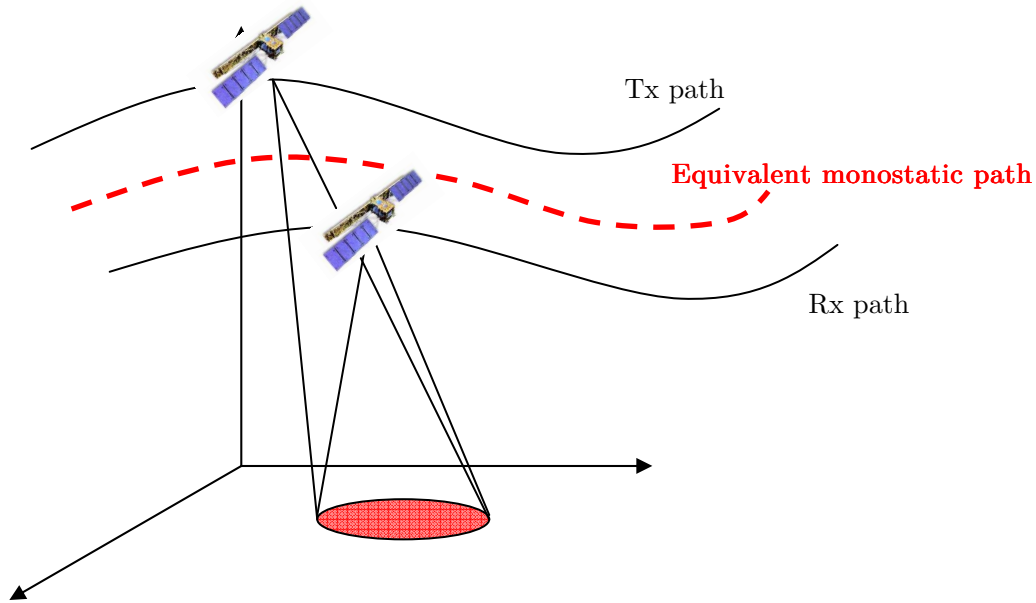


FIGURE 5.8 Bistatic and equivalent monostatic SAR.

by a distribution of a large number of isotropic uncoupled scattering centres (Born Approximation), the complex radar backscattered field provides information of the spatial Fourier Transform of the surface radar reflectivity. The pass-band accessed scene spectrum is defined by the wavenumber vectors of illumination and backscattering as shown in Figure 5.9. The angular sweep provided by the synthetic aperture and the carrier and bandwidth of the transmitted pulses provide the angular and radial extension of the accessed spectrum, resulting in the image spatial resolutions in the cross-range and range directions respectively.

Figure 5.9 shows that the scene spectrum can be accessed in different ways. In particular, under the uncoupled isotropic scattering assumption usual in SAR imaging, a bistatic observation is equivalent to a monostatic observation carried out from the centre of the bistatic base-line with a slight change in the carrier frequency. It is worth noting that the Born approximation will be correct when the illumination field of the observed surface is essentially the direct illumination from the transmitter antenna with negligible reradiation from nearby scatterers. The Born approximation breaks down in presence of strong multiple reflections producing “ghost” targets when river crossing bridges are reflected on the water surface or in the case of dihedral or trihedral structures in cities and industrial areas. In these cases bistatic images will depart from their monostatic equivalent ones.

The study and optimization of the different parameters to obtain the desired system resolution will be presented in the following sections. In these examples, the equivalent monostatic is considered to predict the theoretical results. However, all the results obtained from bistatic simulation have been obtained with a pure bistatic acquisition since the GEOSAR simulator described in section 3.6.3 offers the possibility of working with two separate transmitting and receiving satellites.

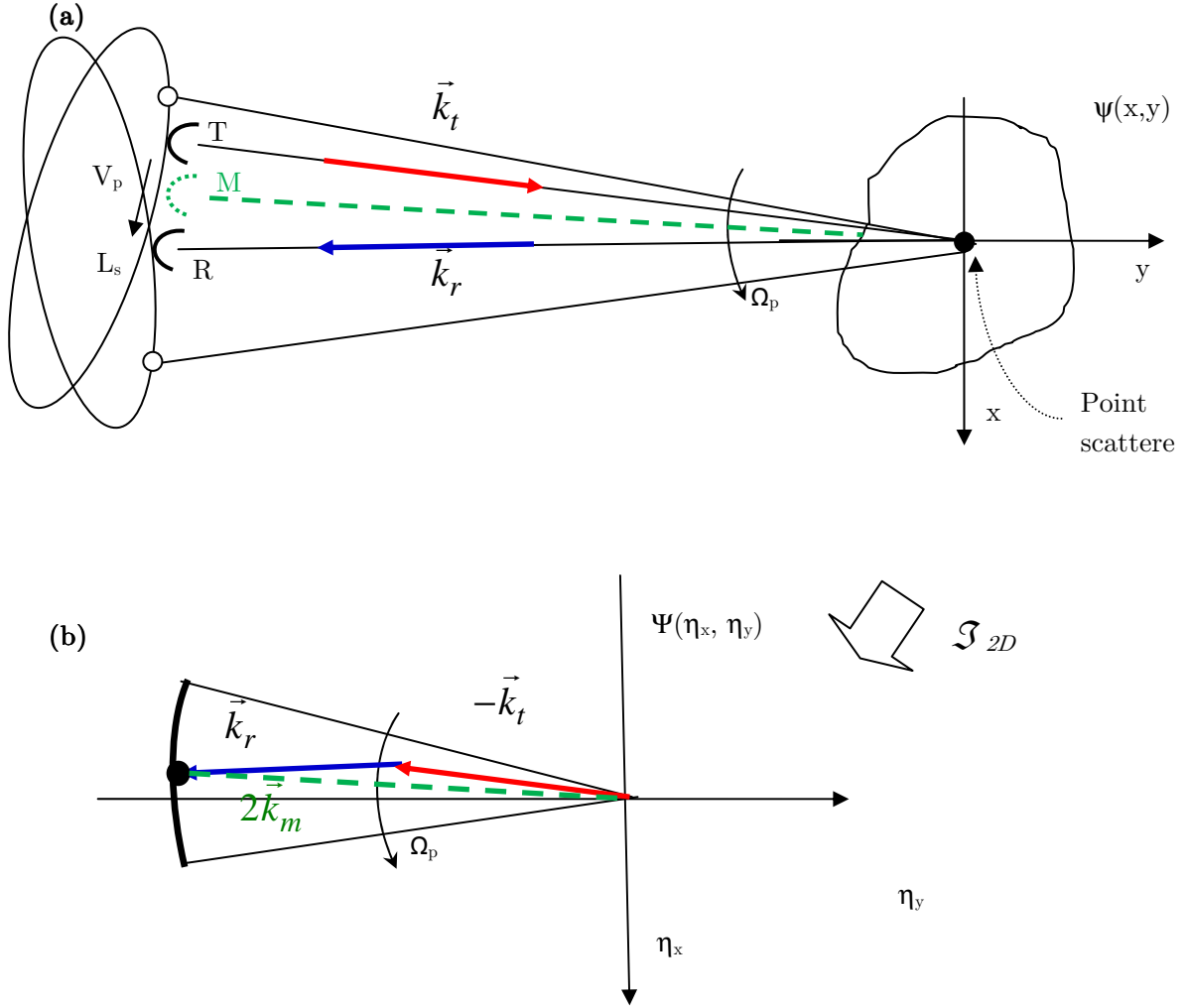


FIGURE 5.9 Spatial (a) and Spectral (b) domains of the imaged scene. The scene spectrum accessed from a bistatic observation is equivalent, to a monostatic observation

So, the equivalent monostatic synthetic aperture is defined as the relative motion of the midpoint of the transmitter-receiver link vector. Then, the same SAR performance would be obtained by considering the bistatic acquisition or a monostatic one moving between both satellites.

The monostatic equivalent of a generic GEOSAR bistatic acquisition will be also found from the orbital behaviour of the transmitter and the receiver. So, as shown in Figure 5.10, the equivalent monostatic trajectory in bistatic GEOSAR will be typically ellipsoidal as in the monostatic cases studied all along this thesis. However, for bistatic GEOSAR the orbital ephemerides of the transmitter and receiver can be adjusted independently obtaining more degrees of freedom in the orbital design. In Figure 5.11, the same example is shown in a 3D representation where the equivalent monostatic is represented as a pink line between both satellite trajectories.

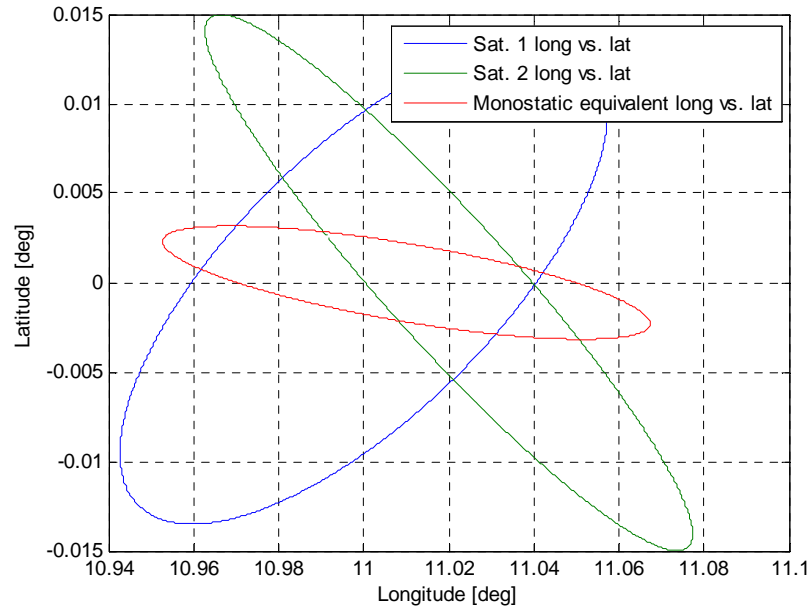


FIGURE 5.10 Bistatic and equivalent monostatic satellite tracks for a generic GEOSAR case.

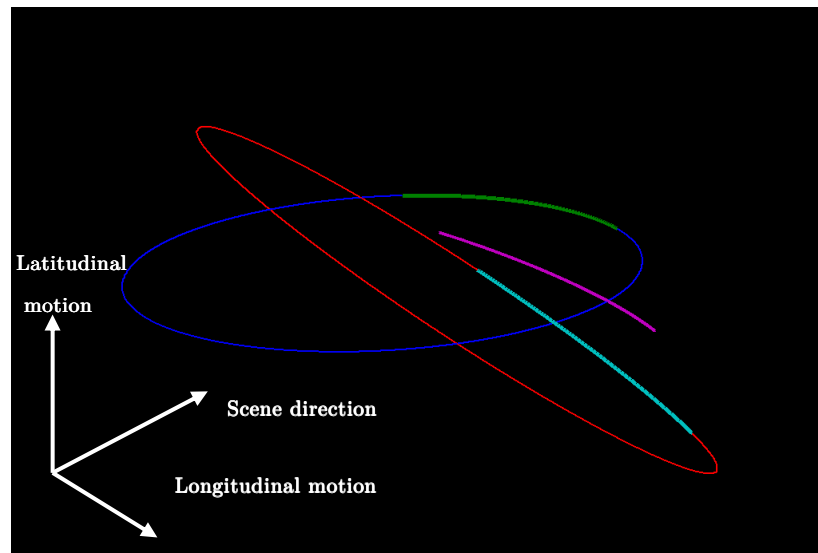


FIGURE 5.11 Bistatic and equivalent monostatic considering 4 hours of acquisition.

Once the equivalent monostatic of the bistatic GEOSAR acquisition is found, the same analysis than the one presented in section 2.4.2 may be performed to determine the bistatic GEOSAR achievable along-track resolution. Since the scene considered in the acquisition of this mission is placed at mid-latitudes, a GEOSAR acquisition with longitudinal motion should be considered in order to get the necessary along-track motion with respect to the scene. As explained in section 2.4.2.2, the achievable along-track resolution will be constrained by the orbital eccentricity which will determine the longitude and by the integration time which will fix the part of the orbital motion that is considered for SAR integration.

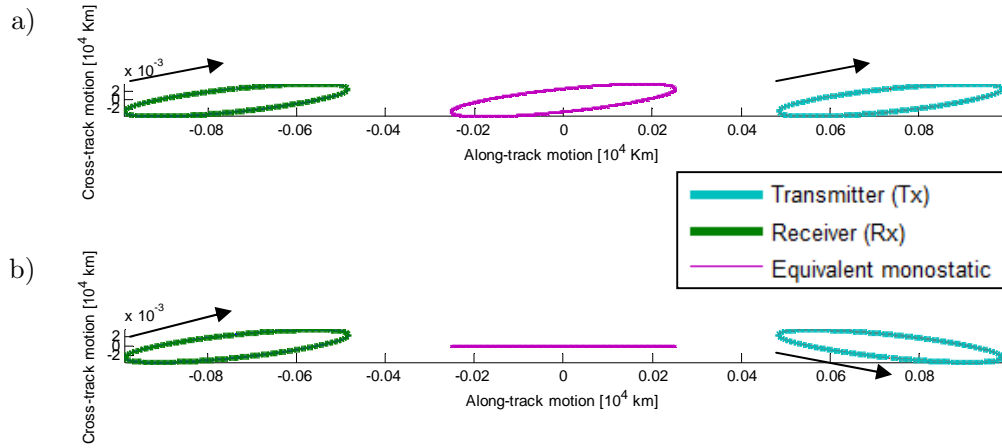


FIGURE 5.12 Possible bistatic formation to reach the desired equivalent monostatic: a) same eccentricity, inclination and argument of the perigee (inclined equivalent monostatic) or b) same eccentricity and inclination and 180° shift in their arguments of the perigee (non-inclined equivalent monostatic)

Therefore, the results presented in Figure 2.41 and Figure 2.42 will be valid for the SPOT and wide coverage beams in the bistatic GEOSAR studied in this section if the equivalent monostatic present an equivalent orbital eccentricity as the ones considered in the analysis of section 2.4.2.2. So, if an along-track resolution of 15 m in 4 hours of integration and 1 km in 30 min for the SPOT Ku-band and wide coverage L-Band acquisitions are desired respectively, a minimum orbital eccentricity of the equivalent monostatic of 0.0003 should be defined.

This can be easily obtained by considering two satellites with the desired eccentricity at different nominal longitudes moving in phase which means with the same time pass through the perigee as shown in equation (2.23). This example is shown in Figure 5.12 a). In this case, the same eccentricity (0.0003), inclination (0.005 degrees) and argument of the perigee (45 degrees) have been selected for transmitter and receiver orbital definition. Regarding the nominal longitude, the transmitter has been placed at 0.1 degrees East while the receiver has been placed at 0.1 degrees West. As seen in this case, the equivalent monostatic has the same behaviour than the transmitting and receiving satellite orbital tracks but it is placed in the middle between them, at 0 degrees of nominal longitude.

Multiple possibilities could be chosen in order to reach a final monostatic equivalent as the one desired, but the one presented in Figure 5.12 a) is the simplest one. However, going a step further, and taking into account the analysis presented in section 4.2 where has been shown that the latitudinal motion given by the inclination of the orbit may be undesired thinking on repeat-pass interferometric applications; the extra degree of freedom given by the bistatic GEOSAR in the orbital design may be used to eliminate the latitudinal component of the equivalent monostatic motion. So, if the same orbital design than in the previous case is considered but a shift of 180 degrees between their arguments of the perigee

is defined, the orbital inclination of the equivalent monostatic is suppressed. As mention, it may be important for interferometric purposes, even more taking into account that it will be difficult to assure a 0 inclination orbit with a single satellite.

This case can be seen in Figure 5.12 b), where two orbits with arguments of the perigee of 225 degrees and 45 degrees for the transmitting and receiving satellites have been plotted, respectively. The black arrows show the direction of the satellite in the orbit. As seen, the equivalent monostatic has zero inclination as it was desired. This can be explained from equation (2.25) considering the 180 degrees shift on the argument of the perigee:

$$\varphi_{SL_T} = i \sin(\omega + \Omega_E(t - t_p)) \quad (5.7)$$

$$\varphi_{SL_R} = i \sin((\omega + \pi) + \Omega_E(t - t_p)) = -i \sin(\omega + \Omega_E(t - t_p)) = -\varphi_{SL_T} \quad (5.8)$$

As it is shown in equations (5.7) and (5.8), the latitude history of the transmitter and receiver will always have the same amplitude but opposite sign and, therefore, their mid latitude point will be always over the equatorial plane.

So, after defining the optimum orbital configuration for bistatic GEOSAR in order to assure a minimum longitudinal motion to reach the along-track resolution requirements and cancel the latitudinal motion, some results obtained from bistatic GEOSAR simulations are presented next.

So, let us consider two satellites with nominal longitudes at 11.1° East and 10.9° East as transmitter and receiver, respectively. In both cases, an orbital eccentricity of 0.0003 and inclination of 0.005 degrees have been set up. As in the previous example, arguments of the perigee of 225 degrees and 45 degrees have been considered. Therefore, with this parameters, an equivalent monostatic orbit with eccentricity of 0.0002 and no-inclination (as shown in Figure 5.12 b)) centred at the middle scene longitude (11° East) is obtained.

In order to check the accuracy of the theoretical approach presented above, two simulations have been performed. In the first one, an integration time of 4 hours with a transmitted frequency at Ku-band (17.25 GHz) has been considered. The resultant focused image considering a single point target in the scene is shown in Figure 5.13. As seen, an along-track resolution (computed as the half null-null distance around the maximum target response) of 19 meters is obtained. Comparing this result with the one obtained in Figure 2.41 for the monostatic case with same transmitting parameters and eccentricity of 0.0002, the fitness of the equivalent monostatic model in bistatic GEOSAR has been demonstrated.

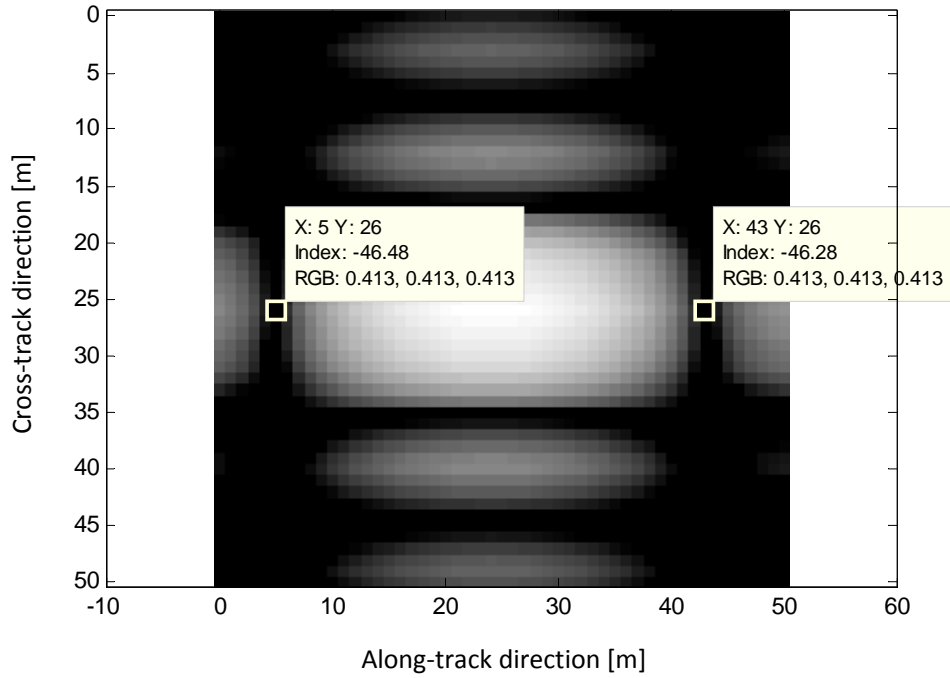


FIGURE 5.13 Focused image with an integration time of 4 hours at Ku-band (19.25 GHz) considering two satellites with orbital eccentricity of 0.0002. An along-track resolution around 19 meters is obtained.

As seen in the previous example, an orbital eccentricity of 0.0002 would not be enough to reach the 15 meters resolution requirement in 4 hours of integrations. Therefore, if the analysis is repeated using an orbital eccentricity of 0.0003 for both the transmitter and receiver, a final along-track resolution of 12.8 meters is obtained. So, an orbital eccentricity around 0.0003 at least should be considered in the orbital design of both satellites for the bistatic mission requirements of this mission.

Similarly, the same analysis may be done at L-band for the wide coverage low-resolution acquisition. In this case, 30 min of acquisition has been considered with a transmitted frequency of 1.625 GHz. As in the previous case, orbital eccentricities of 0.0002 for both satellites have been firstly proposed. The focused image for this case is presented in Figure 5.14. In this case, an along-track resolution of 1.56 km is obtained. Once again, this result is consistent with the ones obtained in the monostatic approach presented in Figure 2.42 for L-band acquisitions.

In this case, the proposed eccentricity is also too small to reach the resolution requirements of the wide coverage beam which was around 1 km. Therefore, if the orbital eccentricity is increased up to 0.0003 as in the previous case, a simulated along-track resolution of 1.02 km is obtained. Thus, a minimum eccentricity of 0.0003 should be also considered for the L-band coarse resolution acquisition to fulfil the mission requirements.

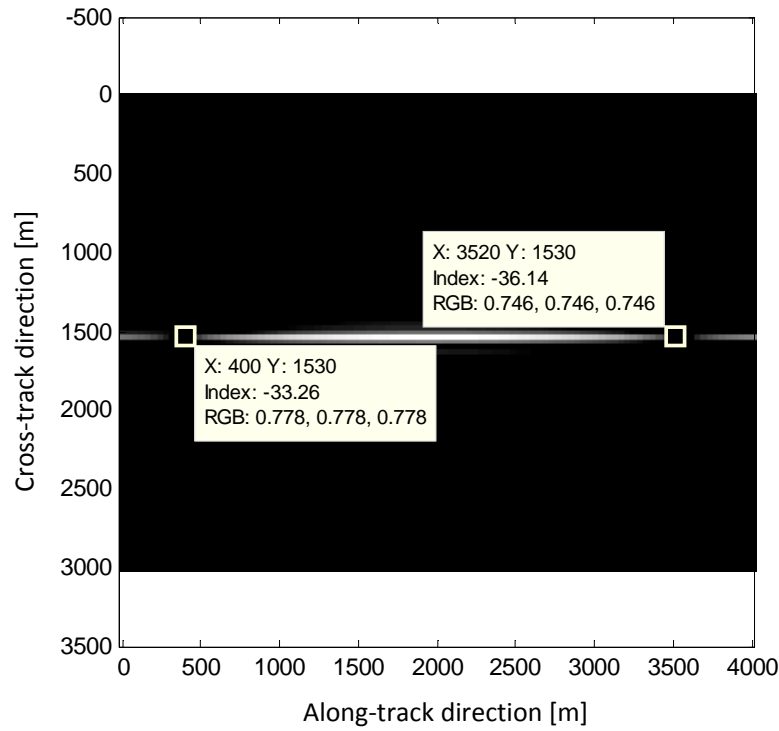


FIGURE 5.14 Focused image with an integration time of 30 min at L-band (1.625 GHz) considering two satellites with orbital eccentricity of 0.0002. An along-track resolution around 1.56 km is obtained.

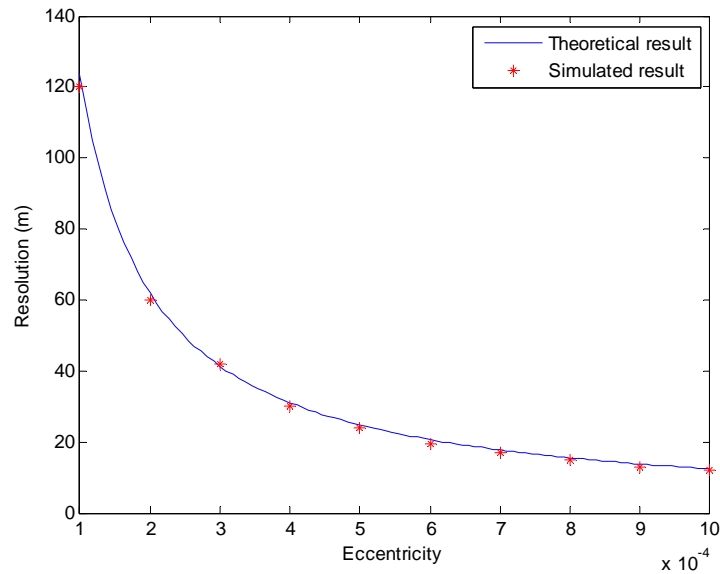


FIGURE 5.15 Achievable resolution of a bistatic GEOSAR acquisition with 4 hours of integration for different orbital eccentricities working at C-band (5.4 GHz).

As explained in section 5.1.2, a third alternative considering a single C-band acquisition at 5.4 GHz for both purposes (wide coverage low-resolution and spot beam with finer resolution) is studied in this analysis. So, the resolution analysis for C-band beam is

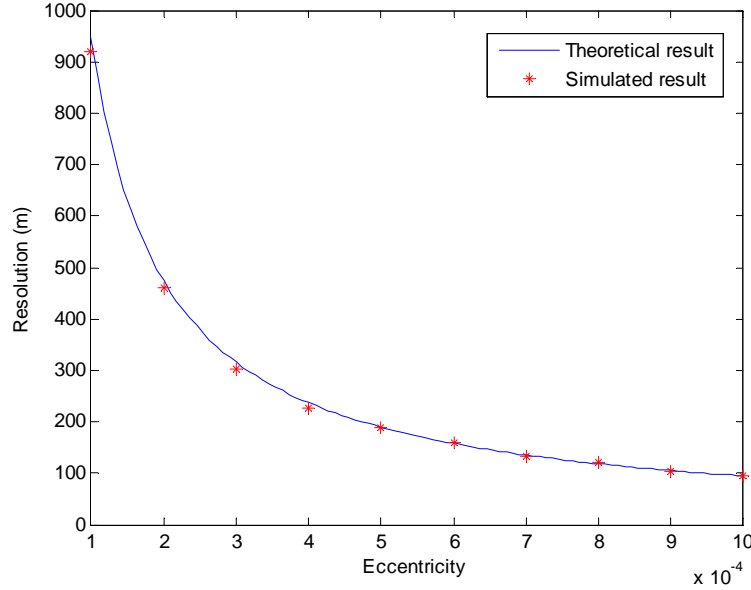


FIGURE 5.16 Achievable resolution of a bistatic GEOSAR acquisition with 30 min of integration for different orbital eccentricities working at C-band (5.4 GHz).

performed for different orbital eccentricities considering an integration time of 4 hours and 30 minutes. The results obtained for each case are presented in Figure 5.15 and Figure 5.16, respectively. As seen, working with a lower frequency than in Ku-band for SPOT beam medium resolution beam results in a coarser resolution. In case of considering the minimum eccentricity obtained in the previous analysis, an along-track resolution of 42 meters is obtained. On the other hand, for the wide coverage low resolution acquisition, a resolution around 304 meters would be obtained working at higher frequency with respect to the original L-band acquisition proposed. The radiometric performance shown in section 5.3 of L-, C- and Ku-band will be useful to determine the best option for the proposed mission.

5.3 GEOSAR radiometric analysis for bistatic acquisition

In this section the necessary antenna parameters to fulfil the coverage and power requirements (sections 3.1 and 3.5) will be particularized for the bistatic GEOSAR mission analysed. As described in section 5.1.2, two simultaneous acquisition beams (wide coverage L-Band beam and spot Ku-Band beam) will be considered in the bistatic/multistatic GEOSAR design of this mission.

Thus, the concepts analysed in Chapter 3 of this thesis are re-defined for a bistatic SAR configuration and the most relevant results are computed for the particular GEOSAR mission studied for the ESA project introduced in section 5.1.

5.3.1 *Antenna design: coverage and pointing requirements*

In section 3.1, the antenna requirements to fulfil the coverage requirements of the system have been studied. So, given a desired coverage, the required antenna gain, size and beamwidth can be obtained from equations (3.5), (3.7) and (3.8), respectively.

Particularizing these equations with the parameters of the L-band wide coverage beam and the Ku-band spot beam, the results presented in Table 5.1 are obtained taking a mean slant range of 37.000 Km. On one hand, for the L-band (at 1.625 GHz) wide beam, with a swath coverage around 3000 Km, an antenna beamwidth of 4.64 degrees is obtained. In order to reach this antenna beamwidth, a parabolic reflector diameter of 2.78 meters is required. Such antenna size results in an antenna gain of 31.6 dB taking an antenna efficiency of 0.65. On the other hand, considering the Ku-band (at 17.25 GHz) spot beam with coverage of 650 Km, a smaller antenna beam of 1.01 degrees is required. In this case, a parabolic reflector of 1.21 meters would be enough to reach the desired beamwidth. The narrower beam results in a higher antenna gain of 44.9 dB considering the same antenna efficiency than in the previous case. All these results are consistent with the plots presented in Figure 3.2, Figure 3.3 and Figure 3.4.

Therefore, two separate antennas could be considered for each frequency each one with the dimensions summarized in Table 5.1 or, alternatively, consider a single antenna with the larger diameter obtained for the L-band beam and two independent feeders which illuminate the necessary part of the antenna reflector for each case.

On the other hand, the antenna requirements working at C-band have been analysed for wide coverage and SPOT beams. The results obtained are summarized in Table 5.2. The required beamwidths and antenna gains have not changed since the same desired coverage than in the L-band and Ku-band configurations have been considered. On the other hand, the required antenna diameters will be smaller (0.84 meters) for wide beam C-band acquisition and larger (3.88 meters) for spot beam acquisition if the coverage requirements are preserved. In that case, a single reflector of around 4 meters diameters could be considered and the different coverage could be obtained by using a tuneable feeder which would illuminate different parts of the reflector.

Additionally, the antenna pointing will be crucial for bistatic acquisition since transmitting and receiving antenna footprints superposition must be assured in order not to reduce the available coverage. In Figure 5.17, the coverage reduction due to antenna pointing mismatches ($\Delta\phi_e$) are schematically presented. In that case, the system coverage given by the antenna footprint (ΔS) is reduced to $\Delta S'$ due to the pointing deviations between the transmitting and the receiving antenna footprints.

	L-Band beam	Ku-Band beam
Frequency	1.625 GHz	17.25 GHz
Wavelength	0.1846 m	0.0174 m
Total efficiency	0.65	0.65
Desired coverage	3000 Km	650 Km
Antenna beamwidth	4.64 deg	1.01 deg
Antenna diameter	2.78 m	1.21 m
Antenna gain	31.6 dB	44.92 dB

TABLE 5.1. Antenna parameters requirements for L-band wide beam and Ku-band spot beam.

	C-Band wide beam	C-Band spot beam
Frequency	5.4 GHz	5.4 GHz
Wavelength	0.056 m	0.056 m
Total efficiency	0.65	0.65
Desired coverage	3000 Km	650 Km
Antenna beamwidth	4.64 deg	1.01 deg
Antenna diameter	0.84 m	3.88 m
Antenna gain	31.6 dB	44.92 dB

TABLE 5.2. Antenna parameters requirements for C-band beam.

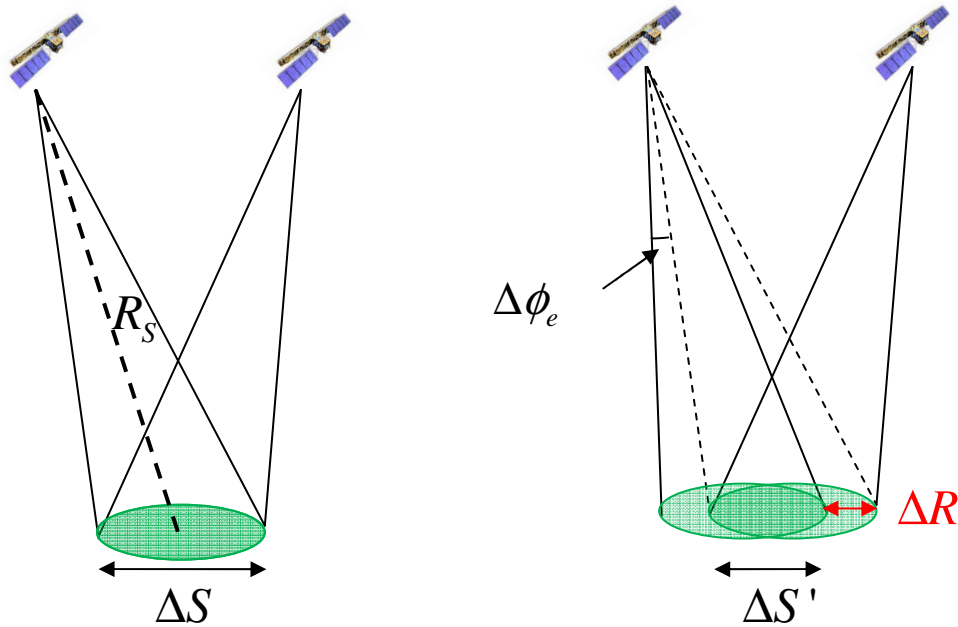


FIGURE 5.17 Coverage reduction due to antenna pointing mismatches.

From the slant range/pointing error direction plane, shown in Figure 5.18, the relation between the coverage reduction (ΔR) and the pointing error can be computed as:

$$\Delta R = \frac{\sin \Delta \phi_e}{\sin(\pi/2 - \arctan(\Delta S / 2R_s) - \Delta \phi_e)} \sqrt{R_s^2 + \frac{\Delta S^2}{4}} \quad (5.9)$$

Equation (5.9) can be simplified by considering small antenna pointing errors ($\Delta \phi_e \ll 1^\circ$) and $R_s \gg \Delta S$. Considering:

$$\sin \Delta \phi_e \approx \Delta \phi_e$$

$$\sqrt{R_s^2 + \frac{\Delta S^2}{4}} \approx R_s$$

$$\sin(\pi/2 - \arctan(\Delta S / 2R_s) - \Delta \phi_e) \approx \sin(\pi/2) = 1$$

the antenna pointing errors and the swath coverage reduction can be related as:

$$\Delta R \approx R_s \Delta \phi_e \quad (5.10)$$

Since the antenna pointing error can be in any direction, in the following analysis, the pointing error direction is projected to the azimuth and ground range directions in order to separate the along-track and cross-track coverage reduction. Moreover, as shown in Figure 5.19, both antenna footprints can be slightly deviated from the nominal pointing (marked as an X in Figure 5.19) and, therefore, both misalignments must be taken into account in the final coverage calculation.

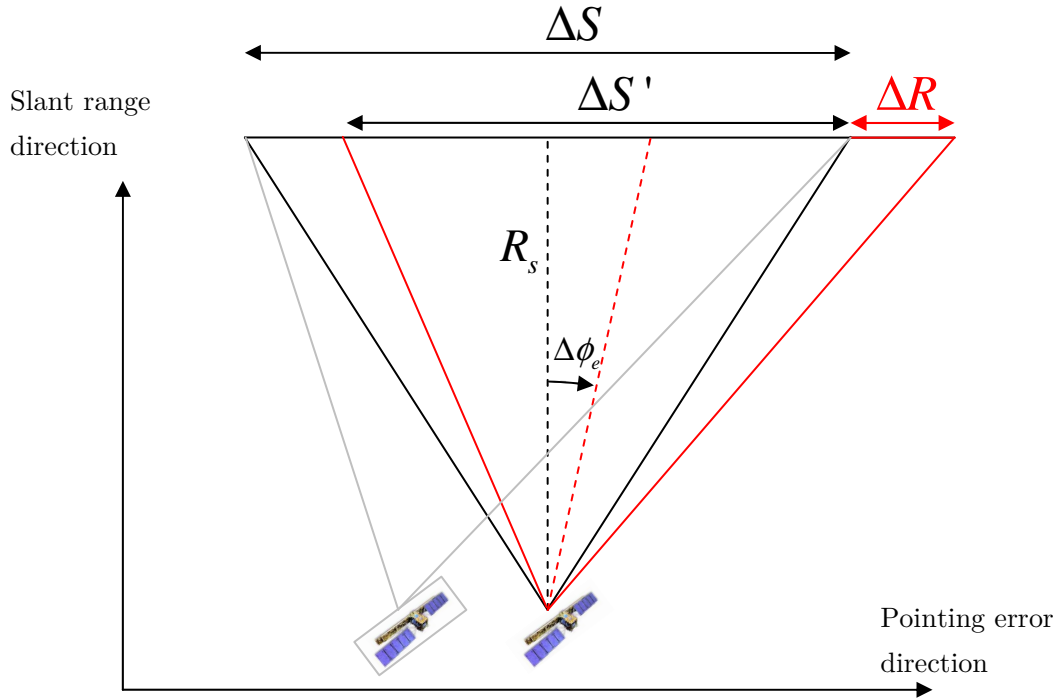


FIGURE 5.18 Coverage reduction in bistatic SAR due to pointing errors (slant range/pointing error direction plane).

So, in Figure 5.19 the transmitting and receiving footprints are plotted in green and red, respectively, in the along-track (\hat{e}_a)/cross-track (\hat{e}_c) plane. Each footprint presents a deviation from the centred position of ΔR (the sub-index t corresponds to the transmitting footprint while r corresponds to the receiving one). Furthermore, the unit vectors \hat{e}_t and \hat{e}_r describes the on ground pointing direction errors of the transmitter and receiver footprints, respectively.

So, projecting the pointing errors from each antenna to the along-track and cross-track directions, the final overlapping between the transmitting and receiving footprints in this two directions ($\Delta S_a', \Delta S_c'$) is related with the ideal coverage ($\Delta S_a, \Delta S_c$) and the pointing errors as:

$$\begin{aligned}\Delta S_a' &= \Delta S_a - \left| \Delta R_t (\hat{e}_t \cdot \hat{e}_a) - \Delta R_r (\hat{e}_r \cdot \hat{e}_a) \right| = \Delta S_a - \left| R_{s,t} \Delta \phi_{e,t} (\hat{e}_t \cdot \hat{e}_a) - R_{s,r} \Delta \phi_{e,r} (\hat{e}_r \cdot \hat{e}_a) \right| \\ \Delta S_c' &= \Delta S_c - \left| \Delta R_t (\hat{e}_t \cdot \hat{e}_c) - \Delta R_r (\hat{e}_r \cdot \hat{e}_c) \right| = \Delta S_c - \left| R_{s,t} \Delta \phi_{e,t} (\hat{e}_t \cdot \hat{e}_c) - R_{s,r} \Delta \phi_{e,r} (\hat{e}_r \cdot \hat{e}_c) \right|\end{aligned}\quad (5.11)$$

The relative coverage loss in each direction can be obtained as:

$$\begin{aligned}\frac{\Delta S_a - \Delta S_a'}{\Delta S_a} &= \frac{\left| R_{s,t} \Delta \phi_{e,t} (\hat{e}_t \cdot \hat{e}_a) - R_{s,r} \Delta \phi_{e,r} (\hat{e}_r \cdot \hat{e}_a) \right|}{\Delta S_a} \\ \frac{\Delta S_c - \Delta S_c'}{\Delta S_c} &= \frac{\Delta S_c - \left| R_{s,t} \Delta \phi_{e,t} (\hat{e}_t \cdot \hat{e}_c) - R_{s,r} \Delta \phi_{e,r} (\hat{e}_r \cdot \hat{e}_c) \right|}{\Delta S_c}\end{aligned}\quad (5.12)$$

In order to obtain an antenna pointing accuracy requirement, the worst case has been taken. So, the same pointing errors ($\Delta \phi_{e,t} = \Delta \phi_{e,r} = \Delta \phi_e$) but in opposite directions ($\hat{e}_r = -\hat{e}_t$) have been considered both in along-track and cross-track cuts. The same transmitter-target and receiver-target slant ranges have been used. With these considerations, equation (5.12) can be re-written as:

$$\frac{\Delta S_{a,c} - \Delta S_{a,c}'}{\Delta S_{a,c}} = \frac{2R_s \Delta \phi_e (\hat{e}_t \cdot \hat{e}_{a,c})}{\Delta S_{a,c}} \quad (5.13)$$

So, taking the desired coverage around 3000 Km and 650 Km analysed for this mission for the wide and spot beams respectively, and imposing a relative error loss under 10% in along-track and cross-track direction separately, the maximum antenna pointing error can be found as:

$$\Delta \phi_{e,a,c} \leq 0.1 \frac{\Delta S_{a,c}}{2R_s (\hat{e}_t \cdot \hat{e}_{a,c})} \quad (5.14)$$

which results in a maximum pointing error of **0.23 degrees** considering the 3000 Km swath and **0.05 degrees** considering the 650 Km one.

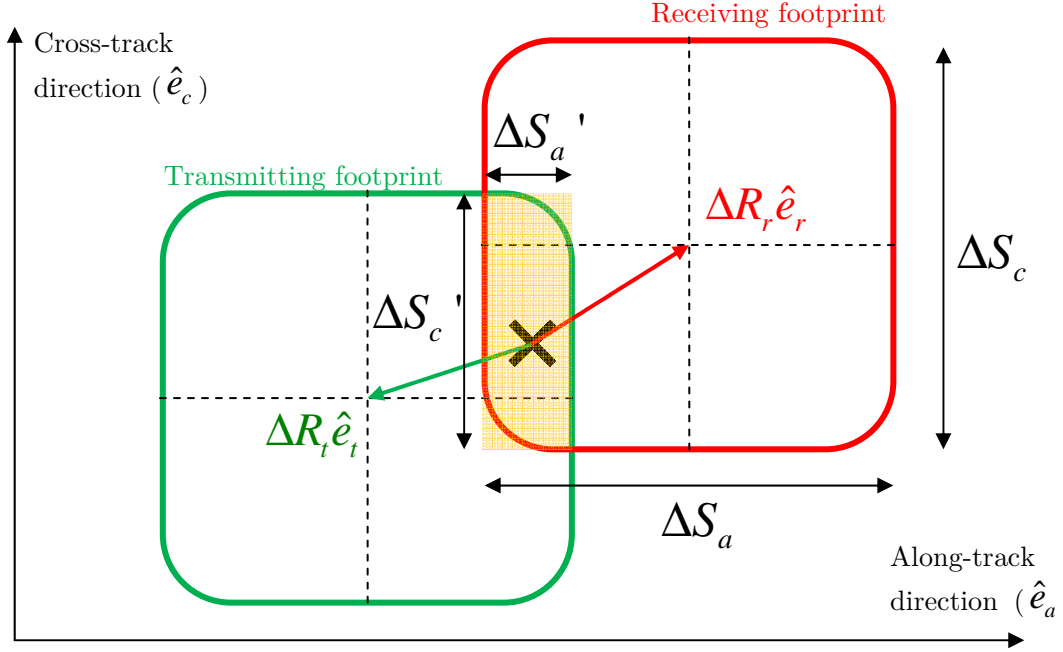


FIGURE 5.19 Transmitting/receiving antenna footprints mismatch in the along-track/cross-track plane.

5.3.2 Backscattering profiles for bistatic acquisition

The SNR computation will depend on the back-scattering properties of the observed scene. At the same time, the surface response is highly dependent on the frequency, the acquisition geometry (incidence angle, bistatic angle), type of surface, etc. [139]–[143]. For bistatic acquisition, the acquisition scheme and bistatic parameters presented in Figure 5.20 have to be taken into account. So, the bistatic scattering properties of the surface will not only depend on the incident angle (θ_{in}) and the scattering angle (θ_s) but also the out-of-plane angle (ϕ_o). These angles can be related to the bistatic angle (β) as [144]:

$$\beta = \cos^{-1}(\cos \theta_{in} \cos \theta_s - \sin \theta_{in} \sin \theta_s \cos \phi_o) \quad (5.15)$$

Simulated results obtained in [142], and shown in Figure 5.21, Figure 5.22 and Figure 5.23), present the scattering behaviour with the out-of-plane angle for different incident angles for desert areas, rangeland and snow, respectively.

The GEOSAR system analysed in this report is intended to image regions at mid-latitudes from 35° to 60° which corresponds to incident and scattering angles from 40° to 70° , approximately. Furthermore, taking two satellites around the equator, the out-of-plane angle will be near to 180° (close monostatic configurations) and will decrease for larger

bistatic angles (until 40° for a bistatic angle of 90°). As shown in Figure 5.21, Figure 5.22 and Figure 5.23, the bistatic scattering coefficient generally decrease with the out-of-plane angle and with the incident angle. For the range of incidence and out-of-plane angles of the GEOSAR bistatic mission analysed, values around -10 to -20 dB are expected for different types of surfaces.

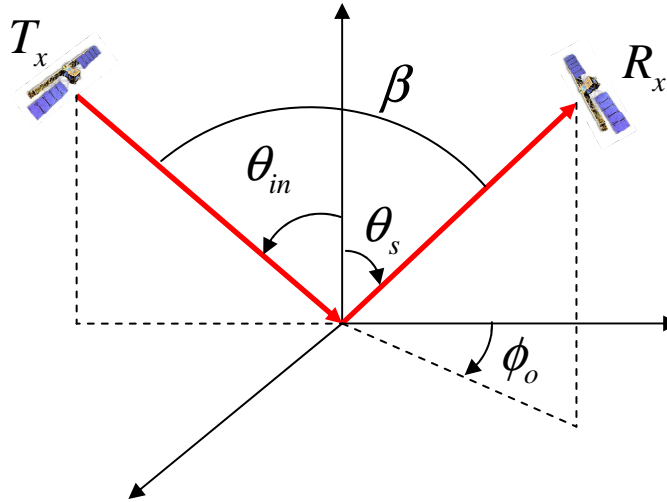


FIGURE 5.20 Bistatic out of plane geometry.

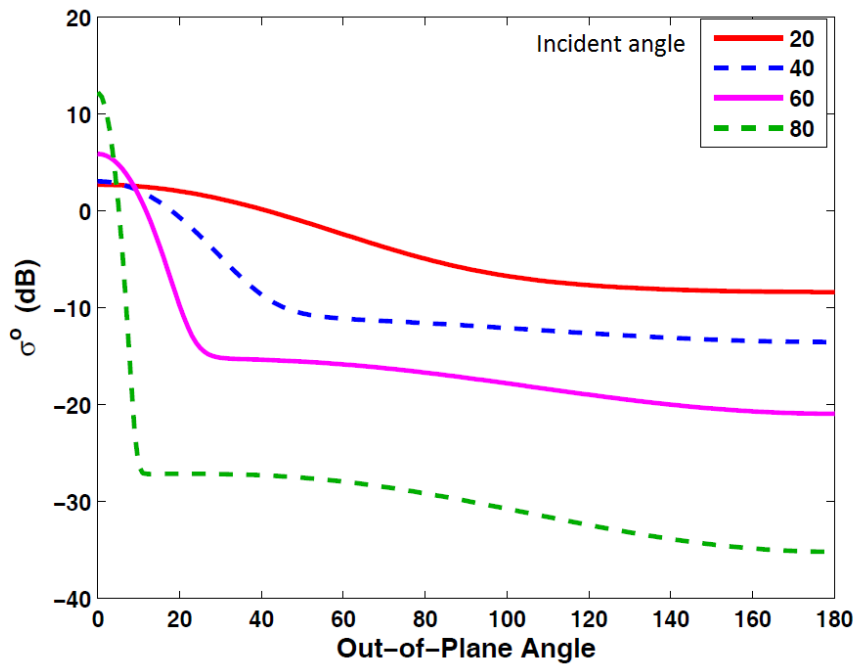


FIGURE 5.21 Scattering behaviour of desert areas vs. out-of-plane angle at different incident angles [142].

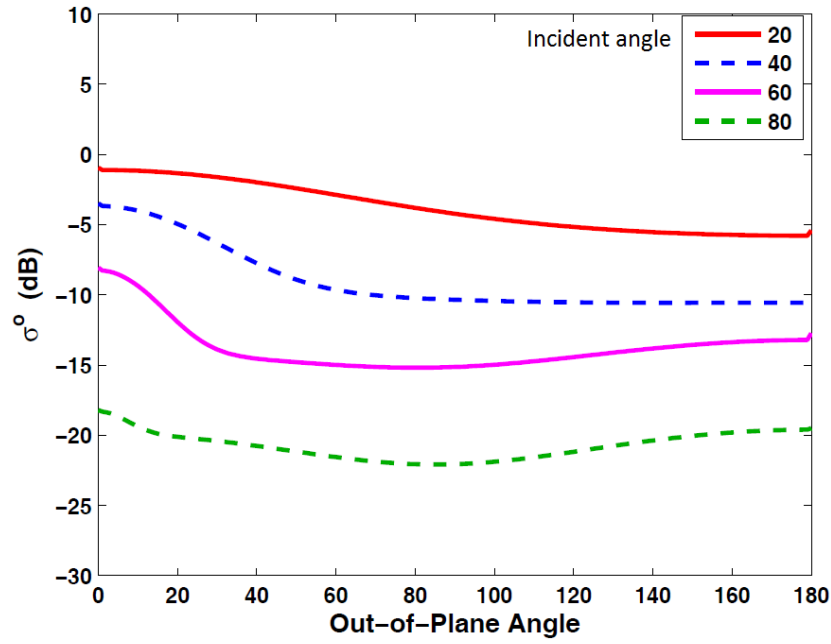


FIGURE 5.22 Scattering behaviour of rangeland vs. out-of-plane angle at different incident angles [142].

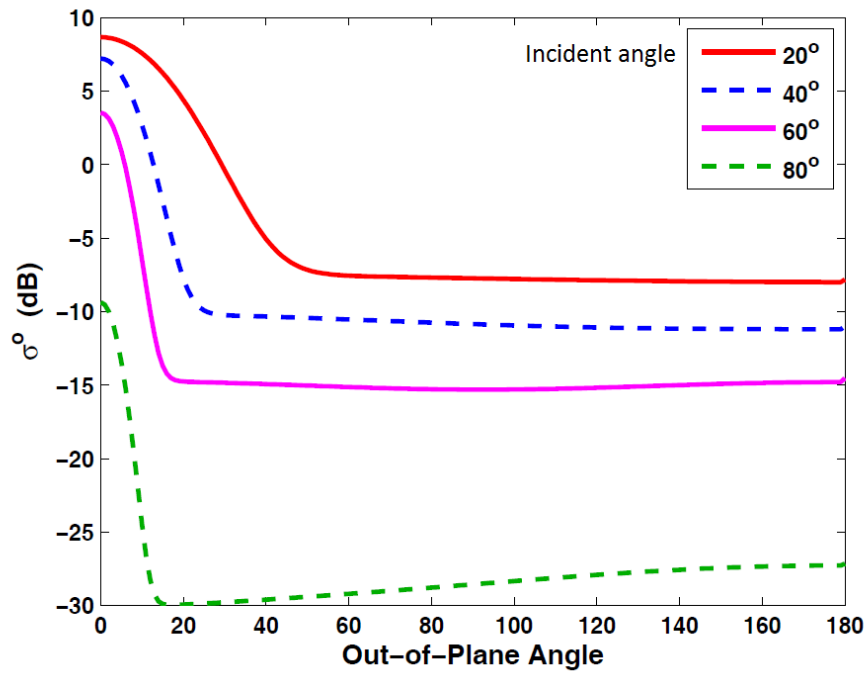


FIGURE 5.23 Scattering behaviour of snow vs. out-of-plane angle at different incident angles [142].

Additionally, the scattering properties of different types of surfaces at incident angle of 60° are plotted in Figure 5.24. As seen, sea surface present low scattering response for large out-of-plane angles, which is the case of the proposed configuration, and, therefore, it will

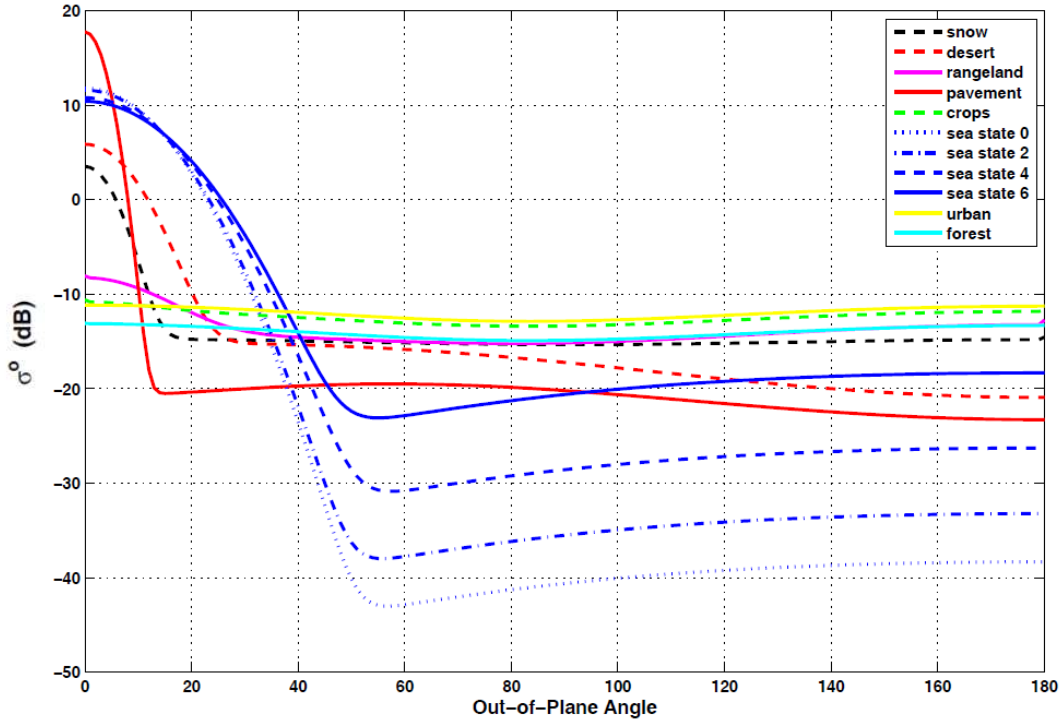


FIGURE 5.24 Scattering behaviour vs. out-of-plane angle for different surfaces with incidence angle of 60 degrees [142].

not be a target of interest for this system. Furthermore, the low coherence of the sea surface makes impossible to image it with integration times of several hours as proposed in this GEOSAR configuration. On the other hand, for land surfaces, the backscattering coefficient varies from -10 dB to -20 dB and it is almost constant for out-of-plane angles going from 40 to 180 degrees. It is important to highlight the response of urban areas with a constant backscattering response around -11 dB since it is expected that they could be interesting regions for GEOSAR acquisition due to their high backscattering response and temporal coherence.

5.3.3 Timing and PRF selection for bistatic acquisition

In this section, the particularities on timing and PRF selection in a bistatic acquisition and the necessary changes with respect to monostatic analysis presented in section 3.3 will be studied. As shown for the monostatic case, the PRF must be selected in order to avoid the transmission and the nadir interferences. In case of open bistatic configuration, with separate transmitting and receiving satellites, the transmission interference could be avoided if the transmitter-receiver direct link is properly isolated. However, for closer bistatic formations, the transmission interferences could be important if no isolation is assured between the transmitting and receiving antennas. On the other hand, in case of bistatic configurations, the nadir point under the satellites will not be a problem but, on the other hand, there will be a point between both satellites where the specular reflection

could result in a strong received echo.

Therefore, regarding the transmission interferences in bistatic case, the equations (3.13), (3.14) and (3.15) must be re-written taking into account the transmitter-scene and receiver-scene slant ranges. Additionally, the receiver will see the transmission events an instant later. So, the transmitter-receiver direct link delay must be taken into account in the PRF selection formulas:

$$Frac\left(\left(R_{1T} + R_{1R}\right)PRF / c\right) / PRF + R_{T-R} / c > \tau_0 + \tau_{RP} \quad (5.16)$$

$$Frac\left(\left(R_{NT} + R_{NR}\right)PRF / c\right) / PRF + R_{T-R} / c < \frac{1}{PRF} - \tau_{RP} \quad (5.17)$$

$$Int\left(\left(R_{NT} + R_{NR}\right)PRF / c\right) = Int\left(\left(R_{1T} + R_{1R}\right)PRF / c\right) \quad (5.18)$$

Taking into account the low PRFs that are considered for GEOSAR acquisition, the direct link delay will be negligible compared with the pulse duration (τ_0) and $1 / PRF$ terms of equations (5.16) and (5.17). Furthermore, the slant range differences between the transmitter-scene and scene-receiver links will be small, reducing the close bistatic PRF selection problem to the monostatic formulas given by (3.13), (3.14) and (3.15). As mentioned, for open bistatic formations or strong isolation between antennas, the transmission interferences could be ignored.

On the other hand, we must be sure that the nadir return does not interfere to the reception windows. For bistatic GEOSAR with two satellites in a quasi-equatorial orbits, the potential point that could mask the reception of echoes from the scene will be the one placed at the equator between both satellites instead of the sub-satellite points. This point can produce a strong echo due to the specular reflection and, therefore, it can be treated as the nadir echo return in the monostatic case. In order to see the importance of the return coming from this point, the results presented in section 5.3.2 for the bistatic clutter response can be compared with the ones expected from the specular reflexion. So, considering the two satellites in the equatorial plane (orbits with small inclinations have been considered all along this thesis) and the central point between them in the Equator, it will correspond to an in-plane bistatic acquisition ($\phi_o = 0^\circ$) with $\theta_{in} = \theta_s$, taking the scheme presented in Figure 5.2.

Taking the results from [142], the bistatic backscattering behaviour of the specular reflectivity point can be computed in function of the bistatic angle between the satellites. The in-plane bistatic reflectivity for different types of surfaces is presented in Figure 5.25 in function of the bistatic angles between satellites. If the results presented in Figure 5.25 are compared with the ones obtained for the out-of-plane configurations (Figure 5.21–Figure 5.24), 15-30 dB higher backscattering coefficient is obtained from the specular reflection point. Therefore, if the antenna diagram does not reduce the contribution of this

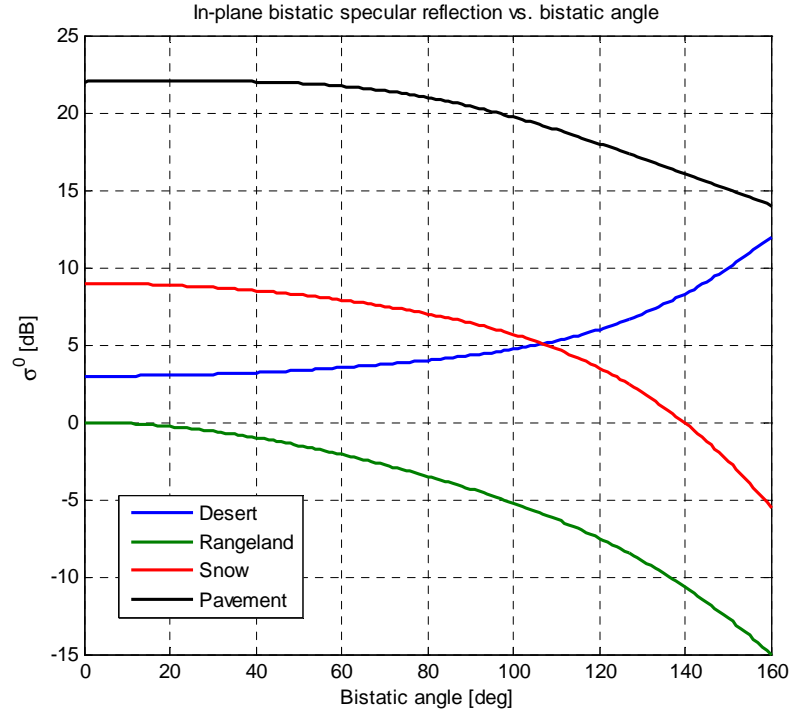


FIGURE 5.25 In-plane backscattering coefficients in bistatic SAR for different surfaces.

point, we must assure that it will not interfere to the desired echoes by proper selection of the PRF, following the monostatic nadir return restrictions, equations (3.16) and (3.17), but changing the term $2h / c$ by the corresponding slant range to the undesired point $2R_{NP} / c$.

In SAR systems, it is common to use the diamond diagram to identify the zones interfered by the transmission events or nadir returns. In the diamond diagram, the interfered zones are plotted in a PRF-incidence angle diagram. In GEOSAR, the range of selectable PRFs will be lower in order to cover a larger area and avoid range ambiguities. As mentioned before, for close bistatic GEOSAR formations, the monostatic PRF selection restrictions will be still valid.

So, similar results than in monostatic case will be obtained for close bistatic GEOSAR acquisition. In Figure 5.26, the diamond diagram obtained for a duty cycle of 20% is presented. It is important to remember that, even though the duty cycle could be increase near the 50%, it will reduce the PRF selection tolerance as studied in section 3.3. In Figure 5.26, the desired system coverage (incidence angles from 40° to 70°) has been plotted. So, taking into account the Doppler bandwidth obtained for L-band wide beam acquisition (around 1.5 Hz) and Ku-band SPOT beam acquisition (around 2.5 Hz), the minimum PRF that should be considered in each case have been plotted in Figure 5.26.

Such low PRFs may not be feasible with current Travelling Wave Tube (TWT) technology and, therefore, minimum PRFs around 40-50 Hz should be considered. This would not be a

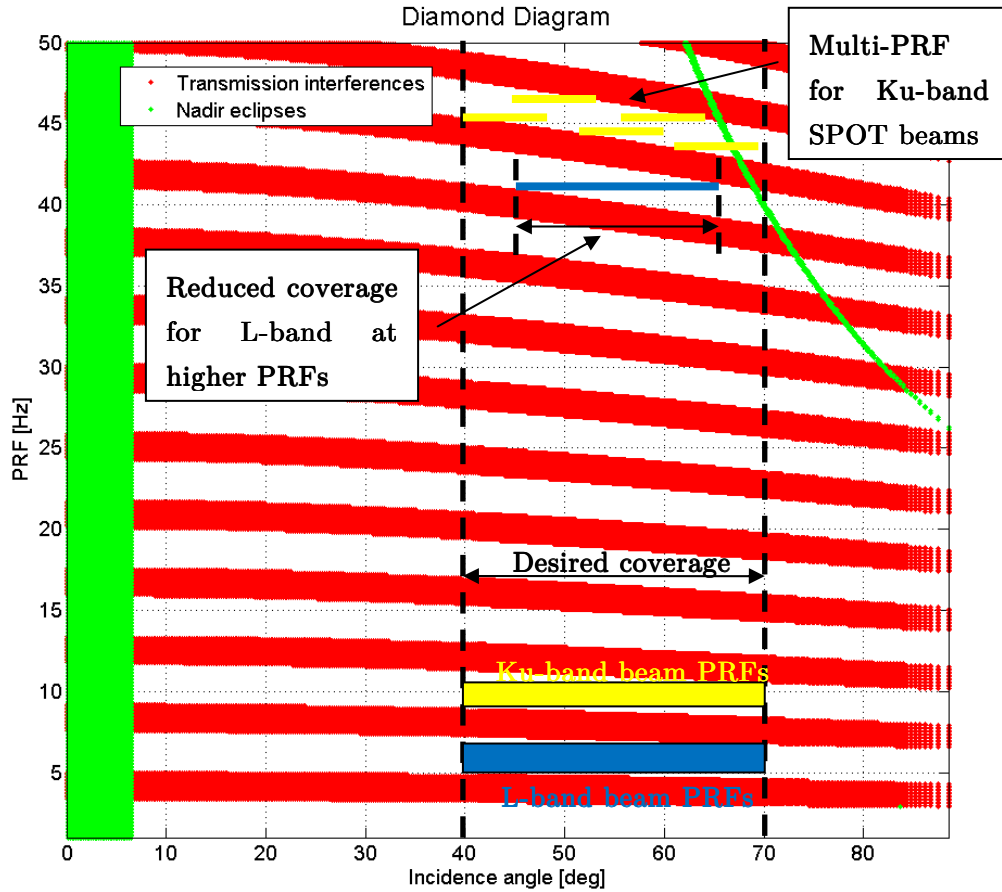


FIGURE 5.26 Diamond diagram for GEOSAR with a 20% duty cycle.

problem for Ku-band SPOT beams, since the PRF could be switched depending on the range of incidence angle illuminated in each acquisition. However, for wide coverage L-band beam the coverage should be reduced since it is not possible to fit the echoes from the scene in between two consecutive transmitted pulses at such range of PRF.

As seen in Figure 5.26, the first nadir interference will be present working at PRF around 40-50 Hz. However, as explained in section 3.3, it could be range compressed and, therefore, just a few pixels on the image will be interfered by this undesired return.

The diamond diagram is frequency independent. Therefore, the same diagrams would be obtained for the last alternative considered working at C-band. However, the PRF should satisfy the Nyquist requirements considering the Doppler bandwidth obtained in for this band. Therefore, a larger PRF above 10 Hz should be considered for wide coverage beam while a PRF above 2 Hz should be enough for SPOT beam working at L-band.

On the other hand, the transmission interferences may be ignored if the satellites are far enough or if the isolation between the transmitting and receiving antenna is high. In this case, only the nadir (or specular reflection point) interferences should be taken into

account. Thus, a wider range of PRFs could be selected for these configurations.

In order to know if the transmission interferences are important in a bistatic GEOSAR configuration, the power backscattered from the scene that arrives to the receiver must be compared with the power coming directly from the transmitter. As explained in section 3.5, the power received from a single pulse will be:

$$P_{echo} = \frac{P_t G_t^0 G_r^0 \sigma_0 \rho_{az} \rho_{gr} \lambda^2}{(4\pi)^3 R_{St}^2 R_{Sr}^2 L_T} \quad (5.19)$$

On the other hand, the power received from the transmitter-receiver direct link can be obtained from the transmission equation as [69]:

$$P_{T-R} = \frac{P_t G_t^\varphi G_r^\varphi}{L_{T-R}} \left(\frac{\lambda}{4\pi R_{T-R}} \right)^2 \quad (5.20)$$

where G_t^φ is the transmission antenna gain in the direction of the receiver and G_r^φ is the receiver antenna gain in the direction of the transmitter. R_{T-R} corresponds to the transmitter receiver direct link range. So, the coupling of the power received from the direct link and the backscattered one can be obtained as:

$$C_{T-R} = \frac{P_{T-R}}{P_{echo}} = \frac{\frac{P_t G_t^\varphi G_r^\varphi}{L_{T-R}} \left(\frac{\lambda}{4\pi R_{T-R}} \right)^2}{\frac{P_t G_t^0 G_r^0 \sigma_0 \rho_{az} \rho_{gr} \lambda^2}{(4\pi)^3 R_{St}^2 R_{Sr}^2 L_T}} = \frac{4\pi \bar{G}_t^\varphi \bar{G}_r^\varphi R_{St}^2 R_{Sr}^2 L_T}{R_{T-R} \sigma_0 \rho_{az} \rho_{gr} L_{T-R}} \quad (5.21)$$

being \bar{G}_t^φ and \bar{G}_r^φ the relative transmitting and receiving antenna gains from the maximum gains G_t^0 and G_r^0 , respectively. Therefore, given a coupling restriction, the maximum value of the $\bar{G}_t^\varphi \bar{G}_r^\varphi$ product should be:

$$\bar{G}_t^\varphi [dB] + \bar{G}_r^\varphi [dB] = C_{T-R} [dB] + 10 \log \left(\frac{R_{T-R} \sigma_0 \rho_{az} \rho_{gr} L_{T-R}}{4\pi R_{St}^2 R_{Sr}^2 L_T} \right) \quad (5.22)$$

As an example, let us consider a maximum coupling of -10 dB between the direct link signal and the backscattered in the scene. Taking transmitting and receiving slant ranges of 37.000 Km, a backscattering coefficient of -10 dB and the resolution cells of 15 x 15 m for Ku-band and 1 x 1 Km for L-band, the transmitter-receiver antenna isolation requirements in function of the bistatic angle shown in Figure 5.27 are obtained.

As seen, higher isolation is required at Ku-band due to the lower backscattered power per echo as a result of the smaller resolution cell. Therefore, if the product of the relative transmitting and receiving antenna gains is below the curves presented in Figure 5.27, the

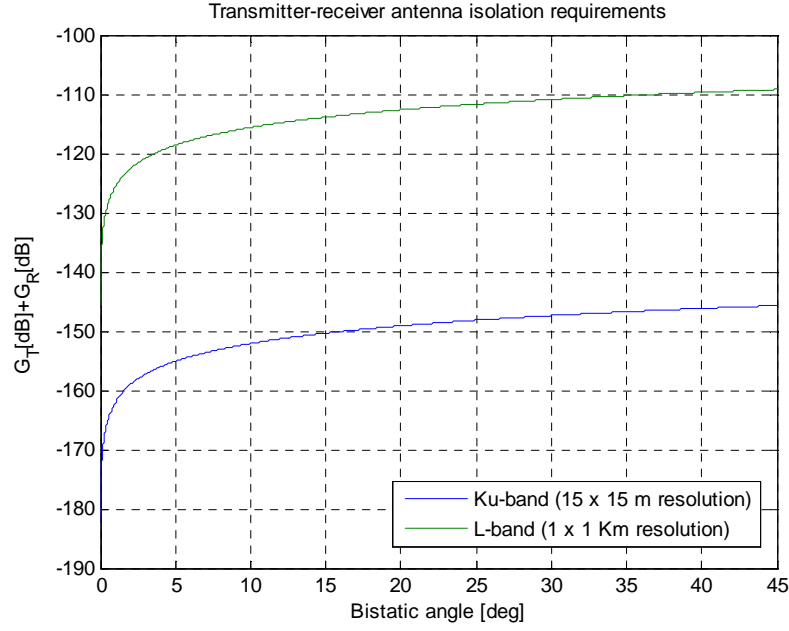


FIGURE 5.27 Transmitter-receiver antenna decoupling requirements to avoid the transmission interferences.

transmission interferences could be ignored and, as a consequence, the duty cycle could be increased up to 100% making the PRF selection easier than in the analysis presented above. Regarding the C-band beam, similar results will be obtained if the same resolution cells are considered.

5.3.4 Power requirements

The power link budget of a bistatic SAR acquisition will not vary significantly from the monostatic analysis presented in section 3.5. In this section, the power link budget of a bistatic GEOSAR is presented taking the mission parameters obtained in the geometric analysis (resolution and integration time) in section 5.2, and in the antenna design presented in section 5.3.1 for this particular mission. Other parameters such as duty cycle, noise parameters, propagation and system losses and target surface reflectivity have been discussed all along the section 5.3. So, the minimum power to reach the SNR requirements will be analysed in both configurations: low-resolution wide swath at L-band and high resolution spot beam at Ku-band. Additionally, the C-band results in both cases will be also computed.

Therefore, the system power requirements can be obtained from the desired SNR rearranging the equation (3.35) as:

$$P_{t_{\min}} = SNR_{0_{\min}} \frac{(4\pi)^3 R_{St}^2 R_{Sr}^2 L_T k T_0 F_n}{G_t G_r \sigma_0 \rho_{az} \rho_{gr} \lambda^2 DC T_i} \quad (5.23)$$

So, in Table 5.3, the parameters obtained from the geometric and radiometric analysis are presented for both configurations. A resolution cell of 1 by 1 Km has been considered for L-band acquisition while 15 by 15 m have been taken for Ku-band. A minimum SNR of 10 dB has been defined to obtain the transmitted power requirements of the system.

The power requirements for the L-band and Ku-band acquisitions are given in the last two rows of Table 5.3. As seen, for L-band beam, a transmitted peak power of 20.85 dBW (15.62 dBW mean power) is required to reach 10 dB of SNR. On the other hand, Ku-band acquisition with the input parameters considered in Table 5.3 is too demanding in terms of power. So, a transmitted peak power of 42.23 dBW (37.00 dBW mean power) is necessary to reach the proposed minimum SNR.

Therefore, in order to reduce the power requirements for Ku-band acquisition, a reduction of the system coverage for this band is proposed. Using a more directive antenna, the transmitted power could be decreased preserving the desired SNR. So, swath coverage of 350 Km will be considered for Ku-band acquisition. Repeating the antenna analysis of section 3.1 with this new parameter, the results presented in Table 5.4 are obtained.

	L-Band beam	Ku-Band beam
Transmitter antenna gain	31.6 dB	44.9 dB
Receiver antenna gain	31.6 dB	44.9 dB
Backscattering coefficient	~ -10 dB	~ -10 dB
Resolution cell	1 x 1 Km	15 x 15 m
Wavelength	0.185 m	0.0174 m
Duty cycle	0.3 (1.0 if isolation between antennas is assured)	0.3 (1.0 if isolation between antennas is assured)
Integration time	30 minutes	4 hours
Transmitting slant range	~ 37.000 Km	~ 37.000 Km
Receiving slant range	~ 37.000 Km	~ 37.000 Km
Propagation losses	3 dB	3 dB
Receiver noise factor	2 dB	2 dB
SNR	> 10 dB	> 10 dB
Required transmitted peak power	20.85 dBW	42.23 dBW
Required transmitted mean power	15.62 dBW	37.00 dBW

TABLE 5.3. Transmitted power requirements to reach a minimum SNR of 10 dB in L-band and Ku-band acquisitions.

Frequency	17.25 GHz
Wavelength	0.0174 m
Total efficiency	0.65
Desired coverage	350 Km
Antenna beamwidth	0.53 deg
Antenna diameter	2.20 m
Antenna gain	50.1 dB
Required transmitted peak power	31.83 dBW
Required transmitted mean power	26.60 dBW

TABLE 5.4. Antenna parameters requirements for Ku-band spot beam with 350 Km coverage.

As seen, a 5.2 dB antenna gain raise is obtained for both antennas. Therefore, the required peak power to reach the 10 dB SNR would decrease to 31.83 dBW (1.52 KW). This corresponds to a mean transmitted power of 26.60 dBW (457 W) which is more reasonable for a SAR system.

On the other hand, the power link budgets considering a C-band acquisition for both cases are presented. For the power link budget, the same parameters that the ones used in Table 5.3 have been considered re-computing the parameters that would change with a different transmitted frequency. This is the case of the resolution cell size. Considering the analysis presented in section 5.2 an azimuth resolution of around 300 m is expected for C-band considering 30 min of integration with an orbital eccentricity of 0.0004. On the other hand, an along-track resolution around 30 meters will be obtained by considering 4 hours of integration with the same orbital configuration. The power requirements obtained for C-band acquisitions with these new parameters are summarized in Table 5.5.

In that case, the power requirements obtained for SPOT beam are not too stringent as in the Ku-band. On the other hand, working at C-band for the wide beam will results in too demanding power requirements. Therefore, the 3000 km coverage in this case should be reduced in order to reduce the necessary power to reach the 10 dB SNR. In this case, if the transmitting and receiving antenna gains are increased 5 dB, the resultant antenna beamwidth is reduced to 2.5 degrees at -3dB cut. It results in a swath coverage of 1600 Km instead of the 3000 km swath initially desired. With the reduced swath, a required transmitted mean power of 26.47 dBW would be necessary.

Therefore, the power requirements results show that L-band is a good choice for wide beam acquisition with coverage around 3000 km and resolutions around 1 by 1 km. On the other hand, Ku-band SPOT beam coverage should be reduced to 350 km to reach the desired

	C-Band wide beam	C-Band SPOT beam
Trans. antenna gain	31.6 dB	44.9 dB
Receiver antenna gain	31.6 dB	44.9 dB
Backscattering coefficient	~ -10 dB	~ -10 dB
Resolution cell	300 x 300 m	30 x 30 m
Wavelength	0.056 m	0.056 m
Duty cycle	0.3 (1.0 if isolation between antennas is assured)	0.3 (1.0 if isolation between antennas is assured)
Integration time	30 minutes	4 hours
Transmitting slant range	~ 37.000 Km	~ 37.000 Km
Receiving slant range	~ 37.000 Km	~ 37.000 Km
Propagation losses	3 dB	3 dB
Receiver noise factor	2 dB	2 dB
SNR	> 10 dB	> 10 dB
Required transmitted peak power	41.69 dBW	26.07 dBW
Required transmitted mean power	36.47 dBW	20.84 dBW

TABLE 5.5. Transmitted power requirements to reach a minimum SNR of 10 dB in C-band for wide coverage and SPOT beams.

SNR with a reasonable mean transmitted power. Alternatively, if SPOT beam coverage of 650 km, as initially described, is desired, C-band would be a good choice in that case obtaining a coarser resolution image (30-45 meters) but using lower transmitted power.

5.4 Bistatic GEOSAR synchronisation

5.4.1 Oscillators analysis for bistatic GEOSAR

Synchronization is a key aspect for any bistatic system. In the bistatic GEOSAR systems the transmitter and the receiver operate from different satellites requiring time, frequency and phase synchronization during the raw data acquisition. In the bistatic GEOSAR there are two independent oscillator chains, one for each satellite, taking into account the required acquisition times, in the order of hours, the synchronization between receiver and transmitter will be very demanding. [121][122][123].

Not only the bistatic design will have a demanding synchronisation step, the stability requirements of a monostatic GEOSAR will be really stringent since to form a distortion-free synthetic aperture, the cumulated phase drift of the oscillators of the transmitter and

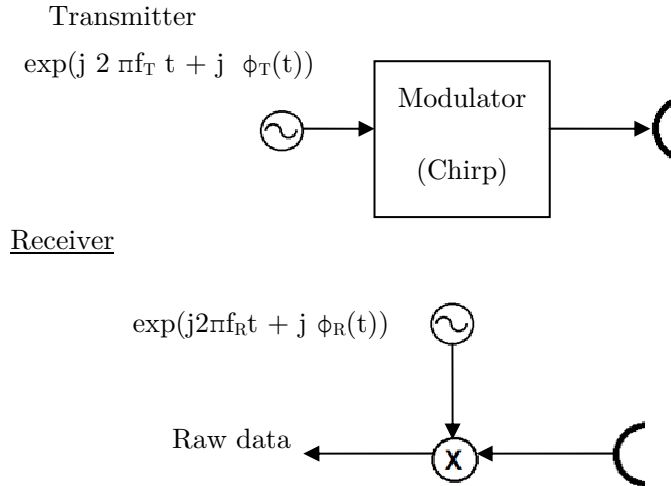


FIGURE 5.28 Simplified block diagram of the transmitter and receiver of a bistatic Radar.

receiver chains must be small during the whole data acquisition. This is usually achieved by using an ultra-stable master clock as the reference for all oscillators of the radar subsystems including those providing the PRF timing and echo sampling in the receiver. In the bistatic case the same degree of coherence must be achieved taking into account the need to include an additional master oscillator to maintain approximately the same time, frequency and phase references in both transmitter and receiver chains.

The simplified block diagram of bistatic radar can be seen in Figure 5.28 and a generic SAR processor able to focus the received echo raw data providing SAR images is shown Figure 5.29.

Taking into account the fact that the master clock is used as a reference of time, frequency and phase in the transmitter and receiver radar subsystems, four different direct or primary errors have been identified.

- Echo sampling frequency errors produce a distance determination error in the slant range axis of the SAR image. Additionally, if the sampling frequency errors produce a substantial phase error in the received pulses the range compression filter will result in amplitude loss and range resolution degradation.
- Transmitted pulse time errors translate directly on an echo delay estimation error and the subsequent slant range error.
- Carrier frequency errors produce a phase drift along the synthetic aperture resulting in a shift in the azimuth compression and a phase error in the image if small error is considered. The carrier frequency error is also affected by PRF ambiguity and loss of amplitude when the signal becomes substantially mismatched with respect

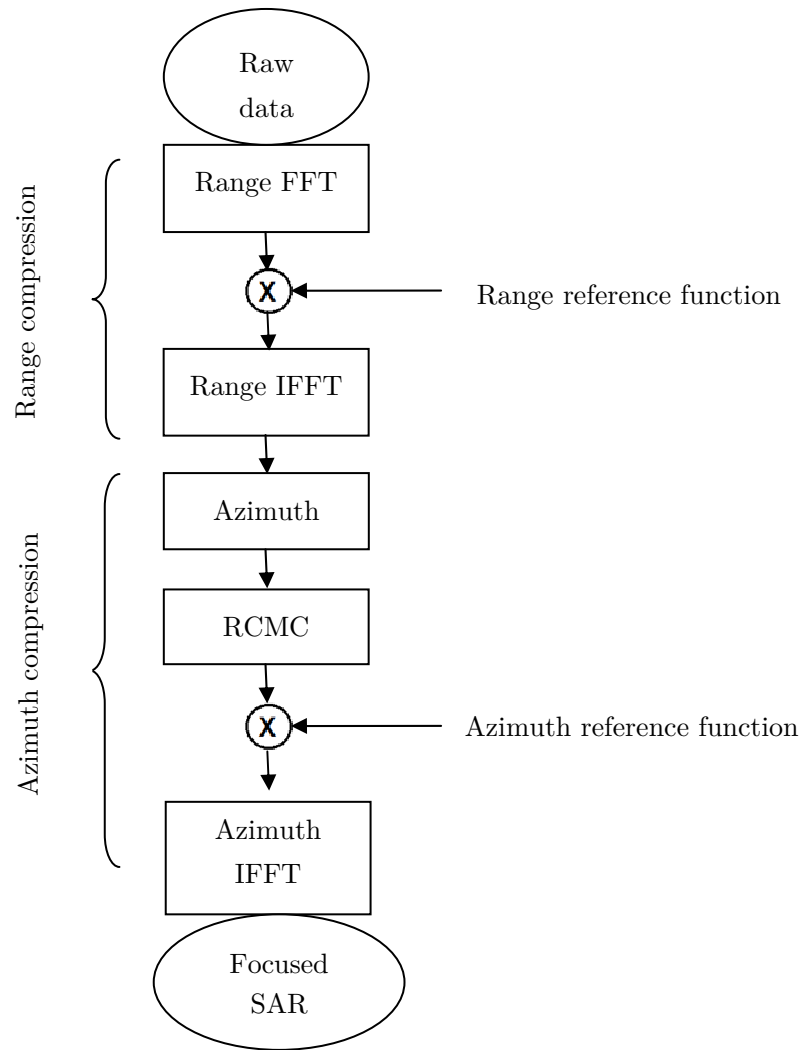


FIGURE 5.29 Simplified block diagram of a SAR processor based on Range & Azimuth compression which can be used to focus bistatic radar raw data.

- the azimuth compression filter. In case of larger frequency errors and longer transmitted chirp pulses, a substantial phase change within the pulse occurs producing a slant range displacement and loss of amplitude due to range compression filter mismatch.
- Phase noise errors. Even in the case of correct time and frequency synchronization phase noise errors will degrade the synthetic aperture coherence resulting in a loss of amplitude, azimuth resolution and increased side lobes.

Thus the possible impacts of the synchronization errors, when imaging a point scatterer in the scene, are one or more of the following:

- Displacement of the focused main lobe in range and/or azimuth
- Amplitude loss of the main lobe
- Spatial resolution loss in range and/or azimuth
- Rising of side lobes

Reconstructed phase errors will affect the estimation of desired phase dependent parameters like the Atmospheric Phase Screen, Earth surface deformation, Change detection, etc.

Additionally, SAR processing in GEOSAR can be considered a 2D correlation of the raw data set with a range-azimuth variant reference function and this implies mutual interaction between range and azimuth compression. For example range compression errors causing range shifts or range defocusing will degrade subsequent azimuth focusing in a Range & Azimuth compression Algorithm. This means that primary errors in range or azimuth will have secondary impacts on the other image domain that should be accounted for analytically or by computer simulations in the synchronization error analysis.

The most relevant results obtained are presented next:

Echo sampling frequency errors: imposing a maximum slant range error equal to 10% of the range resolution, a frequency accuracy requirement of $4 \cdot 10^{-8}$ at Ku-band with a maximum error of 1.5 m and $2.62 \cdot 10^{-6}$ at L-band with a maximum error of 100 m.

Transmitted pulse time errors: a maximum error of 10 ns in the instant of transmission results in a distance error below 1.5 m which may be tolerable with a slant range resolution of 15 m, working at Ku-band. In L-band, less stringent requirements are obtained. In this case, a delay of 0.67 s would produce an error impact of 100 m in slant range corresponding to a 10% of the range resolution in L-band acquisition.

Carrier frequency errors: a maximum tolerable azimuth displacement of 10% of the azimuth resolution results in a frequency stability of $8 \cdot 10^{-16}$ in Ku-band and $5.5 \cdot 10^{-14}$ in L-band.

The stability of a free running oscillator should be $9.67 \cdot 10^{-10}$ in Ku-band and $1.03 \cdot 10^{-8}$ in L-band considering a maximum tolerable error imposing a maximum range displacement of the compressed signal main lobe below 10% of the pulse time resolution.

The slant range displacement can be considered negligible if the previous stabilities of the oscillators are considered.

Phase noise errors: as expected the inherent cumulative phase error of the random walk model results in larger focusing degradation compared to the Gaussian model.

5.4.2 *Bistatic synchronisation strategies*

The azimuth focusing requires knowing with reasonable precision the phase change due to propagation of the radar signal, from transmitter to each ground resolution cell and back to receiver. In an ideal situation we could obtain this information from a perfect knowledge of the satellite track, oscillators phase, APS, etc. Our role in this section is to propose solutions that could work in a real mission with limited accuracy of the orbit, realistic (high grade) oscillators, APS, etc.

In order to avoid phase errors due to transmitter and receiver oscillators and align the receiver acquisition window with the transmitted pulses, a synchronisation method is needed between transmitter and receiver. In this analysis, two possibilities will be presented for the synchronisation link design: a dedicated transmitter-receiver link or on-ground synchronisation links. The two synchronisation schemes are presented in Figure 5.30. As seen in Figure 5.30 a), the oscillators' information is exchanged directly between the transmitter and the receiver which periodically send signals to the other satellite. In this case, different strategies may be considered such as continuous duplex link, pulsed duplex/alternate, etc. [124]. On the other hand, considering on-ground stations in the synchronisation link (Figure 5.30 b)), the signals are sent to on-ground stations which must be in the acquisition illuminated area if the same antennas are used for SAR imaging and for transmitting the synchronisation signals. A simple approach for ground synchronisation is based on ground Active Radar Calibrators (ARC) able to produce high level echoes of the radar illumination. The ground calibrators provide replicas of the illuminating pulses with a stable gain and phase delay that can be processed in the mission ground segment. In this way the ground calibrators' pulses can be identified after raw-data pulse compression but before the synthetic aperture integration to compensate for the oscillators phase shifts. The pros and cons of each design are presented next.

5.4.2.1 Direct link synchronisation design

Let us consider the direct link between the transmitter and the receiver. In this case, the synchronisation is usually established through a bidirectional link between transmitter and receiver [124]. The main advantage of this configuration is that the signals do not have to travel along the atmosphere, which could add extra temporal and spatial varying phase noise to the oscillator synchronism signalling. The transmitted pulses (PRF) time reference can be included by using an additional modulation on the reference signal sent from the transmitter satellite.

However, two dedicated antennas will be necessary in the link design. Alternatively, the side-lobes of the primary transmitting and receiving antennas of the satellites could be considered, but the performance of the synchronisation link could be affected by the gain uncertainty in the side-lobe region of the antenna pattern. Therefore, in this analysis we will focus in the use of two independent antennas for synchronisation.

In order to have an idea of the antenna size and power requirement to be used in this case, a preliminary power link budget is presented next. So, the received power at satellite j coming from satellite i (being i the transmitting or receiving satellite and j the other one) may be obtained as:

$$P_{Rj} = \frac{P_{Ti} G_{Ti} G_{Rj} \lambda^2}{(4\pi r_{ij})^2 L_{ij}} \quad (5.24)$$

being λ the wavelength of the transmitted signal, $G_{Ti} G_{Rj}$ the transmitting and receiving antenna gains, P_{Ti} the transmitted power and r_{ij} the distance between the receiver and the transmitter. Therefore, the SNR of the synchronisation signals will be:

$$SNR_j = \frac{P_{Rj}}{K_B [T_a + (F_j - 1)T_0] B} \quad (5.25)$$

where $K_B = 1.38 \cdot 10^{-23}$ J/K is the Boltzmann constant, F_j the receiver noise factor, T_0 the reference temperature 290 K, T_a the antenna temperature and B the transmitted signal bandwidth. Therefore, if the same antenna is considered for the transmission and reception, the transmitted power requirements can be related to SNR as:

$$P_{Ti} = \frac{(4\pi r_{ij})^2}{G^2 \lambda^2} SNR_j K_B [T_a + (F_j - 1)T_0] B L_{ij} \quad (5.26)$$

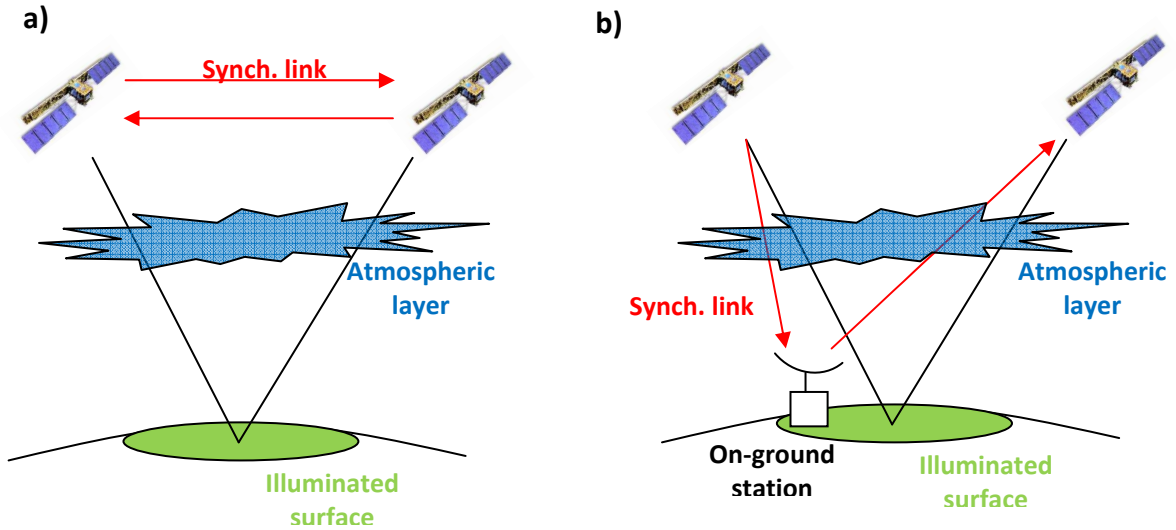


FIGURE 5.30 a) Direct synchronisation link and b) synchronisation link using on-ground station.

So, the transmitted power requirements for synchronization will depend on a large number of factors such as the desired oscillator phase accuracy (given by the noise fluctuations represented by the SNR at the receiver), the selected bistatic formation (close/open bistatic GEOSAR will affect the distance between satellites), the receiver noise level and the antenna gains. For the synchronisation link, smaller antennas may be considered since the transmitter-receiver path length is much shorter and one-way path must be only considered. High antenna gain may be obtained by using higher frequencies (20-40 GHz) for the synchronisation link.

Let us consider an example in order to see the order of magnitude of power requirements for the transmission link. A high frequency carrier of 30 GHz is considered for the synchronisation link. On the other hand, the antenna gain of a square aperture (horn or patch antenna) of side length D can be obtained as:

$$G = \frac{4\pi}{\lambda^2} A_{eff} = \frac{4\pi}{\lambda^2} A_{geo} \eta_t = \frac{4\pi D^2 \eta_t}{\lambda^2} \frac{(4\pi r_{ij})^2}{G^2 \lambda^2} \quad (5.27)$$

Where η_t is the antenna efficiency including the illumination efficiency and ohmic losses. If an antenna of side length $D = 16$ cm and antenna efficiency of 0.6 are considered, an antenna gain of 32.86 dB is obtained. Firstly, a close bistatic formation will be studied. In this case, a nominal longitude separation between satellites under 1 degree is taken. This angular separation results in a maximum distance between satellites under 750 Km. In the synchronisation link, taking into account that ultra-stable oscillators phase errors have decorrelation times in the order of seconds to minutes [125] a narrow bandwidth modulation will be used which will result in a small noise bandwidth. As an example, a 50 KHz bandwidth has been taken. Therefore, if a SNR of 20 dB is desired, the required transmitting peak power for synchronisation in the close bistatic formation will be around $P_T = 14.9$ dBm assuming a noise factor $F = 5$ dB, a conservative antenna temperature $T_a = T_0$ and link system losses of $L = 3$ dB.

In the case of an open bistatic formation, the free space path loss will increase significantly. If a maximum separation between satellite nominal longitudes of 20 degrees is considered, the distance between satellites will be 14643 Km. Taking the parameters of the previous example, to preserve a signal to noise ratio of 20 dB, the transmitted power should be increased to +20 dBm and the gain of the antenna increased to 43.22 dB which can be obtained with a parabolic reflector of 55 cm diameter with an efficiency of 0.7 (including illumination efficiency and ohmic losses).

This scheme would increase the satellites complexity since a new antenna and a transmission and reception payloads for the direct link should be considered. Furthermore, the orbit differences between transmitter and receiver satellites would introduce phase errors that should be determined with a bidirectional link and compensated.

5.4.2.2 On-ground synchronisation design

On the other hand, an on-ground synchronisation link could be also considered. In this case, the L-band radar transmitted signal will be also considered for synchronisation. On ground Active Radar Calibrators (ARC) [126][127][128] should be considered since high RCS will be necessary to estimate the azimuth reference function phase with enough accuracy before azimuth compression. The requirements and design of these calibrators are studied along this section. The received signal phase will be the sum of a large number of terms including satellites slant range affected by orbital uncertainties, clock phase drifts of transmitter and receiver satellites, the phase changes introduced by the Atmospheric Phase Screen (APS), the phase shift introduced by the ARC delay and antenna phase centre uncertainties and the phase errors introduced by noise and clutter interferences:

$$\phi_T = \frac{2\pi}{\lambda}(R_T + R_R) + \phi_{Clk_T} - \phi_{Clk_R} + \Delta\phi_{ARC} + \Delta\phi_{APS} + \Delta\phi_{Clutter} + \Delta\phi_{Noise} \quad (5.28)$$

In the following sections, the phase terms are analysed in order to determine their impact on the signal phase for clock and orbital synchronisation.

5.4.3 *On-ground synchronisation errors*

5.4.3.1 Acquisition window synchronisation

One of the problems of using on ground calibrators is that the receiver will not have precise information of the transmission time instants. However, even in the case of not having a direct link synchronisation subsystem, the receiver will be able to detect the uncompressed transmitted pulses given the limited isolation between transmitter and receiver antennas as analysed in Section 5.3.3. Thus, when the receiver detects the transmitted pulses, the reception window can be set, knowing the satellites positions and the expected bistatic delay of echoes, in order to centre the reception windows at the correct time instant.

Using appropriate guard times at the beginning and end of acquisition windows, with state of the art USO stability, the PRF accuracy should be enough to keep the acquisition windows alignment during the data take after initial setting obtained from direct of transmitted pulses detection. This offset delay from transmitted pulse leading edge can be calculated by the ground segment and included in the acquisition parameters telemetry.

5.4.3.2 Noise and clutter phase impact

The noise and clutter will add random variations to the received signals that could deteriorate the clock phase estimation and the orbital control. As mentioned before, we propose a set of calibrators to track the radar oscillators phase changes. Therefore, in this

section, the RCS requirements of this calibrations as well as the optimum integration time for synchronisation will be analysed in order to minimise the noise and clutter impacts on the total phase error budget. Additionally, a preliminary calibrator design to reach the desired RCS will be presented.

Calibrators RCS requirements and calibration integration time

An important aspect to take into account in the calibration link design is the minimum RCS of the calibrators to assure the correct phase estimation of the master clock drift and orbital errors. The signal received from the calibrator will be affected by noise, clutter and clock phase variations with time. Therefore, the calibrator, as well as the calibration integration time, must be optimized to reduce as much as possible the phase fluctuations of the received signal in order to have a correct estimation of the clock phase. Since high RCS will be necessary to overcome the large distances to the scene and the short integration times for calibrators, active reflectors (two antennas + amplifier) will be considered in this analysis.

A higher RCS of the calibrator will result in better phase accuracy but, at the same time, larger antennas and higher amplification to achieve such RCS. On the other hand, regarding the integration time for calibration, longer acquisitions would reduce the phase fluctuations produced by the noise. However, the temporal resolution to determine the phase fluctuations would be reduced, increasing the phase errors due to clock instabilities. Therefore, an optimum integration time for calibration must be computed.

The first term affecting the received signal phase studied in this section will be the noise. So, the signal to noise ratio for a point target can be computed as:

$$SNR = \frac{P_t G_t G_r \sigma \lambda^2}{(4\pi)^3 R_{st}^2 R_{sr}^2 L_T K_B T_0 F_n} \cdot DC \cdot T_i \quad (5.29)$$

being σ the RCS of the calibrators.

The Signal-to-Clutter Ratio (SCR) impact on the received signal phase must be also considered. In this case, the signal received power will be proportional to:

$$P_s \propto \frac{\sigma \lambda^2}{(4\pi)^3 R_{st}^2 R_{sr}^2} \quad (5.30)$$

While the clutter will be proportional to:

$$P_c \propto \frac{\sigma_0 \rho_{az} \rho_{gr} \lambda^2}{(4\pi)^3 R_{st}^2 R_{sr}^2} \quad (5.31)$$

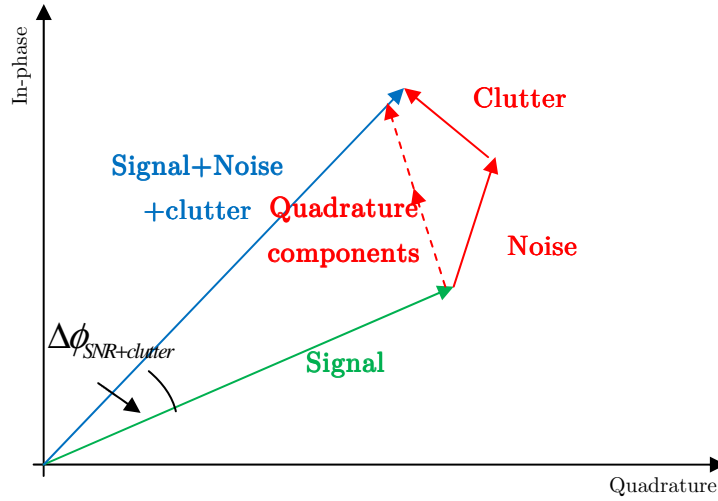


FIGURE 5.31 Noise + clutter phase error.

So, basically, the SCR can be obtained as the ratio between the RCS and the backscattering coefficient of the clutter (σ_0) multiplied by the resolution cell area ($\rho_{az}\rho_{gr}$):

$$SCR = \frac{P_S}{P_C} = \frac{\sigma}{\sigma_0 \rho_{az} \rho_{gr}} \quad (5.32)$$

In both cases, the SNR and SCR increase with the integration time considering a static clutter. While in SNR the relation is directly seen in equation (5.29), the azimuth resolution will improve with longer integration times resulting in better SCR as well. However, the clock phase errors will increase with time and, therefore, an optimum integration time for calibration must be determined in this analysis. An additional reduction of clutter power can be obtained by increasing the transmitted pulses bandwidth B . However, in this case, the increase of receiver bandwidth will result in an increase of noise power.

The impact of noise and clutter in the received signal is schematically presented in Figure 5.31. As seen in Figure 5.31, the noise and clutter are vectors added to the signal, and the components orthogonal to the signal will have the strongest impact in the phase variations in high SNR and SCR scenarios ($>10\text{dB}$).

First, the noise term will be considered. The echo coming from the ground calibrators with amplitude A_0 is considered as phase reference. This corresponds to a signal power of $S_r = A_0^2 / 2$ over a 1Ω Reference impedance. So, from the scheme presented in Figure 5.31, the phase variations of the received signal induced by the thermal noise can be obtained as:

$$\phi_n(t) = \arctan \left(\frac{n_q(t)}{A_0 + n_i(t)} \right) \quad (5.33)$$

Where $n_i(t)$ and $n_q(t)$ correspond to the in-phase and quadrature components of the noise with respect to the signal. However, for low noise condition ($n_q(t), n_i(t) \ll A_0$) the phase variations can be approximated as:

$$\phi_n(t) \approx \frac{n_q(t)}{A_0} \quad (5.34)$$

Thus, the variance of the phase due to noise can be obtained as:

$$\sigma_{\phi_n}^2 = \frac{\sigma_{n_q}^2}{A_0^2} \quad (5.35)$$

So, we have to relate the variance of the quadrature component with the noise power (N). In case of low noise condition ($N \ll S$) we obtain:

$$N = \sigma_n^2 \rightarrow \sigma_{n_q}^2 = E\{n_q^2(t)\} = E\{n_i^2(t)\} = \sigma_n^2 = N \quad (5.36)$$

Since $E\{n_q(t)\} = E\{n_i(t)\} = 0$. Therefore, the phase variance can be related with the SNR as:

$$\sigma_{\phi_n}^2 = \frac{N}{A_0^2} = \frac{N}{2S_r} = \frac{1}{2SNR} \quad (5.37)$$

An equivalent analysis can be done for clutter, obtaining a final variance of the phase given by:

$$\sigma_{\phi_c}^2 = \frac{C}{A_0^2} = \frac{C}{2S_r} = \frac{1}{2SCR} \quad (5.38)$$

with C the clutter power.

So, taking the different phase errors considered in this section, the variance of the total error (considering that the different terms are uncorrelated) can be obtained as:

$$\sigma_{\phi_T}^2 = \sigma_{\phi_n}^2 + \sigma_{\phi_c}^2 + \sigma_{\phi_{clock}}^2 \quad (5.39)$$

And the standard deviation of the final error is given by:

$$\sigma_{\phi_T} = \sqrt{\sigma_{\phi_n}^2 + \sigma_{\phi_c}^2 + \sigma_{\phi_{clock}}^2} = \sqrt{\frac{1}{2SNR} + \frac{1}{2SCR} + \sigma_{\phi_{clock}}^2} \quad (5.40)$$

So, in order to define the minimum RCS and the optimum integration time for synchronisation, the previous formula must be minimized in function of time. Several RCS values may be selected in order to reach a desired maximum phase error.

Finally, we need to know how the clock instabilities evolve with time and the residual error after the ground control phase compensation during the calibration integration time. So, generally, the phase received from a calibrator will have a similar aspect as the one shown in Figure 5.32 a). As seen, the total acquisition time (T_a) is divided into sub-acquisition for calibration of time T_i . From each sub-aperture, the clock phase may be estimated as shown in Figure 5.32 b). So, the uncompensated residual phase error will have a similar aspect as the one shown in Figure 5.32 c). As seen, the low frequency trend of the clock may be compensated ($f < 1 / T_i$). However, the higher frequency components will contribute to the residual error since they cannot be observed nor compensated.

A clock phase error model as the one presented in [129] has been considered with an Allan variance in the order of 10^{-11} for averaging times in the range of 1 to 100s. In this case, the phase spectrum can be modelled as:

$$S_{\phi}(f) = 2(a f^{-4} + b f^{-3} + c f^{-2} + d f^{-1} + e) \quad (5.41)$$

In the paper, an oscillator with frequency of 10 MHz with coefficients $a=-95$ dB, $b=-90$ dB, $c=-200$ dB, $d=-130$ dB and $e=-155$ dB. From the phase spectrum, the clock phase errors of the oscillator that cannot be compensated by the calibration process may be computed as [129]:

$$\sigma_{\phi, clock}^2 = 2 \left(\frac{f_0}{f_{osc}} \right)^2 \int_{1/T_i}^{\infty} S_{\phi}(f) df \quad (5.42)$$

where f_0 is the central radar frequency, f_{osc} is the oscillator frequency and T_i is the integration time.

So, after the theoretical approach presented, a preliminary analysis is presented next. In this case, a maximum phase error of 0.1 radians (5.75 degrees) will be defined as the goal of the synchronisation link design.

First, let us consider the analysis at Ku-band. A transmitted peak power of 31.83 dBW, antenna gain of 50.1 dB, a duty cycle of 0.3, transmission losses of 2 dB and receiver noise factor of 2 dB and a backscattering coefficient of the clutter of -15 dB have been assumed. Therefore, using equation (5.40), the resultant phase errors obtained for different RCS of the calibrators have been computed. For each RCS value, the minimum phase error (with the optimum integration time) obtained has been computed. The results obtained are shown in Figure 5.33. As seen, if an error under 6 degrees is desired, the RCS of the calibrators must be above 66.5 dBsm.

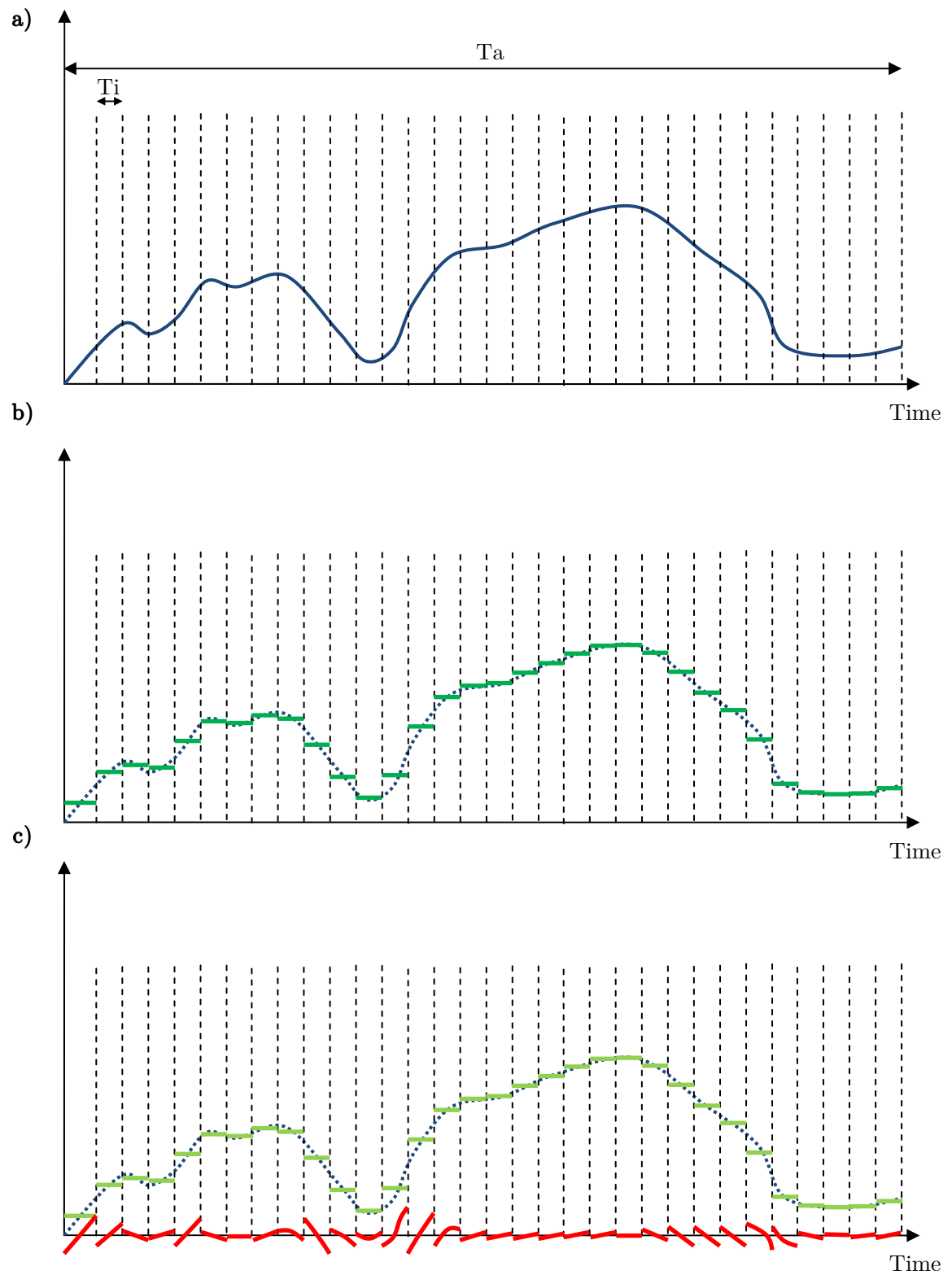


FIGURE 5.32 a) Phase error evolution received from echoes of one of the calibrators. b) Phase estimation from sub-apertures and c) residual error.

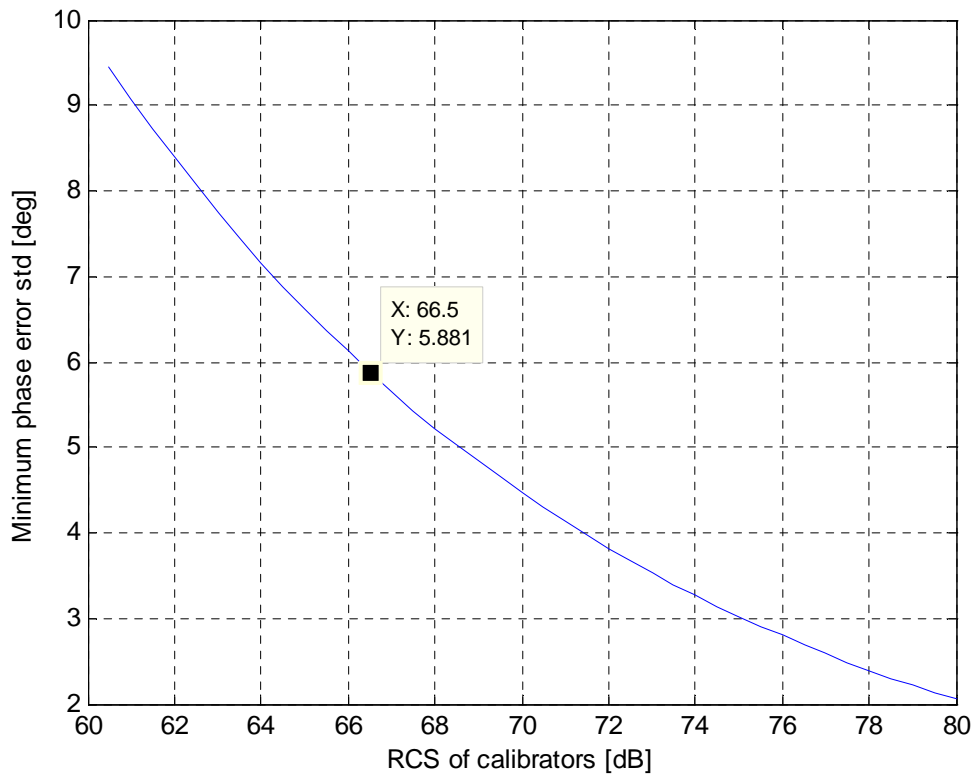


FIGURE 5.33 RCS of the calibrators impact on the phase error in Ku-band.

Thus, once the minimum RCS has been defined, the optimum integration time to reach the minimum phase error must be evaluated. The evolution of phase errors from the different sources (and the total error) with integration time are presented in Figure 5.34. As seen, the minimum phase error computed in Figure 5.33 is obtained for an integration time of 0.95 seconds.

Similarly, the study has been performed at L-band. The power and antenna parameters obtained in Table 5.8 have been considered in the RCS of calibrators calculation: transmitted power of 20.85 dBW, antenna gain of 31.6 dB, duty cycle of 0.3 and backscattering coefficient of the clutter of -15 dB. As seen in Figure 5.35, a minimum RCS of the calibrators of 86 dBsm should be necessary to have a final error under 6 degrees. In this case, as shown in Figure 5.36, the minimum phase error is obtained with an integration time of 6.8 seconds. This larger integration time is the consequence of having a better clock stability at this frequency. As seen, the phase error requirements are much more stringent in Ku-band, where an optimum integration time of 0.95 seconds has been obtained.

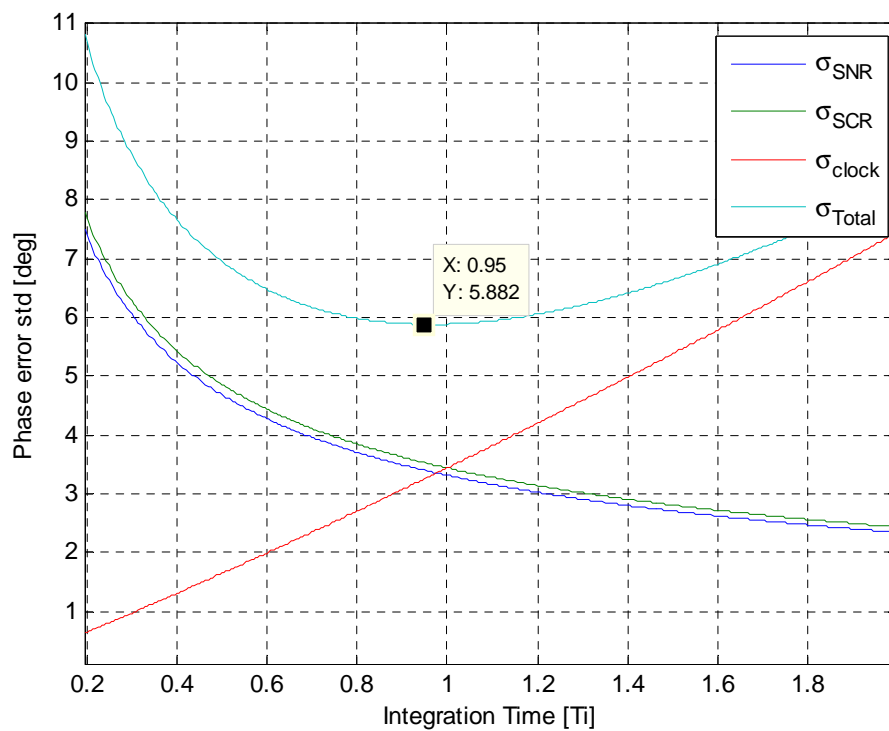


FIGURE 5.34 Evolution of phase errors (Ku-band) related to SNR, SCR and clock with integration time. The total phase error presents a minimum considering an integration time of 0.95 seconds.

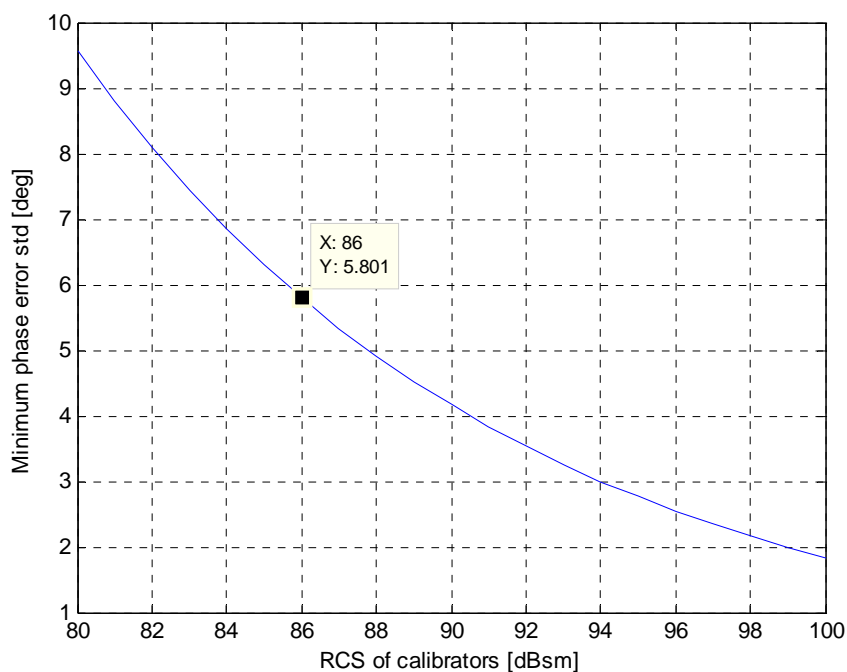


FIGURE 5.35 RCS of the calibrators impact on the phase error in L-band.

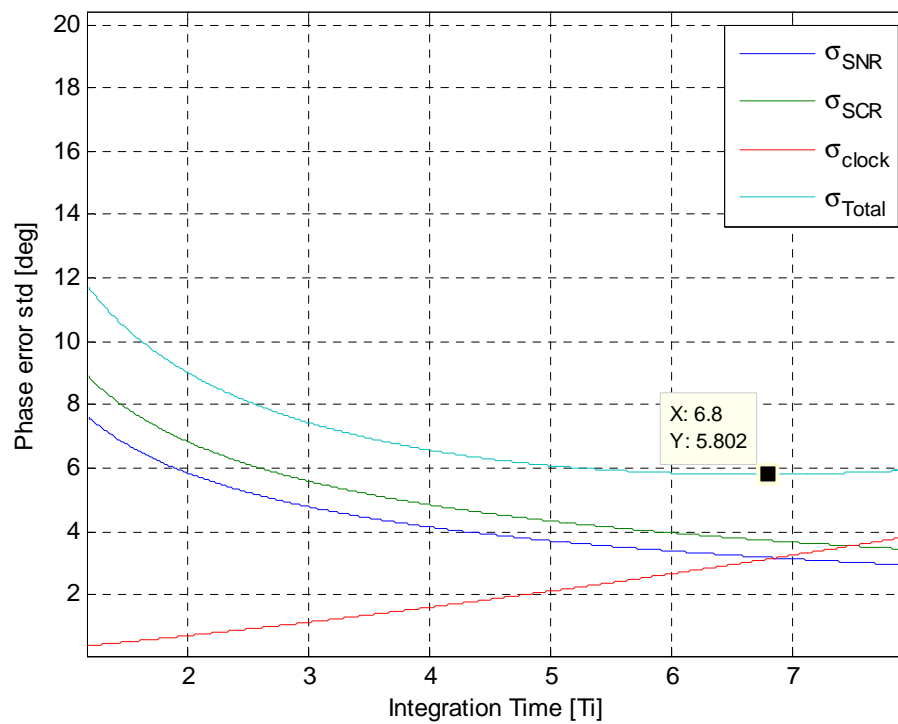


FIGURE 5.36 Evolution of phase errors (L-band) related to SNR, SCR and clock with integration time. The total phase error presents a minimum considering an integration time of 6.8 seconds.

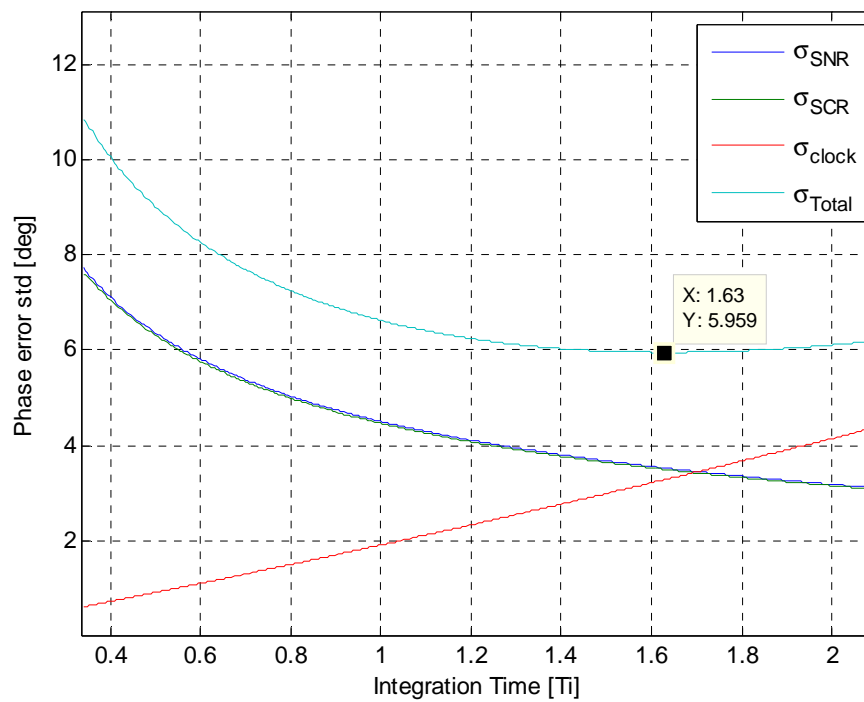


FIGURE 5.37 Evolution of phase errors (X-band) related to SNR, SCR and clock with integration time. The total phase error presents a minimum considering an integration time of 1.63 seconds.

Now, the calibrators must be designed to reach the RCS values previously computed in order to keep the phase error due to clutter and noise under 6 degrees. In the following section the calibrator design is presented as a combination of two antennas plus an amplifier. The results at X-band with an RCS of 62 dBsm are shown in Figure 5.37. The optimum integration time for calibration in this case is 1.63 seconds.

Calibrators design: antenna size + amplifier

Additionally, considering the antenna efficiency, the power intercepted by the antenna that is delivered to the amplifier is obtained as:

$$P_r = P_i \eta_{eff} = \wp_i A_{geo} \eta_{eff} = \wp_i A_{eff} \quad (5.43)$$

The efficiency of the antenna (η_{eff}) is related with the antenna gain as:

$$G = \frac{4\pi}{\lambda^2} A_{eff} = \frac{4\pi}{\lambda^2} A_{geo} \eta_{eff} \rightarrow \eta_{eff} = \frac{G}{A_{geo}} \frac{\lambda^2}{4\pi} \quad (5.44)$$

On the other hand, the power at the output of the amplifier, with power gain (G_A), will be computed as:

$$P_A = P_r G_A \quad (5.45)$$

This power at the output of the amplifier will be reradiated by a second antenna. So, the power density backscattered by the antenna is related to the incidence power density as follows:

$$\begin{aligned} \wp_s &= \frac{P_{ref} G}{4\pi R^2} = \frac{P_r G_A G}{4\pi R^2} = \frac{P_r G_A A_{eff} \frac{4\pi}{\lambda^2}}{4\pi R^2} = \frac{\wp_i A_{eff} G_A A_{eff} \frac{4\pi}{\lambda^2}}{4\pi R^2} = \\ &= \wp_i G_A \frac{A_{eff}^2}{\lambda^2 R^2} \end{aligned} \quad (5.46)$$

Finally, using (3.67) in the RCS equation (3.61), the backscattering coefficient for the calibrator in terms of antenna size (A_{geo}) and amplifier power gain (G_A) will be:

$$\sigma = \lim_{R \rightarrow \infty} 4\pi R^2 \frac{\wp_s}{\wp_i} = \lim_{R \rightarrow \infty} 4\pi R^2 \wp_i G_A \frac{A_{eff}^2}{\lambda^2 R^2} \frac{1}{\wp_i} = \frac{4\pi}{\lambda^2} A_{geo}^2 \eta_{eff}^2 G_A \quad (5.47)$$

Thus, taking the proposed RCS requirements (79.5 dBsm) for the Ku-band calibrator, the results obtained are summarized in Table 5.6. On the other hand, the same antenna size can be used to satisfy the requirements in L-band (Table 5.7) considering the higher RCS requirements of 110 dBsm obtained in the previous section.

Brand	Model	Freq.	Band	Diameter	Area	Gain	η_{eff}	RCS (dBsm)	G _A (dB)
TECATEL	135	17.25 GHz	Ku	135 cm	1.43 m ²	45.74 dB	0.63	66.5	21.72
TECATEL	80	17.25 GHz	Ku	80 cm	0.50 m ²	41.05 dB	0.61	66.5	31.13
XINSHI	XS-KU-60-I	17.25 GHz	Ku	60 cm	0.28 m ²	39.56dB	0.77	66.5	34.14

TABLE 5.6. Amplifier requirements for calibrators to reach the desired RCS of 75 dBsm at Ku-band

Brand	Model	Freq.	Band	Diameter	Area	Gain	η_{eff}	RCS (dBsm)	G _A (dB)
TECATEL	135	1.625 GHz	L	135 cm	1.43 m ²	22.95 dB	0.63	86	61.24
TECATEL	80	1.625 GHz	L	80 cm	0.50 m ²	18.25 dB	0.61	86	71.65
XINSHI	XS-KU-60-I	1.625 GHz	L	60 cm	0.28 m ²	16.77 dB	0.77	86	74.66

TABLE 5.7. Amplifier requirements for calibrators to reach the desired RCS of 110 dBsm at L-band

Re-radiated power from the calibrators

At this point, it is important to evaluate the power reradiated towards the satellite which determines the power amplifier requirements and power consumption of the calibrator. On the other hand the EIRP reradiated power is also needed for EMC control with respect to other radar and telecommunication systems. So, the power intercepted by the antenna of the calibrator (P_R^C) can be obtained from (5.48) where G_T^S and G_T^S are the transmitted power and antenna gain of the satellite, G_R^C is the antenna gain of the calibrator, R_{S-C} is the path length between the satellite and the calibrator and L_{sys} are the total losses of the satellite-calibrator chain.

$$P_R^C = \frac{P_T^S G_T^S G_R^C}{L_{sys}} \left(\frac{\lambda}{4\pi R_{S-C}} \right)^2 \quad (5.48)$$

In this way, the EIRP reradiated by the calibrator towards the satellite can be computed as:

$$EIRP = P_T^C G_T^C = P_R^C G_A G_T^C = \frac{P_T^S G_T^S G_R^C G_T^C}{L_{sys}} \left(\frac{\lambda}{4\pi R_{S-C}} \right)^2 G_A \quad (5.49)$$

Using the parameters obtained in Table 5.6 and Table 5.7, an EIRP of -16.41 dBW (22.85 mW) is obtained at Ku-band and -31.43 dBW (0.72 mW) at L-band.

5.5 Bistatic GEOSAR baseline design

After the geometric, radiometric and synchronisation analysis of the bistatic GEOSAR performance, in this section the most relevant parameters obtained are summarized. Three different beams have been analysed for different purposes. Finally, a wide coverage at L-band low-resolution beam, a C-band mid-coverage mid-resolution beam and a Ku-band SPOT high-resolution beam have been considered. The L-band beam has been taken for atmospheric retrieval while the C-band and Ku-band have been used for surface imaging purposes. The most relevant parameters of each beam are presented in Table 5.8 and Table 5.9.

		L-Band beam	C-band beam	Ku-band beam
Description		Wide beam low-resolution for APS	Mid coverage beam mid-resolution for surface imaging	SPOT beam high-resolution for surface imaging
Frequency		1.625 GHz	5.4 GHz	17.25 GHz
Satellite nominal longitude		Close bistatic: from 0° to 22° East (ideally 11° East) Open bistatic: maximum bistatic angle of 24.1 deg. with satellites between 0° to 22° East.		
Orbital design		1) Minimum eccentricity of 0.0003 2) Zero inclination or same inclination of the two satellites with a shift in their arguments of the perigee of 180 deg. 3) Close time pass through the perigee of the two satellites.		
Beam coverage		3000 km	650 km	350 km
Integration time		30 min	4 hours	4 hours
Signal bandwidth		0.2 MHz	5 MHz	15 MHz
Resolution	Azimuth	1.02 km	41.3 m	12.9 m
	Ground Range	1.17 km (at 40° incidence angle)	46.7 m (at 40° incidence angle)	15.6 m (at 40° incidence angle)
Antenna Parameters		Parabolic reflector		
- Beamwidth		4.64 deg.	1.01 deg.	0.53 deg.
- Efficiency		0.65	0.65	0.65
- Diameter		2.78 m	3.88 m	2.20 m
- Gain		31.6 dB	44.9 dB	50.1 dB
- Pointing accuracy		0.23 deg.	0.05 deg.	0.03 deg.
Doppler bandwidth	Total	30 Hz	90 Hz	280 Hz
	Comp.	2.5 Hz	9 Hz	3 Hz
PRF (min. 40 Hz for TWT current tech.)		43 Hz (single PRF)	40 to 50 Hz (multi PRF for different beams)	40 to 50 Hz (multi PRF for different beams)

TABLE 5.8. Acquisition parameters for bistatic GEOSAR proposed beams (I)

	L-Band beam	C-band beam	Ku-band beam
Duty cycle	0.3 (1.0 if transmitter-receiver isolation may be assured)	0.3 (1.0 if transmitter-receiver isolation may be assured)	0.3 (1.0 if transmitter-receiver isolation may be assured)
Mean trans. power	21.6 dBW	30 dBW	30 dBW
SNR without clutter decorrelation	>10 dB	>10 dB	>10 dB
Clutter decorrelation: max. wind speed to keep SNR>10 dB	40 km/h	20 km/h	5 km/h
RCS of parabolic antennas (Ku-band)	-	-	23 dBsm to 35 dBsm
SCNR with parabolic antennas	-	-	9.22 dB to 21.35 dB
Calibration req.	High RCS Active calibrators at L-band		
- Calibrator RCS	86 dBsm	-	66 dBsm
- Antenna diameter	135 cm	-	135 cm
- Amplifier gain	61.24 dB	-	21.72 dB
-Re-radiated EIRP	0.72 mW	-	22.85 mW

TABLE 5.9. Acquisition parameters for bistatic GEOSAR proposed beams (II)

In Figure 5.38, the azimuth resolution limits for an orbital eccentricity of 0.0003 and 0.0006 are compared with a possible set of applications and requirements [130]. In Figure 5.38, the blue and red dashed lines show the resolution limits for each integration time, but coarser resolutions for a specific integration time could be obtained by multi-look, increasing the image quality. As seen, the requirements for most of the applications can be fulfilled with an orbital eccentricity above 0.0003 which is in accordance with the values used all along this thesis.

On the other hand, the applications for the higher frequency bands (X- and Ku-bands studied in this analysis) are plotted jointly with the azimuth resolution vs. integration time limits in Figure 5.39. In this case, an eccentricity of 0.0003 at Ku-band or 0.0006 at X-band would be enough to fulfil most of the requirements for GEOSAR applications. Better performance could be obtained by considering a Ku-band acquisition with an orbital eccentricity of 0.0006.

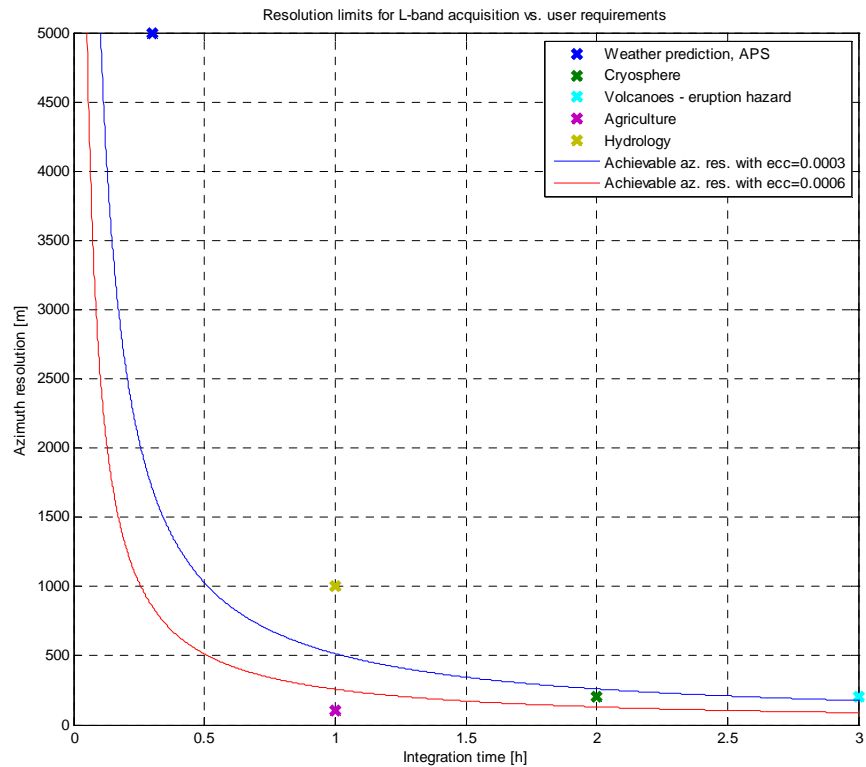


FIGURE 5.38 Resolution limits with orbital eccentricity of 0.0003 and feasibility with user’s requirements for lower band applications.

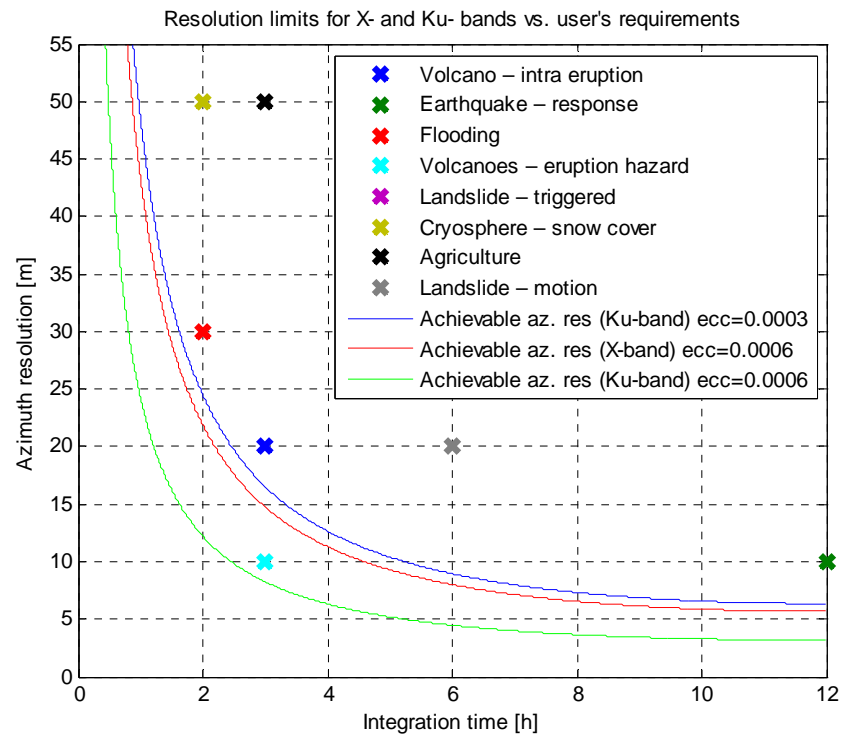


FIGURE 5.39 Resolution limits with orbital eccentricity of 0.0003 and feasibility with user’s requirements for higher band applications.

Chapter 6

Experimental bistatic system with on ground passive receiver and illuminator of opportunity

In this chapter, a bistatic GEOSAR acquisition with the receiver on-ground will be studied. So, the transmitted signal by a broadcasting telecommunications satellite will be used as a signal of opportunity for a ground receiver tuned to one of the transmitted channels. The concept of re-using signal of opportunity in an on-ground receiver was firstly proposed in [50]. In that work, a dual-channel receiver was designed to obtain the signal directly from the satellite with a parabolic antenna pointing towards the satellite and horn antenna pointing to the imaged scene receiving the backscattered echoes. A digital oscilloscope is used to digitise the two channels and process the received raw data. Very preliminary images are obtained in this work.

On the other hand, a similar system will be studied in this section. As in [50], the signal from a broadcasting TV satellite will be used as illumination of opportunity. However, a PC dual-DVB Satellite TV card will be used for receiving the signal. It will be a cheap way to obtain the signal from both direct and backscattered links with small modifications on the hardware. In the following section, the system is presented theoretically and some simulations are performed in order to check their feasibility in terms of focusing and power link budget requirements. The first experimental steps performed in the receiver design will be also explained.

6.1 System description

6.1.1 Geometrical analysis

First of all, the system geometry of the proposed scheme must be analysed. In this case, one of the ASTRA satellites in the 19.2° East constellation will be considered. The on-ground receiver will be placed on the rooftop of one of the Campus Nord of Universitat Politècnica de Catalunya (UPC) buildings with coordinates 41° 23' 20" N, 2° 06' 42" E pointing to the Collserola mountain. The illuminator-receiver-scene scheme is graphically shown in Figure 6.1. This receiver and monitored region has been selected for several reasons:

- a) Accessibility to mount and operate the on-ground receiver. Placing the receiver on the rooftop of the department building makes possible to operate it during hours with no-surveillance. Additionally, it will be easier to perform several tests before the final system design.
- b) Wide field of view. Pointing the one of the receiving antennas to the Collserola Mountain will make possible to cover a wide scene of 1 by 2 km, approximately.
- c) Covered area with expected stable targets: buildings and low-vegetated areas. It is essential considering the long integration necessary to reach the desired resolution.
- d) Scene and illuminator satellite in opposite directions from the receiver to avoid specular reflections.

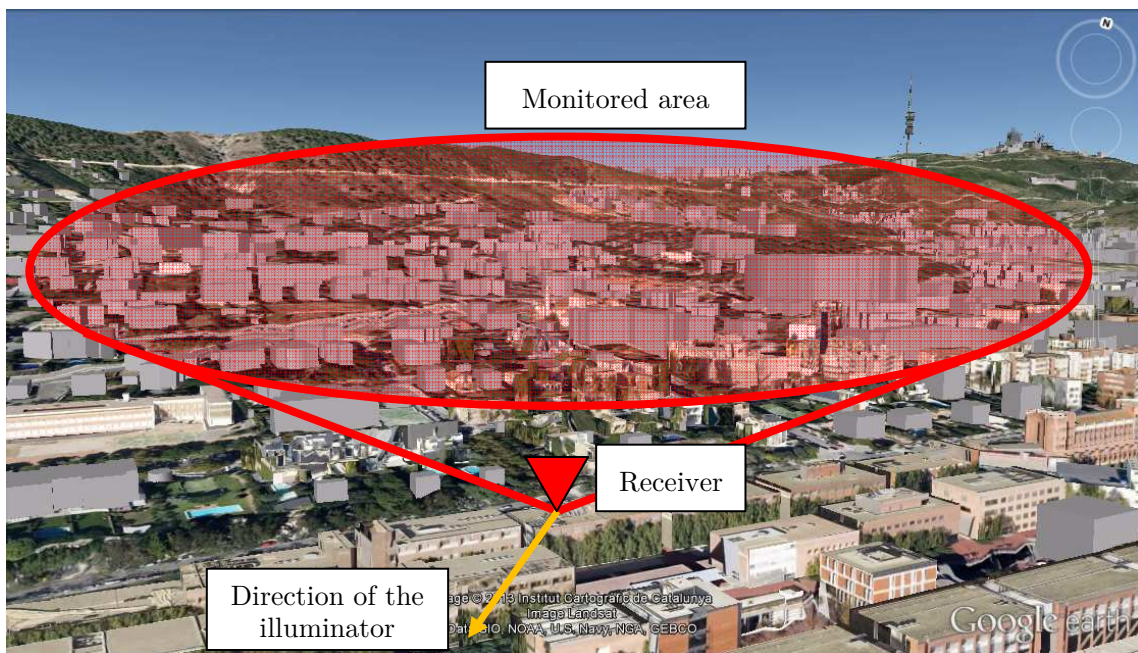


FIGURE 6.1 Illuminator-receiver-scene geometry.

Therefore, the geometrical parameters presented in section 2.2 must be recomputed for this new bistatic configuration. One of the parameters that will be crucial in the SAR focusing and the power link budget computation will be the slant range. In the bistatic configuration studied in this section there will be an important difference between the transmitter-scene slant range and the scene-receiver slant range.

Thus, considering the coordinates of a central point in the scene ($41^{\circ} 23' 36''$ N, $2^{\circ} 06' 31''$ E and 150 m height) and the satellite at 19.2° E in the equatorial plane, a transmitter-scene slant range of 37856 km is obtained by using equation (2.33). The scene-receiver slant range will vary from 500 m to 2.5 km depending on the zone of the covered scene considered. As seen, the receiver-scene slant range is four orders of magnitude shorter than the transmitter-scene slant range.

The look and incidence angle from where the satellite image the scene centre can be found with equations (2.45) and (2.48), respectively. Therefore, considering the satellite and scene locations presented above a look angle of 6.73 degrees and an incidence angle of 50.92 degrees have been obtained. In the computation of the incidence angle the terrain slope has not been considered. For the receiver-scene illumination, a wide range of incidence and look angles will be obtained for the different positions on the scene.

Thus, the most relevant geometrical parameters of the satellite, receiver and scene are summarized in Table 6.1. These parameters will be used all along this chapter to evaluate the SAR performance of the bistatic GEOSAR acquisition with on-ground receiver. In the following sections, the achievable resolution, focusing and power link budget are analysed for this particular configuration.

On-ground receiver GEOSAR configuration geometrical parameters					
Transmitting satellite		On-ground receiver		Scene centre	
Latitude	0 deg	Latitude	$41^{\circ}23'20''$ N	Latitude	$41^{\circ}23'36''$ N
Longitude	19.2° East	Longitude	$02^{\circ}06'42''$ E	Longitude	$02^{\circ}06'31''$ E
Orb. Height	35786 km	Height	115 meters	Height	150 meters
Transmitter-scene slant range			37856 km		
Receiver-scene slant range			500 m to 2.5 km		
Satellite-scene look angle			6.73 degrees		
Satellite-scene incidence angle			50.92 degrees		
Receiver-scene look angle			Variable		
Receiver-scene incidence angle			Variable		

TABLE 6.1. Geometric parameters for bistatic GEOSAR with on-ground receiver.

6.1.2 Achievable resolution

In this section, the range of expected resolutions considering the bistatic GEOSAR configuration with on-ground receiver and illuminator of opportunity will be evaluated. As studied in section 5.2, in a bistatic SAR acquisition an equivalent monostatic acquisition can be defined taking the mid-points between the transmitter and receiver positions. However, in this case, the bistatic angle between transmitter and receiver is large and, therefore, the monostatic equivalence is not as accurate as in the close bistatic GEOSAR formations. For this reason, the achievable resolution results are obtained directly from simulation using the GEOSAR simulator presented in section 3.6.3 using an on ground fixed receiver.

The scheme presented in Figure 6.2 is considered in this analysis. As seen, the receiver location is fixed and it is close to the scene compared with the transmitter-scene slant range. In Figure 6.2, the satellite motion for a generic integration time is plotted in blue. The synthetic aperture length has been exaggerated for better visualization.

Thus, considering the orbital ephemerides of the geosynchronous satellites shown in Figure 2.48, eccentricities around 0.0003 are expected for these satellites. These satellites, used as TV broadcasting transmitters, transmit PSK modulations at a frequency in Ku-band from 10.7 to 12.2 GHz. Then, considering the satellite-scene slant range obtained in Table 6.1, the achievable resolutions with respect to the integration time are presented in Figure 6.3. As seen, considering an integration time of 12 hours, along-track resolution up to 20 meters could be obtained. However, such integration time could be too large for the temporal coherence of the scene. Therefore, reducing the integration time to 4 hours, along-track resolution of 40 meters could be still obtained.

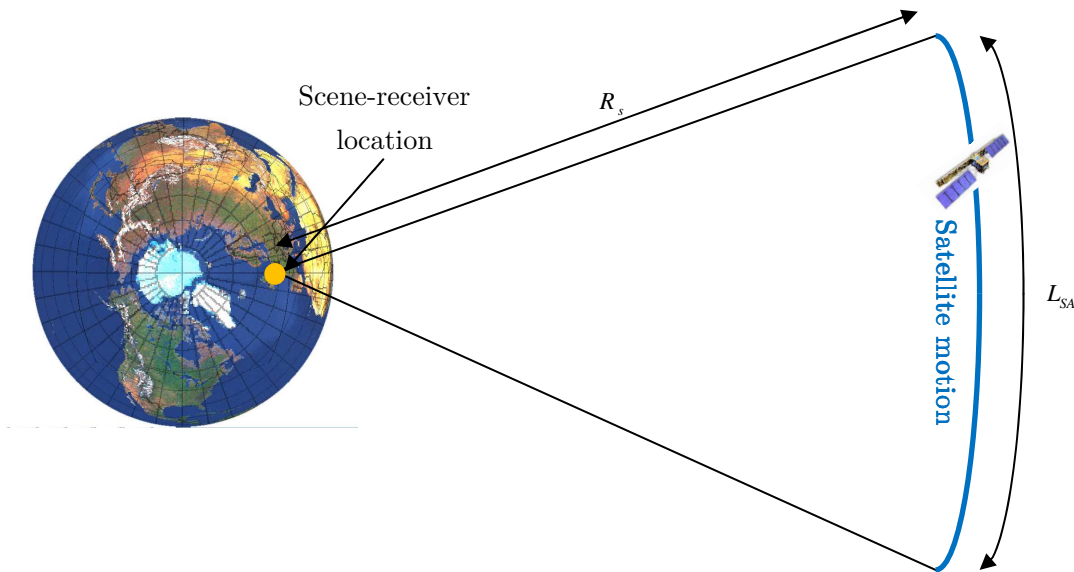


FIGURE 6.2 Equivalent monostatic geometry for GEOSAR with on-ground receiver (top-view).

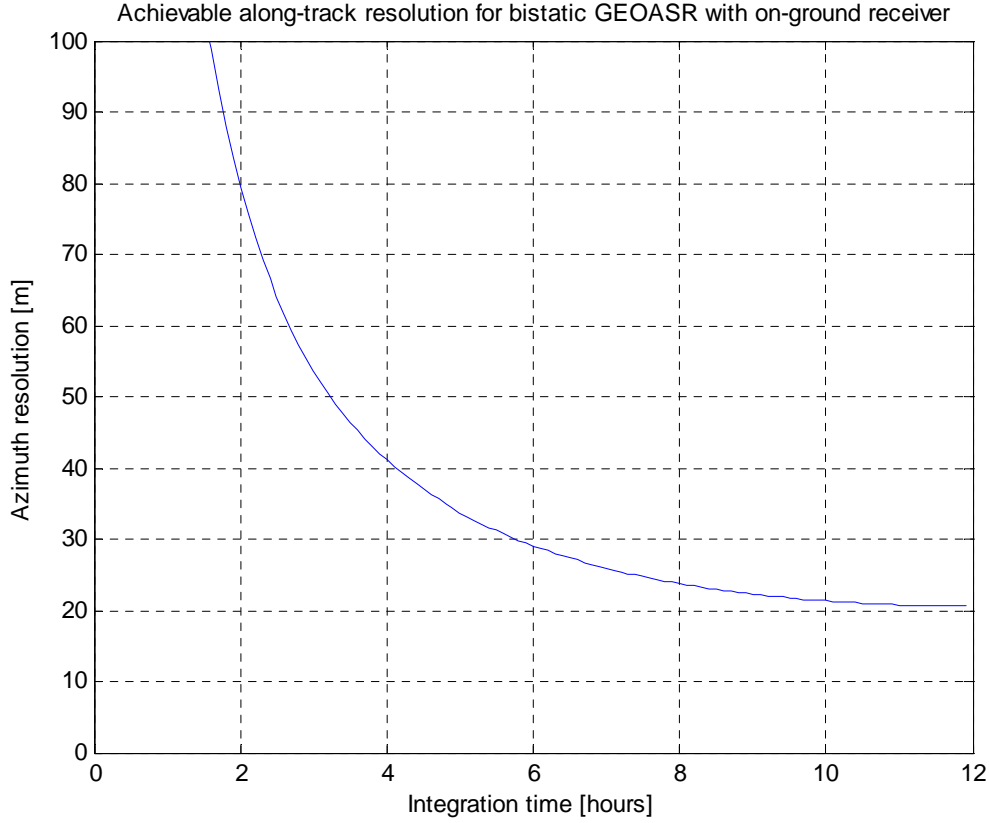


FIGURE 6.3 Achievable resolution for an on-ground bistatic GEOSAR acquisition considering a channel transmitting at 11.5 GHz with orbital eccentricity of 0.0003.

On the other hand, regarding the slant range resolution, it will depend on the transmitted signal bandwidth. In case of DVB-S2 broadcasting transmitted channels, a typical signal bandwidth from 22 MHz to 36 MHz per channel is used. Therefore, the slant range resolution can be obtained:

$$\rho_{sr} = \frac{c}{2B} = 6.8 - 4.2 \text{ m} \quad (6.50)$$

In order to obtain the ground range resolution, the incidence angle of the acquisition as well as the scene slope should be considered for the different positions in the scene. Ground range resolutions below 20 meters will be obtained for incidence angles higher than 20 degrees.

6.1.3 Bistatic GEOSAR with on-ground receiver focusing

So, after defining the problem geometry and analysing the expected resolution for this case, in this section a bistatic GEOSAR acquisition with on-ground received have been performed. In this example, a transmitter placed at a geosynchronous satellite at 19.2 East

with eccentricity of 0.0003 and no inclination is considered. The receiver and scene locations shown in Table 6.1 have been taken.

The signal parameters presented in the previous section have been used: transmitting frequency of 11.5 GHz with a signal bandwidth of 22 MHz. The raw data from a 4 hours acquisition have been simulated. The final focused image considering a scene of 1 by 1 km with 10 targets randomly placed is shown in Figure 6.4. As seen in the zoom-in of one of the target responses shown in Figure 6.5, an along-track resolution of 39 meters and cross-track resolution of 7 meters are obtained, as expected from the theoretical approach presented in the previous section. In this example, the lateral lobes levels could be reduced by using windowing, but in this example it has not been considered.

As it was presented in section 3.6, a time-domain back-projection algorithm has been used to focus the simulated raw data. Additionally, Doppler centroid track and compensation has been considered previous the raw data focusing to compensate the Doppler shift that arises from the orbital radius variations.

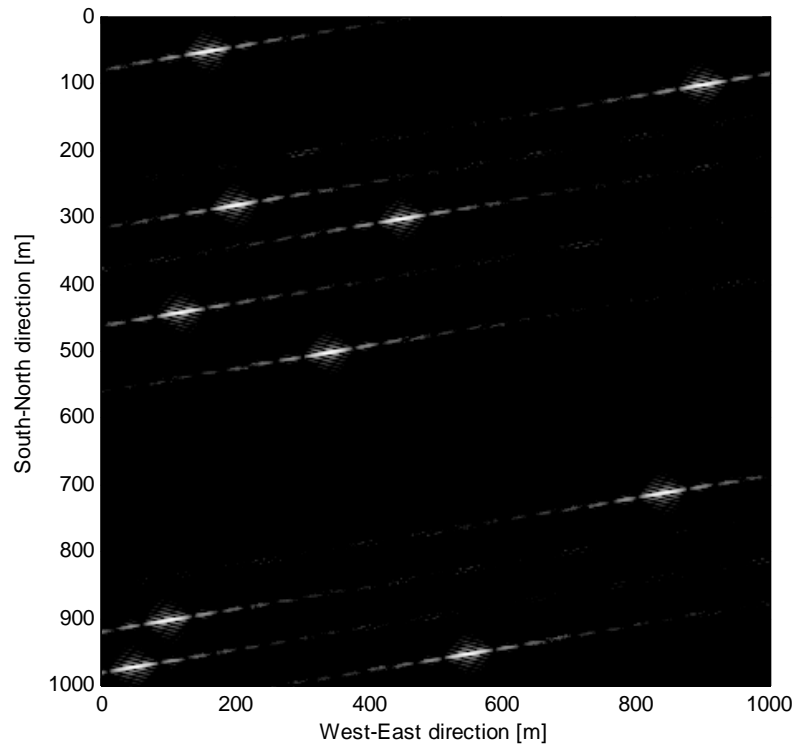


FIGURE 6.4 Focused image from a bistatic GEOSAR with on-ground receiver simulated raw data during 4 hours of acquisition.

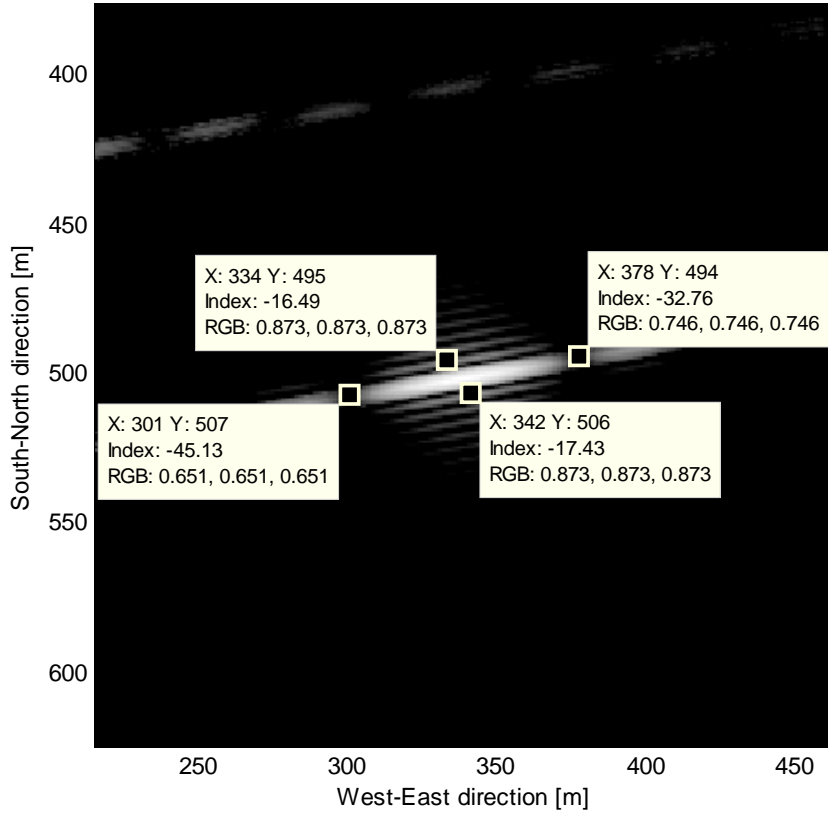


FIGURE 6.5 Along-track and cross-track resolution in the GEOSAR with on-ground receiver simulated case with 4 hours of integration.

6.1.4 Power link budget

Finally, the power link budget for the bistatic system with an on ground receiver will be considered. Additionally, the illumination of opportunity from a TV broadcasting satellite is also used. The main difference with previous analysis will be the location of the receiver on the Earth's surface will avoid the return signal path of thousands of kilometres, giving higher SNR than the previous cases.

In this example, the signal from the ASTRA 2C satellite will be used as a transmitted signal while the receiver location is presented in Table 6.1. Considering the footprint of ASTRA 2C presented in Figure 6.6, the satellite illuminates the region of interest with an EIRP of 50 dBW.

It will be also important to determine the receiving antenna parameters (coverage, size, gain, etc.). Let us consider a scene of 1 by 1 km extension which is observed by a horn antenna. The horn antenna dimensions are shown in Figure 6.7. The size of the horn antenna can be related with the desired coverage (ΔR) and the receiver-target range (R_{T-rec}) as [69]:

$$\Delta R_1 = 0.98 \frac{\lambda}{L} R_{T-rec} \rightarrow L = 0.98 \frac{0.025}{1Km} \cdot 2.03 Km = 4.97cm \quad (6.51)$$

$$\Delta R_2 = 1.36 \frac{\lambda}{W} R_{T-rec} \rightarrow W = 1.36 \frac{0.025}{1Km} \cdot 2.03 Km = 6.90cm \quad (6.52)$$

$$S = L \cdot W = 34.29 cm^2 \quad (6.53)$$

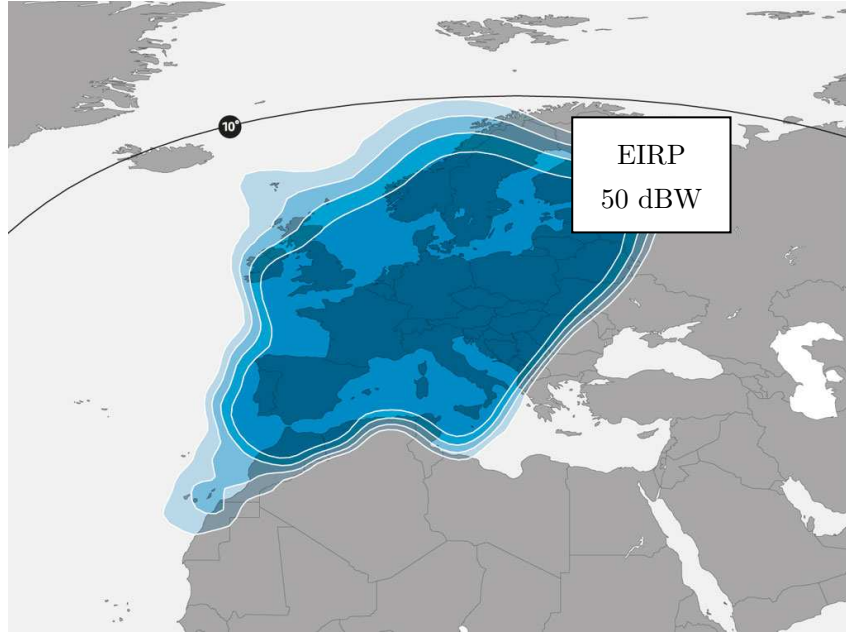


FIGURE 6.6 ASTRA 2C footprint over Europe.

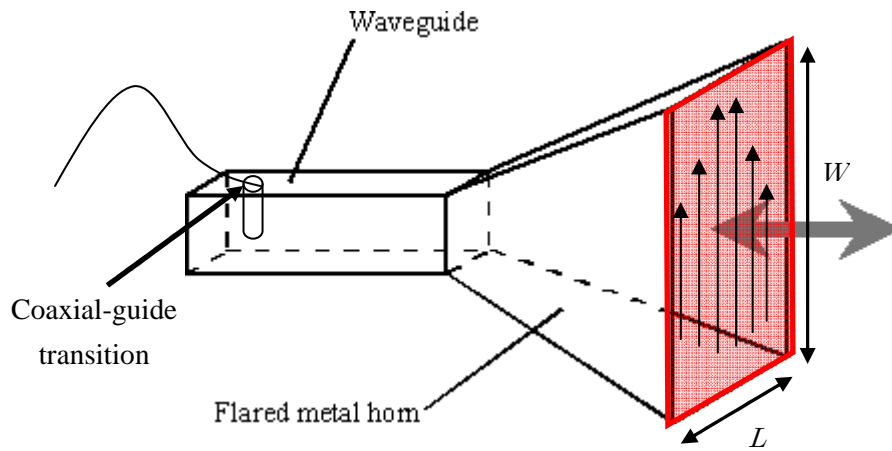


FIGURE 6.7 Horn antenna used as a receiver station on the bistatic on ground receiver configuration.

SNR for bistatic GEOSAR with on-ground receiver					
Parameter	Symbol	Value	SNR impact	SNR budget	Units
Transmitted power	P_t	10 dBW	EIRP	+50	dBW
Gain trans.	G_t	40 dB			
Gain rec.	G_r	12.19 dB	-	+12.19	dB
Slant range transmission	R_t	37856 km	$\frac{\lambda^2}{(4\pi)^3 R_t^2 R_r^2}$	-282.2	dBsm ⁻¹
Slant Range reception	R_r	2 km			
Wavelength	λ	0.026 m			
Pixel area	$\rho_{az}\rho_{gr}$	40 m x 10 m	RCS	+16	dBsm
Backscattering	σ_0	-10 dB			
System losses	L_T	3 dB	-	-3	dB
$k T_0$	-	$4 \cdot 10^{-21}$ J	Noise power	+128.6	dB
Noise factor	F_n	2 dB			
Signal Bandwidth	B	22.0 MHz			
SNR single pulse (per res. cell)			SNR_1	-78.41	dB
Pulse duration	τ_i	0,05 sec	Pulse compression (τ_i / τ_0)	60.4	dB
Compress pulse duration	$\tau_0 = 1 / B$	45.5 nsec			
PRF	-	10 Hz	Integrated pulses ($PRF \cdot T_i$)	51.6	dB
Integration time	T_i	$4 \cdot 3600$ sec			
SNR after SAR processing			SNR_0	33.59	dB
Noise Equivalent Sigma Zero			NESZ	-43.59	dB

TABLE 6.2. Power link budget for the bistatic GEOSAR acquisition with on-ground receiver.

Therefore, from effective illuminated surface of the antenna, the gain is obtained as:

$$G = 6.4 \frac{S}{\lambda^2} \eta_{il} = 12.19 \text{ dB} \quad (6.54)$$

which corresponds to a low-gain antenna due to the wide beam desired to cover large areas relatively near from the receiver. Thus, considering all the parameters computed above, the power link budget presented in Table 6.2 is obtained. As it can be seen, the shorter scene-receptor slant range makes possible to obtain a better SNR than in the previous cases. Therefore, the power requirements and noise will not be a problem for this bistatic GEOSAR configuration.

6.2 Hardware design

In this section, the different parts of the receiver hardware for the bistatic GEOSAR configuration presented in this section will be presented. First of all, the DVB-S2 PC card used as a receiver will be analysed. The hardware used to get the different signal from the two channels will be shown.

After that, the Low-Noise-Blocks (LNBs) used for the acquisition will be studied and the necessity of considering a common external local oscillator will be justified. The necessary modifications on the LNB hardware will be also shown.

Finally, a brief introduction to the parabolic antenna used for the direct and backscattered links will be also presented.

6.2.1 *DVB-S2 receiver: 2-channel simultaneous acquisition*

6.2.1.1 TBS 6981 DVB-S2 Dual Tuner PCIe Card

The purpose of the design presented in this section is to build a low-cost receiver with commercial products without important hardware modifications. So, the first step of the design was to select an appropriate DVB receiver for bistatic GEOSAR purposes. Since two simultaneous acquisitions, direct and backscattered signals, were required, a dual DVB-S2 PCIe card was chosen. In this case, the TBS 6981 Dual Tuner PCIe card was preferred because of its low price and the accessibility to its components. The front and back views of the selected card are presented in Figure 6.8.

This DVB PCIe card allows receiving a frequency range from 950 to 2150 MHz with an input level sensitivity from -69 to -23 dBm. Each channel has an advanced DVB-S2/DVB-S demodulator for 8PSK and QPSK modulations at symbol rates of 1-45 Msps for DVB-S QPSK and 2-36 Msps for DVB-S2 QPSK/8PSK.

The card supports data burst and tone burst as well as DiSEqC2 necessary to control the LNB hardware. The important components used by this card are the CX24132 (tuner), CX24117 (demodulator) and CX23885 (PCIe bus). These chips can be seen in the zoom-in of the TBS 6981 card shown in Figure 6.9.

The tuner and demodulator chips are briefly described next, since this information will be crucial in order to know where to find the necessary raw data of the bistatic GEOSAR processing.

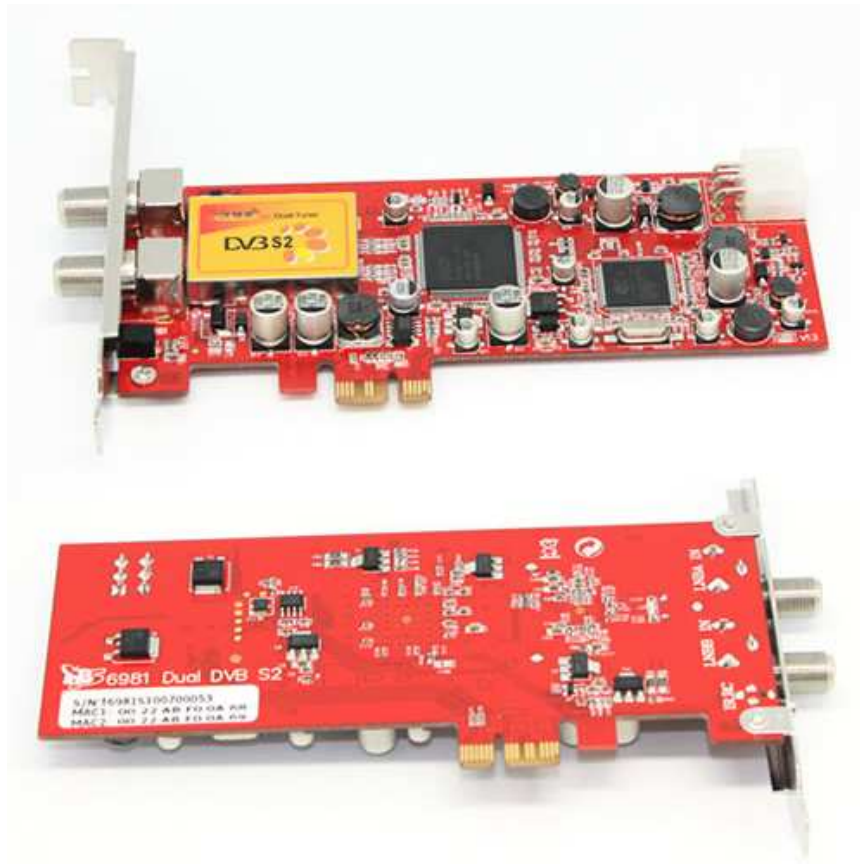


FIGURE 6.8 Front and back views of TBS 6981 PCIe Card used in the receiver for the bistatic GEOSAR acquisition.

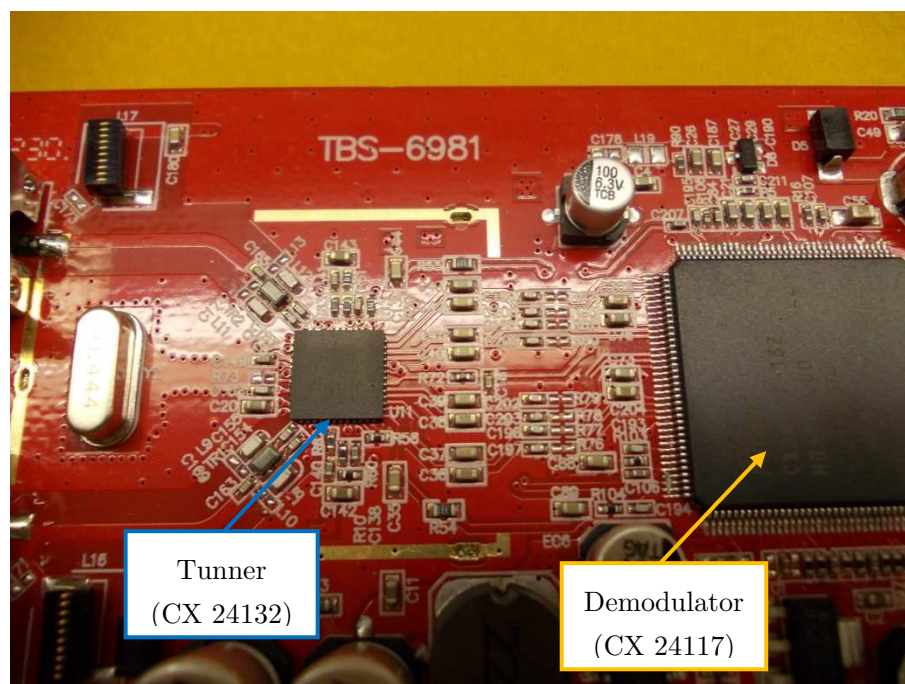


FIGURE 6.9 TBS 6981 components: tuner (CX24132) and demodulator (CX24117).

CX24132 Tuner

The CX24132 is a dual low-power 8PSK Digital satellite tuner. It is also useful for QPSK modulation formats. The chip contains the necessary Low Noise Amplifiers (LNAs), voltage-controlled oscillators (VCOs), synthesizers, mixers and filters to acquire to tune the satellite DVB signals.

The functional block diagram of the CX24132 chip is shown in Figure 6.10. As seen, two RF inputs enter to the chip. Each channel is decomposed into the in-phase (I) and quadrature (Q) components which are delivered through differential output ports to the demodulator. These eight outputs will be the ones of interest to obtain the raw data from direct and backscattering signals (red outputs in Figure 6.10).

CX24117 Demodulator

The CX24117 chip is a dual-integrated demodulator based on an open DVB-S2 standard. It offers the possibility of working with advanced modulation and coding (AMC) with 8PSK and QPSK. The chip is a DiSEqC compliant demodulator that makes possible the two way communications with other elements of the reception chain such as the LNB converters and switches to select the band and polarization of the acquisition.

The block diagram for the CX24117 is presented in Figure 6.11. This block combines and digitises the IQ signal received from each channel. The digital signal is demodulated and a MPEG Transport Stream (TS) is obtained at the outputs of this block.

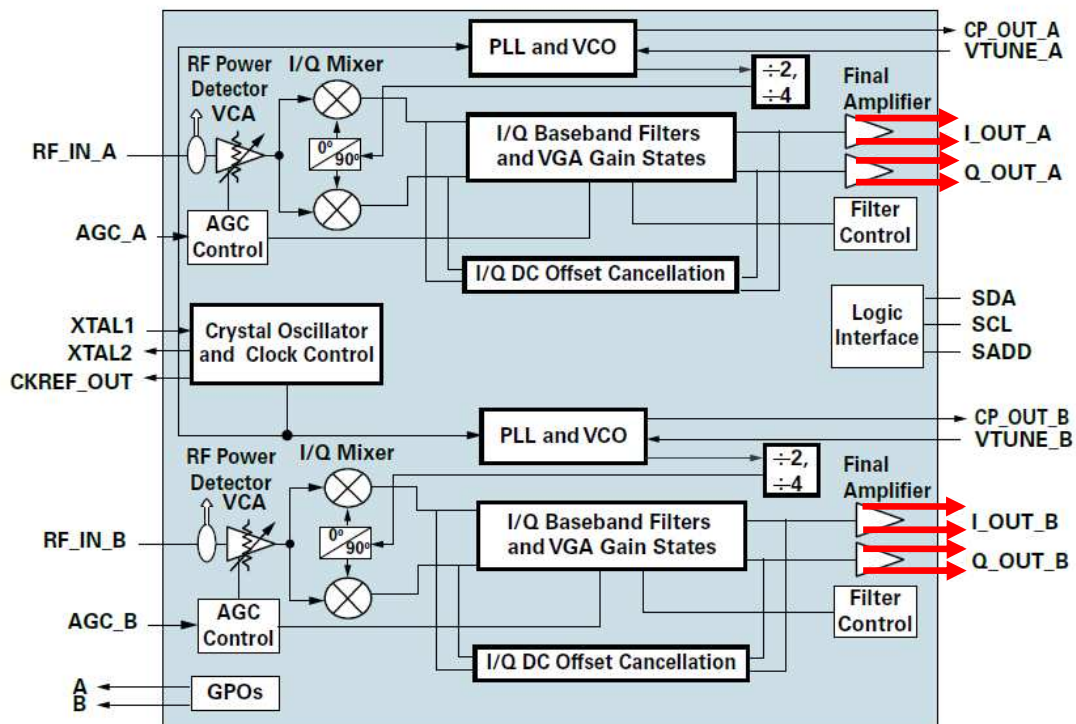


FIGURE 6.10 Block diagram for the CX24132 tuner.

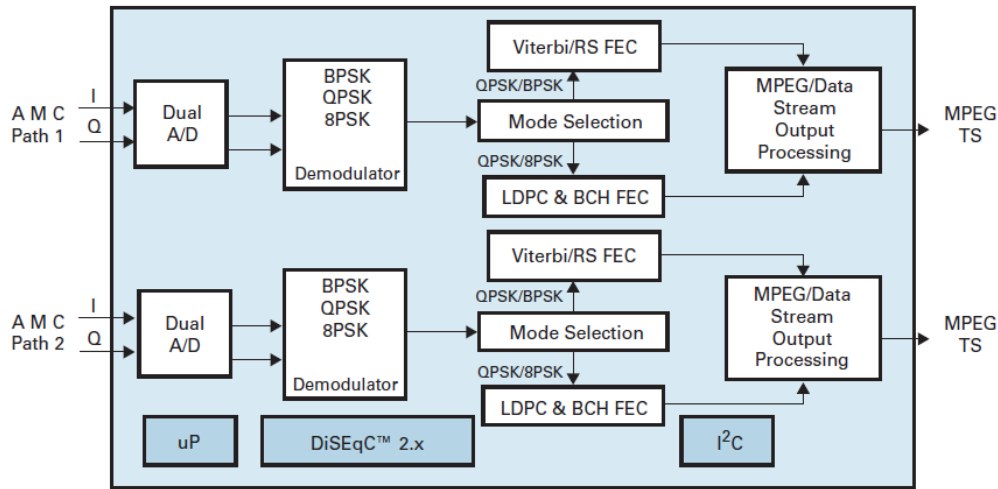


FIGURE 6.11 Block diagram for the CX24117 demodulator.

Since we are interested in the raw data, previous the demodulation, the signal must be obtained at any point between the output of the tuner and the input of the demodulator. In order to acquire the signal, a set of low noise amplifiers with high input impedance have been chosen in order not to overload the circuits on the DVB card. In the following section, the design of the acquisition block is described and the most relevant experimental tests performed are presented.

6.2.1.2 High input impedance buffer design and analysis

So, after presenting the DVB-S2 PCIe card used in the design, the circuit utilized to get the signal from both channels are presented and tested in this section. As mentioned in the previous section, four signals in a differential form will be found at the output of the tuner and at the input of the demodulator corresponding to the In-phase and Quadrature components of the direct and backscattered signals. Therefore, an eight-input four-outputs buffering circuit with high input impedance will be propose in this design in order to get the signal components without distortion of the signals in the DVB-S2 card.

The low power voltage feedback amplifier AD8039 has been selected in this case. This is a low-cost device with low power consumption (1 mA supply current/amp) and high speed (350 MHz, - 3 dB bandwidth). The AD8039 is an 8-pin device which incorporates two equal amplifiers. Each amplifier presents low distortion with a wide supply range from 3 V to 12 V. The pin-out of the AD8039 is shown in Figure 6.12. As seen, the 8 pints correspond to 4-inputs, 2-outputs and 2 for voltage supply.

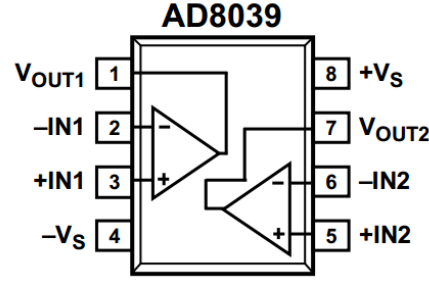


FIGURE 6.12 AD8039 dual amplifier pin-out.

Therefore, two AD8039 will be considered in the buffering circuit design. The differential input of each of the four amplifiers will be assigned to each differential signal coming from the two channels (direct and backscattered signals). However, in order to check the performance of the amplifiers, a simpler design with a single device using only one of the amplifiers has been considered.

So, a simple amplification step with gain 2 has been proposed for amplifier performance testing. The schematic of the testing circuit is presented in Figure 6.13. The design of what it is known as a true differential amplifier assures that the output voltage is zero when $V_{IN1} = V_{IN2}$. From the circuit analysis of the amplifier design the condition to obtain a true differential amplifier can be obtained as [148]:

$$\frac{R_2}{R_1} = \frac{R_F}{R_3} \quad (6.55)$$

Additionally, considering $R_1 = R_3$ and $R_2 = R_F$, the output voltage can be written as [148]:

$$V_O = \frac{R_F}{R_3} (V_{IN1} - V_{IN2}) \quad (6.56)$$

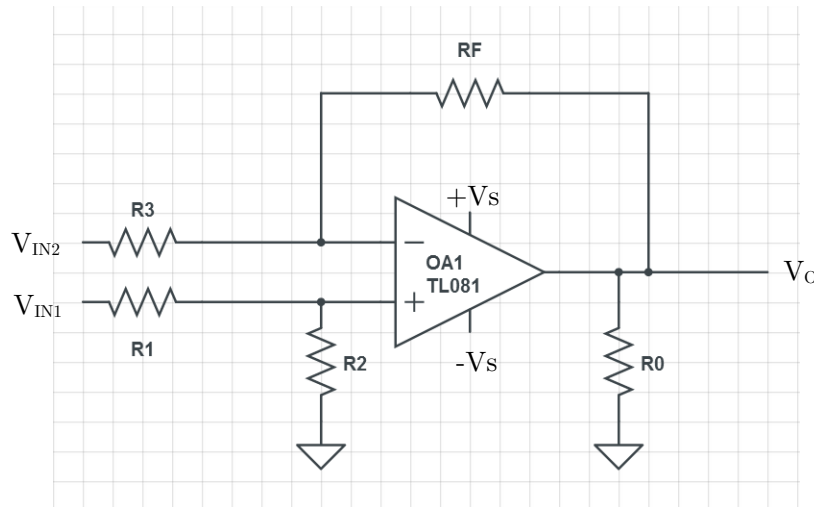


FIGURE 6.13 Single amplifier design schematic.

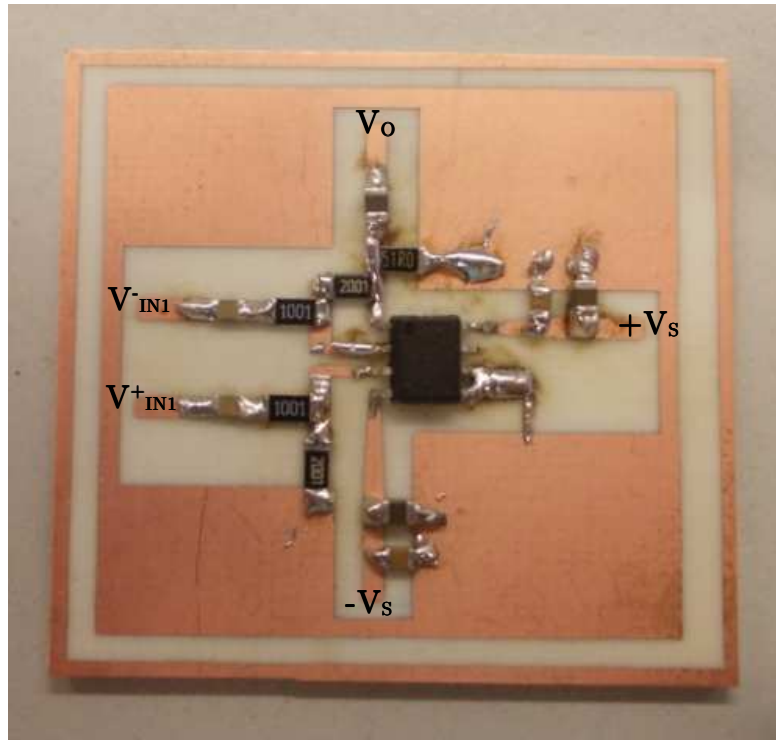


FIGURE 6.14 Single amplifier design circuit.

In Figure 6.14, the final design considered for amplifier testing is presented. In this case, values of $R_1 = R_3 = 1\text{ k}\Omega$ and $R_2 = R_F = 2\text{ k}\Omega$ have been considered. Therefore, a gain 2 (6 dB) should be obtained. Additionally, two capacitors have been placed at each voltage supply line. The results obtained in function of the input signal frequency and amplitude are presented in Figure 6.15 left and right plots, respectively. As seen in the left plot of Figure 6.15, constant gain around 6.56 dB is obtained in the range of frequencies from 0.3 to 50 MHz considering an input voltage of 10 dBm. On the other hand, the voltage gain of the amplifier starts to decrease with input voltages higher than 0 dBm. However, the effect can be neglected since at 10 dBm the 6.5 dB gain is preserved at a frequency of 22 MHz. In this case, a symmetric power supply of $\pm 5\text{ V}$ has been considered.

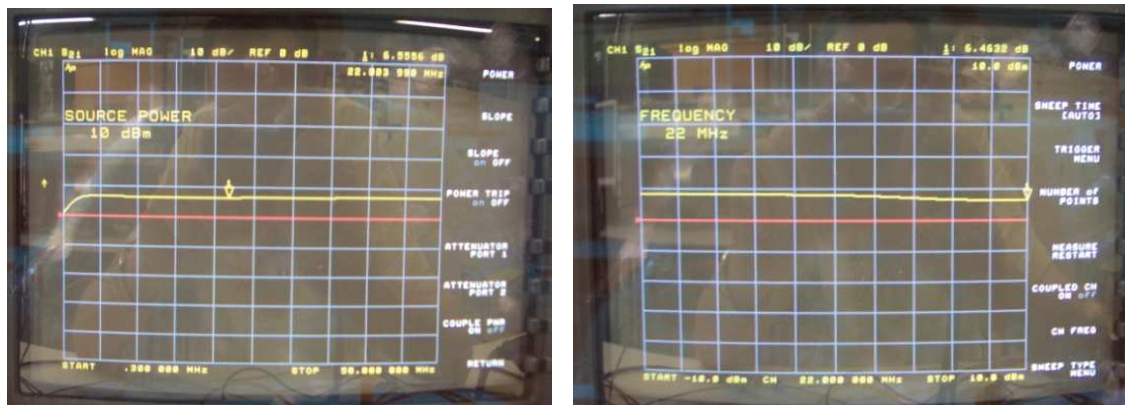


FIGURE 6.15 Single amplifier design circuit.

Once the linearity of the amplifier with frequency and input signal amplitude has been tested, the power supply circuit for the buffer must be designed. The idea is to design a self-supplied power circuit that can get the required voltage supply from the input voltage of the PCIe card used. In this case, three parallel 12 V lines can be found at the input of the TBS6981.

Therefore, instead of considering a symmetric power supply of ± 5 V as in the previous case, a single rail configuration using 0 V in the negative supply voltage ($-V_s$) of the AD8039 and 10 V in the positive one ($+V_s$) can be used. On the other hand, 5 V has been considered as reference voltage for the positive input voltage of the operational amplifier.

The voltage supply is based on the 78L09 regulator which offers an output voltage of 9 V for a range of input voltages from 12 to 24 V. Although the output voltage is 1 V below datasheet specifications, it will be enough for the correct operation of the buffering circuit. So, in Figure 6.16, the schematic of the voltage supply design is presented. In our case, 12 V will be present at the input of the voltage regulator and 9 V at the output. Using a resistive voltage divisor, two voltages of 9 V and 4.5 V can be easily obtained. The final circuit design is presented in Figure 6.16.

Finally, the voltage supply circuit must be connected to the buffering operational amplifiers. As mentioned before, the high voltage output will be connected to the $+V_s$ port of the amplifier while the 4.5 V mid-voltage output will be connected to the $V+$ reference of the buffering circuit. Additionally, the ground voltage of the design presented in Figure 6.16 is connected to the $-V_s$ port of the AD8039 amplifiers. The connection between the voltage supply step and the buffering circuit is schematically presented in Figure 6.18. In this case, only one of the amplifiers has been plotted for simplicity but the voltage supply must be connected to the buffering lines of the four channels of the final design.

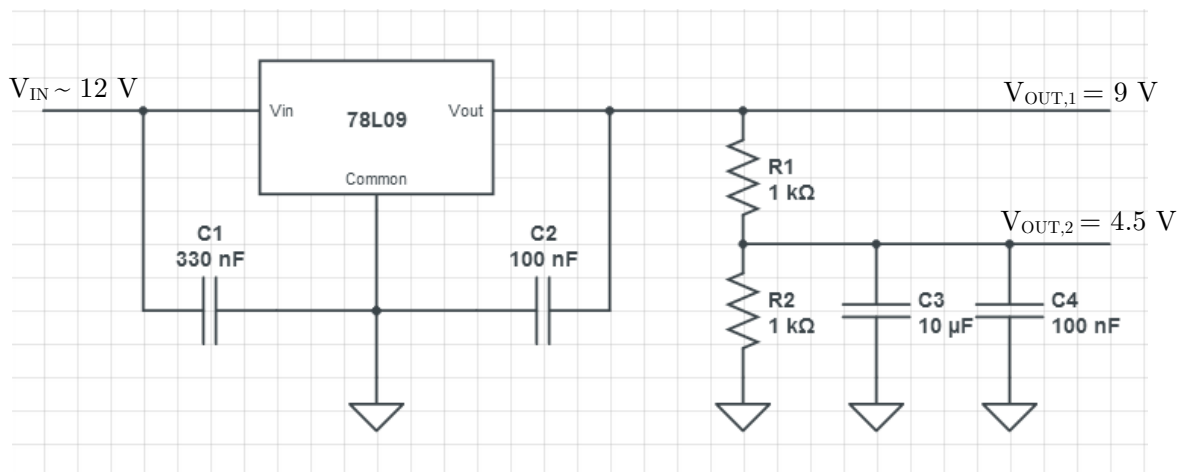


FIGURE 6.16 Voltage supply circuit schematic.

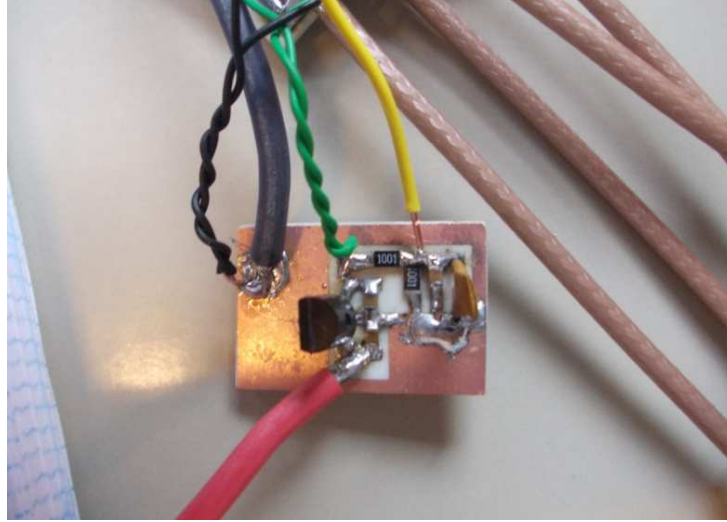


FIGURE 6.17 Voltage supply circuit with the 78L09 voltage regulator and the voltage divisor step.

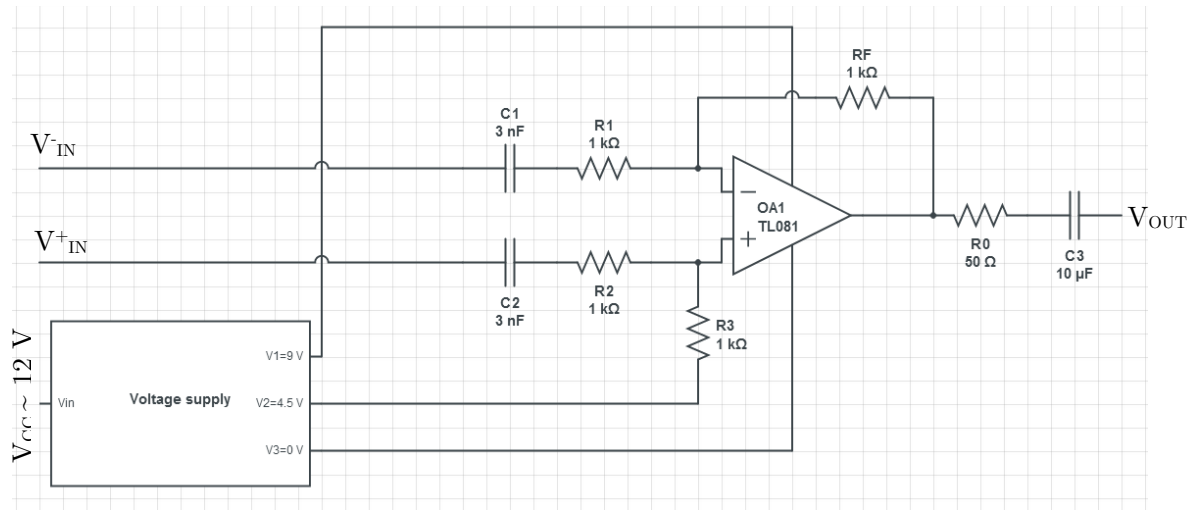


FIGURE 6.18 Voltage supply + buffering circuits schematic and connections.

In the final design schematic presented in Figure 6.18, capacitors at the inputs and output of the operational amplifier have been added to block DC bias. A serial resistor has been also placed at the output to adapt the circuit to a $50\ \Omega$ line. As it can be seen in Figure 6.18, a gain equal to 1 has been chosen for the final design of the buffering circuit.

So, the final Printed Circuit Board (PCB) top and bottom designs are shown in Figure 6.19 top and right pictures, respectively. As it can be seen, the power supply circuit has been integrated to the buffering design. Two AD8039 chips (one at each face of the PCB) have been soldered in order to have the four differential inputs to get the I and Q components of the direct and backscattered signals. The four differential inputs, the four outputs and the continuous voltage supply locations in the PCB are shown in Figure 6.19.

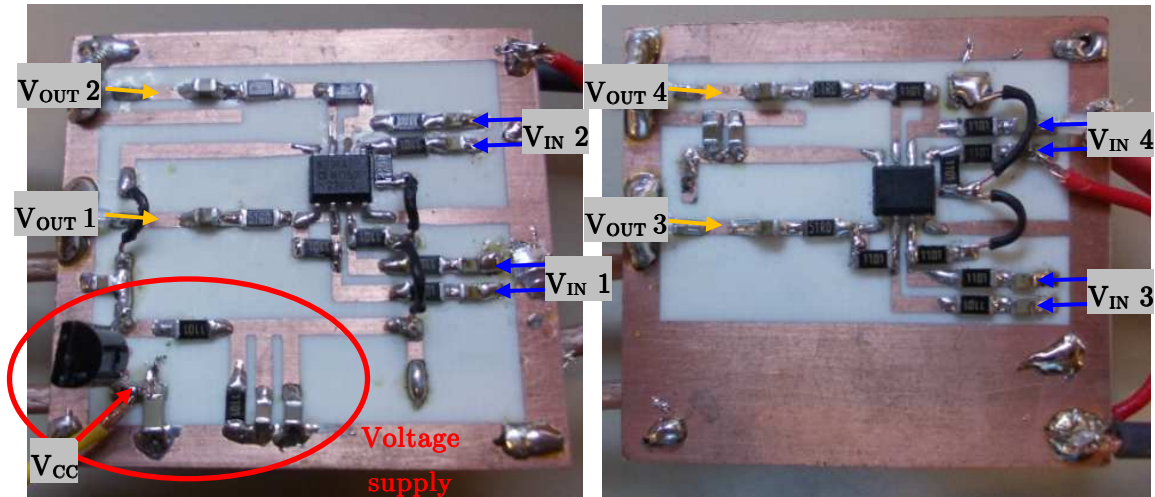


FIGURE 6.19 Final PCB top (left) and bottom (right) designs.

So, once the final circuit was designed, the four buffering channels were tested at different frequencies to see if their responses were as expected. In order to check the amplifier response, a signal generator, an external voltage source and an oscilloscope were used for measurements. The test set is presented in Figure 6.20. So, the sinusoidal signal coming from the generator was connected to the positive input of one of the amplifiers while the negative one was connected to ground. Additionally, the direct signal was sent to the channel 1 of the oscilloscope. On the other hand, the output of the analysed amplifier was connected to the channel 2 of the oscilloscope. Finally, an external voltage of 12.4 V was considered for the input voltage supply of the circuit.

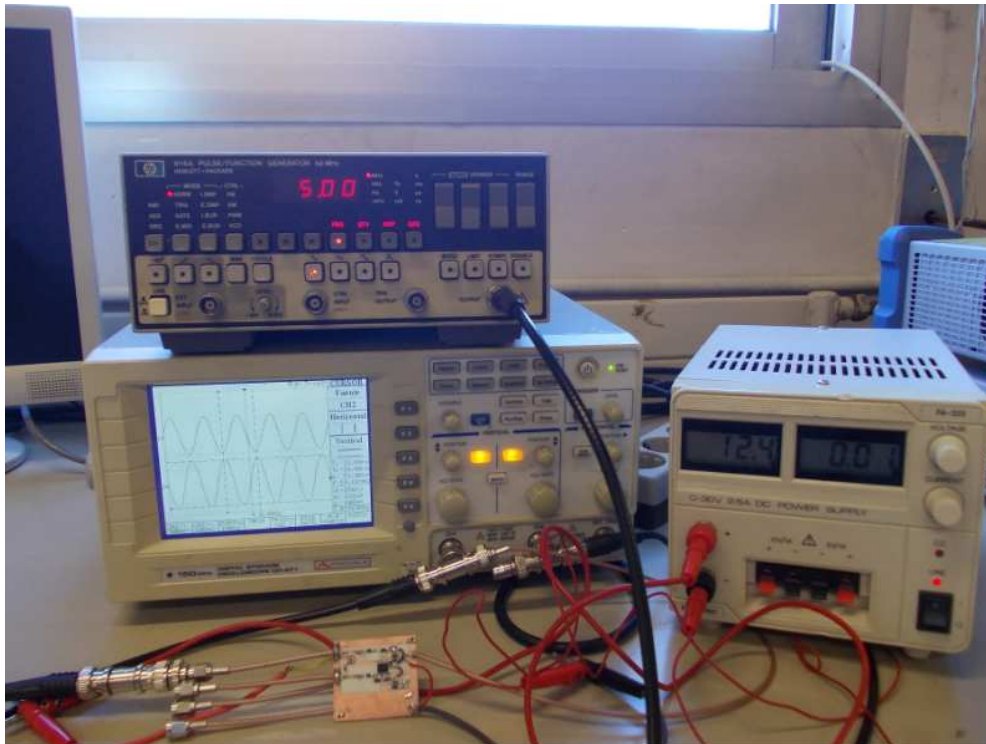


FIGURE 6.20 Final PCB testing.

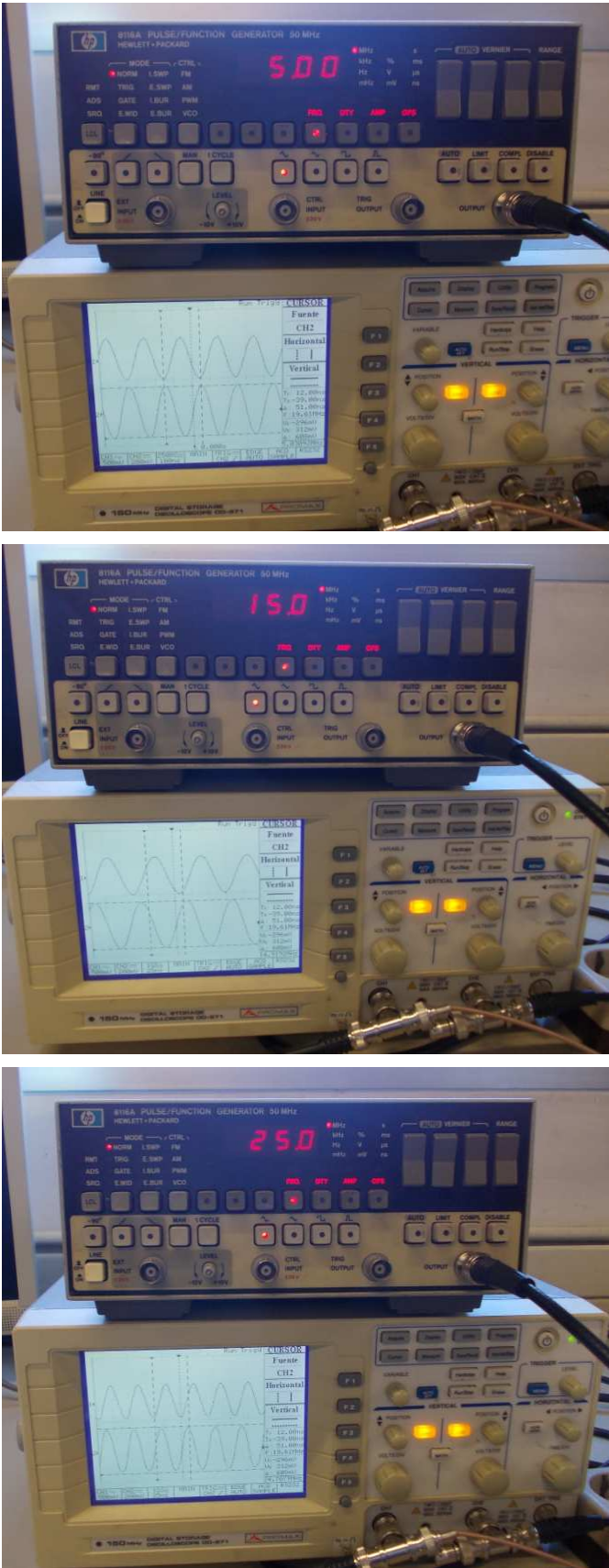


FIGURE 6.21 Buffering circuit testing results.

The results obtained at different frequencies (5 MHz, 15 MHz and 25 MHz) are shown in Figure 6.21. It is important to say that a resistor of $50\ \Omega$ was placed in parallel with the high impedance port of the oscilloscope for proper coaxial line termination. Therefore, as shown in Figure 6.22, the measured voltage in the oscilloscope will be $V_{oc} / 2$ as shown in the equivalent circuit.

So, in Figure 6.21, a measured peak-to-peak voltage around 600 mV is obtained in the three cases. This result is in accordance, considering the voltage divisor due to the parallel resistor at the input of the oscilloscope, with the input voltage selected in the signal generator which was 650 mV of peak. The process was repeated for the four channels in order to verify the correct performance of the four operation amplifiers used in the design.

6.2.1.3 TBS 6981 and buffer connection

After the design and test of the buffering circuit, it must be connected to the TBS6981 PCIe card to acquire the desired signals. As already mentioned, the design of the buffering PCB was made to obtain the required voltage supply from the DVB PC card. So, in this section, the connection and the attachment of the buffering circuit to the PC card is presented. First of all, the points of connection in the TBS6981 card must be identified. As mentioned in section 6.2.1.1, we are interested in the raw data of the acquisition, after down-conversion but previous the MPEG demodulator.

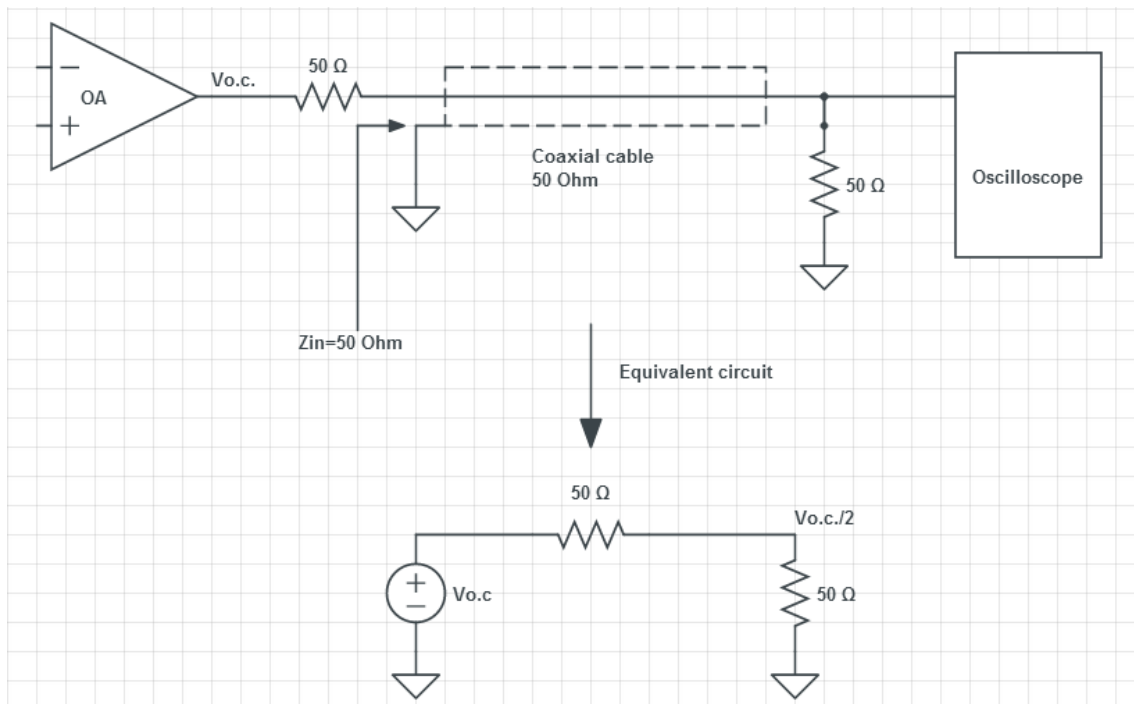


FIGURE 6.22 Buffering circuit testing circuit.

As it was described, the signal is decomposed in the In-phase and Quadrature components at the output of the tuner where they are given in differential form. It makes a total of 8 signals of interest to be acquired corresponding to the signal components of the direct and backscattered signals.

Therefore, a point on the output lines going out the tuner to the demodulator has been selected to get the signals. In Figure 6.23 top picture, the connection points on the TBS6981 card are shown. Each colour pair corresponds to the two differential signals of each signal component. Then, each pair is connected to one of the differential inputs of the operational amplifiers. The correspondence of each pair of signal with the buffering circuit inputs must be seen in bottom pictures of Figure 6.23.

Additionally, the voltage supply sub-system must be connected to the voltage supply of the PC card. It is schematically presented in Figure 6.24 with a blue line. Furthermore, the four output lines have been identified with the corresponding I or Q labels.

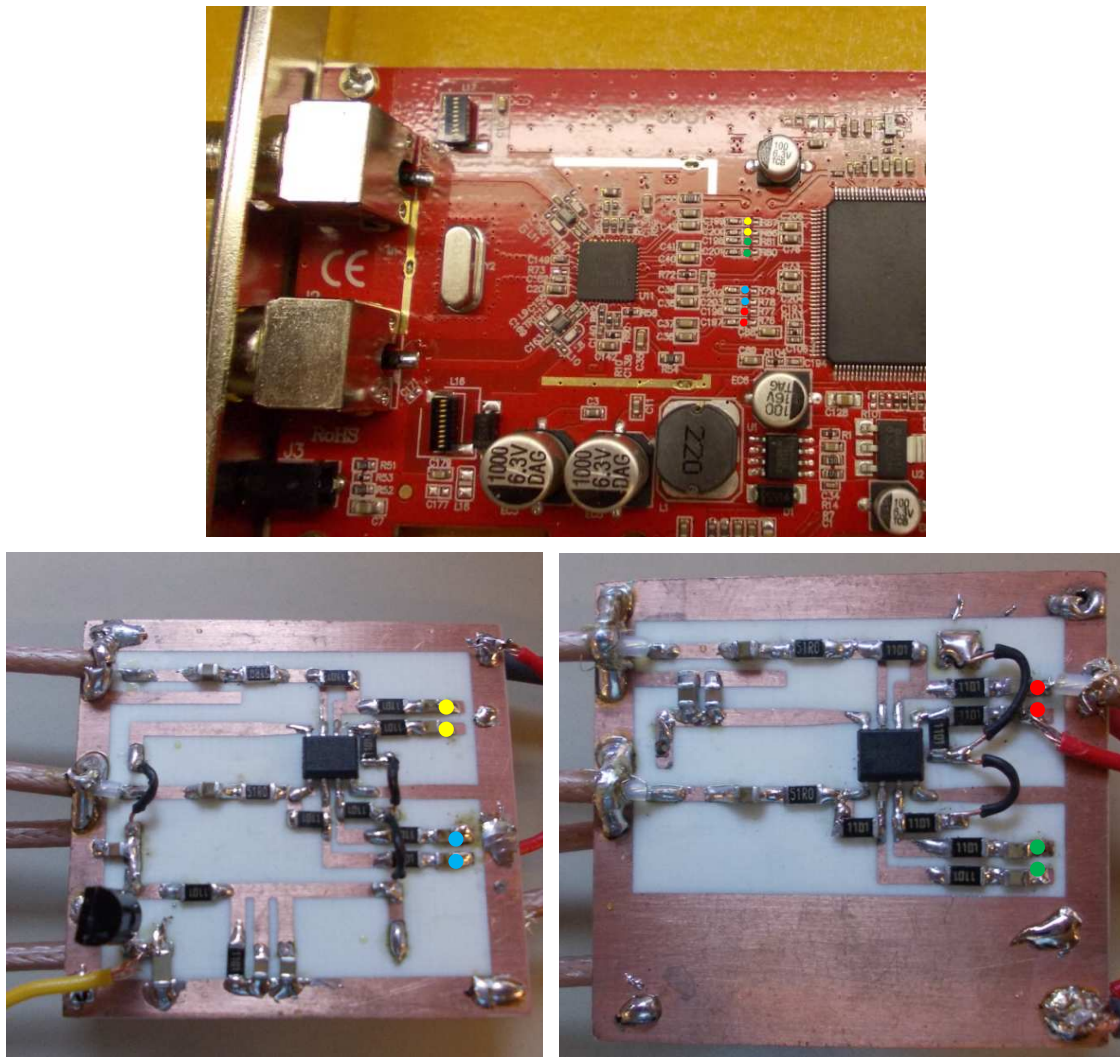


FIGURE 6.23 Buffering circuit connection points in the TBS6981 PC card.

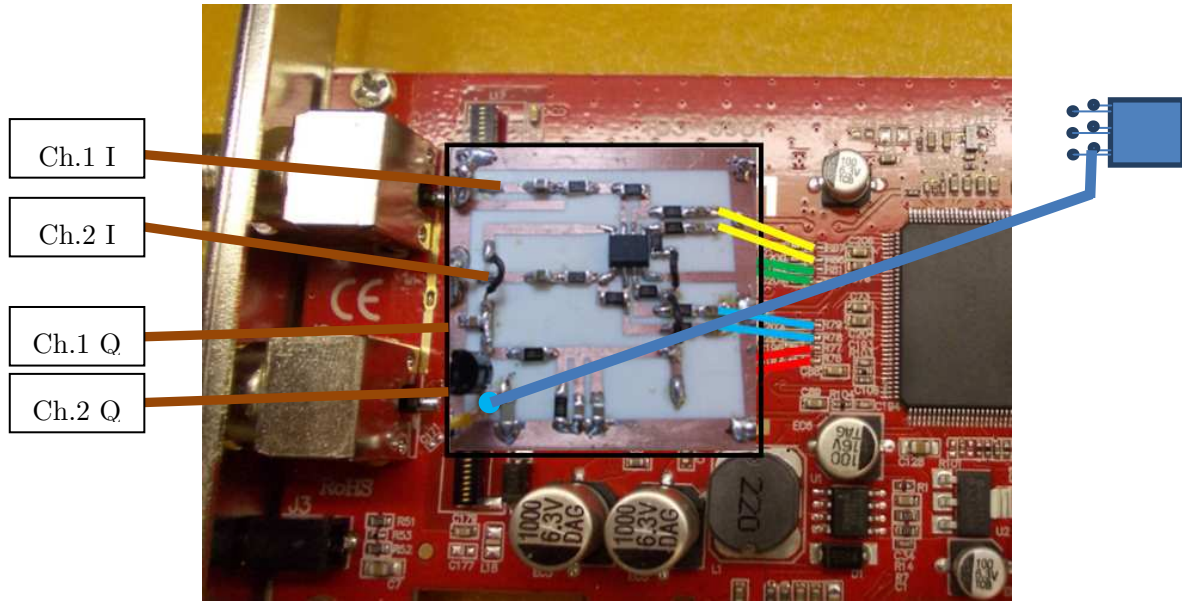


FIGURE 6.24 Buffering circuit connections and output lines.

So, the final design is presented in Figure 6.25, Figure 6.26 and Figure 6.27. In Figure 6.25 a general view of the final design is presented. As seen, the buffering circuit has been placed on a metallic plate over the tuner. The metallic plate makes possible to have a common ground reference between the PCB and the TBS6981 card. In Figure 6.25, the voltage supply connection can be also seen (green wide wire). Additionally, the four outputs of the buffering circuit have been connected to a rack of parallel SMA female connectors.

In Figure 6.26, a detail picture of the SMA female rack is shown. So, it will be easier to install the final design into the PC mother board having the output signal accessible with no necessity of opening the PC for each measurement. Furthermore, having the four outputs fixed in the rack will make possible to connect and disconnect the outputs without risk of damaging the buffer and PC card connections.

Finally, a zoom-in of the buffering circuit integrated in the TBS-6981 card is presented in Figure 6.27. As seen, the buffering PCB has been fixed to the metallic plate with three screws. The coloured cables in the inputs coincide with colours used in Figure 6.23 and Figure 6.24.

So, after presenting all the design steps of the buffering PCB, in the next section the Low-Noise Blocks (LNB) are presented and the necessary modifications for our design studied and tested.

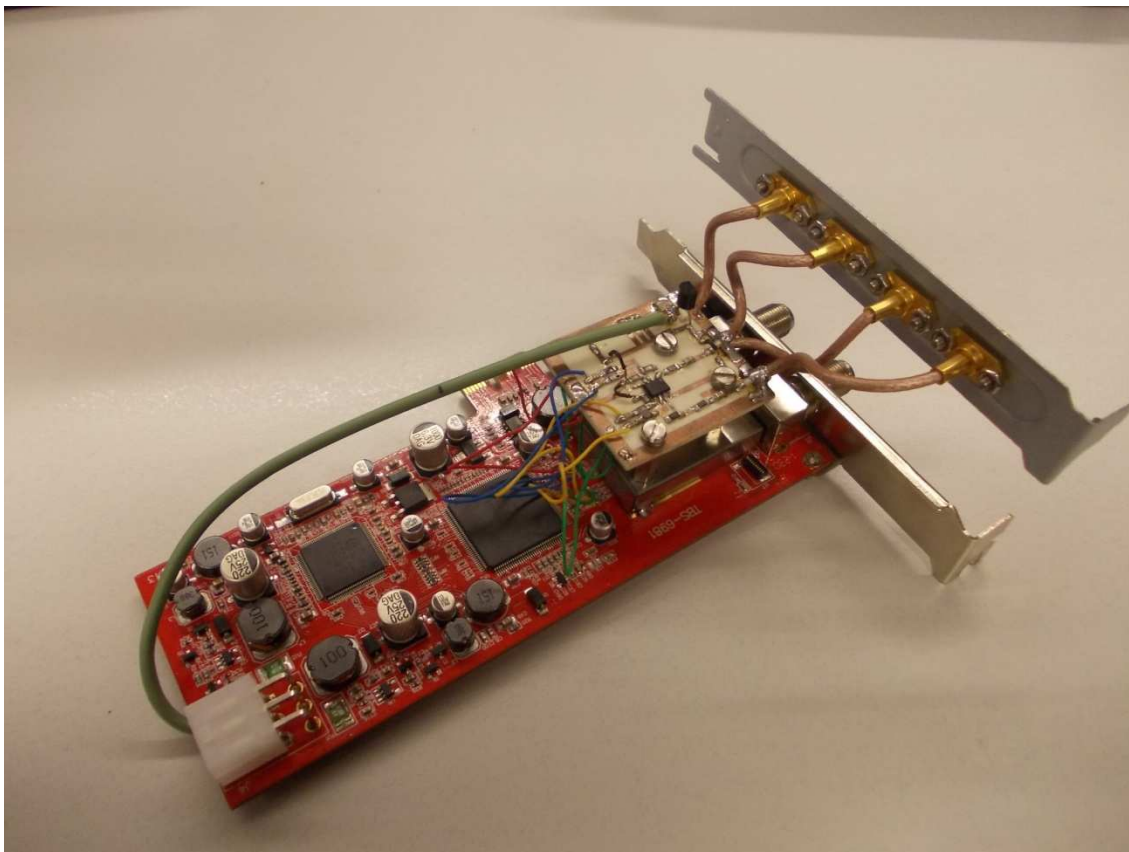


FIGURE 6.25 TBS6981 with buffering circuit final design.

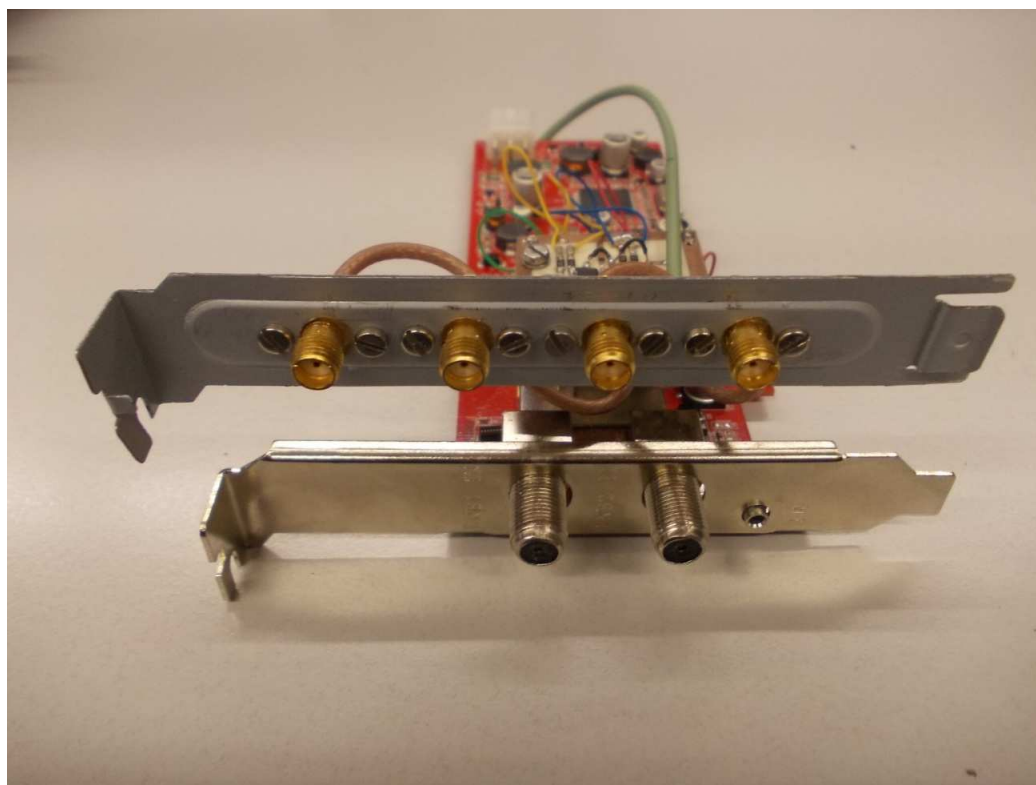


FIGURE 6.26 Final design detail of the two inputs (direct and backscattered signals) and four outputs (I and Q components of each signal).

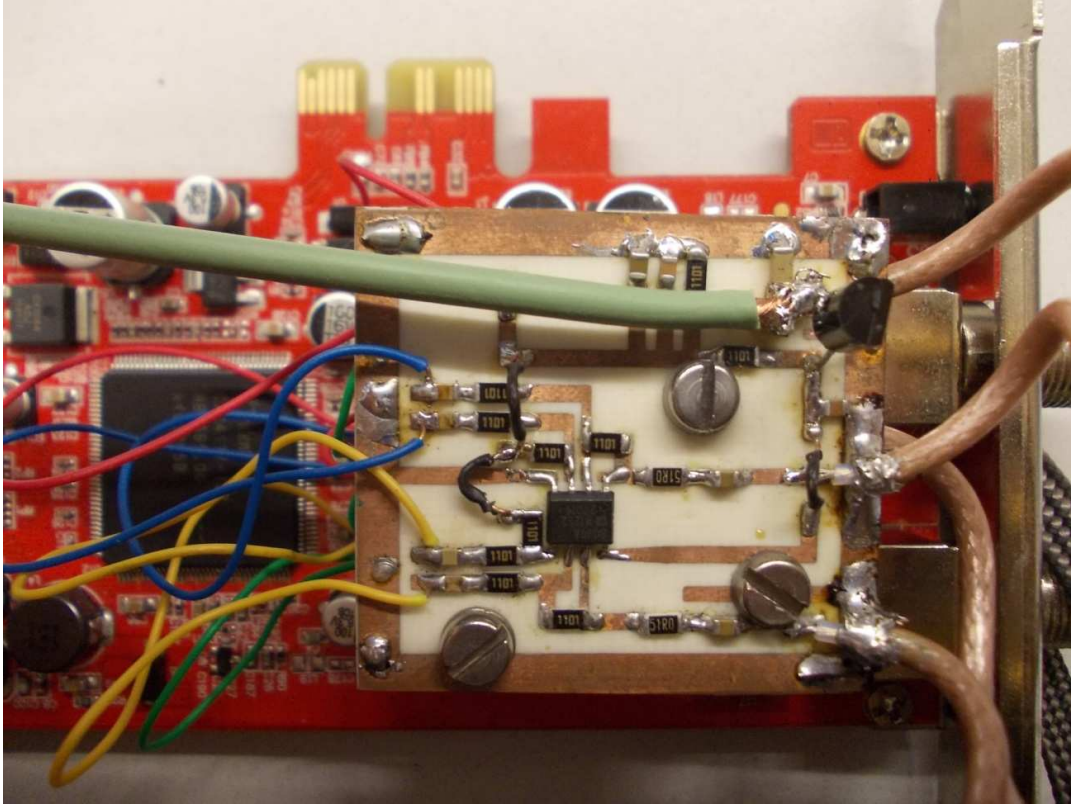


FIGURE 6.27 Detail of the buffering circuit into the TBS6981 card.

6.2.2 LNB study: external oscillator

In this section the LNB will be studied. In this case, Televes low-cost Universal LNBs, as the one shown in Figure 6.28, have been used. This block has an output impedance of $75\ \Omega$ with an output F female connector. Regarding the power consumption, input voltages from 12 to 20 V with a maximum current of 90 mA will be used.

The LNB has two local oscillators (LOs) with central frequencies at 9.75 GHz and 10.6 GHz. The LO selection is made by sending a tone of 0 and 22 KHz, respectively. The communication is automatically made by the TDT card using the DiSEqC protocol. The range of input frequencies is 10.7 GHz to 12.75 GHz. Therefore, the output frequencies will vary from 950 to 1950 MHz for low-band (using the LO at 9.75 GHz) and from 1100 to 2150 MHz for the high-band (considering the LO at 10.6 GHz).

However, the frequency stability of the internal LO is ± 2 MHz. This feature, which is good enough for TV signal reception, may be insufficient for SAR purposes because having two different oscillators, one for each received channel (direct and backscattered signals) with such stabilities could cause important problems in the raw data focusing. Therefore, in the following section, the LNB will be modified in order to operate with an external oscillator which will be common for both acquired signals.

Other interesting features of the presented LNB are a gain of 58 dB, polarity discrimination higher than 18 dB and a noise factor of 0.3 dB. The dimensions of the LNB are 112 x 60 x

60 mm while its weight is around 140 g. It can operate in a range of temperatures from -30 to 60 °C. First of all, one of the LNBs has been opened in order to identify the different parts of the circuit. In Figure 6.29, the inside view of the LNB is presented while in Figure 6.30 the different components of the circuit are depicted.



FIGURE 6.28 TELEVES LNB used in the bistatic GEOSAR with on-ground receiver design.

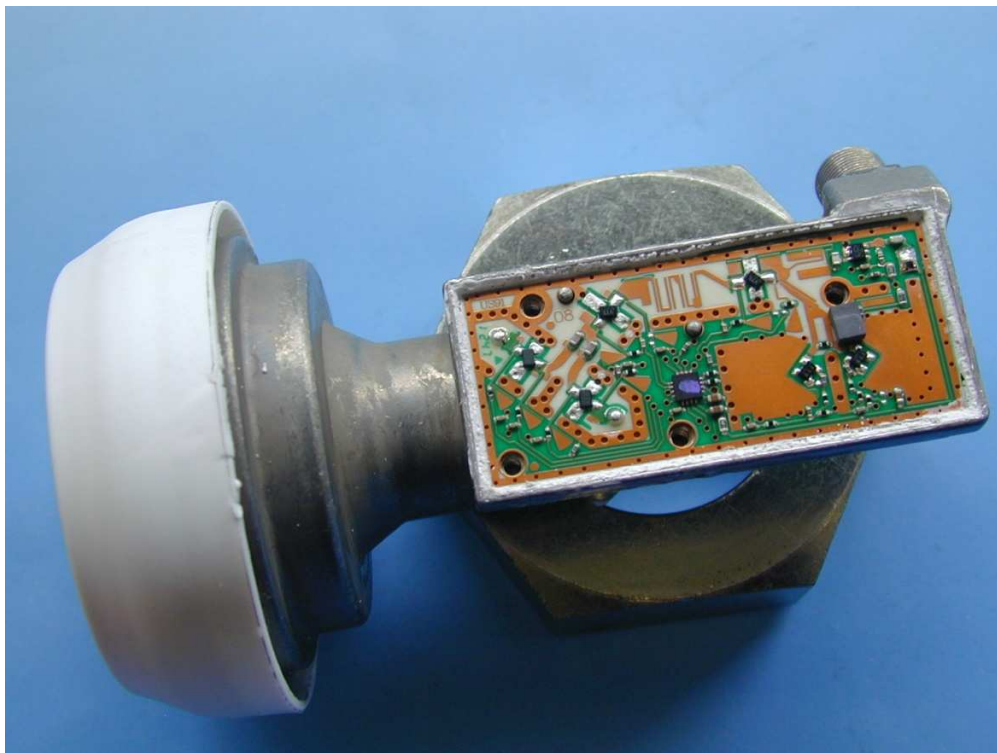


FIGURE 6.29 Inside view of the LNB.

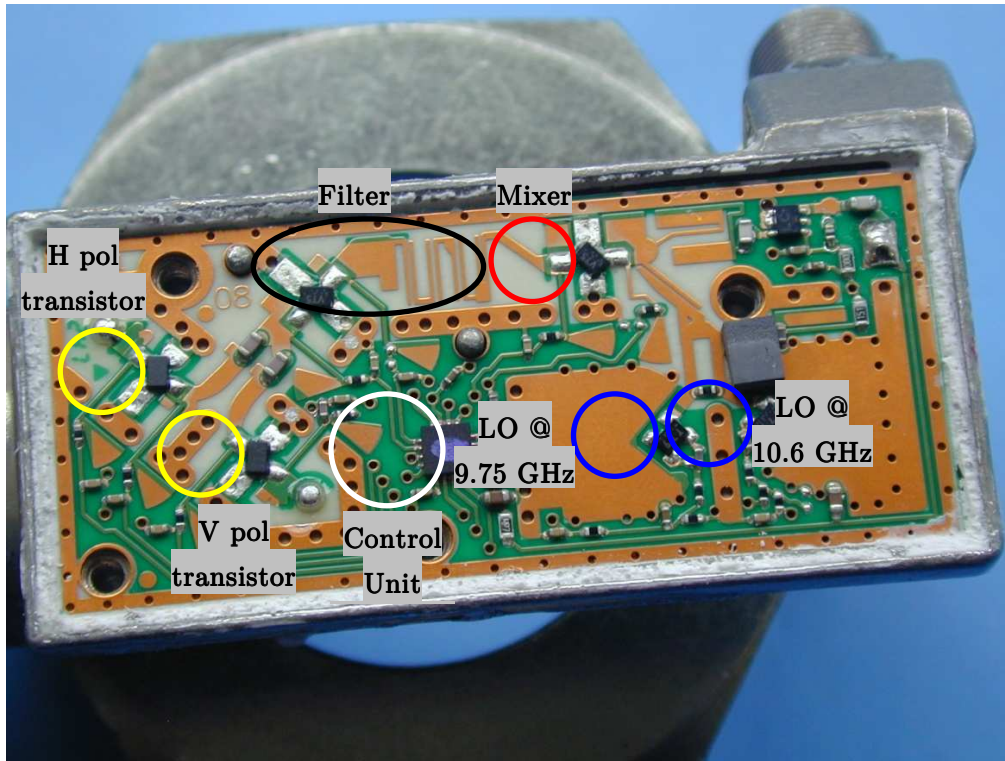


FIGURE 6.30 LNB PCB and components.

So, the yellow circles in Figure 6.30 marks the location of the two transistors used to select the input signal polarization. The signal passes through a band-pass filter until it reaches the mixer. The mixer combines this signal with the one coming from one of the local oscillators (circled in blue in Figure 6.30) in order to down-convert the signal to an intermediate frequency around 1 GHz depending on the operation band. All the transistors of the LNB are controlled by the control unit circled in white. The control unit is the part with direct communication with the TV card in order to select the desired band and polarization of the desired TV channel.

6.2.2.1 LNB measurement with local and external oscillators

So, as presented in the previous section, the local oscillators of the LNBs used in the on-ground receiver design are not stable enough in frequency to assure the correct synchronism between both channels during the acquisition. Therefore, it will be necessary to modify the LNB hardware in order to make possible to use a common external oscillator for both channels. In this section, the different steps in the design are presented and the results obtained from the tests performed with the original and modified LNBs are compared.

The LNB modification has been carried out in the following steps. After removing the metallic, the output coaxial port soldering is removed (*step 1* from Figure 6.31). Once the PCB is extracted, one of the transistors that operate as a local oscillator must be removed. In this particular case, the oscillator transistor working at the higher frequency has been removed. This corresponds to the *step 2* in Figure 6.31. Additionally, the resonator under

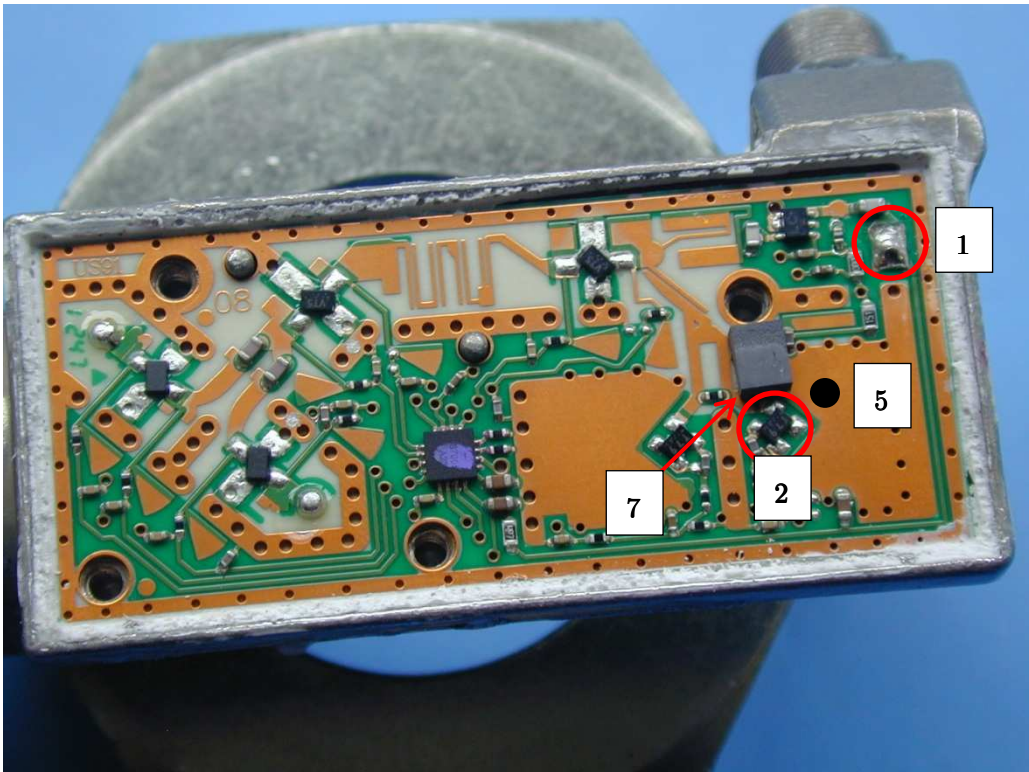


FIGURE 6.31 LNB PCB necessary modifications (I).

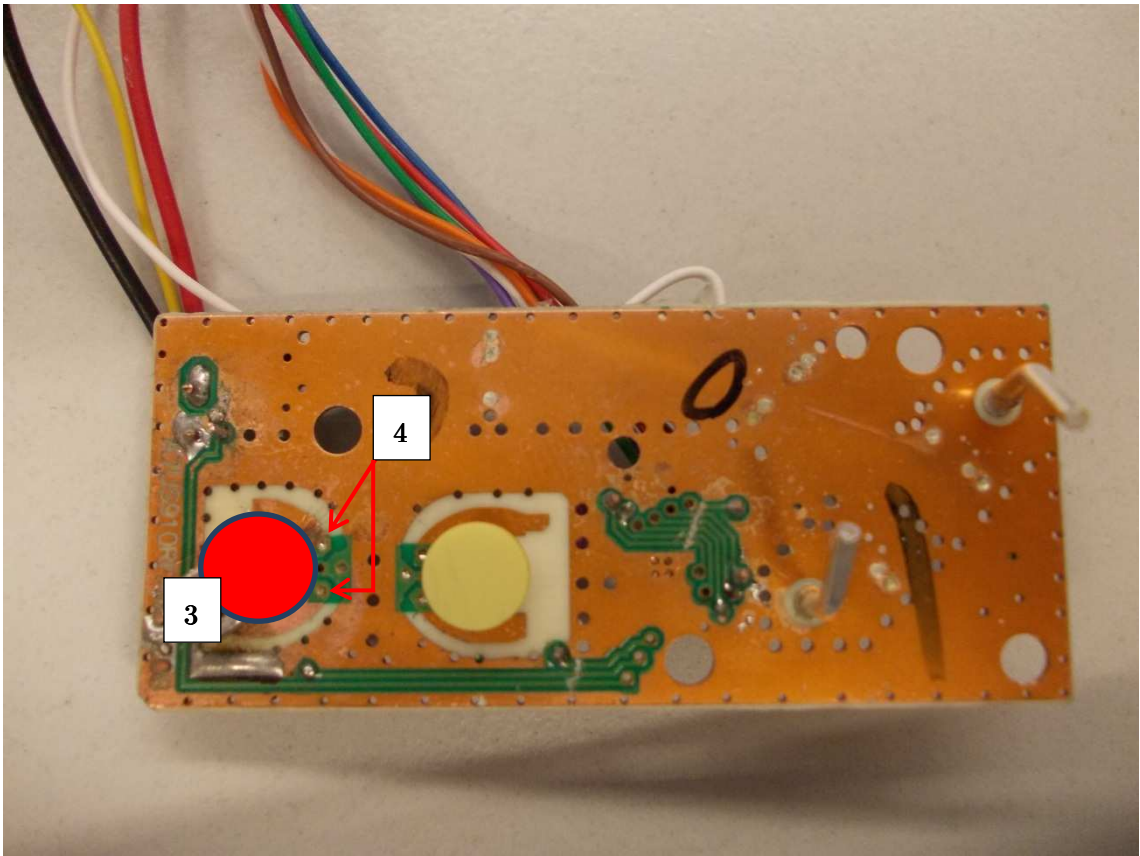


FIGURE 6.32 LNB PCB necessary modifications (II).

the extracted transistor has been also removed since it is worthless without the transistor (*step 3* in Figure 6.32). Furthermore, the tracks that connect the lines around the resonator with the transistor gate and emitter have been eliminated to avoid parasitic phenomena as shown in *step 4* of Figure 6.32.

Once the transistor and resonator have been removed, a hole has been made in the ground plane near to the extracted transistor (*step 5* in Figure 6.31). A coaxial cable has been passed through the hole soldering the cooper shield to the ground plane (*step 6* in Figure 6.33) and the cooper core to the circuit line where the transistor emitter was connected through a 10 pF capacitor (*step 7* and *step 8* in Figure 6.31 and Figure 6.33, respectively).

The other edge of the coaxial cable has been passed through the screw hole shown in *step 7* of Figure 6.34, and a SMA connector has been installed (*step 10* in Figure 6.34). Finally, the PCB output has been soldered again to the LNB (*step 1* of Figure 6.31).

Thus, the final LNB design ready for working with external oscillator is shown in Figure 6.34 and Figure 6.35.

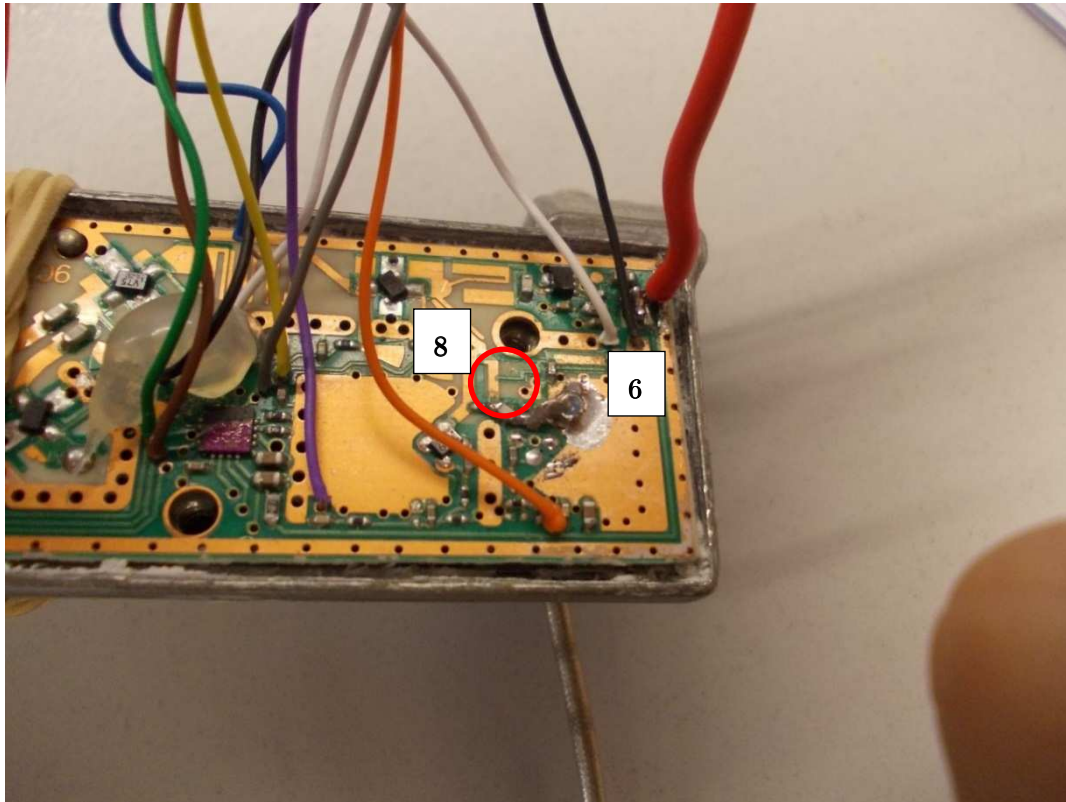


FIGURE 6.33 LNB PCB necessary modifications (III).

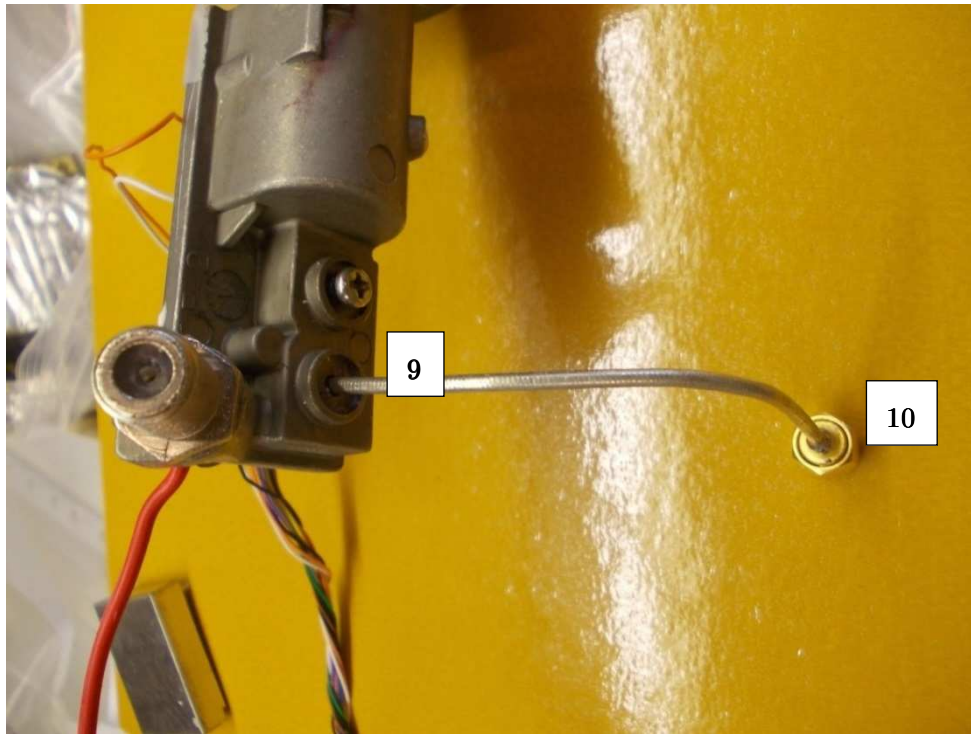


FIGURE 6.34 LNB ready for working with external oscillator (back view).

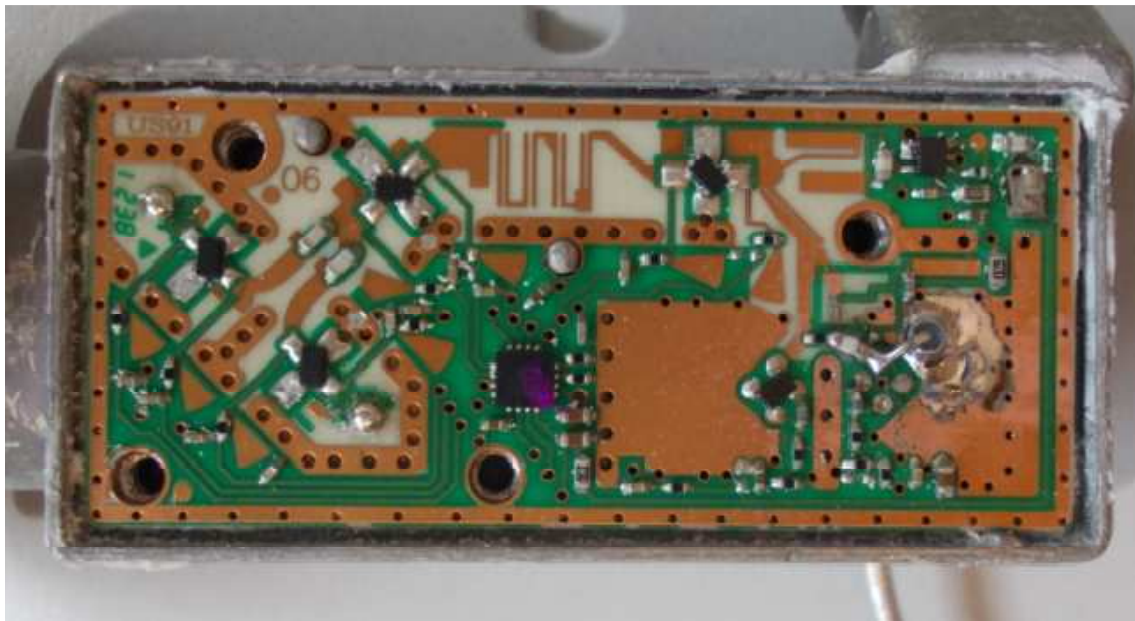


FIGURE 6.35 LNB ready for working with external oscillator (front view).

After the design of the LNB with external oscillator, the performance of the original and modified devices needs to be compared. First of all, the LNB with local oscillator has been tested. In order to do that, the measurement scheme presented in Figure 6.36 has been used. The LNB has been connected to the computer in order to control the local oscillator and the polarization selecting one of the TV channels. In this case, a channel on the higher band with H polarization has been tuned in the computer software in order to use the 10.6 GHz oscillator since it is the one removed in the external oscillator design.

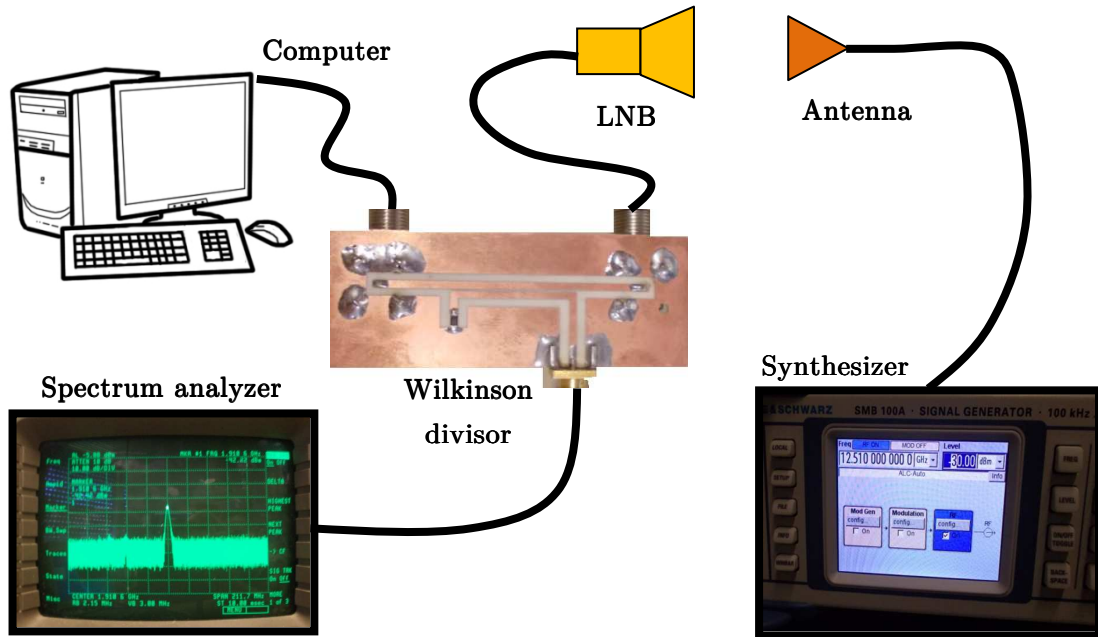


FIGURE 6.36 Measurement scheme for the LNB with local oscillator.

An external signal at the same frequency than the tuned channel (12.50 GHz) with an amplitude of -30 dBm has been generated with a synthesizer. This signal has been sent to a rectangular aperture antenna which has been faced to the LNB. The signal collected by the LNB, and down-converted thanks to the local oscillator used for this configuration, has been sent to a spectrum analyser using a Wilkinson divisor designed with a coupled lines matched at the intermediate frequency. In this case, a peak around 1.90 GHz is expected after down-conversion.

Similarly, an alternative measurement set have been designed to test the LNB performance with external oscillator. The scheme used is presented in Figure 6.37. In this case, the computer control is not necessary since the local oscillator has been removed. However, a second synthesizer, tuned at 10.6 GHz, is being used as external oscillator. The rest of components and parameters are the same than in the previous case. The measurement set up for the external oscillator LNB design is shown in Figure 6.38.

So, considering the external signal source at 12.5 GHz with amplitude of -30 dBm for both cases, the results obtained are presented in Figure 6.39. In the left plot of Figure 6.39, the spectral response of the down-converted signal with the local oscillator is presented. In this case, a peak at 1.917 GHz with amplitude of -42.82 dBm is obtained. On the other hand, taking the response obtained with the external oscillator configuration shown in the right plot in Figure 6.39, a peak at 1.909 GHz with amplitude of -24.17 dBm has been found working with amplitude of the external oscillator signal of 0 dBm. As seen, in both cases, the down-conversion is correctly done, obtaining central frequencies around the expected intermediate frequency. Additionally, the external oscillator amplitude could be decreased up to -20 dBm preserving an output signal amplitude of -39 dBm which is still better than the one in the local oscillator configuration.

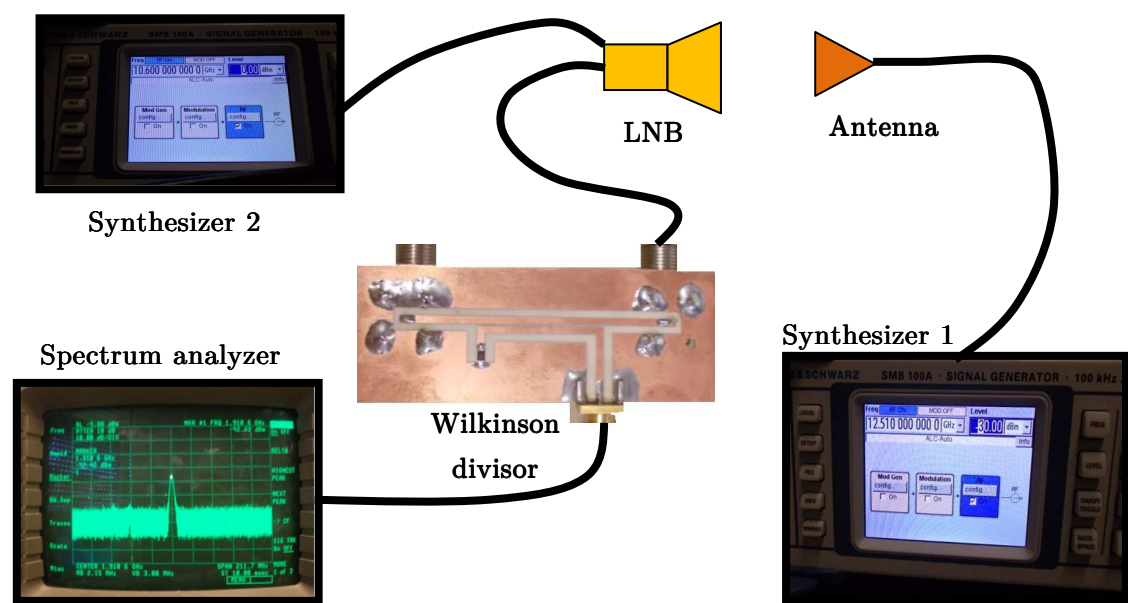


FIGURE 6.37 Measurement scheme for the LNB with external oscillator.

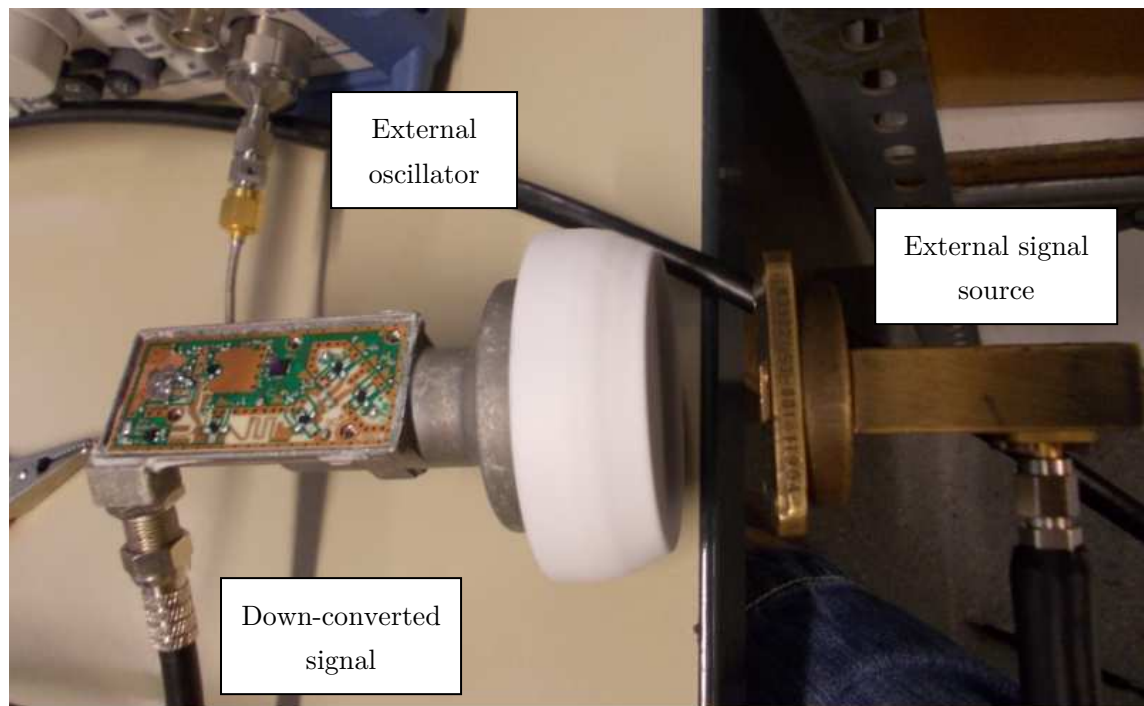


FIGURE 6.38 Measurement set up for the LNB with external oscillator.

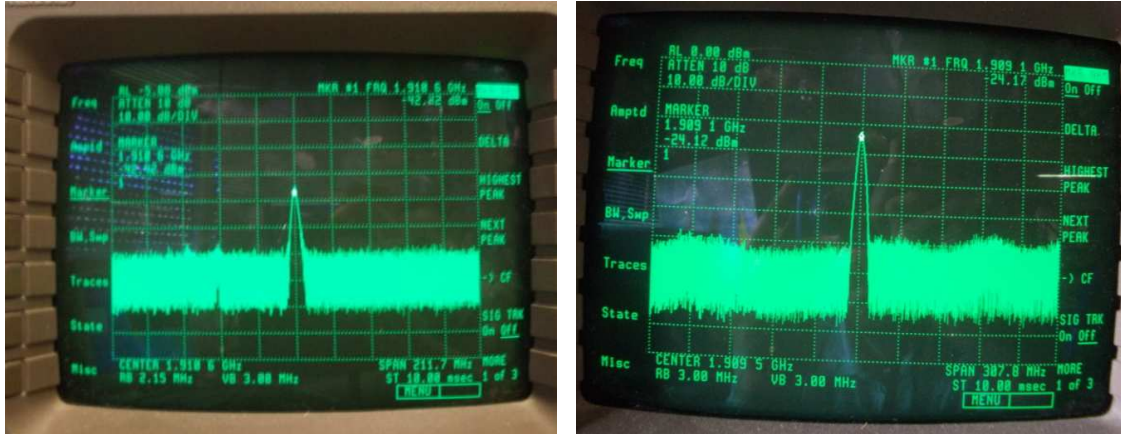


FIGURE 6.39 Down-converted signal from the LNB with local oscillator (left) and with external oscillator with signal amplitude of 0 dBm (right).

Thus, the correct performance of the LNB with an external oscillator has been tested obtaining satisfactory results. So, a common signal reference of around -20 dBm can be used as external oscillator in the bistatic GEOSAR on-ground receiver design using the commercial LNB considered in this analysis.

6.2.3 Acquisition with on-ground receiver scheme

So, after analysing the different parts of the receiver, now a clear vision of the final receiver design and configuration may be presented. The acquisition scheme of the bistatic GEOSAR acquisition with on ground receiver is presented in Figure 6.40.

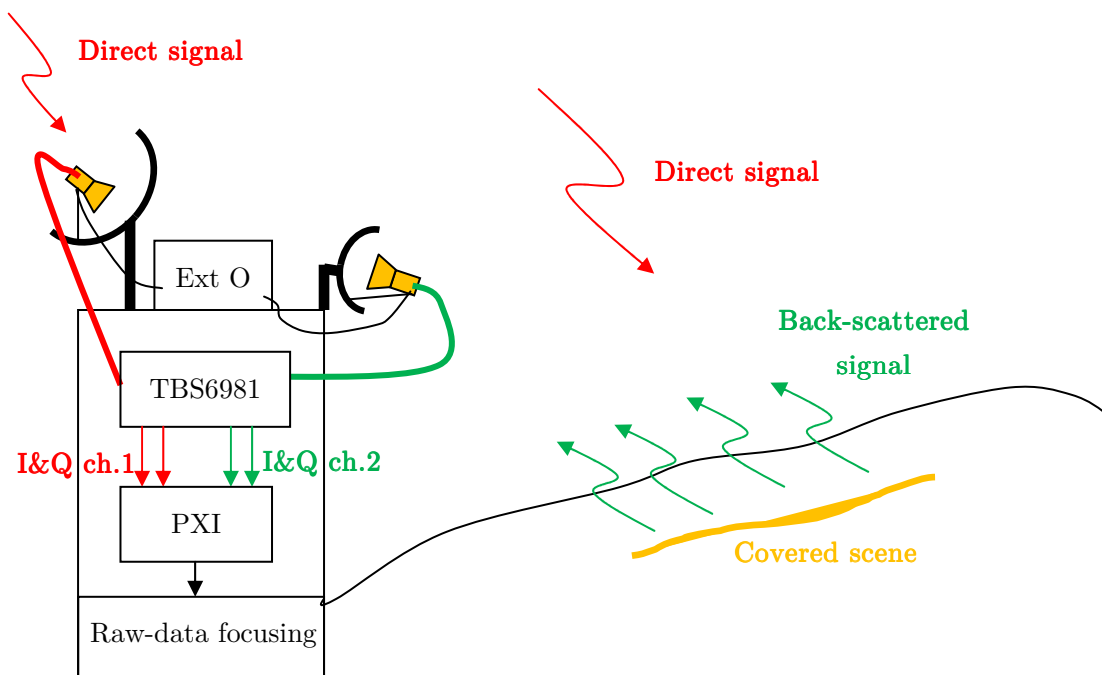


FIGURE 6.40 Bistatic GEOSAR acquisition with on ground receiver.

So, a parabolic antenna will be faced up to the transmitting satellite used as a illuminator of opportunity in order to get the direct signal which will be used as a reference for range compression of the raw-data. Additionally, a second parabolic antenna pointing to the desired scene will be used to obtain the backscattered signals from the targets. Both signals will be acquired by the modified LNBs, described in section 6.2.2, connected to a common external oscillator.

The down-converted signals of each LNB will be sent to the TBS6981 PCIe card with the buffering circuit (presented in section 6.2.1) where the In-phase and Quadrature signal components of each channel will be sent to a PXI. The PXI will be used to digitise the signal and process the raw-data in order to obtain the final focused images.

The system design is completed and the on ground receiver (LNB + DVB receiver) has been finished. It is expected to be tested and get the first results in future studies on the GEOSAR context.

Conclusions and future work

Thus, all along this thesis the most relevant features of future GEOsynchronous Synthetic Aperture Radar missions have been studied. Particularly, a system working in a geosynchronous orbit with nearly-zero inclination has been considered in this analysis. With such particular geometry, a mid-resolution image can be obtained with integration time of hours (or even minutes) with typical power and antenna LEOSAR parameters. In such a way, huge antennas and large transmitted powers as the ones considered in other GEOSAR studies with larger orbital plane inclinations can be avoided. Additionally, permanent monitoring over a large area may be obtained with this particular GEOSAR configuration.

The geometrical analysis of a nearly-zero inclined GEOSAR acquisition has been presented. Orbital parameters as well as integration time plays an important role in the azimuth resolution determination. The theoretical study has shown that using low eccentricities, from 0.0003 to 0.0008, along-track resolution in the order of 10-20 meters can be obtained with integration time of few hours. Such acquisition parameters, useful for stable scenarios, were not valid for phenomena with short temporal correlation. This was the case of APS which needs to be compensated during the raw data processing of several hours to avoid defocusing of the final image.

For this reason, a dual beam concept has been introduced, using a SPOT beam for surface imaging and interferometry and a wide beam at lower frequency for APS monitoring. This second acquisition at lower frequency has been designed to get frequent, each 20-30 minutes, low-resolution images to track the atmospheric behaviour. The validity of this solution has been checked theoretically and via simulation but needs to be further studied with experimental long integration acquisition tests.

One of the most relevant results obtained from the geometric study of a GEOSAR acquisition is related to the non-linear daily motion of the satellite which presents strong accelerations at the edges of the daily relative motion track where slower relative velocity is observed. So, at these points, the azimuth resolution is degraded for a fixed integration time and, furthermore, the lateral lobes increases due to the accumulation of pulses from the satellite positions with slower velocity if constant PRF is considered. Therefore, the acquisition time of these satellite will be constrained to a finite time span during the day which corresponds to acquisitions centred at satellite pass through the perigee and through the apogee.

Additionally, the current TV broadcasting geosynchronous satellite ephemerides have been analysed in order to see their feasibility for SAR purposes in future telecom satellites. This study showed that most of the current satellites present orbital eccentricities high enough to reach the desired resolutions with a few hours of integration. Furthermore, the inclination of these satellites is kept under 0.1° most of the time as desired in the kind of GEOSAR configurations analysed in this thesis.

On the other hand, the radiometric study has provided other important results to take into account in future GEOSAR mission designs. One of the major differences between current LEOSAR acquisition and proposed GEOSAR found in the analysis was the Doppler history of the received echoes. In case of GEOSAR, the orbital radius variations derived of the orbital eccentricity results in a non-constant Doppler centroid common to all the targets within the scene. This Doppler centroid, not useful for in the image processing, must be tracked and compensated. So, small relative Doppler after compensation below 10 Hz are obtained in GEOSAR case which differs significantly from LEOSAR.

This Doppler bandwidth will define the achievable azimuth resolution of the acquisition but, at the same time, it will be important to determine the minimum PRF that could be considered in the timing analysis. The diamond diagrams in GEOSAR case have been computed to see the feasibility of the system in terms of avoiding interferences. An important new result has been obtained in this analysis. Taking into account the particular motion of the geosynchronous satellites considered with nearly fixed position, once the PRF has been selected, the interfered zones can be projected to an Earth map in order to see which are the eclipsed zones over the surface. This new representation of the nadir and transmission interferences has been called Dartboard Diagram.

Regarding the power link budget, the analysis shows that it is possible to reach the desired SNR (above 10 dB) with typical moderate LEOSAR power and antenna parameters. However, the re-using of the signal transmitted by current communication broadcasting geosynchronous satellites is not feasible since the EIRPs of them are not adequate for SAR purposes. Therefore, a dedicated satellite or transponder should be considered in future mission for SAR acquisitions.

The GEOSAR focusing is another important point. The GEOSAR simulator used in the simulations presented in this thesis has been helpful to corroborate part of the theoretical studies. So, the different configurations studied have been simulated and the final focused images for simple ideal scenarios have been provided. Additionally, the impact on the focusing of clutter and APS decorrelation has been also studied. In case of APS, an autofocus technique to compensate the phase variations produced by the atmospheric changes has been presented and tested. However, further analysis in this topic as well as in clutter impact and orbital positioning errors should be performed since these are the critical aspects on the GEOSAR acquisition. Additional experimental test using long integration time GB-SAR data could be used to have a first approximation to clutter and APS

decorrelation issues.

Furthermore, a bistatic GEOSAR baseline design has been studied. This analysis is part of an ESA project carried out jointly with SES ASTRA, Politecnico di Milano, Thales Alenia Space, Aresys, Gamma Remote Sensing, Cranfield University, University of Reading and Universitat Politècnica de Catalunya. The most relevant results obtained in the monostatic analysis were extended to the bistatic configurations. The bistatic design may have special importance thinking on re-using the signal from a telecommunications satellite. However, the complexity on the synchronisation chain can be a limiting factor for those configurations and, therefore, monostatic GEOSAR seems the most suitable for the first experimental tests.

The first steps on the experimental design of an on-ground receiver for a bistatic GEOSAR acquisition with illuminator of opportunity have been presented. So, the theoretical approach to the bistatic GEOSAR with on-ground receiver was presented paying special attention to geometric and radiometric aspects. After that, the hardware and necessary modifications to acquire the direct and backscattered signal were presented. In this case, a dual DVB-S2 PCIe card with a buffering circuit to acquire the I and Q components of the signal have been used. Additionally, the LNBS have been modified in order to operate with a common external oscillator to avoid problems with the synchronism. This experimental work is an important validation for the GEOSAR concept and it is expected to be one of the future lines of investigation in GEOSAR.

To sum up, after all the analysis presented in this thesis, nearly-zero inclination GEOSAR is an interesting alternative of LEOSAR acquisition for future SAR mission. The nearly fixed position of the satellite in the GEOSAR configuration studied is the major advantage allowing permanent monitoring over large areas.

The major drawbacks and limiting factors are related to the long integration time. So, although first theoretical approaches and simulations on atmospheric and clutter decorrelation have been studied, further analysis complemented with experimental tests are necessary to corroborate the studied. Additionally, the orbital positioning errors are another limiting factor of the GEOSAR acquisition. This aspect has been introduced from a theoretical point of view, but it should be studied in depth in order to determine the achievable accuracy at geosynchronous orbit with future technologies since GPS is not a valid possibility in this case. The SAR data itself with ground control points could be used to locate the orbit as described in the thesis but the locations and densities of these calibration have to be determined in future analyses.

So, deeper studies on the atmospheric and clutter dynamics as well as orbit assessment should be necessary in order to predict their behaviour in GEOSAR real acquisitions for different conditions.

Additional future work would be required to completely characterize the GEOSAR acquisition. The on-ground bistatic GEOSAR acquisition campaigns has to be started. The long integration experimental data obtained with this system will make possible to corroborate most of the theoretical and simulated results found in this thesis. Different acquisitions in different scenarios will provide more information on the scene properties considering the integration times of several hours. The use of on-ground GEOSAR receiver can be useful as well to track the orbital position of the satellites and try to determine the possible orbital accuracy of future control points in a future satellite monostatic GEOSAR acquisition.

Other aspects, such as polarimetry, has not been addressed in this thesis and it would be an interesting topic for further analysis. In case of GEOSAR, a full polarimetric acquisition could be interesting in order to track and compensate the ionospheric artefacts presented in Section 4.3.1.2, particularly the Faraday rotation.

Moreover, the analysis presented in this thesis has been focused in mid-latitude scenes. The extension to equatorial and tropical zones, with high occurrence of natural phenomena that could be tracked with GEOSAR (flooding, snow covered regions, rainstorms, earthquakes, etc), would be an interesting extension to the current analysis. In case of Polar regions, working with a low inclination satellite around the terrestrial Equator would result in high incidence angles that would degrade the SAR performance. On the other hand, for Equatorial and Tropical regions at low-latitudes, the GEOSAR orbital configuration should be modified with respect to the one presented in this thesis. So, a latitudinal synthetic aperture should be considered instead of the longitudinal motion taken in our analysis, as shown in Figure 2.26. However, the major drawback of this configuration would be the high ionospheric variations that are observed around the Equator which could degrade significantly the SAR image if they are not previously corrected.

List of Publications

International journals:

- [1] **Ruiz Rodon, J.**; Broquetas, A.; Monti Guarnieri, A.; Rocca, F., "Geosynchronous SAR Focusing With Atmospheric Phase Screen Retrieval and Compensation," *Geoscience and Remote Sensing, IEEE Transactions on* , vol.51, no.8, pp.4397,4404, Aug. 2013.
- [2] **Ruiz-Rodon, J.**; Broquetas, A.; Makhoul, E.; Monti Guarnieri, A.; Rocca, F., "Nearly Zero Inclination Geosynchronous SAR Mission Analysis With Long Integration Time for Earth Observation," *Geoscience and Remote Sensing, IEEE Transactions on* , vol.52, no.10, pp.6379,6391, Oct. 2014
- [3] **Ruiz Rodon, J.**; Broquetas, A.; González Arbesú, J. M.; Closa, J.; Labriola, M.; , "Signal-to-Noise Ratio Equalization for TOPSAR Mode Using a Non-uniform Steering Rate," *Geoscience and Remote Sensing Letters, IEEE* , vol.PP, no.99, pp.1-5, doi: 10.1109/LGRS.2011.2162578
- [4] Makhoul, A. Broquetas, **J. Ruiz-Rodon**, Y. Zhan, and F. Ceba, "A Performance Evaluation of SAR-GMTI MIssion for Maritime Applications," *IEEE Transactions on Geoscience and Remote Sensing*, 2014, accepted for publication.

International conferences:

- [5] **Ruiz, J.** et. al., "Feasibility of Geosynchronous Satellites for Synthetic Aperture Radar Remote Sensing at Ka-Band", Ka and Broadband Communications Conference, Milano 2010.
- [6] **Ruiz Rodon, Josep**; Broquetas, Antoni; Monti Guarnieri, Andrea; Rocca, Fabio; , "A Ku-band geosynchronous Synthetic Aperture Radar mission analysis with medium transmitted power and medium-sized antenna," 2011 IEEE International Geoscience and Remote Sensing Symposium (IGARSS), vol., no., pp.2456-2459, 24-29 July 2011.
- [7] **Ruiz J.** et. al., "Geosynchronous Synthetic Aperture Radar Mission Analysis Based on Long Integration Time Acquisition and Atmospheric Correction", Ka and Broadband Communications Conference, Palermo 2011.

- [8] **Ruiz Rodon, Josep**; Broquetas, Antoni; Monti-Guarnieri, Andrea; Rocca, Fabio; “Atmospheric Phase Screen Retrieval from GEOSAR Long Term Acquisition”, EUSAR, Nuremberg 2012.
- [9] **Josep Ruiz Rodon**, Antoni Broquetas, Eduardo Makhoul, Andrea Monti Guarnieri and Fabio Rocca, “ Results on spatial-temporal Atmospheric Phase Screen retrieval from long-term GEOSAR acquisition”, 2012 IEEE International Geoscience and Remote Sensing Symposium (IGARSS), July 2012.
- [10] Eduardo Makhoul, Antoni Broquetas and **Josep Ruiz Rodon**, “Ground Moving Target Indication using Multi-Channel SAR with Non-Uniform Displaced Phase Centers”, 2012 IEEE International Geoscience and Remote Sensing Symposium (IGARSS), July 2012.
- [11] Andrea Monti Guarnieri, Luca Perletta, Fabio Rocca, Diego Scapin, Stefano Tebaldini, Antoni Broquetas, **Josep Ruiz**, “Design of a geosynchronous SAR system for water vapor maps and deformation estimation”, Fringe Workshop, Frascati (Rome) 2011.
- [12] Recchia, Andrea; Monti Guarnieri, Andrea; Broquetas, Antoni; **Ruiz Rodon, Josep**; Giudici, Davide; Tebaldini, Stefano; “Multi-Aperture Focusing and Atmospheric Phase Screen Estimation in Geosynchronous SAR”, ESA Living Planet Symposium, Edimburg, September 2013.
- [13] Monti Guarnieri, Andrea; Broquetas, Antoni; **Ruiz-Rodon, Josep**; Recchia, Andrea; Giudici, Davide; Schulz, Detlef; Venturini, Roberto; “Wide coverage, fine resolution, geosynchronous SAR for atmosphere and terrain observation”, ESA Living Planet Symposium, Edimburg, September 2013.
- [14] **Josep Ruiz Rodon**, Antoni Broquetas, Andrea Monti Garnieri, Andrea Recchia, ‘Bistatic Geosynchronous SAR for land and atmosphere continuous observation’, 10th European Conference on Synthetic Aperture Radar, June 2014.
- [15] Andrea Recchia, Andrea Monti Garnieri, Antoni broquetas, **Josep Ruiz Rodon**, ‘Impact of clutter decorrelation on Geosynchronous SAR’, 10th European Conference on Synthetic Aperture Radar, June 2014.
- [16] **Josep Ruiz-Rodon**, Antoni Broquetas, Eduardo Makhoul, Andrea Monti-Guarnieri, Andrea Recchia, ‘Internal Clutter Motion Impact on the Long Integration GEOSAR Acquisition’, IEEE *International Geoscience and Remote Sensing Symposium* (IGARSS), July 2014.
- [17] Andrea Recchia, Andrea Monti-Guarnieri, Antoni Broquetas, **Josep Ruiz-Rodon**, ‘Asses,emt of Atmospheric Phase Screen Impact on GEOSynchronous SAR’, IEEE *International Geoscience and Remote Sensing Symposium* (IGARSS), July 2014.

- [18] Eduardo Makhoul, Yu Zhan, Antoni Broquetas, **Josep Ruiz-Rodon**, Stefan Baumgartner, ‘Sea Clutter Statistical Characterization using TERRASAR-X Data’, IEEE *International Geoscience and Remote Sensing Symposium* (IGARSS), July 2014.
- [19] Andrea Recchia, Andrea Monti-Guarnieri, Fabio Rocca, Davide Guidici, Stephen Hobbs, Farid Djelaili, Vu Khang, Deltef Schulz, Ornella Bombaci, Michela Veredice, Claudio Scarchilli, Geoff Wadge, Antoni Broquetas, **Josep Ruiz-Rodon**, ‘Geosynchronous SAR for near-continuous observation of atmosphere and Earth: solutions and challenges’, European Space Agency conference on Advanced RF Sensors and Remote Sensing Instruments” (ARSI), November 2014.

References

- [1] Sharkov, Eugene A., 'Passive Microwave Remote Sensing of the Earth', Physical Foundations, 2003
- [2] Gibson, P., 'Introductory Remote Sensing Principles and Concepts', pp. 17-18 and 63, Routledge London, 2000
- [3] Acker, A.E., 'Understanding Radar: The ABCs of How Radar Systems Work', SciTech Publishing, 2009
- [4] Knott, Eugene F., Shaeffer, John F., Tuley, Michael T., 'Radar Cross Section (2nd Edition)', pp. 7-20, SciTech Publishing, 2004
- [5] Samuel W. McCandless, Jr. and Christopher R. Jackson. 'SAR Marine's User Manual' Chapter 1. Principles of Synthetic Aperture Radar, U.S. Department of Commerce, National Oceanic and Atmospheric Administration, September 2014.
- [6] Werle, D., "Shuttle Imaging Radar (sir-a) Observations Of Large-scale Afforestation Efforts In The Peoples `s Republic Of China," Geoscience and Remote Sensing Symposium, 1989. IGARSS'89. 12th Canadian Symposium on Remote Sensing., 1989 International , vol.3, no., pp.1410-1413, 10-14 Jul 1989.
- [7] Cimino, J.; Elachi, C.; Settle, M., "SIR-B-The Second Shuttle Imaging Radar Experiment," Geoscience and Remote Sensing, IEEE Transactions on , vol.GE-24, no.4, pp.445-452, July 1986
- [8] Martinson, L.W., Gaffney, B.P., Liu, B., Perry, R.P., Ruvin, A., 'Advanced digital SAR processing study', Final Report RCA Government System Div. Moorestown, 1982
- [9] Johnson, W. T K, "Magellan imaging radar mission to Venus," *Proceedings of the IEEE* , vol.79, no.6, pp.777-790, Jun 1991.
- [10] Duchossois, G.; Honvault, C., "The First ESA Remote Sensing Satellite (ERS)--The Programme and the System," OCEANS 81 , vol., no., pp.1014-1018, 16-18 Sept. 1981.
- [11] Nemoto, Y.; Nishino, H.; Ono, M.; Mizutamari, Hitoshi; Nishikawa, K.; Tanaka, K., "Japanese Earth Resources Satellite-1 synthetic aperture radar," Proceedings of the

- IEEE , vol.79, no.6, pp.800-809, Jun 1991.
- [12] Curlander, J.C., "The Shuttle Imaging Radar (sir-c) Digital Processing System," Geoscience and Remote Sensing Symposium, 1989. IGARSS'89. 12th Canadian Symposium on Remote Sensing., 1989 International , vol.3, no., pp.1713-1714, 10-14 Jul 1989.
 - [13] Cuddy, D.; Bicknell, T.; Tankenson, M., "ASF design considerations for Radarsat/ERS-2," Geoscience and Remote Sensing Symposium, 1994. IGARSS '94. Surface and Atmospheric Remote Sensing: Technologies, Data Analysis and Interpretation., International , vol.2, no., pp.906-908 vol.2, 8-12 Aug. 1994.
 - [14] Raney, R., "RADARSAT-Canada's national radar satellite program," Antennas and Propagation Society Newsletter, IEEE , vol.25, no.3, pp.4-8, June 1983.
 - [15] Bartholoma, K.-P.; Benz, R.; Demuth, D.; Dubock, P.; Gardini, B.; Graf, G.; Ratier, G., "ENVISAT-1-on its way to hardware," Geoscience and Remote Sensing Symposium, 1995. IGARSS '95. 'Quantitative Remote Sensing for Science and Applications', International , vol.2, no., pp.1560-1563 vol.2, 10-14 Jul1995
 - [16] Roth, A., "TerraSAR-X: a new perspective for scientific use of high resolution spaceborne SAR data," Remote Sensing and Data Fusion over Urban Areas, 2003. 2nd GRSS/ISPRS Joint Workshop on , vol., no., pp.4-7, 22-23 May 2003.
 - [17] McGuire, M. E.; Parashar, S.; Mahmood, A.; Brule, L., "Evolution of Canadian Earth observation from RADARSAT-1 to RADARSAT-2," Geoscience and Remote Sensing Symposium, 2001. IGARSS '01. IEEE 2001 International , vol.1, no., pp.480-481 vol.1, 2001
 - [18] A.I. Kalmikov, "Real-Aperture radar (RAR) imaging from space", Radio Sci. Bull., No.276, pp. 13-22, 1996.
 - [19] Elachi, C. 'Spaceborne SAR Remote Sensing: Applications and Techniques' , Chapters 3-5, IEEE Press, 1987.
 - [20] Curlander, J.C. and McDonough, R.N., 'Synthetic Aperture Radar: Systems and Signal Processing', Chapter 1: Introduction to SAR, John Wiley & Sons, 1991.
 - [21] Cumming, Ian G., 'Digital Processing of Synthetic Aperture Radar: Algorithms and implementation', Artech House Inc., 2005.
 - [22] Skolnik, M. I. 'Radar Handbook', Chapter 21: Synthetic Aperture Radar, L.J. Cutrona, Sarcutron Inc, Second Edition McGraW Hill, 1990.
 - [23] Bender, M. et al., 'Development of a GNSS water vapour tomography system using algebraic reconstruction techniques'. Adv. Space Res., 47, pp.1704-1720, May 2011.

- [24] Zus, F., Wickert J., Bauer H. S., Schwitalla T., Wulfmeyer V.: Experiments of GPS slant path data assimilation with an advanced MM5 4DVAR system, *Meteorologische Zeitschrift*, 20, 2, pp.173-184, 2011.
- [25] Behrendt, A.; Pal, S.; Aoshima, F.; Bender, M.; Blyth, A.; Corsmeier, U.; Cuesta, J.; Dick, G.; and C. Flamant, M. D.; Girolamo, P. D.; Gorgas, T.; Huang, Y.; Kalthoff, N.; Khodayar, S.; Mannstein, H.; Traeumner, K.; Wieser, A. Wulfmeyer, V. 'Observation of convection initiation processes with a suite of state-of-the-art research instruments during COPS IOP 8b Q. J. R. Meteorol'. Soc., 2011, 137, 81-100.
- [26] Mason, D.C.; Davenport, IJ.; Neal, J.C.; Schumann, G. J-P; Bates, P.D., "Near Real-Time Flood Detection in Urban and Rural Areas Using High-Resolution Synthetic Aperture Radar Images," *Geoscience and Remote Sensing, IEEE Transactions on* , vol.50, no.8, pp.3041-3052, Aug. 2012.
- [27] Trouve, E.; Vasile, G.; Gay, M.; Bombrun, L.; Grussenmeyer, P.; Landes, T.; Nicolas, J-M; Bolon, P.; Petillot, I; Julea, A; Valet, L.; Chanussot, J.; Koehl, M., "Combining Airborne Photographs and Spaceborne SAR Data to Monitor Temperate Glaciers: Potentials and Limits," *Geoscience and Remote Sensing, IEEE Transactions on* , vol.45, no.4, pp.905-924, April 2007.
- [28] Guneriussen, T.; Hogda, K.A; Johnsen, H.; Lauknes, I, "InSAR for estimation of changes in snow water equivalent of dry snow," *Geoscience and Remote Sensing, IEEE Transactions on* , vol.39, no.10, pp.2101-2108, Oct 2001.
- [29] Walters, R. J., J. R. Elliott, N. D'Agostino, P. C. England, I. Hunstad, J. A. Jackson, B. Parsons, R. J. Phillips, and G. Roberts (2009), The 2009 L'Aquila earthquake (central Italy): A source mechanism and implications for seismic hazard, *Geophys. Res. Lett.*, 36, L17312.
- [30] Acocella, V., Neri, M. (2003) What makes flank eruptions? The 2001 Etna eruption and its possible triggering mechanism. *Bulletin of Volcanology - BULL VOLCANOL* , vol. 65, no. 7, pp. 517-529, 2003.
- [31] Coltelli, M., C. Proietti, S. Branca, M. Marsella, D. Andronico, and L. Lodato (2007), Analysis of the 2001 lava flow eruption of Mt. Etna from three-dimensional mapping, *J. Geophys. Res.*, 112, F02029.
- [32] Tsai F. Et al, 'Post-disaster assessment of landslides in southern Taiwan after 2009 Typhoon Morakot using remote sensing and spatial analysis'. *Nat. Hazards Earth Syst.* 10, 2179-2190.
- [33] Casagli N. et al. (2010) Monitoring, prediction, and early warning using ground-based radar interferometry. *Landslides*, Vol. 7, Issue 3, pp.291-301, May 2010.

- [34] Motagh, M., T. R. Walter, M. A. Sharifi, E. Fielding, and A. J. Schenk (2008), Land subsidence in Iran caused by widespread water reservoir overexploitation, *Geophys. Res. Lett.*, 35, L16403.
- [35] Tomiyasu, K.; , "Synthetic aperture radar in geosynchronous orbit," Antennas and Propagation Society International Symposium, 1978 , vol.16, pp. 42-45, May 1978
- [36] Tomiyasu, K.; Pacelli, Jean L., "Synthetic Aperture Radar Imaging from an Inclined Geosynchronous Orbit," *Geoscience and Remote Sensing, IEEE Transactions on* , vol.GE-21, no.3, pp.324-329, July 1983.
- [37] S.N. Madsen et al, 'A Geosynchronous Synthetic Aperture Radar for Tectonic Mapping, Disaster Management and Measurements of Vegetation and Soil Moisture', Jet Propulsion Laboratory, Geoscience and Remote Sensing Symposium, 2001. IGARSS '01.
- [38] Ze Yu ; Jie Chen ; Chunsheng Li ; Zhuo Li ; Yan Zhang; Concepts, properties, and imaging technologies for GEO SAR. Proc. SPIE 7494, MIPPR 2009: Multispectral Image Acquisition and Processing, 749407 (October 30, 2009).
- [39] Yang, Wenfu; Zhu, Yu; Liu, Feifeng; Hu, Cheng; Ding, Zegang; , "Modified Range Migration Algorithm in GEO SAR system," 2010 8th European Conference on Synthetic Aperture Radar (EUSAR), , pp.1-4, 7-10 June 2010.
- [40] Leilei Kou; Xiaoqing Wang; Jinsong Chong; Maosheng Xiang; , "Research on interferometric deformation detection for geosynchronous SAR," Geoscience and Remote Sensing Symposium (IGARSS), 2010 IEEE International., pp.3502-3505, 25-30 July 2010.
- [41] Teng Long; Xichao Dong; Cheng Hu; Tao Zeng; , "A New Method of Zero-Doppler Centroid Control in GEO SAR," Geoscience and Remote Sensing Letters, IEEE , vol.8, no.3, pp.512-516, May 2011.
- [42] Cheng Hu; Teng Long; Tao Zeng; Feifeng Liu; Zhipeng Liu; , "The Accurate Focusing and Resolution Analysis Method in Geosynchronous SAR," Geoscience and Remote Sensing, IEEE Transactions on , vol.49, no.10, pp.3548-3563, Oct. 2011
- [43] Yangte Gao; Cheng Hu; Xichao Dong; Long, Teng; , "Accurate system parameter calculation and coverage analysis in GEO SAR," Synthetic Aperture Radar, 2012. EUSAR. 9th European Conference on , pp.607-610, 23-26 April 2012
- [44] Cheng Hu; Zhipeng Liu; Teng Long; , "An Improved CS Algorithm Based on the Curved Trajectory in Geosynchronous SAR," Selected Topics in Applied Earth Observations and Remote Sensing, IEEE Journal of , vol.5, no.3, pp.795-808, June 2012

- [45] Leilei Kou; Xiaoqing Wang; Jinsong Chong; Maosheng Xiang; , "Research on interferometric deformation detection for geosynchronous SAR," Geoscience and Remote Sensing Symposium (IGARSS), 2010 IEEE International , vol., no., pp.3502-3505, 25-30 July 2010
- [46] Liu Qi; Wei-xian Tan; Yun Lin; Yan-ping Wang; Wen Hong; Yi-rong Wu; , "SAR raw data 2-D imaging model and simulation of GEOCSAR," Radar (Radar), 2011 IEEE CIE International Conference on , vol.1, pp.833-836, 24-27 Oct. 2011
- [47] Leilei Kou; Xiaoqing Wang; Maosheng Xiang; Minhui Zhu; , "Interferometric Estimation of Three-Dimensional Surface Deformation using Geosynchronous Circular SAR," Aerospace and Electronic Systems, IEEE Transactions on , vol.48, no.2, pp.1619-1635, April 2012.
- [48] Ruiz Rodon, J., González, A., Broquetas, A., Monti Guarnieri, A., Carcano, L., Fideli, G., Rocca, F., "Feasibility of geosynchronous satellite for Synthetic Aperture Radar Remote Sensing at Ka-Band", 16th Ka and Broadband Communications, Navigation and Earth Observation Conference, October 2010.
- [49] Prati, C., Rocca, F., Giancola, D. and Monti, A. 'Passive Geosynchronous SAR System Reusing Backscattered Digital Audio Broadcasting Signals'. IEEE Transactions on Geoscience and Remote Sensing, Vol. 36, No. 6, November 1998.
- [50] Cazzani, L. et al, 'A Ground-Based Parasitic SAR Experiment', IEEE Transactions on Geoscience and Remote Sensing, Vol. 38, No. 5, September 2000.
- [51] M. Bonomelli and F. Potra, 'Studio di un sistema SAR geostazionario passivo', Tesi Laurea Ing. Elett., Politec. Milano, Milano, Italy, 1994.
- [52] D. Giancola and G. Quario, 'Studio di fattibilità di un sistema SAR geostazionario', Tesi Laurea Ing. Elett., Politec. Milano, Milano, Italy, 1995.
- [53] Tian, Weiming; Hu, Chen; Zeng, Tao; Ding, Zegang; , "Several Special Issues in GEO SAR system," 8th European Conference on Synthetic Aperture Radar (EUSAR), 2010 , pp.1-4, 7-10 June 2010
- [54] Teng Long; Xichao Dong; Cheng Hu; Tao Zeng; , "A New Method of Zero-Doppler Centroid Control in GEO SAR," Geoscience and Remote Sensing Letters, IEEE , vol.8, no.3, pp.512-516, May 2011.
- [55] Feifeng Liu; Cheng Hu; Tao Zeng; Teng Long; Lihua Jin; , "A novel range migration algorithm of GEO SAR echo data," Geoscience and Remote Sensing Symposium (IGARSS), 2010 IEEE International , pp.4656-4659, 25-30 July 2010.
- [56] Leilei Kou; Xiaoqing Wang; Jinsong Chong; Maosheng Xiang; , "Research on interferometric deformation detection for geosynchronous SAR," Geoscience and

- Remote Sensing Symposium (IGARSS), 2010 IEEE International , pp.3502-3505, 25-30 July 2010.
- [57] Dong, Xichao; Ding, Zegang; Zhao, Zhiwei; , "A method of zero Doppler centroid control in GEO SAR," Synthetic Aperture Radar (EUSAR), 2010 8th European Conference on , pp.1-4, 7-10 June 2010.
- [58] Zhipeng Liu; Di Yao; Teng Long; , "An accurate focusing method in GEO SAR," Radar Conference (RADAR), 2011 IEEE , pp.237-241, 23-27 May 2011.
- [59] Li, Zhuo; Li, Chunsheng; Yu, Ze; Zhou, Jian; Chen, Jie; , "Back projection algorithm for high resolution GEO-SAR image formation," Geoscience and Remote Sensing Symposium (IGARSS), 2011 IEEE International , pp.336-339, 24-29 July 2011.
- [60] Zhipeng Liu; Cheng Hu; Tao Zeng; , "Improved Secondary Range Compression focusing method in GEO SAR," Acoustics, Speech and Signal Processing (ICASSP), 2011 IEEE International Conference on , pp.1373-1376, 22-27 May 2011.
- [61] Yang, Wenfu; Zhu, Yu; Liu, Feifeng; Hu, Cheng; Ding, Zegang; , "Modified Range Migration Algorithm in GEO SAR system," Synthetic Aperture Radar (EUSAR), 2010 8th European Conference on , pp.1-4, 7-10 June 2010.
- [62] Cheng Hu; Feifeng Liu; Wenfu Yang; Tao Zeng; Teng Long; , "Modification of slant range model and imaging processing in GEO SAR," Geoscience and Remote Sensing Symposium (IGARSS), 2010 IEEE International , pp.4679-4682, 25-30 July 2010.
- [63] Cheng Hu; Teng Long; Tao Zeng; Feifeng Liu; Zhipeng Liu; , "The Accurate Focusing and Resolution Analysis Method in Geosynchronous SAR," Geoscience and Remote Sensing, IEEE Transactions on , vol.49, no.10, pp.3548-3563, Oct. 2011.
- [64] M. Capderou, 'Satellites. Orbits and missions', Chapter 2.3 Orbital Elements pp. 51-55, 148-149, Springer, 2005.
- [65] G. Maral and M. Bousquet, 'Satellite Communications Systems. Systems, Techniques and Technology', Wiley, Fourth Edition 2002.
- [66] J.B. Tatum, 'Physics topics. Celestial Mechanics', Chapter 3: Plane and Spherical Trigonometry, Electronic Source.
- [67] Technical report, 'WGS84 implementation manual'K, prepared by EUROCONTROL and IfEN, Version 2.4, February 1998.
- [68] Constantine A. Balanis, 'Antenna Theory: Analysis and Design', Wiley-Interscience, 2005.
- [69] Cardama, A., Jofre, Ll., Rius, J.M., Romeu, J., Blanch, S., Ferrando, M.; 'Antenas', Edicions UPC, 2005.

- [70] Orfanidis, S.J., 'Electromagnetic Waves and Antennas', Rutgers University, 2002.
- [71] Knott, Eugene F., Shaeffer, John F., Tuley, Michael T., 'Radar Cross Section (2nd Edition)', pp. 7-20, SciTech Publishing, 2004
- [72] Bracewell, R., 'The Fourier Transform & Its Applications', McGraw-Hill electric and electronic engineering series, 3rd Edition, 1999.
- [73] Refice, A.; Bovenga, F.; Stramaglia, S.; Conte, D.; , "Use of scaling information for stochastic atmospheric absolute phase screen retrieval", Geoscience and Remote Sensing Symposium, 2002. IGARSS '02. 2002 IEEE International , vol.3, pp. 1729-1731 vol.3, 24-28 June 2002
- [74] Cuozzo, G.; di Bisceglie, M.; Fusco, A.; , "The role of spatial interactions for prediction of the spectral structure of the atmospheric phase screen," Geoscience and Remote Sensing Symposium, 2007. IGARSS 2007. IEEE International , pp.1287-1290, 23-28 July 2007
- [75] Even, Markus; Schunert, Alexander; Schulz, Karsten; Soergel, Uwe; , "Atmospheric phase screen-estimation for PSInSAR applied to TerraSAR-X high resolution spotlight-data," Geoscience and Remote Sensing Symposium (IGARSS), 2010 IEEE International , pp.2928-2931, 25-30 July 2010
- [76] Iannini, L.; Guarnieri, AM., "Atmospheric Phase Screen in Ground-Based Radar: Statistics and Compensation," *Geoscience and Remote Sensing Letters, IEEE* , vol.8, no.3, pp.537,541, May 2011.
- [77] Morello, A.; Mignone, V., "DVB-S2: The Second Generation Standard for Satellite Broad-Band Services," *Proceedings of the IEEE* , vol.94, no.1, pp.210-227, Jan. 2006.
- [78] Hector Henech, Alessia Tomatis, Emmanuel Lance, Maria Kalama, 'Next Generation High Rate Broadband Satellites', 16th Ka and Broadband Communications, Navigation and Earth Observation Conference, October 20-22, 2010, Milan, Italy.
- [79] Dietmar Schmitt, Michael Harverson, 'Challenges in the implementation of Multi-Beam Payload Systems', ESA/ESTEC
- [80] Giuliano Berreta, 'Ka Band Applications and Services from Dream to Reality: the KaSAT Program', 16th Ka and Broadband Communications, Navigation and Earth Observation Conference, October 20-22, 2010, Milan, Italy.
- [81] J.B. Billingsley, 'Low Angle Radar Land Clutter: Measurements and Empirical Models', William Andrew publishing, 2002.
- [82] J.B. Billingsley, 'Exponential decay in windblown radar ground clutter Doppler spectra: multifrequency measurements and model', Technical Report 997, MIT Lincoln

Laboratory, Lexington, MA, July 19, 1996.

- [83] P. Lombardo and J.B. Billingsley, 'A new model for the Doppler spectrum of windblown radar ground clutter', Proceedings of the 1999 IEEE Radar Conference, Waltham, MA, April 20-22, 1999.
- [84] Curlander, J.C. and McDonough, R.N., 'Synthetic Aperture Radar: Systems and Signal Processing', Chapter 3: The matched filter and pulse compression, New York, 1991.
- [85] Ding, Yu; Munson, D.C., Jr., "A fast back-projection algorithm for bistatic SAR imaging," *Image Processing. 2002. Proceedings. 2002 International Conference on*, vol.2, no., pp.II-449-452 vol.2, 2002.
- [86] Xiao, S.; Munson, D.C., Jr.; Basu, S.; Bresler, Y., "An $N^2 \log N$ back-projection algorithm for SAR image formation," *Signals, Systems and Computers, 2000. Conference Record of the Thirty-Fourth Asilomar Conference on*, vol.1, no., pp.3-7 vol.1, Oct. 29 2000-Nov. 1 2000.
- [87] Michel Capderou, 'Satellites. Orbits and missions', Springer, Edition 2005.
- [88] Peret Fortescue, John Stark and Graham Swinerd, 'Spacecraft systems engineering', Wiley, Third edition 2003.
- [89] Madsen, S. N., and Zebker, H. A. 'Imaging radar interferometry. Principles & Applications of Imaging Radar' (Manual of Remote Sensing (3rd ed.), vol. 2), New York: Wiley, 1998.
- [90] Rosen, P.A; Hensley, S.; Joughin, IR.; Fuk K.Li; Madsen, S.N.; Rodriguez, E.; Goldstein, Richard M., "Synthetic aperture radar interferometry," *Proceedings of the IEEE*, vol.88, no.3, pp.333-382, March 2000.
- [91] Gens, R., and Vangenderen, J. L., 'SAR interferometry—Issues, techniques, applications'. International Journal of Remote Sensing, 17, 10 (1996), 1803—1835.
- [92] Massonnet, D., and K. L. Feigl, 'Radar interferometry and its application to changes in the Earth's surface', Rev. Geophys., 36(4), 441–500, 1998.
- [93] Hagberg, J.O.; Ulander, L.M.H.; Askne, J., "Repeat-pass SAR interferometry over forested terrain," Geoscience and Remote Sensing, IEEE Transactions on , vol.33, no.2, pp.331-340, Mar 1995.
- [94] Perissin, D.; Teng Wang, "Repeat-Pass SAR Interferometry With Partially Coherent Targets," Geoscience and Remote Sensing, IEEE Transactions on , vol.50, no.1, pp.271-280, Jan. 2012.
- [95] Zebker, H.A.; Villasenor, J., "Decorrelation in interferometric radar echoes," Geoscience and Remote Sensing, IEEE Transactions on , vol.30, no.5, pp.950-959, Sep 1992.

- [96] Prati, C., Rocca, F., Monti Guarnieri, A., and Damonti, E., Seismic migration for SAR focusing: Interferometrical applications, *IEEE Trans. Geosci. Remote Sens.*, vol. 28, pp. 627-640, July 1990.
- [97] Gatelli, F.; Guarnieri, AM.; Parizzi, F.; Pasquali, P.; Prati, C.; Rocca, F., "The wavenumber shift in SAR interferometry," *Geoscience and Remote Sensing, IEEE Transactions on* , vol.32, no.4, pp.855,865, Jul 1994.
- [98] Tatnall, A. R. L., Farrow, J. B., Bandecchi, M. and Francis, C. R. Spacecraft System Engineering, in *Spacecraft Systems Engineering*, Third Edition, John Wiley & Sons, Ltd, Chichester, UK, 2003.
- [99] Guarnieri, AM.; Tebaldini, S.; Rocca, F.; Broquetas, A, "GEMINI: Geosynchronous SAR for Earth Monitoring by Interferometry and Imaging," *Geoscience and Remote Sensing Symposium (IGARSS), 2012 IEEE International* , vol., no., pp.210,213, 22-27 July 2012.
- [100] C.S. Carrano, K.M. Groves, and R.G. Caton, "Simulating the impacts of ionospheric scintillation on L band SAR image formation," *Radio Science*, vol. 47, p. RS0L20, 2012.
- [101] Chapin, E.; Chan, S.F.; Chapman, B.D.; Chen, C.W.; Martin, J.M.; Michel, T.R.; Muellerschoen, R.J.; Xiaoqing Pi; Rosen, P.A, "Impact of the ionosphere on an L-band space based radar," *Radar, 2006 IEEE Conference on* , pp.8, 24-27 April 2006.
- [102] Nicoll, J.; Meyer, F.; Jehle, M., "Prediction and detection of Faraday rotation in ALOS PALSAR data," *Geoscience and Remote Sensing Symposium, 2007. IGARSS 2007. IEEE International* , pp.5210-5213, 23-28 July 2007.
- [103] Roth, AP.; Huxtable, B.D.; Chotoo, K.; Chotoo, S.D., "Simulating and mitigating ionospheric effects in synthetic aperture radar," *Geoscience and Remote Sensing Symposium (IGARSS), 2010 IEEE International* , pp.2892-2895, 25-30 July 2010.
- [104] N. Jakowski, S. Heise, A. Wehrenpfennig, S. Schlüter, "TEC monitoring by GPS: a possible contribution to space weather monitoring", *Physics and Chemistry of the Earth, Part C: Solar, Terrestrial & Planetary Science*, Volume 26, Issue 8, pp. 609-613, 2001.
- [105] Lin Wu, Ignasi Corbella, Francesc Torres, Nuria Duffo, Manuel Martín-Neira. "Faraday Rotation Angle Retrieval Using SMOS Radiometric Data", 13th Specialist Meeting on Microwave Radiometry and Remote Sensing of the Environment (MicroRad 2014), Pasadena CA (USA) 24-27 March 2014.
- [106] M. Aquino, A. Dodson, J. Souter, T. Moore, "Ionospheric Scintillation Effects on GPS Carrier Phase Positioning Accuracy at Auroral and Sub-auroral Latitudes',

Monitoring and Understanding a Dynamic Planet with Geodetic and Oceanographic Tools IAG Symposium Cairns, Australia 22–26 August, 2005, Part VIII, pp. 859-866, 2007.

- [107] Meyer, Franz J., "Quantifying Ionosphere-Induced Image Distortions in L-band SAR Data Using the Ionospheric Scintillation Model WBMOD," *EUSAR 2014; 10th European Conference on Synthetic Aperture Radar; Proceedings of*, vol., no., pp.1,4, 3-5 June 2014.
- [108] Bagiya, Mala S., Joshi, H. P., Iyer, K. N., Aggarwal, M., Ravindran, S., and Pathan, B. M.: TEC variations during low solar activity period (2005–2007) near the Equatorial Ionospheric Anomaly Crest region in India, *Ann. Geophys.*, 27, 1047-1057, doi:10.5194/angeo-27-1047-2009, 2009.
- [109] Kalpana Patel, A. K. Singh, R. P. Patel and R. P. Singh, "Ionospheric scintillations by sporadic-E irregularities over low latitude", *Bull. Astr. Soc. India* (2007) 35, 625-630, December, 2007.
- [110] A. Rucci, A. Ferretti, A. Monti Guarnieri, F. Rocca, 'Sentinel 1 SAR interferometry applications: the outlook for sub-millimeter measurements', *Remote Sensing of Environment*, Volume 120, pages 156-163, 15 May 2012.
- [111] Sabater, J.M.; Hanssen, R.; Kampes, B.M.; Fusco, A.; Adam, N.; , "Physical analysis of atmospheric delay signal observed in stacked radar interferometric data," *Geoscience and Remote Sensing Symposium*, 2003. IGARSS '03. Proceedings. 2003 IEEE International , vol.3, no., pp.2112- 2115, 21-25 July 2003.
- [112] Tebaldini, Stefano; Guarnieri, Andrea Monti; Rocca, Fabio; , "Recovering time and space varying phase screens through SAR multi-squint differential interferometry," *Synthetic Aperture Radar*, 2012. EUSAR. 9th European Conference on, pp.16-19, 23-26 April 2012
- [113] Pipia, L.; Aguasca, A.; Fabregas, X.; Mallorqui, J.J.; Lopez-Martinez, C.; 'Temporal decorrelation in polarimetric differential interferometry using a ground-based SAR sensor' *Geoscience and Remote Sensing Symposium*, 2005. IGARSS '05. Proceedings. 2005 IEEE International , vol.6, pp. 4108- 4111, 25-29 July 2005
- [114] Smith, Jr., E.K. and Weintraub, S., 'The Constants in the Equation for Atmospheric Refractive Index at Radio Frequencies', *Proceedings of the I.R.E.*, pp. 1035-1037, 1952
- [115] Thayer, G.D., 'An improved Equation for the Radio Refractive Index of Air', *Tadio Science*, 9: 803-807, 1974.
- [116] Davies, J.L., Herring, T.A., Shapiro, I.I., Rogers, A.E.E. and Elgered, G., 'Geodesy

- by radio interferometry: Effects of atmospheric modeling errors on estimates of baseline length', *Radio Science*, 1985.
- [117] Solheim, F.S. Vivekanandan, J., Ware, R.H. and Rocken, C., 'Propagation delays induced in GPS signal by dry air, water vapor, hydrometeors and other particulates', *Journal of Geophysical Research*, 104, 9663-9670, 1999.
- [118] Iannini, L.; Guarnieri, A.M., "Atmospheric Phase Screen in Ground-Based Radar: Statistics and Compensation," *Geoscience and Remote Sensing Letters*, IEEE , vol.8, no.3, pp.537-541, May 2011.
- [119] S. Sukumar, 'Ionospheric Refraction Effects on Radio Interferometer Phase', *J. Astrophysics Astronomy* (1987) vol.8, pp.281-294.
- [120] Atlas, D., Naito, K. and Carbone, R.E., 'Bistatic microwave probing of a refractively perturbed clear atmosphere', *J. Atmospheric Sciences*, vol.25, pp.257-68, 1968.
- [121] Ting Lei, Tao Zeng, Cheng Hu, "Effect of time and frequency synchronization errors on Bistatic SAR image formation", *Beijing Institute of Technology*, 2006.
- [122] Wang, W.Q.; Ding, C.B.; Liang, X.D., "Time and phase synchronisation via direct-path signal for bistatic synthetic aperture radar systems," *Radar, Sonar & Navigation*, IET , vol.2, no.1, pp.1-11, February 2008
- [123] Krieger, G.; Younis, M., "Impact of oscillator noise in bistatic and multistatic SAR," *Geoscience and Remote Sensing Letters*, IEEE , vol.3, no.3, pp.424-429, July 2006.
- [124] Younis, M.; Metzger, R.; Krieger, G., "Performance prediction of a phase synchronization link for bistatic SAR," *Geoscience and Remote Sensing Letters*, IEEE , vol.3, no.3, pp.429-433, July 2006
- [125] Weinerbach, U. Schön S., "Improved GPS receiver clock modeling for kinematic orbit determination of the GRACE satellites" *European Frequency and Time Forum (EFTF)*, 2012.
- [126] Freeman, A.; Shen, Y.; Werner, C.L., "Polarimetric SAR calibration experiment using active radar calibrators," *Geoscience and Remote Sensing*, IEEE Transactions on , vol.28, no.2, pp.224-240, Mar 1990
- [127] Dobson, M.C.; Pierce, L.; Sarabandi, K.; Ulaby, F.T.; Sharik, T., "Preliminary analysis of ERS-1 SAR for forest ecosystem studies," *Geoscience and Remote Sensing*, IEEE Transactions on , vol.30, no.2, pp.203-211, Mar 1992
- [128] Schena, V. D.; Posa, F.; Ponte, S.; De Carolis, G., "Development and performance validation of L-, C- and X-band active radar calibrators (ARC) by means of laboratory

- tests and SIR-C/X-SAR experiments," Geoscience and Remote Sensing Symposium, 1995. IGARSS '95. 'Quantitative Remote Sensing for Science and Applications', International , vol.1, pp.80-82 vol.1, 10-14 Jul1995
- [129] Gerhard Krieger and Marwan Younis, Impact of Oscillator Noise in Bistatic and Multistatic SAR. IEEE Geoscience and Remote Sens. Letters, Vol. 3, No. 3, pp.424-429, June 2006.
- [130] Monti Guarnieri, Andrea; Broquetas, Antoni; Ruiz-Rodon, Josep; Recchia, Andrea; Giudici, Davide; Schulz, Detlef; Venturini, Roberto; "Wide coverage, fine resolution, geosynchronous SAR for atmosphere and terrain observation", ESA Living Planet Symposium, Edimburg, September 2013.
- [131] Dach, R.; Hugentobler, U.; Fridez, P.; Meindl M. (Eds.) ; "Bernese GPS Software v.5.0", Astronomical Institute, Univ. of Bern, 2007.
- [132] Lorga, J.F.M. ; Silva, P.F. ; Dovis, F. ; Di Cintio, A. ; Kowaltschek, S. ; Jimenez, D. ; Jansson, R., "Autonomous orbit determination for future GEO and HEO missions", 2010 5th ESA Workshop on Satellite Navigation Technologies and European Workshop on GNSS Signals and Signal Processing (NAVITEC), Digital Object Identifier: 10.1109/NAVITEC.2010.5708028, Publication Year: 2010 , Page(s): 1 - 14
- [133] Doviak, R.J., Goldhirsh, J. and Miller, A.R., 'Bistatic radar detection of high altitude clear air atmospheric targets,' Radio Science, Vol. 7, pp. 993–1003, 1972.
- [134] Friedlander, B. and Porat, B., 'VSAR: a high resolution radar system for ocean imaging', IEEE Trans., AES-34 (3), pp. 755–71, 1978.
- [135] Pileih Chen; Beard, J.K., "Bistatic GMTI experiment for airborne platforms," *Radar Conference, 2000. The Record of the IEEE 2000 International* , vol., no., pp.42-46, 2000.
- [136] Krieger, G.; Moreira, A.; Fiedler, H.; Hajnsek, I.; Werner, M.; Younis, M.; Zink, M., "TanDEM-X: A Satellite Formation for High-Resolution SAR Interferometry," Geoscience and Remote Sensing, IEEE Transactions on , vol.45, no.11, pp.3317-3341, Nov. 2007.
- [137] K. B. Khadhra, T. Boerner, D. Hounam, and M. Chandra, "Surface parameter estimation using bistatic polarimetric x-band measurements," Progress In Electromagnetics Research B, Vol. 39, pp. 197-223, 2012.
- [138] Duque, S.; Lopez-Dekker, P.; Merlano, J.C.; Mallorqui, J.J., "Bistatic SAR tomography: Processing and experimental results," Geoscience and Remote Sensing Symposium (IGARSS), 2010 IEEE International , pp.154-157, 25-30 July 2010.
- [139] Larson, R.; Maffett, A.L.; Heimiller, R. C.; Fromm, A.; Johansen, E.L.; Rawson, R.;

- Smith, F., "Bistatic clutter measurements," *Antennas and Propagation, IEEE Transactions on*, vol.26, no.6, pp.801-804, Nov 1978
- [140] Ulaby, F.T.; Van Deventer, T.E.; East, J.R.; Haddock, T.F.; Coluzzi, M.E., "Millimeter-wave bistatic scattering from ground and vegetation targets," *Geoscience and Remote Sensing, IEEE Transactions on*, vol.26, no.3, pp.229-243, May 1988.
- [141] Nashashibi, A.Y.; Ulaby, F.T., "MMW Polarimetric Radar Bistatic Scattering From a Random Surface," *Geoscience and Remote Sensing, IEEE Transactions on*, vol.45, no.6, pp.1743-1755, June 2007
- [142] Mudaliar, S., "Bistatic radar clutter simulations using scattering phenomenology," *Radar, 2006 IEEE Conference on*, pp.8, 24-27 April 2006.
- [143] Gustafsson, M.; Herberthson, M.; Rahm, J.; Zdansky, E.; Orbom, A., "A New Methodology for Measuring the Bistatic Ground Scattering Coefficient. Comparisons With the AIEM at Large Bistatic Angles," *Geoscience and Remote Sensing Letters, IEEE*, vol.10, no.5, pp.1167-1170, Sept. 2013
- [144] Skolnik, M., 'Radar handbook. Chapter 25: Bistatic Radar', McGraw-Hill Professional, 2008.
- [145] Loffeld, O.; Nies, H.; Peters, V.; Knedlik, S., "Models and useful relations for bistatic SAR processing," *Geoscience and Remote Sensing, IEEE Transactions on*, vol.42, no.10, pp.2031-2038, Oct. 2004
- [146] Charles V. Jakowats Jr., Daniel E. Wahl, Paul H. Eichel, Dennis C. Ghiglia, Paul A. Thompson, 'Spotlight mode Synthetic Aperture Radar: A signal processing approach' Springer Science+Business Media LLC, 1996.
- [147] Andrea Monti Guarnieri, Luca Perletta, Fabio Rocca, Diego Scapin, Stefano Tebaldini, Antoni Broquetas, Josep Ruiz, 'Design of a geosynchronous SAR system for water-vapor maps and deformation estimation', in *proc FRINGE 2011* (Frascati, Italy), pp 1-5, September 2011.
- [148] W. Marshall Leach, Jr., 'Ideal Op Amp Circuits', Georgia Tech, College of Engineering. Review report.